

Polycyclic Aromatic Hydrocarbon Chemistry
in a Spirit of
Graphene Engineering

Dissertation
zur Erlangung des Grades
“Doktor der Naturwissenschaften”

am Fachbereich Chemie, Pharmazie und Geowissenschaften
der Johannes Gutenberg-Universität Mainz
und in Kooperation mit
dem Max-Planck-Institut für Polymerforschung Mainz

(Ian) Cheng-Yi Hou / 侯正一

geb. in München, Deutschland

Mainz, 2020

1. Betrichterstatter:
2. Betrichterstatter:

Tag der mündlichen Prüfung: 02.09.2020

Die vorliegende Arbeit wurde in der Zeit von Juli 2015 bis März 2020 im Max-Planck-Institut für Polymerforschung in Mainz unter der Betreuung von Prof. Dr. [REDACTED] durchgeführt.

Ich danke Prof. Dr. [REDACTED] für seine wissenschaftliche und persönliche Unterstützung sowie für seine ständige Diskussionsbereitschaft.

To my wife
To Hong Kong and Taiwan
To Freedom

Table of Contents

Abbreviations	4
CHAPTER 1. INTRODUCTION	7
1.1 From an sp ² -carbon to graphene	7
1.1.1 Polycyclic aromatic hydrocarbons	8
1.1.2 Graphene	10
1.2 Quantization of graphene	14
1.2.1 Top-down graphene quantization	14
1.2.2 Bottom-up synthesis of nanographenes on monocrystalline surface	16
1.2.3 Organic synthetic strategy for large nanographenes	17
1.2.4 Organic synthesis of large monodispersed graphene quantum dots	23
1.2.5 Organic synthesis of wide graphene nanoribbons	25
1.3 Defects in graphene and their model compounds	31
1.3.1 Types of defects in graphene	31
1.3.2 Relationship between organic compounds and graphene defects	35
1.3.3 Molecular models representing point defects in graphene	37
1.3.4 Molecular models related to topological non-trivial defects in graphene	41
1.4 Controlling assemblies of nanographenes	47
1.4.1 Controlling 3D supramolecular assemblies of nanographenes	47
1.4.2 Controlling supramolecular assemblies of nanographenes at interfaces	50
1.5 Motivation	54
1.5.1 Synthesis of polyphenylenes as potential precursors for nanographenes approaching length scale of 5 nm	54
1.5.2 Bottom-up approach for nanostructures related to graphene grain boundaries	56
1.5.3 Exploring self-assemblies of hexa- <i>peri</i> -hexabenzocoronene derivatives	58
1.6 References	60
CHAPTER 2. SYNTHESIS OF DENDRITIC POLYPHENYLENES POSSESSING 366 AND 546 CARBONS AS POTENTIAL PRECURSORS FOR GIANT D_{6H}-SYMMETRIC NANOGRAPHENES	72
2.1 Main text	72
2.2 Supporting information	80
2.3 References	97
CHAPTER 3. STEPWISE LATERAL EXTENSION OF PHENYL SUBSTITUTED LINEAR POLYPHENYLENES	99
3.1 Abstract	99
3.2 Introduction	101

3.3 Result and Discussion	104
3.4 Conclusion	113
3.5 Experimental Section.....	114
3.6 Supporting information	123
3.7 References.....	138
 CHAPTER 4. ON-SURFACE SYNTHESIS OF POLYAZULENE WITH 2,6- CONNECTIVITY	140
4.1 Abstract	140
4.2 Main text.....	141
4.3 Supporting information	148
4.4 References	152
 CHAPTER 5. ON-SURFACE SYNTHESIS OF SP²-CARBON-NANOSTRUCTURE WITH A SKELETON OF REGULARLY FUSED ALTERNATING PENTAGONS AND HEPTAGONS.....	154
5.1 Main text.....	154
5.2 Supporting information	159
5.3 References	164
 CHAPTER 6. PHOTO-MODULATION OF 2D-SELF-ASSEMBLY OF AZOBENZENE-HEXA-PERI-HEXABENZOCORONENE-AZOBENZENE TRIADS	167
6.1 Abstract	167
6.2 Introduction.....	169
6.3 Result and discussion.....	171
6.4 Conclusion	177
6.5 Experimental methods.....	178
6.6 Supporting information	181
6.7 References.....	191
 CHAPTER 7. HEXA-PERI-HEXABENZOCORONENE WITH DIFFERENT ACCEPTOR UNITS FOR TUNING OPTOELECTRONIC PROPERTIES.....	194

7.1 Abstract	194
7.2 Main text.....	195
7.3 Supporting information	203
7.4 References.....	223
CHAPTER 8. CHEMISORPTION OF ATOMICALLY PRECISE 42-CARBON GRAPHENE QUANTUM DOTS ON METAL OXIDE FILMS GREATLY ACCELERATES INTERFACIAL ELECTRON TRANSFER	226
8.1 Abstract	226
8.2 Main Text.....	228
8.3 Supporting information	236
8.4 References.....	246
CHAPTER 9. SUMMARY AND OUTLOOK	249
9.1 Synthesis of large-sized Polyphenylenes.....	250
9.2 Synthesis of Sp ² -carbon-nanostructures with multiple heptagon-pentagon-pairs	252
9.3 Stimuli responsive self-assembly of nanographenes.....	254
9.4 References.....	256
ACKNOWLEDGEMENT.....	257

Abbreviations

2D WAXS	2D wide-angle X-ray scattering
nc-AFM	Non-contact atomic force microscopy
AGNR	Armchair graphene nanoribbon
AR	Aspect ratio
APT	Attached proton test
AQ	9,10-Anthraquinone
ATR	Attenuated total reflection
BE	Binding energy
CB	Conduction band
CNTs	Carbon nanotubes
CP	Tetraphenylcyclopenta-2,4-dien-1-one
CT	Charge transfer
CV	Cyclic voltammetry
CVD	Chemical vapor deposition
D-A	Diels-Alder
DCM	Dichloromethane
DCB	1,2-Dichlorobenzene
DCTB	<i>Trans</i> -2-[3-(4- <i>tert</i> -Butylphenyl)-2-methyl-2-propenylidene]malononitrile
DFT	Density functional theory
DLC	Discotic liquid crystalline
DMSO	Dimethylsulfoxide
DMF	<i>N,N</i> -dimethylformaldehyde
DOSY	¹ H NMR diffusion ordered spectroscopy
DS	Drude-Smith
DSC	Differential scanning calorimetry
DV	Double vacancies
E_{ads}	Adsorption energy
EBL	Electron-beam lithography
ET	Electron transfer
FET	Field-effect transistor
GB	Grain boundaries
GPC	Gel permeation chromatography
GO	Graphene oxide

rGO	Reduced graphene oxide
GNR	Graphene nanoribbon
GQD	Graphene quantum dot
HBC	Hexa- <i>peri</i> -hexabenzocoronene
HOMO	Highest occupied molecular orbitals
HOPG	Highly oriented pyrolytic graphite
HPB	Hexaphenylbenzene
HRMS	High-resolution mass spectra
I_{on}/I_{off}	On/off electric current ratio
LDOS	Local density of states
LUMO	Lowest unoccupied molecular orbitals
M_n	Number-average molecular weight
M_w	Weight-average molecular weight
MALDI	Matrix-assisted laser desorption ionization
MM/MD	Molecular mechanics/molecular dynamics
NG	Nanographene
NMI	Naphthalene monoimide
NVT	Constant numbers of particles, volume and temperature
i-NW	Inorganic nanowires
OFET	Organic field-effect transistors
OLED	Organic light emitting diodes
OLCD	Organic liquid crystal display
OLET	Organic light-emitting transistor
OPV	Organic photovoltaic cells
OPTP	Optical pump-terahertz probe
PAH	Polycyclic aromatic hydrocarbon
PBAH	All-benzenoid polycyclic aromatic hydrocarbon
PBC	Periodic boundary condition
PDI	Polydispersity index
PMI	perylene monoimide
PP	Polyphenylene
PPP	Poly(<i>p</i> -phenylene)
PSS	Photostationary state
R_H	Hydrodynamic radius

RFID	Radio-frequency identification
STM	Scanning tunneling microscopy
STS	Scanning tunneling spectroscopy
SI	Supporting information
SV	Single vacancy
SW	Stone-Wales
TBAF	Tetrabutylammonium fluoride
TBAOH	Tetrabutylammonium hydroxide
TCB	1,2,4-Trichlorobenzene
TCNQ	7,7,8,8-Tetracyanoquinodimethane
TEM	Transmission electron microscopy
TEA	Triethylamine
TGA	Thermogravimetry analysis
THF	Tetrahydrofuran
TIPS	Triisopropylsilyl
TLC	Thin layer chromatography
TMS	Trimethylsilyl
UHV	Ultra-high vacuum
UPS	Ultraviolet photoelectron spectroscopy
VB	Valence band
VBXPS	Valence band X-ray photoelectron spectroscopy

Chapter 1. Introduction

1.1 From an sp^2 -carbon to graphene

Carbon is the 15th most abundant element on earth and the 4th in the observable universe by mass. Magnificently, carbon is the basis of lives in our world. It is involved in a large diversity of substances that are stable at the earth's ambient temperature. Furthermore, in (nano)technology, carbon in different forms, such as carbon dots, graphite, (nano)graphene, (nano)diamond, carbon nanotubes (CNTs), fullerenes, and constituent for unlimited numbers of organic compounds, offer applications in electronics, sensing, medicine, and quantum computing, making carbon “the king of all elements”.¹

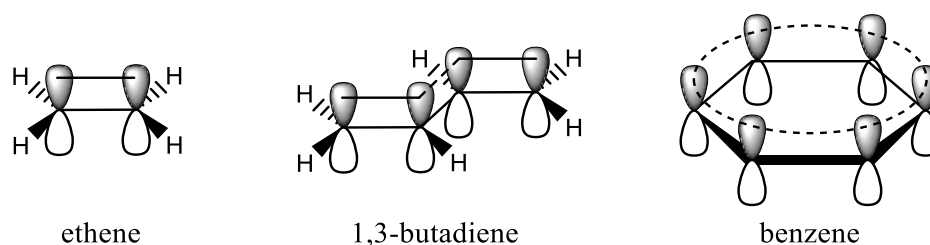


Figure 1.1 Schematic representation of electronic structure of simple sp^2 -carbon systems.

Carbon belongs to group 14, with a ground state electron configuration of $1s^2 2s^2 2p^2$, where the four outer electrons are valence electrons. This provides carbon with a high degree of freedom for covalent bonding. Theoretically, carbon has three kinds of orbital hybridizations in a covalent bond— sp , sp^2 and sp^3 , leading to linear, trigonal, and tetrahedral geometry. In reality, the orbital hybridization and bond angle depend on substitutions. In the sp^2 -hybridization, the three hybridized atomic orbitals stay in the same plane, leaving an intact orthogonal p -orbital. In molecules, the sp^2 -hybridized orbitals form σ -bonding framework, while the orthogonal p -orbitals build up additional π -bondings, leading to a planar geometry, such as the simple example ethene. Furthermore, larger systems arise from connecting more carbon atoms in a similar way. These systems are further stabilized by additional bonding interactions between neighboring π -bonds. In a special case, when $4n + 2$ sp^2 -carbons are linked in a cyclic, planar manner, the system becomes especially stable, and the π -electrons are fully delocalized. The most representative example is benzene, in which every C-C bond possess the same bond length, indicating the same bond-order in all the six bonds. These systems are described as possessing *aromaticity*.

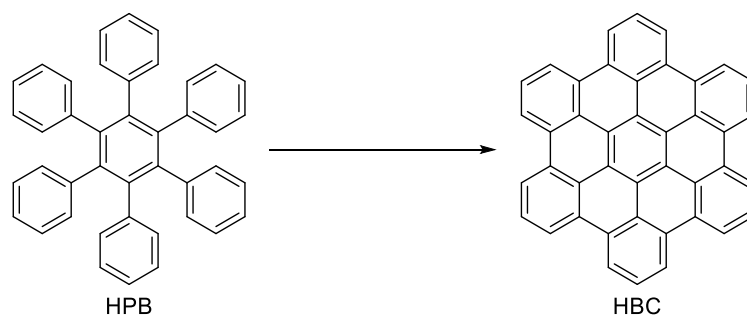
1.1.1 Polycyclic aromatic hydrocarbons

Large π -system composed of multiple fused aromatic rings are called polycyclic aromatic hydrocarbons (PAH). They are a step forward from benzene, but exist in an unlimited diversity. PAH-research has its self-evident importance, since PAHs occur in our environment. Specifically, small PAHs are formed through biosynthesis, and larger ones during combustion of fossil fuels.² The latter has been proven as the major source of PAHs identified in sediments in Massachusetts, USA.³ Besides, as a family of sp²-carbon conjugated system, PAHs have their historical importance in the development of molecular orbital theory.⁴ In addition, NASA suggested in 2014 that more than 20% of carbon by mass in our observable universe may be in form of PAH, and had been already existed in a young universe after the Big Bang.⁵ This implies that PAHs would be components in abiogenesis for formation of carbon-based life in our world. Nevertheless, medium-sized PAHs, such as benzo[a]pyrene, are verified as carcinogens. Metabolites of these PAHs can insert between DNA base pairs, which could then alter DNA sequence, and cause mutation during DNA transcription.⁶ In fact, PAH with more than four rings appear to be absent from biosynthesis.⁷ For this reason, a few decades of PAH-research has focused on their carcinogenic, toxicological, and environmental analysis.

Organic synthetic approaches toward PAHs were pioneered as early as 1910 by ██████████.⁸ and later on by ██████████.⁹ in the 1950s. It was however not until the 90s that organic synthesis of PAHs ushered in an explosive development,¹⁰ partially related to the thriving growth of organic electronics, including organic light emitting diodes (OLED), organic liquid crystal displays (OLCD), organic field-effect transistors (OFET), organic light-emitting transistors (OLET), organic photovoltaic cells (OPV), organic radio-frequency identification tags (RFID), and organic conductors.¹¹ Organic electronics utilize the high-lying π -orbitals of organic molecules as charge conducting channels. PAHs, with their large π -systems perpendicular to its σ -bonding framework, are suitable for this transport mechanism.

Organic synthesis provides an arsenal of tools that can fine-tune the core structure and substituents of PAHs. Core structure and substituents are closely related to crystal packing, energy level, and energy gap of PAHs, which are especially important for electronic applications. In fact, pentacene, a representative example of the acene family, has been developed as a prototype to investigate device fabrication, architecture, aging, and structure-property relationships in different fields of organic electronics.^{12,13}

The synthesis of PAHs often includes a two-steps protocol. First, a molecular precursor with mainly sp^2 -carbons is synthesized, typically featuring a nonplanar overall structure. Then, the precursor is planarized (graphitized) into PAHs. Here, a widely used precursor is polyphenylene (PP), for its high accessibility. For example, hexaphenylbenzene (HPB) can be planarized into hexa-*peri*-hexabenzocoronene (HBC) (Scheme 1.1). PAHs synthesized from a framework of benzene, such as HBC, are called all-benzenoid polycyclic aromatic hydrocarbons (PBAH). More precisely, PBAH is defined as PAHs that can be represented by a resonance form that contains only Clar's aromatic sextets (electronic structure of benzene) with no independent double bond or radical.¹⁴ Since this resonance form is energetically favored over the others, it has a higher weight in the ground state electronic configuration of PBAHs. More details about PBAHs will be discussed in *section 1.2*.



Scheme 1.1 Synthesis of PAH from nonplanar molecular precursor.

Of course, many PAHs cannot be classified as PBAHs. These PAHs can possess more olefinic or open-shell radical characters, and their π -electrons are usually more delocalized than in PBAH. Taking tetracene as an example, in all the close-shell resonance forms of tetracene, there are always twelve π -electrons that are not included in a Clar's sextet. As a result, tetracene is prone to reactions such as hydrogenation, bromination, oxidation, and Diels-Alder (D-A) reaction. In comparison, its isomer triphenylene, which is a PBAH, is an especially chemically inert molecule (Figure 1.2a).¹⁵ In addition, the energy gap between highest occupied molecular orbitals (HOMO) and lowest unoccupied molecular orbitals (LUMO) of tetracene is also much smaller than that of triphenylene.

Most of PAHs, such as those mentioned above, are composed of mainly hexagons. This is naturally related to the fact that PAHs derived from organic synthesis usually have PP precursors. Moreover, the three sp^2 -hybridized orbitals of carbon have a 120° angle between their symmetry axes, leading to a 120° bond angle between two adjacent sp^2 - sp^2 σ -bonds. Thus, there is no ring strain in a hexagon composed of sp^2 -carbons. Nevertheless, PAHs can

also possess non-hexagons in its skeleton, as long as it is still aromatic and polycyclic. Azulene is the simplest example of a PAH with no hexagon in its skeleton, but a fused pentagon-heptagon-pair. Notably, azulene is an isomer of naphthalene, which is composed of two fused benzene rings (Figure 1.2b). Although both azulene and naphthalene are ten- π -electron aromatic systems, they portray fundamentally different characters. First, azulene is blue in color while naphthalene is white. Second, the five-membered ring of azulene has higher electron density than its seven-membered ring, leading to an intrinsic dipole moment of 1.04 Debye, while naphthalene is non-polar. Besides, azulene is very basic as a hydrocarbon, while the basicity of naphthalene is rarely considered.

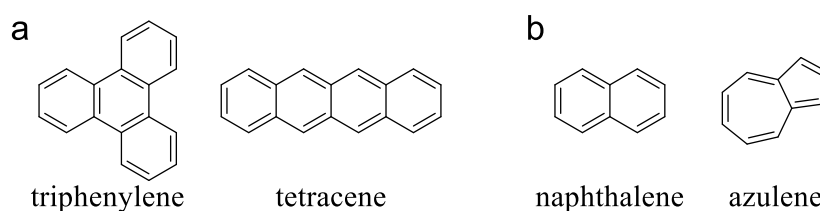


Figure 1.2 Two pairs of isomers that belong to different classes of PAHs. (a) Triphenylene, a PBAH; and tetracene, a non-PBAH (an acene). (b) Naphthalene, an alternant PAH; and azulene, a non-alternant PAH.

Similar to azulene, PAHs having odd-membered rings in their skeleton belong to non-alternant hydrocarbons, while those only holding even-membered rings, such as naphthalene, are called alternant hydrocarbons. The former ones normally have uneven electron density distribution in their ground state electronic configurations. More non-alternant hydrocarbons will be discussed in *section 1.3*.

1.1.2 Graphene

Research on PAHs is embracing its second explosive growth in these two decades.¹⁰ This shall be in close relationship with the first isolation of graphene, which can be considered as an infinitely large PAH with only hexagons in its skeleton (Figure 1.3), by [REDACTED] and [REDACTED] in 2004.¹⁶ The isolation of graphene opened a new carbon era and quickly earned [REDACTED] and [REDACTED] a Nobel Prize in 2010. Notably, graphene is the basis for other carbon allotropes in different dimensions, such as stacking up to 3D graphite, rolling up to 1D CNTs, or enfolding into 0D fullerenes (Figure 1.3).^{17,18} However, although [REDACTED] had already defined a suitable crystal lattice for graphene, and successfully predicted its unique band structure in as early as 1947,¹⁹ for a long time, graphene itself was regarded as unrealistic,

since its long-range 2D order is theoretically easily destroyed by thermal fluctuation.²⁰ In fact, evidence on isolation of CNTs and fullerene appeared much earlier in 1952 and 1985, respectively,^{21,22} while in the 70s and 80s researches related to graphene were focused on adjusting electronic properties of graphite, especially its conductivity, by synthesizing graphite intercalation compounds.²³

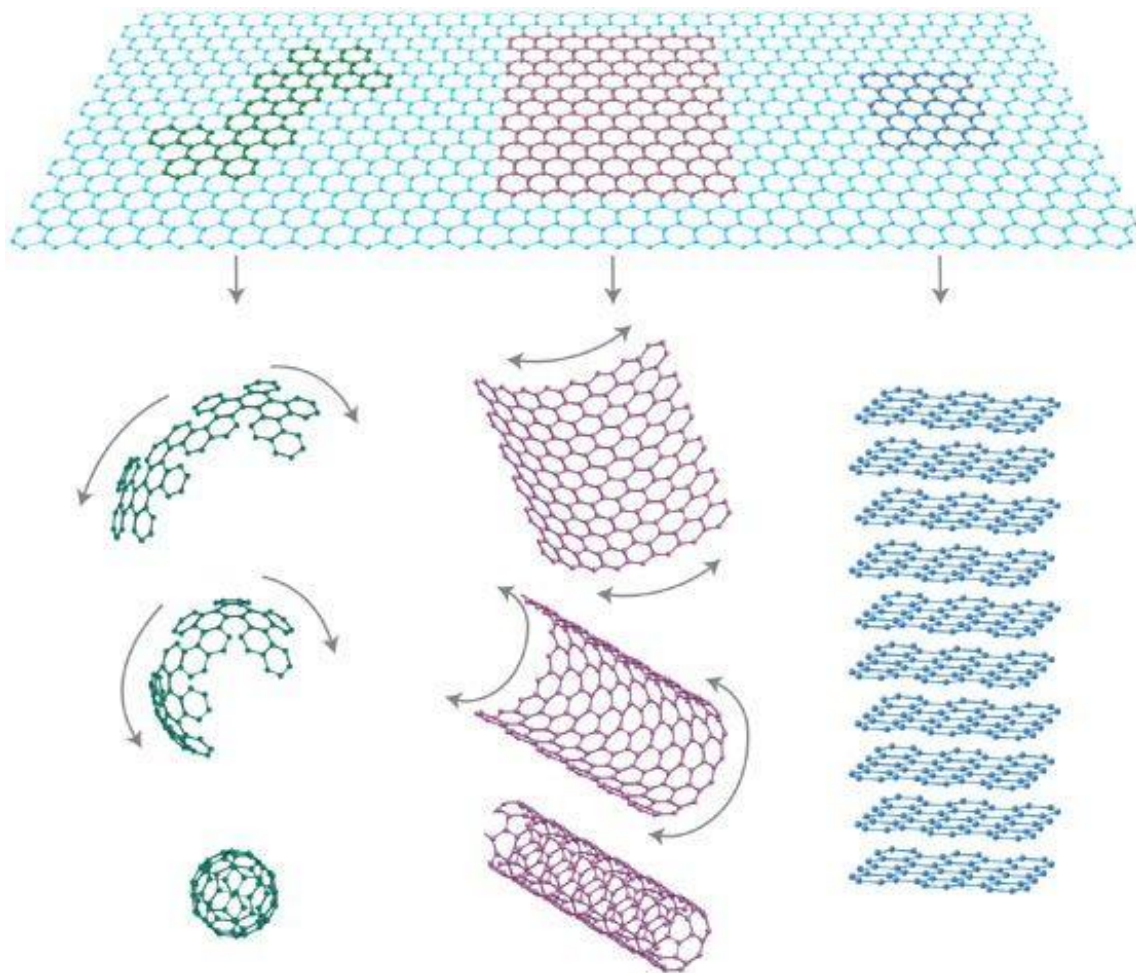


Figure 1.3 Relationship between graphene and other carbon allotropes in different dimensions. Reprinted with permission from Ref. 17; copyright: 2007, Springer Nature.

The ground breaking isolation of single layer graphene by ■■■ and ■■■ in 2004 immediately revealed some of its exotic properties,¹⁶ such as optical transparency, zero band gap, high charge carrier mobility above $10000 \text{ cm}^2\text{V}^{-1}\text{s}^{-1}$, as well as an abnormal ambipolar field-effect carrier concentration change, which does not exist for metallic conductors. Thanks to improved sample preparation, a charge carrier mobility²⁴ as high as $200000 \text{ cm}^2\text{V}^{-1}\text{s}^{-1}$ (100 times higher than that of silicon transistors) and a thermal conductivity²⁵ exceeding $5300 \text{ Wm}^{-1}\text{K}^{-1}$ (10 times higher than that of copper) have been measured. Besides,

graphene is extremely robust and stiff, with the largest ever-measured Young's modulus around 1 TPa.²⁶ The outstanding mechanical strength partially explains why a graphene flake with up to 0.01 mm² size can exist as suspended free-standing membranes without scrolling or folding.²⁷

Uncovering the marvelous nature of graphene requires proper fabrication methods, which has been a never-ending pursue, especially in a view of the balance between product quality and high-throughput production.²⁸ Fabrication principle of graphene can be roughly categorized as “top-down” and “bottom-up”, where the former involves exfoliation of graphite and the latter stems from atomic or molecular precursors. ■■■ and ■■■ originally micromechanically exfoliated highly oriented pyrolytic graphite using adhesive tape.¹⁶ This method can produce graphene with extremely good quality, but is also extremely inefficient, limiting it to only fundamental studies. Besides, other physical exfoliation methods, such as employing shear-force, fulfil requirements for industrial production,^{29–31} but cause more damage to the graphene products, resulting in a drop of mobility to around 100 cm²V⁻¹s⁻¹.²⁸ Recently, electrochemical exfoliation has appeared as a promising high-throughput physical/chemical exfoliation method, which is able to produce graphene with hole mobility up to 400 cm²V⁻¹s⁻¹.^{32–34} Alternatively, chemical exfoliation of graphite by oxidizing them into graphene oxide (GO), followed by back-reduction, can produce reduced graphene oxide (rGO) in high efficiency.³⁵ Nevertheless, rGO is normally heavily damaged graphene, exhibiting mobility only at around 1 cm²V⁻¹s⁻¹. Notably, some recent reports have employed milder chemical conditions, reaching rGO with mobility higher than 1000 cm²V⁻¹s⁻¹, suggesting that chemical exfoliation of graphite is worth a revisit.^{36–39}

Different from a feature of mass production in most of the top-down graphene fabrication techniques, the advantage of bottom-up approaches lies in achieving graphene with high quality and large area, by avoiding possible damage and breaking during graphite exfoliation. This is particularly important for high-performance electronic and optical device applications. Specifically, a graphene sheet with exceptionally good quality can be epitaxially grown on monocrystalline surface of SiC. Typically, C-terminated face of SiC is heated above 1000 °C to produce graphenes with remarkably high charge carrier mobility of 10000–30000 cm²V⁻¹s⁻¹. In parallel, chemical vapor deposition (CVD) of small molecular carbon sources on monocrystalline surfaces, typically a metal surface, is able to fabricate large area (23-cm-wide and 100-m-long⁴⁰) and high field-effect transistor (FET) mobility > 4000 cm²V⁻¹s⁻¹ polycrystalline graphene sheets. Besides, monocrystalline graphene is achieved with large

domain size (diameter $> 1 \text{ cm}^2$) and high FET mobility of $15000\text{--}30000 \text{ cm}^2\text{V}^{-1}\text{s}^{-1}$,⁴¹ making CVD the most promising protocol for growing large-area high-quality graphene.

Graphene, as a transparent, flexible, tough, and super good conductor, holds great potential especially as next generation electronic applications in solar cells, light-emitting diodes, touch panels, smart and wearable devices.⁴² Besides, graphene exhibits outstandingly high surface area, with theoretical and experimental values of > 2500 and $400\text{--}700 \text{ m}^2\text{g}^{-1}$, respectively.^{43,44} Since the π -electrons of graphene are exposed on its surface, they are easily affected by external stimulus. Thus, graphene is also suitable for applications in supercapacitors, sensors, and systems for DNA sequencing.^{45–47} However, the zero band gap semiconducting nature of graphene limits its digital and logic applications. Although transistors using graphene as conducting channel can reach incredible transistor frequencies higher than 100 GHz ,⁴⁸ the on/off electric current ratio ($I_{\text{on}}/I_{\text{off}}$) is generally below 5. There are four ways that could potentially solve this problem—quantization, defect engineering, functionalization, as well as using bilayer graphene.^{49,50} Moreover, these modifications could also adjust the other properties of graphene, and add new stimuli-responsiveness.

1.2 Quantization of graphene

Similar to other metallic and semiconducting materials, when the domain of graphene shrinks from bulk material to a smaller size, quantum confinement can play a role on its electronic properties. When the confinement occurs in both dimensions of graphene, graphene quantum dots (GQDs) are obtained. GQDs can also be considered as large-sized PAHs that contain almost only hexagons. Besides, graphene nanoribbons (GNRs) are characterized by a one-dimensional confinement. Notably, quantum confinement effects dominate electronic transport in FETs based on GQDs with diameters smaller than 100 nm.⁵¹ In parallel, the conductivity of GNRs also exhibits a major drop at a width below 100 nm.⁵² Thus, nanographenes (NG), which include GQDs and GNRs, can be specified as nano-cut-outs of graphene with confinement in at least one of its dimensions in a range of 1–100 nm.²⁸

The synthesis of NGs can be categorized into two strategies, similar to the fabrication of graphene—“top-down” and “bottom-up” methods. The former involves ripping graphene and other higher-dimensional carbon allotropes into lower-dimensional nano-objects, while the latter stems from combining quasi-zero dimensional molecular or atomic building blocks.

1.2.1 Top-down graphene quantization

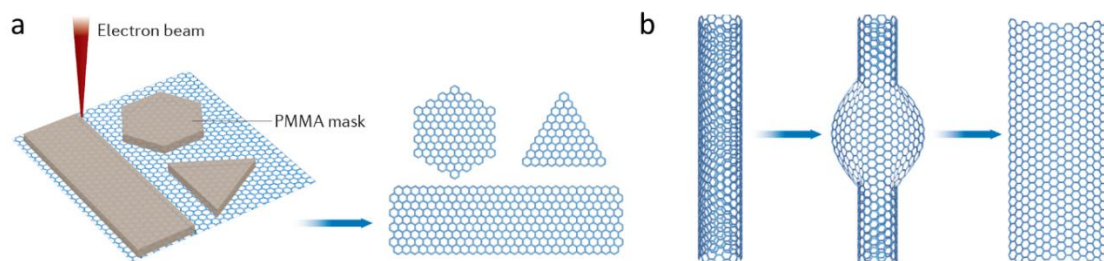


Figure 1.4 Schematic representation of top-down synthesis of NGs by (a) patterned lithography with masking and (b) dimensional reduction of carbon allotropes. Reprinted with permission from Ref. 28; copyright: 2017, Nature publishing group.

The top-down synthesis of NGs from graphene often involves lithography techniques with the help of masking, similar to those in the silicon semiconductor industry (Figure 1.4a). Besides, another well-developed strategy is cage-opening of fullerene or unzipping of CNTs (Figure 1.4b). Top-down synthesis of GNR is more intensely investigated than GQD for two reasons. First, cutting graphene into GNR is easier than GQD, since the former lower the dimension of material from 2D to 1D, while the latter lower to 0D. Second, the most attractive application of graphene is utilizing its ultra-high charge carrier mobility for next

generation semiconductors, and GNRs have advantages in device fabrication, channel alignment, and consistency of performance (when aspect ratio (AR) is high). Nevertheless, GQD has its advantage in other applications such as OLED, OPV, bioimaging, and biosensing.⁵³

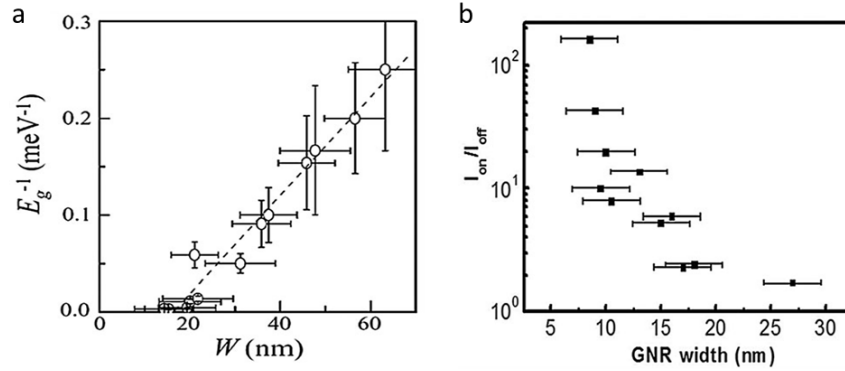


Figure 1.5 (a) Reciprocal value of band gap (E_g) as a function of GNR width (W). Reprinted with permission from Ref. 52; copyright: 2007, American Physical Society. (b) Correlation between $I_{\text{on}}/I_{\text{off}}$ and GNR width of GNR-based FETs. Reprinted with permission from Ref. 54; copyright: 2009, American Chemical Society.

Band gap opening already occurs in relatively wide GNRs (Figure 1.5a).⁵² However, for applying GNR in a transistor, an insufficiently large band gap results in very low $I_{\text{on}}/I_{\text{off}}$, leading to a device that cannot be reasonably switched off. Importantly, it is shown that an $I_{\text{on}}/I_{\text{off}}$ larger than ten can be achieved in FETs using GNR narrower than 10 nm (Figure 1.5b).⁵⁴ As a trade-off, narrowing GNRs causes a drop of charge carrier mobility, due to increase of effective charge carrier masses.^{55,56} Thus, a technique that fabricates GNR with a width of 5–10 nm is immensely desired, where a balance between $I_{\text{on}}/I_{\text{off}}$ and mobility in a FET is plausible.

Electron-beam lithography (EBL) is widely applied for graphene nanopatterning, because of its high resolution.^{51,52} Employing EBL, FET devices fabricated from 10-nm-wide GNR achieve high mobility of $800\text{--}1000 \text{ cm}^2\text{V}^{-1}\text{s}^{-1}$ and $I_{\text{on}}/I_{\text{off}} > 10^6$ at 4 K.⁵⁷ Furthermore, lithography resolution can be enhanced by using heavier particle beams, such as Helium⁵⁵ and Argon⁵⁸ ions, leading to sub-5-nm GNRs. However, EBL is a time- and energy-consuming process, requiring strict operating conditions, making it impractical for industrial manufacturing. To improve this, more productive lithography processes, such as reactive-ion and plasma etching, have been combined with efficient nano-masking protocols, e.g., water adsorption at step-edge of substrate,⁵⁹ inorganic nanowires (i-NW),⁵⁴ printed organic

nanowires,⁶⁰ and self-assembled block copolymers,⁶¹ for potential large-scale production of sub-10-nm GNRs from high quality graphene sheets. Notably, [REDACTED] and [REDACTED] fabricated bilayer-GNR FET by lithography of i-NW masked bilayer graphene. The FET device gave a high room temperature $I_{on}/I_{off} \sim 3000$ with an off-state under external electric field, which came from the behavior of bilayer graphene.⁶²

Besides, solution chemical/physical methods provide another approach for mass-production of GNRs. Remarkably, [REDACTED]'s group reported on a synthesis of GNRs, with a distribution of width from 50 nm down to sub-10-nm, as byproduct during exfoliation of graphite in 1,2-dichloroethane by sonication.⁶³ FETs based on the sub-10-nm GNRs exhibited mobility up to $200 \text{ cm}^2\text{V}^{-1}\text{s}^{-1}$ and the highest I_{on}/I_{off} up to 10^7 ever achieved for GNR-based FETs. The same group also reported on unzipping oxidized multi-wall CNTs by sonication to fabricate 10–30-nm-wide GNRs with FET mobility up to $1500 \text{ cm}^2\text{V}^{-1}\text{s}^{-1}$.⁶⁴

The solution-based wet chemical/physical top-down syntheses of GNRs are usually under milder conditions than the lithography methods. This can often lead to GNRs with smoother edge structure and roughness. Moreover, solution-based methods are more promising for high-throughput GNR production. However, for applications as transistor, especially in an integrated circuit, material processing and device fabrication using the resulting GNRs become a cumbersome task. Conversely, lithography processes gain advantage for patterning densely aligned transistor channels, along with direct circuit design. Notably, [REDACTED]'s group attempted on combining the advantages by slow chemical etching of wide GNR (20 nm) prepared from EBL.⁶⁵ The protocol succeeded in narrowing down the GNRs to sub-5-nm, and rendered a high $I_{on}/I_{off} > 10^4$ for their FET. Such trials of balancing the quality of GNRs, their production rate, and ease of patterning on, especially, insulator or semiconductor surface, is the core-concern of current GNR researches.

1.2.2 Bottom-up synthesis of nanographenes on monocrystalline surface

Bottom-up synthesis is another strategy to achieve NGs with a much better structural control. Specifically, the bottom-up protocols can be categorized into two classes. First, primarily based on CVD methods, NGs are grown on confined templates or starting from a nano-sized seed. Second, NGs with atomically precise structure are derived from organic synthesis with or without surface-assisted reaction steps.

CVD growth of graphene often employs metals as template. Indeed, bottom-up fabrication of NGs on a nano-sized metal substrate is possible. [REDACTED] and [REDACTED] patterned a dumbbell-shape Ni.⁶⁶ When current passed through this nanostructure, the narrower part heated up

more quickly, and became more reactive. Consequently, graphene could be selectively grown on the narrower part. Using this method, 23-nm-wide multi-layer GNR was fabricated with a direct Ni electrode connection, and transistor based on the nano-connection reached $I_{\text{on}}/I_{\text{off}}$ up to 10^4 . Nevertheless, using EBL for Ni nano-patterning was inevitable. Alternatively, GNRs with width down to 20 nm could be grown at edge of a Ni thin film, sandwiched between insulators, avoiding EBL etching.⁶⁷

Besides, direct CVD growth of GNRs on specific facets of SiC or Ge is reported. [REDACTED]'s group reconstructed a deep abrupt step on SiC (001) at 1200–1300 °C to form a SiC (110) nano-facet.⁶⁸ Next, GNR selectively grew on the (110) nano-facet at 1450 °C, because of a lower stability of SiC (110) than SiC (001). Remarkably, a 40-nm-wide GNR could then be *in-situ* fabricated, and a transistor based on such GNR reached $I_{\text{on}}/I_{\text{off}}$ ratio ~ 10 and charge carrier mobility as high as $2700 \text{ cm}^2\text{V}^{-1}\text{s}^{-1}$. In another approach, applying a very slow CVD growing rate ($< 5 \text{ nm h}^{-1}$), Arnold *et al.* demonstrated growth of GNRs with width $< 10 \text{ nm}$ and uniform crystallography and smooth edge on a Ge (001) facet.⁶⁹ These methods are highly valuable for allowing direct growth of GNRs on an insulating substrate. Thus, they avoid transfer of GNRs from otherwise a metal surface, often used in CVD processes. Such a feature largely facilitates device fabrication. For example, large-scale integrated transistors were produced on SiC substrates with a channel density of up to 40000 cm^{-2} .⁶⁸

It is important to stress that, although the NGs synthesized by the above-mentioned methods are frequently described as “smooth” and “straight”, there exists a common drawback—the nano-structure of products, in an atomic aspect, are extremely ill-controlled, especially at the peripheries of NGs.²⁸ This uncertainty leads to NGs with varied property, especially for small-sized ones, where the size is already comparable with the error-scale. For example, a width variation of GNRs provided by block-copolymer-masked lithography resulted in losing synchrony in multichannel transistor, and led to a poor $I_{\text{on}}/I_{\text{off}}$.^{61,70}

1.2.3 Organic synthetic strategy for large nanographenes

Organic synthesis is a bottom-up method with atomically precise control. With such power, syntheses of monodispersed GQDs or width-unified GNRs are possible, which is drastically different from the above-mentioned methods. In *section 1.1.1*, development history of PAH has been introduced. When the size of PAH (with mainly hexagons as skeleton) becomes larger than 1 nm, it can be considered as NGs. Accordingly, HBC (Scheme 1.1), with its size just exceeding 1 nm, serves as a milestone indicating PAHs entering the field of NGs. Yet, to be relevant at a molecular scale larger than 1 nm, organic synthesis faces obstacles in

chemical conversion efficiency, as well as structural characterization of the giant molecules. However, development of proper organic reactions, typically the Scholl reaction, together with advances in characterization techniques, in particular scanning tunneling microscopy (STM), non-contact atomic force microscopy (nc-AFM), and matrix-assisted laser desorption ionization mass spectroscopy (MALDI) (Figure 1.6),^{71–73} have opened the gate toward bottom-up organic synthesis of large NGs.

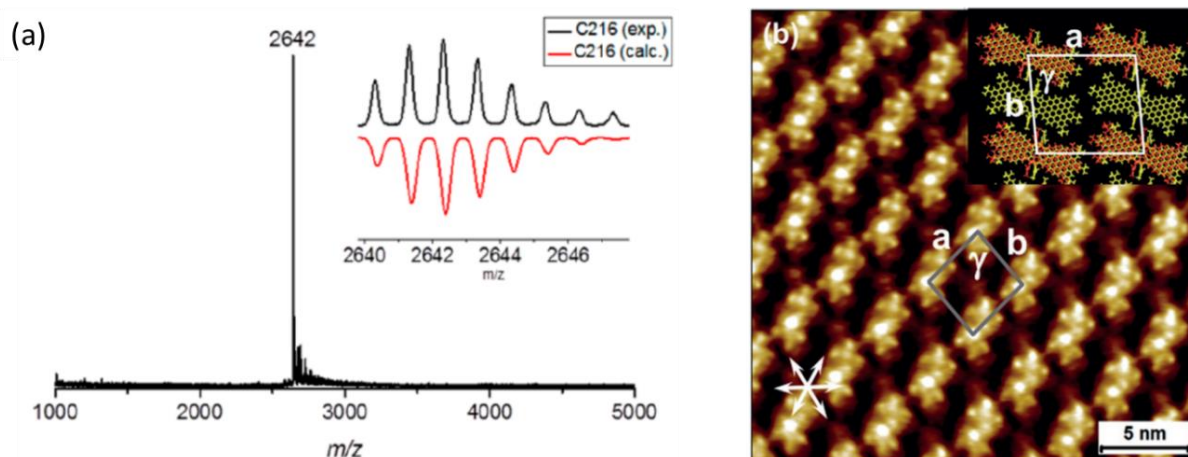


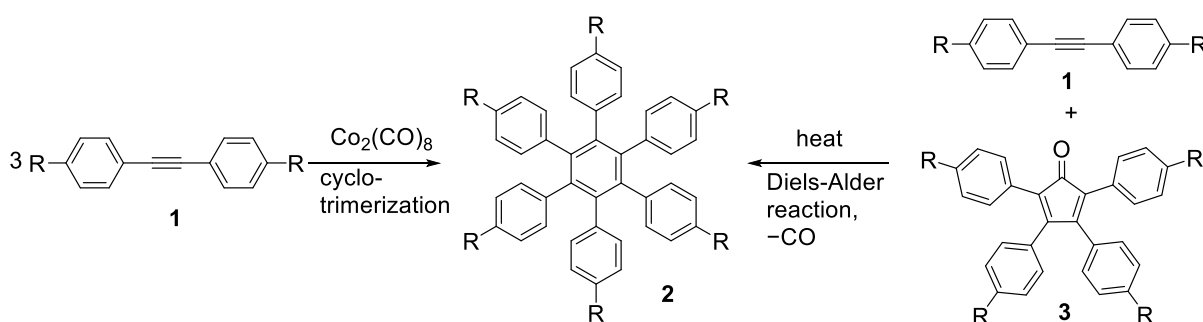
Figure 1.6 (a) MALDI spectrum of a NG containing 216 carbons in its core structure. Inset: comparison between theoretical and experimental isotope distribution of the molecule. (b) STM image of the self-assembly of a porphyrin-embedded NG containing 112 carbons in its core structure. Reprinted with permission from (a) ref. 72, copyright: 2016, American Chemical Society; (b) ref. 73, copyright: 2018, John Wiley and Sons.

Importantly, increasing size of PAHs, such as lateral extension of anthracene to quarteranthene, can quickly decrease their stability.⁷⁴ This is a result of increasing tendency for oxidation and an open-shell electronic structure. Thus, PBAHs, with stable electronic structures containing only Clar's sextet, is a class of PAHs that is especially suitable for size expansion into ultra-large NGs.¹⁴ In this section, we will discuss the development and principle of organic synthetic bottom-up approach for quantized graphene, focusing on the synthesis of large-size BPAHs.

As briefly mentioned in *section 1.1.1*, organic synthesis of PAHs often base on a two-step protocol of precursor synthesis and subsequent planarization. For BPAHs, PPs are especially valuable precursors. To synthesize large BPAHs that can be considered as monodispersed GQDs, dendritic PPs are used. Similarly, synthesis of GNRs employs linearly developed PPs with multiple phenyl substitutions. Importantly, in both cases, to enable complete

planarization of PP precursors, their structures must be carefully designed to allow a 2D projection without overlapping benzene rings in a graphene-related lattice.

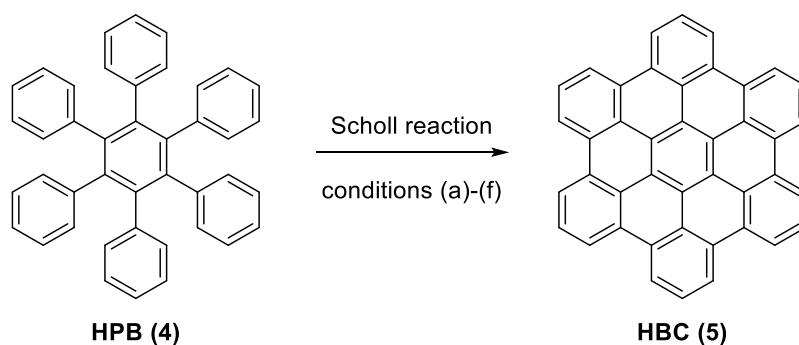
HBC is a good example for understanding both precursor synthesis and the subsequent planarization reaction in PBAH chemistry. Although early approaches used partially planarized precursors,⁷⁵ contemporary synthetic methods are often based on pure PP structures because of their facile synthesis. Particularly, █████ developed a $\text{Co}_2(\text{CO})_8$ -catalyzed cyclotrimerization of tolanes that efficiently produces C_6 -symmetric HPB skeletons (Scheme 1.2).⁷⁶ Furthermore, C_3 -symmetric HPB could also be produced in this way, but tolanes with two substituents that are different in polarity shall be applied, to facilitate product separation.⁷⁷ Besides, synthesis of HPB with other substitution patterns, particularly “para” and “ortho”, employed a D-A reaction between tetraphenylcyclopenta-2,4-dien-1-one (CP) and tolane, which is directly followed by extrusion of carbon monoxide (Scheme 1.2). In addition, metal-catalyzed cross coupling reactions, such as Suzuki-coupling, were also efficient enough for synthesizing HPBs.⁷⁸ From a strategic point of view, the cyclotrimerization works as a convergent method to combine three building blocks, whereas the D-A method can be considered as a divergent method to equip a structural core with multiple phenyl substitutions.



Scheme 1.2 Synthesis of HPB by cyclotrimerization or D-A reaction.

To convert HPB into HBC, six additional C-C bonds are formed, together with loss of twelve hydrogen atoms. This cyclodehydrogenation reaction was attempted in early years by conventional Scholl reaction, namely, coupling aromatic rings in the presence of Lewis acids, though poor yields were encountered (Scheme 1.3, condition (a)).⁷⁹ In contrast, addition of oxidants or using oxidative Lewis acids, such as FeCl_3 ,⁸⁰ MoCl_5 ,⁸¹ or Cu(II)/AlCl_3 ,⁸² significantly improved the conversion (Scheme 1.3, conditions (b)–(d)). █████, █████, and █████ conducted a systematic comparison and suggested that, for the Scholl reaction of pristine HPB, a use of MoCl_5 achieved the highest yield of HBC (Scheme 1.3, condition

(b)).⁸¹ Nevertheless, chlorination or chopping off of substituents were observed as side reactions for Scholl reactions using MoCl₅ or Cu(II)/AlCl₃ (FeCl₃ also led to some chlorination). Notably, an effective reagent system developed by [REDACTED], [REDACTED], and [REDACTED] has risen recently.⁸³ This reagent system employed an organic oxidant 2,3-dichloro-5,6-dicyanobenzoquinone (DDQ), combined with strong acid, typically methanesulfonic acid or triflic acid (Scheme 1.3, condition (f)), and has been proven especially valuable for many cyclodehydrogenation reactions that ill-performed using conventional reagents.

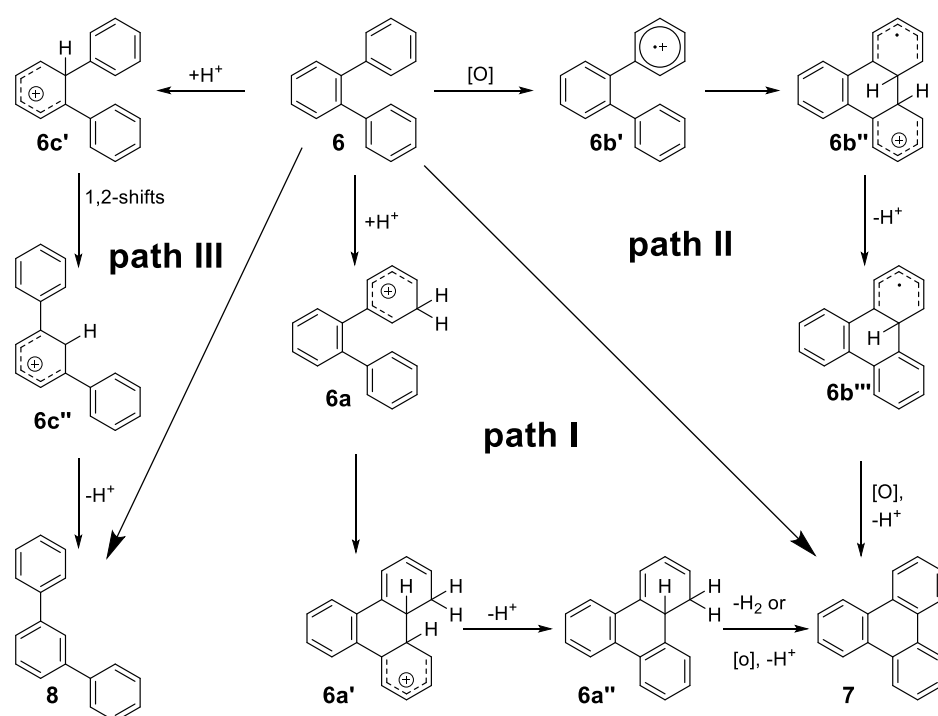


Scheme 1.3 Converting pristine HPB into HBC by the Scholl reaction. Conditions: (a) 18 eq. AlCl₃/NaCl, 120–130 °C, 3%. (b) 12 eq. MoCl₅, dichloromethane (DCM), rt, 99%. (c) 12 eq. CuCl₂/AlCl₃, CS₂, rt, 60%. (d) FeCl₃, DCM, rt, 118% (with inseparable iron residue). (e) 9 eq. PhI(O₂CCF₃)₂/BF₃·Et₂O, DCM, -40 °C, 78%. (f) 6 eq. DDQ, MeSO₃H, DCM, 0 °C, 99% (HPB with alkyl substituent). Data extracted from: (a) ref. 79, (b)–(e) ref. 81, and (f) ref. 83.

The Scholl reaction of HPB is a magnificent chemical conversion, forming multiple C-C bonds in one pot. The successful procedure suggests a high efficiency in each single bond-formation step. Notably, the original Scholl reaction used non-oxidative Lewis acid, such as AlCl₃.⁸⁴ Thus, it was believed to proceed via an arenium cation intermediate, followed by deprotonation and dehydrogenation upon heating (Scheme 1.4, path I). However, the last step was controversial, since quantitative generation of H₂ gas was not observed.⁸⁵ Notably, abundant O₂ gas, which often existed in the experimental environment, could also serve as oxidant to transform easily oxidizable species, such as dihydro intermediate **6a''** (Scheme 1.4), without H₂ extrusion.

Importantly, most of the Lewis acids currently used for Scholl reaction are also oxidants, including FeCl₃ and MoCl₅. Thus, the Scholl reaction can occur via another plausible mechanism using these reagents, that is, the radical cation pathway (Scheme 1.4, path II). In the work of [REDACTED], [REDACTED], and [REDACTED], deriving from computational and experimental evidences, it was suggested that the arenium cation mechanism (Scheme 1.4, path I) was the

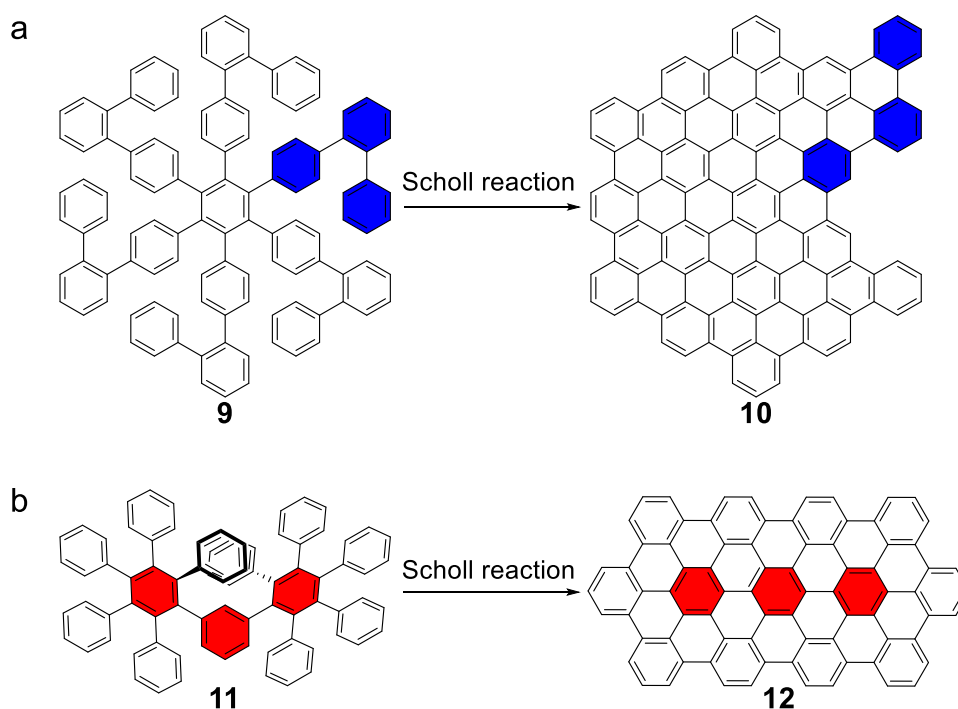
thermodynamically favored pathway.⁸¹ However, in reality, the reaction could be much more complicated, involving various intercrossing steps. Notably, for the Scholl reaction using DDQ/acid, the transformation did not proceed in case of precursors with high oxidation potential. Thus, the reaction under this condition more likely proceeded through a radical cation pathway.⁸⁶



Scheme 1.4 Schematic representation of the mechanism of the Scholl reaction. Path I: arenium cation pathway. Path II: radical cation pathway. Path III: skeleton rearrangement as side reaction.

Notably, rearrangements can occur as side reactions during Scholl reactions (Scheme 1.4, path III). In an extreme example, heating *o*-terphenylene (**6**) at 140 °C in the presence of strong acid led to formation of *m*-terphenylene and *p*-terphenylene as a final mixture in a ratio of 65:35.⁸⁷ The reaction proceeded via a 1,2-phenyl shift, driven by the higher stability of *m*-terphenylene arenium cation (Scheme 1.4, path III). Although contemporary Scholl reactions were performed at much lower temperature, similar side reactions could still occur. For example, our group revealed that, during the Scholl reaction of an extended HPB **9**, a significant amount of the *o*-terphenylene side arms isomerized into *m*-terphenylene (Scheme 1.5a).⁸⁸ On the bright side, in some cases rearrangement could also “correct” kinks in PP precursors, such as a successful complete planarization of PP **11** through a possible equilibrium between isomers with different connectivity of phenylenes (Scheme 1.5b).⁸⁹

Nevertheless, to ensure a desired NG product structure, PP precursors shall be designed to avoid rearrangement during Scholl reaction.⁹⁰

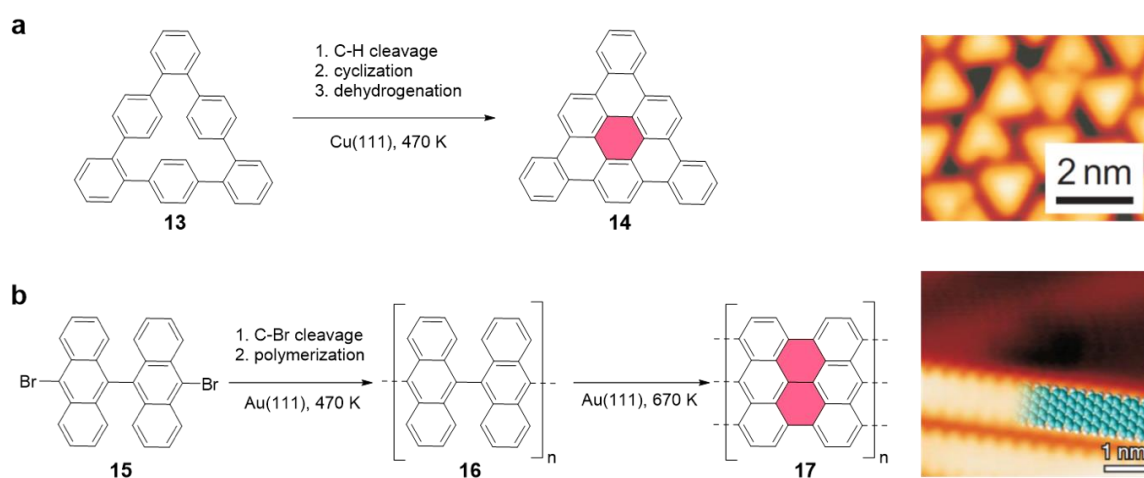


Scheme 1.5 Skeletal rearrangement during Scholl reaction of PP 9 and 11.

Because of lacking solubility, solution-synthesized large NGs are often challenging for conventional characterization, such as NMR, single crystal X-ray diffraction, and mass spectrometry. To overcome this obstacle, our group and [REDACTED]'s group developed a protocol in 2010 to combine advantages of organic synthesis with surface-assisted chemistry.^{91,92} This technique depended on sublimation of molecular precursor, synthesized in solution, onto a monocrystalline metal surface under ultra-high vacuum (UHV) conditions. Upon further heating, the metal surface promoted a homolytic cleavage of, e.g. C-H bond, forming radical species. Then, the radical species further reacted intra- or intermolecularly, followed by dehydrogenation into 2D graphitic structures.⁹³

The power of this method lies in two points. First, the flat monocrystalline metal surface facilitates a perfect planarization of precursors. Second, NG products can be *in-situ* characterized by scanning microscopy, especially STM and nc-AFM, under UHV conditions, to extract structural and electronic information with atomic resolution. For the first demonstration, the cyclohexaphenylene **13** was used, leading to a triangular-shaped monodispersed GQD **14** (Scheme 1.6a).⁹² Although a requirement of sublimable precursors

limited the size of obtainable monodispersed GQDs, for synthesis of GNRs this was not so much a problem. For example, monomeric precursor **15** with halogen substituents was sublimed onto Au(111). Upon heating, **15** underwent C-X cleavage, and the generated radical intermediates polymerized into polymeric precursor **16**. Upon further enhancing the temperature to 670 K, surface-assisted cyclodehydrogenation occurred, and **16** planarized into GNR **17** (Scheme 1.6b).⁹⁴ The solution synthesis combined with a surface-assisted reaction is now widely applied, especially for fundamental studies, to systematically investigate different NGs on surfaces.



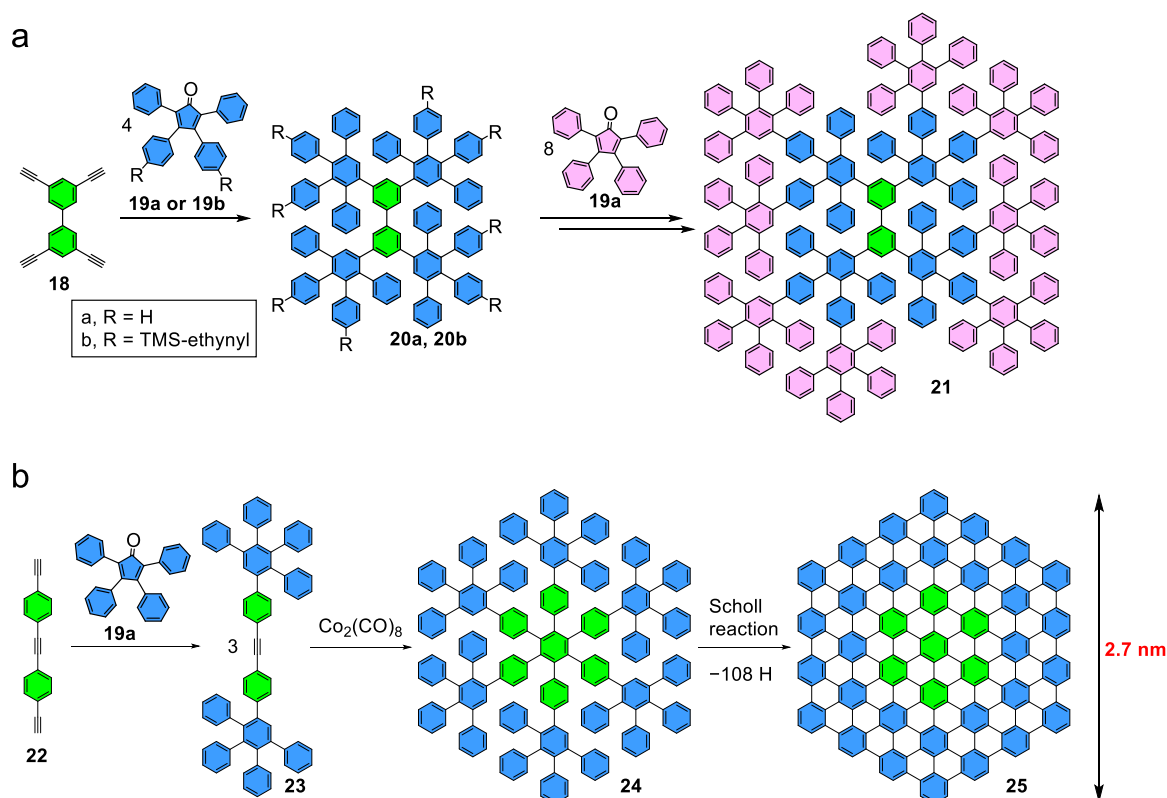
Scheme 1.6 The First demonstration of on-surface synthesis of (a) a GQD and (b) a GNR, and their STM images taken in-situ. Reprinted with permission from (a) ref. 92, copyright: 2011, Nature Publishing group; (b) ref. 94, copyright: 2010, Nature Publishing group.

1.2.4 Organic synthesis of large monodispersed graphene quantum dots

Either applying the divergent or convergent synthetic strategy of HPB mentioned in *section 1.2.3*, PPs rapidly expand into dendritic structures that could be planarized into monodispersed GQDs. Synthesis of PP **21**, serving as potential precursor for GQD with a Z-shape C_{2h} -symmetry, was a representative example (Scheme 1.7a).⁹⁵ This divergent synthesis relied on two-layer-extension of 3,3',5,5'-tetraethenyl-1,1'-biphenyl (**18**) by repetitive D-A reactions with CPs (Scheme 1.7a). Notably, 2D projections of **20** or **21** in a graphene-related lattice (like in Scheme 1.7a) exhibit no spatial overlap benzene ring. This enabled the conversion of **20a** into a square-shape D_{2h} -symmetric GQD with 132-carbon aromatic core.^{96,97} The exact mass of this GQD was observed by MALDI-TOF mass analysis. Despite the successfulness of **20a**, a graphitization of **21** was not reported.

Our group also reported a highly efficient Scholl reaction of an even larger dendritic PP precursor **24**. The reaction led to GQD **25** with a D_{6h} -symmetric 222-carbon π -core (Scheme 1.7b).⁹⁸ This is a perfect demonstration of convergent synthesis of dendritic PP precursors for bottom-up approach of GQDs. Remarkably, **25**, with a diameter close to 3 nm, is the largest GQD ever reported with a relatively clean MALDI-TOF spectrum showing desired product as the dominating peaks. Notably, PP precursors, as well as partially planarized intermediates, exhibit much stronger signals in MALDI-TOF analysis than the fully planarized GQD targets.⁹⁹ Accordingly, observing dominating peak of GQD over the others suggests a high content of fully-converted GQD in the product mixture.

The extension of BPAHs into GQDs gradually lower their HOMO-LUMO gap, roughly proportional to reciprocal of the number of carbon atoms in their π -core.⁹⁶ The 222-carbon **25** possesses a HOMO-LUMO gap approaching 1.4 eV. However, these large PAHs are often insoluble, hindering a thorough investigation of their photophysical properties.



Scheme 1.7 (a) Divergent and (b) convergent synthesis of dendritic PPs that can serve as precursors for large monodispersed GQDs.

The extension of BPAHs into GQDs gradually lower their HOMO-LUMO gap, roughly proportional to reciprocal of the number of carbon atoms in their π -core.⁹⁶ The 222-carbon **25**

possesses an HOMO-LUMO gap approaching 1.4 eV. However, these large PAHs are often insoluble, hindering a thorough investigation of their photophysical properties.

Our group also synthesized highly extended dendritic PPs **26** and **27**, aiming at fabricating monodispersed GQDs with a diameter exceeding 5 nm (Figure 1.7). Both PP precursors were achieved through divergent two-layer-extension by D-A reactions, similar to **21** (Scheme 1.7a). The triangular-shape PP **26** was ideally a precursor for a monodispersed GQD with D_{3h} symmetry and a 474-carbon π -core. However, its full planarization was especially challenging. Interestingly, MALDI-TOF analysis of products after the Scholl reaction compared with model compounds suggested that partial graphitization occurred within each three arms, and a propeller structure likely formed.¹⁰⁰ On the other hand, PP **27** was extended from a HBC core.¹⁰¹ Notably, 2D projection of **27** shows overlap of benzene rings (Figure 1.7). Considering that the rearrangement or extrusion of phenyl groups could occur during the Scholl reaction (section 1.2.3), **27** could be ideally planarized into D_{6h} -symmetric monodispersed GQD with a 546-carbon π -core after losing six phenyl groups. However, Scholl reaction of **27** was complicated and could not be fully clarified.

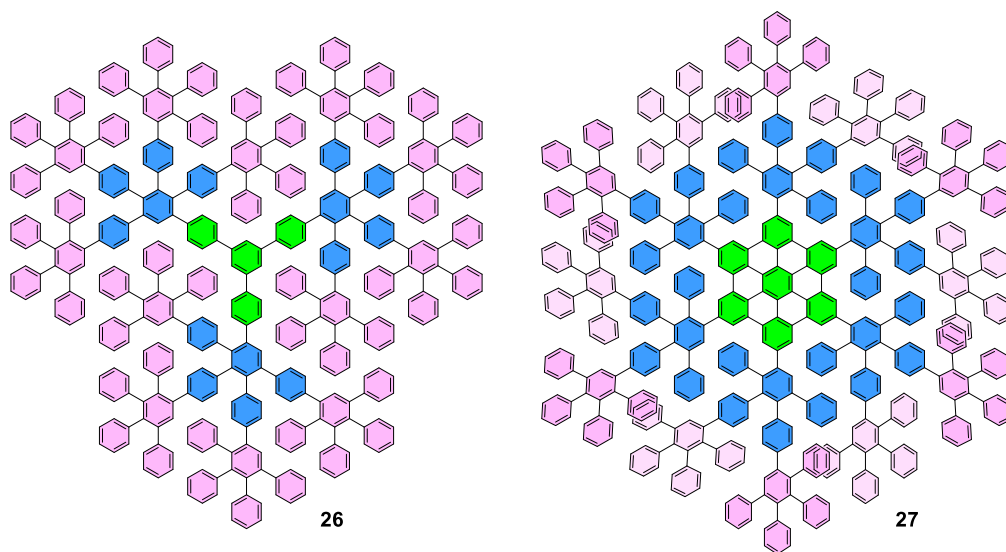


Figure 1.7 Extended dendritic PPs as potential precursors for monodispersed GQDs approaching 5 nm.

1.2.5 Organic synthesis of wide graphene nanoribbons

Organic synthesis provides opportunities for not only atomically precise bottom-up fabrication of GNRs but also their systematic investigation by series of oligomers. Representatively, two series of monodispersed GQDs derived from 1D-extended HBC were synthesized by our group (Figure 1.8). The “armchair” series (**28–30**) extended HBC toward

the “angle” direction,^{96,97} whereas the “superacene” series (**28**, **31**, **32**) on “sides”.^{102,103} These monodispersed GQDs could be considered as GNRs with a width close to 1 nm and a very small AR. Importantly, long alkyl chains were equipped to enhance solubility of the large GQDs, enabling energy gap estimation in solution by UV-Vis absorption spectroscopy (Figure 1.8). Similar to some other conjugated materials, gradual decrease of energy gap along increment of repeating units was observed, and band gap of 1.1 eV and 1.7 eV is predicted for the “armchair” and the “superacene” GNRs, respectively, with infinite repeating units and large ARs.

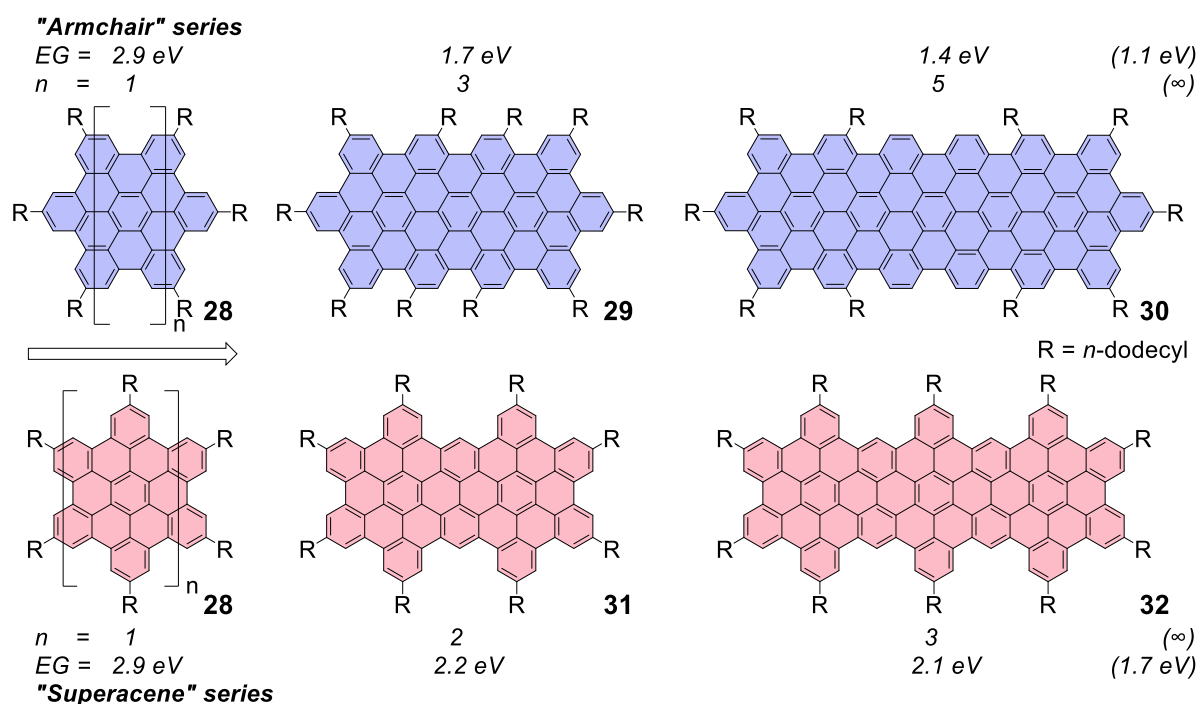
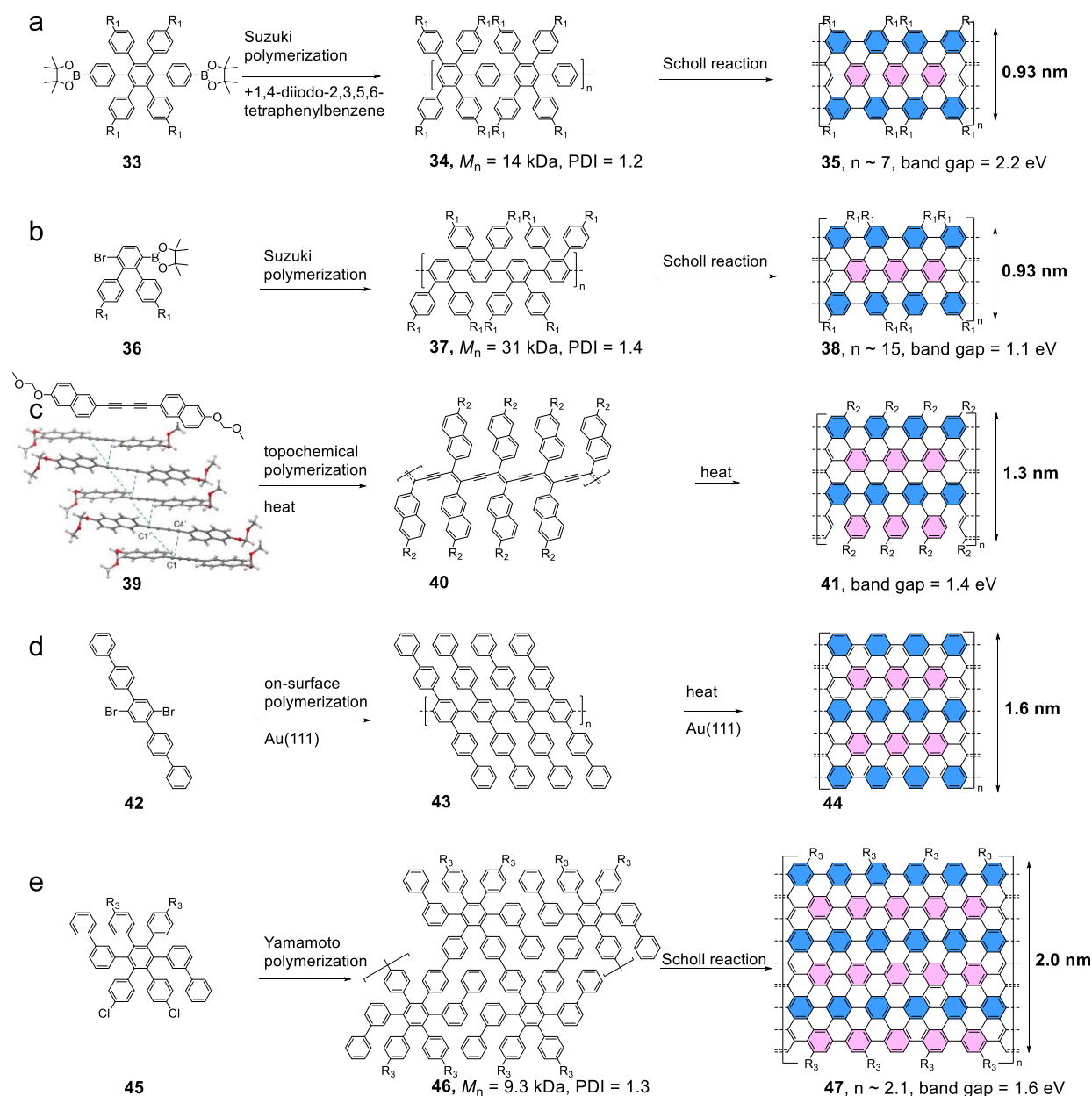


Figure 1.8 Two series of 1D-extended HBCs and their estimated energy gap (EG). Predicted EG for corresponding GNRs are shown in the parentheses.

To synthesize GNRs based on the “armchair” series shown in Figure 1.8, our group pioneered on an A_2B_2 -type Suzuki polymerization between HPB boronic ester **33** and diiodotetraphenylbenzene (Scheme 1.8a).¹⁰⁴ However, because of a high steric hindrance, the efficiency of the Suzuki reaction was low.¹⁰⁵ Nevertheless, the PP precursor **34** was isolated with number average molecular weight (M_n) of up to 14 kDa and a polydispersity index (PDI) as small as 1.2.¹⁰⁴ However, the Scholl reaction of **34** using $FeCl_3$ as oxidant only gave GNR **35** with a band gap at around 2.2 eV. This indicated that the effective conjugated length of **35** would be even smaller than **29** (Figure 1.8 and Scheme 1.8). Excitingly, an improved synthesis has been developed recently by [redacted] and [redacted] (Scheme 1.8b).¹⁰⁶ This approach

utilized AB-type Suzuki-polymerization of 4-bromo-2,3-diphenylboronic ester **36**. Remarkably, M_n of the resulting polymer **37** reached a higher value up to 31 kDa. Moreover, it was found out that DDQ/triflic acid is more efficient over FeCl_3 for converting **37** into GNR **38**. Consequently, GNR **38** possessed a band gap close to 1.1 eV, which agreed with what predicted from oligomers (Figure 1.8). Our group have also utilized similar monomeric structure for on-surface synthesis of pristine GNR **38** without alkyl substituents.¹⁰⁷



$R_1 = 3,7$ -dimethyloctyl, $R_2 =$ methoxymethoxyl, $R_3 = n$ -dodecyl

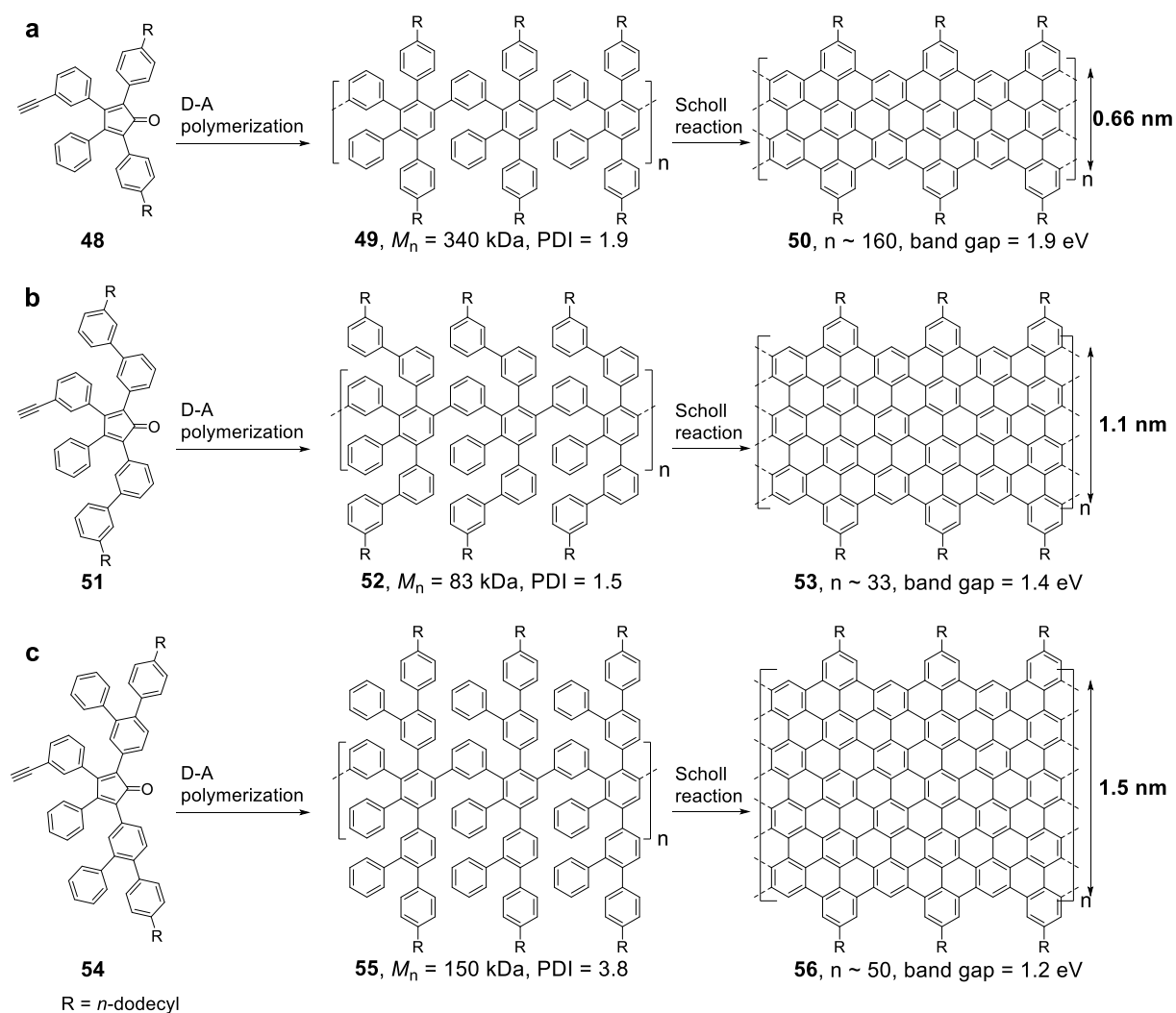
Scheme 1.8 Laterally extended GNRs belonging to BPAHs made by various synthetic strategies and monomer design.

GNRs **35** and **38** can be considered as laterally fused poly(*p*-phenylene) (PPP) chains (Scheme 1.8). In fact, lateral fusion of PPP chains occurred on an Au(111) surface at 650 K. Nevertheless, fusion of more than two chains was challenging.¹⁰⁸ In contrast, syntheses of GNRs that corresponds to lateral fusion of four (GNR **41**), five (GNR **44**), and six (GNR **47**) PPP chains were demonstrated by solution-based organic synthesis with various synthetic methods (Scheme 1.8).

█'s group has reported a novel approach toward GNR **41** utilizing topochemical polymerization.¹⁰⁹ Specifically, by screening substituents of potential monomers, monomer **39** with methoxymethoxyl groups was revealed as possessing proper intermolecular orientation that enabled its polymerization upon heating or UV-light irradiation in monocrystalline state. Further heating the polymer product **40** in solid state resulted in its graphitization into GNR **41** (Scheme 1.8c). For the synthesis of wider GNR **44**, █'s group employed polymerization of dibromo-*p*-pentaphenyl monomer **42** on-surface.¹¹⁰ STM analysis confirmed the formation of GNR, although relatively dense structural defects were observed (Scheme 1.8d). Besides, our group synthesized an even wider GNR **47** by Scholl reaction of a PP precursor **46**, which was obtained from Yamamoto polymerization of diphenyldichloro-HPB monomer **45** (Scheme 1.8e).¹¹¹

GNRs **38**, **41**, **44**, and **47** represent a family of similar structure that belongs to BPAHs, with gradually increased width exceeding 2 nm. Theoretically, their band gap shall be inversely proportional to their width.¹¹² However, as shown in Scheme 1.8, the band gaps increase with the width, portraying the narrowest GNR **38** with the smallest band gap. This could stem from several reasons: (1) The four GNRs were produced from completely different synthetic methods. Some polymer precursors could lead to incomplete cyclodehydrogenation reactions. (2) As already observed by comparing GNR **35** and **38**, AR of GNRs casts a decisive influence on their band gap. Particularly, estimated from M_n of PP precursor **46**, the AR of GNR **47** could be as low as two. Thus, GNR **47** shall be considered as oligomer with an energy gap far from convergence. (3) GNRs often exhibit a strong tendency toward aggregation and intermolecular electronic interaction could influence their band gaps.

On the other hand, our group have recently developed a protocol to synthesize GNRs based on the “superacene” series (Figure 1.10 and Scheme 1.9a). This synthesis utilized AB-type D-A polymerization of monomer **48** featuring a CP and an ethynyl functional group.^{103,113} Moreover, by using monomers **51** and **54** with more phenyl substituents at proper positions, laterally extended PPs **52** and **55** were achieved. Their Scholl reactions led to GNRs **53** and **56** with width approaching 2 nm (Scheme 1.9b,c).^{114,115}



Scheme 1.9 Lateral extension of GNRs by D-A polymerization of extended CP monomers.

Since GNR **50**, **53**, and **56** were synthesized applying the same protocol, their properties can be reasonably compared. Especially, the GNRs exhibited lowering of band gap from 1.9, to 1.4, and to 1.2 eV, while their width increased from 0.66, to 1.1, and to 1.5 nm, respectively (Scheme 1.9). The values agreed with prediction provided by density functional theory (DFT) calculation, which gave band gaps of 2.0, 1.5, and 1.2 eV,¹¹⁶ respectively. Notably, there were several other remarkable features for this D-A-polymerization-based GNR synthesis. First, the D-A polymerization was highly efficient, producing PP precursors with exceptionally large M_n . Consequently, extremely high AR, for example, over 500 for GNR **50**, was developed (Scheme 1.9a). This is way more superior than the GNRs described in Scheme 1.8, and should be one of the reasons for the consistence between the theoretically calculated and experimentally estimated band gaps. Second, according to light scattering analysis results, the PP precursors had an extreme backbone rigidity influenced by enormous substituents on

the polymer backbones. This helped them maintaining a semirigid conformation in solution.^{103,117} Consequently, exceptionally long linear GNRs with no kink were formed after the Scholl reaction. For example, a straight chain of GNR **50** longer than 500 nm was revealed by AFM analysis.¹¹⁸ Third, since the D-A reaction was a metal-free chemical conversion, it tolerated substituents such as halogens, allowing further functionalization of the GNRs with, for example, optically¹¹⁹ or magnetically¹²⁰ active moieties.

Current bottom-up organic synthesis demonstrates fabrication of structurally precise GNRs with a uniform width exceeding 2 nm. This ensures identical intrinsic properties between individual GNR strands, which is drastically different from top-down synthesis. In addition, recent studies have also demonstrated control of the length distribution of bottom-up synthesized GNRs, applying polymer precursors derived from living-polymerizations.^{121,122} Indeed, it is highly intriguing to investigate electronic applications based on solution-synthesized GNRs, especially as transistors. However, FET motilities for solution-synthesized GNRs are often low, in a range of 10^{-3} – 10^{-5} $\text{cm}^2\text{V}^{-1}\text{s}^{-1}$.¹²³ Our group, in collaboration with [REDACTED]'s group, have estimated the intrinsic mobility of GNR **50** to be as high as 150–15000 $\text{cm}^2\text{V}^{-1}\text{s}^{-1}$ by non-contact terahertz conductivity measurement,¹⁰³ despite its transistors only exhibited an $I_{\text{on}}/I_{\text{off}}$ lower than 2.^{118,124} Above all, one foresees that device fabrication using solution-synthesized GNRs are facing more complicated challenges than top-down synthesized ones. A plethora of other substances can obstruct the device performance, such as the dispersing solvent, solubilizing side-chains and additives, and impurities coming from synthesis. Moreover, GNRs strongly aggregate in solution, which can alter their band gaps.¹¹⁸ Development of processing technique and device fabrication for solution-based GNRs are thus equally important as their synthesis.

1.3 Defects in graphene and their model compounds

As a bulk material, graphene inevitably possesses various kinds of defects in its crystal lattice, because of thermodynamics and unideal synthetic conditions. Notably, some similar defects were studied in other carbon allotropes, e.g., CNTs, fullerenes, and graphite, prior to the graphene era.¹²⁵ However, as a flat atomic monolayer, graphene provides more suitable objects for defect analysis, especially after the development of high-resolution transmission electron microscopy (TEM).

Defects in graphene can be in principle understood similarly as those in 3D materials, although the 2D nature of graphene in a sense simplifies the situation by lowering dimension. Besides, 2D nature of graphene alters energetic profile between various types of defects compared to their counterparts in 3D materials. Moreover, sp^2 -hybridized carbons can form various non-hexagon rings, leading to topological defects, which locally or globally affect the graphene crystal lattice. Such scenario distinguishes graphene from the most of other materials.

1.3.1 Types of defects in graphene

The simplest defect in graphene is a single vacancy (SV) of lattice atom, a point defect similar to Schottky defect in 3D crystals. Importantly, migration energy barrier of SV is lower than its formation energy.¹²⁶ Thus, at an elevated temperature, SVs coalesce into other more stable defects, typically a double vacancies (DV). Then, DV undergoes spontaneous reconstruction, forming two bonds between the four dangling bonds, leading to a pentagon-octagon-pentagon topological defect (Figure 1.9a).¹²⁷ Further reconstruction of the pentagon-octagon-pentagon defect into more complicated topological defects can occur at high temperature, driven by release of local strain.

Another representative topological point defect is the Stone-Wales (SW) defect (Figure 1.9b), which was proposed as early as 1986, almost 20 years before the isolation of graphene.¹²⁸ SW defect is formed by rotation of a pair of carbon atoms for 90° , creating a pentagon-heptagon-heptagon-pentagon topology and no lattice vacancy. Practically, at elevated temperature ($> 1000^\circ\text{C}$) or under bombard of high-energy particles, typically during TEM analysis, SW defect can form and be kinetically trapped. Besides, the high-energy electrons used during TEM measurement could also ballistically knock out carbon atoms, forming SVs.¹²⁹ If the carbon atom leaving graphene lattice remained on graphene surface, an adatom-vacancy pair could be formed, which is similar to a Frenkel defect in 3D crystals, although it is

conceptually different since the adatom prefers to stay at the third dimension, namely being excluded from graphene lattice. Furthermore, when carbon adatoms migrating on graphene surface meet, they combine into a pair and insert into graphene crystal lattice (Figure 1.9c). Such topological defect is called inverse SW defect, for a similar heptagon-pentagon-pentagon-heptagon topology but different arrangement compared to SW defect.¹³⁰ Notably, inverse SW defect violates the “isolated pentagon rule”,¹³¹ thus causing severe local buckling on graphene.

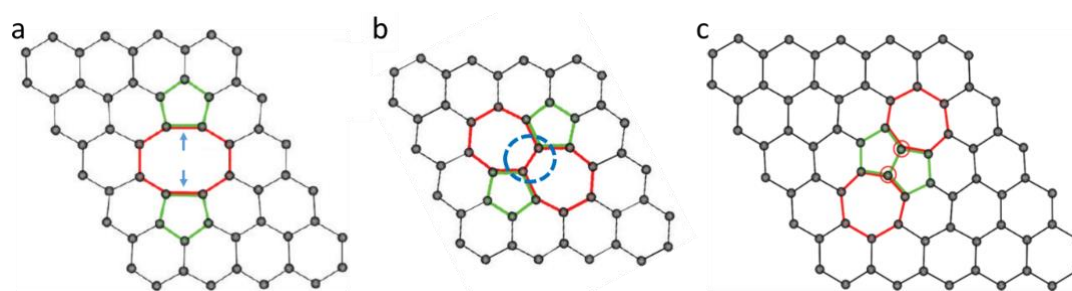


Figure 1.9 Topological trivial point defects observed in graphene. (a) A reconstructed DV. Arrows indicate bonds formed during reconstruction. (b) A SW defect. Circled atoms are rotated in the graphene lattice. (c) Inverse SW defect. Circled atoms are inserted adatoms. Reprinted with permission from Ref. 125; copyright: 2011, American Chemical Society.

Unlike those in a 3D crystal, point defects in 2D graphene lattice are “half-naked”, lacking stabilization from the third dimension. As a result, the energy of formation of these defects in graphene starting from a perfect crystal lattice is much higher than those of similar defects in 3D materials. For example, energy of formation of SV defect in most metals is smaller than 3 eV, while in graphene it is above 7.5 eV.^{126,132} Likewise, the same energy of (inverse) SW defects are high (> 5 eV).^{130,133} Thus, point defect concentration in graphene flake is negligibly low in those synthesized in a thermal equilibrium condition, such as CVD. This is also the reason why CVD can produce high-quality graphene sheet.

As mentioned in *section 1.1.2*, CVD is currently the leading fabrication technique for the synthesis of large-area graphene wafer. At the beginning of CVD graphene growing process, graphene crystallizes from multiple nucleation sites. Then, developed graphene domains eventually merge into a large-area graphene sheet.¹³⁴ However, because of crystal lattice mismatch between different domains, the large-area graphene sheets are always polycrystalline. Thus, in reality, defects that strongly influence graphene properties would be line defects, which define graphene grain boundaries (GB).¹³⁵ It is revealed by TEM imaging

that fused pentagon/heptagon arrays generally dominate the nanostructure of GBs.¹³⁶ To understand this, the nature of topological defects in graphene shall be explained more.

The point defects mentioned above are “topologically trivial”, since the overall symmetry of the surrounding graphene lattice is preserved. In contrast, some “non-trivial” topological defects cast long-range influence on the graphene lattice. Here, disclination and dislocation line defects in 3D materials can be adopted, though as 2D projection, to describe most of “non-trivial” topological defects in graphene lattice. Typically, a pentagon or a heptagon, considered as disclination defect in graphene, cause rotation of graphene crystal lattice surrounding the defect point (Figure 1.10a). Alternatively, the influence of pentagon or heptagon defects can be understood as removing or adding a 60° wedge into graphene lattice, respectively (Figure 1.10a).¹³⁷ These single pentagon/heptagon defects inevitably result in nonplanar local topology, and they have not been experimentally observed in graphene.

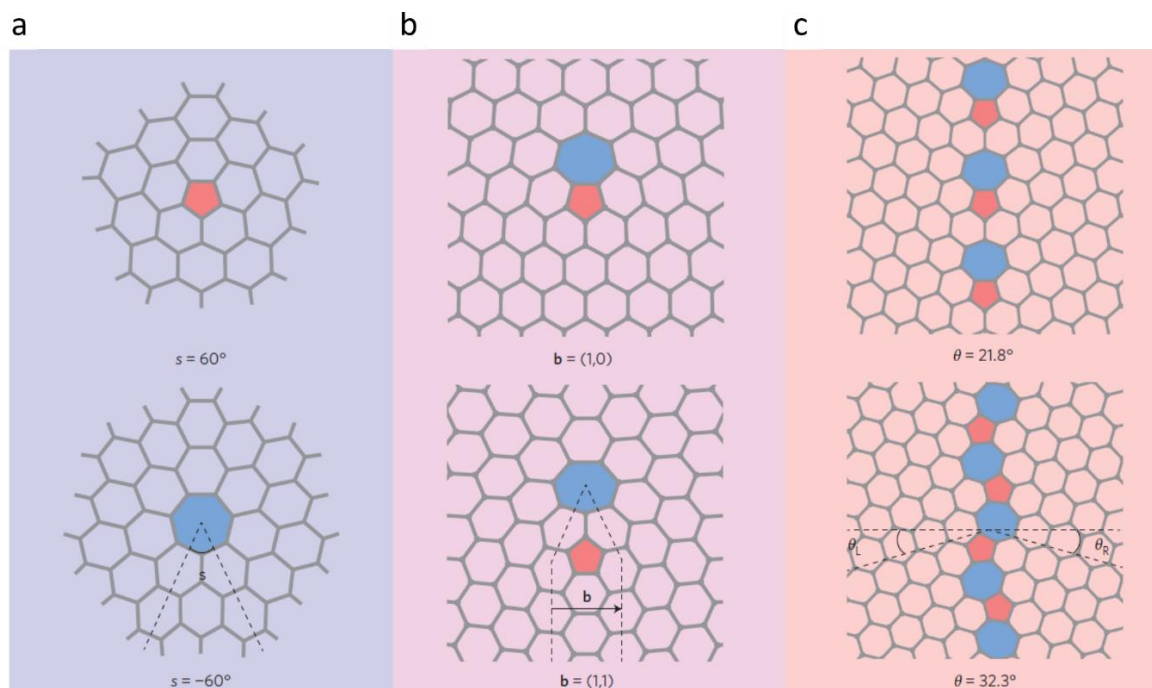


Figure 1.10 Topological non-trivial defects in graphene. (a) Disclinations, s = degree of wedge that is added (negative) or removed (positive). (b) Dislocations, b = Burgers vector. (c) GBs, θ = misorientation angle between two grains. Reprinted with permission from Ref. 135; copyright: 2014, Nature Publishing group.

Importantly, when a pentagon and a heptagon are close in space, they compromise each other's effect, namely rotation of graphene crystal lattice, on local environment. In other words, two disclination defects join as a dislocation defect (Figure 1.10b). A dislocation defect semi-infinitely expands graphene crystal lattice along a translation vector, which is

described by adapted Burgers vector. For example, Figure 1.10b portrays a (1,0) and a (1,1) dislocation defect. Notably, in comparison with a disclination defect, a dislocation defect furnishes only minor perturbation on the crystal lattice (Figure 1.10a,b). As a result, the local area surrounding dislocation defects can be more or less planar,¹³⁷ and the calculated formation energy of dislocation defects in graphene is close to that of SW and SV defects.¹³³ Also, dislocation defects are experimentally observed by microscopies in graphene lattice.¹³⁸ Notably, to maintain a continuous lattice across two graphene grains with different crystal orientation, the crystal lattice requires regular expansion at the GB, namely, periodic alignment of dislocation defects can be the element of graphene GB. The larger is the misorientation angle, the denser are the dislocation defects. For example, Figure 1.10c portrays theoretical nanostructures at two linear GBs between 21.8° and 32.3° misoriented graphene lattices. These two GBs possess particularly low calculated formation energy.¹³⁷

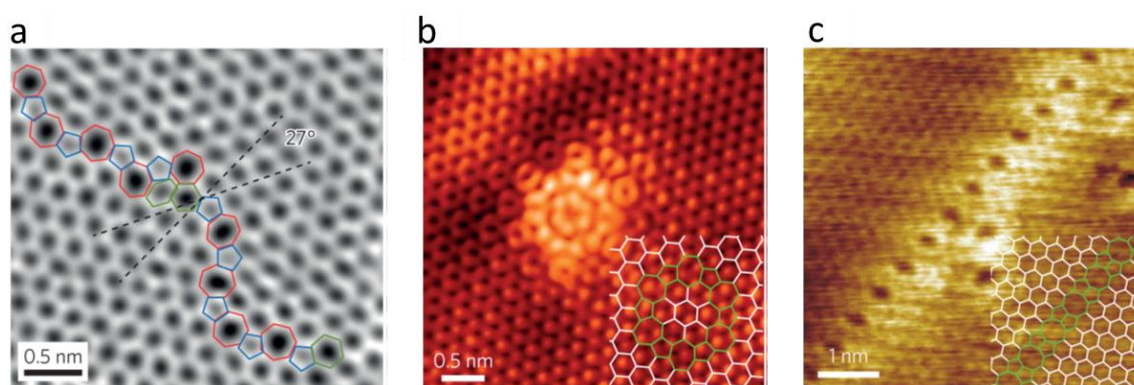


Figure 1.11 Microscopic images of graphene GB nanostructures. (a) TEM image of a boundary of 27° misoriented graphene lattices. (b) STM image of a GB loop. (c) STM image of a GB composed of pentagons and octagons. Reprinted with permission from (a) ref. 136, copyright: 2011, Nature Publishing group; (b) ref. 139, copyright: 2011, American Physical Society; (c) ref. 140, copyright: 2010, Nature Publishing group.

Experimentally observed nanostructures at graphene GBs are more chaotic than ideal cases (Figure 1.11a).¹³⁶ This is understandable because graphene grains can have various misorientation angles, which is normally not ideal for simple GB nanostructures shown in Figure 1.10c. Moreover, the group of [REDACTED] recently has suggested that sinuous GBs are even energetically favored over linear ones.¹⁴¹ Nevertheless, the fused pentagon-heptagon-pairs, namely (1,0) dislocation, or the structure of azulene, still dominate the nanostructure of GBs. Interestingly, a flower-like GB loop is widely observed (Figure 1.11b),¹³⁹ where a very small graphene domain with 30° lattice misorientation is isolated from the bulk graphene lattice. Such a “graphene flower” could be a local minimum in the energy profile of graphene

point defect reconstruction. Besides, GBs can also exist between graphene domains without lattice misorientation. For example, a pentagon/octagon nanoline, or an array of fused reconstructed DV defects, is observed in graphene grown on Ni(111) (Figure 1.11c).¹⁴⁰

Influence on electronic transport properties is one of the most important concerns for graphene GBs. It is generally observed that GBs reduce the conductance of graphene.¹⁴² However, interesting phenomena, such as low temperature magnetoresistance, can be induced, probably due to presence of some local states. Inspiringly, [REDACTED] and [REDACTED] proposed that a through-GB electron transport barrier could be created by controlling the periodicity of GB and crystal lattice misorientation between graphene domains, as a result of electron momentum mismatch.¹⁴³ Thus, it is theoretically possible for a polycrystalline graphene-based transistor with a high I_{on}/I_{off} without opening an intrinsic band gap. Remarkably, the group of [REDACTED] demonstrated intentional creation of an over-7-nm-long line defect with the same structure shown in Figure 1.11c, starting from a hole in graphene, aiming at a potential application in electrostatically gated “valley valve” device.¹⁴⁴ Moreover, taking advantage of the higher reactivity of GBs, [REDACTED]’s group has recently realized reversible passivation of GBs by hydrogenation for regulating conductivity of polycrystalline graphene.¹⁴⁵

GBs also affect other intrinsic properties of graphene. Particularly, presence of GBs reduces mechanical strength of graphene.¹⁴⁶ However, it is also pointed out from theoretical side that such a scenario is strongly related to misorientation angles between grains, and regularity of nanostructure of GB. Especially, the mechanical strength of GB can be close to that of pristine graphene when the tilt angle is large.^{147,148} Besides, although theoretical studies are debating on the thermal transport over GBs,^{149,150} [REDACTED] and [REDACTED] *et al.* have recently experimentally demonstrated a higher grain-size-sensitivity of thermal conductivity over electronic conductivity in polycrystalline graphene, suggesting their potential for thermoelectric material.¹⁵¹ Nevertheless, although interesting phenomena have been predicted or observed in the above-mentioned defect engineering, fabrication techniques still lack precise control on nanostructure at GBs.

1.3.2 Relationship between organic compounds and graphene defects

Pentagons and heptagons exist in various synthetic and natural organic molecules. For example, the simple structure of cyclopentadiene (**57**) and cycloheptatriene (**61**) (Figure 1.12). The polyene structure of **57** and **61** can be easily converted to fully sp^2 -hybridized cyclopentadienide anion **58** and tropylium cation **62**, which are extraordinarily stable for ions of hydrocarbons. Besides, crystal structure analysis suggests no C-C bond length alternation

in both **58** and **62**.¹⁵² Notably, **58** and **62** both contain six π -electrons. Thus, they are aromatic and isoelectronic to benzene, which explains their high stability.

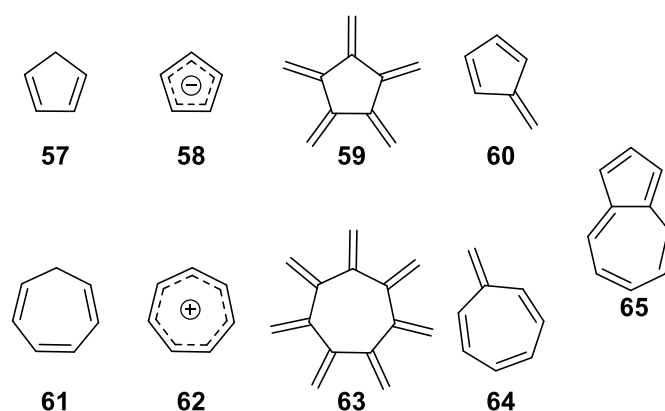


Figure 1.12 Representative structures of single-ring molecules with pentagon or heptagon, and bicyclic azulene.

Aside from the ionic species **58** and **62**, radialenes **59** and **63**, and fulvenes **60** and **64**, are simple examples of neutral monocyclic sp^2 -hydrocarbons with pentagonal or heptagonal skeletons, although they are much less stable. Production of [5]radialene **59** has been reported recently by [REDACTED] and [REDACTED] from low temperature decomposition of an iron complex, though **59** easily oligomerized after formation.¹⁵³ From the diene-rich structure of **59**, it would be expected that D-A reaction could be the reason for the low stability of **59**. However, calculations suggested a biradical intermediate.¹⁵³ Besides, with an increased reactivity, isolation or proof of formation of [7]radialene **63** is not reported yet. On the other hand, pentafulvene **60** and heptafulvene **64** are more stable than radialenes, although they are still sensitive to heat, light, and oxygen.¹⁵⁴ The methylene groups of **60** and **64** are reactive toward nucleophilic and electrophilic attack, respectively.¹⁵⁵ This tendency is rationalized by the ability of forming an aromatic cyclopentadienide anion or tropylium cation. Moreover, azulene **65**, serving as a fused pentafulvene and heptafulvene, is the most stable non-hexagon hydrocarbon among **59–65**, as a result of an aromatic ten- π -electron system. In fact, cyclopentadiene and fulvene derivatives are often used as precursors for azulene synthesis.¹⁵⁶ These simple monocyclic sp^2 -hydrocarbons shown in Figure 1.12 can be considered as “naked” defects of graphene, namely, without the surrounding graphene lattice. Depending on the local electronic structures, defects in graphene could inherit the chemical and physical properties of these small sub-nano architectures. Organic synthesis provides a bottom-up

approach for model compounds related to defects in graphene. The following sections will introduce such PAHs and NGs.

1.3.3 Molecular models representing point defects in graphene

The SV and DV point defects contain dangling bonds, which prefer reconstruction and migration within the graphene lattice. Indeed, they shall be considered as intermediates in an organic reaction point of view, for their high reactivity. Thus, isolation of small molecular models for SV and DV defect is impractical. However, sp^2 -macrocycles, such as annulenes and cycloarenes, can be regarded as model compounds for vacancies in graphene lattice, where all the dangling bonds are passivated with hydrogen atoms (Figure 1.13).

The *cis-trans* alternating isomer of [12]annulene (**66**), with nine outer- and three inner-protons, in its planar conformation, represents the hydrogen-passivated “naked” SV defect of graphene (Figure 1.13). However, the inner-protons cast significant steric hindrance. Thus, [12]annulene **66** is nonplanar. Moreover, it was shown that [12]annulene **66** undergo facile isomerization via a Möbius aromatic transition state through heavy atom tunnelling,¹⁵⁷ which was followed by a six-electron-electrocyclization into a dihydrobenzo[8]annulene.¹⁵⁸

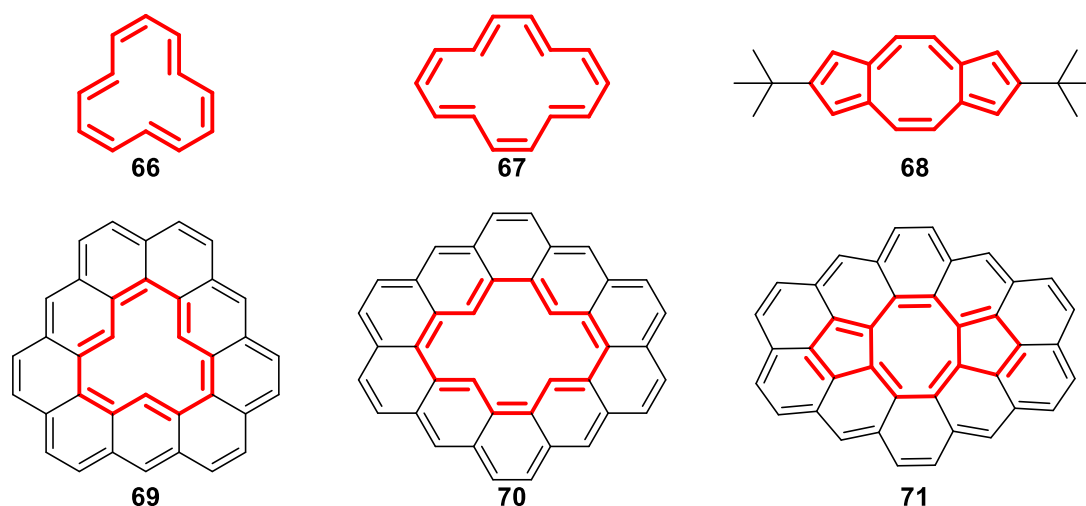





Figure 1.13 Representative molecular model compounds for SV and DV defects in graphene.

In contrary, steric hindrance is smaller in the larger and more stable [14]annulene **67**, which serves as a good model compound for passivated “naked” DV defect in graphene (Figure 1.13). In a single crystal analysis, [14]annulene **67** displayed roughly planar structure, with closely identical bond lengths for every C-C bonds. This suggested a $14\text{-}\pi$ -electron aromatic system.¹⁵⁹ Interestingly, it appeared that [14]annulene **67** adopted a less symmetric

conformation in solution, and the inner protons experienced a weaker diamagnetic shielding effect than what was expected from an aromatic ring current. The result suggested that [14]annulene **67** could enhance its aromaticity when it was transformed from solution to the solid state, as an interplay between intermolecular interaction, steric hindrance, aromatic stabilization, and C-C double bond strength.¹⁶⁰ Besides, 2,7-di-*tert*-butyldicyclopenta[a,e]cyclooctene (**68**), structurally related to **67**, was achieved by , , and  (Figure 1.13), although the synthesis did not involve derivatives of **67**, but started from a bis-cyclopentadiene.¹⁶¹ Importantly, the pentagon-octagon-pentagon architecture of **68** is one of the major topological defects formed after reconstruction of a DV defect, and thus it is more crucial than SV and DV defects for understanding graphene at ambient conditions.¹²⁷ Notably, from single crystal analysis, the perfectly planar structure of **68** was revealed. Moreover, the bond length of the bridging C-C bonds was close to a single bond, and the rest were nearly identical. Similar structural features were also observed in azulene **65**, indicating a high overall aromaticity.¹⁶¹

As a further step from molecular models for “naked” SV and DV defects in graphene, it is important to π -extend **66–68** to a nano-environment more similar to the graphene lattice. However, the synthesis encounters severe obstacles. For cycloarene analogues **69–71** (Figure 1.13), only **70** was synthesized through a long 18-step route.¹⁶² Notably, a mass signal corresponding to **71** was observed in the product mixture of cyclodehydrogenation reaction toward **70**. This could suggest an organic chemical version of DV defects reconstruction.¹⁶² Unfortunately, no follow-up investigation was reported. Indeed, π -extension induced a more severe steric penalty on the inner protons, especially in **69**, which could be the main factor for their challenging synthesis.¹⁶³ Nevertheless, cycloarene **70** already gave a useful insight into electronic structure of passivated DV defect. Particularly, from its ¹H-NMR analysis, it was suggested that macrocyclic diamagnetism, which existed in **67**, disappeared in **70**, indicating a more localized electronic structure.¹⁶²

Recently, our group has synthesized a NG similar to **25** (Scheme 1.7b), the NG containing 222 sp²-carbons, but with a six-carbon hole in its center.⁷² This NG could be considered as model compound for a passivated sextuple vacancy defect of graphene. Although such defects should have little chance to exist in graphene flakes, it gave insight into novel graphene-related nanostructures provided by bottom-up synthesis. Remarkably, our group and Fasel’s group demonstrated on-surface synthesis of a framework of 1,3,5-benzenetriyl, which could be regarded as graphene with regular sub-nano pores.¹⁶⁴ Such a structure was

closely related to the top-down graphene nanomesh, a porous graphene material that could be considered as alternant for GNRs and QGDs for graphene quantization.¹⁶⁵

Aside from SV and DV point defects, the simplest model compound for a “naked” SW point defect can be considered as dicyclopenta[*ef,kl*]heptalene (azupyrene, **73**), an isomer of pyrene (**72**) (Figure 1.14). The first organic synthesis of **73** dated back to as early as 1973, by ████████ *et al.*¹⁶⁶ In fact, it was even 13 years earlier than the proposal of a SW defect.¹²⁸ Later, an elegant synthesis of **73** was developed by the group of ████████, involving a smooth stepwise transformation of azulene into cyclopenta[*cd*]azulene, then aceheptalene, and eventually azupyrene **73**, through cycloaddition-ring-expansion protocol.¹⁶⁷ Notably, among investigation of the chemistry of multianion of various PAHs, our group revealed that trapping a dianion of **73** with methylation reagent resulted in an interesting [14]annulene **75**, where both of the central carbons were methylated (Figure 1.14).¹⁶⁸ This observation indicated highly localized negative charge in the dianion of **73**. In contrast, methylation of dianion of **72** resulted in **74**, where none of the methyl groups attacked on the central carbons (Figure 1.14). The drastic divergence could be rationalized by the nodal positions in LUMOs of **72** and **73**. Moreover, **72** involved benzene sub-ring that possesses large weight in its ground state electronic structure, while **73** did not (Figure 1.14).¹⁶⁸ From a present point of view, this difference in chemical reactivity of **72** and **73** could highlight a possible influence of SW defect on graphene.

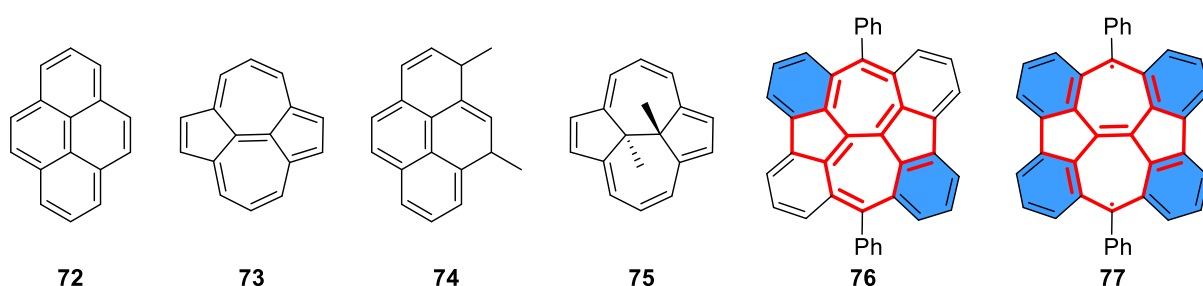
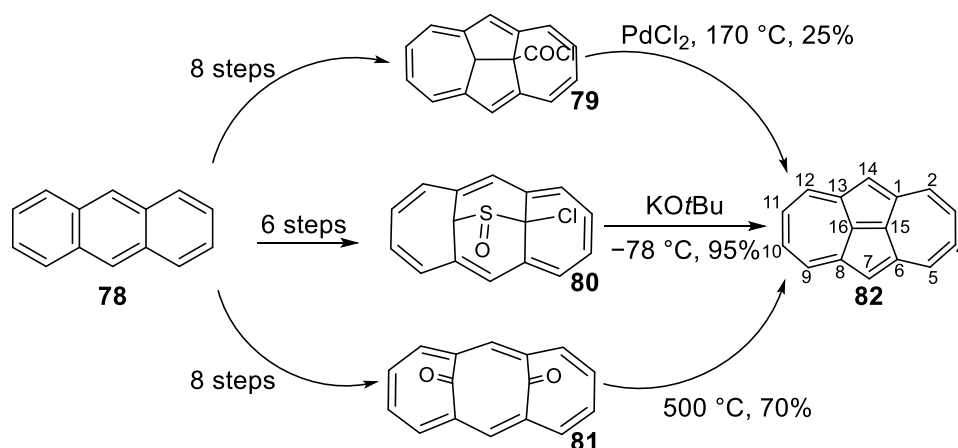


Figure 1.14 Representative molecular model compounds for SW defect in graphene.

Remarkably, PAH **76** representing a slightly π -extended “naked” SW defect has been reported recently by ████████ and ████████ (Figure 1.14).¹⁶⁹ Despite a low stability, the single crystal of **76** was obtained, revealing a fully planar structure. Interestingly, the bond length between central carbons was the shortest among all the others (1.37 Å), close to that of a pure C-C double bond. Combined with the other data such as EPR signals, DFT calculation, and silence in NMR analysis, it was concluded that **76** possessed strong open-shell biradical character, which could be interpreted by the resonance structure **77**, where two more Clar’s

sextets are drawn (Figure 1.14). The electronic difference between **73** and **76** indicates the strong dependence of chemical and physical properties of a SW defect on the surrounding nanostructure.

Dicyclohepta[*cd,gk*]pentalene (**82**), another isomer of pyrene, was also synthesized earlier than the graphene era in 1972 by [redacted] and [redacted], one year before azulopyrene **73** (Scheme 1.10).¹⁷⁰ The initial synthesis involved intermediate **79**. Later, improved syntheses employing intermediates **80** and **81** were developed (Scheme 1.10).^{171,172} Indeed, pyrene isomer **82** can be considered as molecular model for “naked” inverse SW defect, the twin of SW defect in graphene. Remarkably, these syntheses involving intermediate **79–81** can be regarded as organic chemical version of the formation of inverse SW defect in graphene. Creation of an inverse SW defect in graphene is believed proceeding through adatoms insertion into crystal lattice during high-energy particle bombard.¹³⁰ Here, reactions take place with much lower energy barrier by a series of chemical conversion, that eventually also lead to insertion of two sp^2 -carbons into a sub-nano graphene, the anthracene **78** (Scheme 1.10).



Scheme 1.10 Organic synthesis of an isomer of pyrene representing inverse SW defect.

According to the crystal structures of **67**, **68**, and **82** (Figure 1.13 and Scheme 1.10), standard deviations of bond lengths between their peripheral carbons were 1.9, 0.7, and 1.8 pm, respectively. Moreover, the $C_{15}-C_{16}$ bond length in **82** was only 1.35 Å (typical $C=C$ bond length is 1.34 Å). These data suggested that the electronic structure of **82** could be interpreted as a $C=C$ segment surrounded by a 14- π -electron system with aromaticity in between **67** and **68**.¹⁷¹ Indeed, the influence of ring strain, especially in the case of **67** and **82**, should also be considered. Notably, the single crystal of **82** indicated an almost planar structure, which may contradict the fact that an inverse SW defect causes local buckling in graphene lattice.

However, the C₇-C₁₄ atomic distance in **82** was obviously larger than C₂-C₅. Thus, one could imagine that there will be local curvature in a highly π -extended **82**.

1.3.4 Molecular models related to topological non-trivial defects in graphene

The effect of disclination topological defect on graphene lattice (rotation of crystal lattice) can be modeled by radial π -extension of skeletons of radialenes shown in Figure 1.12 with hexagons. Remarkably, the organic synthesis of corannulene (**83**), where a pentagon was embedded in five hexagons, was achieved in as early as 1966 by [redacted] and [redacted] (Figure 1.15).¹⁷³ An interesting interpretation of the electronic structure of **83** lay in its polarized resonance structure **84**, where an aromatic anion of [5]annulene was surrounded by an aromatic cation of [15]annulene (Figure 1.15). In fact, this interpretation gave **83** the name “corannulene”, for “annulene-in-annulene”. However, from single crystal analysis, corannulene exhibited an obvious bond length alternation, indicating localized double bond characteristics similar to the electronic structure of [5]radialene. Thus, the resonance form **83** describes corannulene more properly. Importantly, corannulene **83** is a nonplanar PAH displaying a cone shape, with a cone depth of 0.87 Å.¹⁷⁴ Such observations surely described how disclination defect should induce local buckling in graphene lattice. Notably, a further radially π -extended corannulene **85** has been recently reported by [redacted] and [redacted] (Figure 1.15).¹⁷⁵ The crystal structure of **85** showed a deepened graphitic cone structure, with a cone depth of 4.3 Å, portraying the long-range topological influence of a disclination defect on an NG.

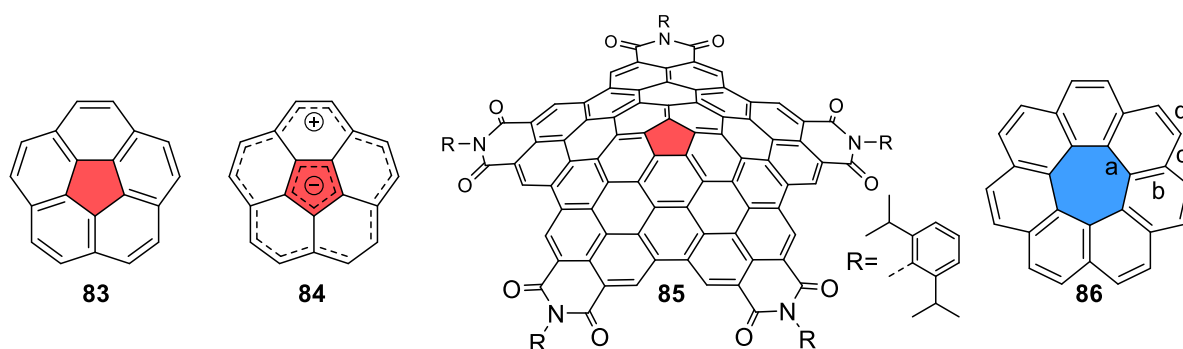


Figure 1.15 Molecular models representing disclination defects in graphene.

Inspired by the synthesis of corannulene **83**, its analogue [7]circulene **86** was achieved 17 years later in 1983 by [redacted], [redacted], and [redacted] (Figure 1.15).¹⁷⁶ It was shown that [7]circulene **86** adopted a saddle-like molecular structure, due to a crowded heptagon center.

Moreover, detailed analysis revealed that bond types a–d shown in Figure 1.15 exhibited average bond length of 1.46, 1.43, 1.41, and 1.34 Å, respectively, where bond length of type b, representing the double bond in a [7]radialene electronic system, was abnormally large.¹⁷⁶ So far, for **86**, there is no report on a similar radial π -extension like **85**. However, several NGs containing two embedded heptagons were reported.^{177,178} These NGs, with extended saddle-architecture, served as potential precursors for the synthesis of nanobelt representing inner part of a torus shape CNT.

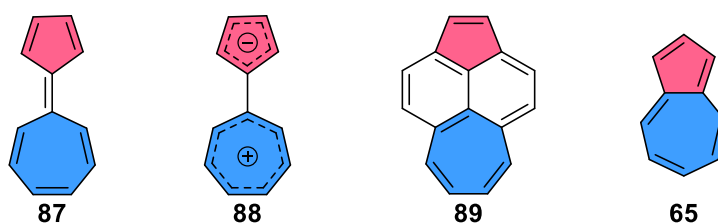


Figure 1.16 Simple organic molecules representing “naked” dislocation defect in graphene.

It can be easily recognized that the two dislocation defects of a pentagon-heptagon-pair in a graphene lattice shown in Figure 1.10b, namely the (1,1) and (1,0) dislocation, correlate to the molecular skeleton of pentaheptafulvalene (**87**) and azulene (**65**), respectively (Figure 1.16). Pentaheptafulvalene **87** was initially considered as highly polar compound, represented by the resonance structure **88**, which consists of an aromatic cyclopentadienide anion and tropylium cation (Figure 1.16). However, from theoretical calculations and a ¹H NMR analysis, a dominantly olefinic character was identified.¹⁷⁹ This is closely related to the high reactivity of pristine **87**, especially toward D-A reactions. Nevertheless, the polarized resonance structure still contributed to the ground state electronic configuration of **87**, and one of its tetrabenzo derivatives has a dipole moment of 0.83 D, comparable with that of azulene **65**.¹⁷⁹

When pentaheptafulvalene **87** was slightly π -extended into acepleiadylene **89**, another isomer of pyrene, its nature fundamentally changed (Figure 1.16). With the presence of a highly aromatic naphthalene sub-ring, the electronic structure of **89** was better described by a naphthalene with an ethene-1,2-diyl and a 1,3-butadiene-1,4-diyl functional groups, according to a crystal structure of acepleiadylene **89** and *s*-trinitrobenzene complex.¹⁸⁰ Consequently, **89** was much more stable than pentaheptafulvalene **87**.

Further π -extension of the “naked” dislocation defects can have a drastic influence on their chemical/physical properties as well as molecular geometry. There are several remarkable

examples of π -extended (1,0) (azulene, Figure 1.17) as well as (1,1) (pentaheptafulvalene, Figure 1.18) dislocation defects. Notably, reports on syntheses of NGs with only one embedded dislocation defect are rare. This is probably due to the fact that both (1,0) and (1,1) dislocation defects are C_{2v} -symmetric, while incorporation of more dislocation defects in a single NG can lift the molecular symmetry to C_{2h} or higher.

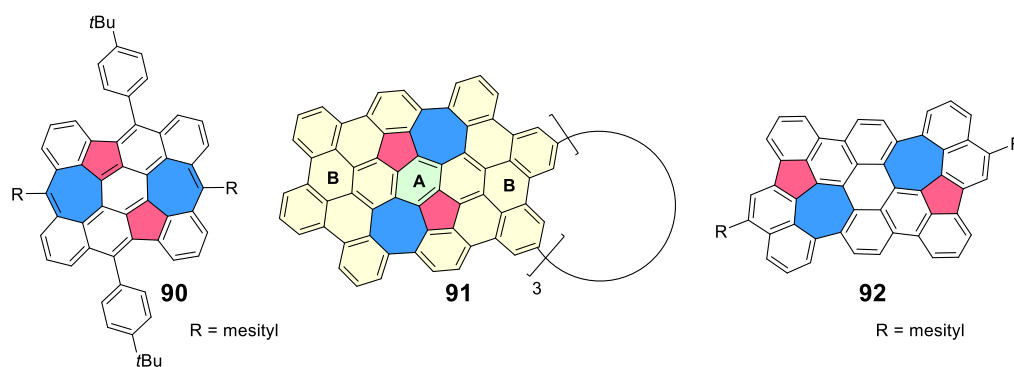


Figure 1.17 NGs with embedded (1,0) dislocation defects (structure of azulene).

■■■■, ■■■■, and our group together have recently reported on the synthesis and characterization of PAH **90** with two embedded (1,0) dislocation defects (Figure 1.17).¹⁸¹ Interestingly, similar to **76**, the *peri*-fused benzo groups delivered **90** a biradical ground state and an optical energy gap as low as 1.13 eV. Moreover, scanning tunneling spectroscopy (STS) confirmed localized states on the apical positions of the heptagons for derivatives of **90** with less substituents.^{181,182} Besides, ■■■■ and ■■■■ have recently achieved NG **91**, a cyclic trimer of a smaller NG possessing the same double embedded (1,0) dislocation defect structure as **90**, by on-surface synthesis (Figure 1.17).¹⁸³ The synthesis involved a tandem cyclodehydrogenation of a “conjoined cove” region, forming the pentagon and the heptagon in the last steps. More recently, ■■■■, ■■■■, and ■■■■ have realized **92** by a similar tandem cyclodehydrogenation reaction, but using solution synthetic protocols (Figure 1.17).¹⁸⁴ Remarkably, derivatives of NG **90** and **91**, which were synthesized on-surface, retained a rather flat conformation.^{181–183} Furthermore, from single crystal analysis of **92**, its local curvature was much smaller than that of corannulene **83** and [7]circulene **86** (Figure 1.15).¹⁸³ These geometric features highlight the counter effect of combining pentagon and heptagon, the two disclination defects with opposite influence, into a dislocation defect.

■■■■ and ■■■■ reported a facile synthesis of NG **93** starting from corannulene **83** (Figure 1.18).¹⁸⁵ The pentagon in **93** was surrounded by five heptagons, which profoundly cancelled the topological effect of the pentagon on **93**. As a result, the central corannulene adopted a

shallow bowl-shape with a bowl depth of only 0.37 Å, drastically different from pristine corannulene (0.87 Å). In addition, the five heptagons caused warped helical structures on the periphery of **93**, which hindered intermolecular interactions, and rendered its derivative a high solubility even in hexane.

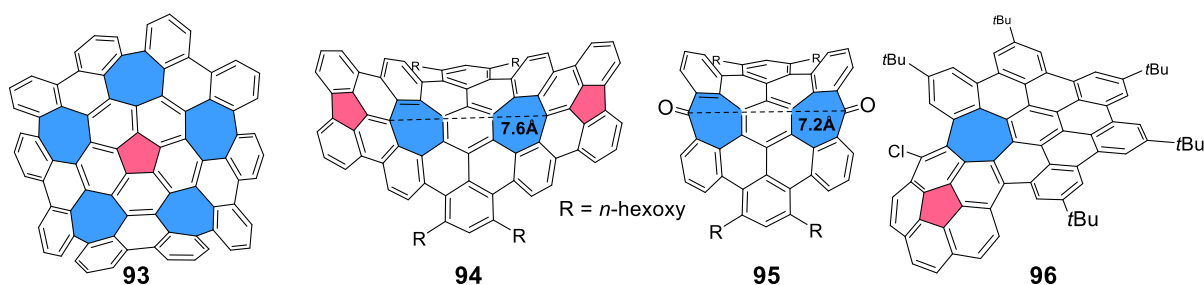


Figure 1.18 NGs with embedded (1,1) dislocation defects (structure of pentaheptafulvalene).

NG **93** can be considered as a model compound for a cluster of (1,1) dislocation defects, where every defect radially points outward. Indeed, this nonplanar warped molecule is of particular interest for nanoscience.¹⁸⁶ However, the existence of such “artificial” defects in graphene flakes is unlikely. [REDACTED], [REDACTED], and [REDACTED] reported on the synthesis of NG **94** with two embedded (1,1) dislocation defects pointing in opposite directions. The synthesis of **94** involved π -extension of an HBC analogue **95** with two heptagons in its skeleton (Figure 1.18).¹⁸⁷ In comparison to NG **93**, NG **94** could better represent the local environment of a (1,1) dislocation defect in the graphene lattice. Interestingly, both NG **94** and **95** adopt saddle shapes, with the hexagon in the structural center being the saddle point. Recently, another NG **96** has been achieved by the group of [REDACTED] (Figure 1.18).¹⁸⁸ Its synthesis employed a π -extension from monofunctionalized corannulene. NG **96** was correlated to the structure of **93**, but with only one embedded (1,1) dislocation defect.

Similar to the (1,0) dislocation defects, the (1,1) dislocation defects also help with the relaxation of local curvature induced by the two disclination defects. This effect could be proven by single crystal analysis of NG **94** and **96** (Figure 1.18). Specifically, The C-C distance of the apical carbons in the heptagons in NG **94** was 7.64 Å, while in its precursor **95** it was 7.22 Å (Figure 1.18). Moreover, it remained basically flat around the pentagons in NG **94**.¹⁸⁷ On the other hand, the bowl depth of the corannulene sub-structure in NG **96** was 0.84 Å, in between **93** and the pristine corannulene **83**.¹⁸⁸

It appears that NGs **90–92** with embedded (1,0) dislocation defects are flatter than NGs **93–96** containing (1,1) dislocation defects (Figure 1.17 and 1.18). This relates to the fact that a

(1,1) dislocation defect expand graphene lattice to a higher extent than (1,0) dislocation defect.¹³⁵ To this end, it is important to stress that none of the dislocation defect in NGs **90–96** is “fully” embedded in hexagons. That is, these dislocation defects are more or less on the periphery of the NGs. Indeed, NG with fully embedded dislocation defect is essential for a first approximation to the force field induced by dislocation defect in the graphene lattice. Thus, the structural correlation of NGs **90–96** to the real situation in graphene lattice shall be address with extra care.

Unidirectionally aligned dislocation defects, or pentagon-heptagon-pairs, can construct a graphene GB (Figure 1.10c).¹⁴³ Several NGs mentioned above provide views on possible structures at graphene GB. For example, the symmetry axis of the two (1,1) dislocation defects in NG **94** are collinear (Figure 1.18), although they point toward opposite directions, making them distinct from graphene GB. Besides, the two (1,0) dislocation defects in NG **91** can be seen as a GB loop that isolate a sub-nano grain A with a size of a benzene from the surrounding larger grain B (Figure 1.17), similar to a “graphene flower” that is often observed in the graphene lattice (Figure 1.10b). Notably, different tilting angles between grain A and grain B are clearly observed in their STM images.¹⁸³

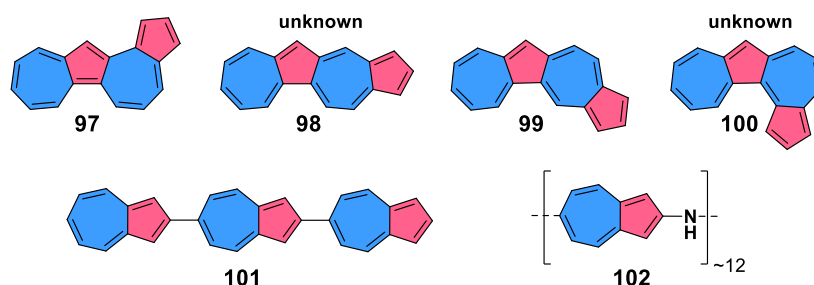


Figure 1.19 PAHs and oligoarenes relate to nanostructures at graphene GBs.

Evidenced by scanning probe microscopies, arrays of *cata*-fused alternant pentagons and heptagons dominate the nanostructure at graphene GBs (Figure 1.11).¹³⁵ However, restricted by synthetic availability, bottom-up synthesis can only offer limited insight into the chemical and physical behavior of these nanostructures. For a vivid example, only **97** and **99** out of the four isomers of *cata*-fused azulenoazulenes **97–100**, which contain alternant pentagon/heptagon skeletons, have been successfully synthesized and isolated to date (Figure 1.19).^{189,190} From spectral analysis it appeared that both **97** and **99** were photophysically and chemically similar to azulene, and the contribution of a [18]annulene resonance form was low

in their ground state electronic configurations. Besides, a further polarization of electrons to the terminal pentagon in **97** has been suggested.¹⁸⁹

Finally, it is worth mentioning that the group of [REDACTED] synthesized a series of different terazulene linked on 2,6-position of azulene, including **101**, in which azulenes are head-to-tail aligned (Figure 1.19).^{191,192} It was revealed that the ordered connection in terazulene **101** rendered it an evenly distributed LUMO over the whole molecule, which enabled a good n-type OFET performance.¹⁹¹ Moreover, DFT calculations suggested a dipole moment of 5.3 D for **101**, more than three times larger than that of azulene (1.04 D), suggesting a further polarized electronic structure. Besides, the group of [REDACTED] synthesized poly[2(6)-aminoazulene] **102**, where all the azulenylene moieties in the polymer chain were head-to-tail aligned.¹⁹³ Interestingly, unlike polyaniline, poly[2(6)-aminoazulene] **102** processed a small band gap, as a result of a more effective conjugation. Nevertheless, a synthesis of head-to-tail connected poly(2,6-azulenylene) has not been reported yet. Although such a structure was not observed at graphene GB for entropy reason,¹³⁵ it was suggested that it could construct a graphene GB nanostructure between specifically 21.8° misoriented graphene grains (Figure 1.10c). Moreover, such GB was calculated to exhibit one of the smallest formation energy and induce very little local buckling in surrounding graphene lattice.¹³⁷

1.4 Controlling assemblies of nanographenes

So far, graphene sheet has not been found in nature. In nature, graphene sheets pile up into graphite, where layers are bonded by London dispersion force, which is around 44 meV per carbon (~ 1 kcal/mol), estimated by thermal desorption of PAHs on graphite surface.^{194,195} This is not a strong force, at least in comparison with C-C bond energy within graphene layer (C-C bond energy in benzene ~ 135 kcal/mol). The anisotropic bonding in graphite is the reason why graphene can be exfoliated from it.

Graphite exists in two forms, alpha graphite and beta graphite, where the graphene layers stack in AB-type or ABC-type, respectively, to avoid carbon atoms directly staying on top of each other. This is a result of reducing electron repulsion between graphene layers. In fact, intermolecular/interlayer interactions in NGs and graphite are a balance between quadrupole-quadrupole repulsion and London dispersion force, and for small π -systems such as benzene and naphthalene, it is even arguable whether there is a favorable π - π interaction over the other London dispersion forces.¹⁹⁶ Nevertheless, it is known that total London dispersion force that could be induced between molecules is related to the polarizability and topology of molecules. Therefore, larger π -systems with increasingly polarizable π -electrons and a planar topology favor parallel-displaced intermolecular interactions. This reflects in a positive correlation between π -core size of NGs and their adhesion energy per carbon atom on graphite.^{194,195,197} The scenario is described as “ π - π stacking”, which often dominates intermolecular interaction between NG molecules.

1.4.1 Controlling 3D supramolecular assemblies of nanographenes

With an diameter just exceeding 1 nm, HBC derivatives have been employed as model compounds to gain an insight into the physical and chemical behavior of NGs.^{14,96,198} When HBC is substituted with multiple long alkyl chains, it not only enhances its solubility in organic solvents but also fundamentally alters its thermal physical behavior as bulk materials. Particularly, our group has systematically investigated the influence of various alkyl side chains with different length and structure, and revealed that mesophase behavior can be introduced to HBC with a controllable phase transition temperature and a wide phase width.^{199,200} Remarkably, although pristine HBC displays a melting point over 700 °C, by substitution of branched alkyl chains, a mesophase transition can occur lower than a room temperature.²⁰¹ Furthermore, alkyl chain substituted GQDs with π -core larger than HBC can keep a mesophase even higher than 550 °C.²⁰²

The thermal behavior of alkyl-chain-substituted HBCs can be understood by phase transition of discotic liquid crystalline (DLC) materials.²⁰⁴ Single crystal structure of pristine HBC exhibits a parallel-displaced packing because of a balance between quadrupole-quadrupole repulsion, π - π , and CH- π dispersion forces.²⁰⁵ Alky-chain-substituted HBCs retain this crystalline phase at lower temperature with nanophase separation between rigid π -cores and flexible alkyl chains. Upon heating, fluctuation of liquid-like flexible alkyl chains reinforces the nanophase separation, and HBC cores become face-to-face packing to maximize region of such phase separation.²⁰⁶ Consequently, DLC mesophase of column-like supramolecular self-assembly is formed (Figure 1.20a). This phenomenon can be easily monitored by 2D wide-angle X-ray scattering (2D WAXS).²⁰⁰ In a typical experiment, HBC materials are processed as fibers by thermal extrusion. It is found that the axial direction of columnar self-assembly is often parallel to the axial direction of the fiber. Then, such fiber can be analysis by 2D WAXS to reveal the anisotropic molecular alignment (Figure 1.20b).

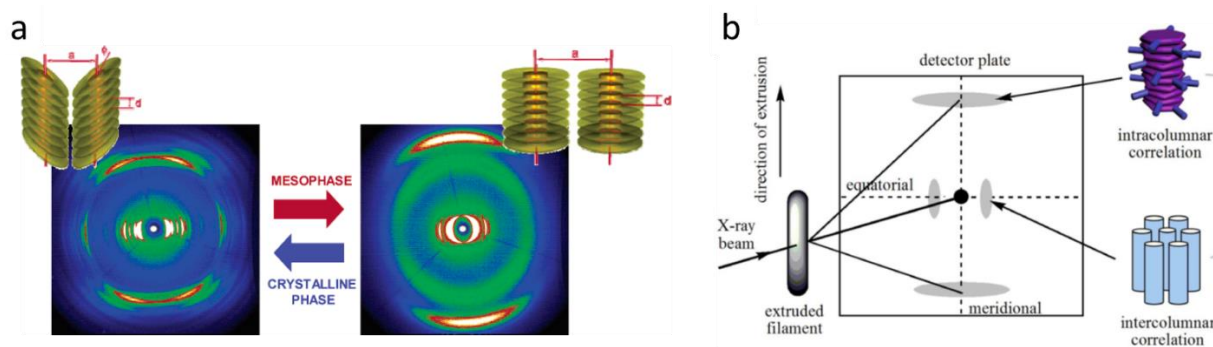


Figure 1.20 (a) Transition between crystalline phase and DLC mesophase of NGs with multiple alkyl chains and the corresponding 2D WAXS patterns. (b) Illustration of a typical 2D WAXS analysis of thermally extruded NG fiber. Reprinted with permission from (a) ref. 198, copyright: 2007, American Chemical Society; (b) ref. 203, copyright: 2012, International Union of Pure and Applied Chemistry.

Employing various functional groups onto alkyl-chain-substituted HBCs can further fine-tune their self-assembly. These functional groups introduce complementary weak force through dipole-dipole interaction, ionic interaction, hydrogen bonding, and hydrophobic effect, and control molecular orientation in columnar self-assembly as well as the DLC phase transition temperature.²⁰⁷ Notably, phenyl substituents on HBC can “lock” the intracolumnar molecular motion and lead to a helical columnar assembly, of which chirality can be controlled by additional chiral substituents.²⁰⁸ In addition, incorporating covalent bonding at DLC phase,

such as triggering polymerization of acrylate groups of HBC **103** at its DLC phase, can fix molecules into a network and avoid back-transition into crystalline phase (Figure 1.21).²⁰⁹

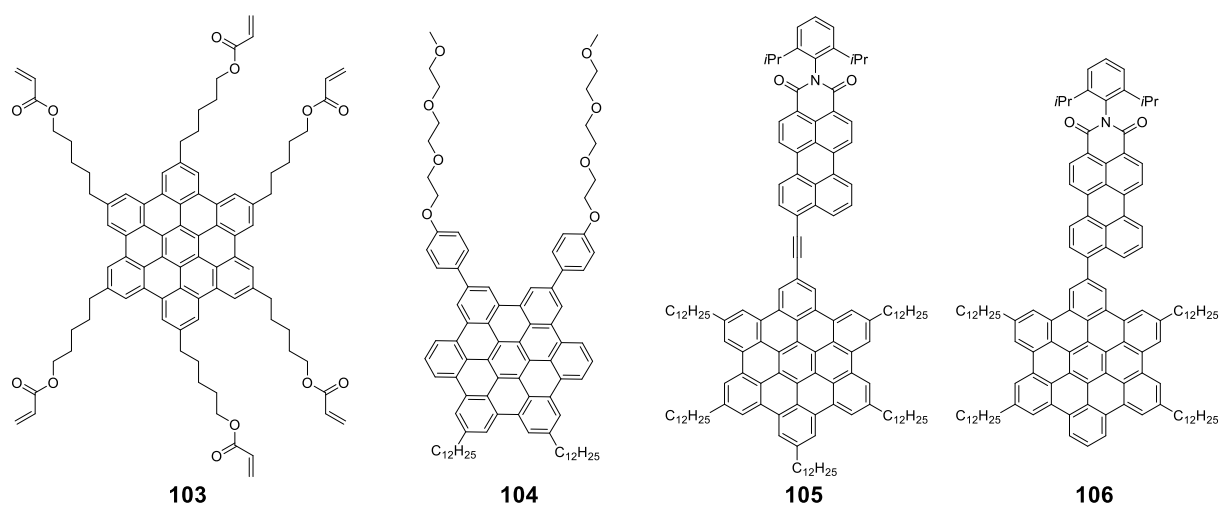


Figure 1.21 HBC derivatives with different kinds of functional group that control their 3D supramolecular assemblies.

Substitution patterns and positions also play an important role on intercolumnar organization and intracolumnar molecular orientation of the 3D assembly of HBC derivatives.²¹⁰ Notably, combining these above-mentioned concepts, the group of Aida synthesized HBC derivative **104**, which assembled into a hollow nanotube with a diameter of 20 nm in solution (Figure 1.21).²¹¹ Besides, larger π -functional groups, such as perylene monoimide (PMI) in HBC derivative **105**, can further regulate the nanomorphology by additional π - π interactions (Figure 1.21). Our group and the group of Samorì revealed that intercolumnar nanophase segregation between electron donor (HBC) and acceptor (PMI) occurred for **105** as bulk material.^{212,213} The nanophase separation led to double-channeled charge transfer (CT) pathway and ambipolar FET performance of device based on **106**.

Despite thermal responsive DLC behaviors of alkyl-substituted NGs, it will be intriguing for controlling self-assemblies of NGs by other stimuli. Yet, the use of other external stimuli has only been occasionally considered. Among different external stimuli, light is particularly attractive for a possible remote application with high spatial and temporal resolution. Notably, molecular photoswitches can isomerize between (quasi)stable states by light irradiation. Such isomerization could change the local physical/chemical environment and have an impact on molecular interaction.²¹⁴ Especially, azobenzene, exhibiting a drastic change on their geometry and polarity upon isomerization between its *trans*- and *cis*-forms, is the most widely applied moiety for photoregulated supramolecular behaviors.²¹⁵

Small PAHs such as triphenylenes have been decorated with multiple azobenzene substituents for controlling their self-assemblies in 3D.^{216,217} Interestingly, thermotropic transition between DLC and calamitic liquid crystalline phase was observed, suggesting a competition between liquid crystalline behaviors of triphenylene and azobenzene.²¹⁷ Furthermore, the phase transition temperature is controllable by adjusting light irradiation intensity, showing an effect on azobenzenes isomerization over the LC behaviors. Nevertheless, NGs with larger π -core functionalized with photoswitches are severely underexplored.

1.4.2 Controlling supramolecular assemblies of nanographenes at interfaces

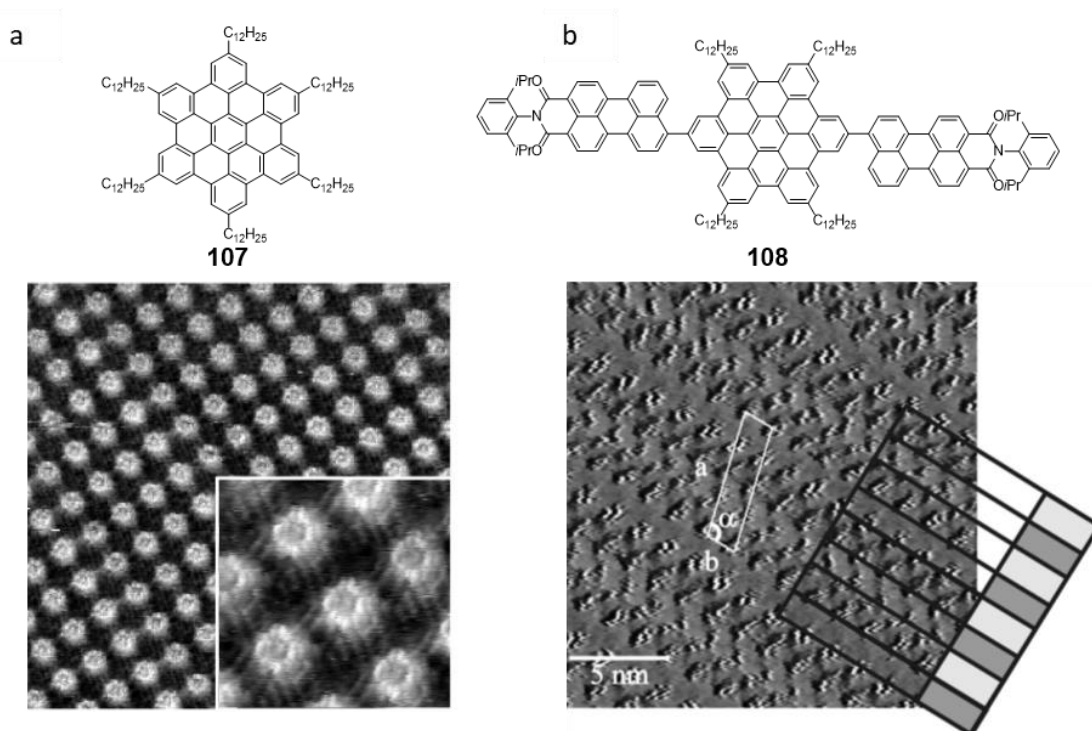
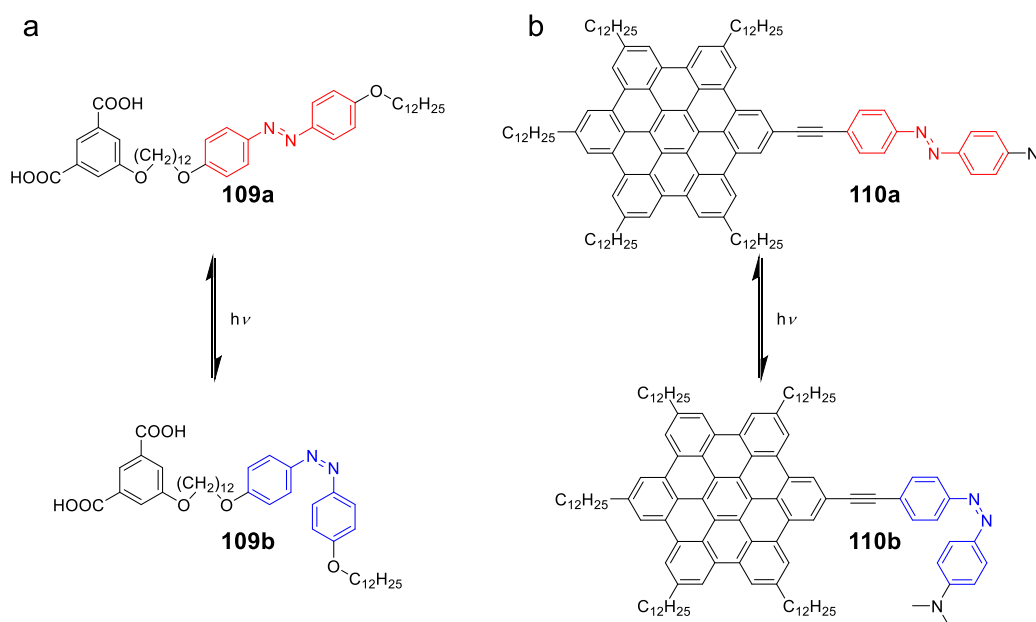


Figure 1.22 STM images of assembly of HBC derivatives (a) **107** at HPOG/*n*-tetradecane interface ($10.4 \times 10.4 \text{ nm}^2$) and (b) **108** at HOPG/TCB interface. Arrays of HBCs (light gray) and PMIs (dark gray) are indicated in (b). Reprinted with permission from (a) ref. ²²⁰, copyright: 2005, American Chemical Society; (b) ref. ²²¹, copyright: 2006, WILEY-VCH.

How molecules assemble at interfaces is important for electronic application, since it affects charge carrier injection and transport. Analysis on vacuum deposited pristine HBCs on surfaces of various substrates, including highly oriented pyrolytic graphite (HOPG), MoS₂, Au, and Cu, reveals a common “face-on” epitaxial growth of molecules.^{218,219} Considering that HBC is the smallest NG, the face-on molecular orders suggest that strong London dispersion forces are generally induced between π -electrons of NGs and flat substrates.

STM provides opportunity for molecularly or atomically precise and a quasi-time-resolved imaging. For this reason, STM is particularly useful for monitoring molecular assembly of NGs at interfaces.¹⁹⁸ For example, STM reveals that hexadodecyl-HBC **107** assembles into 2D crystal with a square unit cell at HOPG/*n*-tetradecane interface (Figure 1.22a).²²⁰ The HBC core can be differentiated from alkyl chains for a different contrast in the image.

From STM analysis of a considerable number of HBC derivatives, it has been shown that their assemblies on HOPG are highly controllable by equipping different functional groups as well as altering substitution patterns.²²² For example, in collaboration with Rabe and Samori, we investigated self-assemblies of PMI-HBC dyad **106** and PMI-HBC-PMI triad **108** at HOPG/TCB interfaces (Figure 1.21 and 1.22b).²²¹ Interestingly, unlike the behavior of its structural analog **105** in 3D, assembly of PMI-HBC dyad **106** on HOPG surface displayed rather isolated molecular organization with no intermolecular interaction between π -cores. In contrast, PMI-HBC-PMI triad **108** exhibited a nanophase segregation between electron donor (HBC) and acceptor (PMI), where PMIs packed in an “edge-on” fashion (Figure 1.22b). The edge-on packing of PMIs led to a more compact assembly of triad **108** and a surprisingly smaller occupied-area-per-molecule on HOPG in comparison with that of dyad **106**.



*Scheme 1.11 Photoisomerization between trans- and cis-forms of azobenzene-containing (a) isophthalic acid **109** and (b) HBC **110**.*

After demonstrating the tunable assemblies of NGs at HOPG/liquid interface by functionalization, the next concern is whether it is possible for remote controlling such

assemblies.²²³ In collaboration with the group of **De Schryver**, we had pioneered on investigating 2D self-assembly of azobenzene derivatives at HOPG/liquid interface.²²⁴ Azobenzene-containing isophthalic acid derivative **109** was found to form stable 2D crystals for both of its *trans*- and *cis*-isomers at HOPG/1-undecanol interface. These self-assemblies were stabilized by London dispersion force between long alkyl chains, and hydrogen bonds between molecules as well as 1-undecanol cocrystalizing on surface. Furthermore, in collaboration with the group of **Rabe**, we studied photoisomerization of azobenzene-containing HBC **110** and its self-assembly on HOPG (Scheme 1.11b).²²⁵ Unfortunately, although the *trans*-form of **110** constituted a 2D pattern at HOPG/TCB interface, no change was observed after light irradiation.

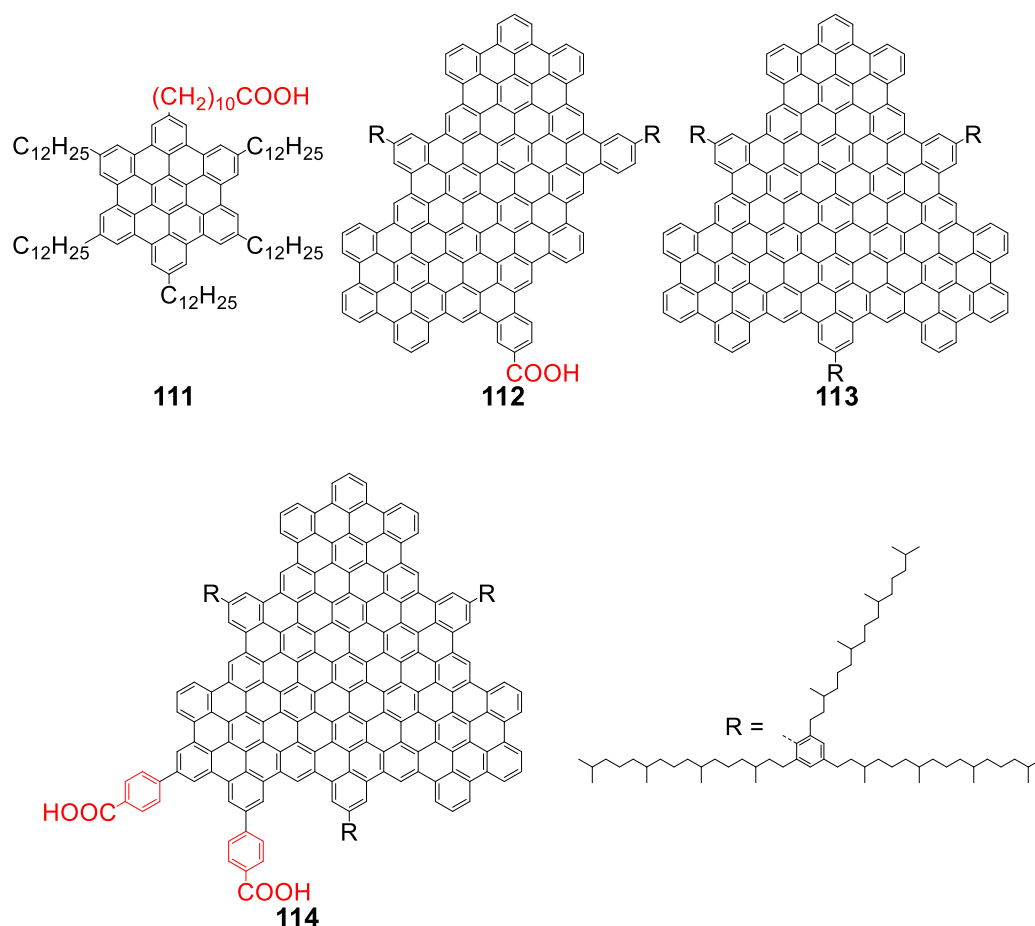


Figure 1.23 Various monodispersed GQDs with carboxyl groups.

In a device application point of view, it is essential to develop protocols that can control assembly of NGs on substrates surface beyond that of HOPG. Particularly, assembly on surface of dielectric materials, such as metal/semimetal oxide, is important for applications in OFET and OPV. In collaboration with **Bjørnholm**'s group, we investigated films of carboxyl-

group-functionalized amphiphilic HBC **111** on mica (Figure 1.23).²²⁶ From X-ray diffraction analysis, it was revealed that HBC **111** assembled in an edge-on fashion. Besides, the group of **111** synthesized a larger carboxyl-group-equipped monodispersed GQD **112** (Figure 1.23).²²⁷ Low surface-coverage film of GQD **112** on mica can be prepared by either Langmuir-Blodgett technique at water/air interface or submerging the substrate in a toluene solution of GQD **112**. From AFM film-thickness-analysis, they concluded that GQD **112** assembled as an edge-on monolayer for the chemical affinity of carboxyl group to mica surface. Interestingly, thin film of the other two monodispersed GQDs **113** and **114** with no carboxyl group or one more carboxyl group, respectively, exhibited face-on arrangement on mica (Figure 1.23). The same group also discovered that dye-sensitized solar cell using monodispersed GQD **113** and TiO₂ gave a low current density, which is attributed to a low affinity of **113** onto TiO₂ surface induced by only physisorption. It was suggested that a chemisorption could improve the performance.²²⁸

1.5 Motivation

In the *previous sections* we have witnessed that the relationship between PAHs, NGs, and graphene is a matter of length scale. Indeed, the most attractive application of graphene is next generation electronics, for its supreme carrier mobility. However, because of the very nature of graphene as zero band gap material, several applications, especially as logic device, are severely hindered. To solve this, it is necessary to resort to nanoscience.

This thesis aims for bottom-up synthesis that provides new possibilities on ultra large and non-hexagon-containing PAHs and NGs, under a frame of graphene quantization and defect engineering, respectively. Furthermore, anchoring on HBC, we also explore, by chemical functionalization, aspects related to assembly of NGs at interface as well as in bulk.

1.5.1 Synthesis of polyphenylenes as potential precursors for nanographenes approaching length scale of 5 nm

We have seen in *section 1.2* that employing both top-down and bottom-up methods can provide NGs.⁷⁰ There, we highlight that carrier mobility and band gap of NGs primarily relate to their size,⁵⁶ and a balance between a reasonable band gap and high carrier mobility could be reached at a spatial scale of 5–10 nm.^{52,54} Thus, proper fabrication technique is highly desired for producing NGs as well as their precursors confined at this scale.

We have introduced in *section 1.2.4* and *1.2.5* that GQDs and GNRs can be achieved currently with a diameter or a width up to 3 nm or 2 nm, respectively. This is still far below the desired 5–10 nm spatial scale. Thus, in *Chapter 2* and *Chapter 3*, we will engage in new synthetic approaches for dendritic and linear PPs that could potentially serve as precursors for larger GQDs and GNRs, respectively.

We have described in *section 1.2.4* our earlier attempts on synthesizing dendritic PP **26** and **27** as precursors for larger GQDs (Figure 1.7).^{100,101} However, their complete graphitization are hindered by a lower symmetry and overlap between benzene ring in 2D projection, respectively. In *Chapter 2*, we will synthesize another two dendritic PPs having 366 and 546 carbons, respectively, by divergent synthesis employing D-A reactions (Figure 1.24). Their structure will be characterized in detail by NMR and MALDI. After achieving the dendritic PPs, their graphitization reactions will be investigated by both solution-based reactions as well as surface-assisted thermal cyclodehydrogenation. An ideal complete planarization of these two PP precursors, featuring no overlap in 2D projection, could lead to D_{6h} -symmetric monodispersed GQDs with diameters approaching 4 nm and 5 nm, respectively.

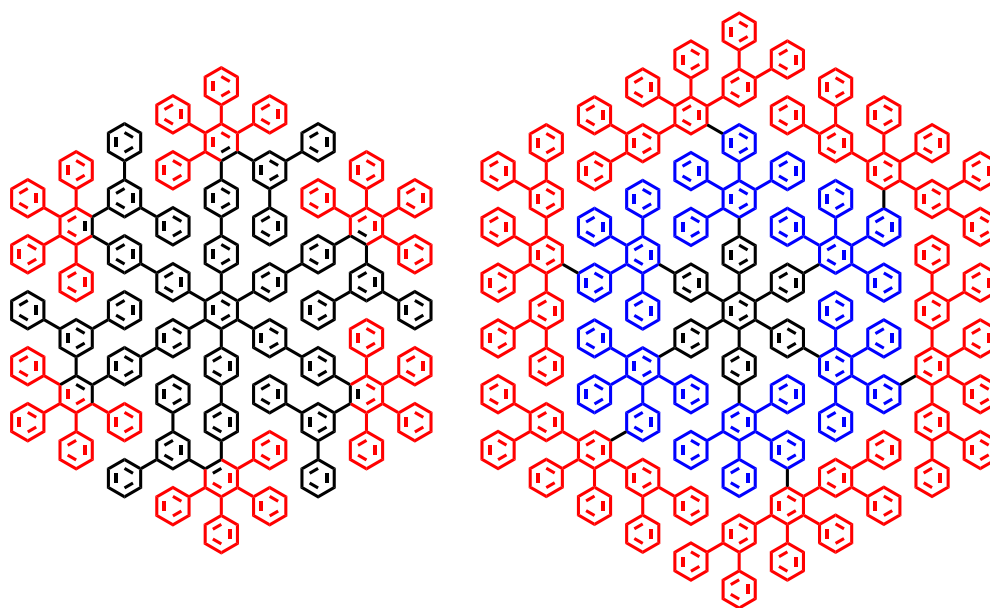


Figure 1.24 Dendritic PPs suitable as precursors for monodispersed GQDs with diameters approaching 5 nm.

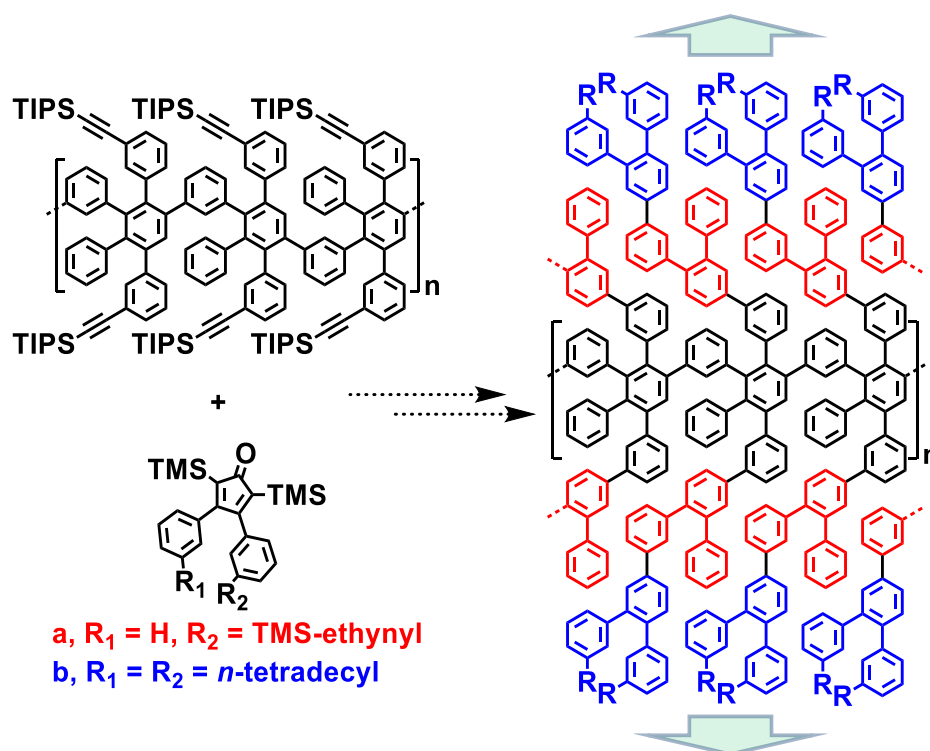


Figure 1.25 New universal synthetic protocol for synthesis of PP precursors for GNRs with customized width.

In section 1.2.5, we have highlighted synthesis of linear PPs that are suitable for bottom-up synthesis of wide GNRs. Especially, our previous approaches using AB-type D-A polymerization provide a series of PP as precursors for GNRs with increased width up to 2

nm.¹¹³ Based on these, in *Chapter 3*, we will develop another approach for lateral extension of PPs, applying two different kinds of D-A reactions (Figure 1.25). Firstly, a linear PP backbone bearing ethynyl functional groups that could react in a second D-A reaction step is synthesized by D-A polymerization. Secondly, CPs with trimethylsilyl (TMS)-protected ethynyl groups can stepwise extend the PP backbone through a sequence of D-A reactions and deprotections. This approach avoids complicated monomer design that is required for our former synthetic protocol. Furthermore, the structures of the PPs are carefully designed to exclude any benzene overlap in a 2D projection, and thus they are suitable precursors for GNRs with tailored width. Cyclodehydrogenations of the resulted PPs will also be studied.

1.5.2 Bottom-up approach for nanostructures related to graphene grain boundaries

Defect engineering can tailor properties of graphene. In particular, understanding and perhaps controlling GB is especially important, since large graphene flakes are always polycrystalline.¹³⁵ Nevertheless, unleashing the potential of GB requires synthetic methods that could precisely control its nanostructure as well as tilt angles between graphene grains. In *section 1.3*, we have described how bottom-up synthesis is employed for constructing various model compounds related to defect structures in graphene. However, it is obvious that reports are extremely rare on model structures that can be correlated to GB in graphene, despite it is in fact more important for understanding graphene.

One can envisage that model structures for graphene GB require an oligomeric or polymeric approach. Thus, solubility issues could complicate their structural characterization. Moreover, some molecular model compounds of defects in graphene already exhibit low stability.^{169,181}

It is expected that the stability of nanostructures representing GB in graphene can be even lower, since a cluster of point defects coexists. Fortunately, on-surface synthesis at UHV condition provides a “super clean” environment and opportunities for *in-situ* structural characterization at an atomic level by scanning probe microscopies (*section 1.2.3*).⁹³ Taking full advantage of this method, in collaboration with ██████’s group, we will explore in *Chapter 4* and *Chapter 5* the synthesis of polyazulenes that give an insight on graphene GB.

In *Chapter 4*, we will synthesize 2,6-diiodoazulene in solution, and study its further polymerization under UHV condition on Au (111) surface (Figure 1.26, path I). The non-negligible intrinsic dipole moment of azulene could play a guiding role during polymerization, forming 2,6-polyazulene with a possible controlled head-to-tail connection. Electronic properties of the resulted polymer will be further characterized by STS. The 2,6-polyazulene, although not experimentally observed at graphene GB, is a theoretical local minimum in an

energy profile of different GB nanostructures.¹³⁷ Besides, the polyazulene is also interesting on its own as a highly polarized nanowire.

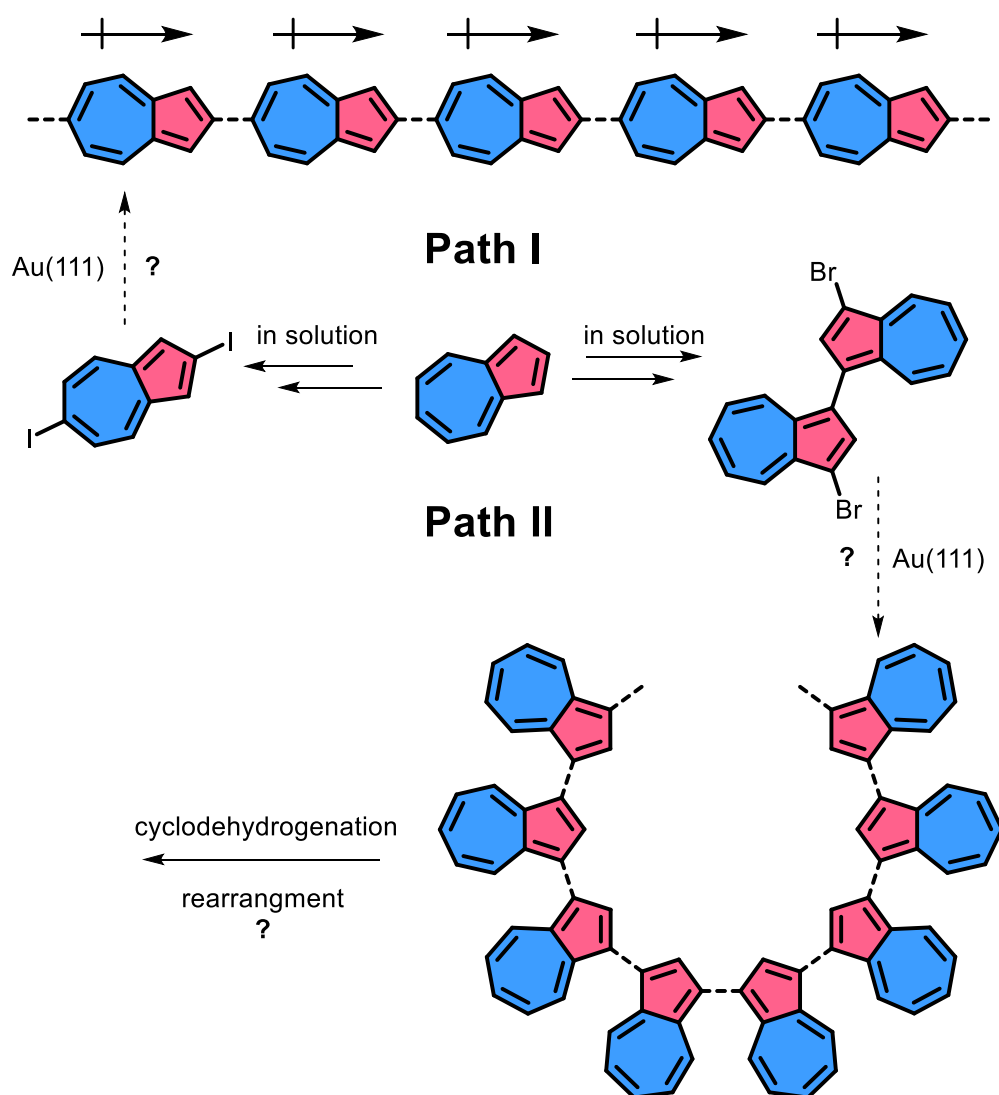


Figure 1.26 Bottom-up approach for nanostructure closely related to graphene GB.

It has been shown in *section 1.3.1* that experimentally observed graphene GB are often composed of fused pentagons-heptagon-pairs (Figure 1.11).¹³⁶ Accordingly, in *Chapter 5*, we will employ 3,3'-dibromo-1,1'-biazulene and polymerize it under UHV condition at Au(111) surface (Figure 1.26, path II). The target product 1,3-polyazulene structurally allows a further cyclodehydrogenation into planar sp^2 -carbon-nanostructure. Notably, azulene is known for isomerizing into naphthalene or indene derivatives, especially when involving radical intermediates.²²⁹ Thus, cyclodehydrogenation of 1,3-polyazulene is expected to be accompanied by skeleton rearrangement, and could possibly lead to cata-fused azulenes.

1.5.3 Exploring self-assemblies of hexa-*peri*-hexabenzocoronene derivatives

We have described in *section 1.4* the self-assembly behaviors of NGs in bulk as well as at interface. Especially, serving as the simplest NG, HBC has been widely employed as model compound for understanding supramolecular organization of NGs and exploring their applications. In *Chapter 6–8*, we will examine some aspects of assembly of chemically functionalized HBCs and their photophysical and photochemical properties.

Alkylated HBCs can have DLC behavior and specific 2D assembly patterns at HOPG/liquid interface. Such supramolecular behaviors are often thermally responsive. However, controlling the assembly of HBC derivatives by other stimuli has remained relatively unexplored. In *section 1.4.2*, we have mentioned that HBC derivative **110** with one azobenzene functional group does not change its 2D-assembly pattern at HOPG/liquid interface after light irradiation. In *Chapter 6*, we will synthesize two more symmetric HBCs decorated with one more azobenzene moiety (Figure 1.27a). We will then investigate their photoisomerization by UV-Vis absorption and NMR spectral change upon UV-irradiation. Furthermore, their 2D assemblies at HOPG/liquid interface will be examined by STM analysis coupled with *in-situ* light irradiation. The additional azobenzene could induce a pronounced local environmental change upon isomerization and enable an observable alteration on assembly patterns.

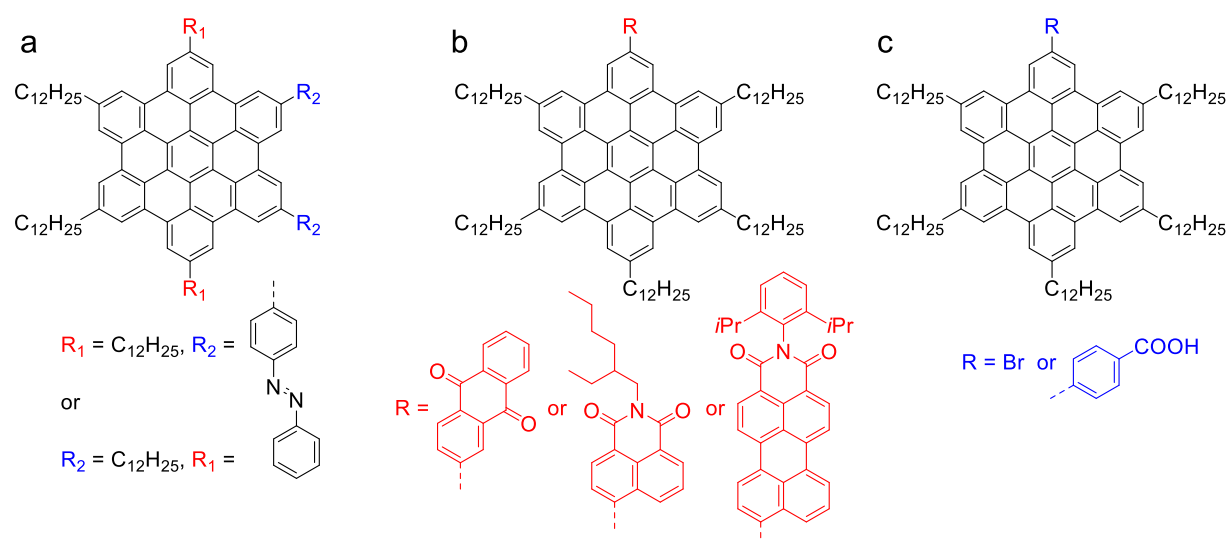


Figure 1.27 HBC functionalized with different moieties for investigation of their assemblies.

We have seen in *section 1.4* that electron withdrawing PMI groups can have a drastic effect on assemblies of HBCs in bulk as well as at interface. Accordingly, in *Chapter 7*, in

collaboration with [REDACTED], we will systematically investigate the 3D assemblies and thermal behavior of HBCs with various electron accepting functional groups (Figure 1.27b). Furthermore, since NGs have an electron-rich nature, functionalizing them with electron accepting moieties could strongly affect their electronic properties. However, there were only limited number of related works in the literatures.²³⁰ Thus, the UV-Vis absorption spectra of the corresponding HBCs will be compared. Also, two different synthetic strategies, namely “pre-functionalization” and “post-functionalization”, will be evaluated. This synthetic studies can pilot further functionalization attempts for larger NGs.¹¹⁹

We have described in *section 1.4.2* that carboxyl groups can induce edge-on chemisorption of GQDs on mica. Attempts on applying them in dye-sensitized solar cell suggest that chemisorption would enhance the performance over physisorption. Considering that there is no systematic proof for this claim, in *Chapter 8*, we will synthesize HBC derivatives with or without carboxyl group (Figure 1.27c). In collaboration with the group of [REDACTED], we will adsorb them onto metal oxide surface and compare their photoinduced CT with metal oxide by Optical pump-terahertz probe (OFTP).

1.6 References

- (1) Demming, A. King of the Elements? *Nanotechnology* **2010**, *21* (30), 300201.
- (2) Sims, R. C.; Overcash, M. R. Fate of Polynuclear Aromatic Compounds (PNAs) in Soil-Plant Systems. In *Residue Reviews*; Springer New York: New York, NY, 1983; Vol. 88, pp 1–68.
- (3) Hites, R. A.; Laflamme, R. E.; Farrington, J. W. Sedimentary Polycyclic Aromatic Hydrocarbons: The Historical Record. *Science* **1977**, *198* (4319), 829–831.
- (4) Fleming, I. *Molecular Orbitals and Organic Chemical Reactions*; John Wiley & Sons Ltd: Chichester, 2009.
- (5) Bauschlicher, C. W.; Boersma, C.; Bauschlicher, C. W.; Ricca, A.; Mattioda, A. L.; Cami, J.; Peeters, E.; De Armas, F. S.; Saborido, G. P.; Hudgins, D. M.; et al. The NASA Ames PAH IR Spectroscopic Database Version 2.00: Content, Web Site, and on(off)Line Tools. *Astrophys. Journal, Suppl. Ser.* **2014**, *211* (1), 8.
- (6) Xue, W.; Warshawsky, D. Metabolic Activation of Polycyclic and Heterocyclic Aromatic Hydrocarbons and DNA Damage: A Review. *Toxicol. Appl. Pharmacol.* **2005**, *206* (1), 73–93.
- (7) Grimmer, G.; Düvel, D. Endogenous Formation of Polycyclic Hydrocarbons in Higher Plants. 8. Carcinogenic Hydrocarbons in the Human Environment. *Z. Naturforsch. B.* **1970**, *25* (10), 1171–1175.
- (8) Scholl, R.; Seer, C.; Weitzenböck, R. Perylen, Ein Hoch Kondensierter Aromatischer Kohlenwasserstoff C₂₀H₁₂. *Berichte der Dtsch. Chem. Gesellschaft* **1910**, *43* (2), 2202–2209.
- (9) Clar, E.; Stewart, D. G. Aromatic Hydrocarbons. LXV. Triangulene Derivatives 1. *J. Am. Chem. Soc.* **1953**, *75* (11), 2667–2672.
- (10) Wang, X.-Y.; Yao, X.; Müllen, K. Polycyclic Aromatic Hydrocarbons in the Graphene Era. *Sci. China Chem.* **2019**, *62* (9), 1099–1144.
- (11) Horowitz, G. Organic Transistors. In *Organic Electronics*; Wiley-VCH Verlag GmbH & Co. KGaA: Weinheim, FRG, 2006; pp 1–32.
- (12) Anthony, J. E. Engineered Pentacenes. In *Organic Electronics*; Wiley-VCH Verlag GmbH & Co. KGaA: Weinheim, FRG, 2006; pp 58–74.
- (13) Kelley, T. High-Performance Pentacene Transistors. In *Organic Electronics*; Wiley-VCH Verlag GmbH & Co. KGaA: Weinheim, FRG, 2006; pp 33–57.
- (14) Wu, J.; Müllen, K. All-Benzenoid Polycyclic Aromatic Hydrocarbons: Synthesis, Self-Assembly and Applications in Organic Electronics. In *Carbon-Rich Compounds*; Wiley-VCH Verlag GmbH & Co. KGaA: Weinheim, FRG, 2006; pp 90–139.
- (15) Bresó-Femenia, E.; Chaudret, B.; Castellón, S. Selective Catalytic Hydrogenation of Polycyclic Aromatic Hydrocarbons Promoted by Ruthenium Nanoparticles. *Catal. Sci. Technol.* **2015**, *5* (5), 2741–2751.
- (16) Novoselov, K. S.; Geim, A. K.; Morozov, S. V.; Jiang, D.; Zhang, Y.; Dubonos, S. V.; Grigorieva, I. V.; Firsov, A. A. Electric Field in Atomically Thin Carbon Films. *Science* **2004**, *306* (5696), 666–669.
- (17) Geim, A. K.; Novoselov, K. S. The Rise of Graphene. *Nat. Mater.* **2007**, *6* (3), 183–191.
- (18) Novoselov, K. S.; Fal'ko, V. I.; Colombo, L.; Gellert, P. R.; Schwab, M. G.; Kim, K. A Roadmap for Graphene. *Nature* **2012**, *490* (7419), 192–200.
- (19) Wallace, P. R. The Band Theory of Graphite. *Phys. Rev.* **1947**, *71* (9), 622–634.
- (20) Lifshitz, E. M.; Pitaevskii, L. P. Fluctuations. In *Course of Theoretical Physics, Vol. 5, Statistical Physics, Part 1*; Landau, L. D., Lifshitz, E. M., Eds.; Pergamon Press Ltd.: Oxford, 1980; pp 333–400.
- (21) Радужевич, Л. В. О Структуре Углерода, Образующегося При Термическом Разложении Окиси Углерода На Железном Контакте. *Журнал Физической Химии* **1952**, *26*, 88–95.
- (22) Kroto, H. W.; Heath, J. R.; O'Brien, S. C.; Curl, R. F.; Smalley, R. E. C₆₀: Buckminsterfullerene. *Nature* **1985**, *318* (6042), 162–163.
- (23) Dresselhaus, M. S.; Dresselhaus, G. Intercalation Compounds of Graphite. *Adv. Phys.* **1981**, *30* (2), 139–326.

- (24) Morozov, S. V.; Novoselov, K. S.; Katsnelson, M. I.; Schedin, F.; Elias, D. C.; Jaszczak, J. A.; Geim, A. K. Giant Intrinsic Carrier Mobilities in Graphene and Its Bilayer. *Phys. Rev. Lett.* **2008**, *100* (1), 016602.
- (25) Balandin, A. A.; Ghosh, S.; Bao, W.; Calizo, I.; Teweldebrhan, D.; Miao, F.; Lau, C. N. Superior Thermal Conductivity of Single-Layer Graphene. *Nano Lett.* **2008**, *8* (3), 902–907.
- (26) Lee, C.; Wei, X.; Kysar, J. W.; Hone, J. Measurement of the Elastic Properties and Intrinsic Strength of Monolayer Graphene. *Science* **2008**, *321* (5887), 385–388.
- (27) Booth, T. J.; Blake, P.; Nair, R. R.; Jiang, D.; Hill, E. W.; Bangert, U.; Bleloch, A.; Gass, M.; Novoselov, K. S.; Katsnelson, M. I.; et al. Macroscopic Graphene Membranes and Their Extraordinary Stiffness. *Nano Lett.* **2008**, *8* (8), 2442–2446.
- (28) Wang, X.-Y.; Narita, A.; Müllen, K. Precision Synthesis versus Bulk-Scale Fabrication of Graphenes. *Nat. Rev. Chem.* **2017**, *2* (1), 0100.
- (29) Paton, K. R.; Varrla, E.; Backes, C.; Smith, R. J.; Khan, U.; O’Neill, A.; Boland, C.; Lotya, M.; Istrate, O. M.; King, P.; et al. Scalable Production of Large Quantities of Defect-Free Few-Layer Graphene by Shear Exfoliation in Liquids. *Nat. Mater.* **2014**, *13* (6), 624–630.
- (30) Hernandez, Y.; Nicolosi, V.; Lotya, M.; Blighe, F. M.; Sun, Z.; De, S.; McGovern, I. T.; Holland, B.; Byrne, M.; Gun’ko, Y. K.; et al. High-Yield Production of Graphene by Liquid-Phase Exfoliation of Graphite. *Nat. Nanotechnol.* **2008**, *3* (9), 563–568.
- (31) Ren, W.; Cheng, H. M. The Global Growth of Graphene. *Nat. Nanotechnol.* **2014**, *9* (10), 726–730.
- (32) Yang, S.; Ricciardulli, A. G.; Liu, S.; Dong, R.; Lohe, M. R.; Becker, A.; Squillaci, M. A.; Samori, P.; Müllen, K.; Feng, X. Ultrafast Delamination of Graphite into High-Quality Graphene Using Alternating Currents. *Angew. Chem. Int. Ed.* **2017**, *56* (23), 6669–6675.
- (33) Yang, S.; Brüller, S.; Wu, Z. S.; Liu, Z.; Parvez, K.; Dong, R.; Richard, F.; Samori, P.; Feng, X.; Müllen, K. Organic Radical-Assisted Electrochemical Exfoliation for the Scalable Production of High-Quality Graphene. *J. Am. Chem. Soc.* **2015**, *137* (43), 13927–13932.
- (34) Yang, S.; Lohe, M. R.; Müllen, K.; Feng, X. New-Generation Graphene from Electrochemical Approaches: Production and Applications. *Adv. Mater.* **2016**, *28* (29), 6213–6221.
- (35) Chua, C. K.; Pumera, M. Chemical Reduction of Graphene Oxide: A Synthetic Chemistry Viewpoint. *Chem. Soc. Rev.* **2014**, *43* (1), 291–312.
- (36) Eigler, S.; Enzelberger-Heim, M.; Grimm, S.; Hofmann, P.; Kroener, W.; Geworski, A.; Dotzer, C.; Röckert, M.; Xiao, J.; Papp, C.; et al. Wet Chemical Synthesis of Graphene. *Adv. Mater.* **2013**, *25* (26), 3583–3587.
- (37) Butz, B.; Dolle, C.; Halbig, C. E.; Spiecker, E.; Eigler, S. Highly Intact and Pure Oxo-Functionalized Graphene: Synthesis and Electron-Beam-Induced Reduction. *Angew. Chem. Int. Ed.* **2016**, *55* (51), 15771–15774.
- (38) Matsumoto, M.; Saito, Y.; Park, C.; Fukushima, T.; Aida, T. Ultrahigh-Throughput Exfoliation of Graphite into Pristine “single-Layer” Graphene Using Microwaves and Molecularly Engineered Ionic Liquids. *Nat. Chem.* **2015**, *7* (9), 730–736.
- (39) Voiry, D.; Fullon, R.; Lee, C.; Jeong, H. Y.; Shin, H. S.; Chhowalla, M. High-Quality Graphene via Microwave Reduction of Solution-Exfoliated Graphene Oxide. *Science* **2016**, *353* (6306), 1430–1433.
- (40) Kobayashi, T.; Bando, M.; Kimura, N.; Shimizu, K.; Kadono, K.; Umezu, N.; Miyahara, K.; Hayazaki, S.; Nagai, S.; Mizuguchi, Y.; et al. Production of a 100-m-Long High-Quality Graphene Transparent Conductive Film by Roll-to-Roll Chemical Vapor Deposition and Transfer Process. *Appl. Phys. Lett.* **2013**, *102* (2), 023112.
- (41) Hao, Y.; Bharathi, M. S.; Wang, L.; Liu, Y.; Chen, H.; Nie, S.; Wang, X.; Chou, H.; Tan, C.; Fallahzad, B.; et al. The Role of Surface Oxygen in the Growth of Large Single-Crystal Graphene on Copper. *Science* **2013**, *342* (6159), 720–723.
- (42) Jang, H.; Park, Y. J.; Chen, X.; Das, T.; Kim, M. S.; Ahn, J. H. Graphene-Based Flexible and Stretchable Electronics. *Adv. Mater.* **2016**, *28* (22), 4184–4202.

1.6 References

- (43) Chang, C. W.; Liao, Y. C. Accelerated Sedimentation Velocity Assessment for Nanowires Stabilized in a Non-Newtonian Fluid. *Langmuir* **2016**, *32* (51), 13620–13626.
- (44) Chae, H. K.; Siberio-Pérez, D. Y.; Kim, J.; Go, Y.; Eddaoudi, M.; Matzger, A. J.; O’Keeffe, M.; Yaghi, O. M. A Route to High Surface Area, Porosity and Inclusion of Large Molecules in Crystals. *Nature* **2004**, *427* (6974), 523–527.
- (45) Stoller, M. D.; Park, S.; Yanwu, Z.; An, J.; Ruoff, R. S. Graphene-Based Ultracapacitors. *Nano Lett.* **2008**, *8* (10), 3498–3502.
- (46) Garaj, S.; Hubbard, W.; Reina, A.; Kong, J.; Branton, D.; Golovchenko, J. A. Graphene as a Subnanometre Trans-Electrode Membrane. *Nature* **2010**, *467* (7312), 190–193.
- (47) Schedin, F.; Geim, A. K.; Morozov, S. V.; Hill, E. W.; Blake, P.; Katsnelson, M. I.; Novoselov, K. S. Detection of Individual Gas Molecules Adsorbed on Graphene. *Nat. Mater.* **2007**, *6* (9), 652–655.
- (48) Lin, Y.-M.; Dimitrakopoulos, C.; Jenkins, K. A.; Farmer, D. B.; Chiu, H.-Y.; Grill, A.; Avouris, P. 100-GHz Transistors from Wafer-Scale Epitaxial Graphene. *Science* **2010**, *327* (5966), 662–662.
- (49) Xia, F.; Farmer, D. B.; Lin, Y. M.; Avouris, P. Graphene Field-Effect Transistors with High on/off Current Ratio and Large Transport Band Gap at Room Temperature. *Nano Lett.* **2010**, *10* (2), 715–718.
- (50) Schwierz, F. Graphene Transistors. *Nat. Nanotechnol.* **2010**, *5* (7), 487–496.
- (51) Ponomarenko, L. A.; Schedin, F.; Katsnelson, M. I.; Yang, R.; Hill, E. W.; Novoselov, K. S.; Geim, A. K. Chaotic Dirac Billiard in Graphene Quantum Dots. *Science* **2008**, *320* (5874), 356–358.
- (52) Han, M. Y.; Özyilmaz, B.; Zhang, Y.; Kim, P. Energy Band-Gap Engineering of Graphene Nanoribbons. *Phys. Rev. Lett.* **2007**, *98* (20), 206805.
- (53) Shen, J.; Zhu, Y.; Yang, X.; Li, C. Graphene Quantum Dots: Emergent Nanolights for Bioimaging, Sensors, Catalysis and Photovoltaic Devices. *Chem. Commun.* **2012**, *48* (31), 3686–3699.
- (54) Bai, J.; Duan, X.; Huang, Y. Rational Fabrication of Graphene Nanoribbons Using a Nanowire Etch Mask. *Nano Lett.* **2009**, *9* (5), 2083–2087.
- (55) Abbas, A. N.; Liu, G.; Liu, B.; Zhang, L.; Liu, H.; Ohlberg, D.; Wu, W.; Zhou, C. Patterning, Characterization, and Chemical Sensing Applications of Graphene Nanoribbon Arrays Down to 5 Nm Using Helium Ion Beam Lithography. *ACS Nano* **2014**, *8* (2), 1538–1546.
- (56) Fischer, M. M.; de Sousa, L. E.; Luiz e Castro, L.; Ribeiro, L. A.; de Sousa, R. T.; Magela e Silva, G.; de Oliveira Neto, P. H. Effective Mass of Quasiparticles in Armchair Graphene Nanoribbons. *Sci. Rep.* **2019**, *9* (1), 17990.
- (57) Hwang, W. S.; Tahy, K.; Li, X.; Xing, H. (Grace); Seabaugh, A. C.; Sung, C. Y.; Jena, D. Transport Properties of Graphene Nanoribbon Transistors on Chemical-Vapor-Deposition Grown Wafer-Scale Graphene. *Appl. Phys. Lett.* **2012**, *100* (20), 203107.
- (58) Wei, D.; Xie, L.; Lee, K. K.; Hu, Z.; Tan, S.; Chen, W.; Sow, C. H.; Chen, K.; Liu, Y.; Wee, A. T. S. Controllable Unzipping for Intramolecular Junctions of Graphene Nanoribbons and Single-Walled Carbon Nanotubes. *Nat. Commun.* **2013**, *4* (1), 1374.
- (59) Abramova, V.; Slesarev, A. S.; Tour, J. M. Meniscus-Mask Lithography for Narrow Graphene Nanoribbons. *ACS Nano* **2013**, *7* (8), 6894–6898.
- (60) Min, S. Y.; Kim, T. S.; Kim, B. J.; Cho, H.; Noh, Y. Y.; Yang, H.; Cho, J. H.; Lee, T. W. Large-Scale Organic Nanowire Lithography and Electronics. *Nat. Commun.* **2013**, *4* (1), 1773.
- (61) Son, J. G.; Son, M.; Moon, K. J.; Lee, B. H.; Myoung, J. M.; Strano, M. S.; Ham, M. H.; Ross, C. A. Sub-10 Nm Graphene Nanoribbon Array Field-Effect Transistors Fabricated by Block Copolymer Lithography. *Adv. Mater.* **2013**, *25* (34), 4723–4728.
- (62) Yu, W. J.; Duan, X. Tunable Transport Gap in Narrow Bilayer Graphene Nanoribbons. *Sci. Rep.* **2013**, *3* (1), 1248.
- (63) Li, X.; Wang, X.; Zhang, L.; Lee, S.; Dai, H. Chemically Derived, Ultrasoft Graphene Nanoribbon Semiconductors. *Science* **2008**, *319* (5867), 1229–1232.

- (64) Jiao, L.; Wang, X.; Diankov, G.; Wang, H.; Dai, H. Facile Synthesis of High-Quality Graphene Nanoribbons. *Nat. Nanotechnol.* **2010**, *5* (5), 321–325.
- (65) Wang, X.; Dai, H. Etching and Narrowing of Graphene from the Edges. *Nat. Chem.* **2010**, *2* (8), 661–665.
- (66) Kato, T.; Hatakeyama, R. Site- and Alignment-Controlled Growth of Graphene Nanoribbons from Nickel Nanobars. *Nat. Nanotechnol.* **2012**, *7* (10), 651–656.
- (67) Martin-Fernandez, I.; Wang, D.; Zhang, Y. Direct Growth of Graphene Nanoribbons for Large-Scale Device Fabrication. *Nano Lett.* **2012**, *12* (12), 6175–6179.
- (68) Sprinkle, M.; Ruan, M.; Hu, Y.; Hankinson, J.; Rubio-Roy, M.; Zhang, B.; Wu, X.; Berger, C.; de Heer, W. A. Scalable Templated Growth of Graphene Nanoribbons on SiC. *Nat. Nanotechnol.* **2010**, *5* (10), 727–731.
- (69) Jacobberger, R. M.; Kiraly, B.; Fortin-Deschenes, M.; Levesque, P. L.; McElhinny, K. M.; Brady, G. J.; Rojas Delgado, R.; Singha Roy, S.; Mannix, A.; Lagally, M. G.; et al. Direct Oriented Growth of Armchair Graphene Nanoribbons on Germanium. *Nat. Commun.* **2015**, *6* (1), 8006.
- (70) Xu, W.; Lee, T. W. Recent Progress in Fabrication Techniques of Graphene Nanoribbons. *Mater. Horizons* **2016**, *3* (3), 186–207.
- (71) Samor, P.; Severin, N.; Simpson, C. D.; Müllen, K.; Rabe, J. P. Epitaxial Composite Layers of Electron Donors and Acceptors from Very Large Polycyclic Aromatic Hydrocarbons. *J. Am. Chem. Soc.* **2002**, *124* (32), 9454–9457.
- (72) Beser, U.; Kastler, M.; Maghsoumi, A.; Wagner, M.; Castiglioni, C.; Tommasini, M.; Narita, A.; Feng, X.; Müllen, K. A C216-Nanographene Molecule with Defined Cavity as Extended Coronoid. *J. Am. Chem. Soc.* **2016**, *138* (13), 4322–4325.
- (73) Chen, Q.; Brambilla, L.; Daukiya, L.; Mali, K. S.; De Feyter, S.; Tommasini, M.; Müllen, K.; Narita, A. Synthesis of Triply Fused Porphyrin-Nanographene Conjugates. *Angew. Chem. Int. Ed.* **2018**, *57* (35), 11233–11237.
- (74) Konishi, A.; Hirao, Y.; Matsumoto, K.; Kurata, H.; Kishi, R.; Shigeta, Y.; Nakano, M.; Tokunaga, K.; Kamada, K.; Kubo, T. Synthesis and Characterization of Quarteranthene: Elucidating the Characteristics of the Edge State of Graphene Nanoribbons at the Molecular Level. *J. Am. Chem. Soc.* **2013**, *135* (4), 1430–1437.
- (75) Clar, E.; Ironside, C. T. Hexabenzocoronene. *Proc. Chem. Soc.* **1958**, 150.
- (76) Hyatt, J. A. Synthesis of a Hexaalkynylhexaphenylbenzene. *Org. Prep. Proced. Int.* **1991**, *23* (4), 460–463.
- (77) Feng, X.; Pisula, W.; Kudernac, T.; Wu, D.; Zhi, L.; De Feyter, S.; Müllen, K. Controlled Self-Assembly of C3-Symmetric Hexa-Peri- Hexabenzocoronenes with Alternating Hydrophilic and Hydrophobic Substituents in Solution, in the Bulk, and on a Surface. *J. Am. Chem. Soc.* **2009**, *131* (12), 4439–4448.
- (78) Yang, X.; Dou, X.; Müllen, K. Efficient Synthesis of Symmetrically and Unsymmetrically Substituted Hexaphenylbenzene Analogues by Suzuki-Miyaura Coupling Reactions. *Chem. - An Asian J.* **2008**, *3* (4), 759–766.
- (79) Feng, X.; Pisula, W.; Müllen, K. Large Polycyclic Aromatic Hydrocarbons: Synthesis and Discotic Organization. *Pure Appl. Chem.* **2009**, *81* (12), 2203–2224.
- (80) Müller, M.; Kübel, C.; Müllen, K. Giant Polycyclic Aromatic Hydrocarbons. *Chem. - A Eur. J.* **1998**, *4* (11), 2099–2109.
- (81) Rempala, P.; Kroulik, J.; King, B. T. Investigation of the Mechanism of the Intramolecular Scholl Reaction of Contiguous Phenylbenzenes. *J. Org. Chem.* **2006**, *71* (14), 5067–5081.
- (82) Stabel, A.; Herwig, P.; Müllen, K.; Rabe, J. P. Diodelike Current–Voltage Curves for a Single Molecule–Tunneling Spectroscopy with Submolecular Resolution of an Alkylated, Peri-Condensed Hexabenzocoronene. *Angew. Chem. Int. Ed.* **1995**, *34* (15), 1609–1611.
- (83) Zhai, L.; Shukla, R.; Rathore, R. Oxidative C–C Bond Formation (Scholl Reaction) with DDQ as an Efficient and Easily Recyclable Oxidant. *Org. Lett.* **2009**, *11* (15), 3474–3477.
- (84) Scholl, R.; Mansfeld, J. Meso-Benzdianthron (Helianthron), Meso-Naphthodianthron, Und Ein Neuer Weg Zum Flavanthren. *Berichte der Dtsch. Chem. Gesellschaft* **1910**, *43* (2), 1734–1746.
- (85) Grzybowski, M.; Skonieczny, K.; Butenschön, H.; Gryko, D. T. Comparison of Oxidative Aromatic Coupling and

1.6 References

- the Scholl Reaction. *Angew. Chem. Int. Ed.* **2013**, *52* (38), 9900–9930.
- (86) Zhai, L.; Shukla, R.; Wadumethrige, S. H.; Rathore, R. Probing the Arenium-Ion (Proton Transfer) versus the Cation-Radical (Electron Transfer) Mechanism of Scholl Reaction Using DDQ as Oxidant. *J. Org. Chem.* **2010**, *75* (14), 4748–4760.
- (87) Ajaz, A.; McLaughlin, E. C.; Skraba, S. L.; Thamam, R.; Johnson, R. P. Phenyl Shifts in Substituted Arenes via Ipso Arenium Ions. *J. Org. Chem.* **2012**, *77* (21), 9487–9495.
- (88) Dötz, F.; Brand, J. D.; Ito, S.; Gherghel, L.; Müllen, K. Synthesis of Large Polycyclic Aromatic Hydrocarbons: Variation of Size and Periphery. *J. Am. Chem. Soc.* **2000**, *122* (32), 7707–7717.
- (89) Müller, M.; Iyer, V. S.; Kübel, C.; Enkelmann, V.; Müllen, K. Polycyclic Aromatic Hydrocarbons by Cyclodehydrogenation and Skeletal Rearrangement of Oligophenylenes. *Angew. Chem. Int. Ed.* **1997**, *36* (15), 1607–1610.
- (90) Feng, X.; Wu, J.; Enkelmann, V.; Müllen, K. Hexa-Peri-Hexabenzocoronenes by Efficient Oxidative Cyclodehydrogenation: The Role of the Oligophenylene Precursors. *Org. Lett.* **2006**, *8* (6), 1145–1148.
- (91) Cai, J.; Ruffieux, P.; Jaafar, R.; Bieri, M.; Braun, T.; Blankenburg, S.; Muoth, M.; Seitsonen, A. P.; Saleh, M.; Feng, X.; et al. Atomically Precise Bottom-up Fabrication of Graphene Nanoribbons. *Nature* **2010**, *466* (7305), 470–473.
- (92) Treier, M.; Pignedoli, C. A.; Laino, T.; Rieger, R.; Müllen, K.; Passerone, D.; Fasel, R. Surface-Assisted Cyclodehydrogenation Provides a Synthetic Route towards Easily Processable and Chemically Tailored Nanographenes. *Nat. Chem.* **2011**, *3* (1), 61–67.
- (93) Sun, Q.; Zhang, R.; Qiu, J.; Liu, R.; Xu, W. On-Surface Synthesis of Carbon Nanostructures. *Adv. Mater.* **2018**, *30* (17), 1705630.
- (94) Cai, J.; Ruffieux, P.; Jaafar, R.; Bieri, M.; Braun, T.; Blankenburg, S.; Muoth, M.; Seitsonen, A. P.; Saleh, M.; Feng, X.; et al. Atomically Precise Bottom-up Fabrication of Graphene Nanoribbons. *Nature* **2010**, *466* (7305), 470–473.
- (95) Iyer, V. S.; Wehmeier, M.; Brand, J. D.; Keegstra, M. A.; Müllen, K. From Hexa-Peri-Hexabenzocoronene to “Superacenes.” *Angew. Chem. Int. Ed.* **1997**, *36* (15), 1604–1607.
- (96) Watson, M. D.; Fechtenkötter, A.; Müllen, K. Big Is Beautiful—“Aromaticity” Revisited from the Viewpoint of Macromolecular and Supramolecular Benzene Chemistry. *Chem. Rev.* **2001**, *101* (5), 1267–1300.
- (97) Simpson, C. Nanoscale Polycyclic Aromatic Hydrocarbons - Synthesis and Characterization, Johannes Gutenberg-Universität, Mainz, 2003.
- (98) Simpson, C. D.; Brand, J. D.; Berresheim, A. J.; Przybilla, L.; Räder, H. J.; Müllen, K. Synthesis of a Giant 222 Carbon Graphite Sheet. *Chem. - A Eur. J.* **2002**, *8* (6), 1424–1429.
- (99) Przybilla, L.; Brand, J.-D.; Yoshimura, K.; Räder, H. J.; Müllen, K. MALDI-TOF Mass Spectrometry of Insoluble Giant Polycyclic Aromatic Hydrocarbons by a New Method of Sample Preparation. *Anal. Chem.* **2000**, *72* (19), 4591–4597.
- (100) Simpson, C. D.; Mattersteig, G.; Martin, K.; Gherghel, L.; Bauer, R. E.; Räder, H. J.; Müllen, K. Nanosized Molecular Propellers by Cyclodehydrogenation of Polyphenylene Dendrimers. *J. Am. Chem. Soc.* **2004**, *126* (10), 3139–3147.
- (101) Dössel, L. Nanographene Als Funktionale Materialien Und Synthetische Herausforderung, Johannes Gutenberg-Universität, Mainz, 2011.
- (102) Wasserfallen, D. Synthetical Engineering of Supramolecular Properties of Large Polycyclic Aromatic Hydrocarbons, Johannes Gutenberg-Universität, Mainz, 2006.
- (103) Narita, A.; Feng, X.; Hernandez, Y.; Jensen, S. A.; Bonn, M.; Yang, H.; Verzhbitskiy, I. A.; Casiraghi, C.; Hansen, M. R.; Koch, A. H. R.; et al. Synthesis of Structurally Well-Defined and Liquid-Phase-Processable Graphene Nanoribbons. *Nat. Chem.* **2014**, *6* (2), 126–132.
- (104) Yang, X.; Dou, X.; Rouhanipour, A.; Zhi, L.; Räder, H. J.; Müllen, K. Two-Dimensional Graphene Nanoribbons. *J. Am. Chem. Soc.* **2008**, *130* (13), 4216–4217.

- (105) Wu, J.; Gherghel, L.; Watson, M. D.; Li, J.; Wang, Z.; Simpson, C. D.; Kolb, U.; Müllen, K. From Branched Polyphenylenes to Graphite Ribbons. *Macromolecules* **2003**, *36* (19), 7082–7089.
- (106) Li, G.; Yoon, K.-Y.; Zhong, X.; Zhu, X.; Dong, G. Efficient Bottom-Up Preparation of Graphene Nanoribbons by Mild Suzuki-Miyaura Polymerization of Simple Triaryl Monomers. *Chem. - A Eur. J.* **2016**, *22* (27), 9116–9120.
- (107) Talirz, L.; Söde, H.; Dumslaff, T.; Wang, S.; Sanchez-Valencia, J. R.; Liu, J.; Shinde, P.; Pignedoli, C. A.; Liang, L.; Meunier, V.; et al. On-Surface Synthesis and Characterization of 9-Atom Wide Armchair Graphene Nanoribbons. *ACS Nano* **2017**, *11* (2), 1380–1388.
- (108) Basagni, A.; Sedona, F.; Pignedoli, C. A.; Cattelan, M.; Nicolas, L.; Casarin, M.; Sambri, M. Molecules–Oligomers–Nanowires–Graphene Nanoribbons: A Bottom-Up Stepwise On-Surface Covalent Synthesis Preserving Long-Range Order. *J. Am. Chem. Soc.* **2015**, *137* (5), 1802–1808.
- (109) Jordan, R. S.; Wang, Y.; McCurdy, R. D.; Yeung, M. T.; Marsh, K. L.; Khan, S. I.; Kaner, R. B.; Rubin, Y. Synthesis of Graphene Nanoribbons via the Topochemical Polymerization and Subsequent Aromatization of a Diacetylene Precursor. *Chem* **2016**, *1* (1), 78–90.
- (110) Abdurakhmanova, N.; Amsharov, N.; Stepanow, S.; Jansen, M.; Kern, K.; Amsharov, K. Synthesis of Wide Atomically Precise Graphene Nanoribbons from Para-Oligophenylene Based Molecular Precursor. *Carbon* **2014**, *77*, 1187–1190.
- (111) El Gemayel, M.; Narita, A.; Dössel, L. F.; Sundaram, R. S.; Kiersnowski, A.; Pisula, W.; Hansen, M. R.; Ferrari, A. C.; Orgiu, E.; Feng, X.; et al. Graphene Nanoribbon Blends with P3HT for Organic Electronics. *Nanoscale* **2014**, *6* (12), 6301–6314.
- (112) Yazyev, O. V. A Guide to the Design of Electronic Properties of Graphene Nanoribbons. *Acc. Chem. Res.* **2013**, *46* (10), 2319–2328.
- (113) Hou, I. C. Y.; Hu, Y.; Narita, A.; Müllen, K. Diels-Alder Polymerization: A Versatile Synthetic Method toward Functional Polyphenylenes, Ladder Polymers and Graphene Nanoribbons. *Polym. J.* **2018**, *50* (1), 3–20.
- (114) Narita, A.; Verzhbitskiy, I. A.; Frederickx, W.; Mali, K. S.; Jensen, S. A.; Hansen, M. R.; Bonn, M.; De Feyter, S.; Casiraghi, C.; Feng, X.; et al. Bottom-up Synthesis of Liquid-Phase-Processable Graphene Nanoribbons with near-Infrared Absorption. *ACS Nano* **2014**, *8* (11), 11622–11630.
- (115) Hu, Y.; Xie, P.; De Corato, M.; Ruini, A.; Zhao, S.; Meggendorfer, F.; Straasø, L. A.; Rondin, L.; Simon, P.; Li, J.; et al. Bandgap Engineering of Graphene Nanoribbons by Control over Structural Distortion. *J. Am. Chem. Soc.* **2018**, *140* (25), 7803–7809.
- (116) Osella, S.; Narita, A.; Schwab, M. G.; Hernandez, Y.; Feng, X.; Müllen, K.; Beljonne, D. Graphene Nanoribbons as Low Band Gap Donor Materials for Organic Photovoltaics: Quantum Chemical Aided Design. *ACS Nano* **2012**, *6* (6), 5539–5548.
- (117) Forero-Martinez, N. C.; Baumeier, B.; Kremer, K. Backbone Chemical Composition and Monomer Sequence Effects on Phenylene Polymer Persistence Lengths. *Macromolecules* **2019**, *52* (14), 5307–5316.
- (118) Abbas, A. N.; Liu, G.; Narita, A.; Orosco, M.; Feng, X.; Müllen, K.; Zhou, C. Deposition, Characterization, and Thin-Film-Based Chemical Sensing of Ultra-Long Chemically Synthesized Graphene Nanoribbons. *J. Am. Chem. Soc.* **2014**, *136* (21), 7555–7558.
- (119) Keerthi, A.; Radha, B.; Rizzo, D.; Lu, H.; Diez Cabanes, V.; Hou, I. C. Y.; Beljonne, D.; Cornil, J.; Casiraghi, C.; Baumgarten, M.; et al. Edge Functionalization of Structurally Defined Graphene Nanoribbons for Modulating the Self-Assembled Structures. *J. Am. Chem. Soc.* **2017**, *139* (46), 16454–16457.
- (120) Slota, M.; Keerthi, A.; Myers, W. K.; Tretyakov, E.; Baumgarten, M.; Ardavan, A.; Sadeghi, H.; Lambert, C. J.; Narita, A.; Müllen, K.; et al. Magnetic Edge States and Coherent Manipulation of Graphene Nanoribbons. *Nature* **2018**, *557* (7707), 691–695.
- (121) Yano, Y.; Mitoma, N.; Matsushima, K.; Wang, F.; Matsui, K.; Takakura, A.; Miyauchi, Y.; Ito, H.; Itami, K. Living Annulative π -Extension Polymerization for Graphene Nanoribbon Synthesis. *Nature* **2019**, *571* (7765), 387–392.

1.6 References

- (122) von Kugelgen, S.; Piskun, I.; Griffin, J. H.; Eckdahl, C. T.; Jarenwattananon, N. N.; Fischer, F. R. Templated Synthesis of End-Functionalized Graphene Nanoribbons through Living Ring-Opening Alkyne Metathesis Polymerization. *J. Am. Chem. Soc.* **2019**, *141* (28), 11050–11058.
- (123) Yoon, K. Y.; Dong, G. Liquid-Phase Bottom-up Synthesis of Graphene Nanoribbons. *Mater. Chem. Front.* **2020**, *4* (1), 29–45.
- (124) Zscheschang, U.; Klauk, H.; Müller, I. B.; Strudwick, A. J.; Hintermann, T.; Schwab, M. G.; Narita, A.; Feng, X.; Müllen, K.; Weitz, R. T. Electrical Characteristics of Field-Effect Transistors Based on Chemically Synthesized Graphene Nanoribbons. *Adv. Electron. Mater.* **2015**, *1* (3), 1400010.
- (125) Banhart, F.; Kotakoski, J.; Krasheninnikov, A. V. Structural Defects in Graphene. *ACS Nano* **2011**, *5* (1), 26–41.
- (126) Krasheninnikov, A. V.; Lehtinen, P. O.; Foster, A. S.; Nieminen, R. M. Bending the Rules: Contrasting Vacancy Energetics and Migration in Graphite and Carbon Nanotubes. *Chem. Phys. Lett.* **2006**, *418* (1–3), 132–136.
- (127) Kotakoski, J.; Krasheninnikov, A. V.; Kaiser, U.; Meyer, J. C. From Point Defects in Graphene to Two-Dimensional Amorphous Carbon. *Phys. Rev. Lett.* **2011**, *106* (10), 105505.
- (128) Wales, D. J.; Stone, A. J. Theoretical Studies Of Icosahedral C60 And Some Related Species. *Chem. Phys. Lett.* **1986**, *128* (5), 501–503.
- (129) Meyer, J. C.; Kisielowski, C.; Erni, R.; Rossell, M. D.; Crommie, M. F.; Zettl, A. Direct Imaging of Lattice Atoms and Topological Defects in Graphene Membranes. *Nano Lett.* **2008**, *8* (11), 3582–3586.
- (130) Lusk, M. T.; Carr, L. D. Nanoengineering Defect Structures on Graphene. *Phys. Rev. Lett.* **2008**, *100* (17), 175503.
- (131) Schmalz, T. G.; Seitz, W. A.; Klein, D. J.; Hite, G. E. Elemental Carbon Cages. *J. Am. Chem. Soc.* **1988**, *110* (4), 1113–1127.
- (132) Maier, K.; Peo, M.; Saile, B.; Schaefer, H. E.; Seeger, A. High-Temperature Positron Annihilation and Vacancy Formation in Refractory Metals. *Philos. Mag. A* **1979**, *40* (5), 701–728.
- (133) Li, L.; Reich, S.; Robertson, J. Defect Energies of Graphite: Density-Functional Calculations. *Phys. Rev. B* **2005**, *72* (18), 184109.
- (134) Li, X.; Cai, W.; An, J.; Kim, S.; Nah, J.; Yang, D.; Piner, R.; Velamakanni, A.; Jung, I.; Tutuc, E.; et al. Large-Area Synthesis of High-Quality and Uniform Graphene Films on Copper Foils. *Science* **2009**, *324* (5932), 1312–1314.
- (135) Yazyev, O. V.; Chen, Y. P. Polycrystalline Graphene and Other Two-Dimensional Materials. *Nat. Nanotechnol.* **2014**, *9* (10), 755–767.
- (136) Huang, P. Y.; Ruiz-Vargas, C. S.; Van Der Zande, A. M.; Whitney, W. S.; Levendorf, M. P.; Kevek, J. W.; Garg, S.; Alden, J. S.; Hustedt, C. J.; Zhu, Y.; et al. Grains and Grain Boundaries in Single-Layer Graphene Atomic Patchwork Quilts. *Nature* **2011**, *469* (7330), 389–392.
- (137) Yazyev, O. V.; Louie, S. G. Topological Defects in Graphene: Dislocations and Grain Boundaries. *Phys. Rev. B* **2010**, *81* (19), 195420.
- (138) Lehtinen, O.; Kurasch, S.; Krasheninnikov, A. V.; Kaiser, U. Atomic Scale Study of the Life Cycle of a Dislocation in Graphene from Birth to Annihilation. *Nat. Commun.* **2013**, *4* (1), 2098.
- (139) Cockayne, E.; Rutter, G. M.; Guisinger, N. P.; Crain, J. N.; First, P. N.; Stroschio, J. A. Grain Boundary Loops in Graphene. *Phys. Rev. B* **2011**, *83* (19), 195425.
- (140) Lahiri, J.; Lin, Y.; Bozkurt, P.; Oleynik, I. I.; Batzill, M. An Extended Defect in Graphene as a Metallic Wire. *Nat. Nanotechnol.* **2010**, *5* (5), 326–329.
- (141) Zhang, Z.; Yang, Y.; Xu, F.; Wang, L.; Yakobson, B. I. Unraveling the Sinuous Grain Boundaries in Graphene. *Adv. Funct. Mater.* **2015**, *25* (3), 367–373.
- (142) Yu, Q.; Jauregui, L. A.; Wu, W.; Colby, R.; Tian, J.; Su, Z.; Cao, H.; Liu, Z.; Pandey, D.; Wei, D.; et al. Control and Characterization of Individual Grains and Grain Boundaries in Graphene Grown by Chemical Vapour Deposition. *Nat. Mater.* **2011**, *10* (6), 443–449.
- (143) Yazyev, O. V.; Louie, S. G. Electronic Transport in Polycrystalline Graphene. *Nat. Mater.* **2010**, *9* (10), 806–809.

- (144) Chen, J.-H.; Autès, G.; Alem, N.; Gargiulo, F.; Gautam, A.; Linck, M.; Kisielowski, C.; Yazyev, O. V.; Louie, S. G.; Zettl, A. Controlled Growth of a Line Defect in Graphene and Implications for Gate-Tunable Valley Filtering. *Phys. Rev. B* **2014**, *89* (12), 121407.
- (145) Balasubramanian, K.; Biswas, T.; Ghosh, P.; Suran, S.; Mishra, A.; Mishra, R.; Sachan, R.; Jain, M.; Varma, M.; Pratap, R.; et al. Reversible Defect Engineering in Graphene Grain Boundaries. *Nat. Commun.* **2019**, *10* (1), 1090.
- (146) Lee, G. H.; Cooper, R. C.; An, S. J.; Lee, S.; Van Der Zande, A.; Petrone, N.; Hammerberg, A. G.; Lee, C.; Crawford, B.; Oliver, W.; et al. High-Strength Chemical-Vapor-Deposited Graphene and Grain Boundaries. *Science* **2013**, *340* (6136), 1074–1076.
- (147) Grantab, R.; Shenoy, V. B.; Ruoff, R. S. Anomalous Strength Characteristics of Tilt Grain Boundaries in Graphene. *Science* **2010**, *330* (6006), 946–948.
- (148) Wei, Y.; Wu, J.; Yin, H.; Shi, X.; Yang, R.; Dresselhaus, M. The Nature of Strength Enhancement and Weakening by Pentagong-Heptagon Defects in Graphene. *Nat. Mater.* **2012**, *11* (9), 759–763.
- (149) Lu, Y.; Guo, J. Thermal Transport in Grain Boundary of Graphene by Non-Equilibrium Green's Function Approach. *Appl. Phys. Lett.* **2012**, *101* (4), 043112.
- (150) Serov, A. Y.; Ong, Z.-Y.; Pop, E. Effect of Grain Boundaries on Thermal Transport in Graphene. *Appl. Phys. Lett.* **2013**, *102* (3), 033104.
- (151) Ma, T.; Liu, Z.; Wen, J.; Gao, Y.; Ren, X.; Chen, H.; Jin, C.; Ma, X.-L.; Xu, N.; Cheng, H.-M.; et al. Tailoring the Thermal and Electrical Transport Properties of Graphene Films by Grain Size Engineering. *Nat. Commun.* **2017**, *8* (1), 14486.
- (152) Kitaigorodskii, A. I.; Struchkov, Y. T.; Khot'syanova, T. L.; Vol'pin, M. E.; Kursanov, D. N. Crystal Structures of Tropylium Perchlorate and Iodide. *Bull. Acad. Sci. USSR Div. Chem. Sci.* **1960**, *9* (1), 32–36.
- (153) Mackay, E. G.; Newton, C. G.; Toombs-Ruane, H.; Lindeboom, E. J.; Fallon, T.; Willis, A. C.; Paddon-Row, M. N.; Sherburn, M. S. [5]Radialene. *J. Am. Chem. Soc.* **2015**, *137* (46), 14653–14659.
- (154) Swan, E.; Platts, K.; Blencowe, A. An Overview of the Cycloaddition Chemistry of Fulvenes and Emerging Applications. *Beilstein J. Org. Chem.* **2019**, *15*, 2113–2132.
- (155) Neuenschwander, M. Low-Temperature Olefin Syntheses in View of Parent Fulvenes and Fulvalenes. *Helv. Chim. Acta* **2015**, *98* (6), 731–762.
- (156) Xin, H.; Gao, X. Application of Azulene in Constructing Organic Optoelectronic Materials: New Tricks for an Old Dog. *ChemPlusChem* **2017**, *82* (7), 945–956.
- (157) Arbitman, J. K.; Michel, C. S.; Castro, C.; Karney, W. L. Calculations Predict That Heavy-Atom Tunneling Dominates Möbius Bond Shifting in [12]- and [16]Annulene. *Org. Lett.* **2019**, *21* (21), 8587–8591.
- (158) Oth, J. F. M.; Röttele, H.; Schröder, G. [12]Annulene. *Tetrahedron Lett.* **1970**, *11* (1), 61–66.
- (159) Chiang, C. C.; Paul, I. C. Crystal and Molecular Structure of [14]Annulene. *J. Am. Chem. Soc.* **1972**, *94* (13), 4741–4743.
- (160) Wannere, C. S.; Sattelmeyer, K. W.; Schaefer, H. F.; Schleyer, P. V. R. Aromaticity: The the Alternating C-C Bond Length Structures of [14]-, [18]- and [22]Annulene. *Angew. Chem. Int. Ed.* **2004**, *43* (32), 4200–4206.
- (161) Hafner, K.; Thiele, G. F.; Mink, C. Synthesis and Structure of 2,7-Di-tert-butylidicyclopenta[a,e]Cyclooctene. *Angew. Chem. Int. Ed.* **1988**, *27* (9), 1191–1192.
- (162) Funhoff, D. J. H.; Staab, H. A. Cyclo[d.e.d.e.d.e.d.e.d.e.]Decakisbenzene, a New Cycloarene. *Angew. Chem. Int. Ed.* **1986**, *25* (8), 742–744.
- (163) Staab, H. A.; Sauer, M. Cycloarene, Eine Neue Klasse Aromatischer Verbindungen, IV. Versuche Zur Synthese Des Cyclo[d.e.d.e.d.e.d.e.d.e.]Nonakisbenzens Und Des Cyclo[d.e.d.e.d.e.d.e.d.e.]Decakisbenzens. *Liebigs Ann. der Chemie* **1984**, *1984* (4), 742–760.
- (164) Bieri, M.; Treier, M.; Cai, J.; Ait-Mansour, K.; Ruffieux, P.; Gröning, O.; Gröning, P.; Kastler, M.; Rieger, R.; Feng, X.; et al. Porous Graphenes: Two-Dimensional Polymer Synthesis with Atomic Precision. *Chem. Commun.* **2009**,

1.6 References

- No. 45, 6919–6921.
- (165) Bai, J.; Zhong, X.; Jiang, S.; Huang, Y.; Duan, X. Graphene Nanomesh. *Nat. Nanotechnol.* **2010**, *5* (3), 190–194.
- (166) Anderson, A. G.; Montana, A. F.; MacDonald, A.; Masada, G. M. Synthesis of Dicyclopenta[ef,kl]Heptalene (Azupyrene). II. Routes from 1,6,7,8,9,9a-Hexahydro-2H-Benzo[c,d]Azulen-6-One and 5-Phenylpentanoic Acid. *J. Org. Chem.* **1973**, *38* (8), 1445–1450.
- (167) Hafner, K.; Diehl, H.; Richarz, W. Cycloadditions of Aceheptylene—A Facile Synthesis of Dicyclopenta[ef,kl]Heptalenes. *Angew. Chem. Int. Ed.* **1976**, *15* (2), 108–109.
- (168) Müllen, K. New Reductive Transformations of Unsaturated Cyclic Hydrocarbons [New Synthetic Methods (66)]. *Angew. Chem. Int. Ed.* **1987**, *26* (3), 204–217.
- (169) Konishi, A.; Horii, K.; Shiomi, D.; Sato, K.; Takui, T.; Yasuda, M. Open-Shell and Antiaromatic Character Induced by the Highly Symmetric Geometry of the Planar Heptalene Structure: Synthesis and Characterization of a Nonalternant Isomer of Bisanthene. *J. Am. Chem. Soc.* **2019**, *141* (26), 10165–10170.
- (170) Reel, H.; Vogel, E. Dicyclohepta[cd,gh]Pentalene—A New Pyrene Isomer. *Angew. Chem. Int. Ed.* **1972**, *11* (11), 1013–1014.
- (171) Vogel, E.; Wieland, H.; Schmalstieg, L.; Lex, J. Novel Synthesis and Molecular Structure of the Pyrene Isomer Dicyclohepta[cd,gh]Pentalene (Azuleno[2,1,8-ija]Azulene). *Angew. Chem. Int. Ed.* **1984**, *23* (9), 717–719.
- (172) Vogel, E.; Markowitz, G.; Schmalstieg, L.; Itô, S.; Breuckmann, R.; Roth, W. R. Thermal Deoxygenation of Syn-15,16-Dioxo-1,6:8,13-bismethano[14]Annulene to the Pyrene Isomer Dicyclohepta[cd,gh]Pentalene (Azuleno[2,1,8-ija]Azulene). *Angew. Chem. Int. Ed.* **1984**, *23* (9), 719–720.
- (173) Barth, W. E.; Lawton, R. G. Dibenz[ghi,mno]Fluoranthene. *J. Am. Chem. Soc.* **1966**, *88* (2), 380–381.
- (174) Hanson, J. C.; Nordman, C. E. The Crystal and Molecular Structure of Corannulene, C₂₀H₁₀. *Acta Cryst.* **1976**, *32* (4), 1147–1153.
- (175) Shoyama, K.; Würthner, F. Synthesis of a Carbon Nanocone by Cascade Annulation. *J. Am. Chem. Soc.* **2019**, *141* (33), 13008–13012.
- (176) Yamamoto, K.; Harada, T.; Nakazaki, M.; Naka, T.; Kai, Y.; Harada, S.; Kasai, N. Synthesis and Characterization of [7]Circulene. *J. Am. Chem. Soc.* **1983**, *105* (24), 7171–7172.
- (177) Cheung, K. Y.; Miao, Q. A Ketone-Functionalized Aromatic Saddle as a Potential Building Block for Negatively Curved Carbon Nanobelts. *Chinese Chem. Lett.* **2019**, *30* (8), 1506–1508.
- (178) Pun, S. H.; Chan, C. K.; Luo, J.; Liu, Z.; Miao, Q. A Dipleadiene-Embedded Aromatic Saddle Consisting of 86 Carbon Atoms. *Angew. Chem. Int. Ed.* **2018**, *57* (6), 1581–1586.
- (179) Halton, B. The Fulvalenes. *Eur. J. Org. Chem.* **2005**, No. 16, 3391–3414.
- (180) Hanson, A. W. The Crystal Structure of the Acepleiadiylene, s⁻-Trinitrobenzene Complex. *Acta Crystallogr.* **1966**, *21* (1), 97–102.
- (181) Liu, J.; Mishra, S.; Pignedoli, C. A.; Passerone, D.; Urgel, J. I.; Fabrizio, A.; Lohr, T. G.; Ma, J.; Komber, H.; Baumgarten, M.; et al. Open-Shell Nonbenzenoid Nanographenes Containing Two Pairs of Pentagonal and Heptagonal Rings. *J. Am. Chem. Soc.* **2019**, *141* (30), 12011–12020.
- (182) Mishra, S.; Lohr, T. G.; Pignedoli, C. A.; Liu, J.; Berger, R.; Urgel, J. I.; Müllen, K.; Feng, X.; Ruffieux, P.; Fasel, R. Tailoring Bond Topologies in Open-Shell Graphene Nanostructures. *ACS Nano* **2018**, *12* (12), 11917–11927.
- (183) Hieulle, J.; Carbonell-Sanromà, E.; Vilas-Varela, M.; Garcia-Lekue, A.; Guitián, E.; Peña, D.; Pascual, J. I. On-Surface Route for Producing Planar Nanographenes with Azulene Moieties. *Nano Lett.* **2018**, *18* (1), 418–423.
- (184) Mastalerz, M.; Yang, X.; Rominger, F. Contorted Polycyclic Aromatic Hydrocarbons with Two Embedded Azulene Units. *Angew. Chem. Int. Ed.* **2019**.
- (185) Kawasumi, K.; Zhang, Q.; Segawa, Y.; Scott, L. T.; Itami, K. A Grossly Warped Nanographene and the Consequences of Multiple Odd-Membered-Ring Defects. *Nat. Chem.* **2013**, *5* (9), 739–744.
- (186) Lin, H. A.; Sato, Y.; Segawa, Y.; Nishihara, T.; Sugimoto, N.; Scott, L. T.; Higashiyama, T.; Itami, K. A Water-

- Soluble Warped Nanographene: Synthesis and Applications for Photoinduced Cell Death. *Angew. Chem. Int. Ed.* **2018**, *57* (11), 2874–2878.
- (187) Cheung, K. Y.; Xu, X.; Miao, Q. Aromatic Saddles Containing Two Heptagons. *J. Am. Chem. Soc.* **2015**, *137* (11), 3910–3914.
- (188) Fernández-García, J. M.; Evans, P. J.; Medina Rivero, S.; Fernández, I.; García-Fresnadillo, D.; Perles, J.; Casado, J.; Martín, N. π -Extended Corannulene-Based Nanographenes: Selective Formation of Negative Curvature. *J. Am. Chem. Soc.* **2018**, *140* (49), 17188–17196.
- (189) Yoshida, Z. ichi; Shibata, M.; Ogino, E.; Sugimoto, T. A New Cata-Condensed Nonalternant Tetracyclic Hydrocarbon Azuleno[2,1-e]Azulene. *Tetrahedron Lett.* **1984**, *25* (31), 3343–3346.
- (190) Takayasu, T.; Nitta, M. On the Reaction of Azuleno-2-Ylmethylene(Triphenyl)Phosphorane. Convenient Preparation of Azuleno[1,2-f]- and Azuleno[1,2-a]-Azulenes and Their Properties. *J. Chem. Soc., Perkin Trans. 1* **1997**, *23*, 3537–3542.
- (191) Yamaguchi, Y.; Ogawa, K.; Nakayama, K. I.; Ohba, Y.; Katagiri, H. Terazulene: A High-Performance n-Type Organic Field-Effect Transistor Based on Molecular Orbital Distribution Control. *J. Am. Chem. Soc.* **2013**, *135* (51), 19095–19098.
- (192) Yamaguchi, Y.; Takubo, M.; Ogawa, K.; Nakayama, K. I.; Koganezawa, T.; Katagiri, H. Terazulene Isomers: Polarity Change of OFETs through Molecular Orbital Distribution Contrast. *J. Am. Chem. Soc.* **2016**, *138* (35), 11335–11343.
- (193) Hou, I. C.-Y.; Shetti, V.; Huang, S.-L.; Liu, K.-L.; Chao, C.-Y.; Lin, S.-C.; Lin, Y.-J.; Chen, L.-Y.; Luh, T.-Y. Poly[2(6)-Aminoazulene]: Synthesis, Photophysical Properties, and Proton Conductivity. *Org. Chem. Front.* **2017**, *4* (5), 773–778.
- (194) Zacharia, R.; Ulbricht, H.; Hertel, T. Interlayer Cohesive Energy of Graphite from Thermal Desorption of Polyaromatic Hydrocarbons. *Phys. Rev. B* **2004**, *69* (15), 155406.
- (195) Weippert, J.; Hauns, J.; Bachmann, J.; Böttcher, A.; Yao, X.; Yang, B.; Narita, A.; Müllen, K.; Kappes, M. M. A TPD-Based Determination of the Graphite Interlayer Cohesion Energy. *J. Chem. Phys.* **2018**, *149* (19), 194701.
- (196) Rashkin, M. J.; Waters, M. L. Unexpected Substituent Effects in Offset π - π Stacked Interactions in Water. *J. Am. Chem. Soc.* **2002**, *124* (9), 1860–1861.
- (197) Silva, N. J.; Machado, F. B. C.; Lischka, H.; Aquino, A. J. A. π - π Stacking between Polyaromatic Hydrocarbon Sheets beyond Dispersion Interactions. *Phys. Chem. Chem. Phys.* **2016**, *18* (32), 22300–22310.
- (198) Wu, J.; Pisula, W.; Müllen, K. Graphenes as Potential Material for Electronics. *Chem. Rev.* **2007**, *107* (3), 718–747.
- (199) Yeh, M. Y.; Liao, Y.; Wu, D.; Huang, C. Columnar Mesophases of Alkylated Hexa-Peri-Hexabenzocoronenes Wirh Remarkably Large Phase Widths. *Adv. Mater.* **1996**, *8* (6), 510–513.
- (200) Pisula, W.; Tomović, Ž.; Simpson, C.; Kastler, M.; Pakula, T.; Müllen, K. Relationship between Core Size, Side Chain Length, and the Supramolecular Organization of Polycyclic Aromatic Hydrocarbons. *Chem. Mater.* **2005**, *17* (17), 4296–4303.
- (201) Liu, C. yang; Fechtenkötter, A.; Watson, M. D.; Müllen, K.; Bard, A. J. Room Temperature Discotic Liquid Crystalline Thin Films of Hexa-Peri-Hexabenzocoronene: Synthesis and Optoelectronic Properties. *Chem. Mater.* **2003**, *15* (1), 124–130.
- (202) Tomović, Ž.; Watson, M. D.; Müllen, K. Superphenalene-Based Columnar Liquid Crystals. *Angew. Chem. Int. Ed.* **2004**, *43* (6), 755–758.
- (203) Seyler, H.; Purushothaman, B.; Jones, D. J.; Holmes, A. B.; Wong, W. W. H. Hexa-Peri-Hexabenzocoronene in Organic Electronics. *Pure Appl. Chem.* **2012**, *84* (4), 1047–1067.
- (204) Fleischmann, E. K.; Zentel, R. Liquid-Crystalline Ordering as a Concept in Materials Science: From Semiconductors to Stimuli-Responsive Devices. *Angew. Chem. Int. Ed.* **2013**, *52* (34), 8810–8827.
- (205) Goddard, R.; Haenel, M. W.; Krüger, C.; Herndon, W. C.; Zander, M. Crystallization of Large Planar Polycyclic

- Aromatic Hydrocarbons: The Molecular and Crystal Structures of Hexabenzob[bc,ef,hi,kl,no,qr]Coronene and Benzo[1,2,3-bc:4,5,6-b'c']Dicononene. *J. Am. Chem. Soc.* **1995**, *117* (1), 30–41.
- (206) Demus, D.; Goodby, J.; Gray, G. W.; Spiess, H. -W.; Vill, V. *Handbook of Liquid Crystals*; Wiley, 1998.
- (207) Pisula, W.; Feng, X.; Müllen, K. Tuning the Columnar Organization of Discotic Polycyclic Aromatic Hydrocarbons. *Adv. Mater.* **2010**, *22* (33), 3634–3649.
- (208) Pisuia, W.; Tomović, Ž.; Watson, M. D.; Müllen, K.; Kussmann, J.; Ochsenfeld, C.; Metzroth, T.; Gauss, J. Helical Packing of Discotic Hexaphenyl Hexa-Peri-Hexabenzocoronenes: Theory and Experiment. *J. Phys. Chem. B* **2007**, *111* (26), 7481–7487.
- (209) Kastler, M.; Pisula, W.; Davies, R. J.; Gorelik, T.; Kolb, U.; Müllen, K. Nanostructuring with a Crosslinkable Discotic Material. *Small* **2007**, *3* (8), 1438–1444.
- (210) Wang, Z.; Watson, M. D.; Wu, J.; Müllen, K. Partially Stripped Insulated Nanowires: A Lightly Substituted Hexa-Peri-Hexabenzocoronene-Based Columnar Liquid Crystal. *Chem. Commun.* **2004**, *4* (3), 336–337.
- (211) Hill, J. P.; Jin, W.; Kosaka, A.; Fukushima, T.; Ichihara, H.; Shimomura, T.; Ito, K.; Hashizume, T.; Ishii, N.; Aida, T. Self-Assembled Hexa-Peri-Hexabenzocoronene Graphitic Nanotube. *Science* **2004**, *304* (5676), 1481–1483.
- (212) Mativetsky, J. M.; Kastler, M.; Savage, R. C.; Gentilini, D.; Palma, M.; Pisula, W.; Müllen, K.; Samorì, P. Self-Assembly of a Donor-Acceptor Dyad across Multiple Length Scales: Functional Architectures for Organic Electronics. *Adv. Funct. Mater.* **2009**, *19* (15), 2486–2494.
- (213) Dössel, L. F.; Kamm, V.; Howard, I. A.; Laquai, F.; Pisula, W.; Feng, X.; Li, C.; Takase, M.; Kudernac, T.; De Feyter, S.; et al. Synthesis and Controlled Self-Assembly of Covalently Linked Hexa-Peri-Hexabenzocoronene/Perylene Diimide Dyads as Models to Study Fundamental Energy and Electron Transfer Processes. *J. Am. Chem. Soc.* **2012**, *134* (13), 5876–5886.
- (214) Frath, D.; Yokoyama, S.; Hirose, T.; Matsuda, K. Photoresponsive Supramolecular Self-Assemblies at the Liquid/Solid Interface. *J. Photochem. Photobiol. C* **2018**, *34*, 29–40.
- (215) Feringa, B. L.; Browne, W. R. *Molecular Switches, Second Edition*; Feringa, B. L., Browne, W. R., Eds.; Wiley-VCH Verlag GmbH & Co. KGaA: Weinheim, Germany, 2011; Vol. 1.
- (216) Rahman, M. L.; Tschierske, C.; Yusoff, M.; Silong, S. Synthesis and Liquid Crystalline Properties of a Disc-Shaped Molecule with Azobenzene at the Periphery. *Tetrahedron Lett.* **2005**, *46* (13), 2303–2306.
- (217) Tanaka, D.; Ishiguro, H.; Shimizu, Y.; Uchida, K. Thermal and Photoinduced Liquid Crystalline Phase Transitions with a Rod-Disc Alternative Change in the Molecular Shape. *J. Mater. Chem.* **2012**, *22* (48), 25065–25071.
- (218) Keil, M.; Samorì, P.; Dos Santos, D. A.; Kugler, T.; Stafström, S.; Brand, J. D.; Müllen, K.; Brédas, J. L.; Rabe, J. P.; Salaneck, W. R. Influence of the Morphology on the Electronic Structure of Hexa-Peri-Hexabenzocoronene Thin Films. *J. Phys. Chem. B* **2000**, *104* (16), 3967–3975.
- (219) Ruffieux, P.; Gröning, O.; Biemann, M.; Simpson, C.; Müllen, K.; Schlapbach, L.; Gröning, P. Supramolecular Columns of Hexabenzocoronenes on Copper and Gold (111) Surfaces. *Phys. Rev. B* **2002**, *66* (7), 073409.
- (220) Piot, L.; Marchenko, A.; Wu, J.; Müllen, K.; Fichou, D. Structural Evolution of Hexa-Peri-Hexabenzocoronene Adlayers in Heteroepitaxy on n-Pentacotane Template Monolayers. *J. Am. Chem. Soc.* **2005**, *127* (46), 16245–16250.
- (221) Samorì, P.; Fechtenkötter, A.; Reuther, E.; Watson, M. D.; Severin, N.; Müllen, K.; Rabe, J. P. Self-Assembly of Perylene Monoimide Substituted Hexa-Peri-Hexabenzocoronenes: Dyads and Triads at Surfaces. *Adv. Mater.* **2006**, *18* (10), 1317–1321.
- (222) Ito, S.; Wehmeier, M.; Brand, J. D.; Kübel, C.; Epsch, R.; Rabe, J. P.; Müllen, K. Synthesis and Self-Assembly of Functionalized Hexa-Peri-Hexabenzocoronenes. *Chem. - A Eur. J.* **2000**, *6* (23), 4327–4342.
- (223) Mali, K. S.; Pearce, N.; De Feyter, S.; Champness, N. R. Frontiers of Supramolecular Chemistry at Solid Surfaces. *Chem. Soc. Rev.* **2017**, *46* (9), 2520–2542.
- (224) Vanoppen, P.; Grim, P. C. M.; Rücker, M.; De Feyter, S.; Moessner, G.; Valiyaveetil, S.; Müllen, K.; De Schryver,

- F. C. Solvent Codeposition and Cis-Trans Isomerization of Isophthalic Acid Derivatives Studied by STM. *J. Phys. Chem.* **1996**, *100* (50), 19636–19641.
- (225) Ai, M.; Groeper, S.; Zhuang, W.; Dou, X.; Feng, X.; Müllen, K.; Rabe, J. P. Optical Switching Studies of an Azobenzene Rigidly Linked to a Hexa-Peri-Hexabenzocoronene Derivative in Solution and at a Solid-Liquid Interface. *Appl. Phys. A* **2008**, *93* (2), 277–283.
- (226) Reitzel, N.; Hassenkam, T.; Balashev, K.; Jensen, T. R.; Howes, P. B.; Kjaer, K.; Fechtenkötter, A.; Tchegotareva, N.; Ito, S.; Müllen, K.; et al. Langmuir and Langmuir-Blodgett Films of Amphiphilic Hexa-Peri-Hexabenzocoronene: New Phase Transitions and Electronic Properties Controlled by Pressure. *Chem. - A Eur. J.* **2001**, *7* (22), 4894–4901.
- (227) Hamilton, I. P.; Li, B.; Yan, X.; Li, L. S. Alignment of Colloidal Graphene Quantum Dots on Polar Surfaces. *Nano Lett.* **2011**, *11* (4), 1524–1529.
- (228) Yan, X.; Cui, X.; Li, B.; Li, L. S. Large, Solution-Processable Graphene Quantum Dots as Light Absorbers for Photovoltaics. *Nano Lett.* **2010**, *10* (5), 1869–1873.
- (229) Alder, R. W.; East, S. P.; Harvey, J. N.; Oakley, M. T. The Azulene-to-Naphthalene Rearrangement Revisited: A DFT Study of Intramolecular and Radical-Promoted Mechanisms. *J. Am. Chem. Soc.* **2003**, *125* (18), 5375–5387.
- (230) Hinkel, F.; Cho, D.; Pisula, W.; Baumgarten, M.; Müllen, K. Alternating Donor-Acceptor Arrays from Hexa-Perihexabenzocoronene and Benzothiadiazole: Synthesis, Optical Properties, and Self-Assembly. *Chem. - A Eur. J.* **2015**, *21* (1), 86–90.

Chapter 2. Synthesis of Dendritic Polyphenylenes Possessing 366 and 546 Carbons as Potential Precursors for Giant D_{6h} -Symmetric Nanographenes

Ian Cheng-Yi Hou,¹ [REDACTED],² [REDACTED],² [REDACTED],² [REDACTED]^{1,3,*}
and [REDACTED]^{1,4,*}

¹Max Planck Institute for Polymer Research, Ackermannweg 10, D-55128 Mainz, Germany

²Department of Physics, University of Basel, Klingelbergstrasse 82, 4056 Basel, Switzerland

³Organic and Carbon Nanomaterials Unit, Okinawa Institute of Science and Technology Graduate University, 1919-1 Tancha, Onna-son, Kunigami, Okinawa 904-0495, Japan

⁴Institute of Physical Chemistry, Johannes Gutenberg-University Mainz, Duesbergweg 10-14, D-55128 Mainz, Germany

Published in: Unpublished manuscript.

Contribution: Organic synthesis and characterization. First draft preparation and correction. DOSY NMR analysis.

2.1 Main text

Dendritic polyphenylene (PP) is a class of hyper-branched macromolecules that are composed of substituted benzenes as their scaffold. Semi-rigid quasi-spherical nanostructures, high intramolecular free volume, and supreme thermal stability of dendritic PPs render them wide applications in the fields of imaging, sensing, and biomedicine.^{1,2} Moreover, carefully designed dendritic PPs, which can be represented by 2D-projection without overlapping of benzene rings, serve as potential precursors for nanographenes (NG), nano-sized graphene fragments.³⁻⁵

More than two decades ago, an efficient organic synthesis of hexa-*peri*-hexabenzocoronene, the smallest NG, was achieved through oxidative cyclodehydrogenation of hexaphenylbenzene (HPB) **2** (Figure 1).⁶ Since then, properly designed dendritic PPs give birth to various NGs with tailored shapes, such as hexagon,⁷ triangle,⁸ dumbbell,⁹ star,¹⁰ donut,¹¹ and ribbon¹². These NGs offer an opportunity for systematic investigating their size-dependent energy gaps.^{13,14} Notably, NGs with a size of 5–10 nm display a proper balance between charge carrier mobility and band gap, thus are of great interest for application in logic devices.^{15,16} We have recently developed a method to synthesize PP serving as potential precursor for the synthesis of graphene nanoribbon with a width wider than 3 nm.¹⁷ However, so far, organic bottom-up synthesis can only provide NG flakes with a size up to 3 nm, employing dendritic PP **3** as the precursor (Figure 1).⁷ The synthesis of NG flakes with a diameter larger than 3 nm are partially hindered by availability of proper PP precursors, as well as difficulties in a complete graphitization.^{18,19} To this end, we synthesized PPs **4** and **5**,

which consist of 366 and 546 sp^2 -carbons, respectively, as potential precursors for unprecedentedly large D_{6h} -symmetric NGs with size approaching 5 nm (Figure 1). Structure of **4** and **5** were characterized by ^1H NMR, ^{13}C NMR, and matrix-assisted laser desorption/ionization (MALDI) mass spectra. Their van der Waal radius are estimated by ^1H NMR diffusion ordered spectroscopy (DOSY) and compared with smaller PPs **2** and **3**. We also describe our initial attempts on oxidative cyclodehydrogenation of PPs **4** and **5** in solution, as well as surface-assist thermal cyclodehydrogenation under ultra-high vacuum (UHV) conditions.

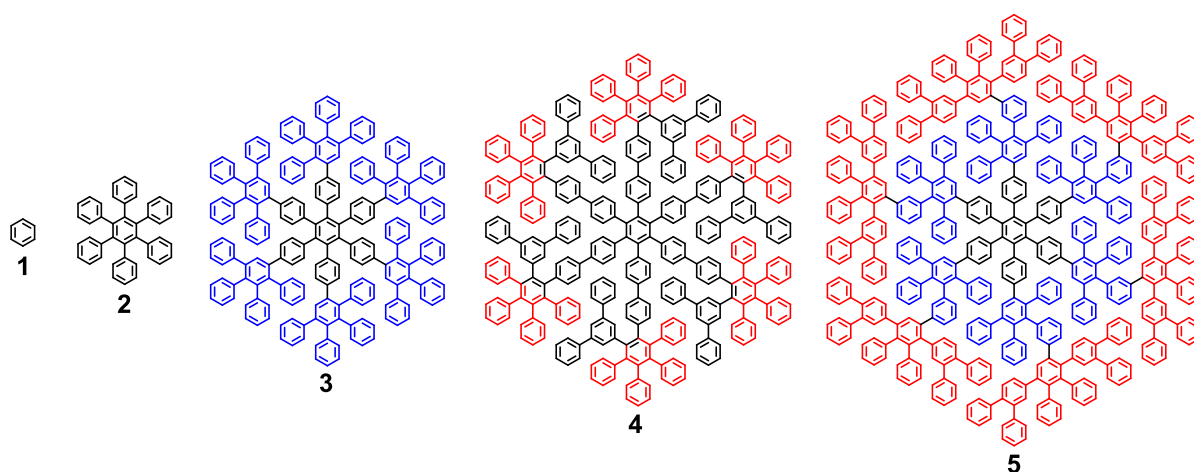
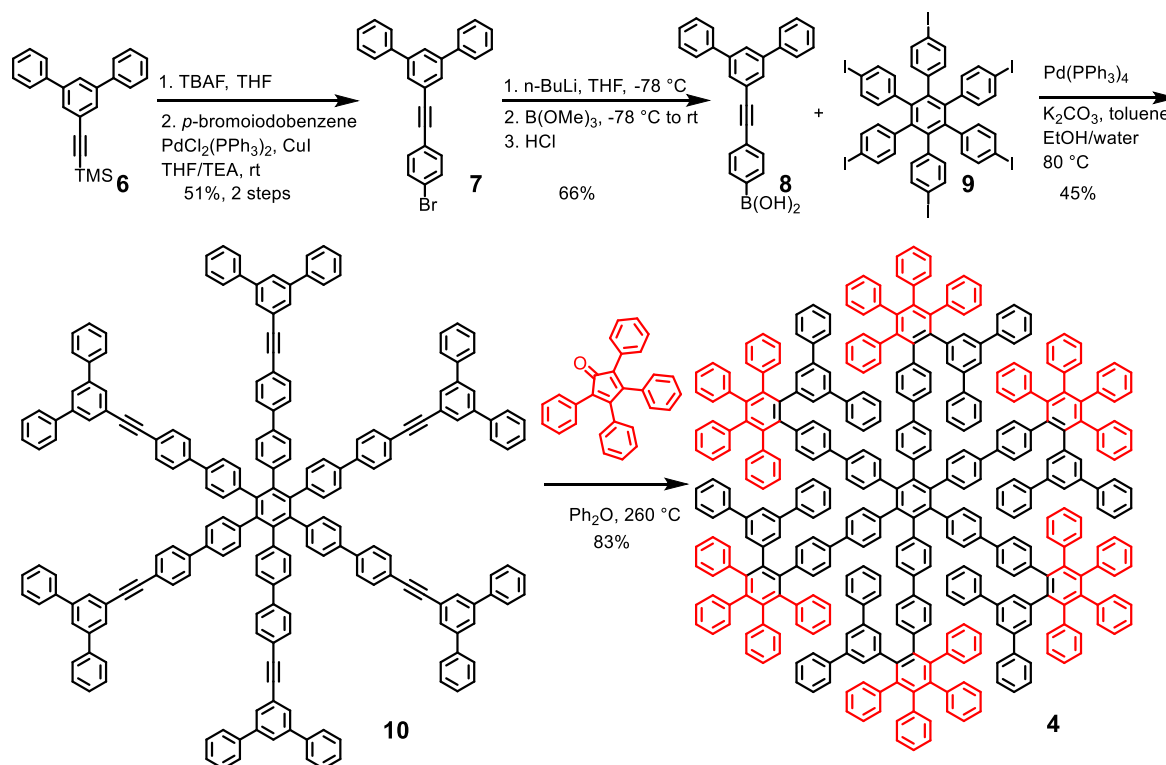


Figure 1. Dendritic PPs correlated to D_{6h} -symmetric “super benzenes”.

Synthesis of dendritic PP **4** was achieved by first constructing a star-shape skeleton **10**, that contains six internal alkynes, followed by its six-fold Diels-Alder (D-A) reaction with tetraphenylcyclopenta-2,4-dien-1-one (CP) (Scheme 1). First, the trimethylsilyl protecting group of 1-(trimethylsilylethynyl)-3,5-diphenylbenzene (**6**)²⁰ was removed by reacting with tetrabutylammonium fluoride. Then, the ethynyl group was allowed to selectively react with the iodo group of *p*-bromiodobenzene through a Sonogashira reaction at room temperature to give 1-(4-bromophenylethynyl)-3,5-diphenylbenzene (**7**). Next, the bromo group of **7** was lithiated and converted to boronic acid functional group by reacting with $\text{B}(\text{OMe})_3$. Subsequently, a six-fold Suzuki reaction between **8** and HPB core **9**²¹ converted them to **10** in 45% yield, under standard Suzuki reaction condition using $\text{Pd}(\text{PPh}_3)_4$ as catalyst and K_2CO_3 as base. Notably, although **8** and **9** can be isolated as pure substances, **8**, **9**, and **10**, especially the latest, exhibited poor solubility in common organic solvents, which hindered a thorough purification of **10**. Thus, a crude product of the star-shape core **10** was directly subjected to the six-fold D-A reaction with CP in a suspension in Ph_2O . During the reaction, the

2.1 Main text

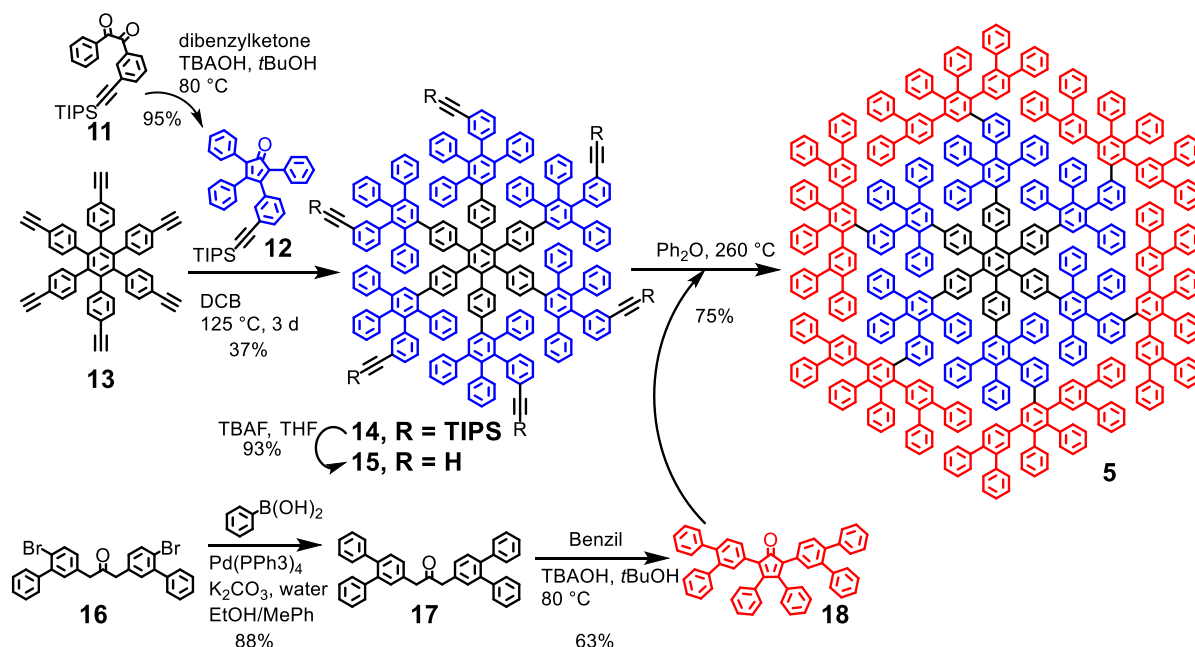
suspension became a transparent solution, indicating conversion of **10** into more soluble D-A adducts. Finally, the adduct mixture was purified by recycling gel permeation chromatography (GPC) to afford PP **4** in 66% yield (83% yield before GPC).



Scheme 1. Synthesis of dendritic PP **4**. TBAF: tetrabutylammonium fluoride. THF: tetrahydrofuran. TEA: triethylamine.

Synthesis of PP **5** was accomplished based on the previous synthesis of PP **3** (Scheme 2). Namely, HPB core **13**²¹ with six ethynyl functional groups was step-wise extended by D-A reaction with two different functionalized CPs 3-*m*-(triisopropylsilylethynyl)phenyl-2,4,5-triphenylcyclopenta-2,4-dien-1-one (**12**) and 2,5-bis(3,4-diphenyl)phenyl-3,4-diphenylcyclopenta-2,4-dien-1-one (**18**). Synthesis of **12** was achieved by Knoevenagel condensation between 3-(triisopropylsilylethynyl)benzyl (**11**)²² and 1,3-diphenylacetone in 95% yield. Synthesis of **18** was conducted by introducing two additional phenyl groups to 1,3-di[(4-bromo-3-phenyl)phenyl]acetone (**16**)²³ with a double Suzuki reaction, followed by Knoevenagel condensation with benzil. Notably, these two functionalized CPs share same core structures as monomers we previously used for synthesis of lateral extended graphene nanoribbons.^{23,24} After both **12** and **18** were isolated, hexaethynyl-HPB core **13**²¹ was firstly reacted with **12** through a six-fold D-A reaction, followed by deprotection, to afford dendritic PP **15** as an ethynyl-group-functionalized PP **3**. Dendritic PP **15** was then further extended by

a six-fold D-A reaction with **18** in Ph₂O at 260 °C toward dendritic PP **5** in 75% yield. Crude mixture of PP **5** was purified by GPC to remove smaller molecular weight impurities. It is important to note that both **4** and **5** can be projected into a 2D graphene-related structure without any cavity nor overlapping of a single benzene rings (Scheme 1 and 2).



Scheme 2. Synthesis of dendritic PP **5**. TBAOH: tetrabutylammonium hydroxide. DCB: 1,2-dichlorobenzene.

PP **4** possesses several protons under different environment. Unfortunately, their signals severely overlap in the ¹H NMR spectrum of **4**. As a result, the spectrum cannot be fully assigned (Figure S4). With the same reason but also a problem of existence of various possible isomers (Figure S1), peaks in the ¹H NMR spectrum of **5** are broad (Figure S5), hindering an unambiguous structural characterizations based on NMR. Nonetheless, MALDI-TOF spectra of **4** and **5** show peaks at $m/z = 4639.9246$ and 6920.8087 , respectively, in agreement with their theoretical exact mass $m/z = 4639.9250$ and 6920.8640 (Figure 2). Moreover, the isotope distribution for both **4** and **5** match well with theoretical patterns (Figure 2, insets). Furthermore, we estimated molecular size of PPs **2–5** in solution, by their DOSY spectra (Figure 3a). Their self-diffusion constants in CD₂Cl₂ were determined as 8.47, 4.04, 3.33 and 2.79×10^{-6} cm²/s, respectively. These values correspond to hydrodynamic radiuses (R_H) of around 0.618, 1.19, 1.57 and 1.88 nm. R_H of these PP molecules exhibit a linear relationship with cubic root of numbers of benzene rings in each structure (Figure 3b). Although **5** possesses different molecular shape from **2–4**, where the backbone of the later

2.1 Main text

four are composed of only rigid *p*-phenylenes, while **5** contains more flexible *m*-phenylenes, their R_H are in good agreement with their increasing mass, suggesting a similar molecular shape in solution.

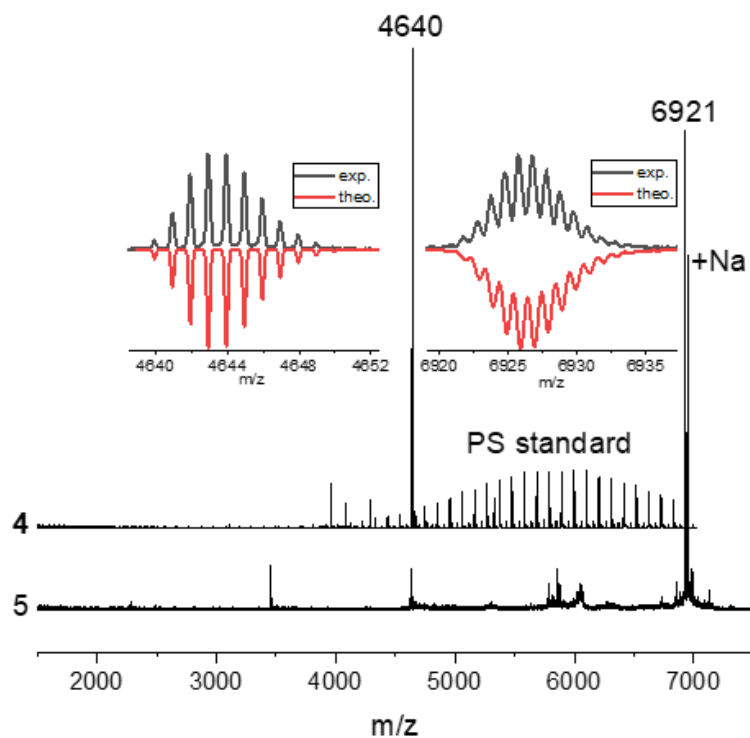


Figure 2. MALDI-TOF spectra of **4** and **5**. Insets: comparison of isotopes distribution and the corresponding theoretical pattern for the formula.

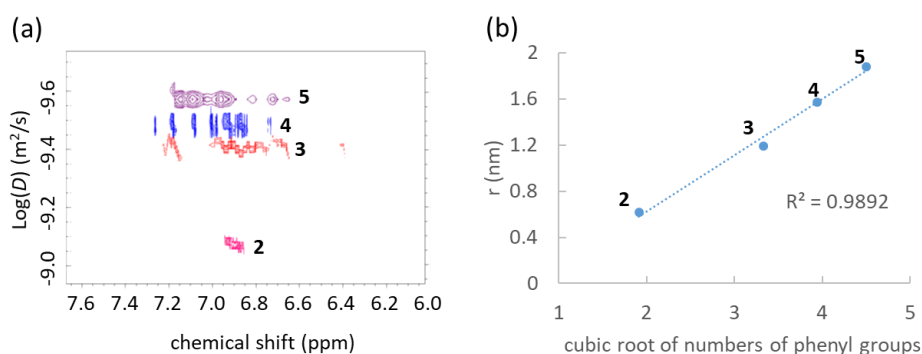


Figure 3. (a) DOSY NMR signal of **2–5** in CD_2Cl_2 at 25 °C and (b) correlation of their R_H (r) derived from (a) with their cubic root of numbers of benzene rings.

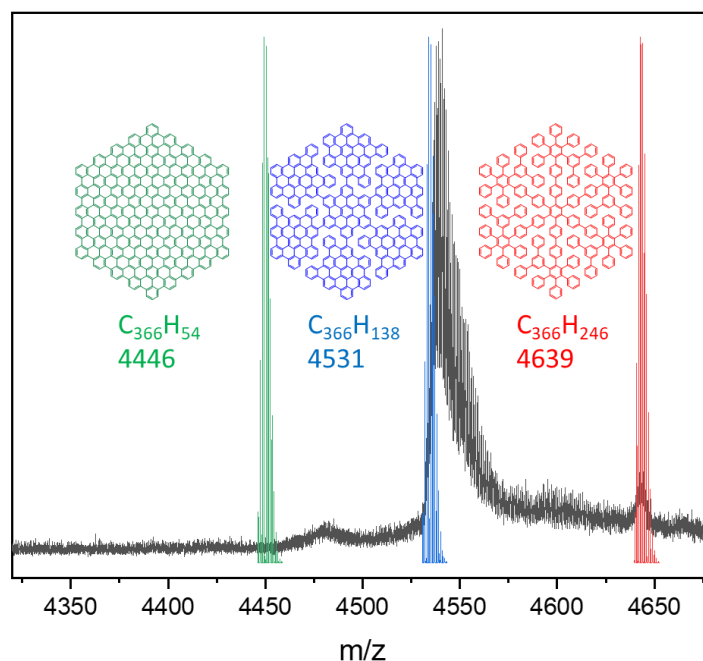


Figure 4. Black lines: MALDI-TOF spectra of **4** after cyclodehydrogenation. Condition: DDQ, TfOH, CH_2Cl_2 , 12 h. Red, blue and green lines correspond to theoretical isotope pattern of reactant **4**, partially and fully cyclodehydrogenated products, respectively, with structures shown in the same color.

After confirming the structure of **4** and **5**, we investigated their cyclodehydrogenation reaction in solution. We employed common conditions for solution cyclodehydrogenation reactions, such as $\text{Cu}(\text{CF}_3\text{SO}_3)_2/\text{AlCl}_3/\text{CS}_2$, $\text{FeCl}_3/\text{CH}_2\text{Cl}_2/\text{MeNO}_2$, or 2,3-dichloro-5,6-dicyano-*p*-quinone(DDQ)/ $\text{CF}_3\text{SO}_3\text{H}/\text{CH}_2\text{Cl}_2$. In addition, unconventional conditions were also examined, such as $\text{NaPF}_6/(\text{CF}_3\text{SO}_3)_2\text{O}/\text{CF}_3\text{SO}_3\text{H}/\text{SO}_2\text{Cl}_2$, $\text{Cu}(\text{CF}_3\text{SO}_3)_2/\text{AlCl}_3/h\nu$, or using silica as template (Table S1 and S2). Unfortunately, these trials often lead to unresolvable product mixture. In general, long reaction time (> 24h) resulted in powder with no detectable signal in MALDI-TOF analysis. Notably, in the cases of **5**, when using $\text{Cu}(\text{CF}_3\text{SO}_3)_2/\text{AlCl}_3/\text{CS}_2$ or DDQ/ $\text{CF}_3\text{SO}_3\text{H}/\text{CH}_2\text{Cl}_2$ as reagent system and a shorter reaction time, very broad undefined band were observed by MALDI-TOF with an onset close to 6700 (110 bonds formed) and 6660 (130 bonds formed) m/z, respectively (Table S2). Besides, in the case of **4**, signals close to 4531 m/z, which is the exact mass of partial cyclodehydrogenation of the HPB core and the six HPB side arms, were observed after cyclodehydrogenations using $\text{Cu}(\text{CF}_3\text{SO}_3)_2/\text{AlCl}_3/\text{CS}_2$ or DDQ/ $\text{CF}_3\text{SO}_3\text{H}/\text{CH}_2\text{Cl}_2$ and a 12 h reaction time (Figure 4 and Table S1). However, their isotope distribution is much wider than theoretical prediction, indicating existence of multiple structural defects. Importantly, we have observed in our previous work that a complete cyclodehydrogenation reaction of large

2.1 Main text

PP was extremely difficult, and cyclodehydrogenation reaction of a dendritic PP with 474 carbons led to a propeller nanostructure.¹⁹ These results indicate that partial graphitization into NG fragments would hinder a complete planarization of dendritic PPs. In addition, for complete planarization of **4** and **5**, the reactions require formation of 96 and 150 new bonds, respectively. To reach a 50% reaction yield of complete planarized products of **4** and **5**, they demand higher than 99.2% and 99.5% yield, respectively, for each single C-C bond formation step. Indeed, these scenarios are challenging for any kind of chemical transformation.

Despite the intrinsic difficulty of cyclodehydrogenation of dendritic PP **4** and **5** in solution, formation of poorly soluble intermediate could lead to incomplete conversion or side reactions. In contrary, on-surface thermal cyclodehydrogenation are not limited by solubility of reactant nor product in organic solvent. Furthermore, on-surface synthesis offers an opportunity for *in-situ* characterization of reaction products at an atomic level by scanning probe microscopies.^{25,26}

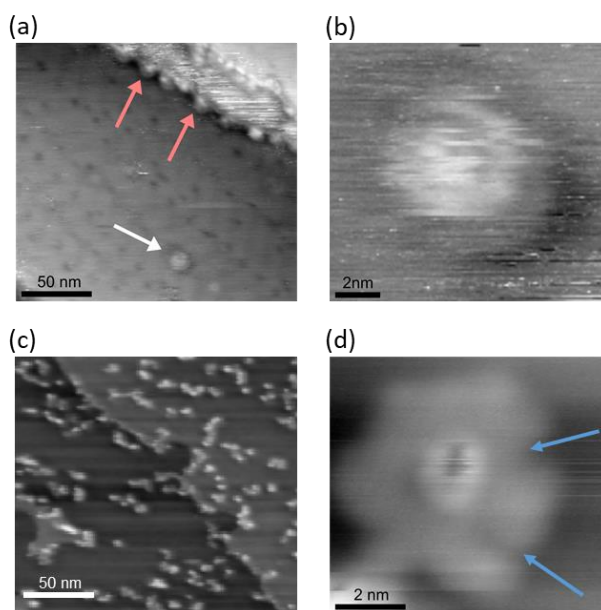


Figure 5. nc-AFM images of dendritic PP **5** on Au(111) surface under UHV condition (a)(b) before and (c)(d) after annealing at 300 °C. Parameters: (a,b) $f_2 = 1.02$ MHz, $A_2 = 400$ pm, $\Delta f = -25$ Hz; (c) $f_1 = 170$ kHz, $A_1 = 4$ nm, $\Delta f = -10$ Hz; (d) $f_2 = 1.01$ MHz, $A_2 = 400$ pm, $\Delta f = -30$ Hz. Scale bar: (a,c) 50 nm; (b,d) 2 nm.

On-surface synthesis of NGs often employs sublimation of PP precursors onto single crystalline metal surfaces, followed by their surface-assisted thermal cyclodehydrogenation.^{26,27} However, both dendritic PP **4** and **5** are too large for sublimation

at a temperature before decomposition. Thus, we resorted to electrospray deposition, which has been utilized for depositing high molecular weight oligomeric or polymeric materials onto single crystalline substrates under UHV conditions.^{28–31} Figure 5a exhibits a room temperature non-contact atomic force microscopy (nc-AFM) image of dendritic PP **5** deposited on Au(111) surface by electrospray deposition without any further surface treatment. Notably, molecules prefer stacking at steppedges (indicated by red arrow), while isolated single molecule is also observed on terrace (indicated by white arrow). An enlargement of a single molecule reveals a disc-like structural feature (Figure 5b). Such topology agrees with our previous investigation on other large PP dendrimers on surface.³² Next, to induce possible surface-assisted cyclodehydrogenation of dendritic PP **5**, we annealed the sample at 300 °C for 20 min. Notably, according to the nc-AFM image taken after the annealing, molecules became relatively evenly distributed (Figure 5c). Furthermore, in an enlarged image of a single molecule, a hexagonal topology is revealed, which is drastically different from those observed before annealing (Figure 5d). Similar structural feature is also observed for dendritic PP **4** after annealing (Figure S2). Estimated from the nc-AFM images, these hexagonal structures exhibit a diameter of 5 and 6.5 nm for annealed dendritic PP **4** and **5**, respectively. Although obvious structural defects exist (Figure 5d, indicated in blue arrow), the size and symmetry of the molecules observed are in reasonable agreement with the D_{6h} -symmetric NGs that could be derived from cyclodehydrogenation of dendritic PP **4** and **5** (Figure S3). Our experimental results suggest that surface-assisted cyclodehydrogenation possess great potential for achieving unprecedentedly large NG flakes from large dendritic PPs.

In conclusion, we synthesized two dendritic PPs with 366 and 546 carbons in their skeleton. These dendritic PPs can be represented by 2D projections without cavity nor overlapping of phenyl rings, thus are suitable as precursors for synthesis of super large NGs with D_{6h} symmetry. The DOSY spectra of these two large dendritic PP revealed 1.57 and 1.88 nm van der Waals radiuses in CD_2Cl_2 . Although the complete in-solution cyclodehydrogenation of these two PPs into NGs was difficult, formation of an intermediate with propeller structure was suggested during the reaction. Furthermore, on surface thermal cyclodehydrogenation of both dendritic PPs resulted in nanostructure with hexagonal topologies. Cyclodehydrogenation conditions and on surface microscopic characterization are currently optimized in our lab.

2.2 Supporting information

1. General Information

Unless otherwise noted, materials were purchased from Fluka, Aldrich, Acros, abcr, Merck, and other commercial suppliers, and were used as received unless otherwise specified. Au substrates were purchased from Mateck GmbH. Compounds **6**, **9**, **11**, **13**, and **16** were synthesized according to ref²⁰, ref²¹, ref²², ref²¹, and ref²³, respectively. All reactions working with air- or moisture-sensitive compounds were carried out under argon atmosphere using standard Schlenk line techniques. Thin layer chromatography (TLC) was performed on silica gel-coated aluminum sheets with F254 indicator. Preparative column chromatography was performed on silica gel from Merck with a grain size of 0.063–0.200 mm (silica gel) or 0.04–0.063 mm (flash silica gel, Geduran Si 60). Melting points were determined on a Büchi hot stage apparatus without correction. Membrane filtration was performed on polyvinylidene fluoride membranes with a pore size of 0.45 μm (Merck). NMR spectra were recorded in deuterated solvents using Bruker AVANCE III 300 and Bruker AVANCE III 700 MHz NMR spectrometers. Chemical shifts (δ) were expressed in ppm relative to the residual of solvent (CD_2Cl_2 @ 5.32 ppm for ^1H NMR, 53.84 ppm for ^{13}C NMR; dimethylsulfoxide- d_6 (DMSO- d_6) @ 2.50 ppm for ^1H NMR, 39.52 ppm for ^{13}C NMR). Coupling constants (J) were recorded in Hertz (Hz) with multiplicities explained by the following abbreviations: s = singlet, d = doublet, t = triplet, q = quartet, dd = doublet of doublets, dt = doublet of triplets, m = multiplet, br = broad. The ^{13}C NMR spectra of compound **4** and **5** were recorded with spin-echo attached-proton test sequence with CH, CH_3 showing negative signal and C, CH_2 showing positive signal. High-resolution mass spectra (HRMS) were recorded by matrix-assisted laser decomposition/ionization (MALDI) using 7,7,8,8-tetracyanoquinodimethane (TCNQ) or *trans*-2-[3-(4-*tert*-Butylphenyl)-2-methyl-2-propenylidene]malononitrile (DCTB) as matrix with a Bruker Reflex II-TOF spectrometer (MALDI-TOF HRMS). Non-contact atomic force microscopy (nc-AFM) measurements were performed with a home-built microscope with Nanonis RC5 electronics. PPP-NCL cantilevers (Nanosensors) were used as sensors (typical resonance frequencies of $f_1 = 160$ kHz and $f_2 = 1$ MHz).

2. Summary of cyclodehydrogenation reaction of dendritic PP 4 and 5 in solution

Table S1. Cyclodehydrogenation of dendritic PP 4 under different conditions monitored by MALDI-TOF analysis.

entry	conditions ¹	intermediate mass ^{2,3}	final mass ^{2,4}
1	Cu(OTf) ₂ , AlCl ₃ , CS ₂ , 40 °C	~4532	~4532
2	NaPF ₆ , (OTf) ₂ O, TfOH, SO ₂ Cl ₂ , air	very broad	-
3	FeCl ₃ , CH ₂ Cl ₂ /MeNO ₂ , rt	very broad and weak	-
4	Cu(OTf) ₂ , AlCl ₃ , hv	similar as entry 3	-
5	FeCl ₃ , CH ₂ Cl ₂ /MeNO ₂ , silica, rt	similar as entry 3	-
6	DDQ, TfOH, CH ₂ Cl ₂ , rt	~4532 ⁵	similar as entry 3

¹Tf = trifluoromethanesulfonyl group. ²Onset of signal band of interest in MALDI-TOF analysis. ³Analyzed after 12 h reaction. ⁴Analyzed after 24 h reaction. ⁵Signal band is narrower than entry 1.

Table S2. Cyclodehydrogenation of dendritic PP 5 under different conditions monitored by MALDI-TOF analysis.

entry	conditions ¹	intermediate mass ^{3,4}	final mass ^{3,5}
1	Cu(OTf) ₂ , AlCl ₃ , CS ₂ , 40 °C ²	~6699, broad	~6699, broad
2	Cu(OTf) ₂ , AlCl ₃ , CS ₂ , <i>o</i> -chloranil, 30 °C	very broad	no signal
3	FeCl ₃ , CH ₂ Cl ₂ /MeNO ₂ , rt	similar as entry 2	no signal
4	DDQ, TfOH, CH ₂ Cl ₂	~6660, broad ⁶	~6660, broad, weak ⁴

¹Tf = trifluoromethanesulfonyl group. ²No signal when equivalent of reagent was doubled. ³Onset of signal band of interest in MALDI-TOF analysis. ⁴Analyzed after 12 h reaction. ⁵Analyzed after 24 h reaction. ⁶Analyzed after 4 h reaction.

3. Experimental details

Isomers of dendritic PP 5

The D-A reaction of CP and ethynyl group is not regioselective.²⁴ This leads to two different connection of the side arms in dendritic PP 5 (Figure S1). Thus, there can be six types of isomer A₆, A₅B, A₄B₂ (three regioisomers), A₃B₃ (three regioisomers), A₂B₄ (three regioisomers), AB₅, and B₆. If every isomer exist, then the dendritic PP we synthesized is a mixture of total 13 different regioisomers. This scenario can also complicate their cyclodehydrogenation reactions.

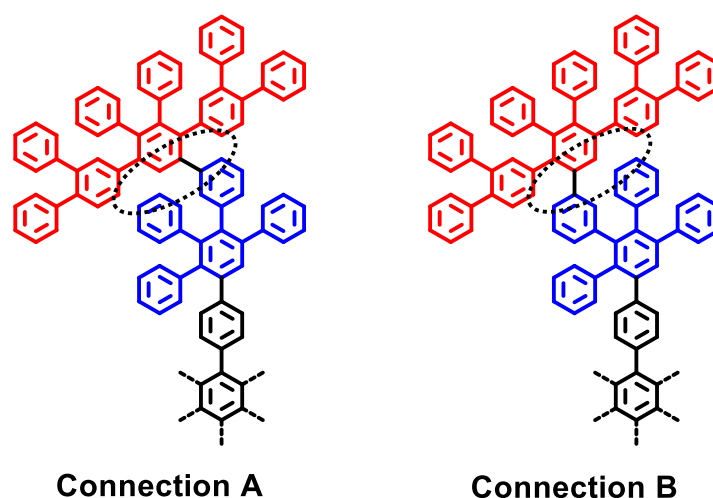


Figure S1. The two kinds of connection of the six arms of dendritic PP 5.

DOSY NMR analysis

Van der Waals radius was estimated using the Stokes-Einstein equation:

$$r = \frac{kT}{6\pi\eta D}$$

where k is Boltzmann constant (1.380×10^{-23} J/K), T is temperature in Kelvin, η is viscosity of solution (CD_2Cl_2 , 4.17×10^{-4} Pa·s at 25 °C) and D is the self-diffusion constants extracted from DOSY spectra (m^2/s). The diffusion constants were calibrated by CH_2Cl_2 in CD_2Cl_2 solvent ($D = 3.03 \times 10^{-5}$ cm^2/s) as internal standard.

Dendritic PP 4 and 5 on Au(111) surface under ultra-high vacuum (UHV) conditions

Au(111) single crystal substrates were prepared in UHV conditions by several cycles of Ar^+ sputtering and annealing at 550°C. After the treatment, atomically flat surfaces were obtained

with large terraces separated by atomic steps. The electro spray deposition was performed on Au(111) samples kept at a room temperature following our previous procedure³⁰ using a commercial system (MolecularSpray), with a typical applied voltage of 1.5 kV. The setup was connected to preparation chambers of the UHV system. Dendritic PPs **4** and **5** were deposited for 10 min from toluene/methanol solution (five to one, ratio in volume). During the spray deposition, pressure of vacuum chamber rose up to 1×10^{-6} mbar. Samples were first scanned prior to any annealing process. The surface-assisted thermal cyclodehydrogenation where perform by *in-situ* annealing for 20 min at 300°C. nc-AFM imaging was performed at a room temperature. Scanning tips were annealed for 1 h at 100 °C followed by Ar⁺ sputtering for 90 s at 680 eV at an Ar⁺ pressure of 3×10^{-6} bar before measurements. Base pressure of UHV system was maintained at 2×10^{-11} mbar during measurements.

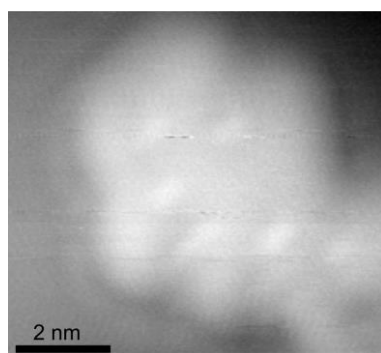
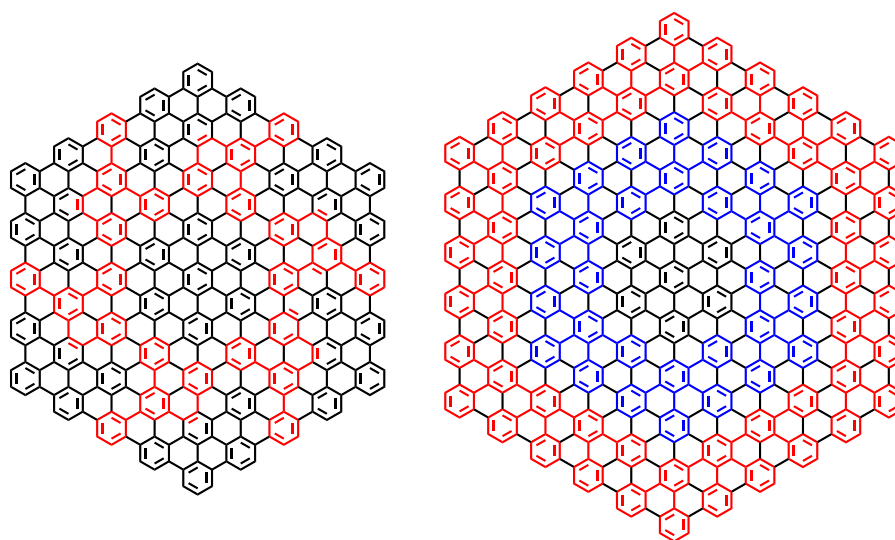


Figure S2. nc-AFM image of dendritic PP **5** on Au(111) surface under UHV condition after annealing at 300 °C. Parameters: $(d) f_2 = 0.99$ MHz, $A_2 = 800$ pm, $\Delta f = -60$ Hz.



Figures S3. Structure of ideal D_{6h} -symmetric NGs from complete cyclodehydrogenations of dendritic PPs **4** and **5**.

2.2 Supporting information

Synthetic procedure and characterization data for unreported compounds

Synthesis of dendritic PP 4: A mixture of star-shape skeleton **10** (30 mg, 0.012 mmol), 2,3,4,5-tetraphenyl-cyclopenta-2,4-dien-1-one (46 mg, 0.12 mmol) and diphenyl ether (0.5 mL) was degassed by freeze-pump-thaw technique for three cycles. This mixture was heated at 260 °C overnight, during which it became a clear solution, and the purple color lightened. After cooling to a room temperature, methanol was added to the solution. A white precipitate (47 mg, 0.010 mmol, 83%) was collected. This precipitate was further purified by recycling gel permeation chromatography to yield **4** as a white solid (37 mg, 0.079 mmol, 66%): mp > 410 °C; ¹H NMR (700 MHz, CD₂Cl₂): δ 7.22 (s, 6H), 7.17–7.12 (m, 36H), 7.08–7.02 (m, 24H), 6.99–6.93 (m, 36H), 6.93–6.86 (m, 84H), 6.86–6.79 (m, 48H), 6.70 (d, *J* = 8 Hz, 12H); ¹³C NMR (176 MHz, CD₂Cl₂) δ 141.49, 141.34, 141.21, 141.18, 141.07, 140.90, 140.84, 140.41, 140.39, 140.33, 140.24, 140.04, 139.91, 137.98, 137.57, 132.46, 132.17, 132.13, 131.88, 131.84, 131.81, 130.38, 128.83, 127.35, 127.19, 127.05, 126.98, 126.94, 125.85, 125.70, 125.63, 125.49, 125.26, 123.36; HRMS (MALDI-TOF) *m/z*: [M]⁺ calcd for C₃₆₆H₂₄₆ 4639.9250; Found 4639.9246.

Synthesis of dendritic PP 5: A solution of dendritic PP **14** (55 mg, 0.014 mmol) in tetrahydrofuran (3 mL) was degassed by freeze-pump-thaw technique for 3 cycles. To this solution was injected a tetrahydrofuran solution of tetrabutylammonium fluoride (0.1 mL, 0.09 mmol, 1 M). The solution was allowed to react for 1 h, and poured into methanol (30 mL) to induce precipitation of product. The precipitate was collected by filtration with a membrane filter, and washed with methanol to give dendritic PP **15** as a white powder (38 mg, 0.013 mmol, 93%), which was directly used in the next step without further purification. A solution of **15** (35 mg, 0.012 mmol) and 2,5-di([1,1':2',1''-terphenyl]-4'-yl)-3,4-diphenylcyclopenta-2,4-dien-1-one (**18**) (73 mg, 0.11 mmol) in diphenyl ether (1 mL) was degassed by freeze-pump-thaw technique for 3 cycles. This mixture was heated at 260 °C overnight. After cooling to a room temperature, methanol (10 mL) was added to the solution to induce precipitation of product. The precipitate was collected by filtration with a membrane filter, and washed with methanol to give crude **5** as a white powder (62 mg, 0.0090 mmol, 75%). The crude **5** was further purified by recycling gel permeation chromatography to yield **5** as a white solid (44 mg, 0.0064 mmol, 53%): mp > 410 °C; ¹H NMR (700 MHz, CD₂Cl₂): δ 7.56–7.36 (br, 6H), 7.33–6.48 (m, 348H), 6.48–6.29 (m, 12H); ¹³C NMR (176 MHz, CD₂Cl₂): δ 142.36, 142.30, 142.25, 142.11, 141.96, 141.90, 141.80,

141.65, 141.02, 140.97, 140.84, 140.70, 140.60, 140.49, 140.44, 140.39, 140.29, 140.23, 140.04, 139.49, 139.45, 139.32, 138.95, 138.79, 138.01, 134.58, 133.64, 132.93, 132.31, 132.18, 132.12, 132.05, 132.02, 131.78, 131.72, 131.58, 131.54, 130.25, 130.24, 130.17, 129.62, 129.43, 128.73, 128.19, 128.11, 128.06, 127.91, 127.52, 127.23, 126.97, 126.77, 126.59, 126.14, 125.93, 125.84; HRMS (MALDI-TOF) m/z : $[M]^+$ calcd for $C_{546}H_{366}$ 6920.8640; Found 6920.8087.

Synthesis of 1-(4-bromophenylethynyl)-3,5-diphenylbenzene (7): To a solution of 1-(trimethylsilylethynyl)-3,5-diphenylbenzene (**6**)²⁰ (5.07 g, 15.5 mmol) in THF (50 mL) was injected a THF solution of TBAF (23 mL, 1 M, 23 mmol). The solution was stirred at a room temperature for 1 h, and then passed through a short pad of silica gel with THF as eluent. Solvent was then removed *in vacuo* to afford 1-ethynyl-3,5-diphenylbenzene as a white solid (3.92 g, 15.4 mmol, 99% crude yield), which was directly used in the next step without further purification. A mixture of 1-ethynyl-3,5-diphenylbenzene (3.92 g, 15.4 mmol), $PdCl_2(PPh_3)_2$ (0.22 g, 0.31 mmol), CuI (0.059 g, 0.31 mmol), tetrahydrofuran (20 mL) and triethylamine (10 mL) was degassed by Argon bubbling under vigorous stirring for 15 min. To this mixture was then added *p*-bromiodobenzene (4.81 g, 17.0 mmol) at 0 °C, portion by portion. The mixture was gradually warmed up to a room temperature and stirred overnight. Diethyl ether and ice was added into the mixture and the organic layer was washed with HCl (aq., 2 M), water, and brine, and dried over $MgSO_4$. The solution was concentrated *in vacuo* and the residue was purified by recrystallization from ethanol to afford **7** as a pale yellow crystal (3.21 g, 7.86 mmol, 51%, over two steps): mp 121.9–123.2 °C; 1H NMR (300 MHz, CD_2Cl_2): δ 7.83 (d, $J = 1.7$ Hz, 1H), 7.77 (d, $J = 1.7$ Hz, 2H), 7.69 (d, $J = 7.3$ Hz, 4H), 7.54 (d, $J = 8.4$ Hz, 2H), 7.50 (t, $J = 7.3$ Hz, 4H), 7.46 (d, $J = 8.4$ Hz, 2H), 7.41 (t, $J = 7.3$ Hz, 2H); ^{13}C NMR (75 MHz, CD_2Cl_2): δ 142.62, 140.72, 133.67, 132.28, 129.57, 129.48, 128.41, 127.71, 126.88, 124.38, 123.16, 122.71, 90.92, 88.94; HRMS (MALDI-TOF) m/z : $[M]^+$ calcd for $C_{26}H_{17}Br$ 408.0514; Found 408.0548.

Synthesis of (4-([1,1':3',1''-terphenyl]-5'-ylethynyl)phenyl)boronic acid (8): To a solution of 1-(4-bromophenylethynyl)-3,5-diphenylbenzene (**7**) (3.11 g, 7.62 mmol) in tetrahydrofuran (25 mL) was injected a hexane solution of *n*BuLi (5.3 mL, 8.4 mmol) at -78 °C. The mixture was allowed to react for 30 min, and then $B(OMe)_3$ (1.7 mL, 15 mmol) was syringed. The solution was then gradually warmed up to a room temperature, and further stirred for 3 h. A water solution of HCl (20 mL, 2 M) was added at 0 °C to quench the reaction. The mixture

2.2 Supporting information

was then warmed up to a room temperature and vigorously stirred for 4 h. Diethyl ether (200 mL) was added and the organic phase was washed with water and brine, and dried over MgSO₄. Solvent was then removed *in vacuo* and the residue was purified by recrystallization (CHCl₃) to afford **8** as a white powder (1.89 g, 5.05 mmol, 66%): mp 227.7–230.6 °C; ¹H NMR (300 MHz, DMSO-d₆): δ 8.20 (s, 2H), 7.94 (s, 1H), 7.89 – 7.77 (m, 8H), 7.58 (d, *J* = 7.8 Hz, 2H), 7.51 (t, *J* = 7.4 Hz, 4H), 7.42 (t, *J* = 7.4 Hz, 2H); ¹³C NMR (75 MHz, DMSO-d₆): δ 141.54, 139.16, 134.38, 130.46, 129.09, 128.54, 128.10, 127.13, 125.76, 123.70, 123.65, 94.78, 90.18, 90.02; HRMS (MALDI-TOF) *m/z*: [M]⁺ calcd for C₂₆H₁₉BO₂ 373.1514; Found 373.1502.

Synthesis of star-shape skeleton 10: A mixture of (4-([1,1':3',1''-terphenyl]-5'-ylethynyl)phenyl)boronic acid (**8**) (0.26 g, 0.70 mmol), hexa(*p*-iodophenyl)benzene (**9**)²¹ (90 mg, 0.069 mmol), a water (4.5 mL) solution of K₂CO₃ (1.2 g, 8.7 mmol), EtOH (1.5 mL), and toluene (20 mL) was degassed by freeze-pump-thaw technique for one cycle. Pd(PPh₃)₄ (4 mg, 0.003 mmol) was then added, and the mixture was further degassed by freeze-pump-thaw technique for two cycles. The mixture was then heated at 80 °C under vigorously stirring for 2 days. After cooling to a room temperature, the mixture was poured into methanol. A white solid was collected as crude **10** (79 mg, 0.031 mmol, 45%). This solid was used for the next step without further purification: mp > 410 °C; HMR spectra cannot be recorded because of a very low solubility in common organic solvent; HRMS (MALDI-TOF) *m/z*: [M]⁺ calcd for C₁₉₈H₁₂ 2502.9860; found 2502.9988.

Synthesis of 2,3,5-triphenyl-4-{3-[(triisopropylsilyl)ethynyl]phenyl}cyclopenta-2,4-dien-1-one (12): To a *t*BuOH (300 mL) solution of 1,3-diphenylacetone (1.13 g, 5.37 mmol) and 3-[(triisopropylsilyl)ethynyl]benzil (**11**)²² (2.14 g, 5.48 mmol) was added at 80 °C tetrabutylammonium hydroxide (0.71 g, 1.1 mmol, 40% w/w in EtOH, two portions). The solution turned dark purple immediately. The reaction was tracked by thin layer chromatography until starting material was consumed. After cooling to a room temperature, diethyl ether was added, and the organic phase was washed with NH₄Cl (aq., sat.), water, and brine, and dried over MgSO₄. Solvent was removed *in vacuo* and residue was purified by silica gel column chromatography (dichloromethane/hexane = 1/6) to yield **12** as a purple solid (2.9 g, 5.1 mmol, 95%): mp 75.6–77.7 °C; ¹H NMR (300 MHz, CD₂Cl₂): δ 7.41–7.17 (m, 14H), 7.13 (t, *J* = 7.8 Hz, 1H), 7.02–6.88 (m, 4H), 1.07 (s, 21H); ¹³C NMR (75 MHz, CD₂Cl₂): δ 200.72, 155.22, 154.05, 133.76, 133.63, 133.60, 132.11, 131.43, 131.25, 130.67,

129.89, 129.75, 129.20, 128.61, 128.61, 128.53, 128.25, 128.06, 126.41, 125.98, 123.72, 118.74, 106.86, 91.86, 18.94, 11.81; HRMS (MALDI-TOF) m/z : $[M]^+$ calcd for $C_{40}H_{40}OSi$ 564.2848; found 564.2789.

Synthesis of dendritic PP 14: A mixture of hexa(4-ethynylphenyl)benzene (**13**)²¹ (30 mg, 0.044 mmol), 2,3,5-triphenyl-4-{3-[(triisopropylsilyl)ethynyl]phenyl}cyclopenta-2,4-dien-1-one (**12**) (226 mg, 0.398 mmol), and *o*-xylene (0.6 mL) was degassed by freeze-pump-thaw technique for three cycles. This mixture was heated at 125 °C for 3 days. After cooling to a room temperature methanol (3 mL) was added to induce precipitation of product. The precipitate was collected by filtration with a membrane filter and washed with methanol to give **13** as a white powder (61 mg, 0.015 mmol, 37%): mp > 410 °C; ¹H NMR (300 MHz, CD₂Cl₂): δ 7.45–7.37 (br, 6H), 7.26–7.08 (m, 30H), 7.06–6.68 (m, 84H), 6.68–6.57 (br, 12H), 6.43–6.30 (m, 12H), 1.08 (s, 126H); ¹³C NMR (75 MHz, CD₂Cl₂): δ 142.16, 142.11, 141.97, 141.20, 141.03, 140.74, 140.64, 140.38, 140.20, 139.51, 139.38, 138.97, 138.54, 135.98, 131.99, 131.59, 130.31, 128.68, 128.02, 127.91, 127.74, 127.28, 127.16, 127.01, 126.74, 126.14, 125.88, 122.38, 122.08, 107.58, 107.51, 90.34, 90.22, 18.83, 18.81, 11.70; HRMS (MALDI-TOF) m/z : $[M]^+$ calcd for $C_{288}H_{270}Si_6$ 3895.9743; Found 3895.9639.

Synthesis of 1,3-di([1,1':2',1''-terphenyl]-4'-yl)propan-2-one (17): The procedure was modified from our previous work describing synthesis of a similar structure.²³ A mixture of 1,3-bis(3-phenyl-4-bromophenyl)acetone (**16**)²³ (113 mg, 0.218 mmol), phenyl boronic acid (80 mg, 0.65 mmol), a water (3 mL) solution of K₂CO₃ (180 mg, 1.3 mmol), EtOH (3 mL), and toluene (12 mL) was degassed by freeze-pump-thaw technique for one cycle. Pd(PPh₃)₄ (25 mg, 0.022 mmol) was then added, and the mixture was further degassed by freeze-pump-thaw technique for two cycles. The mixture was then heated at reflux under vigorously stirring for 4 h. After cooling to a room temperature, the mixture was diluted with diethyl ether and washed with NaOH (aq., 2 M), water, and brine, and dried over MgSO₄. Solvent was then removed *in vacuo*, and the residue was purified by silica gel column chromatography (dichloromethane/hexane = 2/3) to yield **17** as a white solid (99 mg, 0.19 mmol, 88%): mp 138.8–140.2 °C; ¹H NMR (300 MHz, CD₂Cl₂): δ 7.39 (d, J = 7.8 Hz, 2H), 7.34–7.17 (m, 16 H), 7.17–7.06 (m, 8 H), 3.91 (s, 4 H); ¹³C NMR (75 MHz, CD₂Cl₂): δ 205.74, 141.88, 141.78, 141.34, 139.86, 134.05, 132.39, 131.41, 130.42, 130.39, 129.27, 128.39, 127.10, 127.02, 118.73, 49.44; HRMS (MALDI-TOF) m/z : $[M]^+$ calcd for $C_{40}H_{40}OSi$ 514.2297; found 514.2258.

2.2 Supporting information

Synthesis of 2,5-di([1,1':2',1''-terphenyl]-4'-yl)-3,4-diphenylcyclopenta-2,4-dien-1-one (18): To a *t*BuOH (150 mL) solution of 1,3-di([1,1':2',1''-terphenyl]-4'-yl)propan-2-one (**17**) (1.01 g, 1.96 mmol) and benzil (412 mg, 1.96 mmol) was added at 80 °C tetrabutylammonium hydroxide (0.19 mg, 0.29 mmol, 40% w/w in EtOH). The solution turned dark purple immediately. The reaction was tracked by thin layer chromatography until consumption of starting material. After cooling to a room temperature, diethyl ether was added, and the organic phase was washed with NH₄Cl (aq., sat.), water, and brine, and dried over MgSO₄. Solvent was removed *in vacuo*, and the residue was purified by silica gel column chromatography (dichloromethane/hexane = 1/6) to yield **18** as a purple solid (0.88 g, 1.2 mmol, 63%): mp 143.8–145.0 °C; ¹H NMR (300 MHz, CD₂Cl₂): δ 7.50–7.25 (m, 12H), 7.25–7.18 (m, 6H), 7.18–7.06 (m, 14H), 7.01–6.90 (m, 4H); ¹³C NMR (75 MHz, CD₂Cl₂): δ 200.91, 155.76, 141.83, 141.73, 140.62, 140.17, 133.96, 133.01, 130.91, 130.60, 130.34, 129.86, 129.61, 129.13, 128.76, 128.39, 128.29, 127.10, 126.99, 125.44; HRMS (MALDI-TOF) *m/z*: [M]⁺ calcd for C₅₃H₃₆O 688.2766; found 688.2763.

4. ^1H NMR and ^{13}C NMR spectra of unreported compounds

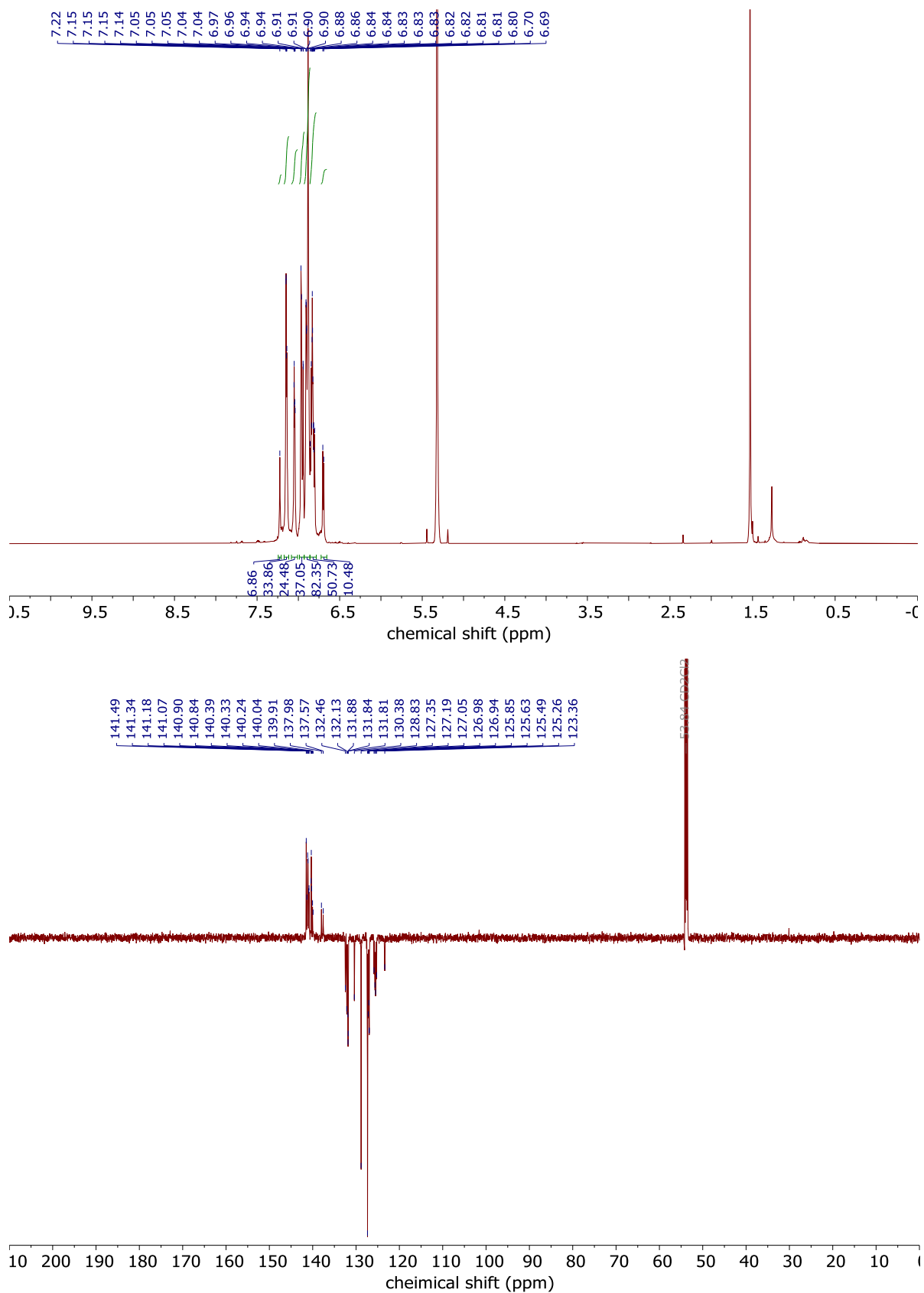


Figure S4. ^1H NMR (up, 700 MHz, CD_2Cl_2) and ^{13}C NMR APT spectra (down, 176 MHz, CD_2Cl_2) of 4.

2.2 Supporting information

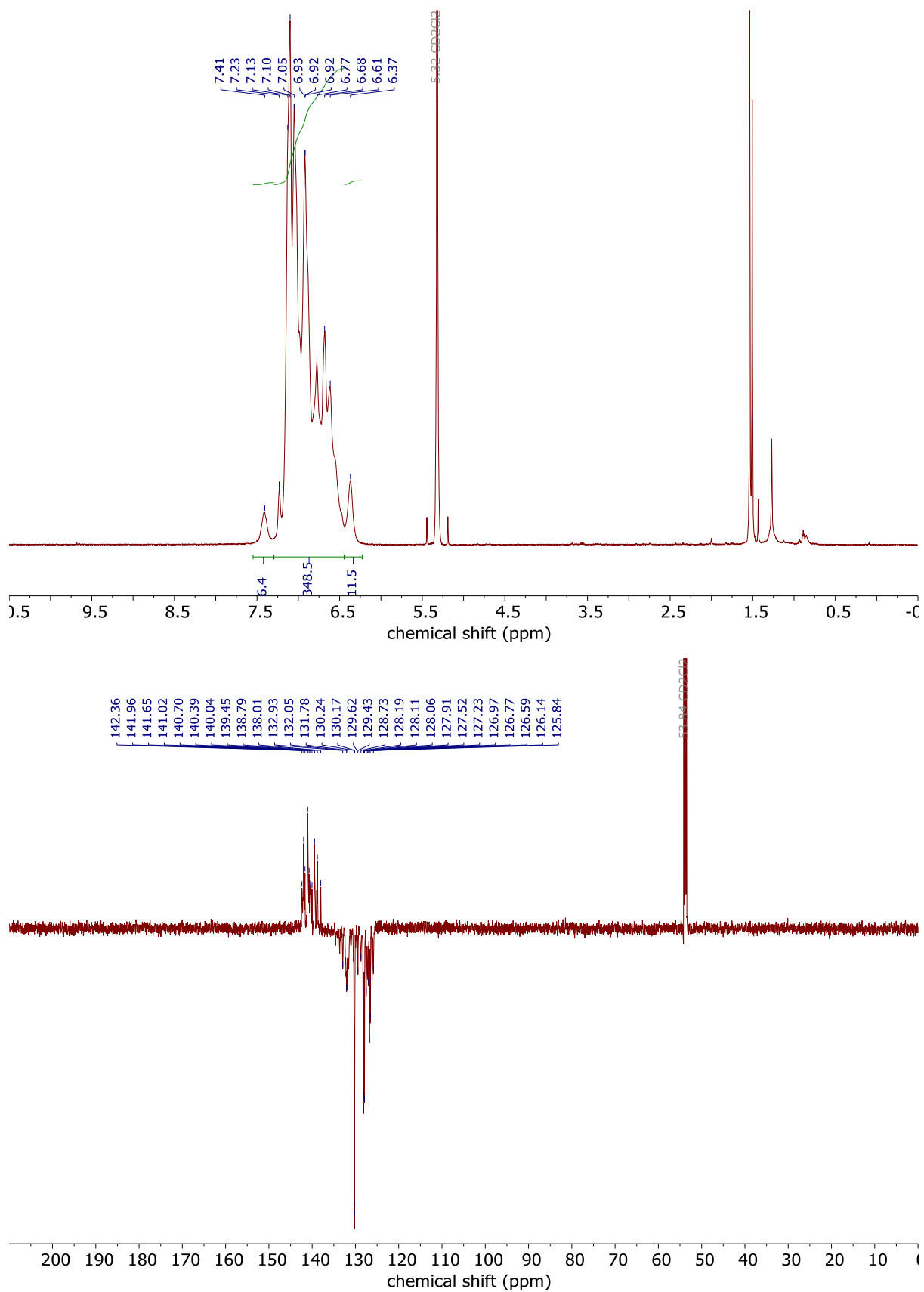


Figure S5. ^1H NMR (up, 700 MHz, CD_2Cl_2) and ^{13}C NMR APT spectra (down, 176 MHz, CD_2Cl_2) of 5.

Chapter 2. Synthesis of Dendritic Polyphenylenes Possessing 366 and 546 Carbons as Potential Precursors for Giant D_{6h} -Symmetric Nanographenes

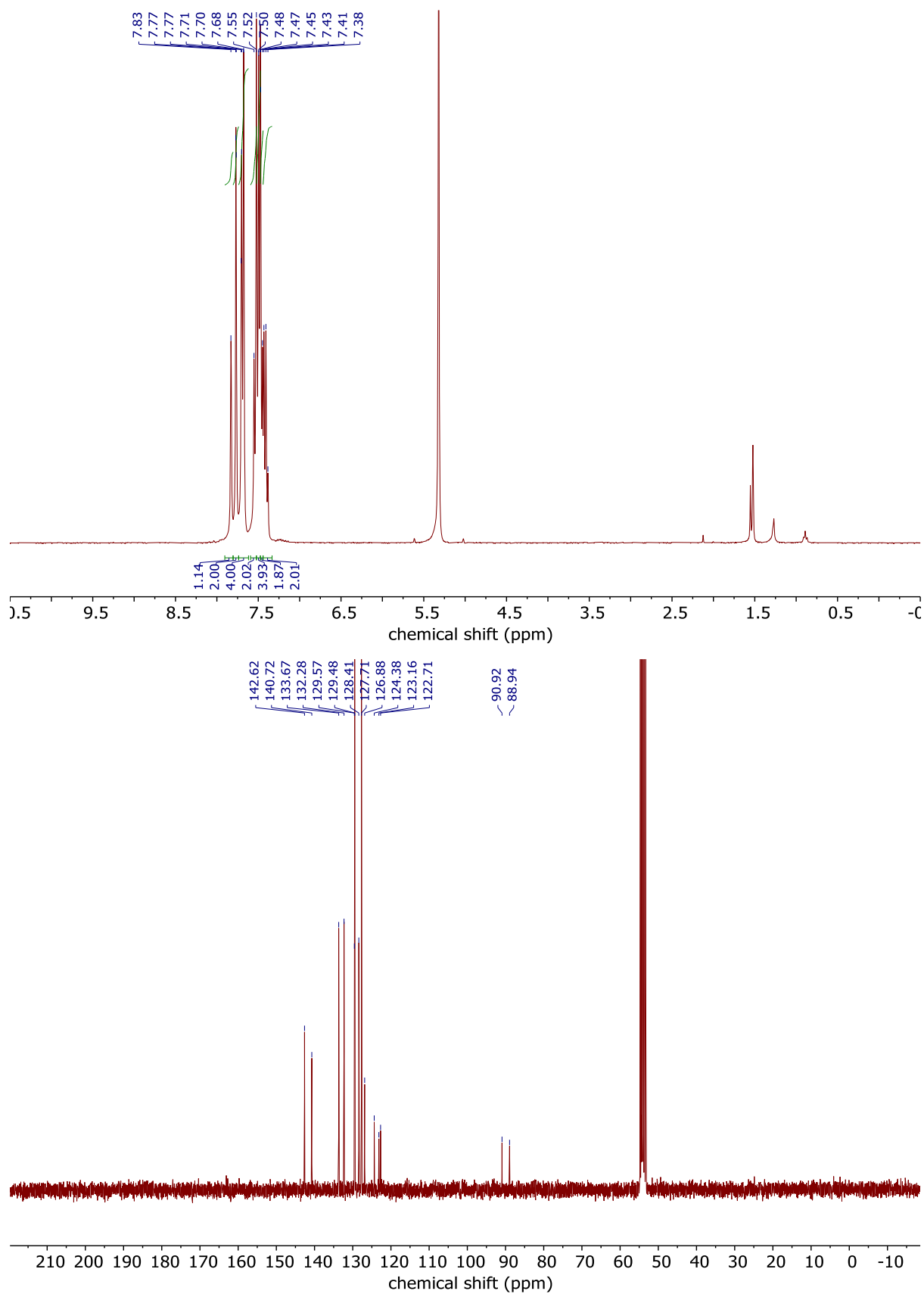


Figure S6. ^1H NMR (up, 300 MHz, CD_2Cl_2) and ^{13}C NMR spectra (down, 75 MHz, CD_2Cl_2) of 7.

2.2 Supporting information

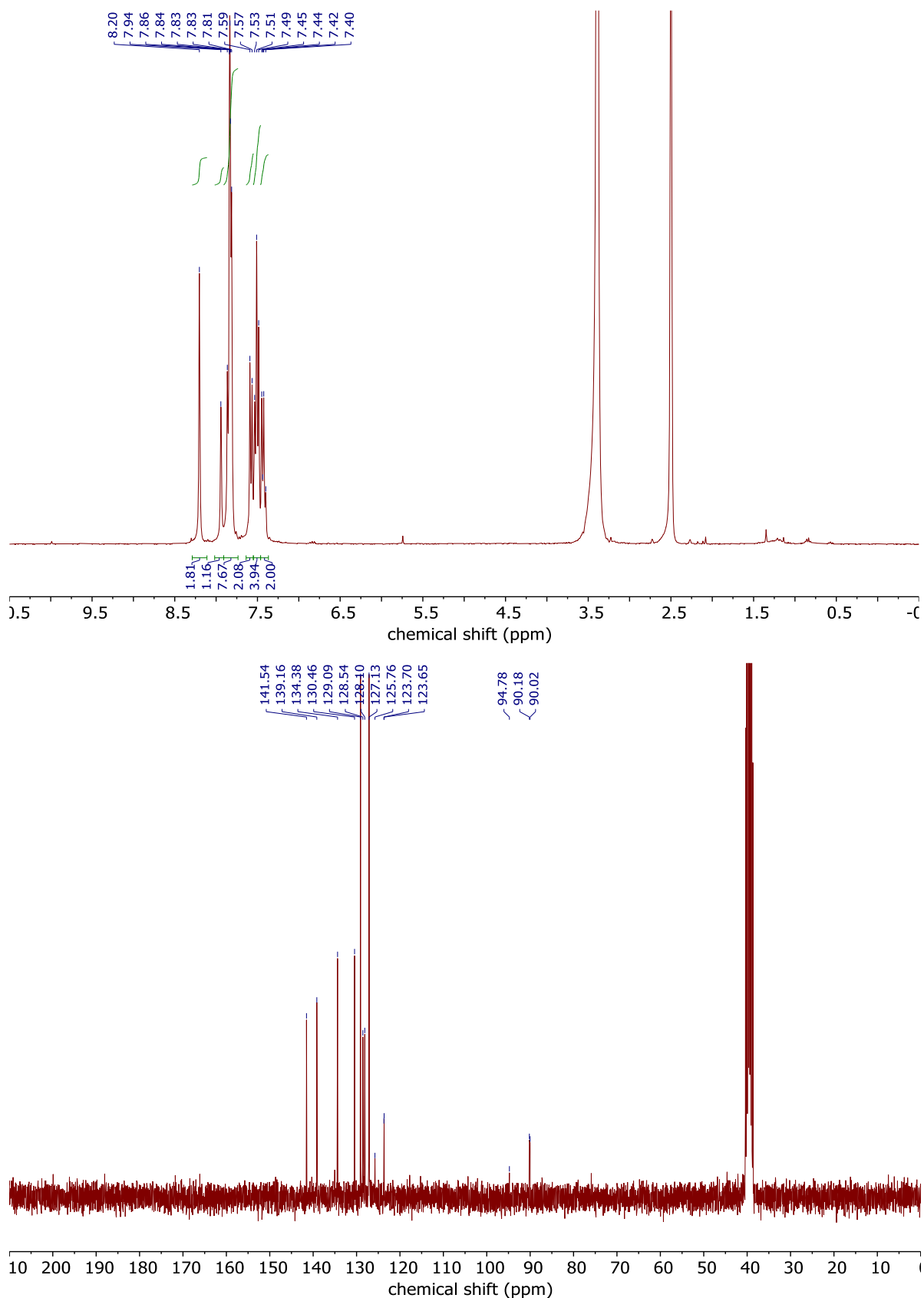


Figure S7. ^1H NMR (up, 300 MHz, DMSO-d_6) and ^{13}C NMR spectra (down, 75 MHz, DMSO-d_6) of **8**.

Chapter 2. Synthesis of Dendritic Polyphenylenes Possessing 366 and 546 Carbons as Potential Precursors for Giant D_{6h} -Symmetric Nanographenes

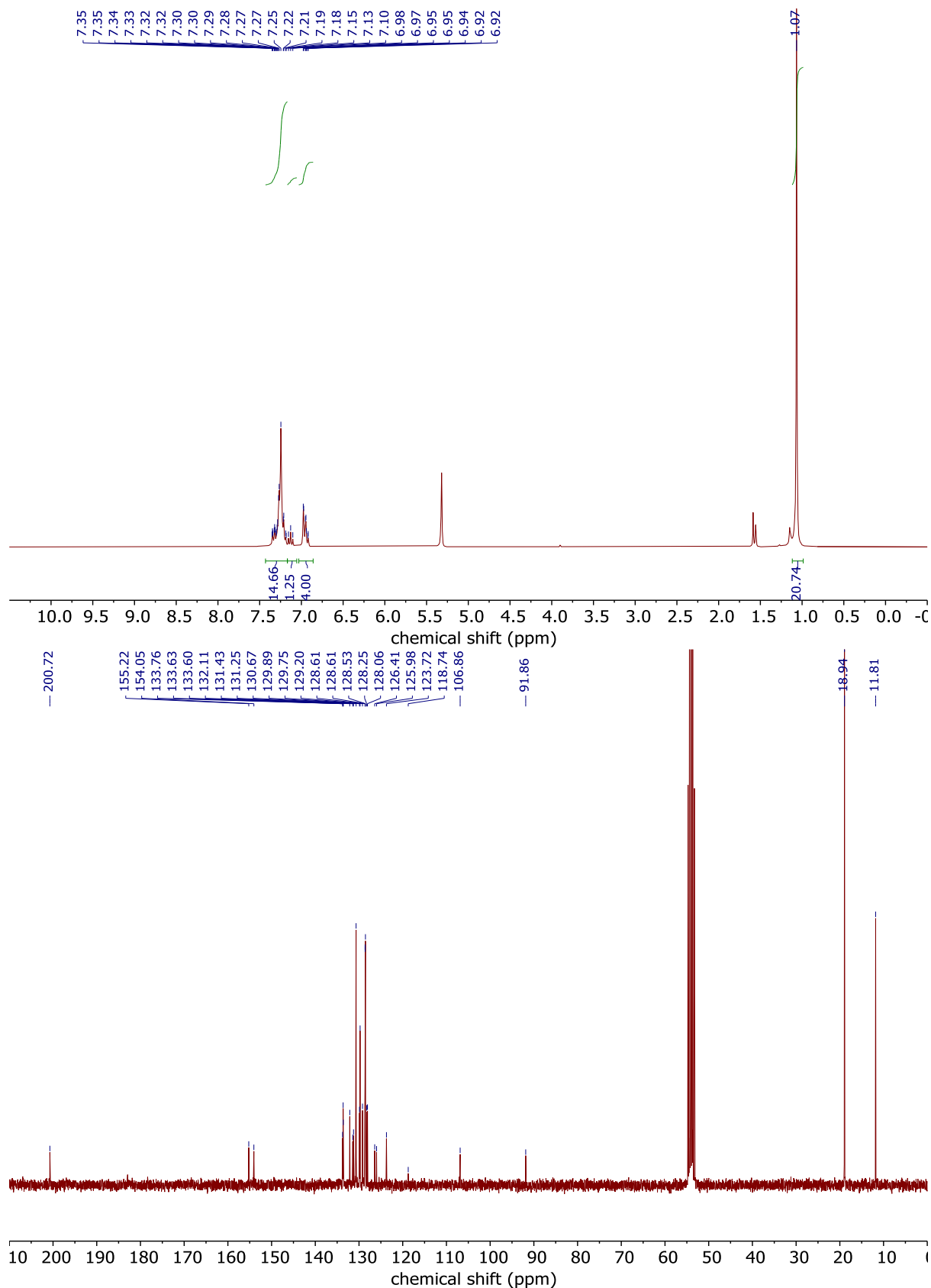


Figure S8. ^1H NMR (up, 300 MHz, CD_2Cl_2) and ^{13}C NMR spectra (down, 75 MHz, CD_2Cl_2) of 12.

2.2 Supporting information

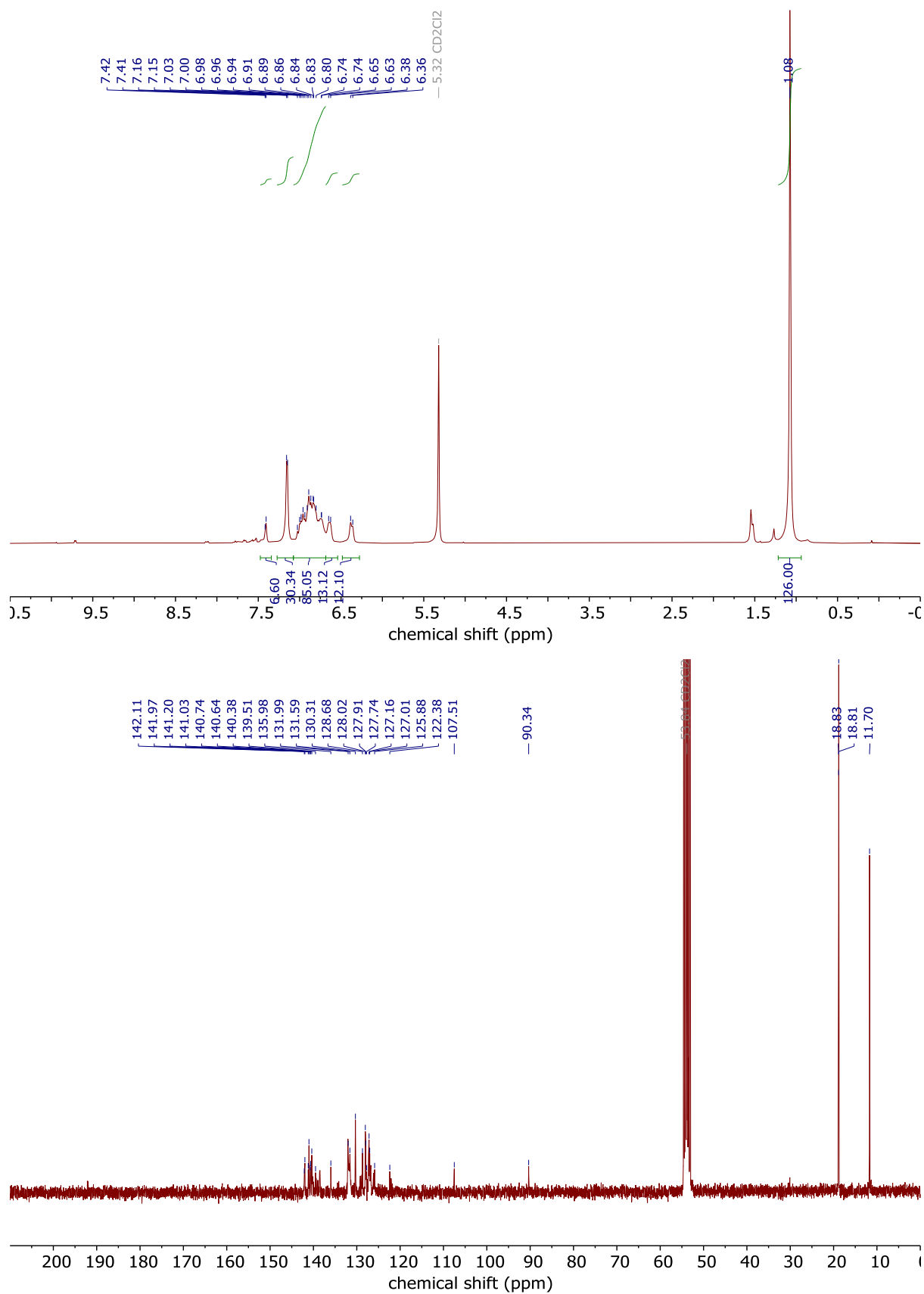


Figure S9. ^1H NMR (up, 300 MHz, CD_2Cl_2) and ^{13}C NMR spectra (down, 75 MHz, CD_2Cl_2) of **14**.

Chapter 2. Synthesis of Dendritic Polyphenylenes Possessing 366 and 546 Carbons as Potential Precursors for Giant D_{6h} -Symmetric Nanographenes

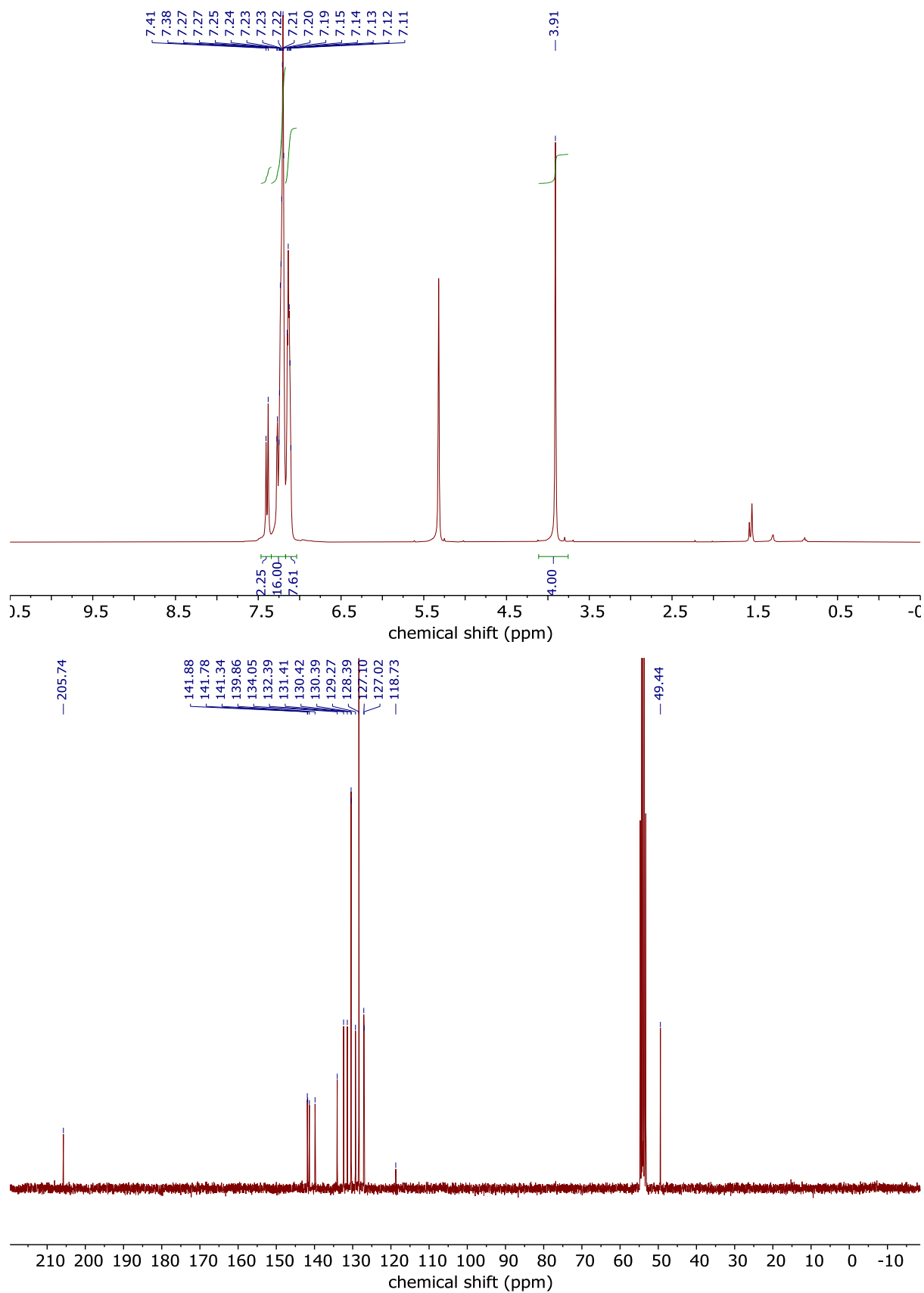


Figure S10. ^1H NMR (up, 300 MHz, CD_2Cl_2) and ^{13}C NMR spectra (down, 75 MHz, CD_2Cl_2) of 17.

2.2 Supporting information

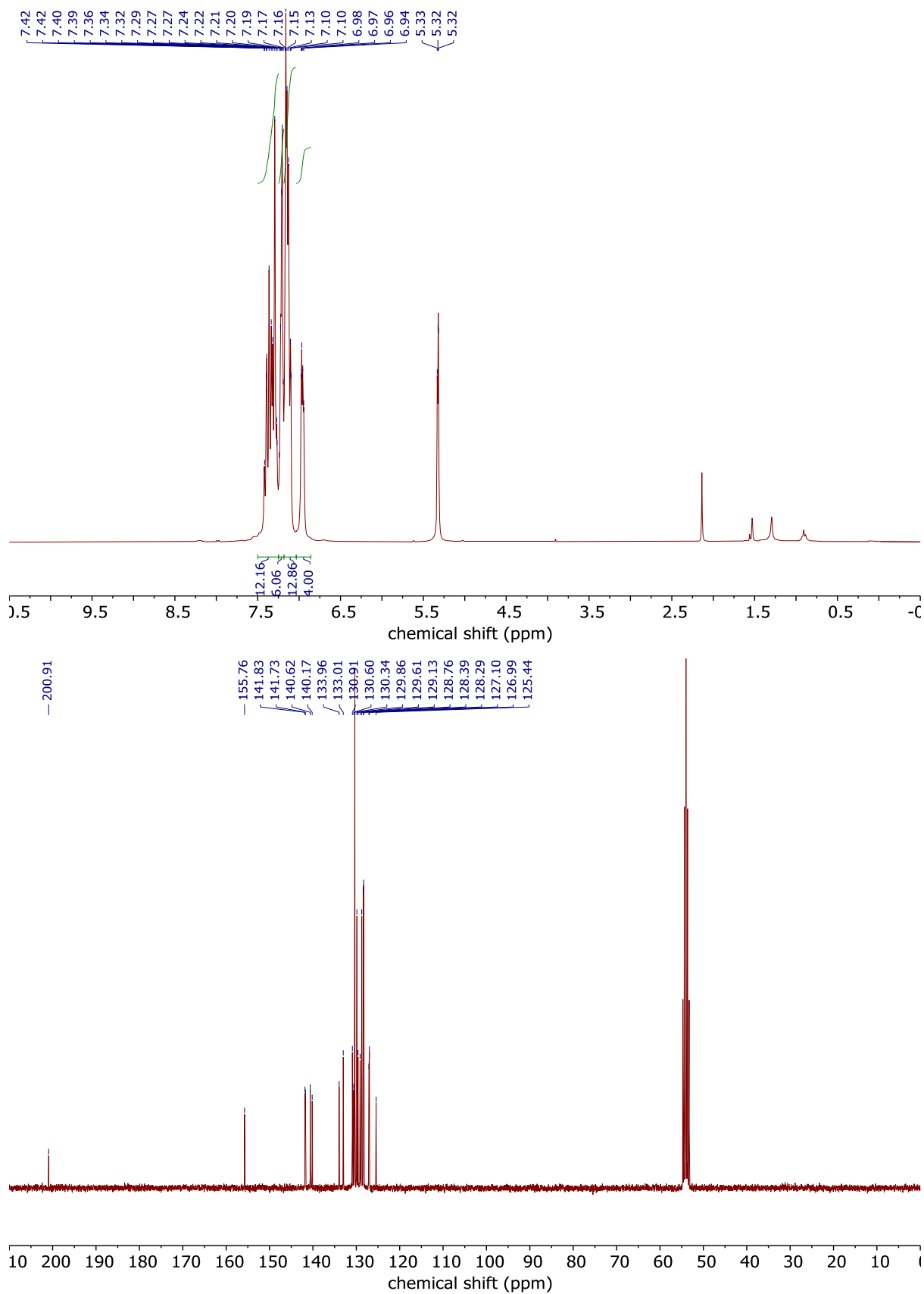


Figure S11. ^1H NMR (up, 300 MHz, CD_2Cl_2) and ^{13}C NMR spectra (down, 75 MHz, CD_2Cl_2) of 18.

2.3 References

- (1) Hammer, B. A. G.; Müllen, K. Expanding the Limits of Synthetic Macromolecular Chemistry through Polyphenylene Dendrimers. *J. Nanoparticle Res.* **2018**, *20* (10), 262.
- (2) Hammer, B. A. G.; Müllen, K. Dimensional Evolution of Polyphenylenes: Expanding in All Directions. *Chem. Rev.* **2016**, *116* (4), 2103–2140.
- (3) Wang, X.-Y.; Yao, X.; Müllen, K. Polycyclic Aromatic Hydrocarbons in the Graphene Era. *Sci. China Chem.* **2019**, *62* (9), 1099–1144.
- (4) Narita, A.; Wang, X. Y.; Feng, X.; Müllen, K. New Advances in Nanographene Chemistry. *Chem. Soc. Rev.* **2015**, *44* (18), 6616–6643.
- (5) Güçlü, A. D.; Potasz, P.; Korkusinski, M.; Hawrylak, P. *Graphene Quantum Dots*; NanoScience and Technology; Springer Berlin Heidelberg: Berlin, Heidelberg, 2014.
- (6) Wu, J.; Pisula, W.; Müllen, K. Graphenes as Potential Material for Electronics. *Chem. Rev.* **2007**, *107* (3), 718–747.
- (7) Simpson, C. D.; Brand, J. D.; Berresheim, A. J.; Przybilla, L.; Räder, H. J.; Müllen, K. Synthesis of a Giant 222 Carbon Graphite Sheet. *Chem. - A Eur. J.* **2002**, *8* (6), 1424–1429.
- (8) Feng, X.; Wu, J.; Ai, M.; Pisula, W.; Zhi, L.; Rabe, J. P.; Müllen, K. Triangle-Shaped Polycyclic Aromatic Hydrocarbons. *Angew. Chem. Int. Ed.* **2007**, *46* (17), 3033–3036.
- (9) Müller, M.; Iyer, V. S.; Kübel, C.; Enkelmann, V.; Müllen, K. Polycyclic Aromatic Hydrocarbons by Cyclodehydrogenation and Skeletal Rearrangement of Oligophenylenes. *Angew. Chem. Int. Ed.* **1997**, *36* (15), 1607–1610.
- (10) Tomović, Ž.; Watson, M. D.; Müllen, K. Superphenalene-Based Columnar Liquid Crystals. *Angew. Chem. Int. Ed.* **2004**, *43* (6), 755–758.
- (11) Beser, U.; Kastler, M.; Maghsoumi, A.; Wagner, M.; Castiglioni, C.; Tommasini, M.; Narita, A.; Feng, X.; Müllen, K. A C216-Nanographene Molecule with Defined Cavity as Extended Coronoid. *J. Am. Chem. Soc.* **2016**, *138* (13), 4322–4325.
- (12) Yang, X.; Dou, X.; Rouhanipour, A.; Zhi, L.; Räder, H. J.; Müllen, K. Two-Dimensional Graphene Nanoribbons. *J. Am. Chem. Soc.* **2008**, *130* (13), 4216–4217.
- (13) Tan, Y. Z.; Yang, B.; Parvez, K.; Narita, A.; Osella, S.; Beljonne, D.; Feng, X.; Müllen, K. Atomically Precise Edge Chlorination of Nanographenes and Its Application in Graphene Nanoribbons. *Nat. Commun.* **2013**, *4* (May), 1–7.
- (14) Watson, M. D.; Fechtenkötter, A.; Müllen, K. Big Is Beautiful—“Aromaticity” Revisited from the Viewpoint of Macromolecular and Supramolecular Benzene Chemistry. *Chem. Rev.* **2001**, *101* (5), 1267–1300.
- (15) Han, M. Y.; Özyilmaz, B.; Zhang, Y.; Kim, P. Energy Band-Gap Engineering of Graphene Nanoribbons. *Phys. Rev. Lett.* **2007**, *98* (20), 206805.
- (16) Bai, J.; Duan, X.; Huang, Y. Rational Fabrication of Graphene Nanoribbons Using a Nanowire Etch Mask. *Nano Lett.* **2009**, *9* (5), 2083–2087.
- (17) Hou, I. C. Y.; Narita, A.; Müllen, K. Stepwise Lateral Extension of Phenyl-Substituted Linear Polyphenylenes. *Macromol. Chem. Phys.* **2020**, *221* (1), 1900374.
- (18) Dössel, L. *Nanographene Als Funktionale Materialien Und Synthetische Herausforderung*. Johannes Gutenberg-Universität, Mainz, 2011.
- (19) Simpson, C. D.; Mattersteig, G.; Martin, K.; Gherghel, L.; Bauer, R. E.; Räder, H. J.; Müllen, K. Nanosized Molecular Propellers by Cyclodehydrogenation of Polyphenylene Dendrimers. *J. Am. Chem. Soc.* **2004**, *126* (10), 3139–3147.
- (20) Zhao, W.; Huang, L.; Guan, Y.; Wulff, W. D. Three-Component Asymmetric Catalytic Ugi Reaction - Concinnity from Diversity by Substrate-Mediated Catalyst Assembly. *Angew. Chem. Int. Ed.* **2014**, *53* (13), 3436–3441.
- (21) Shen, X.; Ho, D. M.; Pascal, R. A. Synthesis of Polyphenylene Dendrimers Related to “Cubic Graphite.” *J. Am.*

2.3 References

- Chem. Soc.* **2004**, *126* (18), 5798–5805.
- (22) Hu, Y.; Xie, P.; De Corato, M.; Ruini, A.; Zhao, S.; Meggendorfer, F.; Straasø, L. A.; Rondin, L.; Simon, P.; Li, J.; et al. Bandgap Engineering of Graphene Nanoribbons by Control over Structural Distortion. *J. Am. Chem. Soc.* **2018**, *140* (25), 7803–7809.
- (23) Narita, A.; Verzhbitskiy, I. A.; Frederickx, W.; Mali, K. S.; Jensen, S. A.; Hansen, M. R.; Bonn, M.; De Feyter, S.; Casiraghi, C.; Feng, X.; et al. Bottom-up Synthesis of Liquid-Phase-Processable Graphene Nanoribbons with near-Infrared Absorption. *ACS Nano* **2014**, *8* (11), 11622–11630.
- (24) Narita, A.; Feng, X.; Hernandez, Y.; Jensen, S. A.; Bonn, M.; Yang, H.; Verzhbitskiy, I. A.; Casiraghi, C.; Hansen, M. R.; Koch, A. H. R.; et al. Synthesis of Structurally Well-Defined and Liquid-Phase-Processable Graphene Nanoribbons. *Nat. Chem.* **2014**, *6* (2), 126–132.
- (25) Treier, M.; Pignedoli, C. A.; Laino, T.; Rieger, R.; Müllen, K.; Passerone, D.; Fasel, R. Surface-Assisted Cyclodehydrogenation Provides a Synthetic Route towards Easily Processable and Chemically Tailored Nanographenes. *Nat. Chem.* **2011**, *3* (1), 61–67.
- (26) Sun, Q.; Zhang, R.; Qiu, J.; Liu, R.; Xu, W. On-Surface Synthesis of Carbon Nanostructures. *Adv. Mater.* **2018**, *30* (17), 1705630.
- (27) Zhong, Q.; Hu, Y.; Niu, K.; Zhang, H.; Yang, B.; Ebeling, D.; Tschakert, J.; Cheng, T.; Schirmeisen, A.; Narita, A.; et al. Benzo-Fused Periacenes or Double Helicenes? Different Cyclodehydrogenation Pathways on Surface and in Solution. *J. Am. Chem. Soc.* **2019**, *141* (18), 7399–7406.
- (28) Saywell, A.; Sprafke, J. K.; Esdaile, L. J.; Britton, A. J.; Rienzo, A.; Anderson, H. L.; O’Shea, J. N.; Beton, P. H. Conformation and Packing of Porphyrin Polymer Chains Deposited Using Electrospray on a Gold Surface. *Angew. Chem. Int. Ed.* **2010**, *49* (48), 9136–9139.
- (29) Kondratuk, D. V.; Perdigão, L. M. A.; Esmail, A. M. S.; O’Shea, J. N.; Beton, P. H.; Anderson, H. L. Supramolecular Nesting of Cyclic Polymers. *Nat. Chem.* **2015**, *7* (4), 317–322.
- (30) Hinaut, A.; Pawlak, R.; Meyer, E.; Glatzel, T. Electrospray Deposition of Organic Molecules on Bulk Insulator Surfaces. *Beilstein J. Nanotechnol.* **2015**, *6* (1), 1927–1934.
- (31) Hinaut, A.; Meier, T.; Pawlak, R.; Feund, S.; Jöhr, R.; Kawai, S.; Glatzel, T.; Decurtins, S.; Müllen, K.; Narita, A.; et al. Electrospray Deposition of Structurally Complex Molecules Revealed by Atomic Force Microscopy. *Nanoscale* **2018**, *10* (3), 1337–1344.
- (32) Nguyen, T. T. T.; Baumgarten, M.; Rouhanipour, A.; Räder, H. J.; Lieberwirth, I.; Müllen, K. Extending the Limits of Precision Polymer Synthesis: Giant Polyphenylene Dendrimers in the Megadalton Mass Range Approaching Structural Perfection. *J. Am. Chem. Soc.* **2013**, *135* (11), 4183–4186.

Chapter 3. Stepwise Lateral Extension of Phenyl Substituted Linear Polyphenylenes

Ian Cheng-Yi Hou¹, [REDACTED]^{1,2,*} and [REDACTED]^{1,3,*}

¹Max Planck Institute for Polymer Research, Ackermannweg 10, D-55128 Mainz, Germany

²Organic and Carbon Nanomaterials Unit, Okinawa Institute of Science and Technology Graduate University, 1919-1 Tancha, Onna-son, Kunigami, Okinawa 904-0495, Japan

³Institute of Physical Chemistry, Johannes Gutenberg-University Mainz, Duesbergweg 10-14, D-55128 Mainz, Germany

Published in: *Macromol. Chem. Phys.* **2020**, *221* (1), 1900374. DOI: 10.1002/macp.201900374. Reprinted with permission. Copyright: 2020, WILEY-VCH.

Contribution: Organic synthesis and characterization. First draft preparation and correction. Submission and revision.

3.1 Abstract

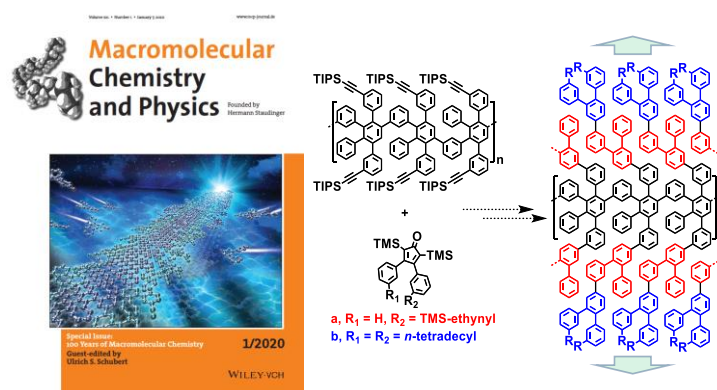


Table Of Content. Polyphenylenes (PPs) have been employed as polymer precursors for the synthesis of graphene nanoribbons (GNRs) with a width up to 2 nm. Here, a synthetic protocol is proposed for lateral extension of PPs toward a series of polymer that is structurally suitable for the synthesis of GNRs wider than 2 nm via repetitive Diels-Alder reactions.

Polyphenylenes (PPs) are unique polymers showing high mechanical strength and chemical stability with potential applications, for example, in proton transfer and gas-separation membranes. Moreover, recent studies have demonstrated that phenyl substituted linear PPs can serve as precursors for bottom-up syntheses of graphene nanoribbons (GNRs), a new class of nanoscale carbon materials promising for nanoelectronics. Notably, lateral extension of such linear PPs with appropriate “branched” design, namely by avoiding spatial overlap of benzene rings in their projection into a plane, can lead to wider GNRs with modulated electronic and optical properties. GNRs with width up to ~2 nm have thus been obtained, but there is a lack of synthetic methods for further expanding PPs laterally to achieve even wider GNRs. Here, phenyl substituted linear PPs bearing two ethynyl groups at “outer” positions in

each repeating unit together with 3,4-diphenylcyclopentadienones bearing a trimethylsilyl(TMS)-protected ethynyl group are used for stepwise lateral extension of the PPs based on a sequence of Diels-Alder cycloadditions and deprotections. Each successive reaction step could be corroborated by ^1H NMR and IR spectroscopy as well as gel permeation chromatography, providing a new pathway towards linear PPs that could potentially serve as precursors of wider GNRs with tunable electronic bandgap.

3.2 Introduction

Polyphenylenes (PPs) are polymers with exceptional properties^{1,2} including outstanding mechanical strength as well as thermal and chemical stability. This qualifies PPs for applications under harsh conditions such as proton-transfer³⁻⁷, electrodialysis⁸ and gas separation^{9,10} membranes. Linear PPs with phenyl substituents can also serve as precursors for graphene nanoribbons (GNRs), nanometer-wide strips of graphene. The underlying concept is to appropriately design branched PP structures that can be fully planarized by C-C bond formation between the benzene rings, typically through oxidative cyclodehydrogenation.^{1,2,11-13} GNRs synthesized by such bottom-up methods have not only contributed to fundamental studies in condensed matter physics, but also exhibited potential for future applications in nanoelectronics, photonics, and quantum computing.¹⁴⁻¹⁶

One of the most efficient methods to synthesize PPs is through the use of Diels-Alder cycloadditions between cyclopentadienone (CP) derivatives, usually a 2,3,4,5-tetraarylcyclopentadienone, and alkynes leading to, both, linear and dendritic PPs.^{1,2} In comparison with other polymerization methods typically through transition-metal catalyzed/mediated reactions, Diels-Alder reaction, which underdoes without metal catalyst or other reagents, has advantages also with high efficiency.^{12,17} An A₂B₂-type Diels-Alder polymerization between an A₂ monomer having two CP moieties and a bisalkyne serving as a B₂ monomer has been known for more than 70 years^{18,19} and provided numerous linear PPs with a backbone of poly[(*p*-phenylene)-*ran*-(*m*-phenylene)].² On the other hand, CP derivatives carrying an alkyne functional group can serve as bifunctional monomers which undergo AB-type Diels-Alder polymerization to yield linear PPs with surprisingly high persistence length.^{17,20} Moreover, PPs synthesized by this procedure exhibit higher degrees of polymerizations (DP) than that of those made by A₂B₂-type polymerization.^{17,21,22}

In 2014, we have reported an AB-type Diels-Alder polymerization of tetraphenyl-CP **1a** leading to linear **PP-Ia** with the poly[(*p*-phenylene)-*ran*-(*m*-phenylene)] backbone (**Figure 1a**). The weight-average molecular weight (M_w) of **PP-Ia** exceeded 600,000 g/mol, which was much larger than the values obtained with previous PPs prepared by the A₂B₂-type Diels-Alder polymerization. The structure of **PP-Ia** can be projected into a plane without spatial overlap of benzene rings. “Planarization” of **PP-Ia** through oxidative cyclodehydrogenation could, thus, provide structurally defined GNRs.¹⁷

Moreover, we have demonstrated the synthesis of laterally extended linear **PP-Ib** by using CP-based monomer **1b** having four extra phenyl rings in addition to the structure of **1a**

(Figure 1a).²¹ **PP-Ib** was planarized by cyclodehydrogenation furnishing an even wider GNR with a width of ca. 2 nm. Remarkably, this quasi one-dimensional GNR exhibited a smaller electronic bandgap compared to that of the narrower GNRs obtained from **PP-Ia**.²¹ However, synthesis of linear PPs broader than **PP-Ib** has remained elusive, although it would lead to even wider GNRs with tunable bandgaps essential for the development of GNR-based nanoelectronics.

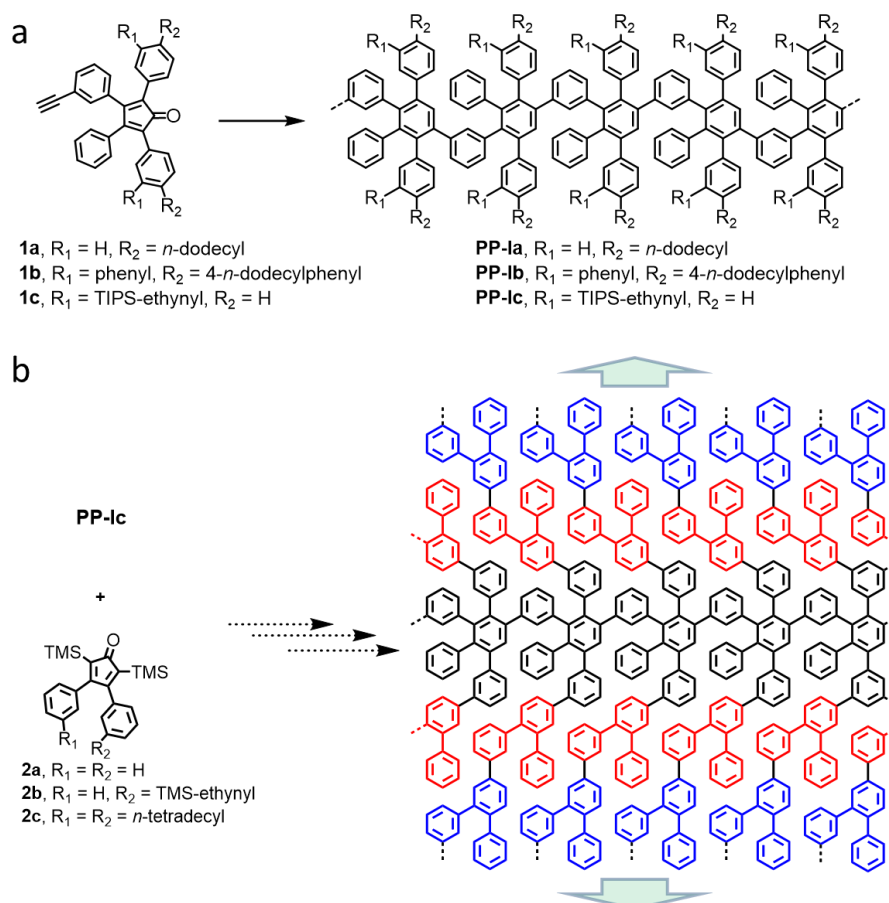


Figure 1. (a) Diels-Alder polymerization of tetraphenyl-CPs **1a–c** to **PP-Ia–c**, respectively. (b) Proposed strategy for the lateral extension of **PP-Ic** by a sequence of deprotections and Diels-Alder reactions with diphenyl-CPs **2b,c** to form PPs with architectures that are suitable for planarization into wider GNRs.

Considering synthetic complexity expected for further extension of monomer **1b** with more phenyl rings, as well as the importance of making PPs with different degrees of lateral extension, we have conceived a universal approach to “broaden” linear PPs in a stepwise manner. To this end, we employ linear PPs bearing two ethynyl groups at the “outer” positions in each repeating unit which can be subjected to Diels-Alder reactions for “growth” in the lateral direction. We choose CPs that have trimethylsilyl (TMS)-protected ethynyl

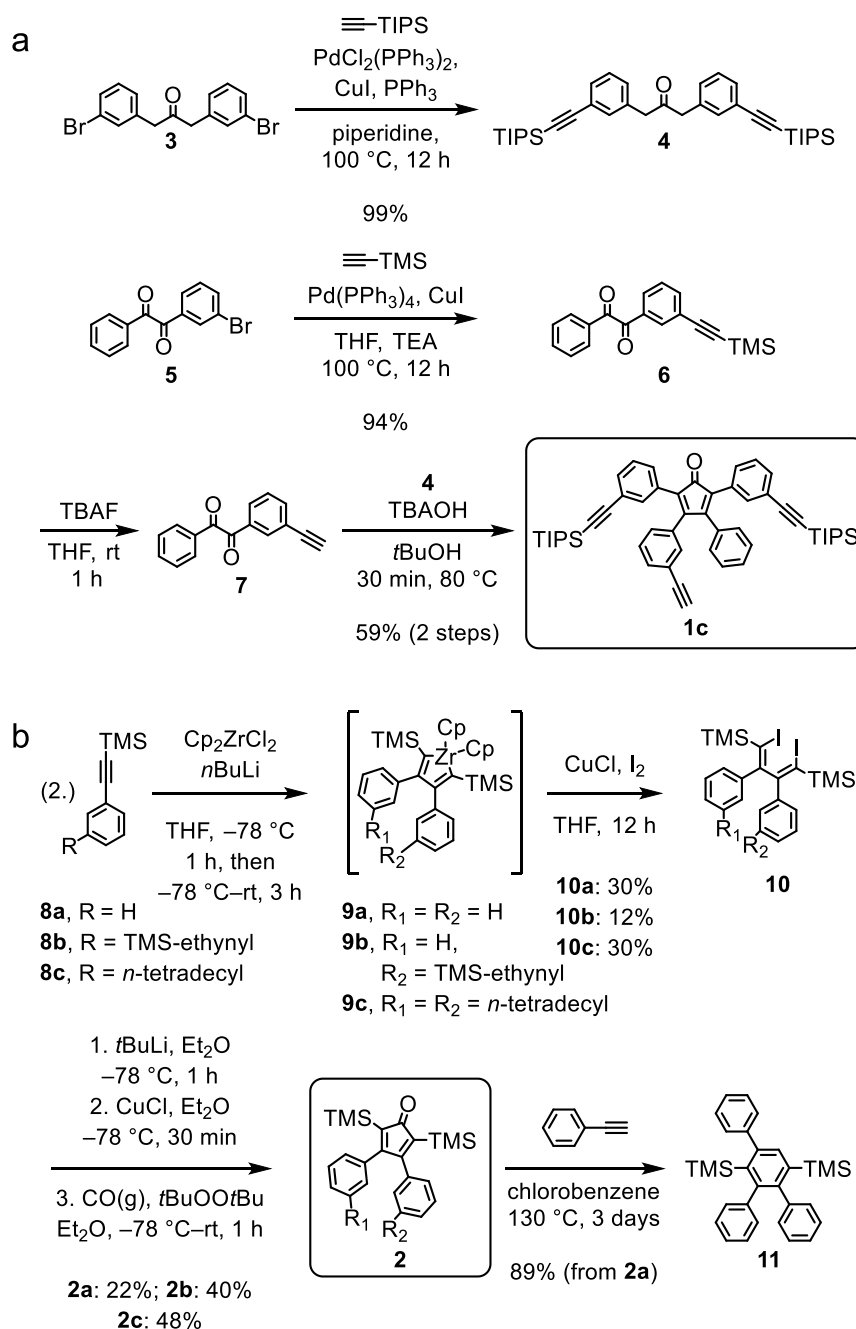
groups which allows for the lateral expansion of PPs step by step through a sequence of Diels-Alder reaction and deprotection. Such a synthetic strategy based on sequential Diels-Alder reactions has been used for the divergent construction of dendritic PPs, but not previously considered for linear PPs (**Figure 1b**).^{1,23,24}

Here, we synthesized CP-based monomer **1c** bearing two triisopropylsilyl(TIPS)-protected ethynyl groups on the peripheral phenyl rings. Polymerization of **1c** provided **PP-Ic** which was subjected to deprotection to **PP-Id** having ethynyl groups for the further lateral growth (**Figure 1a**). As to the diene counterpart, 3,4-diphenyl-CP **2b** with TMS-protected ethynyl groups was utilized instead of the typical tetraphenyl-CP. It is this “trick” which avoids the spatial overlap of benzene rings in the 2D projection of the resulting PPs (**Figure 1b**). After reaching the desired degree of lateral extension by repeating the sequence of the Diels-Alder cycloaddition with **2b** and deprotection, a reaction with 3,4-diphenyl-CP **2c** carrying solubilizing long alkyl chains can serve as an end-capping. The 2,5-positions of the CP cores of **2b,c** were substituted with TMS moieties as protecting groups, because non-substituted 3,4-diphenyl-CP can undergo irreversible Diels-Alder dimerization even at a room temperature.²⁵ Diels-Alder cycloadditions of **PP-Id** with **2b**, deprotection and subsequent Diels-Alder reaction with **2c** were corroborated by gel permeation chromatography (GPC), NMR, and FTIR spectroscopy. Our preliminary attempts to planarize the resulting PPs through oxidative cyclodehydrogenation failed to give wider GNRs without defects, based on an analysis by UV-vis absorption spectrum. Nevertheless, our strategy for the step-by-step lateral extension of PPs can be applicable to syntheses of different linear PPs with various degree of lateral expansion, including those that potentially serve as precursors of GNRs with distinct structures.

3.3 Result and Discussion

3.3.1. Synthesis of Tetraphenyl- and Diphenyl-substituted CP Building Blocks

3.3.1.1 Synthesis of Tetraphenyl-CP **1c**



Scheme 1. Synthesis of (a) tetraphenyl-CP **1c** and (b) diphenyl-CP **2a-c**. THF: tetrahydrofuran. TEA: triethylamine. TBAOH: tetra-*n*-butylammonium hydroxide. Cp₂ZrCl₂: zirconocene dichloride.

For the synthesis of 3-(*m*-ethynylphenyl)-4-phenyl-2,5-bis{*m*-[(triisopropyl)silylethynyl]phenyl}cyclopenta-2,4-dien-1-one (**1c**) as the CP-based monomer for the polymerization to **PP-1c**, 1,3-bis(3-bromophenyl)acetone²⁶ (**3**) was initially reacted

with TIPS-acetylene under Sonogashira conditions to give bis(TMS-ethynylphenyl)acetone **4**. In parallel, 3-bromobenzil¹⁷ (**5**) was functionalized with TMS-ethynyl group and then deprotected with tetra-*n*-butylammonium fluoride (TBAF) to provide 3-ethynylbenzil (**7**). Subsequently, a Knoevenagel condensation between **4** and **6** afforded monomer **1c** in 59% yield (**Scheme 1a**).

3.3.1.2 Synthesis of Diphenyl-CP **2a–c**

To synthesize 3,4-diphenyl-CPs **2a** and **2c**, we first carried out a zirconocene-mediated dimerization of aryl TMS-acetylene derivatives **8a** and **8c**²⁷, forming Zr-metallacycle intermediates **9a** and **9c**, respectively (**Scheme 1b**).²⁸ Attempts at direct iodination of **9a** with I₂ failed.²⁸ However, after converting **9a,c** into organo-copper species in situ by reaction with CuCl, iodination of the copper species smoothly produced (1*Z*,3*Z*)-1,4-diiodo-2,3-diphenylbutadiene derivatives **10a,c** with high regio- and stereoselectivity, but moderate yields of 30% for both (**Scheme 1b**).^{28–30} **10b** was synthesized similarly but starting from a mixture of **8a** and **8b**. Because of formation of a large amount of homocoupled products, which rendered a purification process tedious, **10b** was isolated in a much lower yield of 12%. We have also tried, but failed, to synthesize **10b** in a controlled manner through a tandem addition of **8a,b**, following literature-known conditions for the coupling of other TMS-alkynes.^{28,31,32} Next, iodo groups of **10a–c** were lithiated by treatment with *t*BuLi and converted again into the organo-copper reagents by reacting with CuCl (**Scheme 1b**). We then tried to react the resulting organo-copper intermediates with different carbonyl sources for the formation of the corresponding CPs **2a–c**. After failures with carbon dioxide gas³³ and oxalyl chloride³⁴ we found that the reaction proceeded with carbon monoxide gas successfully yielding 3,4-diphenyl-CPs **2a–c** after oxidation in 22–48% yield (**Scheme 1b**).³⁵ It was not possible to perform a one-pot synthesis of CP derivatives **2a–c** directly from **8a–c**, respectively, without isolation of the diiodo species **9a–c**.³⁴

After obtaining diphenyl-CPs **2a–c**, we first tested their stability and reactivity under conditions commonly used for a Diels-Alder reaction between tetraphenyl-CPs and aromatic compounds bearing ethynyl groups. **2a** was heated in a concentration of 0.2 M at 130 °C in *o*-xylene for three days with no observable reaction, but could be recovered in more than 95% yield demonstrating a largely increased stability of the CP core with the TMS-substituents.³³ This condition was later-on used in the Diels-Alder reactions for the lateral extension of PPs (*vide infra*). Next, **2a** was heated with 1.1 eq. of phenylacetylene at 120 °C in chlorobenzene for three days until it was fully consumed. 1,4-Bis(trimethylsilyl)-2,3,6-triphenylbenzene (**11**)

was isolated as product in 89% yield with no byproduct, for the first time demonstrating the high reactivity of these diphenyl-CPs for a Diels-Alder reaction (**Scheme 1b**).

3.3.2 Optimized Polymerization Conditions for Tetraphenyl-substituted CP **1c**

We initially attempted the Diels-Alder polymerization of CP **1c** in neat phase, but only polymers with number average molecular weights (M_n) lower than 7 kg/mol were obtained, although such conditions were reported to provide high-molecular weight **PP-Ia** from **1a**.²¹ Nevertheless, polymerization of **1c** in a highly concentrated Ph₂O solution (>2 M) at approximately 140–150 °C proceeded efficiently, reaching M_n above 25 kg/mol in 12 h. Polymerization of **1c** at even higher temperature (>180 °C) led to **PP-Ic** with a larger M_n of 65 kg/mol. However, such high molecular-weight **PP-Ic** turned out to be unsuitable for subsequent lateral extension studies (*vide infra*) since the products became insoluble in organic solvents after Diels-Alder reaction with **2b** or **2c**. Moreover, ¹H NMR analyses of **PP-Ic** polymerized at approximately 140 and 180 °C, both, showed a signal at 1.25 ppm (**Figure 2a**). This could be assigned to protons of TIPS-groups that were attached to a benzene ring instead of an ethynylene unit,³⁶ indicating an undesirable Diels-Alder reaction at the protected TIPS-ethynyl groups.

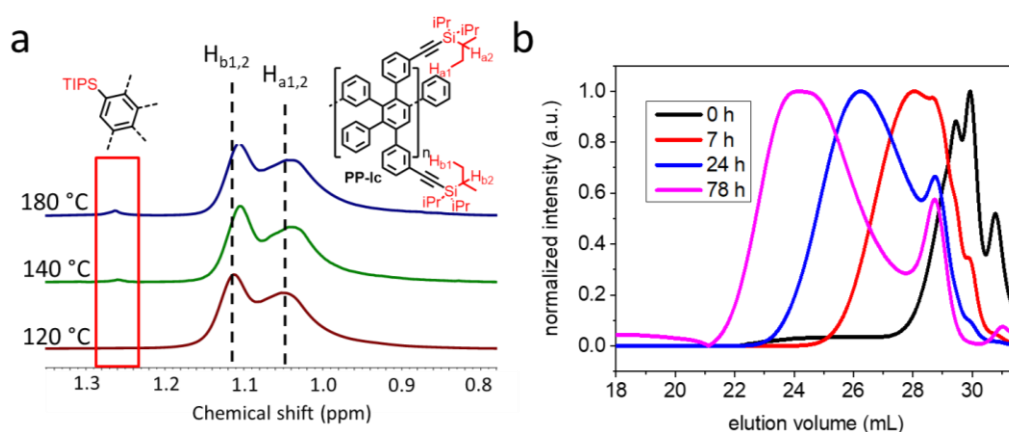


Figure 2. (a) ¹H NMR signals of TIPS-group of **PP-Ic** polymerized at different temperatures, measured in CD₂Cl₂ at 290 K. (b) GPC analysis taken at different time during polymerization of **1c** into **PP-Ic** at 120 °C. (Solvent: THF. Flow rate: 1 mL/min. Temperature: 30 °C.)

We thus aimed at **PP-Ic** with a smaller molecular weight by carrying out the polymerization of **1c** at a lower concentration of 0.65 M and lower temperature of 120 °C that was applied also to avoid the side reaction at TIPS-ethynyl groups. The polymerization under these conditions became slower compared to those of the higher-concentration experiments. The increase of DP could be monitored by GPC (**Figure 2b**), and the M_n of **PP-Ic** gradually

developed to around 13 kg/mol after 78 h together with disappearance of oligomers. The obtained **PP-Ic** still gave a pale purple color in solution indicating the presence of a tetraphenyl-CP moiety at a chain-end, which could interfere with the Diels-Alder reaction in the next step for the lateral extension (*vide infra*). **PP-Ic** was thus end-capped by reaction with phenylacetylene at 160 °C overnight. After the reaction, the purple color disappeared, suggesting the absence of CP groups in the polymer chain. To our delight, **1c** exclusively reacted at the terminal alkyne moieties under these polymerization conditions at 120 °C without showing a signal at 1.25 ppm (**Figure 2a**). Interestingly, the proton signals of TIPS-ethynyl groups split into two broad bands peaking at 1.11 and 1.05 ppm. This can be attributed to *m*-(TIPS-ethynyl)phenyl groups that are present in different environments where those with two *ortho* phenyl groups (H_{a1} and H_{a2}) are more shielded (**Figure 2a**). Moreover, matrix-assisted laser desorption-ionization time-of-flight mass spectrometric (MALDI-TOF) analysis of the treated **PP-Ic** revealed peaks at m/z corresponding to the mass of tetramer to decamer. There, all TIPS-protecting-groups remain intact while a phenyl group is attached through the end-capping, although an ethynyl group at the other end is presumably oxidized (**Figure S1**).

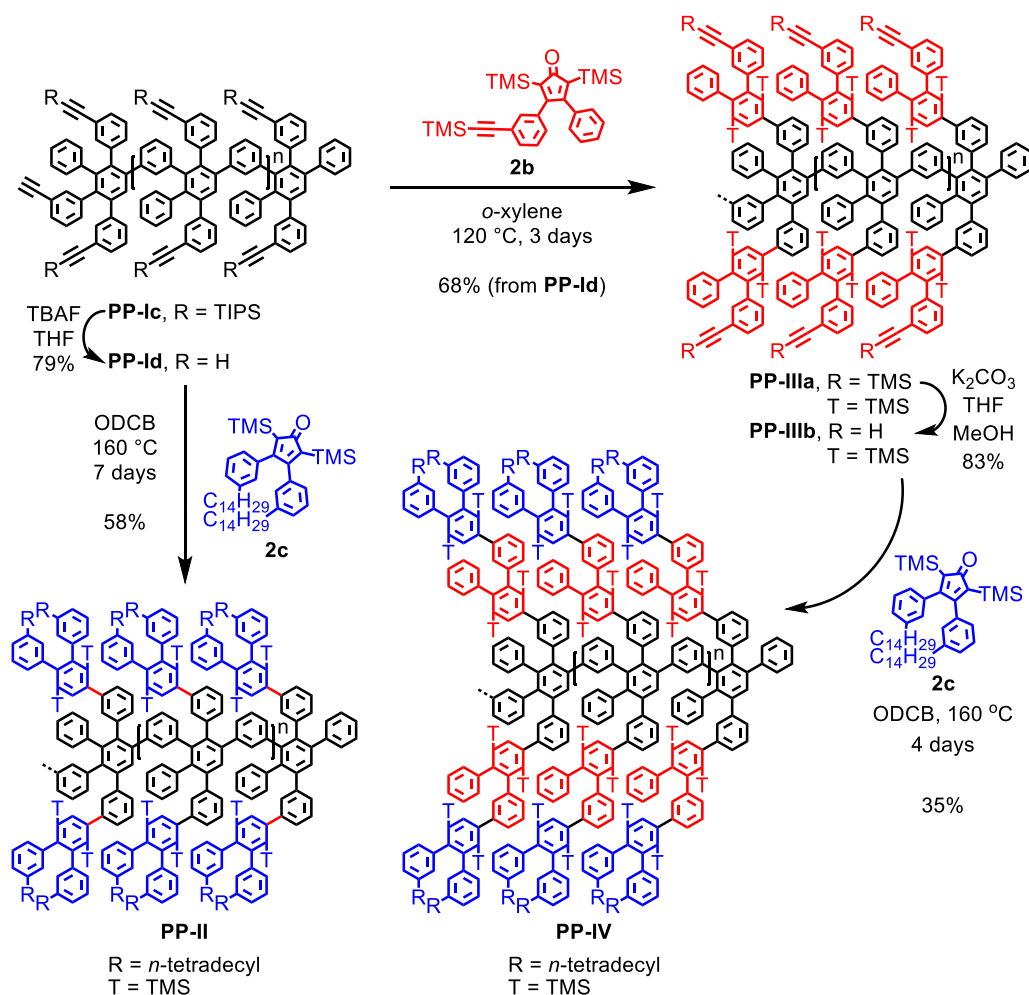
3.3.3 Lateral Extension of PP-Ic

2.3.1 Extension of **PP-Ic** toward **PP-II** and **PP-IIIa**

PP-Ic with a M_n around 13 kg/mol was next subjected to a sequence of deprotection and Diels-Alder cycloaddition with the diphenyl-CPs **2b** and/or **2c** for lateral growth (**Scheme 2**). Firstly, a diluted solution of **PP-Ic** in THF was reacted with TBAF to remove TIPS-protecting groups, furnishing **PP-Id** with multiple peripheral ethynyl functional groups as evidenced by ^1H NMR. The split signals of TIPS functional groups (*vide supra*) of **PP-Ic** at 0.9–1.2 ppm completely disappeared in the ^1H NMR spectrum of **PP-Id**, with simultaneous appearance of signals of ethynyl groups centered at 3.0 ppm, suggesting complete deprotection (**Figure 3**). The ethynyl signals of **PP-Id** were also present as two bands induced by different environments surrounding *m*-ethynylphenyl moieties (*vide supra*).

PP-Id retained good solubility in THF and other common organic solvents which allowed the further Diels-Alder reactions of the terminal alkynes. **PP-Id** was thus reacted either with diphenyl-CP **2c** to afford **PP-II** decorated with alkyl chains, or **2b** to give **PP-IIIa** possessing TMS-ethynyl groups ready for further expansion. The reaction of **PP-Id** with **2c** in *o*-dichlorobenzene (ODCB) at 150 °C produced **PP-II** in 48% yield. The reaction of **PP-Id** with **2b** in *o*-xylene at 120 °C, where the lower reaction temperature allowed one to avoid

reaction of TMS-protected internal alkynes (*vide supra*), produced **PP-IIIa** in 65% yield (**Scheme 2**). During the conversions, gel formation was commonly observed. This fact could explain the relatively low yields, especially for **PP-II**. The ^1H NMR spectrum of **PP-IIIa** demonstrates complete conversion of all the ethynyl groups since their signals at 3.0 ppm vanish (**Figure 3**). On the other hand, TMS signals at -1.0–0.5 ppm emerge, which can be assigned to three different TMS groups introduced by the addition of diphenyl-CP **2b**. The signals of TMS groups on benzene rings at -1.0–0.0 ppm are also split into two bands for similar reasons as in **PP-Ic** and **PP-Id**. The TMS-groups on ethynylene moieties are less shielded, and their signals appear at lower field of about 0.0–0.5 ppm (**Figure 3**). Similar spectral features can also be observed in the ^1H NMR spectrum of **PP-II** (**Figure S23**).



Scheme 2. Lateral extension reactions of **PP-Ic**.

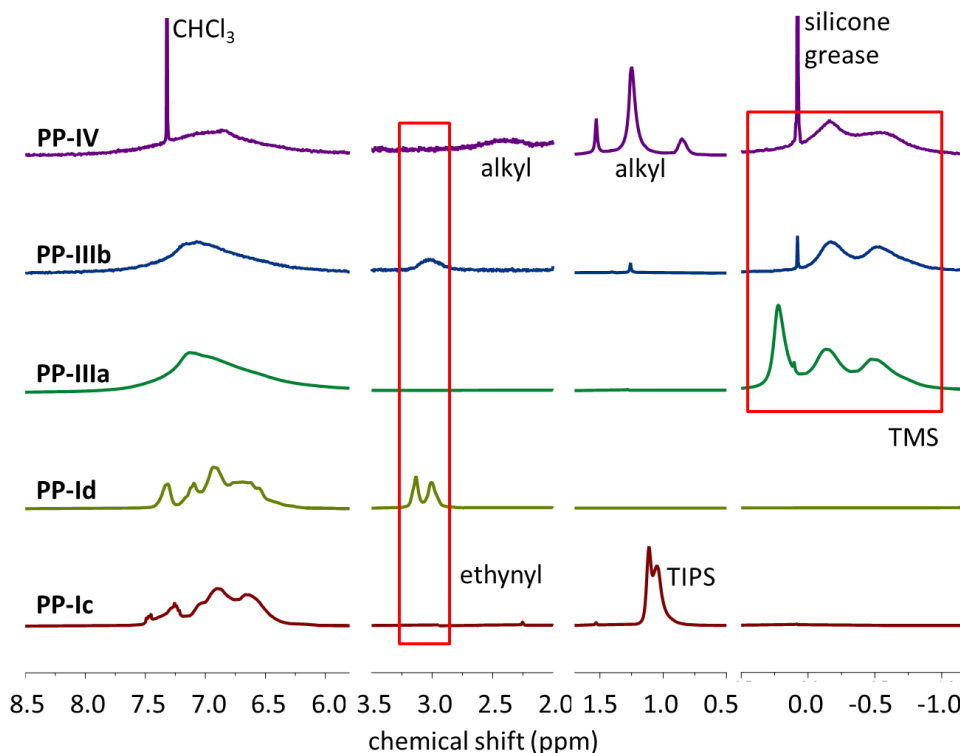


Figure 3. ^1H NMR spectra of **PP-Ic**, **PP-Id**, **PP-IIIa**, **PP-IIIb** and **PP-IV**, measured in CD_2Cl_2 at 290 K. Regions in red circle show the characteristic signals of different functional groups.

2.3.2 Extension of **PP-IIIa** toward **PP-IV**

The TMS protecting groups of **PP-IIIa** can be removed regenerating Diels-Alder reactive ethynyl groups for further reactions. To prevent the possible removal of TMS-groups on phenylenes, the deprotection reaction was conducted under a milder condition by reacting with K_2CO_3 in THF/MeOH (2/1) as cosolvents. To our delight, the polymer retained good solubility even in such a polar solvent combination during deprotection, resulting in fully deprotected **PP-IIIb** in high yield (**Scheme 2**). In the ^1H NMR spectrum of **PP-IIIb** the signals of TMS-ethynyl groups are completely gone, while those attached to benzene rings remain, confirming good selectivity and efficiency of the deprotection reaction (**Figure 3**). Unlike those for **PP-Id**, the signals of the ethynyl groups on **PP-IIIb** exhibit a single broad band centered at 3.0 ppm as a result of similar local environments for every *m*-ethynylphenyl moieties.

Finally, to prove that **PP-IIIb** can still grow further, it was allowed to react with the end-capping diphenyl-CP **2c** in ODCB at 150 °C to give **PP-IV** in 35% yield (**Scheme 2**). The low yield was again a result of the gel forming tendency of the polymer product. Signals of the long alkyl chains arise at 0.75–1.5 ppm together with disappearance of the signals of

ethynyl groups at 3.0 ppm in the ^1H NMR spectrum of **PP-IV**. A broad signal at 2.0–3.0 ppm is attributed to protons on α -positions of the alkyl chains. The relative signal intensities agreed with theoretical values for **PP-Ic**, **PP-Id**, **PP-II**, **PP-IIIa**, **PP-IIIb** and **PP-IV** in their ^1H NMR spectra, corroborating their chemical structures (**Figure S21–27**). It is important to note that, since both **PP-IIIa** and **PP-IIIb** still retain good solubility in common organic solvents, **PP-IIIb** can also react repeatedly with diphenyl-CP **2b** using the same procedure toward a series of wider and wider linear PPs.

2.3.3 Attempts of Planarization of **PP-II** into GNR

Having these expanded PPs in hand, we made preliminary attempts at their planarization into GNRs. It is reported that TMS-groups can be removed during oxidative cyclodehydrogenation reactions.³⁷ Thus, we first tried the cyclodehydrogenation of **PP-II** under the standard conditions used for syntheses of GNRs¹⁷ using FeCl_3 (15 eq. per C-C bond to be formed) in a mixture of dichloromethane and nitromethane at room temperature for three days. However, the resulting product exhibited a broad absorption extending up to ~800 nm with a shoulder at around 400–550 nm in the UV-Vis spectrum measured for a suspension in 1,2,4-trichlorobenzene (**Figure S2**). In comparison to the previously reported GNR derived from **PP-Ib**, showing a defined absorption band with a maximum at 660 nm and an onset at ~1000 nm, the blue-shifted and rather featureless absorption of the product indicated incomplete planarization of **PP-II**. We then removed the TMS-groups by treatment of **PP-II** with HBr under microwave conditions (see Supporting Information for details) considering that the TMS-groups might have hampered the efficient planarization. The UV-vis absorption spectrum of the resulting product after the cyclodehydrogenation was similar to the one obtained without removal of TMS-substituents. The incomplete cyclodehydrogenation of **PP-II** might be due to the formation of isomers through C-C bond closure at undesired positions. This would, of course, prohibit further planarization (**Figure S3**). Optimization of the cyclodehydrogenation conditions as well as the design of the PP for the fabrication of wider GNRs are planned in our laboratory.

3.3.4 IR and GPC Analysis of PPs

2.4.1 IR Analyses of PPs

To gain further insight into the structures of the obtained PPs, powders of **PP-Ic**, **PP-II**, **PP-IIIa** and **PP-IV** were analyzed by IR spectroscopy (**Figure 4**). All four PPs show IR bands at

3100–3000 cm^{-1} and 3000–2800 cm^{-1} which correspond to sp^2 and sp^3 C-H stretching, respectively. Interestingly, **PP-IIIa** has relatively weak sp^3 C-H stretching signals, reflecting its less abundant alkyl groups. It is important to note that there is no signal above 3300 cm^{-1} in all cases suggesting the absence of terminal alkynes. **PP-Ic** and **PP-IIIa** possess a peak at 2154 cm^{-1} which is not observed for **PP-II** nor **PP-IV**. This peak can be assigned to weak absorption of the $\text{C}\equiv\text{C}$ stretching of silylethynyl groups which exist in the structure of **PP-Ic** and **PP-IIIa**.³⁸ The presence of TMS-groups is demonstrated in the spectra of **PP-II**, **PP-IIIa** and **PP-IV** by observation of sharp C-Si stretching peaks at 1247 cm^{-1} and strong absorption bands at 837 cm^{-1} (**Figure 4**). There are weak bands at around 1715 cm^{-1} for **PP-II**, **PP-IIIa** and **PP-IV** (**Figure S4**)³⁸ which are most likely overtones of the strong absorption band at 837 cm^{-1} . However, they could also point toward residual carbonyl groups due to incomplete carbon monoxide extrusion after Diels-Alder reaction. The characteristic C-H bending peaks of 1,3-phenylenes are clearly observed for **PP-Ic** at around 880 and 780 cm^{-1} which appear as relatively weaker peaks for **PP-II**, **PP-IIIa** and **PP-IV**. The IR observations are in good agreement with structural feature of each PPs and suggest efficient functional group conversions.

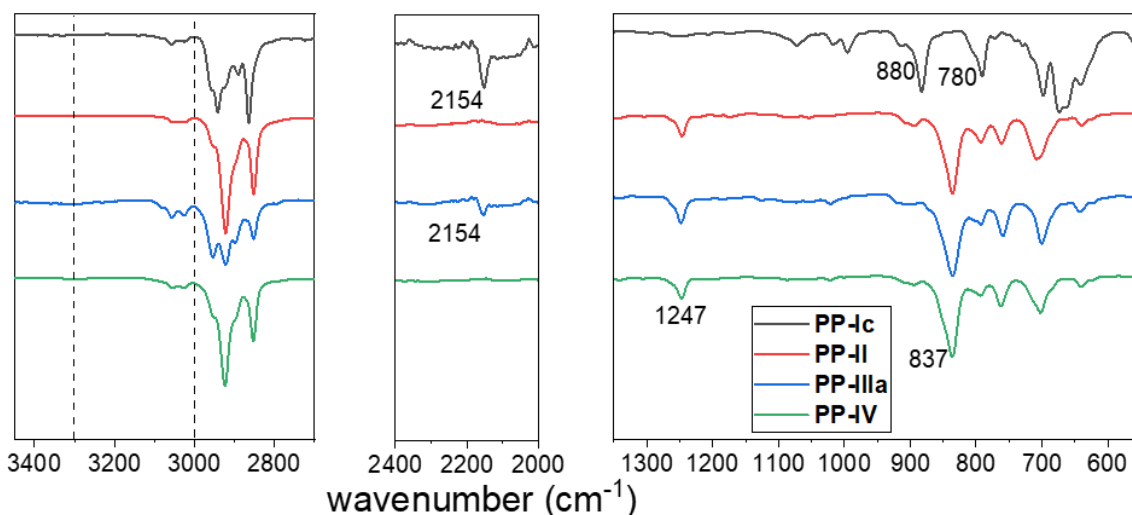


Figure 4. IR spectra of **PP-Ic**, **PP-II**, **PP-IIIa** and **PP-IV**.

2.4.2 GPC Analyses of PPs

Molecular weight distributions of **PP-Ic**, **PP-II**, **PP-IIIa** and **PP-IV** were analyzed by GPC with polystyrene as standards (**Figure 5** and **Table 1**). Assuming an ideal conversion in each lateral extension steps, a theoretical M_n of each PPs can be calculated based on M_n of **PP-Ic** (**Table 1**). The experimental M_n ratio of **PP-Ic/PP-II/PP-IIIa** is in good agreement with the

theoretical values (**Table 1**). However, the M_n of **PP-IV** appears to be much lower than predicted. This can be explained by the formation of insoluble gels during reaction since higher molecular-weight polymers have a lower solubility and a stronger tendency toward aggregation (*vide supra*). Note that the GPC plots of **PP-II**, **PP-IIIa** and **PP-IV** display small shoulder peaks at retention times around 16, 16, and 13 min, respectively, corresponding to higher molecular-weight species (**Figure 5**). In contrast, **PP-Ic** shows a simple Gaussian distribution, which suggests aggregation of **PP-II**, **PP-IIIa** and **PP-IV** in solution. Nevertheless, after complete removal of solvent to form their dry solid powders they can be dissolved again into organic solvents as transparent solutions without any visible particles or undissolved gel. One concludes that this aggregation process is reversible.

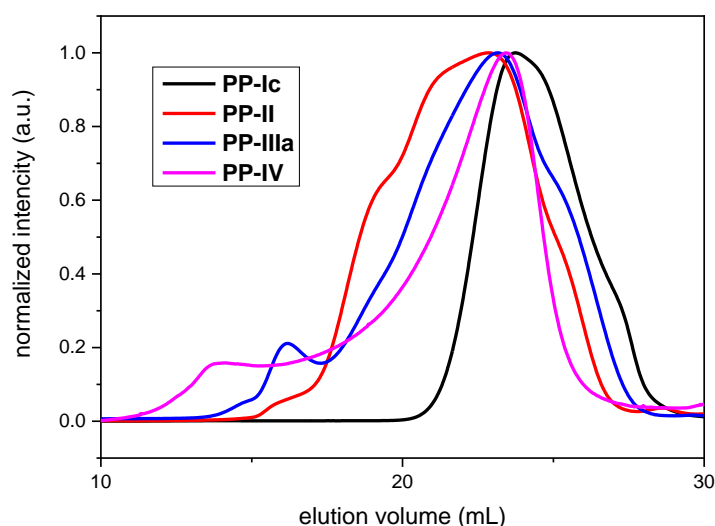


Figure 5. GPC spectra of **PP-Ic**, **PP-II**, **PP-IIIa** and **PP-IV** (Solvent: THF. Flow rate: 1 mL/min. Temperature: 30 °C).

Table 1. Molecular weight data extracted from GPC analysis^{a)} of polymer **PP-Ic**, **PP-II**, **PP-IIIa** and **PP-IV**.

PPs	M_n (g/mol)	M_n (calcd) ^{b)} (g/mol)	M_p (g/mol)	M_w (g/mol)	PDI
PP-Ic	21000	21000	42500	38500	1.83
PP-II	66200	52900	74100	211000	3.19
PP-IIIa	46400	36700	60200	154000	3.33
PP-IV	57500	73200	49000	222000	3.87

^{a)}Polystyrene as standard. ^{b)}Calculated based on M_n of **PP-Ic**.

3.4 Conclusion

We have developed an elegant way for lateral expansion of a linear PP by reaction with diphenyl-CP derivatives using a stepwise Diels-Alder cycloaddition/deprotection protocol. This route is commonly used in the field of dendritic PPs, but has so far not been applied within the synthesis of linear PPs. Each individual step of the extension procedure was monitored by recording ^1H NMR and IR spectra, showing successful functional group transformations. The resulting extended PPs were analyzed by GPC revealing the step-wise evolution of the molecular weight. Preliminary attempts at cyclodehydrogenation of these PPs were not successful. However, our synthetic protocol opens up further opportunities for the synthesis of wider GNRs and their band-gap engineering. Moreover, such laterally expanded PPs can also be regarded as a new class of polymers that have implications for the field of macromolecular chemistry and physics.^{20,39} For example, light scattering studies are desired to elucidate the effect of such lateral expansion on their persistence lengths, although the issue of the aggregations needs to be addressed first by devising the chemical structures. Further, substitution of their peripheral positions with different functional groups might lead to formation of unique self-assembled nanostructures.³⁹

3.5 Experimental Section

General Information: Unless otherwise noted, materials were purchased from Fluka, Aldrich, Acros, abcr, Merck and other commercial suppliers and used as received unless otherwise specified. Compound **3**, **5**, **8c** and **10a** were synthesized according to ref ²⁶, ref ¹⁷, ref ²⁷ and ref ³⁰, respectively. All reactions working with air- or moisture-sensitive compounds were carried out under argon atmosphere using standard Schlenk line techniques. Thin layer chromatography (TLC) was performed on silica gel coated aluminum sheets with F254 indicator. Preparative column chromatography was performed on silica gel from Merck with a grain size of 0.063–0.200 mm (silica gel) or 0.04–0.063 mm (flash silica gel, Geduran Si 60). Melting points were determined on a Büchi hot stage apparatus without correction. Membrane filtration was performed on polyvinylidene fluoride membrane with a pore size of 0.45 μm (Merck). NMR spectra were recorded in deuterated solvents using Bruker AVANCE III 250 and Bruker AVANCE III 300 MHz NMR spectrometers. Chemical shifts (δ) were expressed in ppm relative to the residual of solvent (CD_2Cl_2 @ 5.32 ppm for ^1H NMR, 53.84 ppm for ^{13}C NMR; CDCl_3 @ 7.26 ppm for ^1H NMR, 77.16 ppm for ^{13}C NMR). Coupling constants (J) were recorded in Hertz (Hz) with multiplicities explained by the following abbreviations: s = singlet, d = doublet, t = triplet, q = quartet, dd = doublet of doublets, dt = doublet of triplets, m = multiplet, br = broad. IR was measured on a Nicolet 730 FT-IR spectrometer equipped with an attenuated total reflection (ATR) setup. The samples were deposited as pristine material on the diamond crystal and pressed on it with a stamp. Analytical GPC was performed using a PSS SECcurity Agilent 1260 Infinity Setup (Polymer Standards Service GmbH (PSS)). A column combination from PSS (SDV 10^6 , 10^4 , 500 \AA , 300x8 mm) was connected and maintained at 30 $^\circ\text{C}$. THF was used as eluent with a flow rate of 1 mL/min. The relative molecular weights were calculated based on a universal polystyrene calibration using the signal recorded by a PSS SECcurity UV detector (254 nm). High-resolution mass spectra (HRMS) were recorded by matrix-assisted laser decomposition/ionization (MALDI) using 7,7,8,8-tetracyanoquinodimethane (TCNQ) or *trans*-2-[3-(4-*tert*-Butylphenyl)-2-methyl-2-propenylidene]malononitrile (DCTB) as matrix with a Bruker Reflex II-TOF spectrometer (MALDI-TOF HRMS).

Synthesis of 3-(3-ethynylphenyl)-4-phenyl-2,5-bis[3-(triisopropylsilylethynyl)phenyl]cyclopenta-2,4-dien-1-one (1c): To a solution of 1-phenyl-2-[3-(trimethylsilylethynyl)phenyl]ethane-1,2-dione (**6**) (1.00 g, 3.28 mmol) in THF (20 mL) was

injected a THF solution of TBAF (4.5 mL 1 M, 4.5 mmol). The solution was stirred at a room temperature for 1 h, and then passed through a short pad of silica gel with THF as eluent. Solvent was then removed in vacuo to afford 1-phenyl-2-(3-ethynylphenyl)ethane-1,2-dione (**7**) as a yellow solid (770 mg, 3.27 mmol, 99% crude yield), which was directly used in the next step without further purification. To a solution of 1,3-bis[3-(triisopropylsilylethynyl)phenyl]propan-2-one (**4**) (1.62 g, 3.11 mmol) and **7** (770 mg, 3.27 mmol) in *t*BuOH (180 mL) was added at 80 °C a solution of tri-*n*-butylammonium hydroxide (0.2 g, 0.3 mmol, 40% w/w) in EtOH under vigorous stirring. The reaction was tracked by TLC until consumption of starting materials (ca. 30 min). During the time the solution gradually turned into dark purple. The solution was then allowed to cool down to a room temperature, and diluted with ether and water. The aqueous phase was extracted three times and the combined organic phases were washed with water, brine and dried over MgSO₄. The solvent was then removed in vacuo and the residue was purified by triethylamine-neutralized silica gel column chromatography (eluent: dichloromethane/hexane = 1/3) to afford **1c** as a purple solid (1.40 g, 59%, over 2 steps from **6**): mp 130.1–131.9 °C; ¹H NMR (300 MHz, CD₂Cl₂, δ): 7.49 – 7.28 (m, 5H), 7.30 – 7.12 (m, 7H), 7.08 (s, 1H), 7.03 – 6.91 (m, 4H), 3.05 (s, 1H), 1.09 (s, 42H); ¹³C NMR (75 MHz, CD₂Cl₂, δ): 199.93, 155.80, 154.68, 134.23, 133.83, 133.05, 132.95, 132.88, 131.47, 131.44, 131.34, 131.16, 130.59, 130.56, 130.13, 129.63, 129.48, 128.83, 128.74, 128.66, 128.59, 125.69, 125.14, 123.92, 123.84, 122.72, 107.27, 107.21, 91.44, 91.32, 83.19, 78.22, 18.98, 11.86; MS (MALDI-TOF) *m/z*: [M]⁺ calcd for C₅₃H₆₀OSi₂, 768.4 (100%), 769.4 (68%), 770.4 (29%), 771.4 (7.6%); Found 768.4 (95%), 769.4 (100%), 770.4 (43%), 771.4 (22%).

Synthesis of 3,4-diphenyl-2,5-bis(trimethylsilyl)cyclopenta-2,4-dien-1-one (2a): Synthesis of **2a** was carried out following a reported procedure.³⁵ To a solution of [(1*Z*,3*Z*)-1,4-diiodo-2,3-diphenylbuta-1,3-diene-1,4-diyl]bis(trimethylsilane) (**10a**)³⁰ (301 mg, 0.500 mmol) in diethyl ether (5 mL) was injected a hexane solution of *t*BuLi (1.18 mL, 1.7 M, 2.0 mmol) at –78 °C. After stirring at –78 °C for 1 h, CuCl (1.4 mg, 1.05 mmol) was added into the reaction mixture. The mixture was further stirred at –78 °C for 30 min. CO (g.) was then bubbled through the mixture under vigorous stirring for 10 min. Di-*tert*-butyl peroxide (0.19 mL, 1.1 mmol) was then injected into the mixture, which was allowed to warm up to 0 °C and stirred at this temperature for 1 h. Water was then added to quench the reaction and the organic phase was diluted with diethyl ether. The organic layer was washed with Na₂S₂O₃ (aq., 5%), water, brine and dried over MgSO₄. The solvent was then removed in vacuo and the residue

was purified by triethylamine-neutralized silica gel column chromatography (eluent: dichloromethane/hexane = 1/8) to afford **2a** as a yellow solid (40.6 mg, 22%): ¹H NMR (300 MHz, CD₂Cl₂, δ): 7.25–7.14 (m, 6H), 7.00–6.88 (m, 4H), -0.03 (s, 18H). The NMR data agreed with a previously reported one in a literature.⁴⁰

Synthesis of 3-phenyl-2,5-bis(trimethylsilyl)-4-[3-(trimethylsilylethynyl)phenyl]cyclopenta-2,4-dien-1-one (2b): Synthesis of **2b** was carried out following a reported procedure.³⁵ To a solution of {(1Z,3Z)-1,4-diiodo-2-phenyl-3-[3-(trimethylsilylethynyl)phenyl]buta-1,3-diene-1,4-diyl}bis(trimethylsilane) (**10b**) (4.3 g, 6.2 mmol) in diethyl ether (60 mL) was injected a hexane solution of *t*BuLi (15 mL, 1.7 M, 26 mmol) at -78 °C. After stirring at -78 °C for 1 h, CuCl (1.3 g, 13 mmol) was added into the reaction mixture. The mixture was further stirred at -78 °C for 30 min. CO (g.) was then bubbled through the mixture under vigorous stirring for 10 min. Di-*tert*-butyl peroxide (2.4 mL, 13 mmol) was then injected into the mixture, which was allowed to warm up to 0 °C and stirred at this temperature for 1 h. Water was then added to quench the reaction and the organic phase was diluted with diethyl ether. The organic layer was washed with Na₂S₂O₃ (aq., 5%), water, brine and dried over MgSO₄. The solvent was then removed in vacuo and the residue was purified by triethylamine-neutralized silica gel column chromatography (eluent: dichloromethane/hexane = 1/10) to afford **2b** as a yellow solid (1.2 g, 40%): mp 120.7–123.0 °C; ¹H NMR (300 MHz, CD₂Cl₂, δ): 7.30 (d, *J* = 7.7 Hz, 1H), 7.26–7.17 (m, 3H), 7.12 (t, *J* = 7.7 Hz, 1H), 7.09 (s, 1H), 6.99 – 6.90 (m, 2H), 6.85 (d, *J* = 7.7 Hz, 1H), 0.22 (s, 9H), -0.01 (s, 9H), -0.02 (s, 9H); ¹³C NMR (75 MHz, CD₂Cl₂, δ): 210.22, 171.48, 170.54, 136.66, 136.08, 132.02, 131.89, 131.78, 131.06, 128.86, 128.78, 128.68, 128.11, 123.15, 104.84, 95.21, 0.10, 0.04; MS (MALDI-TOF) *m/z*: [M]⁺ calcd for C₂₈H₃₆OSi₃ 472.2 (100%), 473.2 (46%), 474.2 (19%); Found 472.2 (100%), 473.2 (73%), 474.2 (30%).

Synthesis of 3,4-bis(3-tetradecylphenyl)-2,5-bis(trimethylsilyl)cyclopenta-2,4-dien-1-one (2c): Synthesis of **2c** were accomplished following a previously reported procedure.³⁵ To a solution of [(1Z,3Z)-1,4-diiodo-2,3-bis(3-tetradecylphenyl)buta-1,3-diene-1,4-diyl]bis(trimethylsilane) (**10c**) (1.77 g, 1.78 mmol) in diethyl ether (20 mL) was injected at -78 °C a hexane solution of *t*BuLi (4.30 mL, 1.7 M, 7.30 mmol). The solution was allowed to react for 1 h, and CuCl (0.370 g, 3.74 mmol) was added into the solution. The mixture was further stirred at -78 °C for 30 min. CO (g.) was then bubbled through the mixture under vigorous stirring for 10 min. Di-*tert*-butyl peroxide (0.684 mL, 3.74 mmol) was then injected

into the solution, which was then warmed up to 0 °C and allowed to react for 1 h. Water was added to quench the reaction and the organic phase was diluted with diethyl ether. The organic layer was washed with Na₂S₂O₃ (aq., 5%), water, brine and dried over MgSO₄. The ether was then removed in vacuo and the residue was purified by triethylamine-neutralized silica gel column chromatography (dichloromethane/hexane = 1/25) to afford **2c** as a yellow solid (0.659 g, 48%): mp 37.2–38.7 °C; ¹H NMR (300 MHz, CD₂Cl₂, δ): 7.08 (t, *J* = 7.4 Hz, 2H), 7.01 (d, *J* = 7.6 Hz, 2H), 6.74 (d, *J* = 7.2 Hz, 2H), 6.72 (s, 2H), 2.45 (t, *J* = 7.6 Hz, 4H), 1.40 (quin, *J* = 8.2, 7.3 Hz, 4H), 1.34 – 1.07 (br, 44H), 0.88 (t, *J* = 6.4 Hz, 6H), -0.02 (s, 18H); ¹³C NMR (75 MHz, CD₂Cl₂, δ): 210.68, 172.32, 142.70, 136.23, 130.46, 128.93, 128.72, 127.77, 126.12, 36.26, 32.52, 31.97, 30.29, 30.25, 30.17, 30.08, 29.95, 29.69, 23.28, 14.46, 0.14; HRMS (MALDI-TOF) *m/z*: [M]⁺ calcd for C₅₁H₈₄OSi₂ 768.6061; Found 768.6130.

Synthesis of 1,3-bis[3-(triisopropylsilylethynyl)phenyl]propan-2-one (4): A mixture of 1,3-bis(3-bromophenyl)acetone (**3**)²⁶ (5.0 g, 14 mmol), (triisopropylsilyl)acetylene (7.6 mL, 34 mmol), PdCl₂(PPh₃)₂ (0.48 g, 0.68 mmol), CuI (0.26 g, 1.4 mmol), PPh₃ (0.36 g, 1.4 mL) and piperidine (50 mL) was degassed by argon bubbling under vigorous stirring for 15 min. The mixture was then stirred at 100 °C overnight. After cooling down to a room temperature, ether and ice was added into the mixture and the organic layer was washed with HCl (aq., 2 M), water and brine and dried over MgSO₄. Ether were removed in vacuo and the residue was purified by silica gel column chromatography (eluent: ethyl acetate/hexane = 1/6) to afford **4** as a pale yellow oil (7.7 g, 99%): ¹H NMR (300 MHz, CD₂Cl₂, δ): 7.39 (d, *J* = 7.5 Hz, 2H), 7.34–7.22 (s, 2H, with an embedded t, *J* = 7.4 Hz, 2H), 7.12 (d, *J* = 7.3 Hz, 2H), 3.74 (s, 4H), 1.14 (s, 42H); ¹³C NMR (75 MHz, CD₂Cl₂, δ): 205.10, 134.85, 133.57, 131.17, 130.29, 129.09, 124.38, 107.27, 91.40, 49.37, 19.02, 11.91; HRMS (MALDI-TOF) *m/z*: [M + H]⁺ calcd for C₃₇H₅₅OSi₂ 571.3791; Found 571.3765.

Synthesis of 1-phenyl-2-[3-(trimethylsilylethynyl)phenyl]ethane-1,2-dione (6): A mixture of 3-bromobenzil (**5**)¹⁷ (2.1 g, 7.3 mmol), (trimethylsilyl)acetylene (3.0 mL, 22 mmol), Pd(PPh₃)₄ (0.26 g, 0.22 mmol), CuI (0.046 g, 0.22 mmol), THF (10 mL) and trimethylamine (10 mL) was degassed by argon bubbling under vigorous stirring for 15 min. The mixture was then stirred at 100 °C overnight. After cooling down to a room temperature, ether and ice was added into the mixture and the organic layer was washed with HCl (aq., 2 M), water and brine and dried over MgSO₄. The solvents were removed in vacuo and the residue was

purified by silica gel column chromatography (eluent: ethyl acetate/hexane = 1/10) to afford **6** as a pale yellow solid (2.1 g, 94%): mp 50.2–51.3 °C; ¹H NMR (300 MHz, CD₂Cl₂, δ): 8.04 (s, 1H), 7.96 (d, *J* = 8.0 Hz, 2H), 7.92 (d, *J* = 7.5 Hz, 1H), 7.72 (d, *J* = 7.8 Hz, 1H), 7.66 (t, *J* = 7.3 Hz, 1H), 7.51 (t, *J* = 7.7 Hz, 2H), 7.45 (t, *J* = 7.7 Hz, 1H), 0.25 (s, 9H); ¹³C NMR (75 MHz, CD₂Cl₂, δ): 194.05, 193.75, 137.95, 135.15, 133.38, 133.15, 132.91, 130.08, 129.52, 129.18, 129.14, 124.53, 103.29, 96.57, -0.07; MS (MALDI-TOF) *m/z*: [M – H]⁺ calcd for C₁₉H₁₇O₂Si 305.1 (100%), 306.1 (26%), 306.1 (5.1%); Found 305.1 (100%), 306.1 (15%), 306.1 (3.6%).

Synthesis of ((1Z,3Z)-1,4-diiodo-2-phenyl-3-[3-(trimethylsilylethynyl)phenyl]buta-1,3-diene-1,4-diyl)bis(trimethylsilane) (10b): The synthetic procedure was modified from literature reports.^{28,29} To a suspension of zirconocene dichloride (18 g, 63 mmol) in THF (200 mL) was added a hexane solution of *n*BuLi (83 mL, 1.6 M, 0.13 mol) at –78 °C. The solution turned pale yellow upon the addition. The mixture was stirred at –78 °C for 1 h to generate an active zirconocene species. Trimethyl(phenylethynyl)silane (**8a**) (11 g, 63 mmol) and 1,3-bis[(trimethylsilyl)ethynyl]benzene (**8b**) (17 g, 63 mmol) were then simultaneously added to the mixture under argon flow. The mixture was stirred for 3 h while it was allowed to gradually warm up to a room temperature. The mixture turned into a dark brown solution during the process. The mixture was then cooled down to 0 °C, and CuCl (7.5 g, 75 mmol) was added in one portion, followed by addition of I₂ (38 g, 0.15 mmol) in 5 portions. The mixture was allowed to gradually warm up to a room temperature and stirred overnight. The reaction was then quenched with water and diluted with ether. The organic layer was washed with Na₂S₂O₃ (aq., 5%), water, brine and dried over MgSO₄. The solvents were then removed in vacuo and the residue was purified by triethylamine-neutralized silica gel column chromatography (eluent: cyclohexane) to afford **10b** as a pale-yellow solid (5.2 g, 12%, first band): mp 136.2–137.3 °C; ¹H NMR (300 MHz, CD₂Cl₂, δ): 7.40 (d, *J* = 7.4 Hz, 1H), 7.37 – 7.26 (m, 3H), 7.24 (m, 2H), 7.20 (d, *J* = 8.0 Hz, 2H), 7.15 (t, *J* = 5.5 Hz, 1H), 0.26 (s, 9H), 0.01 (s, 9H), 0.00 (s, 9H); ¹³C NMR (75 MHz, CD₂Cl₂, δ): 163.31, 162.60, 139.93, 139.66, 132.77, 132.13, 129.86, 129.70, 128.77, 128.25, 123.17, 114.06, 113.69, 104.76, 99.93, 95.01, 0.94, 0.85, -0.04; MS (MALDI-TOF) *m/z*: [M – I]⁺ calcd for C₂₇H₃₆ISi₃ 571.1 (100%), 572.1 (45%), 573.1 (19%); found 571.3 (100%), 572.3 (44%), 573.3 (20%).

Synthesis of [(1Z,3Z)-1,4-diiodo-2,3-bis(3-tetradecylphenyl)buta-1,3-diene-1,4-diyl)bis(trimethylsilane) (10c): The synthetic procedure was modified from reported

procedures.^{28,29} A hexane solution of *n*BuLi (8.1 mL, 1.6 M, 13 mmol) was injected into a suspension of zirconocene dichloride (1.8 g, 6.2 mmol) in THF (6 mL) at -78 °C. The solution turned into pale yellow upon the injection. The mixture was allowed to react at -78 °C for 1 h to generate an active zirconocene species. Trimethyl[(3-*n*-tetradecylphenyl)ethynyl]silane (**8c**)²⁷ (3.28 g, 12.3 mmol) was then injected into the mixture in one portion. The mixture was stirred for 3 h while it was allowed to gradually warm up to a room temperature. The mixture turned into a dark brown solution during the process. The mixture was then cooled down to 0 °C, and CuCl (0.73 g, 7.4 mmol) was added in one portion, followed by addition of I₂ (3.76 g, 14.8 mmol) in 5 portions. The mixture was then gradually warmed up to a room temperature and allowed to react under stirring overnight. The reaction was then quenched with water and diluted with ether. The organic layer was washed with Na₂S₂O₃ (aq., 5%), water, brine and dried over MgSO₄. The ether was then removed in vacuo and the residue was purified by triethylamine-neutralized silica gel column chromatography (eluent: cyclohexane) to afford **10c** as pale-yellow oil (1.85 g, 30%): ¹H NMR (300 MHz, CD₂Cl₂, δ): 7.19 – 7.10 (br, 4H), 7.10 – 7.01 (br, 2H), 7.01 – 6.88 (br, 2H), 2.53 (t, *J* = 7.5 Hz, 4H), 1.53 (quin, *J* = 7.5 Hz, 4H), 1.44 – 1.16 (br, 44H), 0.92 (t, *J* = 6.5 Hz, 6H), 0.00 (s, 18H); ¹³C NMR (75 MHz, CD₂Cl₂, δ): 164.21, 143.01, 139.98, 130.27, 128.99, 128.17, 127.08, 112.44, 36.28, 32.60, 31.98, 30.39, 30.37, 30.33, 30.27, 30.16, 30.04, 29.76, 23.36, 14.57, 1.22; MS (MALDI-TOF) *m/z*: [M – C₂(TMS)₂I₂]⁺ calcd for C₄₂H₆₆ 570.5 (100%), 571.5 (45%), 572.5 (10%); found 571.1 (100%), 572.1 (42%), 573.1 (18%).

Synthesis of 1,4-bis(trimethylsilyl)-2,3,5-triphenylbenzene (11): A solution of 3,4-diphenyl-2,5-bis(trimethylsilyl)cyclopenta-2,4-dien-1-one (**2a**) (33 mg, 0.089 mmol) and phenylacetylene (14 mg, 0.13 mmol) in ODCB (0.5 mL) was degassed by freeze-pump-thaw technique for three cycles. The solution was then stirred at 120 °C for 3 days. The solvent was removed in vacuo and the residue was purified by silica gel column chromatography (eluent: dichloromethane/hexane = 1/20) to afford **11** as a white solid (36 mg, 89%): mp 160.4–162.0 °C; ¹H NMR (300 MHz, CD₂Cl₂, δ): 7.56 – 7.33 (m, 6H), 7.18 – 7.01 (m, 8H), 7.01 – 6.93 (m, 2H), -0.08 (s, 9H), -0.47 (s, 9H); ¹³C NMR (75 MHz, CD₂Cl₂, δ): 149.40, 148.95, 146.60, 146.41, 143.56, 143.17, 140.07, 138.80, 135.77, 132.63, 131.87, 130.43, 128.48, 127.60, 127.34, 127.25, 126.74, 126.63, 3.08, 0.66; MS (MALDI-TOF) *m/z*: [M]⁺ calcd for C₃₀H₃₄Si₂ 450.2 (100%), 451.2 (43%), 452.2 (15%); Found 450.2 (100%), 451.2 (41%), 452.2 (12%).

Synthesis of PP-Ic: A solution of **1c** (0.50 g, 0.65 mmol of repeating unit) in Ph₂O (1 mL) was degassed by freeze-pump-thaw technique for three cycles. The solution was then stirred at 120 °C for 78 h. During the reaction, small amounts of solution were taken from the mixture by syringes and the molecular weight was monitored by GPC analysis with PS standards (see Results and discussion for details). Phenylacetylene (0.13 g, 1.3 mmol) was then added and the solution was stirred at 160 °C overnight, during which purple color of the solution completely disappeared. After cooling down to a room temperature, MeOH (10 mL) was added to induce precipitation of polymeric products. A white precipitate was collected by filtration with a membrane filter and washed with methanol to afford **PP-Ic** (465 mg, 91%): ¹H NMR (250 MHz, CD₂Cl₂, δ): 7.53 – 6.02 (br, 18H), 1.23 – 1.08 (br, 21H), 1.08 – 0.73 (br, 21H); IR: ν = 3059 (w), 2941 (m), 2864 (w), 2154 (m), 1597 (w), 1463 (m), 1383 (w), 1244 (w), 1170 (w), 1072 (w), 995 (m), 882 (s), 791 (m), 674(s), 553 (m), 499 (m), 462 (m).

Synthesis of PP-Id: A solution of **PP-Ic** (0.23 g, 0.31 mmol of repeating unit) in THF (10 mL) was degassed by freeze-pump-thaw technique for three cycles. To this solution was injected a THF solution of TBAF (1 M, 3 mL). After the injection the mixture was degassed by freeze-pump-thaw technique for another three cycles. The solution was then allowed to react at a room temperature for one day before pouring into methanol (100 mL). White precipitates were collected by filtration with a membrane filter and washed with methanol to afford as **PP-Id** (105 mg, 79%): ¹H NMR (250 MHz, CD₂Cl₂, δ): 7.64 – 5.95 (br, 18H), 3.26 – 3.07 (br, 1H), 3.07 – 2.82 (br, 1H).

Synthesis of PP-II: A solution of **PP-Id** (51 mg, 0.12 mmol of repeating unit) and **2c** (0.27 g, 0.36 mmol) in ODCB (1 mL) was degassed by freeze-pump-thaw technique for three cycles. This solution was stirred at 160 °C for seven days. After cooling to a room temperature, the solution was poured into methanol (20 mL) to induce precipitation of polymer products. The precipitates were collected by filtration with a membrane filter and washed with methanol to afford crude product of **PP-II** (0.15 g, 67%), which was further purified by recycling GPC to yield **PP-II** as a white powder (0.13 g, 58%): ¹H NMR (250 MHz, CD₂Cl₂, δ): 8.84 – 5.48 (br, 36H), 3.08 – 1.93 (br, 8H), 1.93 – 0.95 (br, 96H), 0.95 – 0.44 (br, 12H), 0.37 – -0.36 (br, 18H), -0.36 – -1.31 (br, 18H); IR: ν = 3054 (w), 2923 (m), 2853 (m), 1713.13065 (w), 1600.16127 (w), 1463 (w), 1400 (w), 1247 (m), 1174 (w), 1087 (w), 1054 (w), 837 (s), 762 (m), 708 (m), 641 (w), 556 (w), 446 (w).

Synthesis of PP-IIIa: A solution of **PP-Id** (54 mg, 0.13 mmol of repeating unit) and **2b** (0.17 g, 0.36 mmol) in chlorobenzene (1 mL) was degassed by freeze-pump-thaw technique for three cycles. This solution was stirred at 125 °C for five days. After cooling to a room temperature, the solution was poured into methanol (20 mL) to induce precipitation of polymer products. The polymer precipitates were collected by filtration with a membrane filter and washed with methanol to give a crude product of **PP-IIIa** (white powder, 0.11 g, 68%). The yellow filtrate was concentrated in vacuo and the residue was purified by silica gel column chromatography (eluent: dichloromethane/hexane = 1/6) to recover unreacted **2b** as a yellow solid (49 mg, 0.11 mmol). The crude product was further purified by recycling GPC to yield **PP-IIIa** as a white powder (0.10 g, 62%): ¹H NMR (250 MHz, CD₂Cl₂, δ): 8.02 – 5.72 (br, 38H), 0.44 – 0.04 (br, 18H), 0.44 – -0.34 (br, 18H), -0.34 – -1.00 (br, 18H); IR: ν = 3057 (w), 2923 (w), 2853 (w), 2154 (w), 1719 (w), 1597 (w), 1479 (w), 1409 (w), 1341 (w), 1248 (m), 1185 (w), 1125 (w), 1072 (w), 1021 (w), 837 (s), 759 (m), 701 (m), 642 (m), 566 (w), 450 (w).

Synthesis of PP-IIIb: A solution of **PP-IIIa** (15 mg, 0.012 mmol of repeating unit) in THF (2 mL) and methanol (1 mL) was degassed by freeze-pump-thaw technique for three cycles. To this solution was added K₂CO₃ (3.3 mg, 0.024 mmol) under a flow of argon. The mixture was vigorously stirred overnight at a room temperature and poured into methanol (20 mL) to induce precipitation of polymer product. The precipitates were collected by filtration with a membrane filter and washed with methanol to afford a white powder of **PP-IIIb** (12 mg, 83%): ¹H NMR (250 MHz, CD₂Cl₂, δ): 8.11 – 5.79 (br, 38H), 3.22 – 2.77 (br, 2H) 0.44 – 0.04 (br, 18H), 0.37 – -0.36 (br, 18H), -0.36 – -1.13 (br, 18H).

Synthesis of PP-IV, Procedure A: A mixture of **PP-IIIb** (14 mg, 0.012 mmol of repeating unit) and **2c** (36 mg, 0.047 mmol) in ODCB (0.2 mL) was degassed by freeze-pump-thaw technique for three cycles. This mixture was stirred at 160 °C for four days, during which a gel was formed. After cooling to a room temperature, THF (5 mL) was added to the mixture. The mixture was sonicated for 15 min and filtrated. The solution was poured into methanol (20 mL) to induce precipitation of polymer product. The precipitates were collected by filtration with a membrane filter and washed with methanol to afford a white powder of **PP-IV** (6.0 mg, 20%).

Procedure B: A solution of **PP-IIIa** (10 mg, 0.0077 mmol of repeating unit) in THF (2 mL) and methanol (1 mL) was degassed by freeze-pump-thaw technique for three cycles. To this

solution was added K_2CO_3 (2.1 mg, 0.015 mmol) under a flow of argon. The mixture was vigorously stirred overnight and then dichloromethane (20 mL) was added. The organic phase was washed with water and brine and dried over Na_2SO_4 . **2c** (24 mg, 0.031 mmol) and ODCB (0.2 mL) were added into the solution and the mixture was concentrated in vacuo to remove dichloromethane. After degassing by freeze-pump-thaw technique for three cycles, the residual solution was stirred at 160 °C for four days. After cooling to a room temperature, the solution was poured into methanol (20 mL) to induce precipitation of polymer product. The precipitates were collected by filtration with a membrane filter and washed with methanol to afford a white powder of **PP-IV** (6.7 mg, 34% over two steps): ^1H NMR (250 MHz, CD_2Cl_2 , δ): 8.26 – 5.76 (br, 56H), 2.95 – 2.05 (br, 8H), 1.85 – 0.96 (br, 96H), 0.96 – 0.62 (br, 12H), 0.34 – -0.37 (br, 36H), -0.37 – -1.28 (br, 36H); IR: ν = 3054 (w), 2924 (m), 2853 (w), 1717 (w), 1600 (w), 1463 (w), 1404 (w), 1343 (w), 1247 (m), 1087 (w), 1021 (w), 837 (s), 762 (m), 702 (m), 641 (w), 429 (w).

3.6 Supporting information

General

Microwave-assisted reactions were performed using a CEM microwave reactor Discover-S-Class. Solution UV–vis absorption spectra were recorded at a room temperature on a Perkin-Elmer Lambda 900 spectrophotometer. The baseline was corrected by subtracting a measurement of the cuvette filled with pure solvent used for the measurement.

Removal of trimethylsilyl groups from **PP-II**

We have tried several different reagents to remove trimethylsilyl (TMS) groups from **PP-II**. We first used the most common reagent tetra-*n*-butylammonium fluoride (TBAF). It is interesting to note that, **PP-II** was initially insoluble in *N,N*-dimethylformaldehyde (DMF). However, after adding TBAF to a mixture of **PP-II** and DMF, it turned into a clear solution, presumably forming Si-F ionic adduct. However, a reaction at a room temperature overnight only showed very little desilylation, based on ¹H NMR spectrum. Elevation of the reaction temperature had minor effect on the reaction and insoluble product was eventually formed at a reaction temperature of 80 °C. Refluxing a solution of **PP-II** in tetrahydrofuran (THF) and concentrated HCl (aq.) resulted in no reaction. On the other hand, there was also no reaction in a solution of **PP-II** in THF and HBF₄ (aq.) at a room temperature, while heating to 85 °C led to again formation of insoluble products. Eventually, we found out that heating of **PP-II** in a solution of THF and concentrated HBr (aq.) at 100 °C allowed smooth removal of the silyl groups. The efficiency of the reaction was further improved under microwave irradiation, leading to complete removal of the TMS groups.

*Desilylation of **PP-II***: A solution of **PP-II** (32.6 mg, 0.0171 mmol of repeating units) in THF (25 mL) in a microwave reaction tube was degassed by argon bubbling for 5 min. To this solution was added 1 mL of concentrated aqueous solution of HBr (48 w/w %). The solution was subjected to microwave irradiation in a microwave reactor at 110 °C with max power of 300 W with activated cooling, for 2 days. After cooling to a room temperature, the solution was poured into methanol (100 mL) to induce precipitation of polymeric product. The precipitate was collected as a light brownish flake through filtration with a membrane filter (26 mg, 94%). The product was hardly soluble in dichloromethane, but soluble after adding a small amount of HBr (aq.) or using THF as solvent. ¹H NMR suggested a complete removal of all TMS groups (**Figure S24**). ¹H NMR (250 MHz, CD₂Cl₂, δ): 8.2–6.0 (br, 40H), 2.7–2.0 (br, 8H), 1.5–0.9 (br, 96H), 0.9–0.7 (br, 12H).

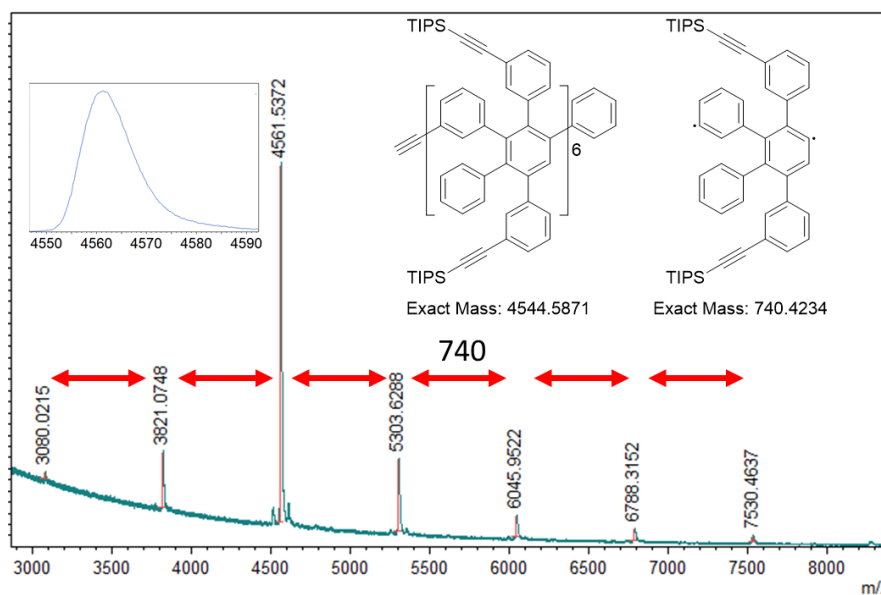


Figure S1. Matrix assist laser desorption ionization time of flight mass spectrum of **PP-1c** recorded in linear mode (matrix: *trans*-2-[3-(4-*tert*-Butylphenyl)-2-methyl-2-propenyldene]malononitrile). Inset: enlargement of the hexamer signal.

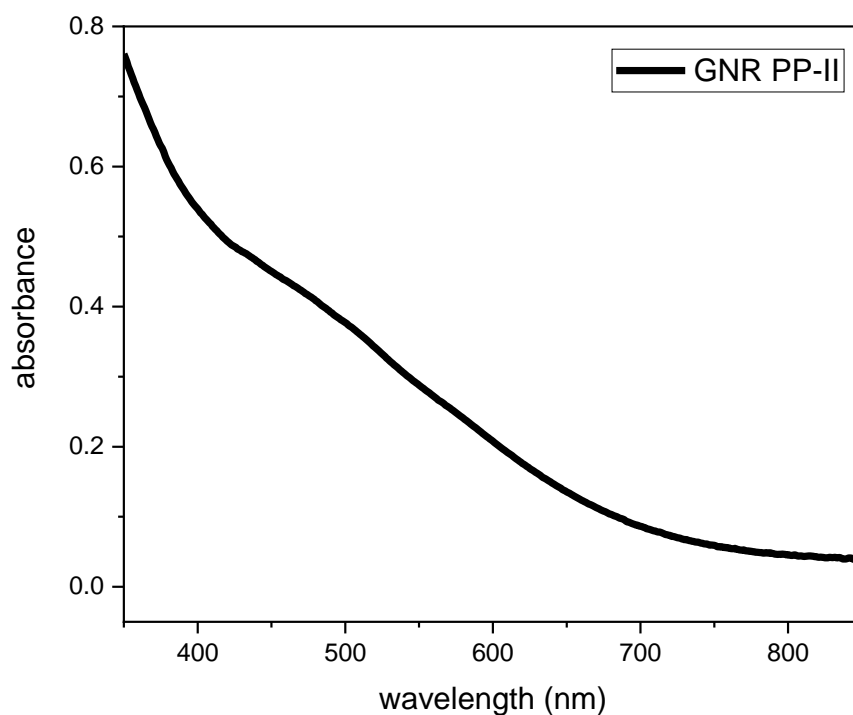


Figure S2. UV-Vis absorption spectrum of product after the oxidative cyclodehydrogenation of **PP-II**, recorded in 1,2,4-trichlorobenzene.

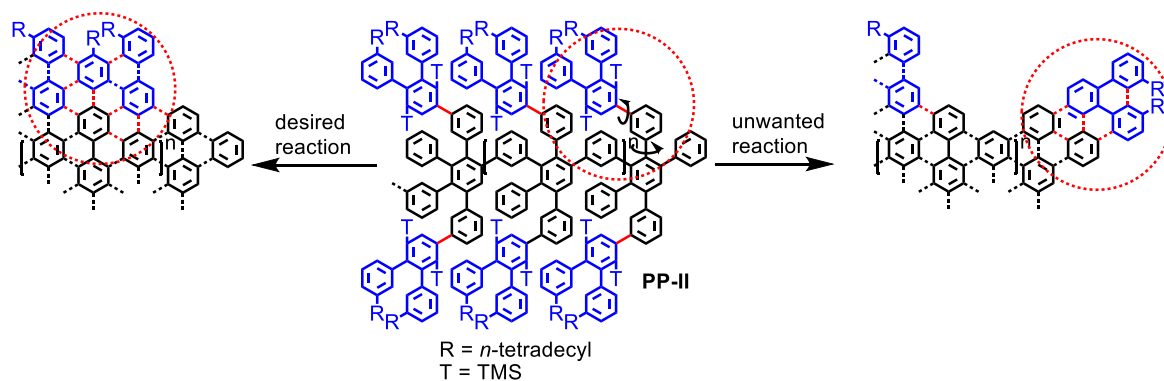


Figure S3. Possible cyclodehydrogenation of **PP-II** at undesired position.

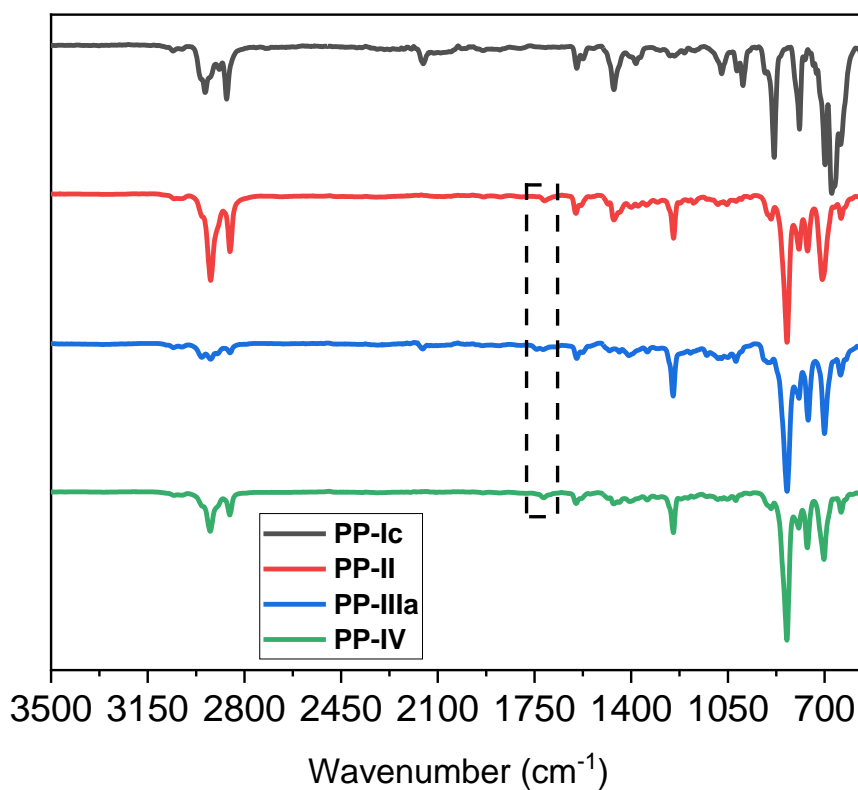


Figure S4. FT-IR spectra of **PP-Ic**, **PP-II**, **PP-IIIa** and **PP-IV** at the full spectral region of 3500–600 cm^{-1} .

3.6 Supporting information

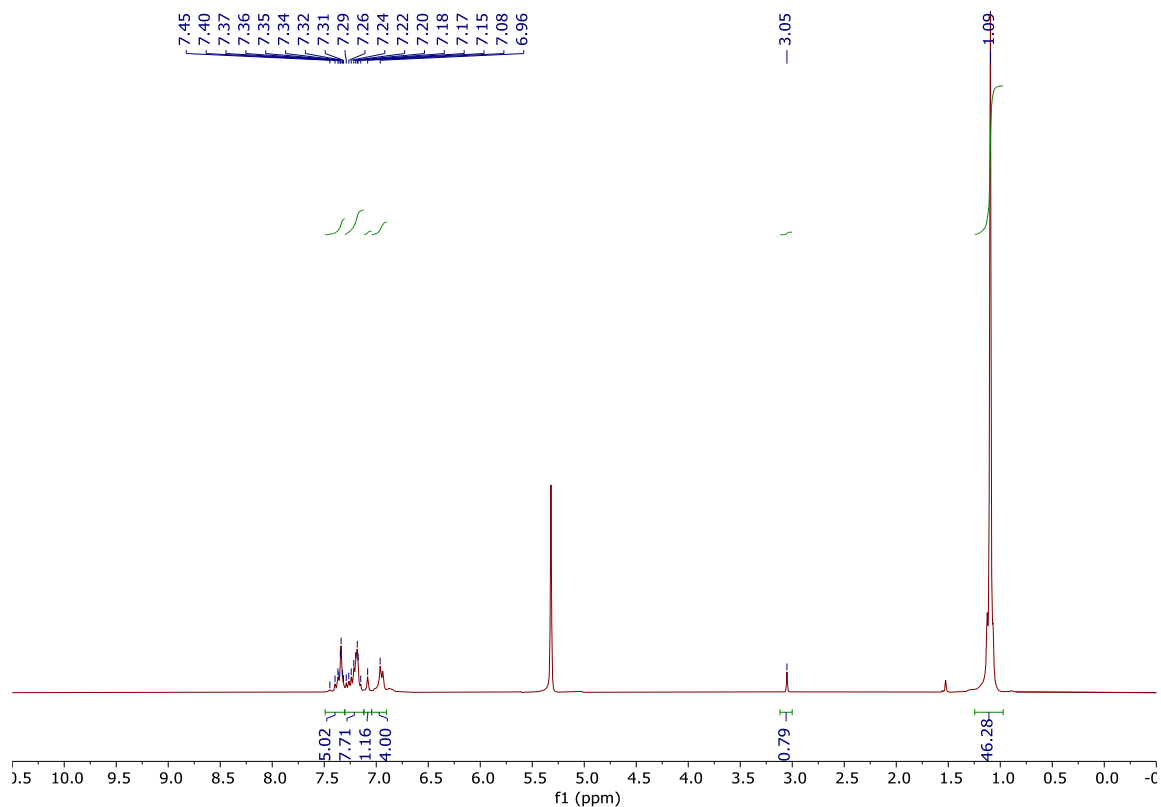


Figure S5. ^1H NMR spectrum of **1c**. (300 MHz, CD_2Cl_2)

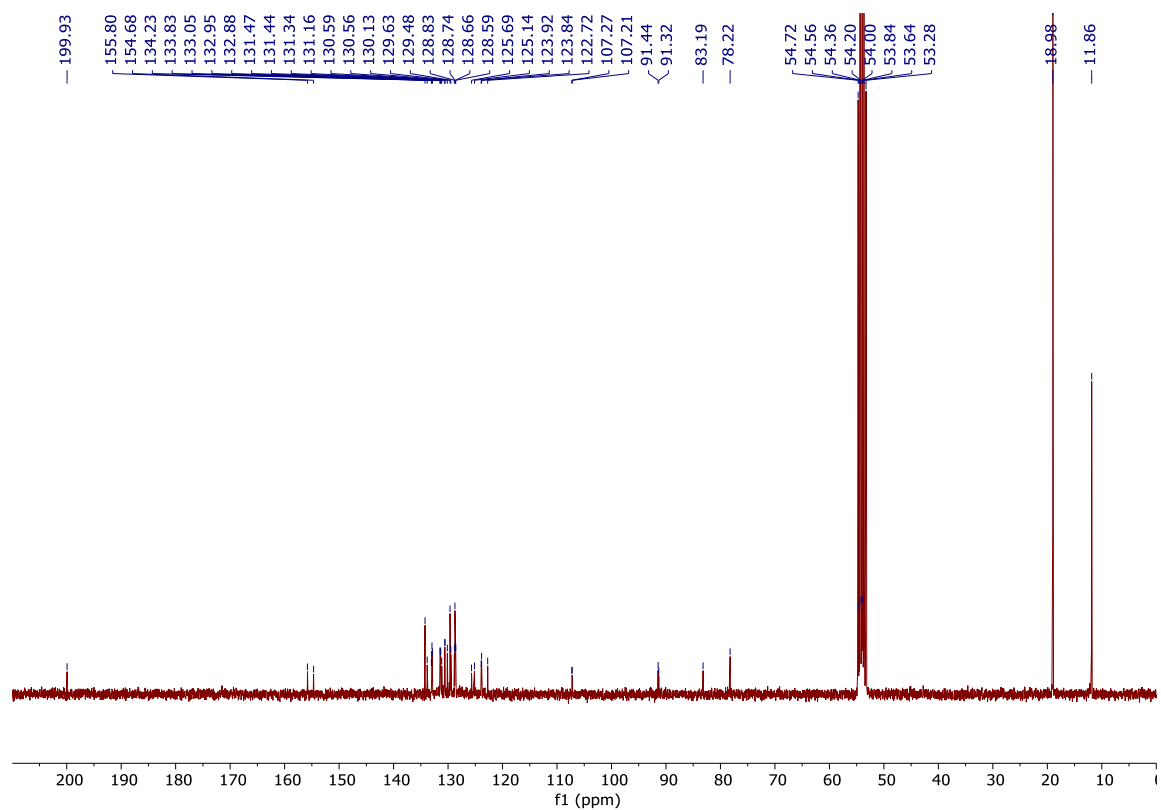


Figure S6. ^{13}C NMR spectrum of **1c**. (75 MHz, CD_2Cl_2)

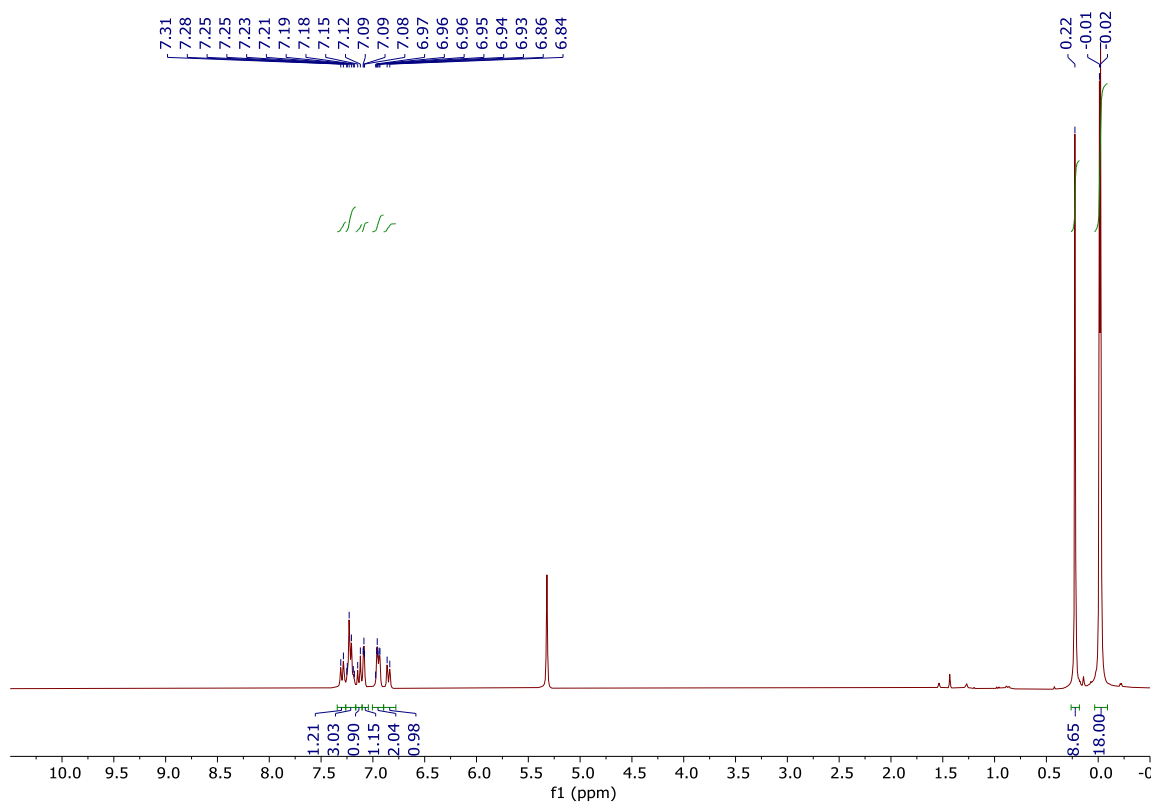


Figure S7. ^1H NMR spectrum of **2b**. (300 MHz, CD_2Cl_2)

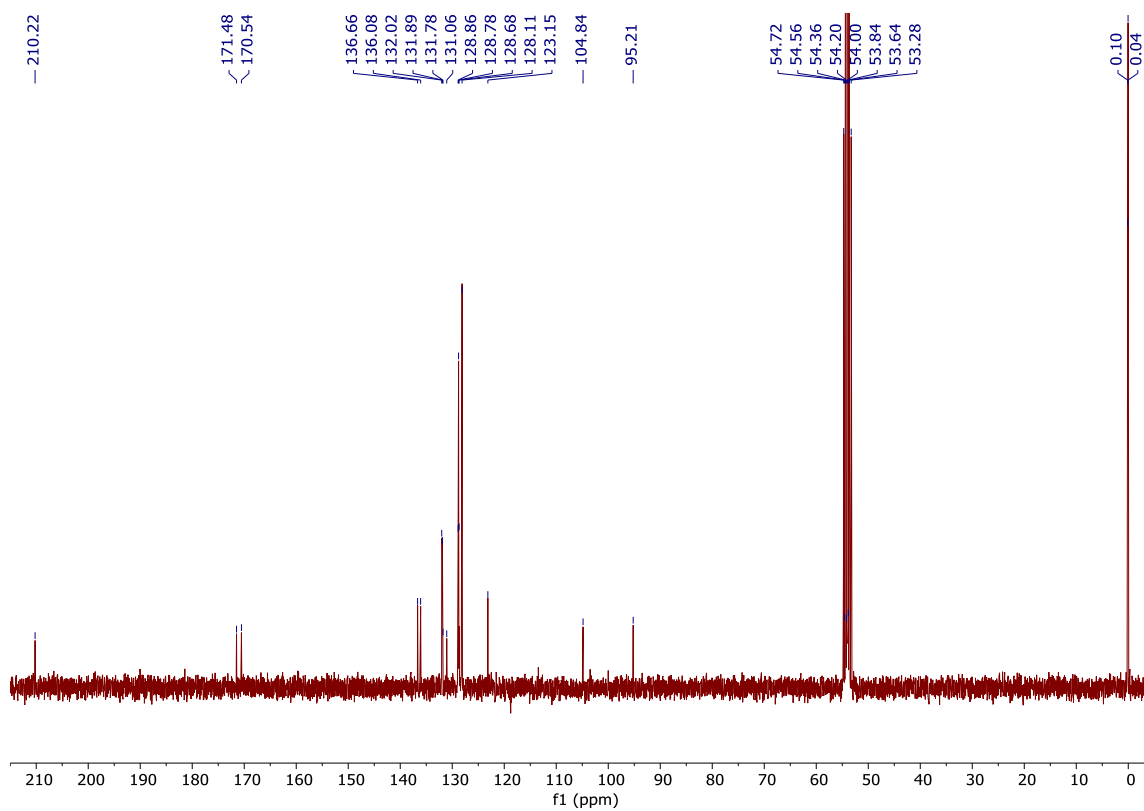
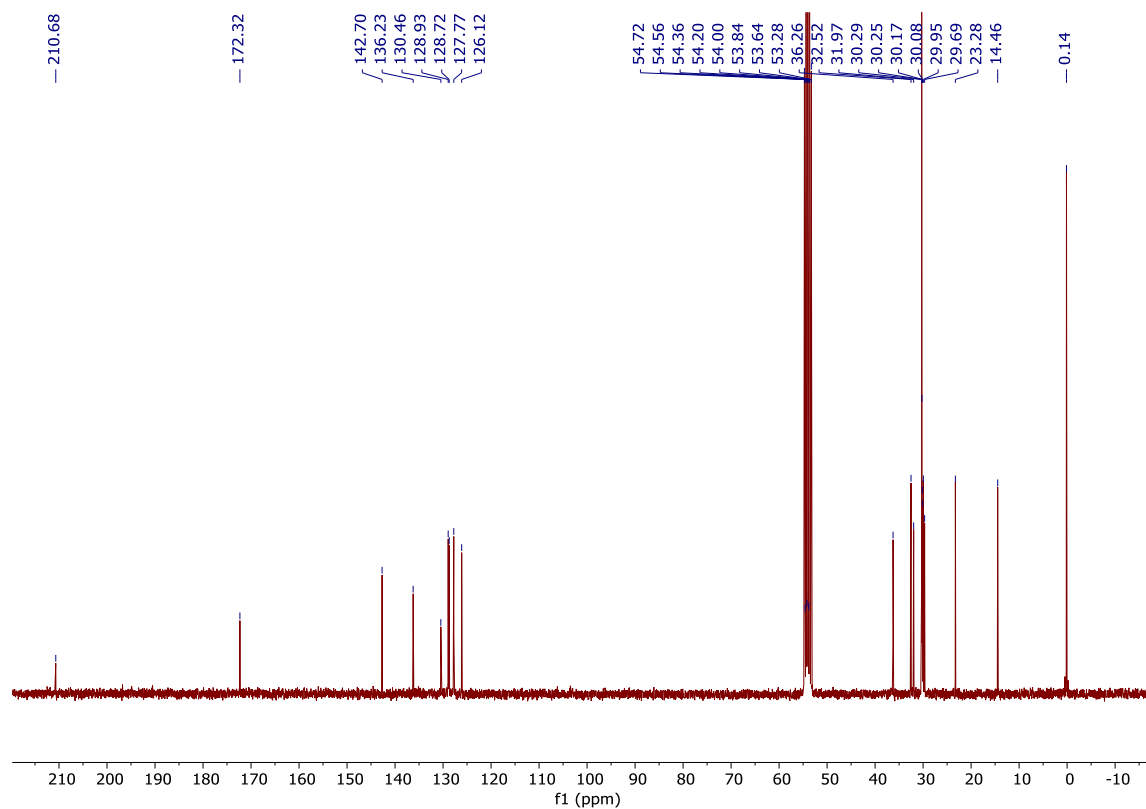
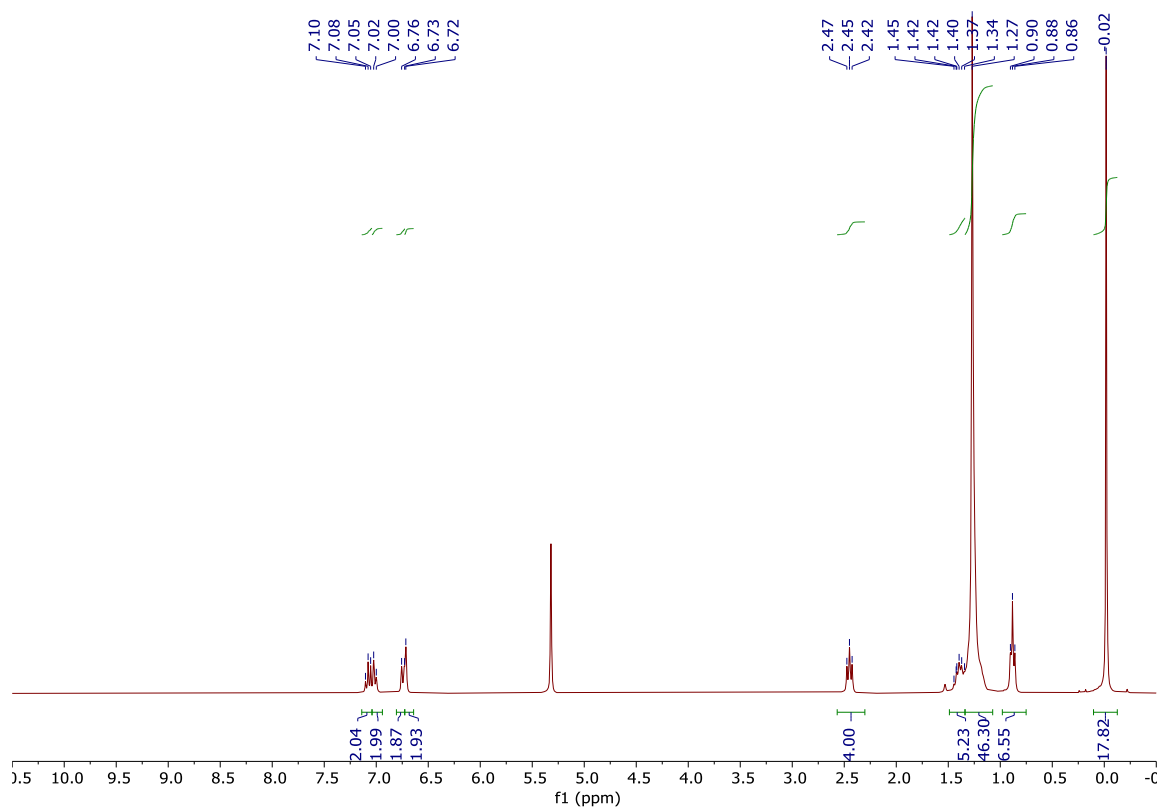


Figure S8. ^{13}C NMR spectrum of **2b**. (75 MHz, CD_2Cl_2)

3.6 Supporting information



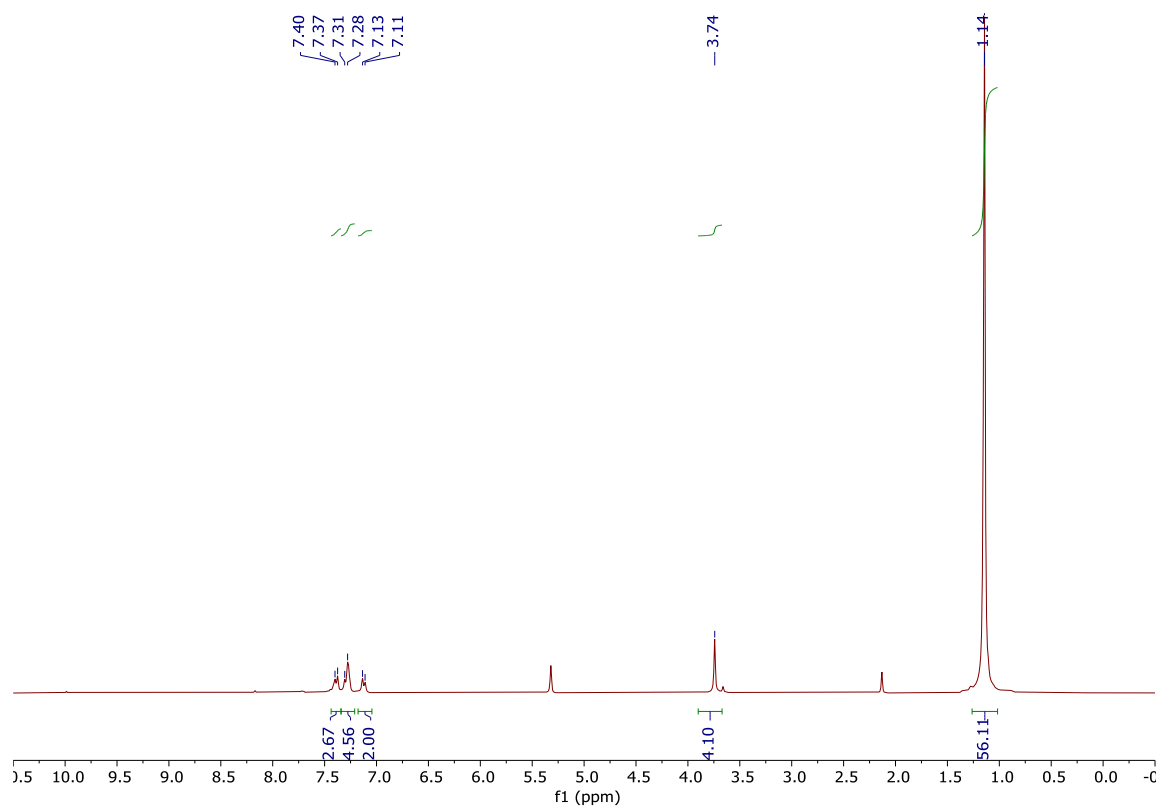


Figure S11. ^1H NMR spectrum of **4**. (300 MHz, CD_2Cl_2)

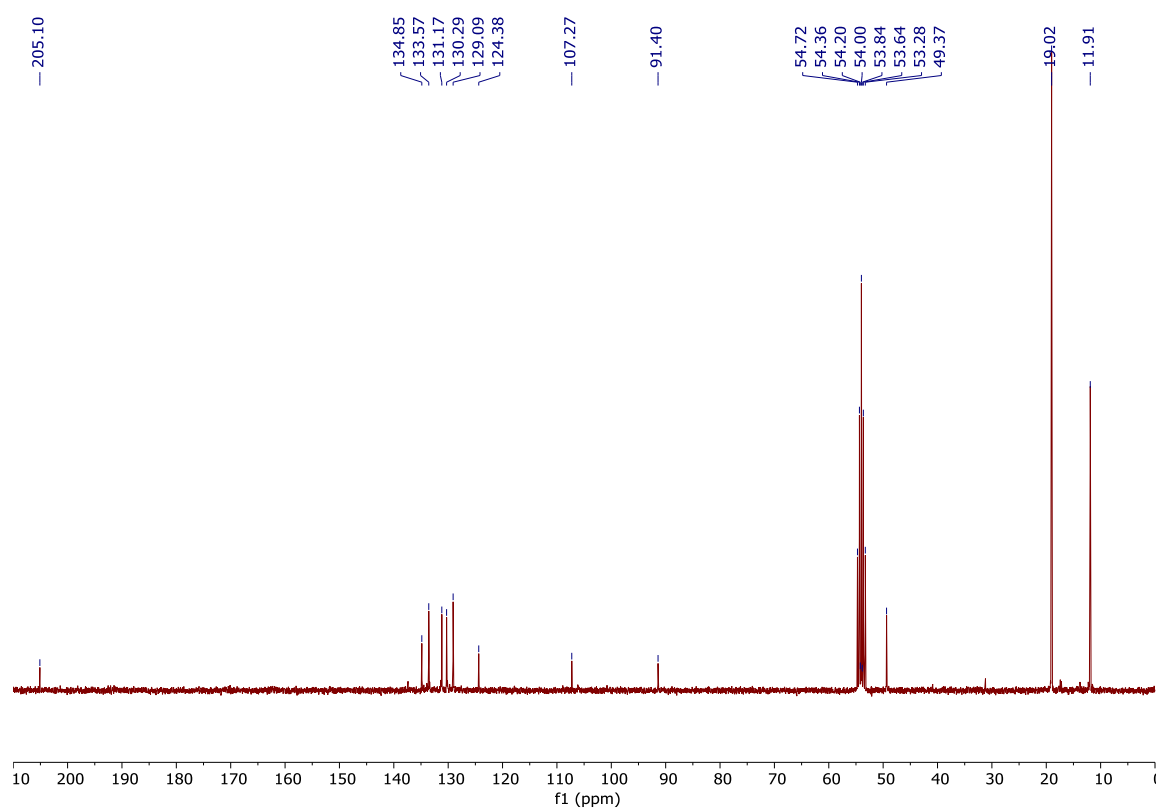


Figure S12. ^{13}C NMR spectrum of **4**. (75 MHz, CD_2Cl_2)

3.6 Supporting information

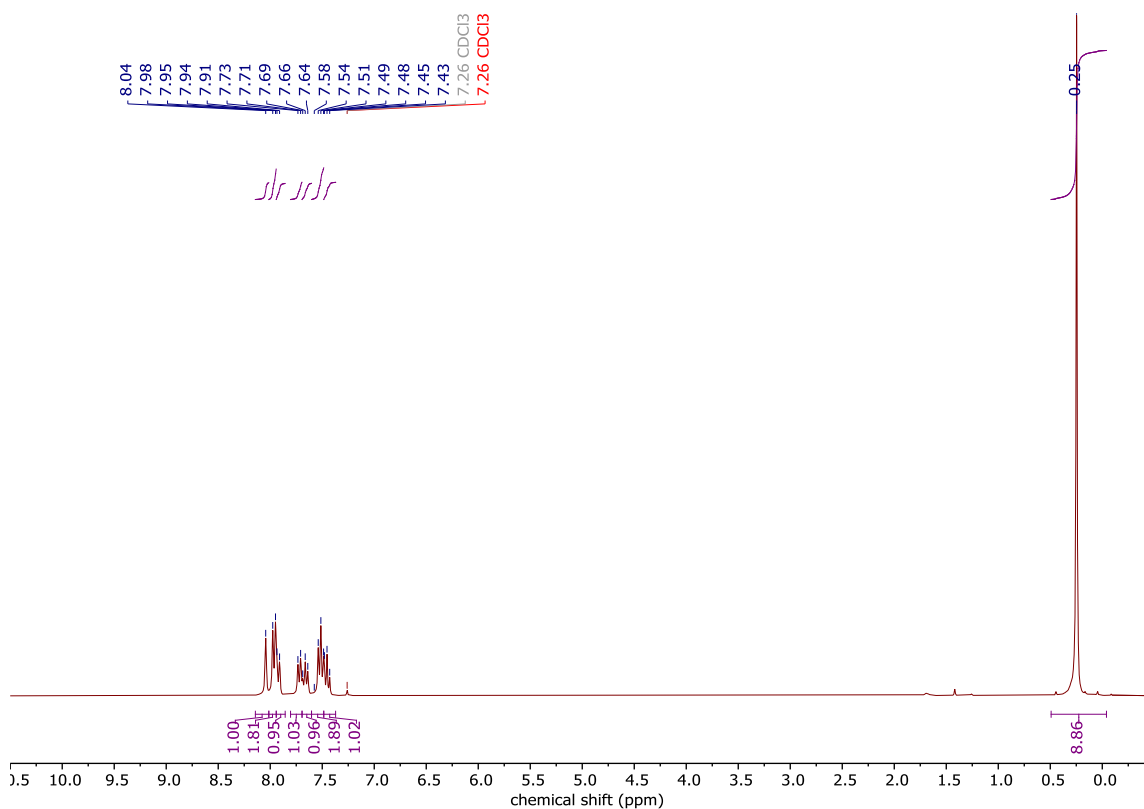


Figure S13. ^1H NMR spectrum of **6**. (300 MHz, CDCl_3)

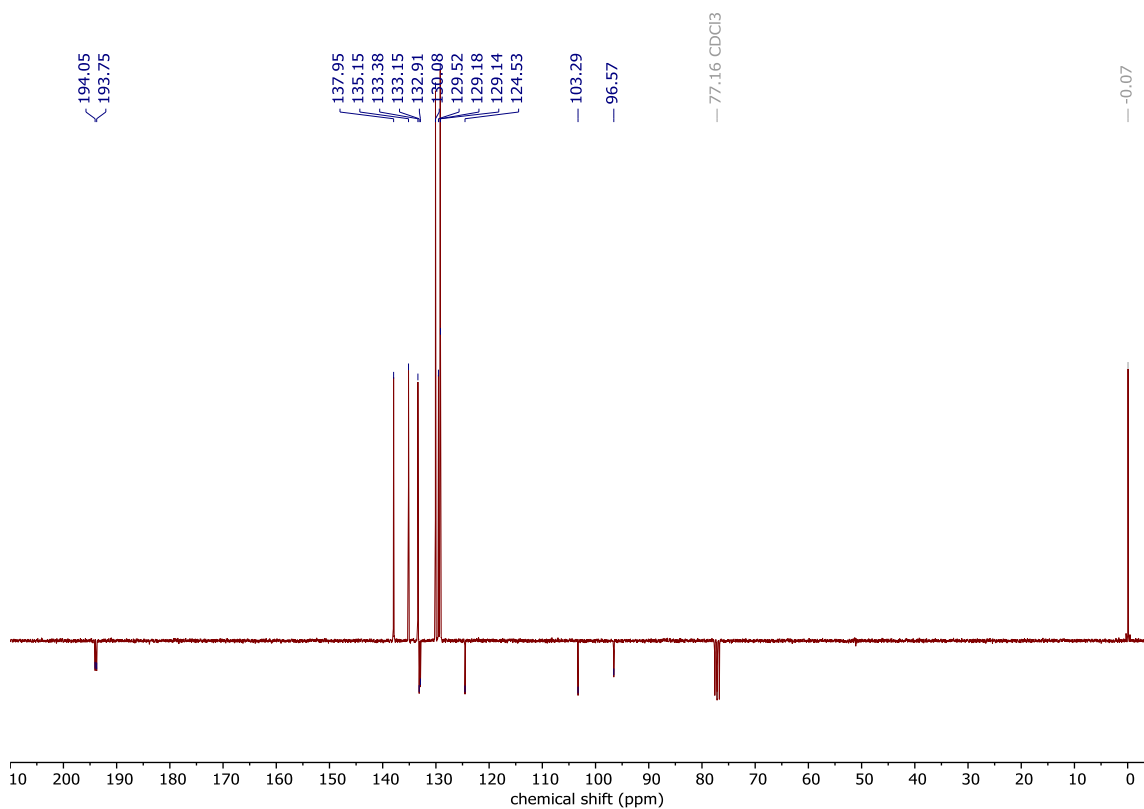


Figure S14. ^{13}C NMR spectrum of **6**. (75 MHz, CDCl_3)

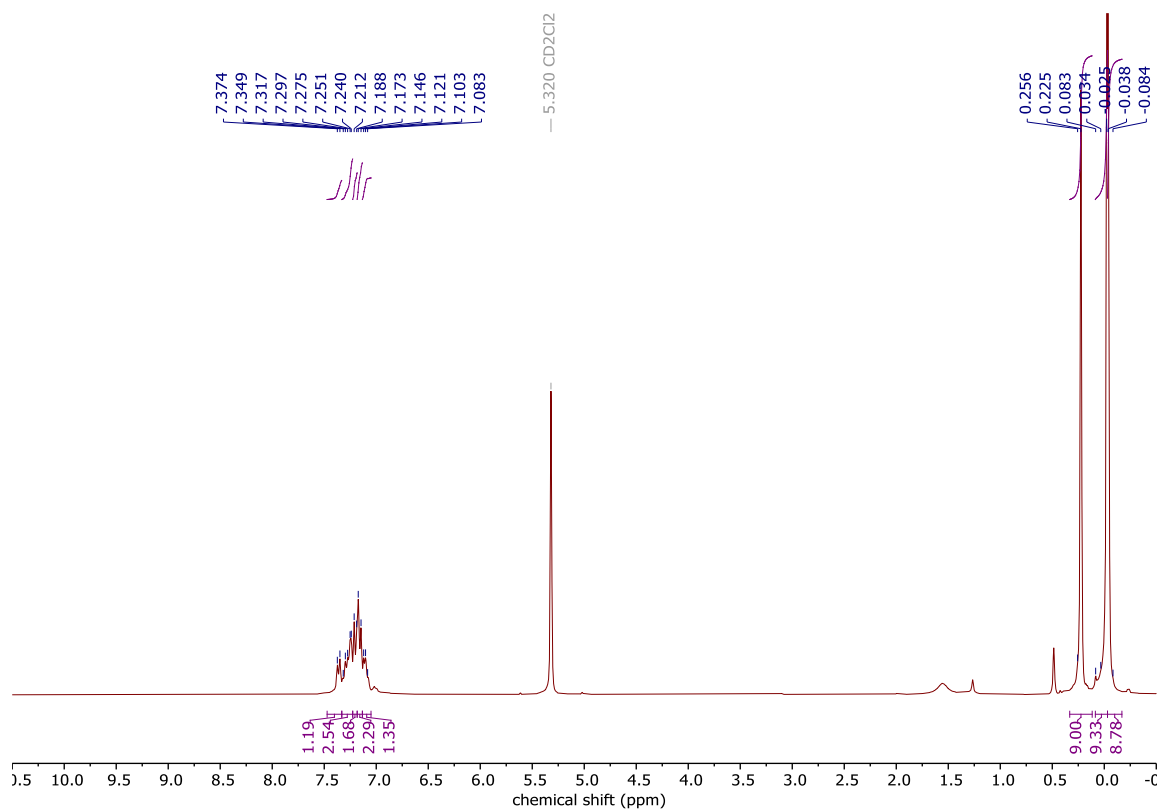


Figure S15. ¹H NMR spectrum of **10b**. (300 MHz, CD₂Cl₂)

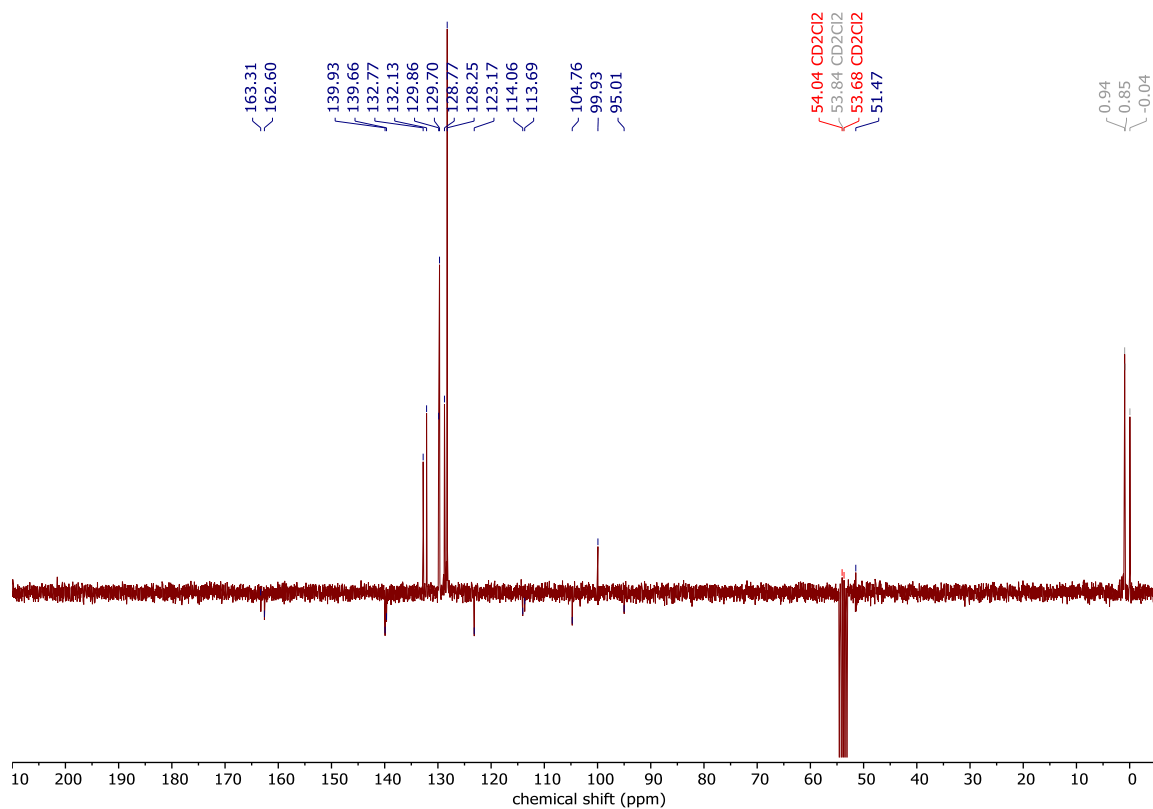


Figure S16. ¹³C NMR spectrum of **10b**. (75 MHz, CD₂Cl₂)

3.6 Supporting information

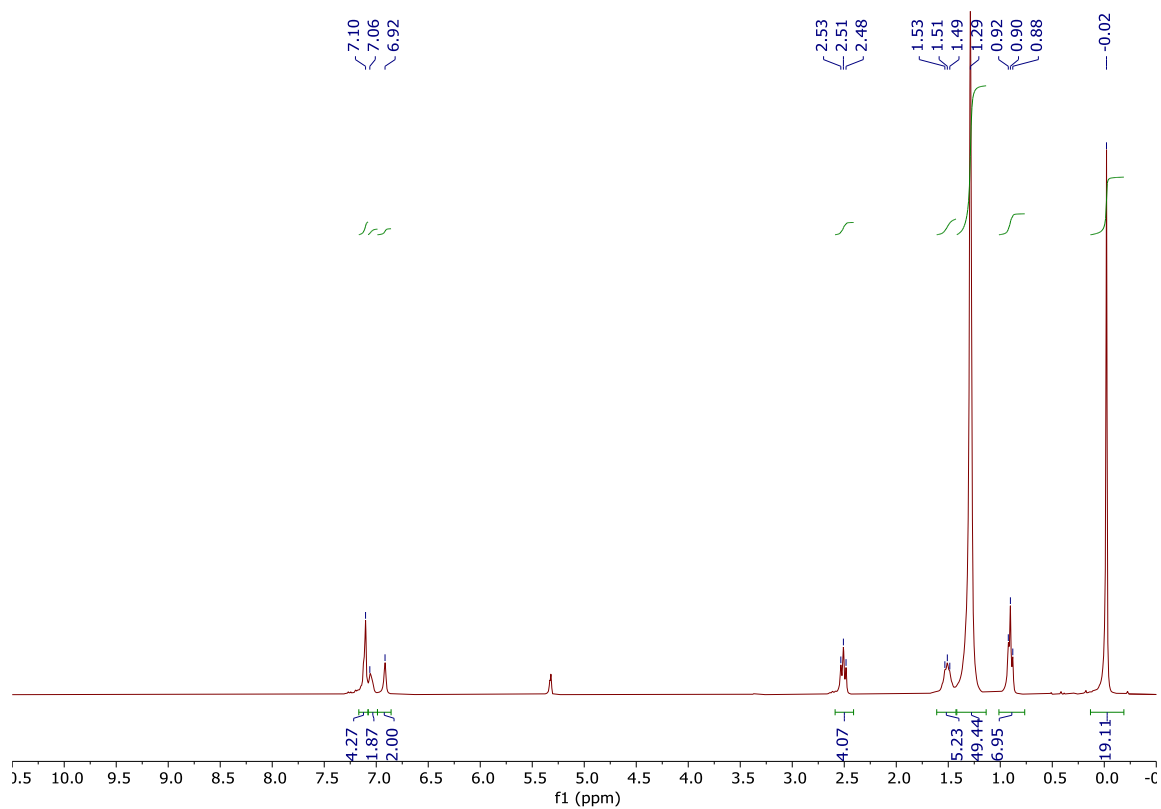


Figure S17. ¹H NMR spectrum of **10c**. (300 MHz, CD₂Cl₂)

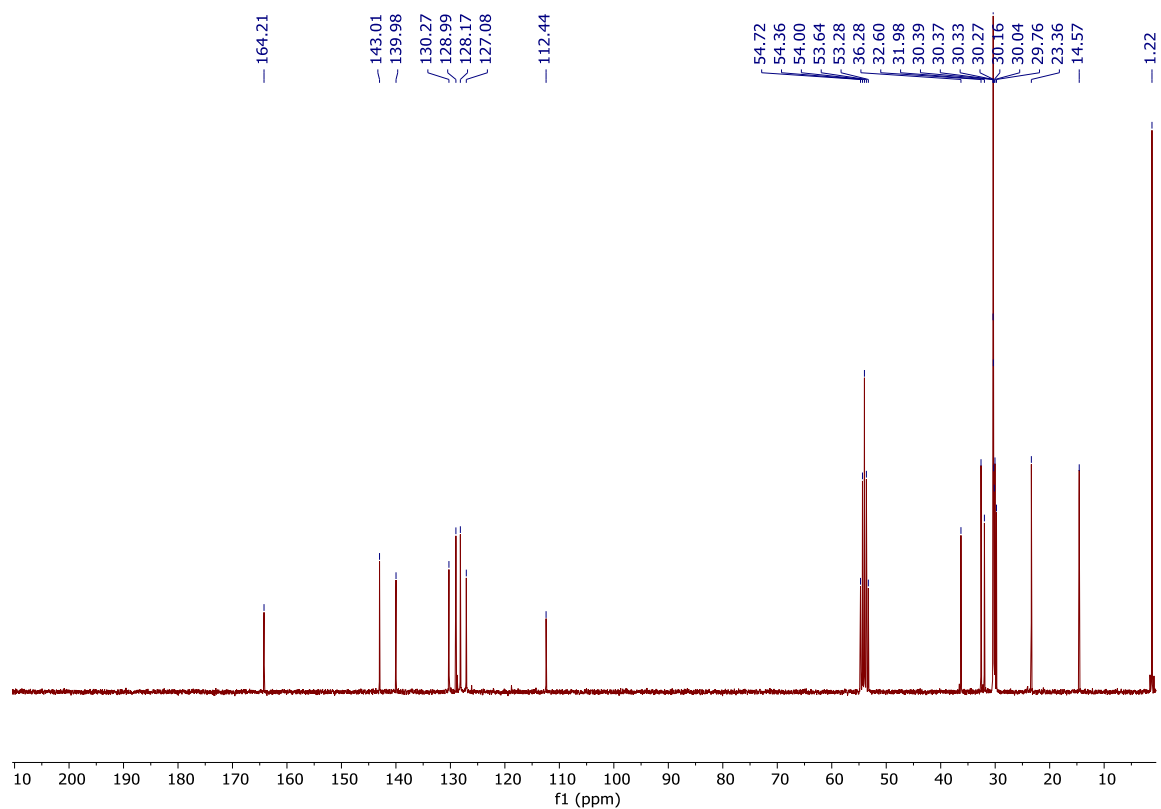


Figure S18. ¹³C NMR spectrum of **10c**. (75 MHz, CD₂Cl₂)

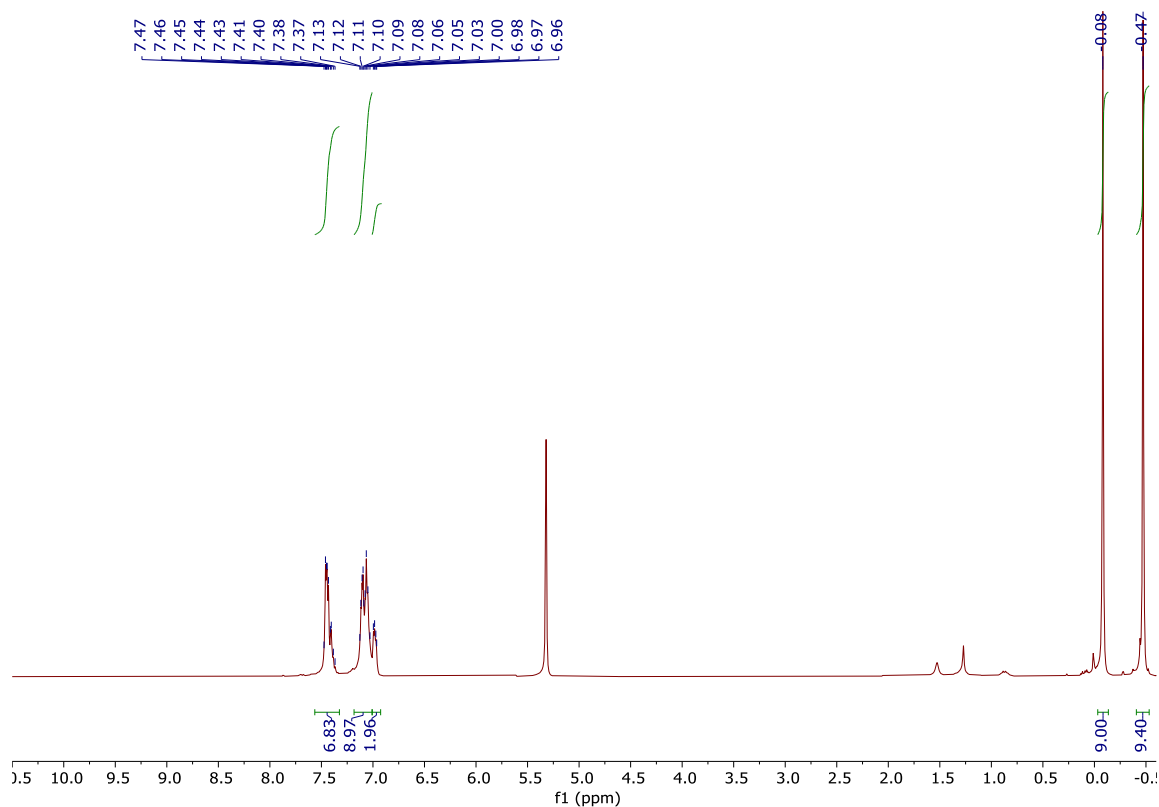


Figure S19. ^1H NMR spectrum of **11**. (300 MHz, CD_2Cl_2)

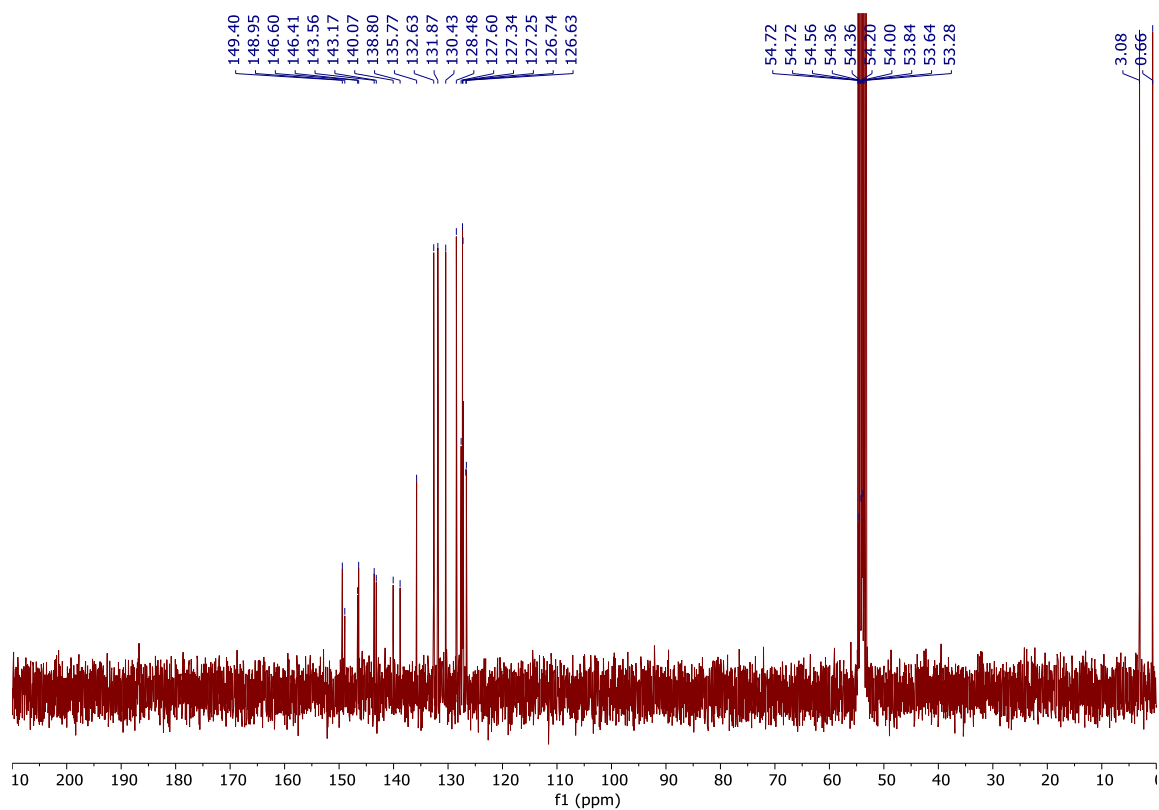


Figure S20. ^{13}C NMR spectrum of **11**. (75 MHz, CD_2Cl_2)

3.6 Supporting information

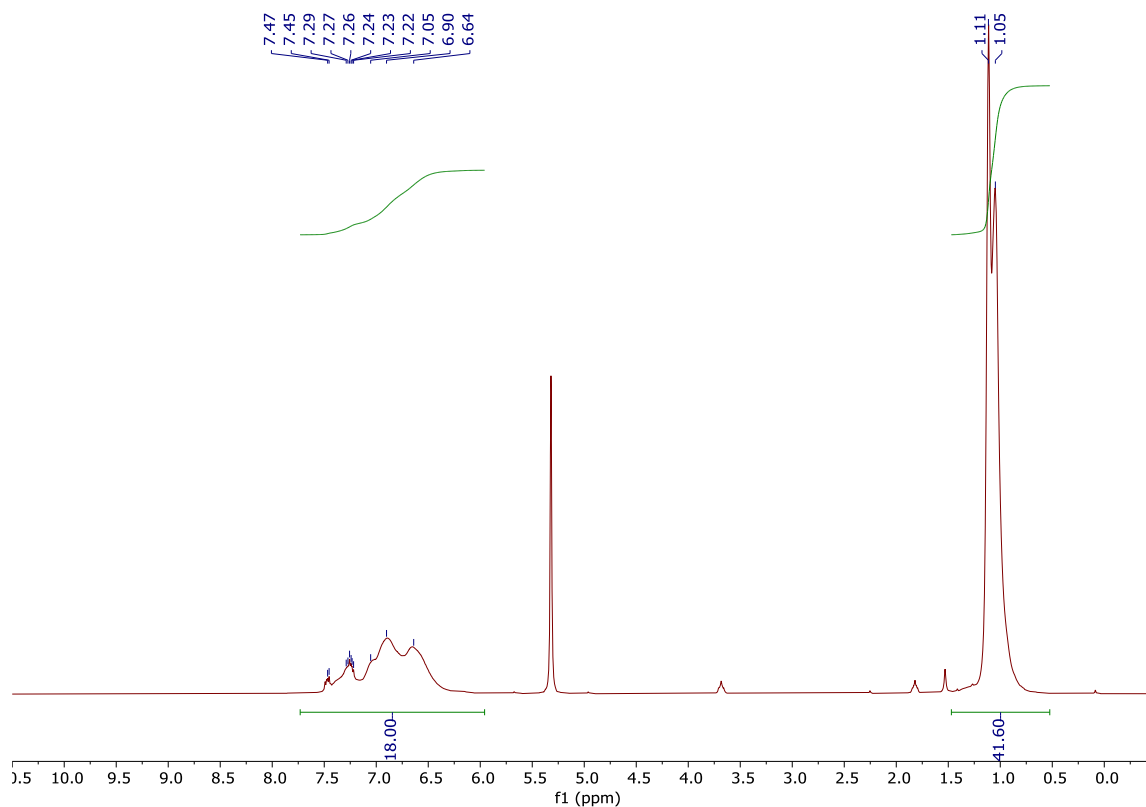


Figure S21. ^1H NMR spectrum of PP-Ic. (250 MHz, CD_2Cl_2)

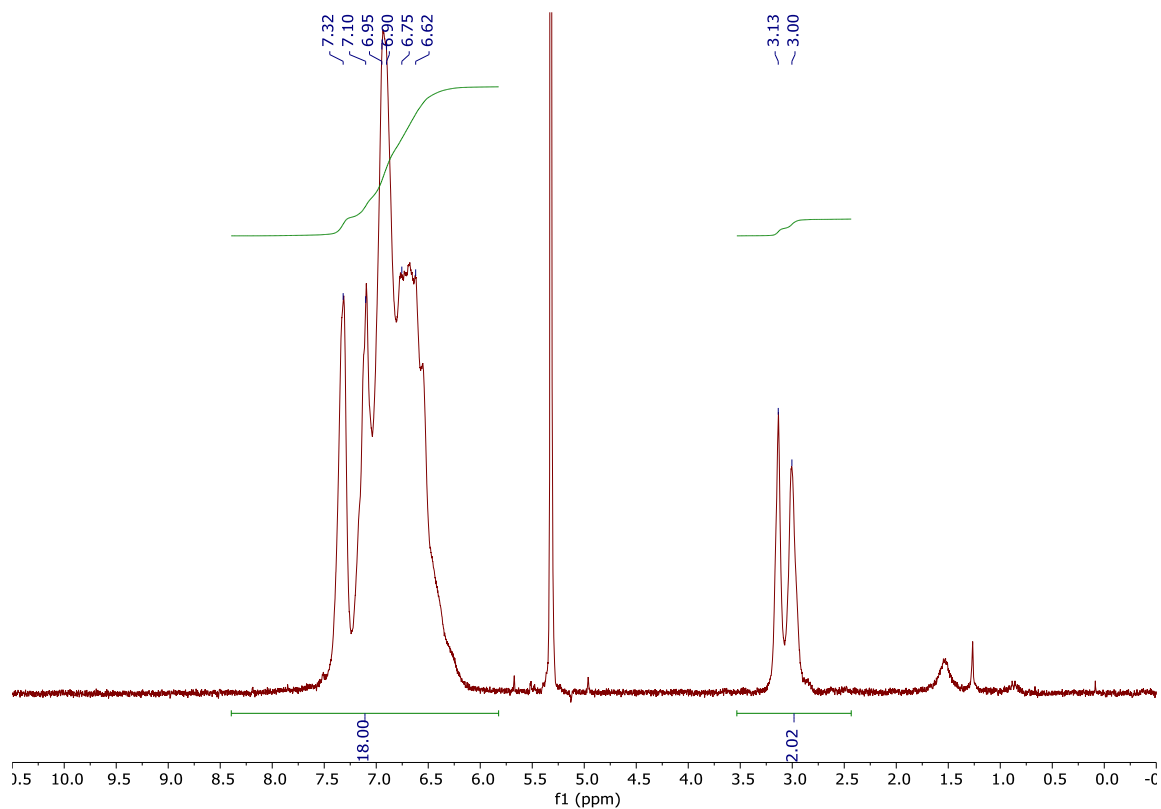


Figure S22. ^1H NMR spectrum of PP-Id. (250 MHz, CD_2Cl_2)

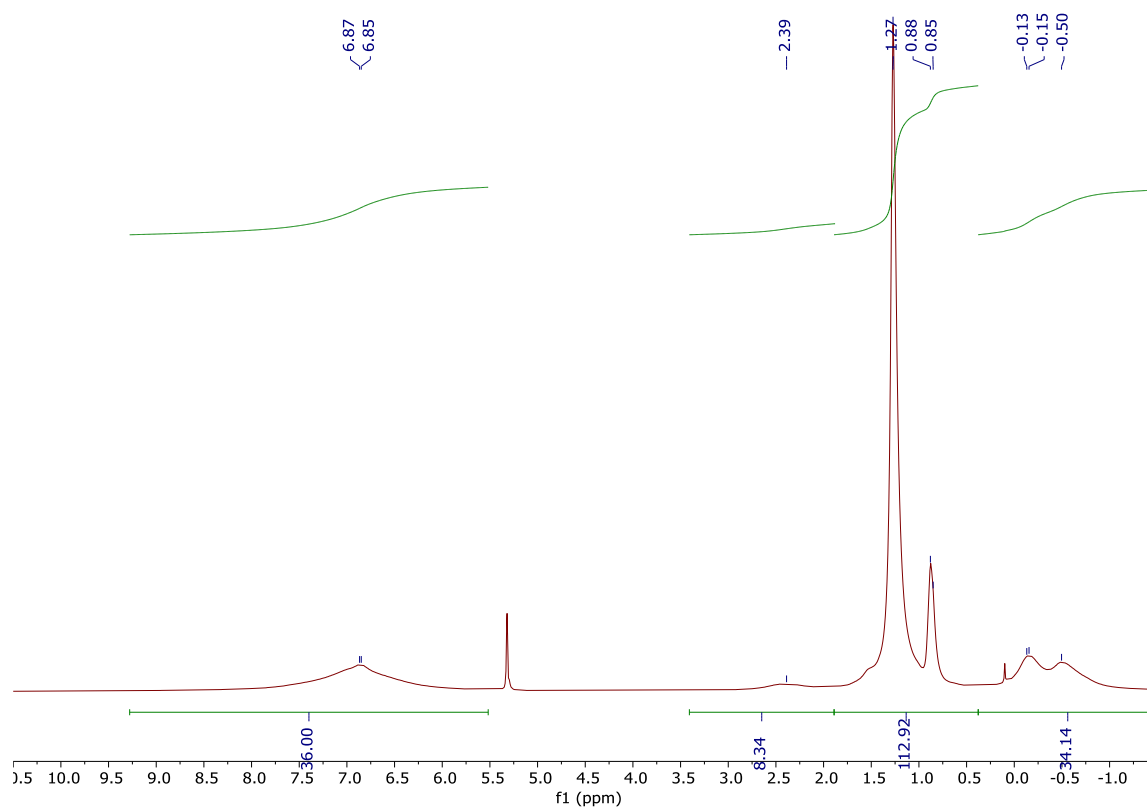


Figure S23. ^1H NMR spectrum of **PP-II**. (250 MHz, CD_2Cl_2)

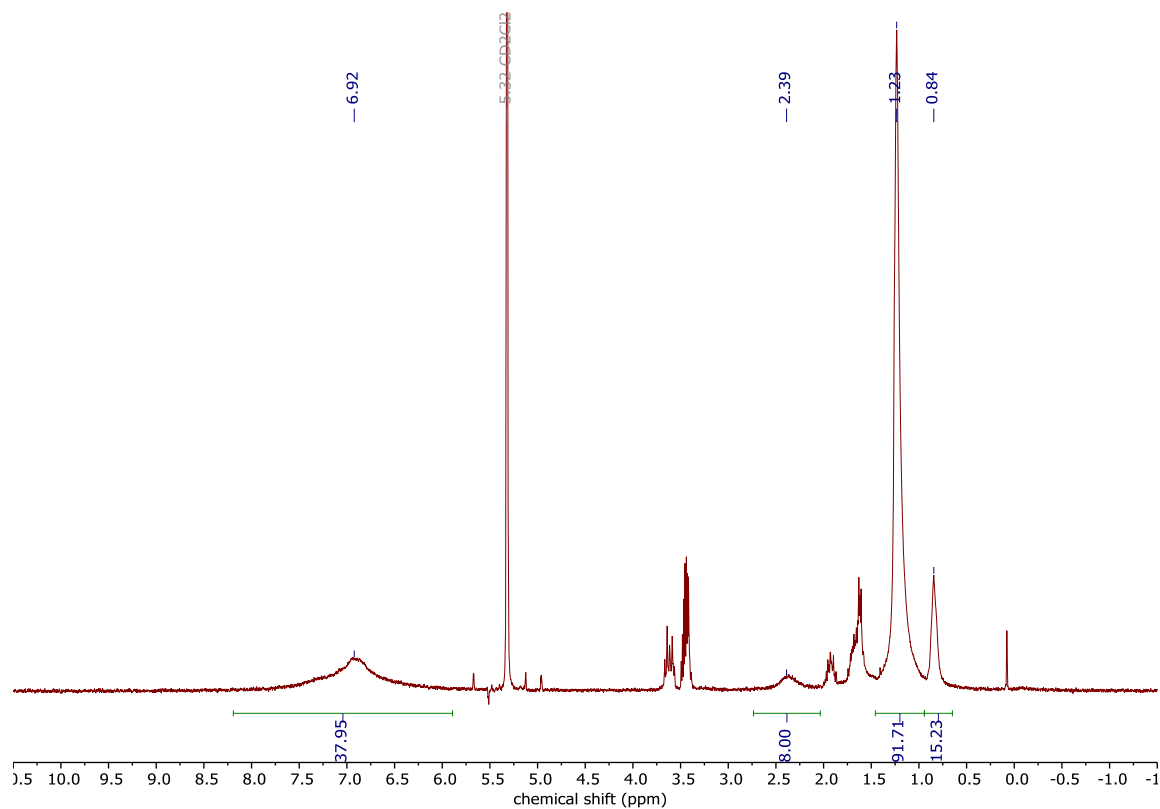


Figure S24. ^1H NMR spectrum of **PP-II** after desilylation. (250 MHz, CD_2Cl_2)

3.6 Supporting information

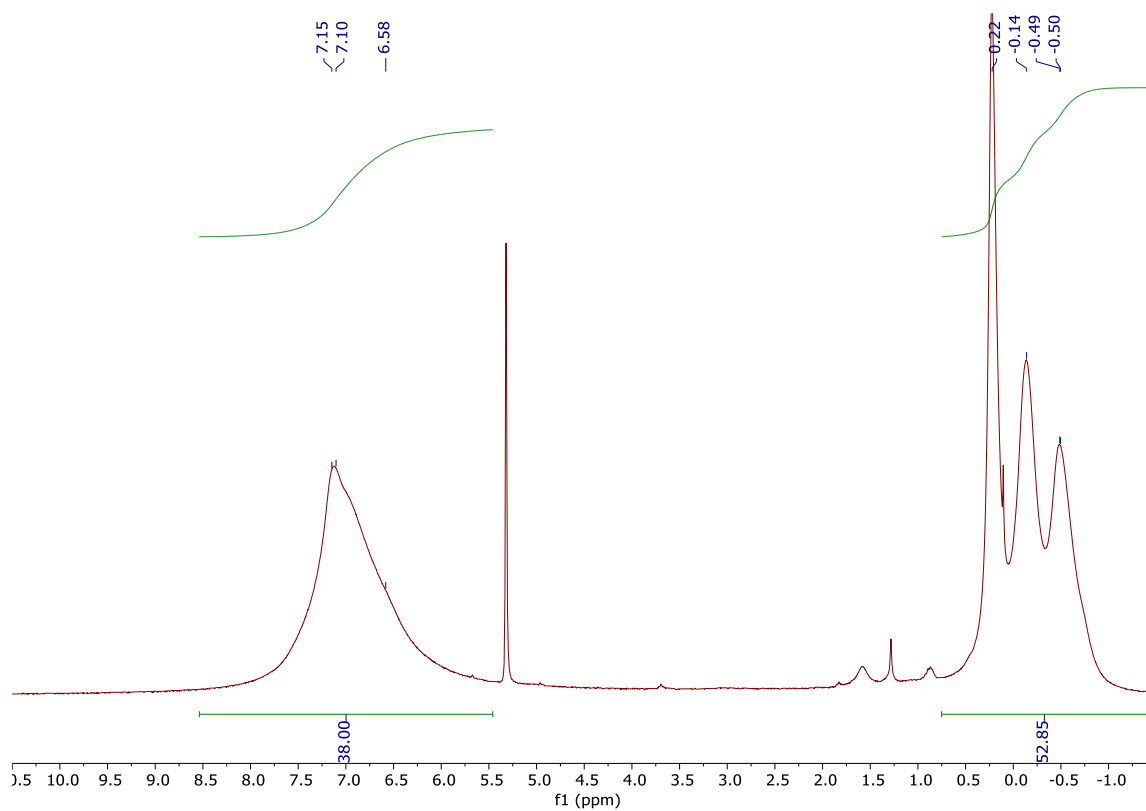


Figure S25. ^1H NMR spectrum of **PP-IIIa**. (250 MHz, CD_2Cl_2)

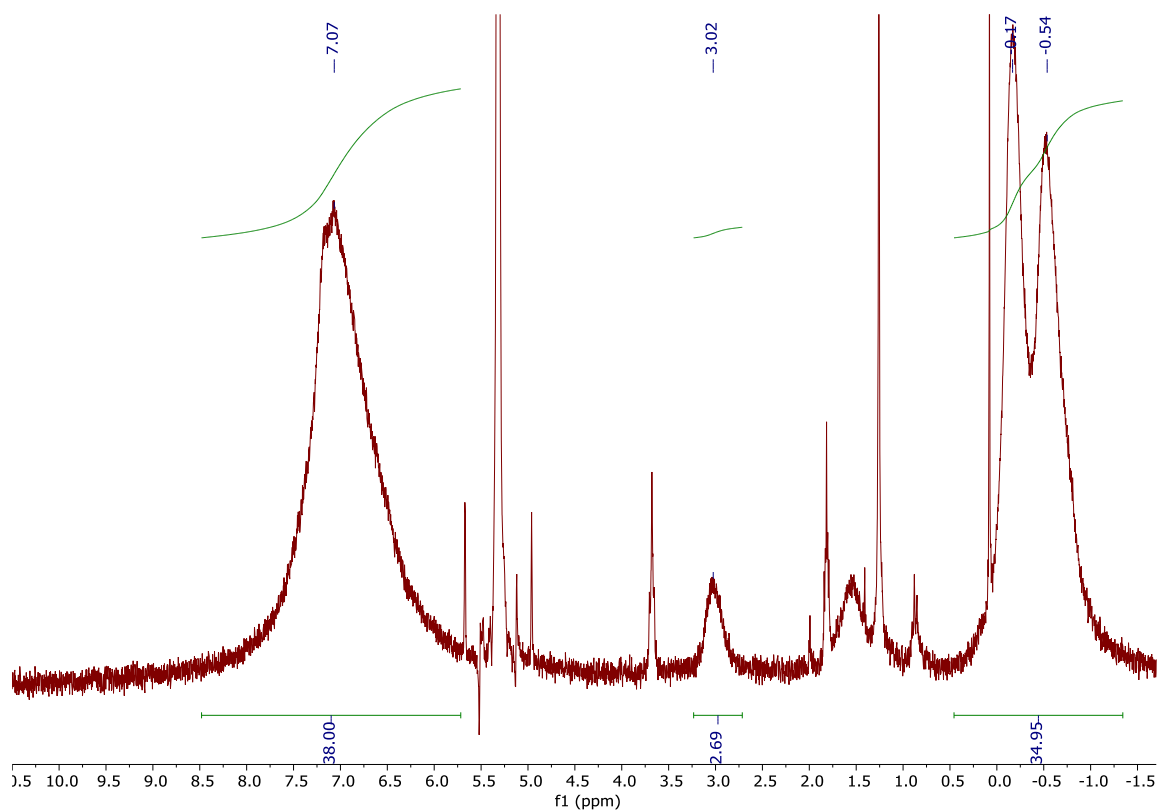


Figure S26. ^1H NMR spectrum of **PP-IIIb**. (250 MHz, CD_2Cl_2)

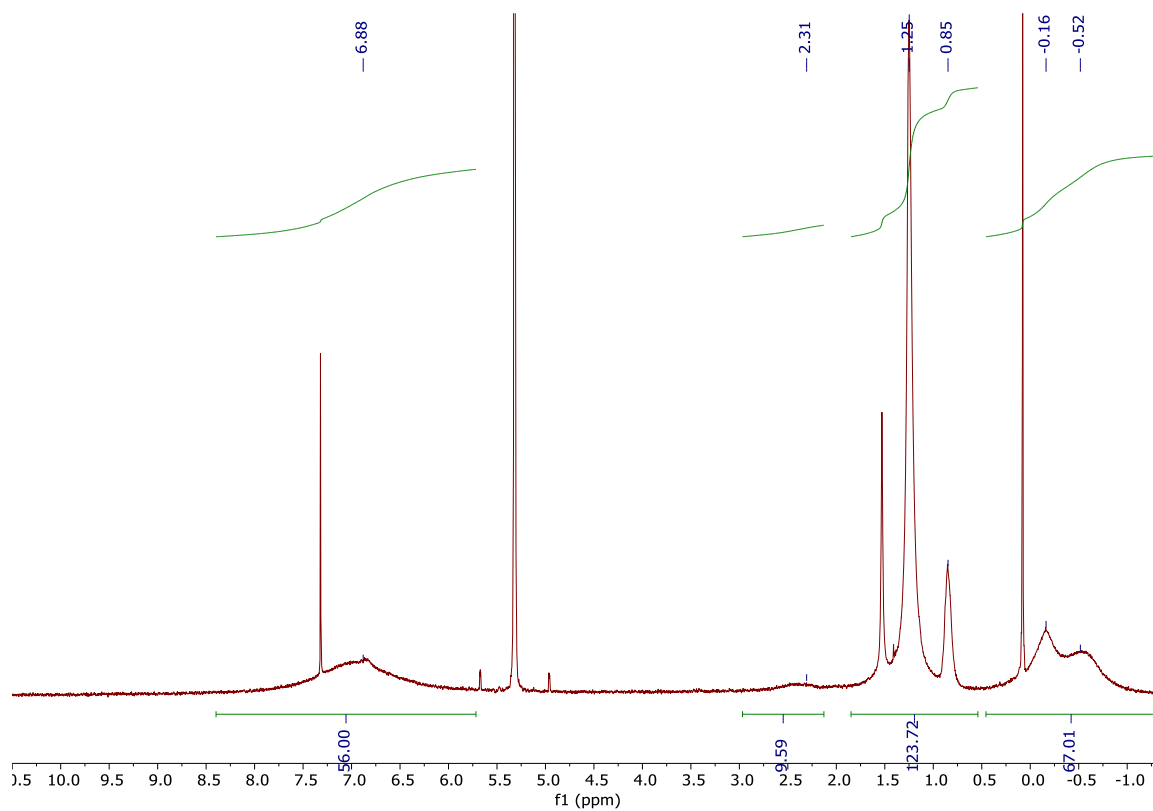


Figure S27. ^1H NMR spectrum of PP-IV. (250 MHz, CD_2Cl_2)

3.7 References

- (1) Hammer, B. A. G.; Müllen, K. Dimensional Evolution of Polyphenylenes: Expanding in All Directions. *Chem. Rev.* **2016**, *116* (4), 2103–2140.
- (2) Hou, I. C. Y.; Hu, Y.; Narita, A.; Müllen, K. Diels-Alder Polymerization: A Versatile Synthetic Method toward Functional Polyphenylenes, Ladder Polymers and Graphene Nanoribbons. *Polym. J.* **2018**, *50* (1), 3–20.
- (3) Si, K.; Wycisk, R.; Dong, D.; Cooper, K.; Rodgers, M.; Brooker, P.; Slattery, D.; Litt, M. Rigid-Rod Poly(Phenylenesulfonic Acid) Proton Exchange Membranes with Cross-Linkable Biphenyl Groups for Fuel Cell Applications. *Macromolecules* **2013**, *46* (2), 422–433.
- (4) Adamski, M.; Skalski, T. J. G.; Britton, B.; Peckham, T. J.; Metzler, L.; Holdcroft, S. Highly Stable, Low Gas Crossover, Proton-Conducting Phenylated Polyphenylenes. *Angew. Chem. Int. Ed.* **2017**, *56* (31), 9058–9061.
- (5) Holmes, T.; Skalski, T. J. G.; Adamski, M.; Holdcroft, S. Stability of Hydrocarbon Fuel Cell Membranes: Reaction of Hydroxyl Radicals with Sulfonated Phenylated Polyphenylenes. *Chem. Mater.* **2019**, *31* (4), 1441–1449.
- (6) Shiino, K.; Miyake, J.; Miyatake, K. Highly Stable Polyphenylene Ionomer Membranes from Dichlorobiphenyls. *Chem. Commun.* **2019**, *55* (49), 7073–7076.
- (7) Motealleh, B.; Huang, F.; Largier, T. D.; Khan, W.; Cornelius, C. J. Solution-Blended Sulfonated Polyphenylene and Branched Poly(Arylene Ether Sulfone): Synthesis, State of Water, Surface Energy, Proton Transport, and Fuel Cell Performance. *Polymer (Guildf.)* **2019**, *160*, 148–161.
- (8) Largier, T. D.; Wang, D.; Mueller, J.; Cornelius, C. J. Improving Electrodialysis Based Water Desalination Using a Sulfonated Diels-Alder Poly(Phenylene). *J. Memb. Sci.* **2017**, *531*, 103–110.
- (9) Largier, T.; Huang, F.; Cornelius, C. J. Homopolymer and Multi-Block Diels-Alder Polyphenylenes: Synthesis, Physical Properties, X-Ray Diffraction, and Gas Transport. *Eur. Polym. J.* **2017**, *89*, 301–310.
- (10) Largier, T.; Huang, F.; Kahn, W.; Cornelius, C. J. Poly(Phenylene) Synthesized Using Diels-Alder Chemistry and Its Sulfonation: Sulfonate Group Complexation with Metal Counter-Ions, Physical Properties, and Gas Transport. *J. Memb. Sci.* **2019**, *572*, 320–331.
- (11) Wang, X.-Y.; Yao, X.; Müllen, K. Polycyclic Aromatic Hydrocarbons in the Graphene Era. *Sci. China Chem.* **2019**, *62* (9), 1099–1144.
- (12) Narita, A.; Wang, X. Y.; Feng, X.; Müllen, K. New Advances in Nanographene Chemistry. *Chem. Soc. Rev.* **2015**, *44* (18), 6616–6643.
- (13) Narita, A.; Chen, Z.; Chen, Q.; Müllen, K. Solution and On-Surface Synthesis of Structurally Defined Graphene Nanoribbons as a New Family of Semiconductors. *Chem. Sci.* **2019**, *10* (4), 964–975.
- (14) Gröning, O.; Wang, S.; Yao, X.; Pignedoli, C. A.; Borin Barin, G.; Daniels, C.; Cupo, A.; Meunier, V.; Feng, X.; Narita, A.; et al. Engineering of Robust Topological Quantum Phases in Graphene Nanoribbons. *Nature* **2018**, *560* (7717), 209–213.
- (15) Rizzo, D. J.; Veber, G.; Cao, T.; Bronner, C.; Chen, T.; Zhao, F.; Rodriguez, H.; Louie, S. G.; Crommie, M. F.; Fischer, F. R. Topological Band Engineering of Graphene Nanoribbons. *Nature* **2018**, *560* (7717), 204–208.
- (16) Slota, M.; Keerthi, A.; Myers, W. K.; Tretyakov, E.; Baumgarten, M.; Ardavan, A.; Sadeghi, H.; Lambert, C. J.; Narita, A.; Müllen, K.; et al. Magnetic Edge States and Coherent Manipulation of Graphene Nanoribbons. *Nature* **2018**, *557* (7707), 691–695.
- (17) Narita, A.; Feng, X.; Hernandez, Y.; Jensen, S. A.; Bonn, M.; Yang, H.; Verzhbitskiy, I. A.; Casiraghi, C.; Hansen, M. R.; Koch, A. H. R.; et al. Synthesis of Structurally Well-Defined and Liquid-Phase-Processable Graphene Nanoribbons. *Nat. Chem.* **2014**, *6* (2), 126–132.
- (18) Ried, W.; Freitag, D. Synthese von Polyphenyl-Poly-Phenylen. *Naturwissenschaften* **1966**, *53* (12), 306.
- (19) Stille, J. K.; Harris, F. W.; Rakutis, R. O.; Mukamal, H. Diels-Alder Polymerizations: Polymers Containing Controlled Aromatic Segments. *J. Polym. Sci. Part B Polym. Lett.* **1966**, *4* (10), 791–793.
- (20) Forero-Martinez, N. C.; Baumeier, B.; Kremer, K. Backbone Chemical Composition and Monomer Sequence Effects on Phenylene Polymer Persistence Lengths. *Macromolecules* **2019**, *52* (14), 5307–5316.
- (21) Narita, A.; Verzhbitskiy, I. A.; Frederickx, W.; Mali, K. S.; Jensen, S. A.; Hansen, M. R.; Bonn, M.; De Feyter, S.;

- Casiraghi, C.; Feng, X.; et al. Bottom-up Synthesis of Liquid-Phase-Processable Graphene Nanoribbons with near-Infrared Absorption. *ACS Nano* **2014**, 8 (11), 11622–11630.
- (22) Hu, Y.; Xie, P.; De Corato, M.; Ruini, A.; Zhao, S.; Meggendorfer, F.; Straasø, L. A.; Rondin, L.; Simon, P.; Li, J.; et al. Bandgap Engineering of Graphene Nanoribbons by Control over Structural Distortion. *J. Am. Chem. Soc.* **2018**, 140 (25), 7803–7809.
- (23) Hammer, B. A. G.; Müllen, K. Expanding the Limits of Synthetic Macromolecular Chemistry through Polyphenylene Dendrimers. *J. Nanoparticle Res.* **2018**, 20 (10), 262.
- (24) Nguyen, T. T. T.; Baumgarten, M.; Rouhanipour, A.; Räder, H. J.; Lieberwirth, I.; Müllen, K. Extending the Limits of Precision Polymer Synthesis: Giant Polyphenylene Dendrimers in the Megadalton Mass Range Approaching Structural Perfection. *J. Am. Chem. Soc.* **2013**, 135 (11), 4183–4186.
- (25) Fuchs, B.; Pasternak, M.; Pazhenchevsky, B. Chemical and Photochemical Behavior of Nondissociating Cyclopentadienone Dimers. *J. Org. Chem.* **1981**, 46 (10), 2017–2020.
- (26) Sauriat-Dorizon, H.; Maris, T.; Wuest, J. D.; Enright, G. D. Molecular Tectonics. Construction of Porous Hydrogen-Bonded Networks from Bisketals of Pentaerythritol. *J. Org. Chem.* **2003**, 68 (2), 240–246.
- (27) Chen, X. C.; Nishinaga, S.; Okuda, Y.; Zhao, J. J.; Xu, J.; Mori, H.; Nishihara, Y. A Divergent Synthesis of 3,10-Dialkylpicenes. *Org. Chem. Front.* **2015**, 2 (5), 536–541.
- (28) Negishi, E. ichi; Holmes, S. J.; Tour, J. M.; Miller, J. A.; Cederbaum, F. E.; Swanson, D. R.; Takahashi, T. Novel Bicyclization of Enynes and Diynes Promoted by Zirconocene Derivatives and Conversion of Zirconabicycles into Bicyclic Enones via Carbonylation. *J. Am. Chem. Soc.* **1989**, 111 (9), 3336–3346.
- (29) Xi, C.; Hou, S.; Afifi, T. H.; Hara, R.; Takahashi, T. Remarkable Effect of Copper Chloride on Diiodination of Zirconacyclopentadienes. *Tetrahedron Lett.* **1997**, 38 (23), 4099–4102.
- (30) Xi, Z.; Song, Z.; Liu, G.; Liu, X.; Takahashi, T. Preparation of Partially Substituted 1-Halo- and 1,4-Dihalo-1,3-Dienes via Reagent-Controlled Desilylation of Halogenated 1,3-Dienes. *J. Org. Chem.* **2006**, 71 (8), 3154–3158.
- (31) Xi, Z.; Hara, R.; Takahashi, T. Highly Selective and Practical Alkyne-Alkyne Cross-Coupling Using Cp₂ZrBu₂ and Ethylene. *J. Org. Chem.* **1995**, 60 (14), 4444–4448.
- (32) Buchwald, S. L.; Nielsen, R. B. Selective, Zirconium-Mediated Cross-Coupling of Alkynes: Synthesis of Isomerically Pure 1,3-Dienes and 1,4-Diiodo 1,3-Dienes. *J. Am. Chem. Soc.* **1989**, 111 (8), 2870–2874.
- (33) Xi, Z.; Song, Q. Efficient Synthesis of Cyclopentadienone Derivatives by the Reaction of Carbon Dioxide with 1,4-Dilithio-1,3-Dienes. *J. Org. Chem.* **2000**, 65 (26), 9157–9159.
- (34) Chen, C.; Xi, C.; Jiang, Y.; Hong, X. 1,1-Cycloaddition of Oxalyl Dichloride with Dialkenylmetal Compounds: Formation of Cyclopentadienone Derivatives by the Reaction of 1,4-Dilithio-1,3-Dienes or Zirconacyclopentadienes with Oxalyl Chloride in the Presence of CuCl. *J. Am. Chem. Soc.* **2005**, 127 (22), 8024–8025.
- (35) Luo, Q.; Wang, C.; Zhang, W.-X.; Xi, Z. CuCl-Mediated Tandem CO Insertion and Annulation of 1,4-Dilithio-1,3-Dienes: Formation of Multiply Substituted Cyclopentadienones and/or Their Head-to-Head Dimers. *Chem. Commun.* **2008**, No. 13, 1593.
- (36) Hilt, G.; Janikowski, J. Regiocontrolled Cobalt-Catalyzed Diels-Alder Reactions of Silicon-Functionalized, Terminal, and Internal Alkynes. *Org. Lett.* **2009**, 11 (3), 773–776.
- (37) Pradhan, A.; Dechambenoit, P.; Bock, H.; Durola, F. Twisted Polycyclic Arenes by Intramolecular Scholl Reactions of C₃-Symmetric Precursors. *J. Org. Chem.* **2013**, 78 (6), 2266–2274.
- (38) Launer, P. J. Infrared Analysis of Organosilicon Compounds: Spectra-Structure Correlations. In *Silicone Compounds Register and Review*; Arkles, B., Larson, G. L., Eds.; Gelest, Inc.: Morrisville, 1987; pp 100–103.
- (39) Huang, Y.; Mai, Y.; Yang, X.; Beser, U.; Liu, J.; Zhang, F.; Yan, D.; Müllen, K.; Feng, X. Temperature-Dependent Multidimensional Self-Assembly of Polyphenylene-Based “Rod-Coil” Graft Polymers. *J. Am. Chem. Soc.* **2015**, 137 (36), 11602–11605.
- (40) Liu, L.; Wei, J.; Chi, Y.; Zhang, W. X.; Xi, Z. Structure and Reaction Chemistry of Magnesium Organocuprates Derived from Magnesiacyclopentadienes and Copper(I) Salts. *Angew. Chem. Int. Ed.* **2016**, 55 (47), 14762–14765.

Chapter 4. On-surface Synthesis of Polyazulene with 2,6-Connectivity

■■■■^{1†}, **Ian Cheng-Yi Hou**^{2†}, ■■■■¹, ■■■■¹, ■■■■¹, ■■■■^{2,3,*}, ■■■■^{1,4*}

¹Empa, Swiss Federal Laboratories for Materials Science and Technology, Überlandstrasse 129, CH-8600 Dübendorf,

²Max Planck Institute for Polymer Research, 55128 Mainz, Germany.

³Organic and Carbon Nanomaterials Unit, Okinawa Institute of Science and Technology Graduate University, 1919-1 Tancha, Onna-son, Kunigami, Okinawa 904-0495, Japan.

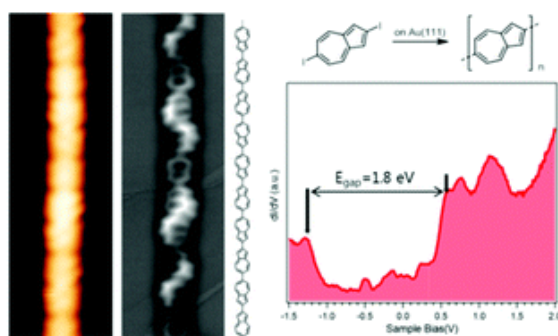
⁴Department of Chemistry and Biochemistry, University of Bern, Freiestrasse 3, CH-3012 Bern, Switzerland.

†These authors contributed equally to this work

Published in: *Chem. Commun.* **2019**, 55 (89), 13466–13469. DOI: 10.1039/c9cc07168g. Reprinted with permission. Copyright: 2019, the Royal Society of Chemistry.

Contribution: Organic synthesis and characterization. Preparing first draft with the co-first author. Manuscript revision.

4.1 Abstract

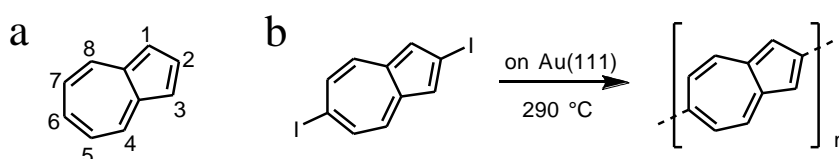


ToC Figure. We report the on-surface synthesis and characterization of the homopolymer of azulene connected exclusively at 2,6-positions.

Azulene, the smallest neutral nonalternant aromatic hydrocarbon, serves as not only a prototype for fundamental studies but also a versatile building block for functional materials because of its unique opto(electronic) properties. Here, we report the on-surface synthesis and characterization of the homopolymer of azulene connected exclusively at the 2,6-positions using 2,6-diiodoazulene as the monomer precursor. As an intermediate to the formation of polyazulene, a gold-(2,6-azulenylene) chain is observed.

4.2 Main text

Properties of carbon-based aromatic systems are sensitively determined by their bond topologies.^{1,2} So far, much attention has been paid to the design and synthesis of aromatic materials like conjugated polymers and nanographenes constituted by alternant hydrocarbons, which do not possess odd-membered rings. In contrast, incorporation of non-alternant hydrocarbons has only rarely been explored. Electronic and optical properties of alternant and non-alternant hydrocarbons differ profoundly. Azulene (Scheme 1), for example, an aromatic hydrocarbon containing 10 π -electrons, has several characteristics that differ from its isomer naphthalene.^{3,4} Azulene has an intrinsic dipole moment of 1.08 D,⁵ while naphthalene is non-polar. The dipole moment of azulene arises from an unequal distribution of electron density between its electron-deficient 7-membered ring and electron-rich 5-membered ring due to an aromatic stabilization according to Hückel's rule. In addition, azulene exhibits an "anomalous" fluorescence from its second excited singlet state in violation of Kasha's rule,⁶ which makes it a promising candidate in optoelectronics.^{7,8}



Scheme 1. (a) The chemical structure of azulene with carbon atom numbering. (b) On-surface synthetic route toward the 2,6-polyazulene.

Because of its unique electronic and optical properties, azulene has been employed as core structure of functional materials for different applications such as stimuli-responsive materials,⁹ organic field-effect transistors,^{10,11} solar cells¹² and others.^{13,14} The connectivity of azulenylyne units (Scheme 1a) in the derived structures has a substantial influence on their optical and electronic properties.¹⁵ One remarkable example is that the lowest unoccupied molecular orbital (LUMO) of 2,6':2'',6''-terazulene is fully delocalized over the whole molecule, showing strong bonding between the azulene moieties, resulting in a good n-type semiconductor performance.^{10,16} This motivates the study of 2,6-polyazulene. However, despite a number of theoretical studies on 2,6-polyazulenes, reports on the synthesis of azulene-based polymers predominantly focus on the incorporation of 1,3-azulenylenes.^{17,18} Recent studies showed that integration of 2,6-azulenylenes into copolymers had great potential for field-effect transistors and proton-conducting materials.^{11,19} Nevertheless, the synthesis of azulene homopolymers with 2,6-connectivity remained elusive.

On-surface synthesis has recently developed as a complementary strategy for chemical synthesis. A significant number of structures/materials which are challenging by conventional solution chemistry have been achieved by this method.^{20–22} Due to its potentially interesting properties, 2,6-polyazulene is starting to gain attention from the community of on-surface synthesis.²³ Here, we report the on-surface synthesis of polyazulene with exclusive 2,6-connectivity using 2,6-diiodoazulene as the molecular precursor (Scheme 1b). The electronic property of the synthesized polyazulene is investigated by scanning tunneling spectroscopy (STS) and density functional theory (DFT) calculations. The electronic gap of the polyazulene is determined to be 1.8 eV on Au(111), which is further supported by differential conductance dI/dV mapping. This work demonstrates not only the synthesis but also the first detailed electronic characterization of azulene homopolymers with pure 2,6-connectivity.

The 2,6-diiodoazulene was synthesized following a previous work.²⁴ To access the pristine 2,6-diiodoazulene molecules, we first deposit the molecule under ultrahigh vacuum condition onto an Au(111) surface maintained at 160 K to avoid possible deiodination that would occur at room temperature.²⁵ As shown in the scanning tunneling microscopy (STM) images (Fig. 1a and 1b), 2,6-diiodoazulene forms porous structures on Au(111). A zoom-in image reveals the monomers appearing as rod structures with brighter iodine protrusions at both ends according to the chemical model overlaid in Fig. 1b. Note that it is not possible to differentiate the 7- and 5-membered rings and the exact orientation of azulenes solely based on the STM images. After annealing the sample to 350 K, a chain structure is observed on the surface (Fig. 1c and 1d). The molecular chains are composed of two alternating subunits (Fig. 1d), assigned to 2,6-azulenylene moieties and to gold adatoms, respectively. We superimpose an equally scaled chemical structure of a chain segment onto a small-scale STM image in Fig. 1d, which shows a good match. It is not surprising that gold atoms are involved in nanostructures obtained upon dehalogenation of molecules on Au substrates, and there are many reports of organo-metallic species on Au(111).^{26–28} The detached iodine atoms are detected as round protrusions staying aside the organo-metallic chains (indicated by a blue arrow in Fig. 1d), forming some honeycomb-type structure at the left part of Fig. 1c. This is consistent with the fact that iodine desorption from Au(111) starts only at around 540 K.²⁵ Closer inspection of the structures formed at 350 K reveals that a few 2,6-connected oligoazulenes without the involvement of Au atoms have already been formed (one of them is indicated by a green arrow in Fig. 1d). The one-dimensional organometallic chains are straight due to the formation of the C-Au-C organo-metallic motifs as aryl radicals on Au(111).^{26–28} Further annealing the sample to 580 K triggers the release of all Au atoms from

the organo-metallic chains and the formation of the carbon-carbon bonded polymer, as well as partial desorption of iodines (Fig. 1e and 1f). A high-resolution STM image of the polymer reveals that the azulene units are connected along their long axis, implying the formation of 2,6-connected polyazulene.

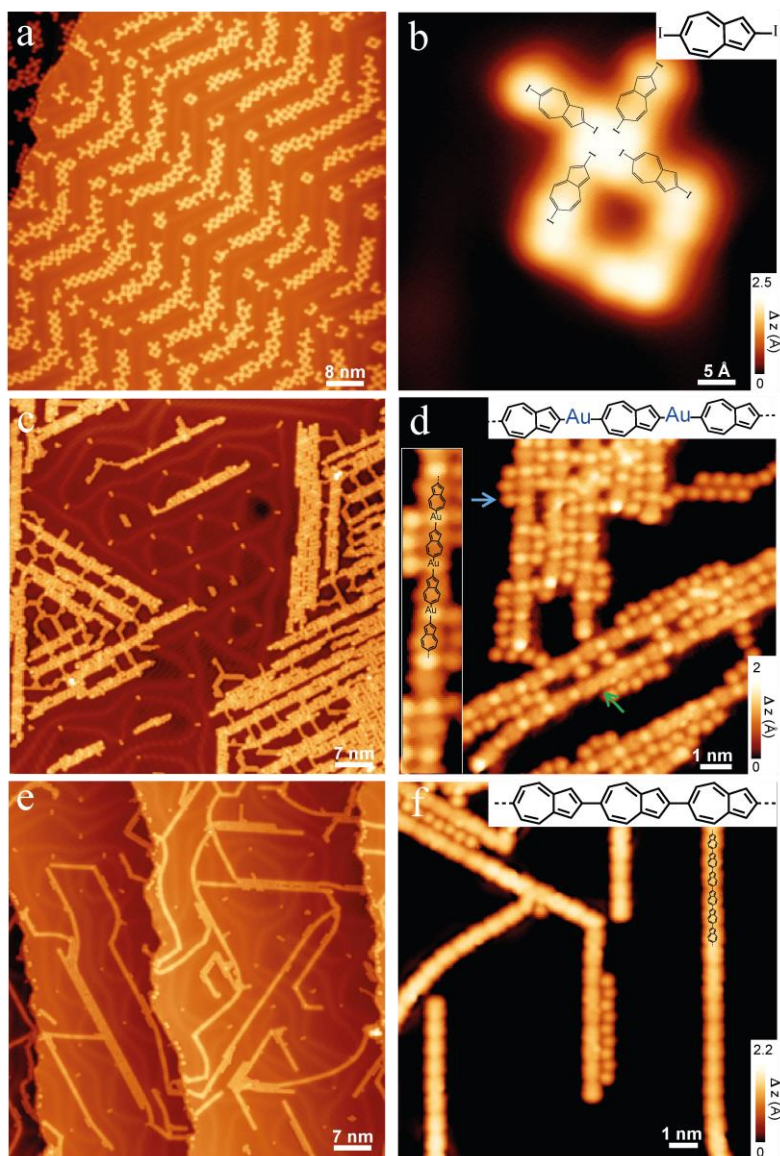


Figure 1. (a,b) STM images after deposition of 2,6-diiodoazulene on Au(111) held at 160 K. Chemical structures of four molecules are overlaid on the corresponding STM image in (b). (c,d) STM images of the sample after annealing to 350 K. An inset in (d) highlights the organo-metallic chain. The blue arrow indicates a detached iodine atom. The green arrow indicates oligomeric 2,6-connected azulene segments. (e,f) STM images after annealing the sample to 580 K. A scaled chemical model of a 2,6-oligoazulene is overlaid on a chain in (f). Scanning parameters: (a) $V_s = -1$ V, $I_t = 0.09$ nA; (b) $V_s = -0.02$ V, $I_t = 0.25$ nA; (c) $V_s = -1$ V, $I_t = 0.06$ nA; (d) $V_s = -0.005$ V, $I_t = 0.1$ nA; (e) $V_s = -1$ V, $I_t = 0.08$ nA; (f) $V_s = -0.01$ V, $I_t = 1$ nA.

To further support the formation of polyazulene and determine the connectivity between azulene units, we resort to bond-resolved non-contact atomic force microscopy (nc-AFM).²⁹ As shown in Fig. 2a, the structure of the polymer can be clearly resolved, with the 5- and 7-membered rings being imaged with different sizes. Typical defects in the straight 2,6-connected polyazulene are kinks (cf. Fig. S1) arising from 1,6-connected azulene units, which are attributed to a small amount of impurity from the precursor²⁴ or to a 2,1-sigmatropic rearrangement. Within a 2,6-polyazulene chain, neighboring 2,6-azulenylenes can be connected in three different ways, namely pentagon *vs.* heptagon (p-h), pentagon *vs.* pentagon (p-p), or heptagon *vs.* heptagon (h-h), which correspond to 2,6-, 2,2- and 6,6-connectivity, respectively (see the arrows in Fig. 2a). The h-h-connectivity is the most easily recognized, since it results in a non-zero dihedral angle between neighboring azulenylyene units due to the steric hindrance between the hydrogen atoms at 5,7-positions of azulenylyene, which is clearly reflected in the nc-AFM images. High resolution images however also allow identification of p-h- and p-p-connectivity. An interesting aspect about the reaction between azulenylenes is whether there is any preference for the p-h-connectivity, since azulene has an intrinsic dipole moment of 1.08 D which might direct the polymerization process *via* dipole-dipole interactions. To this end, we have performed a statistical analysis of the linkages between neighboring azulenylenes. It turns out that the ratio between p-h-, p-p- and h-h-linkages is 2 : 1 : 1 (Fig. 2b), which indicates a non-selective, random connection between the 5- and 7-membered rings (see discussion in Fig. S2). Thus, the intrinsic dipole moment of pristine azulene does not play a role in orienting the azulenylenes during on-surface polymerization. We attribute this to the screening effect of the electrons of the metal which produces an image dipole, with the resulting dipolar interaction being inconsequentially small for molecular dipoles oriented parallel to the surface.³⁰ A possible way to align the azulenylenes and to obtain p-h linkages only may thus be the use of an insulating substrate.

To study the electronic properties of 2,6-polyazulene, we first carry out DFT calculations of an azulene molecule and polyazulene. Fig. 3a shows the frontier orbitals from HOMO-2 to LUMO+1 of azulene, while Fig. 3b gives the band structure of the 2,6-polyazulene originating from these orbitals. The bands originating from the highest occupied molecular orbital (HOMO), HOMO-2 and LUMO+1 are relatively flat due to the orbitals having low amplitudes at the 2,6-positions where azulene units are connected. In contrast, the bands originating from HOMO-1 and LUMO show significant dispersion due to considerable orbital overlap between the neighboring azulenylenes. To further investigate how the random distribution of p-h-, p-p- and h-h-linkages affects the electronic structure, we performed band

structure calculations for three different structures consisting of a supercell with four azulene units. The first structure with only the p-h-linkage between all the azulenylenes reproduces the band structure of 2,6-polyazulene (Fig. 3c), but folded to a four times smaller Brillouin zone. The second structure (star) in Fig. 3c has alternating p-p- and h-h-linkages, and the third structure (diamond) has every third unit flipped compared to the others. Besides a splitting of the bands due to lifting of degeneracy near k-vectors corresponding to the modified periodicity, the band structures near the valence band (VB) and conduction band (CB) onsets do not differ much from each other. All of the three structures have an electronic band gap of 0.94 ± 0.03 eV, and their frontier bands display similar dispersions. This is in line with the fact that the molecular orbitals of azulene possess no weight at 2,6-positions for HOMO-2 and HOMO but considerable weight for HOMO-1 and LUMO (Fig. 3a). Although three different linkages are randomly distributed within our experimentally obtained polymers, the electronic properties of the synthesized polyazulene shall remain very similar to the ones of the perfectly regular poly(2,6-azulenylene).

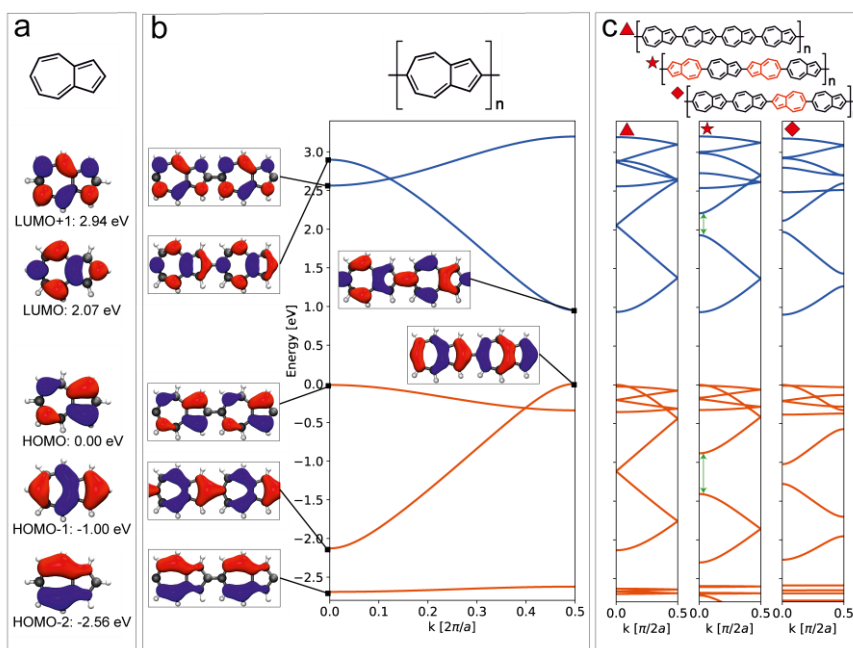


Figure 3. Electronic structure of azulene and polyazulenes with 2,6-connectivity. (a) The shape of frontier orbitals of an azulene molecule. (b) Band structure of 2,6-polyazulene and the orbital shapes of the frontier bands which evolve from the corresponding molecular orbital of azulene shown in (a). (c) Band structures of three polyazulenes with different connectivity patterns in a supercell containing four 2,6-azulenylenes with all units oriented in the same way (triangle); first and third unit flipped (star); and only third unit flipped (rhombus). The green arrows show two examples of degeneracy liftings caused by the flipped units. In all band structure plots, top of the valence band is taken as zero energy, orange lines are occupied bands while blue lines correspond to unoccupied bands. In all orbital plots wavefunction isosurfaces at $\pm 0.03 \text{ \AA}^{-3/2}$ are shown. a is the length of one azulene unit within the homopolymer.

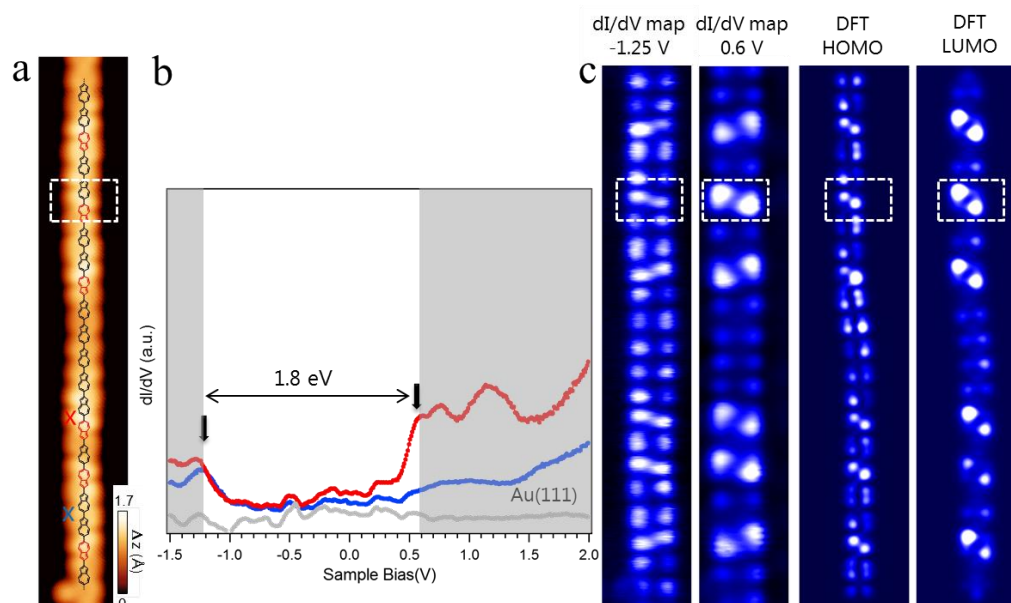


Figure 4. (a) STM image of a polyazulene segment ($V_s = -1.5$ V, $I_t = 0.9$ nA) and (b) its differential conductance dI/dV spectra. The spectra were taken at the locations marked by crosses with corresponding colors in (a). The grey spectrum has been acquired on a clean Au(111) area nearby. Spectra are vertically offset for clarity. (c) Constant-current dI/dV maps of the HOMO and LUMO, and the corresponding DFT-calculated LDOS maps. The h-h-linkage which shows a higher contrast is highlighted by dashed rectangles in both dI/dV and LDOS maps.

We have used dI/dV spectroscopy to experimentally characterize the electronic properties. The point spectra of the polymer reveal two peaks at around -1.25 V and 0.6 V, which correspond to its VB and CB onsets, respectively (Fig. 4a and 4b). To verify the assignment of the molecular orbitals, we have performed dI/dV mapping at two corresponding bias voltages (Fig. 4c). The dI/dV maps show clear patterns confirming their origin from molecular orbitals. Moreover, the position of the h-h-linkage has a higher contrast in dI/dV mapping of the CB onset, which is highlighted by the white rectangle in Fig. 4. This feature could also be seen in the constant-current STM imaging at a bias voltage of 0.6 V (Fig. S3), and is consistent with the fact that the LUMO of an azulene monomer is mainly located at the 7-membered ring (see also Fig. 3a).¹⁷ To further support our experimental findings, we determine the electronic properties of the experimentally observed polyazulene segment shown in Fig. 4a by DFT calculations (Fig. S4). The DFT calculated local density of states (LDOS) maps at the VB and CB onsets (i.e. HOMO and LUMO) are in good agreement with the experimental dI/dV maps at both negative and positive biases (Fig. 4c), and thus confirm the peaks at -1.25 V and 0.6 V in Fig. 4b originating from the VB and CB onsets. Note that the energy positions of the DFT computed LDOS are determined from the calculated DOS

shown in Fig. S4. Notably, the h-h-linkage displays characteristic contrast in both DFT calculated maps, and appears particularly bright in the experimental map (highlighted by dashed rectangles).

The frontier states (i.e. the first occupied and unoccupied states) of the polymer are positioned symmetrically with respect to a negative bias voltage of around -0.3 V (Fig. 4b). In contrast, the frontier states of most carbon nanowires/ribbons composed of alternant (poly)benzenoids are positioned symmetrically to positive bias voltages on Au(111).³¹ This is due to the systems having different valence and conduction band alignments with respect to the vacuum level, which determines the corresponding positioning with respect to the Au Fermi level upon adsorption for weakly interacting systems. This is reflected in our DFT calculations, which demonstrate that for polyazulene the VB and CB onsets are respectively at -5.0 eV and -4.1 eV with respect to the vacuum level. In contrast, the band onsets for armchair graphene nanoribbons of width 7 (7AGNR) are found at -4.7 eV and -3.2 eV (Fig. S5).

In conclusion, the homopolymer of azulene with exclusive 2,6-connectivity has been synthesized by dehalogenative coupling of 2,6-diiodoazulene on Au(111). Although azulene has an intrinsic dipole moment, dipole-dipole interactions do not yield a preferential pentagon-heptagon-linkage along the polymer. However, the electronic properties of 2,6-polyazulene do not significantly depend on the ratio of the p-p, p-h and h-h linkages. STS yields an electronic gap of 1.8 eV for polyazulene on Au(111), confirmed by STS mapping and DFT-based LDOS simulations. The study route may enable future applications of azulene-based functional materials.

4.3 Supporting information

Methods

STM/STS/nc-AFM. A commercial low-temperature STM/nc-AFM (Scienta Omicron) system was used for sample preparation and *in situ* characterization under ultra-high vacuum conditions (base pressure below 1×10^{-10} mbar). The Au(111) single crystal was cleaned by argon sputtering ($p = 6 \times 10^{-6}$ mbar) and annealing cycles to 750 K for 15 minutes. Deposition of the molecular precursors was done by thermal evaporation from a 6-fold organic evaporator (Mantis GmbH). STM images were recorded in constant-current mode, and the dI/dV spectra were recorded using the lock-in technique ($U_{\text{RMS}} = 20$ mV). nc-AFM images were recorded with a CO-functionalized tip attached to a quartz tuning fork sensor (resonance frequency 23.5 kHz, peak-to-peak oscillation amplitude below 100 pm).

Density functional theory calculations. DFT orbitals of the isolated azulene and the band structures were calculated with the Quantum Espresso software package using the PBE exchange correlation functional. A plane wave basis with an energy cutoff of 400 Ry for the charge density was used together with PAW pseudopotentials (SSSP)³². For the band structure of the primitive (super) cell calculations a Monkhorst k-mesh of $40 \times 1 \times 1$ ($10 \times 1 \times 1$) was used. The models of the gap-phase calculated polyazulenes were constructed in flat geometries. The cell and atomic geometries were relaxed until forces were smaller than 1 e^{-4} a.u. To perform these calculations we used the AiiDA platform.³³

The equilibrium geometry of the polyazulene polymer on the Au(111) substrate was obtained with the CP2K code.³⁴ The gold slab consisted of 4 atomic layers of Au along the [111] direction and a layer of hydrogen to suppress one of the two Au(111) surface states. 40 \AA of vacuum were included in the cell to decouple the system from its periodic replicas in the direction perpendicular to the surface. We used the TZV2P Gaussian basis set³⁵ for C and H and the DZVP basis set for Au together with a cutoff of 600 Ry for the plane wave basis set. We used norm conserving Goedecker-Teter-Hutter³⁶ pseudopotentials, the PBE³⁷ parametrization for the exchange correlation functional and the Grimme's DFT-D3 dispersion corrections³⁸. To obtain the equilibrium geometries we kept the atomic positions of the bottom two layers of the slab and hydrogen layer fixed to the ideal bulk positions, all other atoms were relaxed until forces were lower than 0.005 eV/\AA .

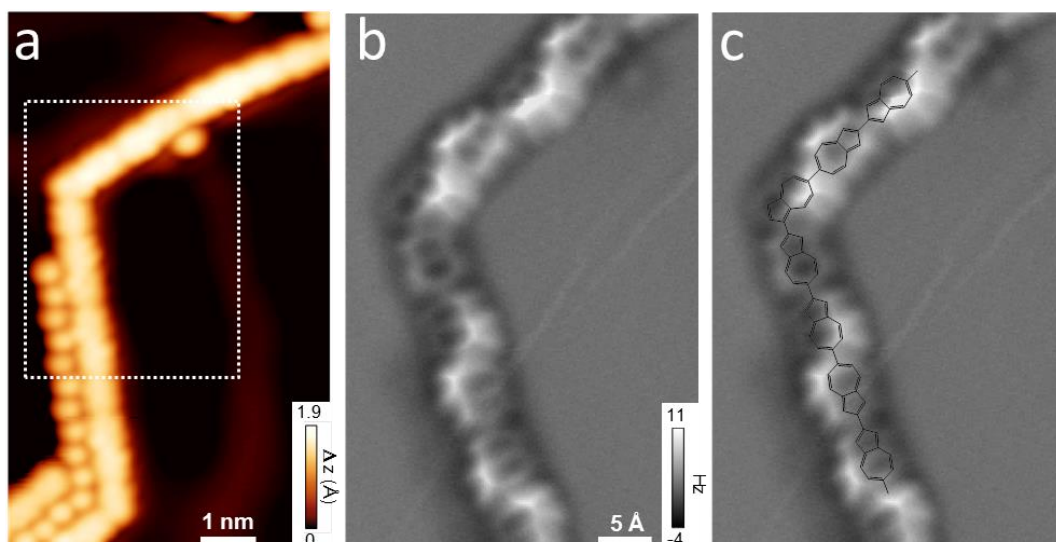


Figure S1. (a) STM image of a kinked polymer. (b) nc-AFM image of the area which is highlighted by a dashed rectangle in (a). (c) The same nc-AFM image as (b) with the chemical structure of the polymer overlaid, where we clearly see that the kink is due to a 1,6-connected azulenylenyl unit. The protrusions beside the polymer in the STM image are the detached iodine atoms, which are not seen in the nc-AFM image.

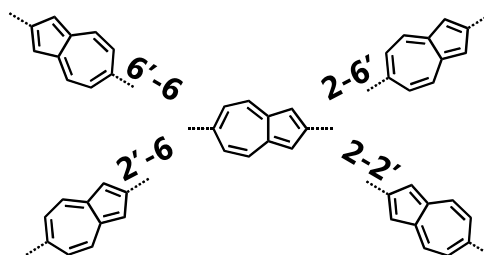


Figure S2. The possible linkages between the 2,6-azulenylenyl units in non-biased situations. If we take the middle azulenylenyl as the starting point, it can connect to a second azulenylenyl in four different ways, that is, 6',6, 2,6', 2',6, and 2,2', where 2,6' and 2',6 lead to the same connectivity (2,6-connectivity) in the polymer chain. Thus, a non-biased statistic ratio of 2,6 (*p-h*), 2,2 (*p-p*) and 6,6 (*h-h*) linkages in the polymer chain would be 2 : 1 : 1.

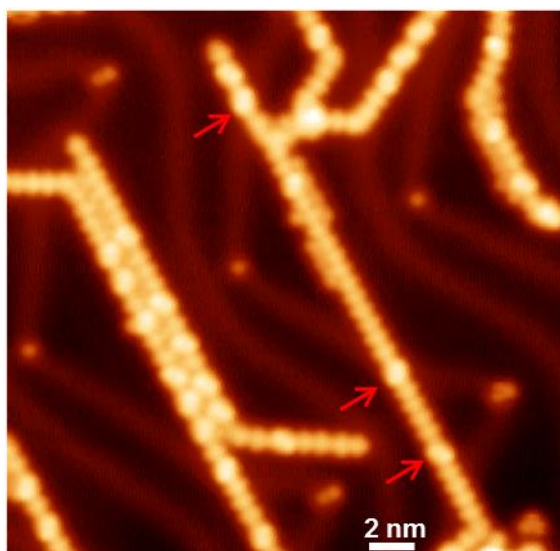


Figure S3. A typical STM image of polyazulene product on Au(111) at a bias voltage of 0.6 V. The h-h-linkage is clearly seen as a bump in the chains, three of them being indicated by red arrows.

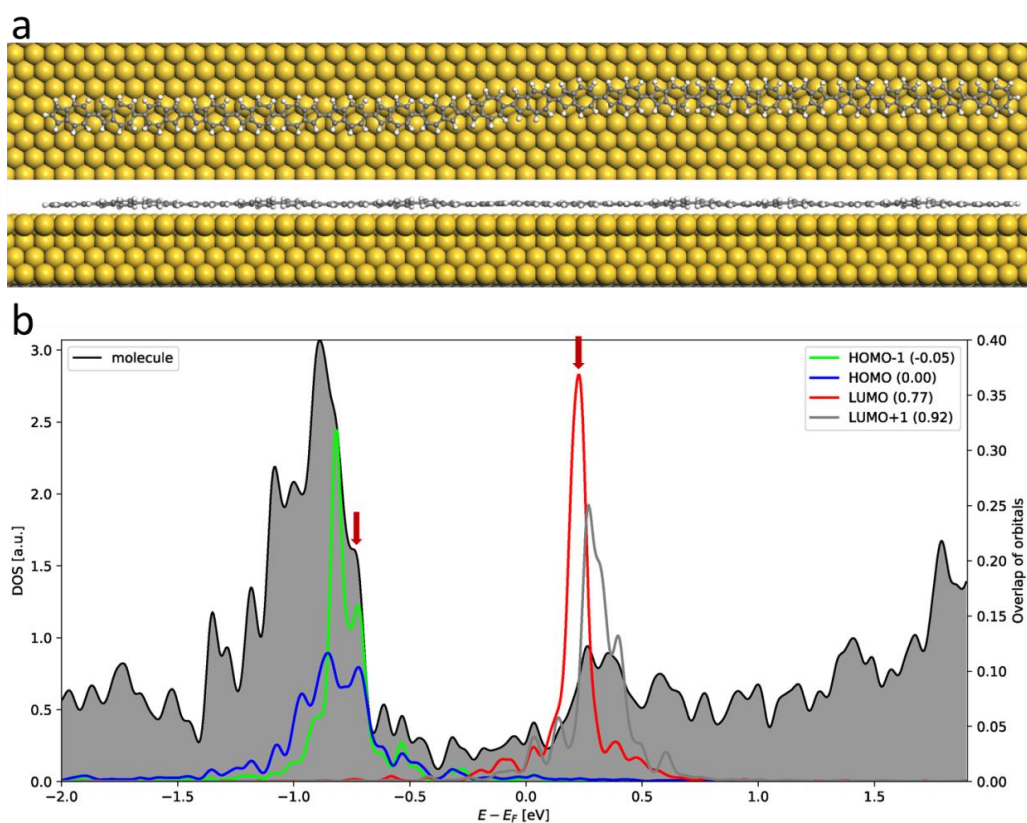


Figure S4. (a) Top and side views of a DFT optimized structure of a finite polyazulene chain on Au(111). (b) Gray filled area shows the DFT calculated density of states (DOS) of the polymer on the surface scaled by a factor of 0.1. Projections of the HOMO-1, HOMO, LUMO and LUMO+1 orbitals from the gas-phase polymer onto the orbitals of the molecule/substrate system are shown in colored lines. The energy positions used for the LDOS map simulations are indicated by red arrows.

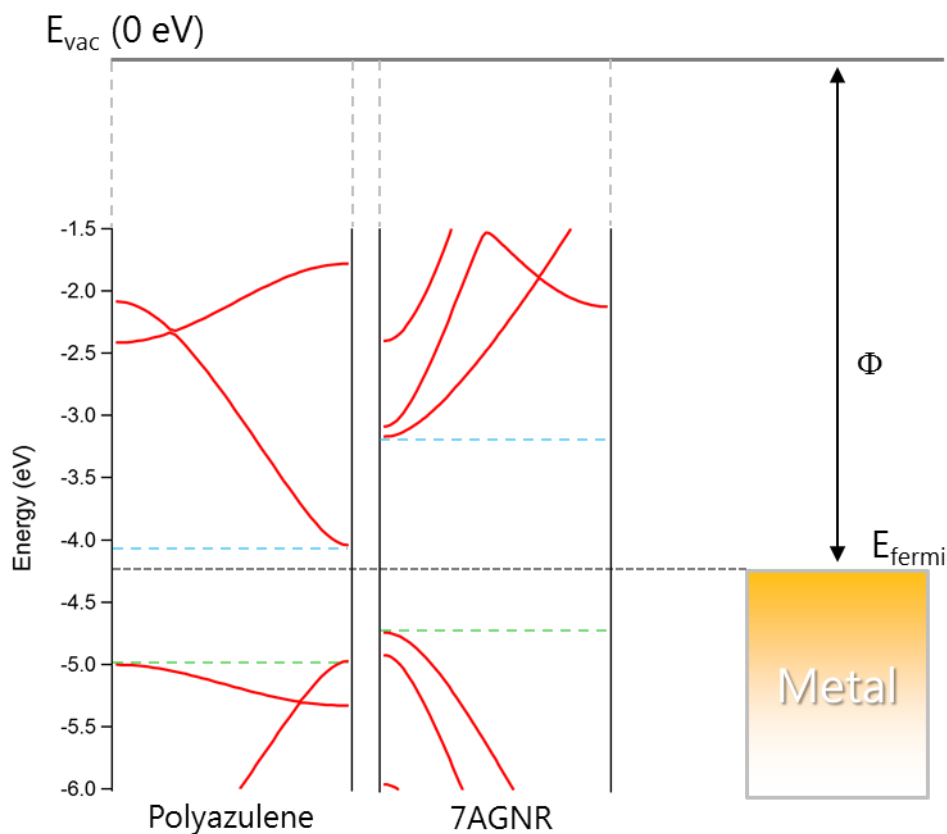


Figure S5. A schematic illustration of the energy level alignment of polyazulene, 7AGNR and the metal substrate. The band structures of polyazulene and 7AGNR are shown with energies taken with respect to the vacuum level. We use blue(green) dashed lines to indicate the onsets of their VB(CB). A metal surface is schematically shown on the right, whose Fermi level position is determined by the work function ϕ and an arbitrary value is chosen here.

4.4 References

- (1) Klein, B. P.; van der Heijden, N. J.; Kachel, S. R.; Franke, M.; Krug, C. K.; Greulich, K. K.; Ruppenthal, L.; Müller, P.; Rosenow, P.; Parhizkar, S.; et al. Molecular Topology and the Surface Chemical Bond: Alternant Versus Nonalternant Aromatic Systems as Functional Structural Elements. *Phys. Rev. X* **2019**, *9* (1), 011030.
- (2) Mishra, S.; Lohr, T. G.; Pignedoli, C. A.; Liu, J.; Berger, R.; Urgel, J. I.; Müllen, K.; Feng, X.; Ruffieux, P.; Fasel, R. Tailoring Bond Topologies in Open-Shell Graphene Nanostructures. *ACS Nano* **2018**, *12* (12), 11917–11927.
- (3) Sidman, J. W.; McClure, D. S. Electronic and Vibrational States of Azulene. *J. Chem. Phys.* **1956**, *24* (4), 757–763.
- (4) Michl, J.; Thulstrup, E. W. Why Is Azulene Blue and Anthracene White? A Simple Mo Picture. *Tetrahedron* **1976**, *32* (2), 205–209.
- (5) Anderson, A. G.; Steckler, B. M. Azulene. VIII. A Study of the Visible Absorption Spectra and Dipole Moments of Some 1- and 1,3-Substituted Azulenes 1,2. *J. Am. Chem. Soc.* **1959**, *81* (18), 4941–4946.
- (6) Zhou, Y.; Baryshnikov, G.; Li, X.; Zhu, M.; Ågren, H.; Zhu, L. Anti-Kasha's Rule Emissive Switching Induced by Intermolecular H-Bonding. *Chem. Mater.* **2018**, *30* (21), 8008–8016.
- (7) Tétrault, N.; Muthyala, R. S.; Liu, R. S. H.; Steer, R. P. Control of the Photophysical Properties of Polyatomic Molecules by Substitution and Solvation: The Second Excited Singlet State of Azulene. *J. Phys. Chem. A* **1999**, *103* (15), 2524–2531.
- (8) Mitchell, D. R.; Gillispie, G. D. The S₂ → S₁ Absorbance Spectrum of Azulene Determined by Two-Color Two-Photon Fluorescence Excitation. *J. Phys. Chem.* **1989**, *93* (11), 4390–4393.
- (9) Murai, M.; Amir, E.; Amir, R. J.; Hawker, C. J. Azulene-Based Conjugated Polymers: Unique Seven-Membered Ring Connectivity Leading to Stimuli-Responsiveness. *Chem. Sci.* **2012**, *3* (9), 2721.
- (10) Yamaguchi, Y.; Ogawa, K.; Nakayama, K.; Ohba, Y.; Katagiri, H. Terazulene: A High-Performance n-Type Organic Field-Effect Transistor Based on Molecular Orbital Distribution Control. *J. Am. Chem. Soc.* **2013**, *135* (51), 19095–19098.
- (11) Xin, H.; Ge, C.; Jiao, X.; Yang, X.; Rundel, K.; McNeill, C. R.; Gao, X. Incorporation of 2,6-Connected Azulene Units into the Backbone of Conjugated Polymers: Towards High-Performance Organic Optoelectronic Materials. *Angew. Chemie* **2018**, *130* (5), 1336–1340.
- (12) Nishimura, H.; Ishida, N.; Shimazaki, A.; Wakamiya, A.; Saeki, A.; Scott, L. T.; Murata, Y. Hole-Transporting Materials with a Two-Dimensionally Expanded π -System around an Azulene Core for Efficient Perovskite Solar Cells. *J. Am. Chem. Soc.* **2015**, *137* (50), 15656–15659.
- (13) Dong, J.-X.; Zhang, H.-L. Azulene-Based Organic Functional Molecules for Optoelectronics. *Chinese Chem. Lett.* **2016**, *27* (8), 1097–1104.
- (14) Xin, H.; Gao, X. Application of Azulene in Constructing Organic Optoelectronic Materials: New Tricks for an Old Dog. *ChemPlusChem* **2017**, *82* (7), 945–956.
- (15) Amir, E.; Murai, M.; Amir, R. J.; Cowart, J. S.; Chabinyo, M. L.; Hawker, C. J. Conjugated Oligomers Incorporating Azulene Building Blocks – Seven- vs. Five-Membered Ring Connectivity. *Chem. Sci.* **2014**, *5* (11), 4483–4489.
- (16) Yamaguchi, Y.; Takubo, M.; Ogawa, K.; Nakayama, K.; Koganezawa, T.; Katagiri, H. Terazulene Isomers: Polarity Change of OFETs through Molecular Orbital Distribution Contrast. *J. Am. Chem. Soc.* **2016**, *138* (35), 11335–11343.
- (17) Nöll, G.; Lambert, C.; Lynch, M.; Porsch, M.; Daub, J. Electronic Structure and Properties of Poly- and Oligoazulenes. *J. Phys. Chem. C* **2008**, *112* (6), 2156–2164.
- (18) Steer, R. P. Photophysics of Molecules Containing Multiples of the Azulene Carbon Framework. *J. Photochem. Photobiol. C* **2019**, *40*, 68–80.
- (19) Hou, I. C.-Y.; Shetti, V.; Huang, S.-L.; Liu, K.-L.; Chao, C.-Y.; Lin, S.-C.; Lin, Y.-J.; Chen, L.-Y.; Luh, T.-Y. Poly[2(6)-Aminoazulene]: Synthesis, Photophysical Properties, and Proton Conductivity. *Org. Chem. Front.* **2017**, *4* (5), 773–778.
- (20) Björk, J.; Hanke, F. Towards Design Rules for Covalent Nanostructures on Metal Surfaces. *Chem. - A Eur. J.* **2014**, *20* (4), 928–934.
- (21) Held, P. A.; Fuchs, H.; Studer, A. Covalent-Bond Formation via On-Surface Chemistry. *Chem. - A Eur. J.* **2017**, *23* (25), 5874–5892.
- (22) Sun, Q.; Zhang, R.; Qiu, J.; Liu, R.; Xu, W. On-Surface Synthesis of Carbon Nanostructures. *Adv. Mater.* **2018**, *30* (17), 1705630.

- (23) Fan, Q.; Martin-Jimenez, D.; Ebeling, D.; Krug, C. K.; Brechmann, L.; Kohlmeyer, C.; Hilt, G.; Hieringer, W.; Schirmeisen, A.; Gottfried, J. M. Nanoribbons with Nonalternant Topology from Fusion of Polyazulene: Carbon Allotropes beyond Graphene. *J. Am. Chem. Soc.* **2019**, *141* (44), 17713–17720.
- (24) Narita, M.; Murafuji, T.; Yamashita, S.; Fujinaga, M.; Hiyama, K.; Oka, Y.; Tani, F.; Kamijo, S.; Ishiguro, K. Synthesis of 2-Iodoazulenes by the Iododeboronation of Azulene-2-Ylboronic Acid Pinacol Esters with Copper(I) Iodide. *J. Org. Chem.* **2018**, *83* (3), 1298–1303.
- (25) Di Giovannantonio, M.; Deniz, O.; Urgel, J. I.; Widmer, R.; Dienel, T.; Stolz, S.; Sánchez-Sánchez, C.; Muntwiler, M.; Dumschlaff, T.; Berger, R.; et al. On-Surface Growth Dynamics of Graphene Nanoribbons: The Role of Halogen Functionalization. *ACS Nano* **2018**, *12* (1), 74–81.
- (26) Urgel, J. I.; Hayashi, H.; Di Giovannantonio, M.; Pignedoli, C. A.; Mishra, S.; Deniz, O.; Yamashita, M.; Dienel, T.; Ruffieux, P.; Yamada, H.; et al. On-Surface Synthesis of Heptacene Organometallic Complexes. *J. Am. Chem. Soc.* **2017**, *139* (34), 11658–11661.
- (27) Sun, Q.; Cai, L.; Ma, H.; Yuan, C.; Xu, W. Dehalogenative Homocoupling of Terminal Alkynyl Bromides on Au(111): Incorporation of Acetylenic Scaffolding into Surface Nanostructures. *ACS Nano* **2016**, *10* (7), 7023–7030.
- (28) Zhang, H.; Lin, H.; Sun, K.; Chen, L.; Zagranski, Y.; Aghdassi, N.; Duhm, S.; Li, Q.; Zhong, D.; Li, Y.; et al. On-Surface Synthesis of Rylene-Type Graphene Nanoribbons. *J. Am. Chem. Soc.* **2015**, *137* (12), 4022–4025.
- (29) Gross, L.; Mohn, F.; Moll, N.; Liljeroth, P.; Meyer, G. The Chemical Structure of a Molecule Resolved by Atomic Force Microscopy. *Science* **2009**, *325* (5944), 1110–1114.
- (30) Kunkel, D. A.; Hooper, J.; Simpson, S.; Miller, D. P.; Routaboul, L.; Braunstein, P.; Doudin, B.; Beniwal, S.; Dowben, P.; Skomski, R.; et al. Self-Assembly of Strongly Dipolar Molecules on Metal Surfaces. *J. Chem. Phys.* **2015**, *142* (10), 101921.
- (31) Ruffieux, P.; Cai, J.; Plumb, N. C.; Patthey, L.; Prezzi, D.; Ferretti, A.; Molinari, E.; Feng, X.; Müllen, K.; Pignedoli, C. A.; et al. Electronic Structure of Atomically Precise Graphene Nanoribbons. *ACS Nano* **2012**, *6* (8), 6930–6935.
- (32) Lejaeghere, K.; Bihlmayer, G.; Bjorkman, T.; Blaha, P.; Blugel, S.; Blum, V.; Caliste, D.; Castelli, I. E.; Clark, S. J.; Dal Corso, A.; et al. Reproducibility in Density Functional Theory Calculations of Solids. *Science* **2016**, *351* (6280), aad3000–aad3000.
- (33) Pizzi, G.; Cepellotti, A.; Sabatini, R.; Marzari, N.; Kozinsky, B. AiiDA: Automated Interactive Infrastructure and Database for Computational Science. *Comput. Mater. Sci.* **2016**, *111*, 218–230.
- (34) Hutter, J.; Iannuzzi, M.; Schiffmann, F.; Vandevondele, J. Cp2k: Atomistic Simulations of Condensed Matter Systems. *Wiley Interdiscip. Rev. Comput. Mol. Sci.* **2014**, *4* (1), 15–25.
- (35) Vandevondele, J.; Krack, M.; Mohamed, F.; Parrinello, M.; Chassaing, T.; Hutter, J. Quickstep: Fast and Accurate Density Functional Calculations Using a Mixed Gaussian and Plane Waves Approach. *Comput. Phys. Commun.* **2005**, *167* (2), 103–128.
- (36) Goedecker, S.; Teter, M.; Hutter, J. Separable Dual-Space Gaussian Pseudopotentials. *Phys. Rev. B* **1996**, *54* (3), 1703–1710.
- (37) Perdew, J. P.; Burke, K.; Ernzerhof, M. Generalized Gradient Approximation Made Simple. *Phys. Rev. Lett.* **1996**, *77* (18), 3865–3868.
- (38) Grimme, S.; Antony, J.; Ehrlich, S.; Krieg, H. A Consistent and Accurate Ab Initio Parametrization of Density Functional Dispersion Correction (DFT-D) for the 94 Elements H–Pu. *J. Chem. Phys.* **2010**, *132* (15), 154104.

Chapter 5. On-Surface Synthesis of sp^2 -Carbon-Nanostructure with a Skeleton of Regularly Fused alternating Pentagons and Heptagons

Ian Cheng-Yi Hou^{1†}, ^{2†}, ², ^{1,3,*}, ^{2,4,*}, ^{1,5,*}

¹Max Planck Institute for Polymer Research, 55128 Mainz, Germany

²Empa, Swiss Federal Laboratories for Materials Science and Technology, 8600 Dübendorf, Switzerland

³Organic and Carbon Nanomaterials Unit, Okinawa Institute of Science and Technology Graduate University, 1919-1 Tancha, Onna-son, Kunigami, Okinawa 904-0495, Japan

⁴Department of Chemistry and Biochemistry, University of Bern, 3012 Bern, Switzerland

⁵Institute of Physical Chemistry, Johannes Gutenberg-University Mainz, Duesbergweg 10-14, D-55128 Mainz, Germany

†These authors contributed equally to this work

Published in: Unpublished manuscript.

Contribution: Organic synthesis and characterization. Prepare the first draft.

5.1 Main text

sp^2 -carbon-materials are attracting attention for their great potential in mechanical, sensing, optic, spintronic, and electronic applications.¹⁻³ They are normally graphene-based with fused hexagons as their skeletons. Nevertheless, arrays of fused pentagon-heptagon-pairs, namely azulenes, are widely observed, especially at graphene grain boundaries (Figure 1a,b).⁴⁻⁹ It has been suggested that their nanostructures fundamentally influence intrinsic properties of graphene-based materials.^{8,10-14} However, although synthetic methods have been developed for various nanostructures containing two fused pentagon-heptagon-pairs,¹⁵⁻²² constructing sp^2 -carbon-nanostructures with multiple fused pentagon-heptagon-pairs is challenging.

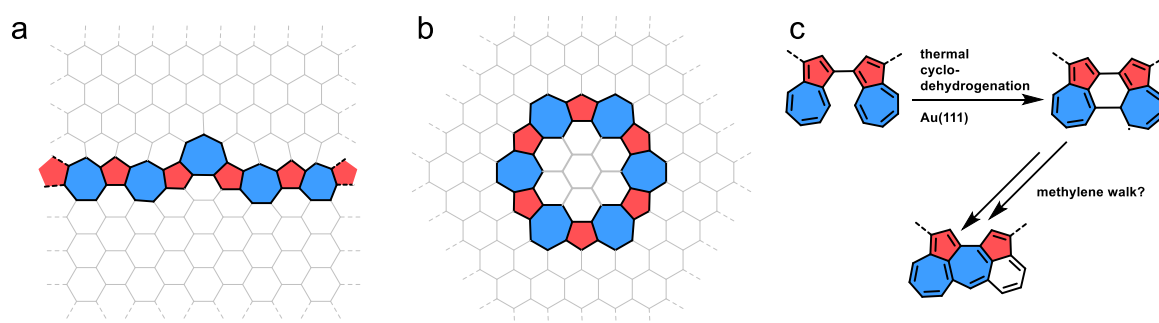
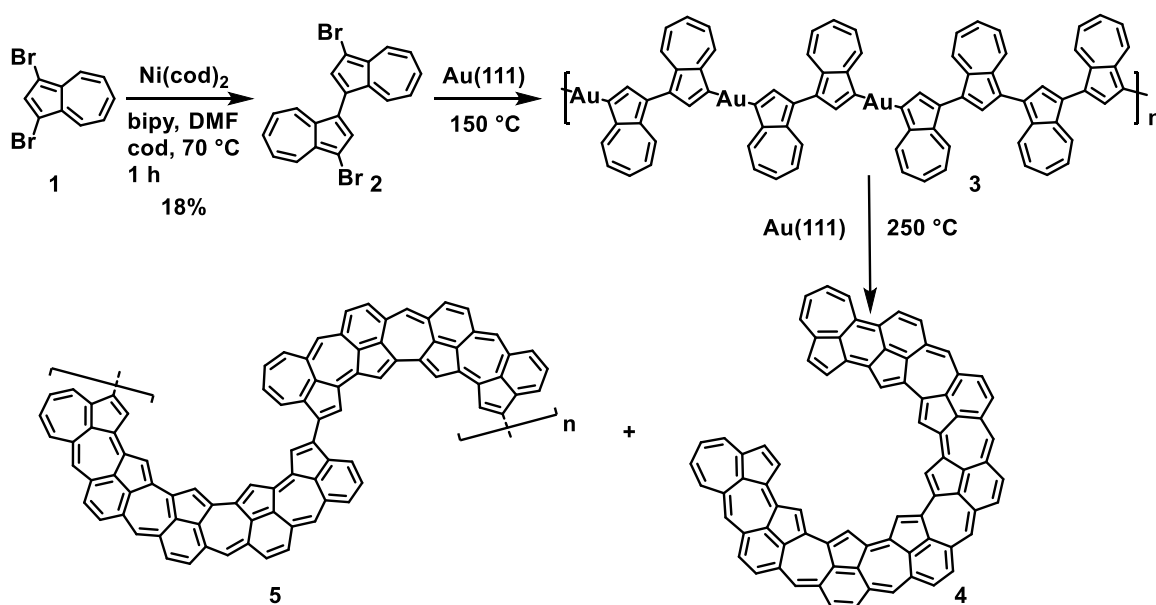


Figure 1. Schematic representation of fused azulene array at (a) grain boundary⁷ and (b) grain boundary loop⁴ in graphene, and (c) a possible method proposed in this work for construction of array of fused azulenes by on-surface reactions.

On-surface synthesis has recently achieved great success in fabrication of novel sp^2 -carbon-nanostructures.^{23–27} This method is conducted by sublimation of molecular precursors under ultra-high vacuum (UHV) on monocrystalline metal surfaces, followed by surface-assisted reactions at an elevated temperature.²³ Especially, surface-assisted cyclodehydrogenations can convert partially planarized polycyclic aromatic hydrocarbons (PAH) into larger π -systems. Such reaction often proceeds between hexagons of PAHs through formation of radical-adduct intermediates.²⁸ Importantly, it is known that radical-adducts of azulene could undergo skeletal rearrangement at elevated temperature.^{29,30} However, although cyclodehydrogenation of PAHs on surface could lead to formation of azulene skeleton,^{31,32} and on-surface reactions of azulene derivatives have been studied,^{33–36} surface-assisted cyclodehydrogenation between azulenes remains unexplored. We envisage that intramolecular cyclodehydrogenation of oligoazulenes can convert the isolated hexagon-pentagon-pairs into a nanostructure of fused pentagons and heptagons via skeletal rearrangements (Figure 1c). To this end, we polymerized 1,1'-dibromo-3,3'-biazulene (**2**) on Au(111) surface via dehalogenation coupling, and triggered surface-assisted cyclodehydrogenation of the polymeric product by heating until 250 °C. Cyclodehydrogenated product with rearranged azulene skeleton was unambiguously characterized by high-resolution scanning tunneling microscopy (STM) and non-contact atomic force microscopy (nc-AFM). For the first time, sp^2 -carbon-nanostructures were synthesized with a skeleton of regularly fused pentagon-heptagon-pairs.



*Scheme 1. Synthesis of **2** in solution and its polymerization and graphitization on Au(111) surface.*

Biazulene **2** was synthesized under a similar Yamamoto reaction condition used for polymerization of 1,3-dibromoazulene (**1**)³⁷, while controlling stoichiometry of Ni(cod)₂ reagent to suppress formation of oligomers.³⁸ Biazulene **2** was isolated as the major product with a plausible 18% yield, and a 25% recovery of **1** (Scheme 1).

Biazulene **2** was deposited on Au(111) held at a room temperature. The molecules self-assembled into different aggregates stabilized by Br-Br halogen bonding (see supporting information for further description).³⁹ In a next step, we annealed the sample at 150 °C to initiate a debromination and a subsequent polymerization of **2** into organometallic polymer **3** (Scheme 1). In the STM images of **3** (Figure 2a), chain structures are indeed formed. From a close-up image (Figure 2b), single 1,3-biazulenylene units can be resolved, and the bright protrusions are assigned as heptagons of azulenes.

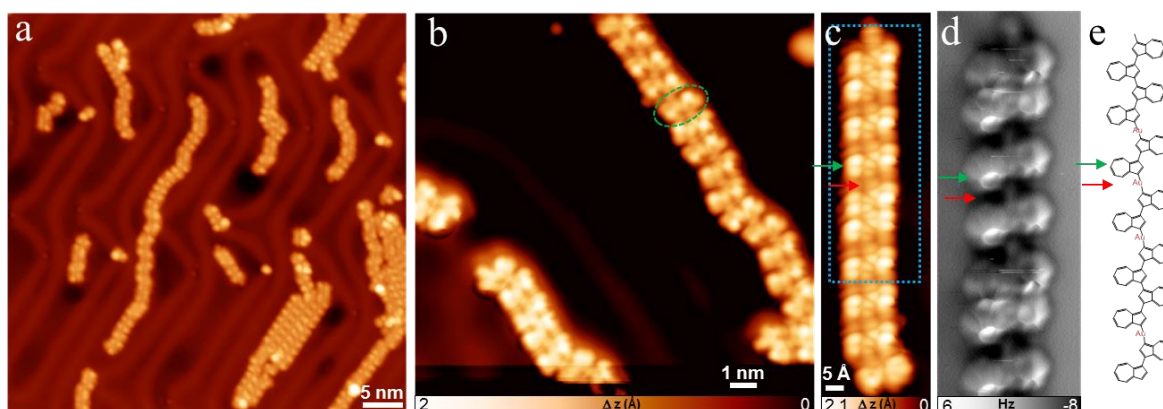
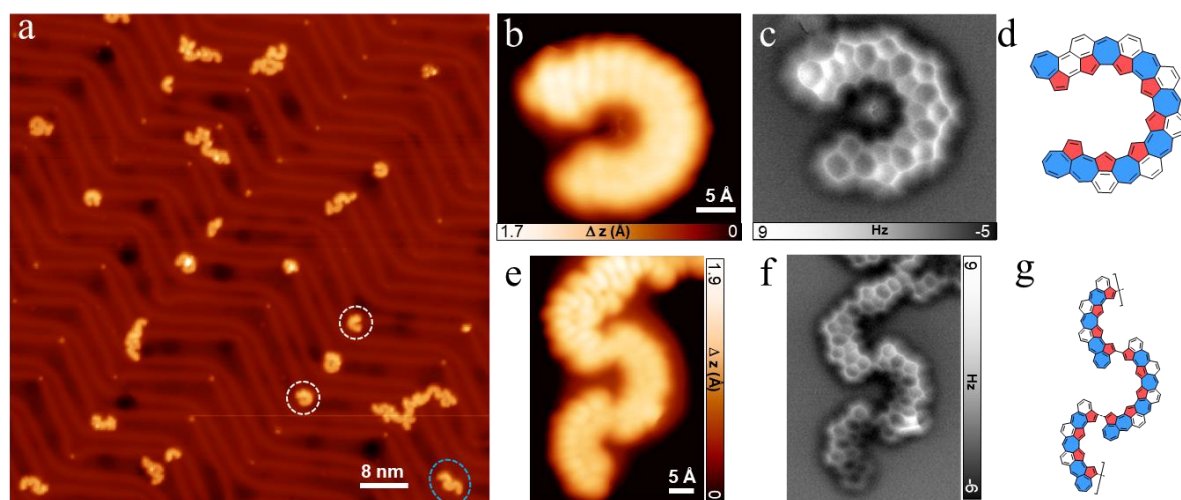


Figure 2. (a) A large-scale STM image after annealing the sample to 150 °C. ($V_s = -1.5$ V, $I_t = 0.07$ nA). (b) A close-up STM image of the organometallic chain structure ($V_s = -0.1$ V, $I_t = 0.11$ nA). A biazulenylene within the organometallic chain is indicated by the green ellipse. (c) The high-resolution STM image of the organometallic chain imaged by a CO-functionalized tip ($V_s = -0.05$ V, $I_t = 0.1$ nA). (d) The bond-resolved nc-AFM image of the region marked by a dashed rectangle in (c) ($V_s = -5$ mV, oscillation amplitude: ~ 80 pm). (e) The corresponding chemical structure of the chain in (d).

To further identify the chemical structure of **3**, we resorted to nc-AFM imaging. A non-planar structure of **3** is clearly illustrated (Figure 1d), since the nc-AFM only resolves the heptagons of 1,3-biazulenylenes due to a distorted geometry of the chain. However, by comparing the STM and nc-AFM images with the chemical structure of 1,3-biazulenylene, we can reasonably assign the 1,3-biazulenylenes in the chain which are indicated by green arrows in Figure 2c–e. Most of the 1,3-biazulenylenes display a distance around 1 nm between each other, which is much larger than a single C-C bond. Thus, we assume the presence of a C-Au-C organometallic linkage. Formation of C-Au-C bonds after debromination of molecules are

often observed on the more reactive Copper surfaces^{40,41} or between terminal alkynyl bromides⁴². However, the C-Au-C bonds could also be formed when the steric hindrance between the debrominated species hampers the direct C-C bond formation.⁴³ In this work, the direct C-C bond formation between two biazulenylene units also faces a substantial steric hindrance, which would favor the formation of the C-Au-C organometallic bonds. This also reflects in the observation of protrusions of Au atoms in the STM image (indicated by a red arrow in Fig. 2c). Despite a majority of C-Au-C linkage in **3**, interestingly, there also exists some higher 1,3-oligoazulenylenes in the polymer chain, as a result of C-C bond formation between 1,3-biazulenylenes (Figure 2c–e).



*Figure 3. (a) A large-scale STM image after further annealing **3** to 250 °C. ($V_s = -1$ V, $I_t = 0.1$ nA). (b) A close-up STM image of a small segment ($V_s = -0.02$ V, $I_t = 0.1$ nA) and its corresponding (c) bond-resolved nc-AFM image ($V_s = -5$ mV, oscillation amplitude: ~ 80 pm) and (d) chemical structure with numbers indicating ring size. (e) A close-up STM image of a large object ($V_s = -0.02$ V, $I_t = 0.1$ nA) and its corresponding (f) bond-resolved nc-AFM image ($V_s = -5$ mV, oscillation amplitude: ~ 80 pm) and (g) an illustrative chemical structure. White and blue circles in (a) corresponds to structures in (b,c) and (e,f), respectively.*

After confirming the formation of **3** on surface, we annealed the sample to 250 °C. In the STM images of the resulted materials (Figure 3a,b,e), curved nanostructures that are distinctly different from those in Figure 2 are observed. In an nc-AFM image of a short segment with 23 polygons, a skeleton of multiple fused pentagon-heptagon-pairs is clearly identified (Figure 3c,d). This nanostructure is likely a product of 1,3-octaazulene, which is formed by extrusion of all Au atoms in **3** (Scheme S1 and Figure 2c–e). Importantly, a simple cyclodehydrogenation of 1,3-oligoazulene shall lead to oligo(*peri*-azulene) (Scheme S1),

while formation of the structure shown in Figure 3c must involve rearrangement of the azulene skeleton. Interestingly, except the end-groups, all the pentagons are in the inner ring, while hexagons stay in the outer ring, and heptagons in the middle (Figure 3c,d). Such arrangement suggests a chain-reaction mechanism (*vide infra*). Besides, shorter segments of cyclodehydrogenated 1,3-hexaazulene was also detected with the same structural feature (Figure S2). Unfortunately, no nanoring (Figure S3), which could be the possible cyclodehydrogenated product of 1,3-decaazulene, was observed. However, there existed several nanostructures of longer segments that stemmed from polymeric precursors (Figure 3a). In an enlarged image of one of these structures, it is revealed as cyclodehydrogenated products of oligoazulenyls linked by C-C single bonds (Figure 3e-g). Notably, a complete cyclodehydrogenation of poly(1,3-azulenyl)s shall lead to helical architectures and structural overlap that are not favored on surface. Thus, planarization into oligomer of short fragments occurred. Nevertheless, the nanostructure still represents the feature of a regularly rearranged skeleton (Figure 3f,g).

The ordered rearrangement can be explained by “methylene-walk” of radical adduct of azulenes.^{29,30} Although previous studies showed that azulene in a polymer chain hardly rearranges on surface below 400 °C,³³⁻³⁵ radical-adduct of azulene can have a much lower reaction barrier for rearrangements. First, we assume that surface-assisted C-H bond cleavage occurred at azulenyl end-groups since they have higher degree of freedom, which facilitates interactions with Au surface (Scheme S1). Then, the formed radical species attacked on the neighboring azulenyls, which triggered a chain-reaction through repetitive steps of cyclopropylcarbinyl-homoallyl-rearrangement/1,2-hydrogen-shift/inter-azulene-radical-attack (Scheme S1), and eventually led to the structure what we observed. Detailed mechanistic study is progressing in our group.

In conclusion, to study surface-assisted cyclodehydrogenation between heptagons of PAHs, we synthesized 1,3-biazulenyl-Au organometallic polymers on Au(111) from 1,1'-dibromo-3,3'-biazulene. After annealing at 250 °C, novel sp²-carbon-nanostructures were identified with skeletons of multiple regularly fused pentagon-heptagon-pairs. Formation of such nanostructures involved rearrangement of azulene skeletons in a controlled manner. The results demonstrate the great potential using azulene as precursor for on-surface synthesis of unconventional sp²-carbon-nanostructures. This shall benefit the understanding of defects in graphene-related materials⁹ as well as development of novel sp²-carbon-2D/3D materials^{44,45}.

5.2 Supporting information

General Information

Unless otherwise noted, materials were purchased from Fluka, Aldrich, Acros, abcr, Merck, and other commercial suppliers, and were used as received unless otherwise specified. 1,3-Dibromoazulene (**1**) was synthesized following ref³⁷. All reactions working with air- or moisture-sensitive compounds were carried out under argon atmosphere using standard Schlenk line techniques. Preparative column chromatography was performed on silica gel from Merck with a grain size of 0.04–0.063 mm (flash silica gel, Geduran Si 60). NMR spectra were recorded in deuterated solvents using Bruker AVANCE III 300 spectrometers. Chemical shifts (δ) were expressed in ppm relative to the residual of solvent (CD₂Cl₂ @ 5.32 ppm for ¹H NMR, 53.84 ppm for ¹³C NMR). Coupling constants (J) were recorded in Hertz (Hz) with multiplicities explained by the following abbreviations: s = singlet, d = doublet, t = triplet, q = quartet, dd = doublet of doublets, dt = doublet of triplets, m = multiplet, br = broad. The ¹³C NMR spectrum was recorded with spin-echo attached-proton test sequence with CH, CH₃ showing negative signal and C, CH₂ showing positive signal. High-resolution mass spectra (HRMS) were recorded by matrix-assisted laser decomposition/ionization (MALDI) using *trans*-2-[3-(4-tert-Butylphenyl)-2-methyl-2-propenylidene]malononitrile (DCTB) as matrix with a Bruker Reflex II-TOF spectrometer (MALDI-TOF HRMS).

Synthetic procedure of 1,1'-dibromo-3,3'-biazulene (**2**)

To a schlenk tube containing 1,3-dibromoazulene³⁷ (792 mg, 2.77 mmol) was added bis(1,5-cyclooctadiene)nickel (457 mg, 1.66 mmol), 1,5-cyclooctadiene (180 mg, 1.66 mmol), 4,4'-bipyridine (290 mg, 1.85 mmol) and dimethylformaldehyde (20 mL) in a glove box. The color of the mixture immediately turned into dark purple. The mixture was then heated at 70 °C under vigorous stirring for 1h. After reaching a room temperature, diethyl ether (200 mL) was added and the solution was washed with water, 1M HCl (aq.), brine and dried over Mg₂SO₄. Solvent was then removed *in vacuo* and the residue was purified by silica gel column chromatography (DCM/hexane = 1/20). First band from the column was unreacted 1,3-dibromoazulene (220 mg, 25%) and the second was **2** (201 mg, 18%) and the rest was higher 1,3-oligoazulenes (170 mg). **2** was collected as a green powder and recrystallized seven times (hexane) before next step: ¹H NMR (300 MHz, CD₂Cl₂): δ 8.40 (d, J = 9.7 Hz, 2H), 8.27 (d, J = 9.7 Hz, 2H), 8.01 (s, 2H), 7.66 (t, J = 9.9 Hz, 2H), 7.27 (t, J = 9.8 Hz, 2H), 7.14 (t, J = 9.8 Hz, 2H); ¹³C NMR (75 MHz, CD₂Cl₂): δ 140.20, 138.99, 137.45, 137.05,

5.2 Supporting information

136.90, 136.63, 124.65, 124.51, 124.05, 104.25; HRMS (MALDI-TOF) m/z : $[M]^+$ calcd for $C_{20}H_{12}Br_2$ 409.9306; Found $[M]^+$ 409.9294.

STM/nc-AFM analysis

A commercial low-temperature STM/nc-AFM (Scienta Omicron) system was used for sample preparation and *in situ* characterization under ultra-high vacuum conditions (base pressure below 1×10^{-10} mbar). The Au(111) single crystal was cleaned by cycles of argon sputtering ($p = 6 \times 10^{-6}$ mbar) and annealing at 750 K for 15 minutes. Deposition of **2** on Au(111) was conducted by thermal evaporation from a six-fold organic evaporator (Mantis GmbH). STM images were recorded in constant-current mode, and the dI/dV spectra were recorded using the lock-in technique ($U_{RMS} = 20$ mV). nc-AFM images were recorded with a CO-functionalized tip attached to a quartz tuning fork sensor (resonance frequency 23.5 kHz, peak-to-peak oscillation amplitude below 100 pm).

Self-assembly of **2** on Au (III)

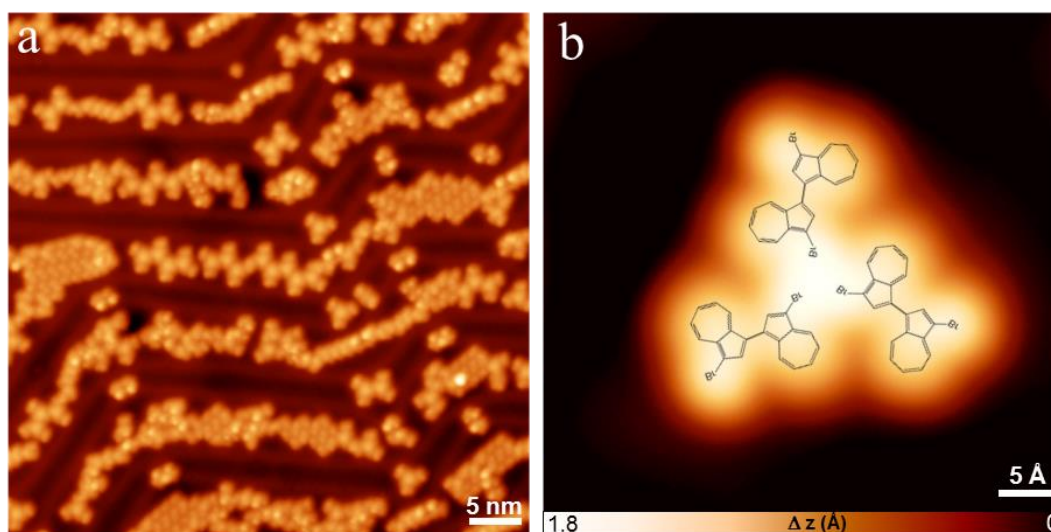


Figure S1. (a) A large-scale STM image after deposition of **2** on Au(111) at a room temperature ($V_s = -1.5$ V, $I_t = 0.06$ nA). (b) A high-resolution STM image of a typical self-assembled structure of **2** ($V_s = -0.02$ V, $I_t = 0.1$ nA). The corresponding chemical models of three **2** molecules are overlaid on the STM image.

Biazulenyl **2** was deposited on Au(111) held at a room temperature. The molecules tend to stay at the fcc regions between the herringbone reconstruction of the Au(111) and self-assembled into different aggregates, implying a weak intermolecular interaction (Figure S1a). Due to a nonplanar geometry of **2**, the heptagons exhibited higher contrast. In addition, the bromine atoms also show higher contrasts in the STM image. After overlapping the

corresponding chemical structures of **2** onto a high resolution STM image, it can be seen that the self-assembled structures are stabilized by Br-Br halogen bonding (Figure S1b).³⁹

Complementary figures and scheme

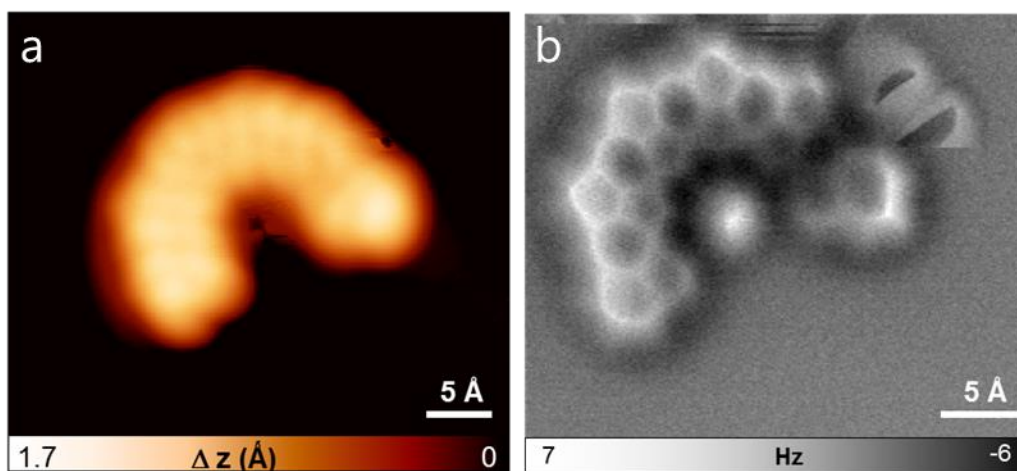


Figure S2. (a) A close-up STM image of a cyclodehydrogenated product of 1,3-hexaazulenylylene on Au(111) and (b) its corresponding bond-resolved nc-AFM image. Parameters: (a) $V_s = -0.02$ V, $I_t = 0.1$ nA; (b) $V_s = -5$ mV, oscillation amplitude ~ 80 pm.

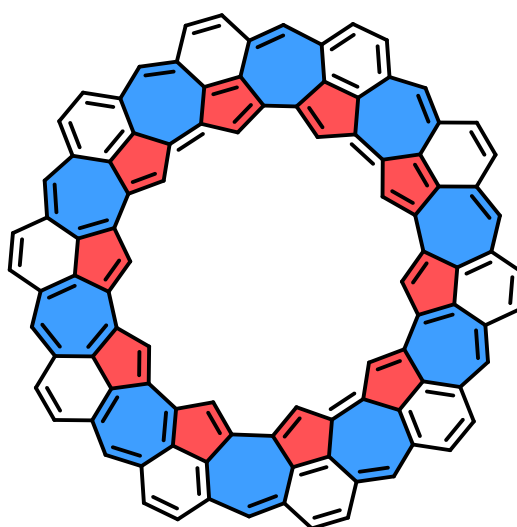
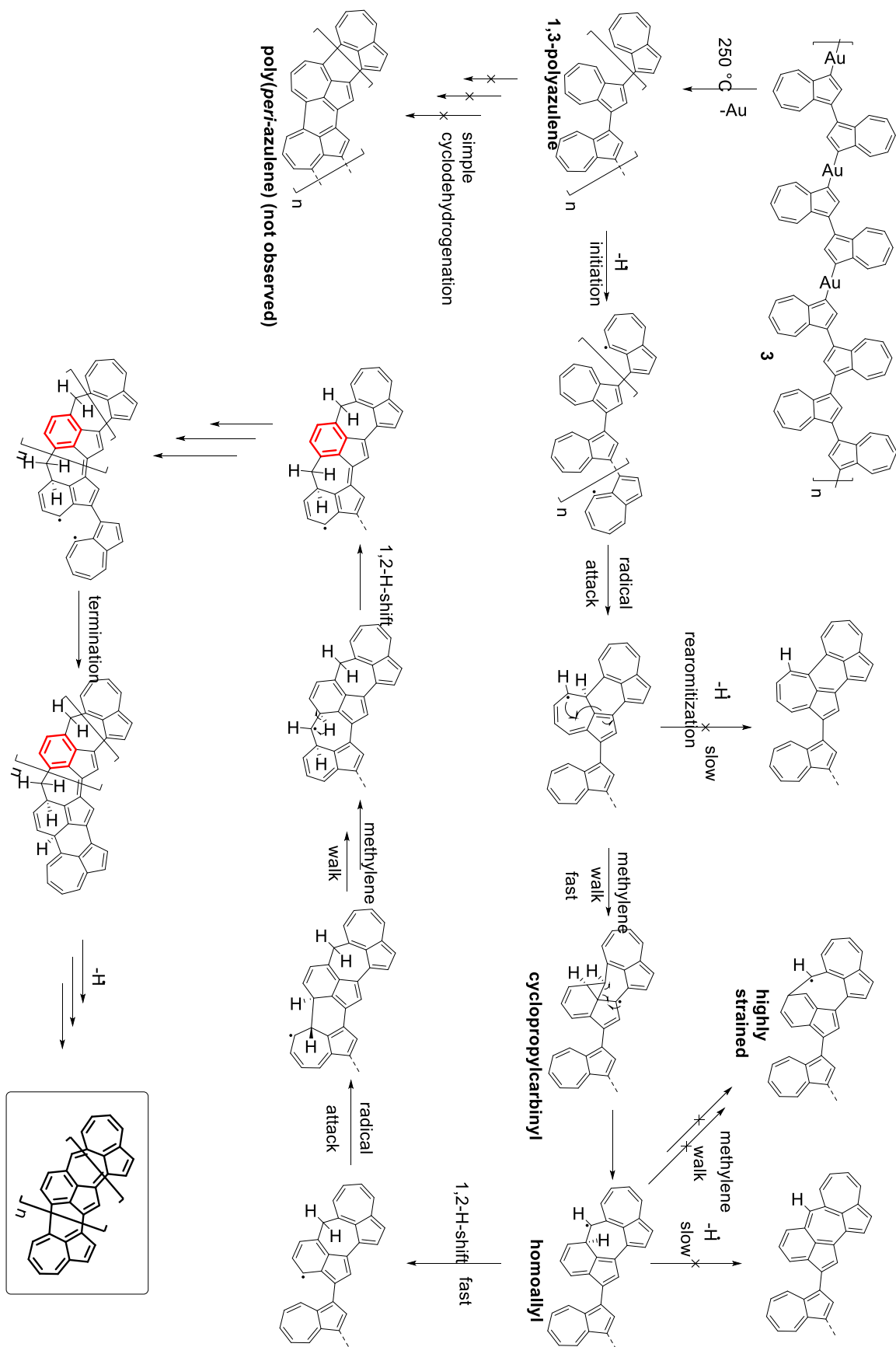


Figure S3. A nanoring structure (not observed) that could be formed from cyclodehydrogenation of 1,3-decaazulene.



Scheme S1. Proposed reaction mechanism from 1,3-azulenylen-Au polymer to the fused pentagon-heptagon-pairs.^{29,30}

Chapter 5. On-Surface Synthesis of Sp^2 -Carbon-Nanostructure
with a Skeleton of Regularly Fused alternating Pentagons and Heptagons

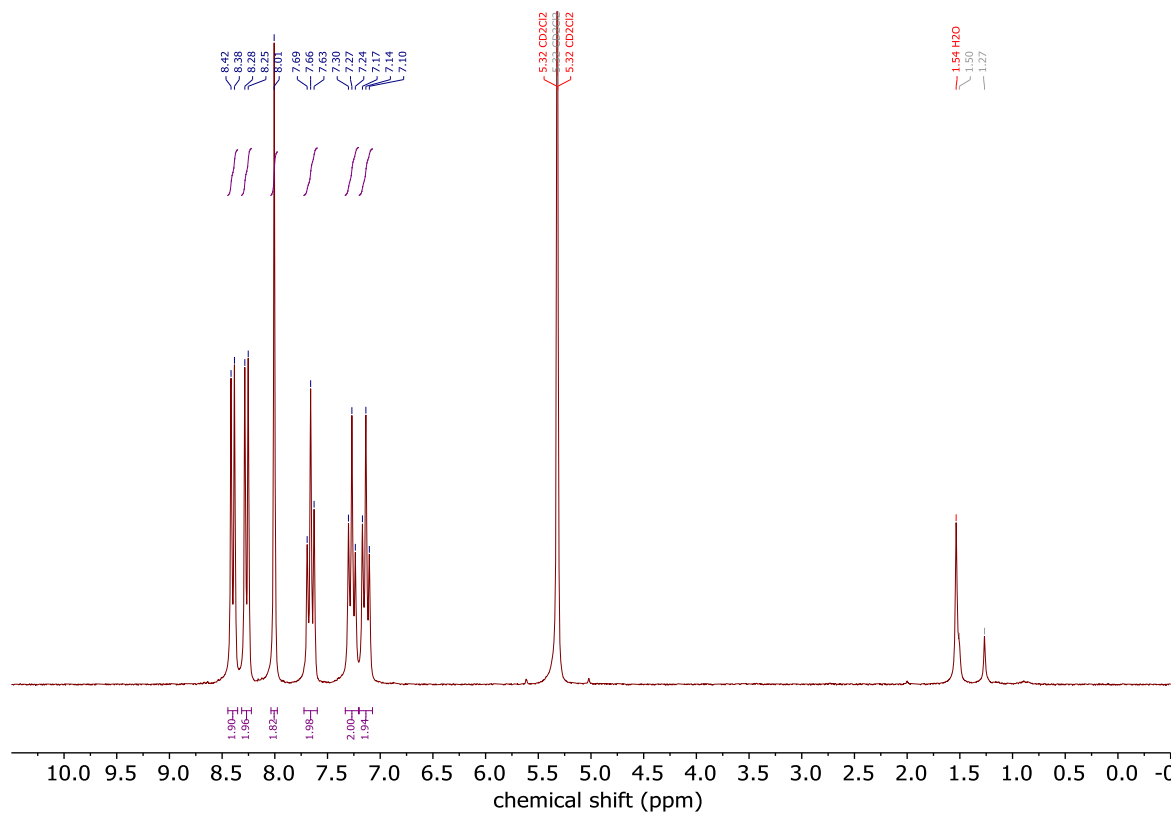


Figure S4. 1H NMR spectrum (300 MHz) of **2** in CD_2Cl_2 .

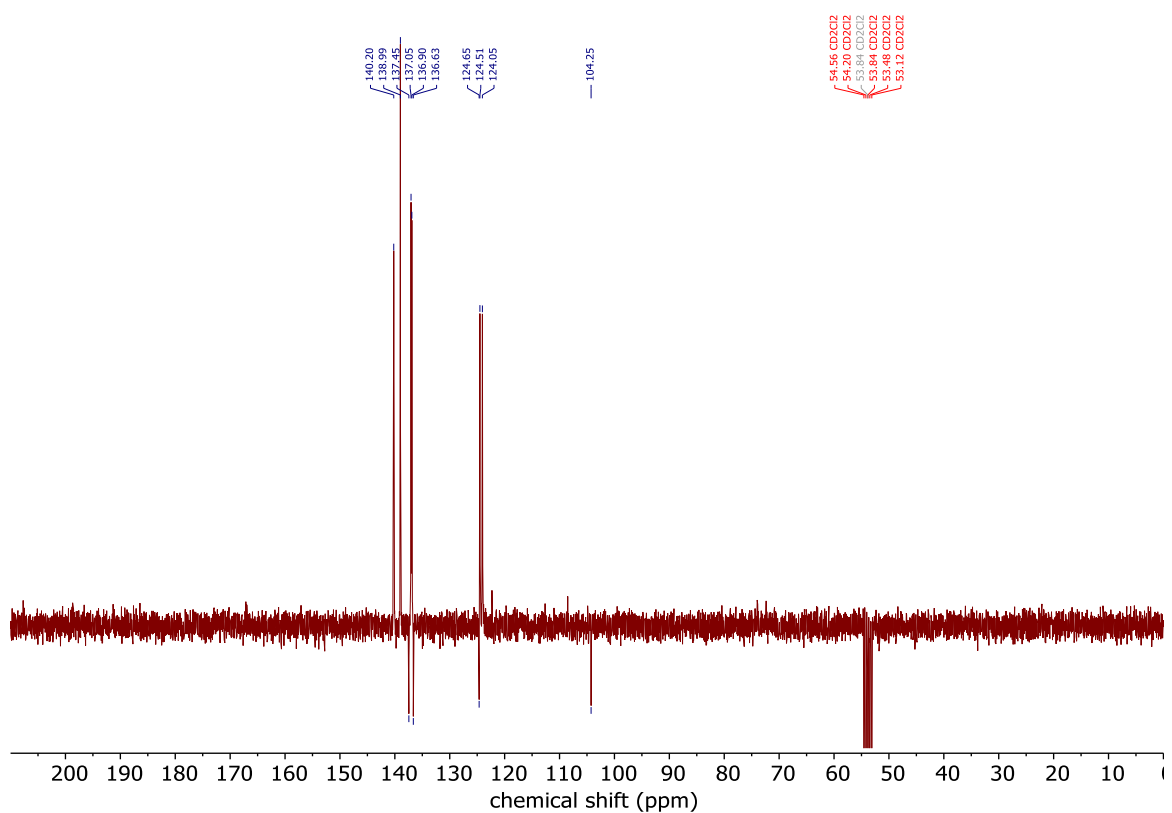


Figure S5. Spin-echo ^{13}C NMR (75 MHz) spectrum of **2** in CD_2Cl_2 .

5.3 References

- (1) Fukuzumi, S. *Chemical Science of π -Electron Systems*; Akasaka, T., Osuka, A., Fukuzumi, S., Kandori, H., Aso, Y., Eds.; Springer Japan: Tokyo, 2015.
- (2) Matsumoto, K. *Frontiers of Graphene and Carbon Nanotubes: Devices and Applications*; Matsumoto, K., Ed.; Springer Japan: Tokyo, 2015.
- (3) Müllen, K.; Feng, X. *From Polyphenylenes to Nanographenes and Graphene Nanoribbons*; Müllen, K., Feng, X., Eds.; Advances in Polymer Science; Springer International Publishing: Cham, 2017.
- (4) Cockayne, E.; Rutter, G. M.; Guisinger, N. P.; Crain, J. N.; First, P. N.; Stroschio, J. A. Grain Boundary Loops in Graphene. *Phys. Rev. B* **2011**, *83* (19), 195425.
- (5) Huang, P. Y.; Ruiz-Vargas, C. S.; Van Der Zande, A. M.; Whitney, W. S.; Levendorf, M. P.; Kevek, J. W.; Garg, S.; Alden, J. S.; Hustedt, C. J.; Zhu, Y.; et al. Grains and Grain Boundaries in Single-Layer Graphene Atomic Patchwork Quilts. *Nature* **2011**, *469* (7330), 389–392.
- (6) Rasool, H. I.; Ophus, C.; Klug, W. S.; Zettl, A.; Gimzewski, J. K. Measurement of the Intrinsic Strength of Crystalline and Polycrystalline Graphene. *Nat. Commun.* **2013**, *4* (1), 2811.
- (7) Yazyev, O. V.; Chen, Y. P. Polycrystalline Graphene and Other Two-Dimensional Materials. *Nat. Nanotechnol.* **2014**, *9* (10), 755–767.
- (8) Balasubramanian, K.; Biswas, T.; Ghosh, P.; Suran, S.; Mishra, A.; Mishra, R.; Sachan, R.; Jain, M.; Varma, M.; Pratap, R.; et al. Reversible Defect Engineering in Graphene Grain Boundaries. *Nat. Commun.* **2019**, *10* (1), 1090.
- (9) Banhart, F.; Kotakoski, J.; Krasheninnikov, A. V. Structural Defects in Graphene. *ACS Nano* **2011**, *5* (1), 26–41.
- (10) Ma, T.; Liu, Z.; Wen, J.; Gao, Y.; Ren, X.; Chen, H.; Jin, C.; Ma, X.-L.; Xu, N.; Cheng, H.-M.; et al. Tailoring the Thermal and Electrical Transport Properties of Graphene Films by Grain Size Engineering. *Nat. Commun.* **2017**, *8* (1), 14486.
- (11) Zhang, Z.; Yang, Y.; Xu, F.; Wang, L.; Yakobson, B. I. Unraveling the Sinuous Grain Boundaries in Graphene. *Adv. Funct. Mater.* **2015**, *25* (3), 367–373.
- (12) Serov, A. Y.; Ong, Z.-Y.; Pop, E. Effect of Grain Boundaries on Thermal Transport in Graphene. *Appl. Phys. Lett.* **2013**, *102* (3), 033104.
- (13) Chen, J.-H.; Autès, G.; Alem, N.; Gargiulo, F.; Gautam, A.; Linck, M.; Kisielowski, C.; Yazyev, O. V.; Louie, S. G.; Zettl, A. Controlled Growth of a Line Defect in Graphene and Implications for Gate-Tunable Valley Filtering. *Phys. Rev. B* **2014**, *89* (12), 121407.
- (14) Yazyev, O. V.; Louie, S. G. Electronic Transport in Polycrystalline Graphene. *Nat. Mater.* **2010**, *9* (10), 806–809.
- (15) Yoshida, Z. ichi; Shibata, M.; Ogino, E.; Sugimoto, T. A New Cata-Condensed Nonalternant Tetracyclic Hydrocarbon Azuleno[2,1-e]Azulene. *Tetrahedron Lett.* **1984**, *25* (31), 3343–3346.
- (16) Takayasu, T.; Nitta, M. On the Reaction of Azuleno-2-ylmethylene(Triphenyl)Phosphorane. Convenient Preparation of Azuleno[1,2-f]- and Azuleno[1,2-a]-Azulenes and Their Properties. *J. Chem. Soc., Perkin Trans. 1* **1997**, *23*, 3537–3542.
- (17) Anderson, A. G.; Montana, A. F.; MacDonald, A.; Masada, G. M. Synthesis of Dicyclopenta[ef,kl]Heptalene (Azupyrene). II. Routes from 1,6,7,8,9a-Hexahydro-2H-Benzo[c,d]Azuleno-6-One and 5-Phenylpentanoic Acid. *J. Org. Chem.* **1973**, *38* (8), 1445–1450.
- (18) Hafner, K.; Diehl, H.; Richarz, W. Cycloadditions of Aceheptylene—A Facile Synthesis of Dicyclopenta[ef,kl]Heptalenes. *Angew. Chem. Int. Ed.* **1976**, *15* (2), 108–109.
- (19) Konishi, A.; Horii, K.; Shiomi, D.; Sato, K.; Takui, T.; Yasuda, M. Open-Shell and Antiaromatic Character Induced by the Highly Symmetric Geometry of the Planar Heptalene Structure: Synthesis and Characterization of a Nonalternant Isomer of Bisanthene. *J. Am. Chem. Soc.* **2019**, *141* (26), 10165–10170.
- (20) Reel, H.; Vogel, E. Dicyclohepta[cd,gh]Pentalene—A New Pyrene Isomer. *Angew. Chem. Int. Ed.* **1972**, *11* (11),

- 1013–1014.
- (21) Vogel, E.; Wieland, H.; Schmalstieg, L.; Lex, J. Novel Synthesis and Molecular Structure of the Pyrene Isomer Dicyclohepta[cd,gh]Pentalene (Azuleno[2,1,8-ija]Azulene). *Angew. Chem. Int. Ed.* **1984**, *23* (9), 717–719.
- (22) Vogel, E.; Markowitz, G.; Schmalstieg, L.; Itô, S.; Breuckmann, R.; Roth, W. R. Thermal Deoxygenation of Syn-15,16-Dioxo-1,6:8,13-bismethano[14]Annulene to the Pyrene Isomer Dicyclohepta[cd,gh]Pentalene (Azuleno[2,1,8-ija]Azulene). *Angew. Chem. Int. Ed.* **1984**, *23* (9), 719–720.
- (23) Sun, Q.; Zhang, R.; Qiu, J.; Liu, R.; Xu, W. On-Surface Synthesis of Carbon Nanostructures. *Adv. Mater.* **2018**, *30* (17), 1705630.
- (24) Gröning, O.; Wang, S.; Yao, X.; Pignedoli, C. A.; Borin Barin, G.; Daniels, C.; Cupo, A.; Meunier, V.; Feng, X.; Narita, A.; et al. Engineering of Robust Topological Quantum Phases in Graphene Nanoribbons. *Nature* **2018**, *560* (7717), 209–213.
- (25) Rizzo, D. J.; Veber, G.; Cao, T.; Bronner, C.; Chen, T.; Zhao, F.; Rodriguez, H.; Louie, S. G.; Crommie, M. F.; Fischer, F. R. Topological Band Engineering of Graphene Nanoribbons. *Nature* **2018**, *560* (7717), 204–208.
- (26) Di Giovannantonio, M.; Urgel, J. I.; Beser, U.; Yakutovich, A. V.; Wilhelm, J.; Pignedoli, C. A.; Ruffieux, P.; Narita, A.; Müllen, K.; Fasel, R. On-Surface Synthesis of Indenofluorene Polymers by Oxidative Five-Membered Ring Formation. *J. Am. Chem. Soc.* **2018**, *140* (10), 3532–3536.
- (27) Mishra, S.; Beyer, D.; Eimre, K.; Kezilebieke, S.; Berger, R.; Gröning, O.; Pignedoli, C. A.; Müllen, K.; Liljeroth, P.; Ruffieux, P.; et al. Topological Frustration Induces Unconventional Magnetism in a Nanographene. *Nat. Nanotechnol.* **2020**, *15* (1), 22–28.
- (28) Treier, M.; Pignedoli, C. A.; Laino, T.; Rieger, R.; Müllen, K.; Passerone, D.; Fasel, R. Surface-Assisted Cyclodehydrogenation Provides a Synthetic Route towards Easily Processable and Chemically Tailored Nanographenes. *Nat. Chem.* **2011**, *3* (1), 61–67.
- (29) Alder, R. W.; East, S. P.; Harvey, J. N.; Oakley, M. T. The Azulene-to-Naphthalene Rearrangement Revisited: A DFT Study of Intramolecular and Radical-Promoted Mechanisms. *J. Am. Chem. Soc.* **2003**, *125* (18), 5375–5387.
- (30) Stirling, A.; Iannuzzi, M.; Laio, A.; Parrinello, M. Azulene-to-Naphthalene Rearrangement: The Car-Parrinello Metadynamics Method Explores Various Reaction Mechanisms. *ChemPhysChem* **2004**, *5* (10), 1558–1568.
- (31) Hieulle, J.; Carbonell-Sanromà, E.; Vilas-Varela, M.; Garcia-Lekue, A.; Guitián, E.; Peña, D.; Pascual, J. I. On-Surface Route for Producing Planar Nanographenes with Azulene Moieties. *Nano Lett.* **2018**, *18* (1), 418–423.
- (32) Mishra, S.; Lohr, T. G.; Pignedoli, C. A.; Liu, J.; Berger, R.; Urgel, J. I.; Müllen, K.; Feng, X.; Ruffieux, P.; Fasel, R. Tailoring Bond Topologies in Open-Shell Graphene Nanostructures. *ACS Nano* **2018**, *12* (12), 11917–11927.
- (33) Shiotari, A.; Nakae, T.; Iwata, K.; Mori, S.; Okujima, T.; Uno, H.; Sakaguchi, H.; Sugimoto, Y. Strain-Induced Skeletal Rearrangement of a Polycyclic Aromatic Hydrocarbon on a Copper Surface. *Nat. Commun.* **2017**, *8* (1), 16089.
- (34) Sun, Q.; Hou, I. C. Y.; Eimre, K.; Pignedoli, C. A.; Ruffieux, P.; Narita, A.; Fasel, R. On-Surface Synthesis of Polyazulene with 2,6-Connectivity. *Chem. Commun.* **2019**, *55* (89), 13466–13469.
- (35) Fan, Q.; Martin-Jimenez, D.; Ebeling, D.; Krug, C. K.; Brechmann, L.; Kohlmeyer, C.; Hilt, G.; Hieringer, W.; Schirmeisen, A.; Gottfried, J. M. Nanoribbons with Nonalternant Topology from Fusion of Polyazulene: Carbon Allotropes beyond Graphene. *J. Am. Chem. Soc.* **2019**, *141* (44), 17713–17720.
- (36) Klein, B. P.; Van Der Heijden, N. J.; Kachel, S. R.; Franke, M.; Krug, C. K.; Greulich, K. K.; Ruppenthal, L.; Müller, P.; Rosenow, P.; Parhizkar, S.; et al. Molecular Topology and the Surface Chemical Bond: Alternant Versus Nonalternant Aromatic Systems as Functional Structural Elements. *Phys. Rev. X* **2019**, *9* (1), 011030.
- (37) Dubovik, J.; Bredihhin, A. A Convenient Synthesis of Functionalized Azulenes via Negishi Cross-Coupling. *Synth.* **2015**, *47* (4), 538–548.
- (38) Wang, F.; Lai, Y. H.; Kocherginsky, N. M.; Kosterki, Y. Y. The First Fully Characterized 1,3-Polyazulene: High Electrical Conductivity Resulting from Cation Radicals and Polycations Generated upon Protonation. *Org. Lett.*

5.3 References

- 2003, 5 (7), 995–998.
- (39) Shang, J.; Wang, Y.; Chen, M.; Dai, J.; Zhou, X.; Kuttner, J.; Hilt, G.; Shao, X.; Gottfried, J. M.; Wu, K. Assembling Molecular Sierpiński Triangle Fractals. *Nat. Chem.* **2015**, 7 (5), 389–393.
- (40) Wang, W.; Shi, X.; Wang, S.; Van Hove, M. A.; Lin, N. Single-Molecule Resolution of an Organometallic Intermediate in a Surface-Supported Ullmann Coupling Reaction. *J. Am. Chem. Soc.* **2011**, 133 (34), 13264–13267.
- (41) Di Giovannantonio, M.; Tomellini, M.; Lipton-Duffin, J.; Galeotti, G.; Ebrahimi, M.; Cossaro, A.; Verdini, A.; Kharche, N.; Meunier, V.; Vasseur, G.; et al. Mechanistic Picture and Kinetic Analysis of Surface-Confined Ullmann Polymerization. *J. Am. Chem. Soc.* **2016**, 138 (51), 16696–16702.
- (42) Sun, Q.; Cai, L.; Ma, H.; Yuan, C.; Xu, W. Dehalogenative Homocoupling of Terminal Alkynyl Bromides on Au(111): Incorporation of Acetylenic Scaffolding into Surface Nanostructures. *ACS Nano* **2016**, 10 (7), 7023–7030.
- (43) Urgel, J. I.; Hayashi, H.; Di Giovannantonio, M.; Pignedoli, C. A.; Mishra, S.; Deniz, O.; Yamashita, M.; Dienel, T.; Ruffieux, P.; Yamada, H.; et al. On-Surface Synthesis of Heptacene Organometallic Complexes. *J. Am. Chem. Soc.* **2017**, 139 (34), 11658–11661.
- (44) Rickhaus, M.; Mayor, M.; Juriček, M. Chirality in Curved Polyaromatic Systems. *Chem. Soc. Rev.* **2017**, 46 (6), 1643–1660.
- (45) Ni, B.; Zhang, T.; Li, J.; Li, X.; Gao, H. Topological Design of Graphene. In *Handbook of Graphene*; Wiley, 2019; pp 1–44.

Chapter 6. Photo-modulation of 2D-Self-assembly of Azobenzene-Hexa-*peri*-hexabenzocoronene-Azobenzene Triads

Ian Cheng-Yi Hou,¹ [redacted],² [redacted],³ [redacted],⁴ [redacted],^{4,5} [redacted],² [redacted],^{1,6,*} [redacted],^{3,*} and [redacted],^{1,7,*} [redacted]

¹Max Planck Institute for Polymer Research, Ackermannweg 10, D-55128 Mainz, Germany

²Laboratory for Chemistry of Novel Materials, University of Mons, Place du Parc 20, B-7000 Mons, Belgium

³Université de Strasbourg, CNRS, ISIS UMR 7006, 8 allée Gaspard Monge, 67000 Strasbourg, France

⁴Karlsruhe Institute of Technology KIT, Institute of Nanotechnology, P.O. Box 3640, 76021 Karlsruhe, Germany

⁵Department of Chemistry, University of Basel, St. Johannisring 19, 4056 Basel, Switzerland

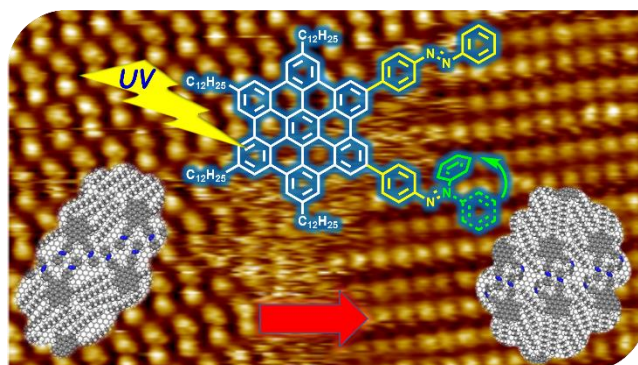
⁶Organic and Carbon Nanomaterials Unit, Okinawa Institute of Science and Technology Graduate University
1919-1 Tancha, Onna-son, Kunigami, Okinawa 904-0495, Japan

⁷Institute of Physical Chemistry, Johannes Gutenberg-University Mainz, Duesbergweg 10-14, D-55128 Mainz, Germany

Published in: *Chem. Mater.* **2019**, *31* (17), 6979–6985. DOI: 10.1021/acs.chemmater.9b01535. Reprinted with permission. Copyright: 2019, American Chemical Society.

Contribution: Organic synthesis and characterization (excluding azobenzene building blocks). Photoswitching analysis in solution. STM analysis. Prepare and correcting the first draft. Submission and revision the manuscript.

6.1 Abstract



ToC Figure.

Achieving exquisite control over self-assembly of functional polycyclic aromatic hydrocarbons (PAH) and nanographene (NG) is essential for their exploitation as active elements in (nano)technological applications. In the framework of our effort to leverage their functional complexity, we designed and synthesized two hexa-*peri*-hexabenzocoronene (HBC) triads, *pAHA* and *oAHA*, decorated with two light-responsive azobenzene moieties at the pseudo-*para* and *ortho* positions, respectively. Their photoisomerization in solution is demonstrated by UV-Vis absorption. ¹H NMR measurements of *oAHA* suggested 23% of *Z*-form can be obtained at a photostationary state with UV irradiation (366 nm). Scanning

tunneling microscopy imaging revealed that the self-assembly of ***p*AHA** and ***o*AHA** at the solid-liquid interface between highly oriented pyrolytic graphite (HOPG) and their solution in 1,2,4-trichlorobenzene can be modulated upon light irradiation. This is in contrast to our previous work using HBC bearing a single azobenzene moiety, which did not show such photomodulation of the self-assembled structure. Upon *E-Z* isomerization both ***p*AHA** and ***o*AHA** displayed an increased packing density on the surface of graphite. Moreover, ***p*AHA** revealed a change of self-assembled pattern from an oblique unit cell to a dimer row rectangular crystal lattice whereas the assembly of ***o*AHA** retained a dimer row structure before and after light irradiation, yet with a modification of the inter-row molecular orientation. Molecular mechanics/molecular dynamics simulations validated the self-assembly patterns of ***p*AHA** and ***o*AHA**, comprising azobenzenes in their *Z*-forms. These results pave the way toward use of suitably functionalized large PAHs, as well as NGs, to develop photo-switchable devices.

6.2 Introduction

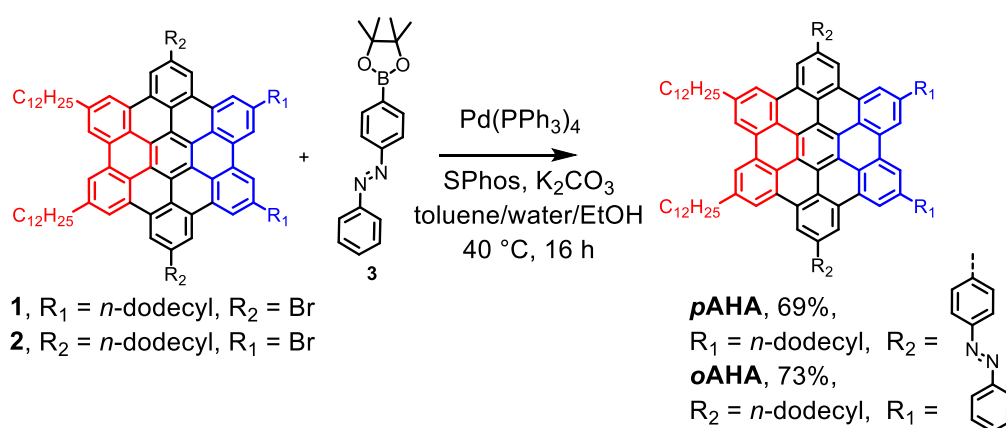
Hexa-*peri*-hexabenzocoronene (HBC), a molecule containing 42 sp^2 carbons and possessing a D_{6h} symmetry, is one of the most representative and well-studied polycyclic aromatic hydrocarbons (PAHs). With a diameter slightly exceeding 1 nm, it is considered one of the smallest possible nanographene (NG), i.e. molecularly defined subunits of the graphene lattice which is confined in at least one of its lateral dimensions.¹⁻³ For this reason, HBC is frequently used as a model system to gain insight into the behavior of NG-based materials.⁴⁻⁸ The large π -conjugated core of HBC gives rise to strong, non-covalent interactions among adjacent molecules, as well as between molecules and the basal plane of graphite. Understanding the resulting self-assembly processes is essential for advances in HBC-based (nano)technologies.^{5,6,9} Self-assembly of HBC derivatives has been studied in various environments, namely in solution and in bulk, where 3D columnar supramolecular structures are formed,^{6,10-17} and on surfaces, enabling programmed 2D nano-patterning.^{14,18,19} Substituents at peripheral positions play a key role in controlling self-assembly behavior of HBC. For example, HBCs with appropriate alkyl substituents show thermal phase transitions between crystalline and liquid-crystalline phases, where the phase-transition temperature can be tuned by the length of the side chains.^{6,11,20,21} Self-assembly of HBCs can thus be controlled by heat, yet the use of other external stimuli as remote controls to regulate self-assembly of HBC-based materials has only been occasionally considered.^{19,22} Among external stimuli, light is particularly attractive, as photons may be remotely applied with high spatial and temporal resolution. A plausible way of imparting photo-switchable characteristics to HBCs is to functionalize their peripheries with photochromic moieties.²³⁻²⁶ In particular, azobenzene exhibits a pronounced geometric change between its *E/Z*-isomers, which has been applied to light-controllable, self-assembled materials and photo-mechanical devices.²⁷⁻³¹ Photoresponsive self-assembly of azobenzene-containing materials has been intensively investigated, especially at solid-air³²⁻³⁶ and solid-liquid^{19,37-42} interfaces. Surface confinement restricts assembly in 2D and provides an opportunity for detailed examination of structures and dynamics of these molecules in real space by scanning probe microscopy techniques. In this context, it is extremely interesting to combine carbon-based nanostructures with photochromic molecules like azobenzene to develop optically responsive systems and materials.²⁶ HBC bearing one azobenzene unit was previously reported, but self-assembly of its *Z*-form could not be observed on a graphite surface by scanning tunneling microscopy (STM).¹⁹ Here we synthesized azobenzene-HBC-azobenzene triads, ***p*AHA** and ***o*AHA** (Scheme 1), featuring an HBC core and two peripheral azobenzene moieties in the

6.2 Introduction

pseudo-*para* and pseudo-*ortho* positions, respectively. Geometries of ***p*AHA** and ***o*AHA** are employed to explore intermolecular interactions that affect their self-assembly. Photoisomerization of the azobenzene moieties in solution is confirmed by UV-Vis absorption, combined with ^1H NMR spectroscopy. Self-assembly of these two HBCs at the solid-liquid interface before and after UV light irradiation was monitored by STM, and corroborated with molecular mechanics/molecular dynamics (MM/MD) simulations. Formation of stable self-assemblies for both ***p*AHA** and ***o*AHA** after isomerization of their azobenzene moieties reveals the potential of using large PAHs, as well as NGs, for photo-responsive devices and smart surfaces.

6.3 Result and discussion

Synthesis of azobenzene-HBC-azobenzene triads. *pAHA* and *oAHA* were synthesized from the corresponding HBCs **1** and **2** bearing two bromo groups at desired positions, in addition to four *n*-dodecyl chains⁴³, which guarantee the molecule's good solubility in organic solvents and high affinity to graphite surfaces (Scheme 1). The azobenzene moieties were introduced by a two-fold Suzuki coupling reaction between **1** or **2** with azobenzene boronic ester **3**.⁴⁴ *pAHA* and *oAHA* were isolated in 69% and 73% yields, respectively.



Scheme 1. Synthesis of azobenzene-HBC-azobenzene *pAHA* and *oAHA*.

Photoisomerization in solution. Reversible photoisomerization of both *pAHA* and *oAHA* could be observed in solution upon alternating irradiation at 366 and 436 nm (Figures S1–S3). The spectral changes upon photoisomerization were relatively small, and could be attributed to overlapping absorption features of the azobenzene units and the HBC core. HBC has a higher extinction coefficient,^{15,45} which could overshadow spectral variation of the azobenzene units. Nevertheless, *oAHA* showed sufficient solubility to enable ¹H NMR spectroscopic analysis at room temperature, which demonstrated that approximately 23% of Z-form was obtained in a photostationary state (PSS) after irradiation at 366 nm (Figure S4).

STM investigation of 2D self-assembly. The UV-Vis absorption and ¹H NMR results, indicating the efficient photoisomerization of *pAHA* and *oAHA* in solution, motivated us to investigate the influence of isomerization on their self-assembly at the solid-liquid interface between graphite and their supernatant solutions. 2D self-assembly patterns of *pAHA* and *oAHA* were monitored by STM at the interface between 1,2,4-trichlorobenzene (TCB) solutions and highly oriented pyrolytic graphite (HOPG) before and after *in-situ* UV light irradiation (Figure 1, 2; Table 1). In all cases, brighter areas with a diameter of ~1 nm can be

assigned to HBC cores as a result of more favorable resonant tunneling between the Fermi level of HOPG and the frontier orbitals of the large aromatic core. Non-irradiated **pAHA** exhibits an oblique unit cell containing one molecule and an area of $6.8 \pm 0.6 \text{ nm}^2$ per molecule (Figure 1a and Table 1), while **oAHA** forms a dimer-row structure with two molecules per unit cell and an area of $5.9 \pm 0.3 \text{ nm}^2$ per molecule (Figure 2a and Table 1). A different assembly was also observed for **oAHA** (Figure S5; Table S1). These crystal packings are all assigned to assemblies of *E,E*-isomers, which have both azobenzenes in *E*-form (Figure 1a, 2a and S5).

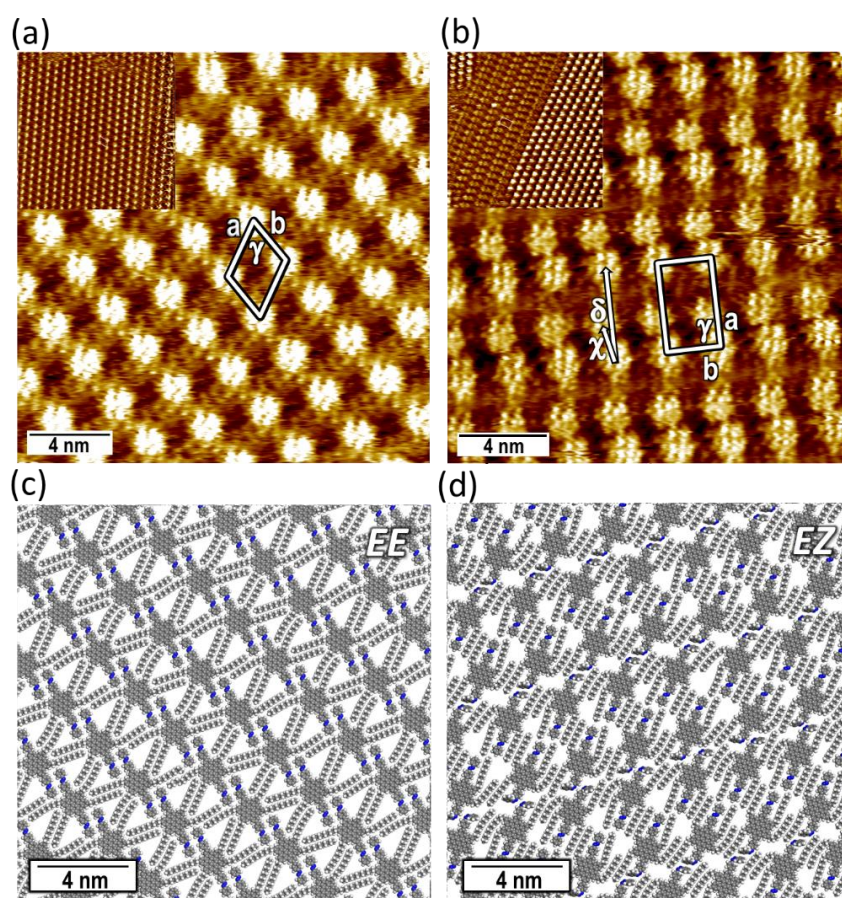


Figure 1. STM images recorded at the interface between HOPG and a 0.1 mM solution of **pAHA** in TCB and their 2D crystal packing models derived from MM/MD simulations. (a) An STM image taken without irradiation (**pAHA** ori in Table 1) and (c) a corresponding packing model of *E,E*-isomers. (b) An image recorded after irradiation at 366 nm (**pAHA** irr in Table 1) and (d) a corresponding packing model of *E,Z*-isomers. Inset in (a,b): images of the same crystal packing taken for a larger area of $50 \text{ nm} \times 50 \text{ nm}$. The newly formed dimer row crystal packing coexists with the oblique packing of *E,E*-isomers with a clear border, as can be seen in the inset of (b). Tunneling parameters: (a) bias voltage tunneling (V_T) = -300 mV , average tunneling current (I_T) = 20 pA ; (c) $V_T = -300 \text{ mV}$, $I_T = 20 \text{ pA}$. Atom color coding: (c,d) carbon (gray), nitrogen (blue), hydrogen (white).

It is interesting to note that, although ***p*AHA** and ***o*AHA** are a pair of isomers themselves, their assemblies show significantly different density where that of ***o*AHA** is much more compact. Different packing motifs between ***p*AHA** and ***o*AHA** demonstrate that connectivity of the azobenzene-HBC-azobenzene triads strongly affects molecular self-assembly at the solid-liquid interface. The same supramolecular packing is extended over a larger area (50 nm × 50 nm) (Figure 1a and 2a, insets). Analysis of ***p*AHA** over even larger areas demonstrated that the crystalline domains end when terraces in the HOPG surface were encountered. These domains remained intact for hours without transforming into other self-assembled structures, thus confirming high stability of the crystal packing.

*Table 1. Experimental lattice constants of *p*AHA and *o*AHA self-assembly at the HOPG/TCB interface.*

	a (nm)	b (nm)	γ (°)	χ (nm)b	δ (°) ^b	Area ^c (nm ²)	E _{ads} ^d (kcal/mol)	BE ^e (kcal/mol)
<i>p</i>AHA <i>ori</i>	3.0 ± 0.2	2.5 ± 0.1	65 ± 5	-	-	6.8 ± 0.6	-210.89 ^f	-23.35 ^f
<i>p</i>AHA <i>irr</i> ^a	4.2 ± 0.1	2.52 ± 0.05	88 ± 1	1.6 ± 0.1	11 ± 3	5.3 ± 0.2	-204.57 ^g	-13.83 ^g
<i>o</i>AHA <i>ori</i>	4.4 ± 0.1	2.7 ± 0.1	81 ± 3	2.0 ± 0.2	25 ± 4	5.9 ± 0.3	-211.58 ^f	-17.27 ^f
<i>o</i>AHA <i>irr</i> ^a	5.2 ± 0.2	1.77 ± 0.09	83 ± 5	2.4 ± 0.3	-4 ± 4	4.6 ± 0.3	-205.72 ^g	-19.50 ^g

^aOnly formed after irradiation at 366 nm. ^bInter-row distance and angle, specified in STM Figures. ^cArea per molecule. ^dAdsorption energy between molecule and the HOPG surface. Derived from MM/MD simulation. ^eIntermolecular binding energy. Derived from MM/MD simulation. ^fCalculated for the *E,E*-form. ^gCalculated for the *E,Z*-form.

STM investigation after light irradiation. After the 2D-self-assembly patterns of ***p*AHA** and ***o*AHA** were illustrated, their solution on the HOPG substrate was irradiated *in situ* with UV light ($\lambda_{irr} = 366$ nm) to examine effect of photoisomerization of the azobenzene moieties on the 2D crystalline assemblies. After 3 minutes of irradiation at a power density of 2 mW/cm², new domains with radically different lattice parameters were observed for both ***p*AHA** and ***o*AHA**, along with the simultaneous presence of the aforementioned domains formed by their *E,E*-isomers (Figure 1b and 2b, respectively). Molecules in the photo-modified domains assemble in dimer rows with a rectangular crystal lattice for both ***p*AHA** and ***o*AHA** showing an area of 5.3 ± 0.2 nm² and 4.6 ± 0.3 nm² per molecule, respectively (Figure 1b, 2b and Table 1). Additionally, another dimer row structured self-assembly pattern with δ close to 0° and a parallelogram unit cell was observed for ***p*AHA** (Figure S6 and Table S1). HBC cores in the photo-modified domains appear darker, compared with those in intact domains of the *E,E*-isomers, coexisting on the same STM image (inset of Figures 1b and 2b).

This could indicate a larger HOPG/HBC distance⁴⁶ possibly induced by nonplanar Z-form azobenzene arms. Moreover, the photo-modified domains exhibit denser packing than those in the original domains of the *E,E*-isomers, as evidenced by their smaller average area per molecule (Table 1). These observations support an assumption that the photo-modified domains consist of molecules containing nonplanar Z-form isomers, with azobenzene arms presumably back-folded in the supernatant solution, reducing the molecular footprint visualized by STM. However, although rarely observed on HOPG for HBC species,^{10,47,48} occurrence of a change in a 2D-assembly pattern for the *E,E*-isomers themselves cannot be completely excluded.

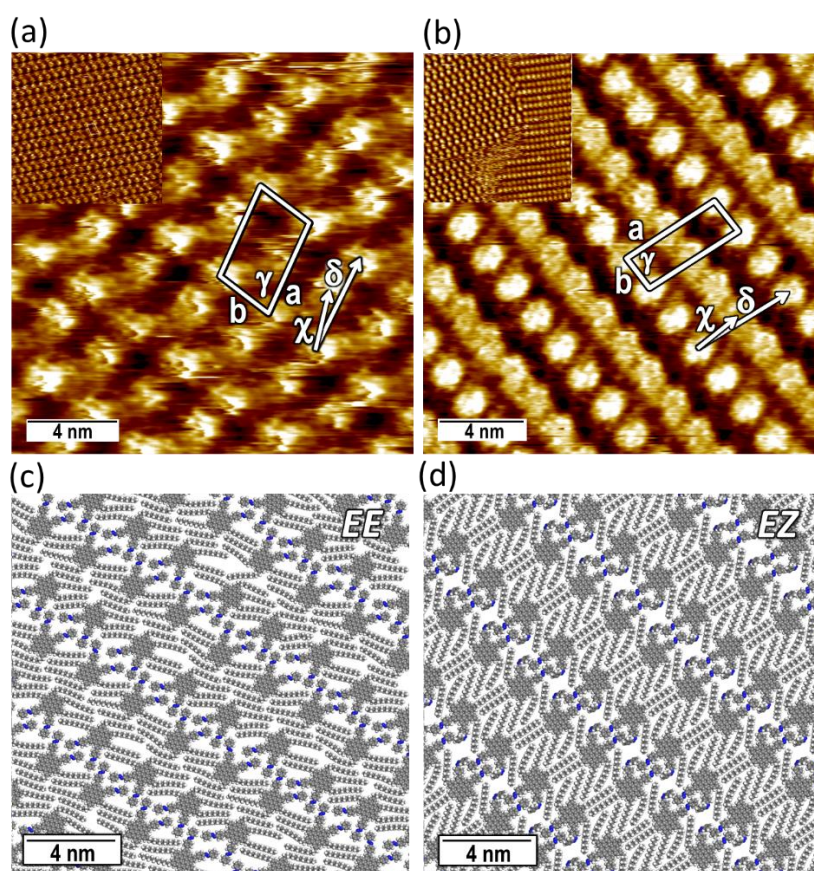


Figure 2. STM images recorded at the interface of HOPG and a 0.1 mM TCB solution of **oAHA** and their 2D crystal packing models derived from MM/MD simulations. (a) An STM image taken without irradiation (**oAHA** ori in Table 1) and (c) a corresponding packing model of *E,E*-isomers. (b) An image taken after irradiation at 366 nm (**oAHA** irr in Table 1) and (d) a corresponding packing model of *E,Z*-isomers. Inset in (a, b): images of the same crystal packing taken over a larger area 50 nm × 50 nm. The newly formed rectangular dimer row crystal packing coexists with the domain of *E,E*-isomers with a clear border, as can be seen in the inset of (b). Tunneling parameters (a) $V_T = -550$ mV, $I_T = 20$ pA; (c) $V_T = -700$ mV, $I_T = 20$ pA. Atom color coding: (c,d) carbon (gray), nitrogen (blue), hydrogen (white).

Simulation of the assembly patterns. MM/MD calculations were performed to further support the assumed formation of self-assembled domains consisting of isomers with *Z*-form azobenzenes, as well as to gain a greater understanding of how the azobenzene moieties govern the self-assembly of *pAHA* and *oAHA* by unraveling the packing at the atomistic level. Although lattice constants extracted from simulated results are generally larger than those experimentally determined, there is a reasonable agreement between experiment and simulation, allowing for a detailed interpretation of the STM images (Figure S7 and Table S2). Considering the relatively low *Z/E*-ratio at the PSS suggested by ¹H NMR measurements for *oAHA* (Figure S4) and assuming similar behavior for *pAHA*, we infer that the assembly patterns arising after irradiation in both cases are composed of *E,Z*-isomers, but not *Z,Z*-isomers. The best matching simulated patterns of *E,Z*-isomers are displayed in Figure 1c, d and 2c, d. Interestingly, nanophase separations between flexible alkyl chains and rigid azobenzenes is suggested for the packing of *E,E*-isomers of both *pAHA* and *oAHA* (Figure 1c and 2c, respectively). The nanophase separation disappears in the self-assembly of the *E,Z*-isomer of *pAHA* (Figure 1d). In the case of *oAHA*, azobenzenes intercalate in a zig-zag fashion. Spatial demand of azobenzenes on the surface determines the length *b* of the short lattice axis (Figure 2c): when one of the azobenzenes is switched into the *Z*-form, molecular size is reduced and the packing becomes tighter (Figure 2d). In contrast to *pAHA*, the nanophase separation in *oAHA* is retained in the self-assembly of both *E,Z*- and *Z,Z*-isomers (Figure S7). The incremental increase of binding energy with the number of *Z*-units in the *oAHA* molecule indicates that interaction between *Z*-azobenzenes benefits retention of the nanophase separation patterns (Table S2).

It is important to stress that observation of stable self-assemblies of molecules containing *Z*-isomers of azobenzene-based photoswitches at the solid-liquid interface by STM represents a challenging task.^{37,40} This is a result of the non-planarity of the *Z*-isomers and lone-pair electrons of nitrogens interacting with the graphite surfaces, thereby causing molecular desorption. Formation of stable assemblies for different photoactive states without desorption/readsorption of molecules is essential for development of responsive surfaces and devices.^{45,49,50} In our case, the packing density increased upon irradiation with UV light and we did not monitor the presence of regions with fuzzy contrast between domains of different assembly. It is therefore likely that the physisorbed molecules undergo a process that involves the subsequential desorption, isomerization in solution and re-adsorption onto the surface where void space is created by the shrinking of the assemblies. On the same time, some other molecules may undergo isomerization directly on the surface. Moreover, large PAHs such as

6.3 Result and discussion

HBC, namely NGs, exhibit very high adsorption energy toward HOPG surfaces.⁵¹ In this regard, desorption of molecules from the surface might not occur while molecules may move on the surface during irradiation and rearrange to form the new domains. However, the absence of a monitoring of the switch on the time scale of the event does not allow us to provide a conclusive mechanism for this process. Note also from the MM/MD calculation that absolute values of adsorption energies for the different isomers of *pAHA* and *oAHA* are similar (<9% energy difference from the most to the least stable isomers, see Table S2). Such a scenario is consistent with our observation of self-assembly of the *Z*-azobenzene-containing isomers for both *pAHA* and *oAHA*.

6.4 Conclusion

In summary, we have synthesized two model compounds, *p*AHA and *o*AHA, to cast light onto the photo-responsive behavior of large PAHs, as well as NGs, decorated with azobenzenes. UV-Vis absorption and ¹H NMR measurements demonstrated their photoisomerization in solution. STM images and MM/MD simulation of *p*AHA and *o*AHA revealed the photo-modulation of self-assembled structures into more compact packings, formed by *Z*-azobenzene-containing isomers at TCB/HOPG interface. The MM/MD simulation suggests similar nanophase separation between alkyl chains and azobenzenes in all three isomers of *o*AHA while it disappears in *E,Z*-isomer of *p*AHA. The markedly different packings of the different isomers of *p*AHA and *o*AHA on the graphite surface provide clear evidence for the potential of using large PAHs, as well as NGs, for the design of new photo-responsive materials that are suitable for the development of switchable surfaces and devices. We are actively working towards gaining a complete understanding on the mechanism of this photo-modulated self-assembly and exploring HBC derivatives possessing more azobenzene substituents and higher symmetry.

6.5 Experimental methods

General. All reactions working with air- or moisture-sensitive compounds were carried out under argon atmosphere using standard Schlenk line techniques. Thin layer chromatography (TLC) was performed on silica gel coated aluminum sheets with F254 indicator. Silica gel column chromatography separation was performed with 0.063–0.200 mm particle size. NMR spectra were recorded in deuterated solvents using Bruker AVANCE III 500 and Bruker AVANCE III 700 MHz NMR spectrometers. The ^{13}C NMR spectra were recorded with spin-echo attached-proton test (APT) sequence with CH, CH_3 showing negative signal and C, CH_2 showing positive signal. Chemical shifts (δ) were expressed in ppm relative to the residual of solvent ($\text{C}_2\text{D}_2\text{Cl}_4$ @ 6.00 ppm for ^1H NMR, 73.78 ppm for ^{13}C NMR). Coupling constants (J) were recorded in Hertz (Hz) with multiplicities explained by the following abbreviations: s = singlet, d = doublet, t = triplet, q = quartet, dd = doublet of doublets, dt = doublet of triplets, m = multiplet, br = broad. The UV–Vis absorption spectra were measured with a Perkin-Elmer Lambda 900 spectrophotometer in a quartz cuvette (Hellma) with a light path of 1 cm at room temperature. High-resolution mass spectra (HRMS) were recorded by matrix-assisted laser decomposition/ionization (MALDI) using 7,7,8,8-tetracyanoquinodimethane (TCNQ) as matrix with a Bruker Reflex II-TOF spectrometer (MALDI-TOF HRMS).

Materials. Unless otherwise noted, all starting materials and reagents were purchased from commercial sources (Alfa Aesar, Sigma-Aldrich, Acros and TCI) and used without further purification. HBCs **1** and **2** containing two bromo functional groups⁴³ and the azobenzene boronic ester **3**⁴⁴ were synthesized according to the previously published literature procedures.

Synthesis of pAHA. To a suspension of dibromo-HBC **1** (40 mg, 0.030 mmol), SPhos (4.4 mg, 0.011 mmol), and azobenzene boronic ester **3** (26 mg, 0.084 mmol) in toluene (8 mL) was added a solution of K_2CO_3 (1.4 g, 10 mmol) in water (1.5 mL) and ethanol (1.5 mL). This mixture was degassed by freeze-pump-thaw technique (1 cycle). $\text{Pd}(\text{PPh}_3)_4$ (8.0 mg, 0.0069 mmol) was then added to the mixture, which was further degassed by freeze-pump-thaw technique for another 2 cycles. The mixture was then heated at 40 °C under vigorous stirring for 16 h. After cooling to a room temperature, the mixture was poured into methanol. The yellow precipitates was collected by vacuum filtration and washed with methanol and then purified by silica gel column chromatography (two times, eluent: hot toluene) to afford the title compound as a bright yellow solid (32 mg, 69%). ^1H NMR (500 MHz, $\text{C}_2\text{D}_2\text{Cl}_4$, 373 K): δ 8.60–8.40 (br, 4H), 8.35–8.20 (m, 4H), 8.20–8.05 (m, 8H), 8.05–7.95 (m, 8H), 7.75–

7.55 (m, 6H), 3.15–2.85 (br, 8H), 2.15–1.90 (br, 8H), 1.85–1.60 (br, 16H), 1.60–1.20 (m, 56H), 1.10–0.85 (br, 12H). ¹³C NMR (126 MHz, C₂D₂Cl₄, 373 K): δ 153.11, 151.95, 144.02, 139.17, 135.56, 130.54, 129.28, 128.86, 128.59, 127.72, 123.47, 122.90, 122.08, 121.99, 120.70, 120.66, 120.39, 118.67, 118.50, 118.42, 36.83, 31.70, 31.58, 29.99, 29.78, 29.71, 29.67, 29.62, 29.49, 29.12, 22.39, 13.74. HRMS (MALDI-TOF) Mass. calcd. for C₁₁₄H₁₃₀N₄ [M]⁺ 1555.0296. Found [M]⁺ 1555.0505.

Synthesis of *o*AHA. To a suspension of dibromo-HBC **2** (45 mg, 0.034 mmol), SPhos (5.4 mg, 0.014 mmol), and azobenzene boronic ester **3** (41 mg, 0.13 mmol) in toluene (6 mL) was added a solution of K₂CO₃ (0.7 g, 5 mmol) in water (1 mL) and ethanol (1 mL). This mixture was degassed by freeze-pump-thaw technique (1 cycle). Pd(PPh₃)₄ (7.6 mg, 0.0066 mmol) was then added to the mixture, which was further degassed by freeze-pump-thaw technique for another 2 cycles. The mixture was then heated at 40 °C under vigorous stirring for 16 h. After cooling to a room temperature, the mixture was poured into methanol. The yellow precipitates were collected by vacuum filtration and washed with methanol and then purified by silica gel column chromatography (two times, eluent: hot toluene) to afford the title compound as a brownish solid (38 mg, 73%). ¹H NMR (500 MHz, C₂D₂Cl₄, 373 K): δ 8.20–8.05 (m, 8H), 8.00–7.87 (br, 2H), 7.85–7.80 (br, 2H), 7.80–7.76 (br, 2H), 7.76–7.71 (br, 2H), 7.71–7.60 (m, 12H), 7.58–7.50 (br, 2H), 3.00–2.80 (br, 4H), 2.80–2.65 (br, 4H), 2.05–1.93 (br, 4H), 1.93–1.78 (br, 4H), 1.78–1.20 (m, 72H), 1.10–0.90 (m, 12H). ¹³C NMR (126 MHz, C₂D₂Cl₄, 373 K): δ 153.15, 151.72, 143.32, 138.73, 138.51, 134.22, 130.48, 128.85, 128.61, 128.55, 128.27, 128.20, 128.01, 127.91, 127.19, 123.24, 122.90, 122.65, 121.68, 121.48, 120.27, 120.20, 119.85, 118.09, 118.00, 117.80, 117.62, 117.10, 36.89, 36.66, 31.74, 31.63, 31.35, 30.11, 30.09, 29.84, 29.74, 29.70, 29.68, 29.61, 29.54, 29.42, 29.17, 22.43, 13.78. HRMS (MALDI-TOF) Mass. calcd. for C₁₁₄H₁₃₀N₄ [M]⁺ 1555.0296. Found [M]⁺ 1555.0420.

Photoswitching in solution. The photoswitching in solution was conducted by direct irradiation of a THF solution of *p*AHA or *o*AHA in a quartz cuvette used for UV-Vis absorption spectral measurement. The absorption spectra were directly recorded using a UV-Vis spectrophotometer after irradiation. The light source used for switching was a Mercury arc lamp (HBO 200W/2, OSRAM). The irradiation wavelength was controlled by using optical filters (Schott Glaswerke). More details of experiments can be found in the supporting information.

STM Investigation. The STM imaging was conducted at ambient pressure and room temperature at constant current mode with a Veeco Multimode III (Bruker) connected with a STM head (tip: mechanically cut Pt/Ir wire, 4:1, $\phi = 0.25$ mm, Goodfellow) and a 1 μm piezoelectric scanner (A-Piezo, Veeco). The substrates (HOPG, Momentive Performance) were glued on (silver conductive paint, Aldrich) a metal disk (Ted Pella) that magnetically attached to the STM base. In our instrumental configuration, the sample is grounded. The experiments were performed at the solid/liquid interface between the HOPG and a drop (4 μL) of TCB solution of the molecule under investigation. The photo-controlled assembly was achieved by *in situ* irradiation of the solution on the HOPG substrate with optical fiber-coupled LED light source (ThorLabs, 365 nm, $P_d = 2$ mW cm^{-2}) by placing the collimator lens at a distance of 5 cm for 3 minutes. The raw STM data were processed by SPIP (Image Metrology). Drift of every image was calibrated by the images of the HOPG crystal lattice *in situ* ($V_T = 60$ mV, $I_T = 20$ pA). The unit cell constants were estimated from the average of multiple images (**pAHA** *ori*: 75, **pAHA** *irr*: 18, **pAHA** *irr2*: 6, **oAHA** *ori*: 13, **oAHA** *ori2*: 20, **oAHA** *irr*: 26).

MM/MD Simulations. The methodology employed in the MM/MD simulation is the same as the one used in our previous work for multi-azobenzene compounds.³⁷ The details about the description of the modified Dreiding force field⁵² used to reproduce the geometries of the multi-azobenzene groups adsorbed on graphite are given in the previously mentioned work. All the MM/MD simulations were performed using Materials Studio 7.0 package.⁵³ Details of the simulation methods and description can be found in the supporting information.

6.6 Supporting information

Experimental details

Photoswitching in solution. Solution used were heated at 80 °C overnight prior to investigation to ensure that all molecules were in *E*-form. The 365 nm light irradiation was achieved by using a 3 mm GG320 combined with a UG11 filter to eliminate the high energy UV peaks and the visible light peaks of the light source to reveal only the 366 nm peak ($P_d = 70 \text{ mW cm}^{-2}$). The 436 nm light irradiation was achieved by using 3 mm GG395 filter to block the UV light from the light source ($P_d = 310 \text{ mW cm}^{-2}$). Lower energy peaks of the light source were not blocked. The experiments were conducted at room temperature. If not specified, the irradiation interval was 10 s. The light source used for the photoisomerization in THF- d_8 for tracking the reaction by ^1H NMR spectra is the same for UV-Vis measurement. Because the solution is 100-times more concentrated than that for UV-Vis experiments, as well as the partial absorption of 366 nm light by the NMR tube (glass), the irradiation time was longer.

STM investigation. The surface of the HOPG substrate was peeled off (Scotch tape) several times until visually flat before use. Solution used were heated at 80 °C overnight before investigation to ensure all materials were in *E*-form. At the concentration used for investigation, the materials will eventually slowly precipitate out from the solution because of strong intermolecular π - π -stacking. Nevertheless, the molecule-substrate interaction still overcome the intermolecular stacking and the 2D supramolecular self-assembly pattern was observed.

MM/MD simulations. Following the reported methodologies^{37,52}, an orthorhombic unit cell of dimensions $a = 487\text{\AA}$, $b = 324\text{\AA}$ and $c = 50\text{\AA}$ coupled to Periodic Boundary Conditions (PBC) was used to reproduce structural packing of the graphene substrate. This graphene layer has been considered as an infinite rigid body to reduce the computational cost. In this unit cell, a self-assembly group of 144 molecules (12 rows and columns) was placed on the graphene substrate, whereas the big dimensions of the unit cell ensure a large lateral vacuum distance ($>40\text{\AA}$) between the replicated group of molecules. The simulation have been carried out in vacuum following the NVT ensemble (constant number of particles, volume and temperature) with a temperature of $T=100\text{K}$. The thermostat used to monitor the temperature was Velocity Scale. The atomic charges were calculated following the Gasteiger method,⁵⁴ while a cut-off distance of 12.5\AA was used in the non-bonded interactions. Firstly, the unit cell was

6.6 Supporting information

optimized at MM level. The resulting optimized unit cell was used as starting point for the quenched simulation (MM/MD). The run simulation time used was 25 ps, whereas the time step was 1 fs. The geometries of the MM/MD run were extracted every 500 steps, thus resulting in a total of 50 geometries per run. The geometry with lower energy was used as starting point for a new quenched simulation. All this process has been repeated till the energy difference between the starting and the most stable geometry is very low.

Some of the assumptions used in our model are: (i) the 2D self-assembly is formed by one single layer of HBC monomers, all of them made of a single isomer (*E,E*; *E,Z* or *Z,Z*); (ii) all alkyl chains of the HBC compounds are adsorbed on the graphite layer, implying that all atoms of the alkyl chains are in the same plane as the HBC core; and (iii) only the best fitting models which ended up in clear self-assembled pattern from several starting models have been shown here; our models thus represent one of the possible suitable patterns with similar structural parameters as the STM images.

In order to obtain a more complete interpretation of the experimental findings, we casted down the different energies driving the 2D self-assembly of the two HBC compounds on graphite. For this purpose, we have computed two parameters: adsorption energy (E_{ads}) and binding energy (BE), giving us a hint on the relative strength of the molecule-substrate and molecule-molecule interactions. The adsorption energy (E_{ads}) has been computed as the average adsorption energy of an individual HBC molecule on the graphite surface, following eq. 1:

$$E_{ads} = \frac{E_{tot} - E_{Gr} - E_{HBC}}{n} \quad (1)$$

With E_{tot} the total energy of the system, E_{Gr} the energy of the graphite layer, E_{HBC} the energy of the monolayer of HBC molecules and n the number of HBC molecules that form the assembly. In our case we have taken $n = 64$. The binding energy (BE) has been defined as the average interaction energy between HBC molecules in the assembly following eq. 2:

$$BE = \frac{E_{HBC} - \sum_{i=1}^n E_i}{n} \quad (2)$$

With E_i the energy of the individual molecules that form the monolayer. As in the last case we considered a representative assembly made of 64 molecules. These energies are also collected in Table S2.

UV-Vis absorption spectra Figure S1, S2, S3 and ^1H NMR spectra Figure S4

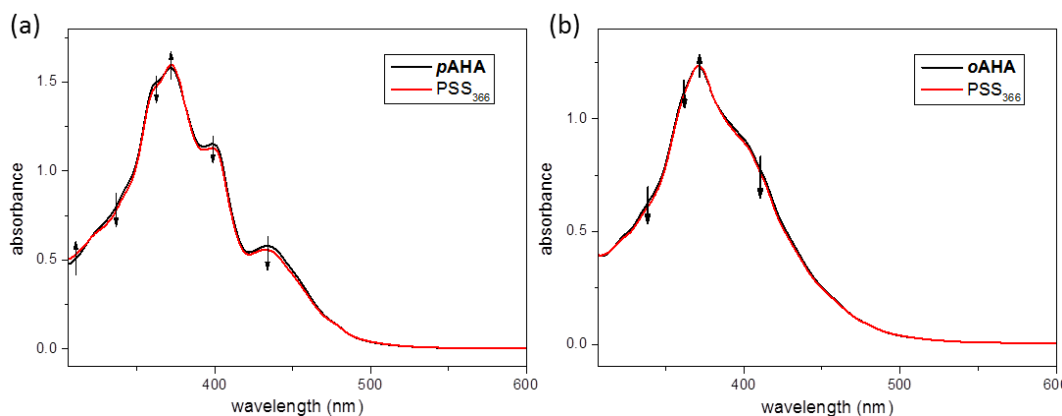


Figure S1. UV-Vis absorption spectra of the THF solutions of (a) pAHA (9.1×10^{-6} M) and (b) oAHA (1.3×10^{-5} M) without light irradiation (black line) and at the PSS of 366 nm irradiation (red line). Arrows show the trend of the spectral change at different spectral region.

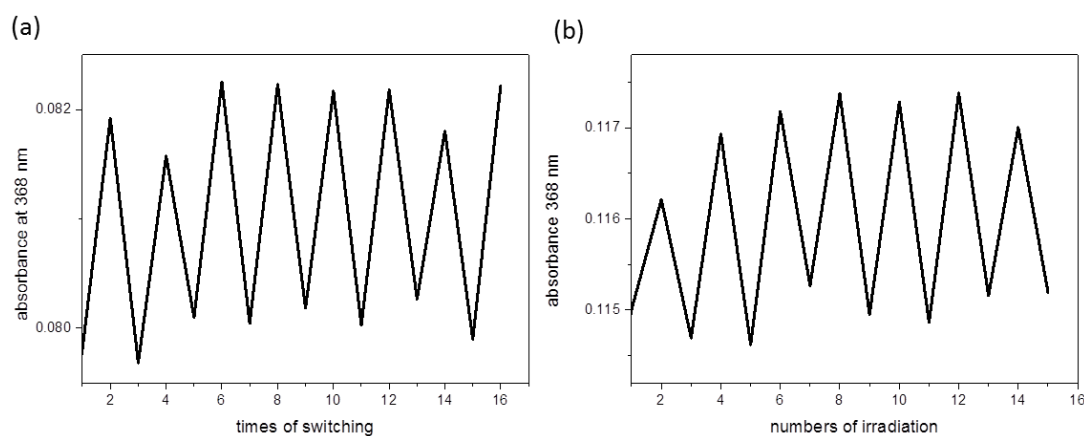


Figure S2. Absorbance variation of (a) pAHA (4.5×10^{-7} M) and (b) oAHA (1.3×10^{-6} M) in THF monitored at 368 nm starting from PSS₃₆₆ upon alternated irradiation with 436 and 366 nm light.

6.6 Supporting information

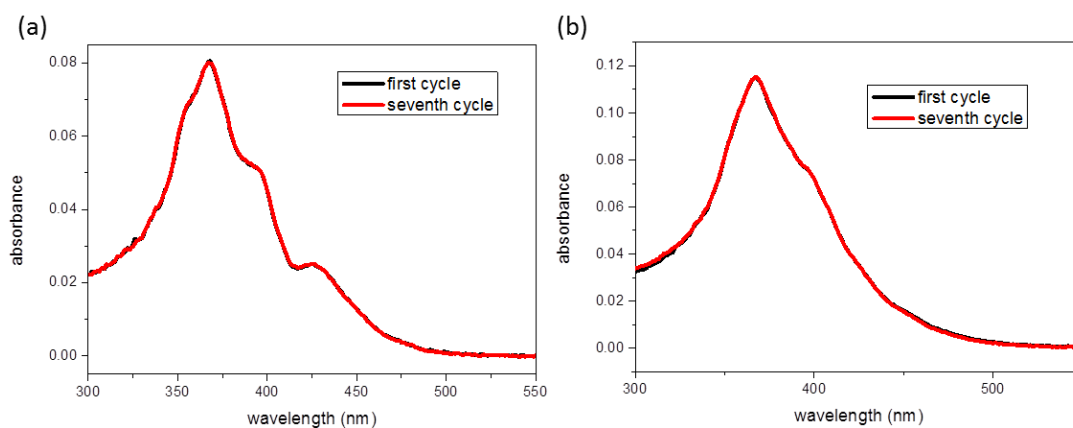


Figure S3. UV-Vis absorption spectra of (a) **pAHA** (4.5×10^{-7} M) and (b) **oAHA** (1.3×10^{-6} M) in THF after the first cycle and the seventh cycle of photoswitching.

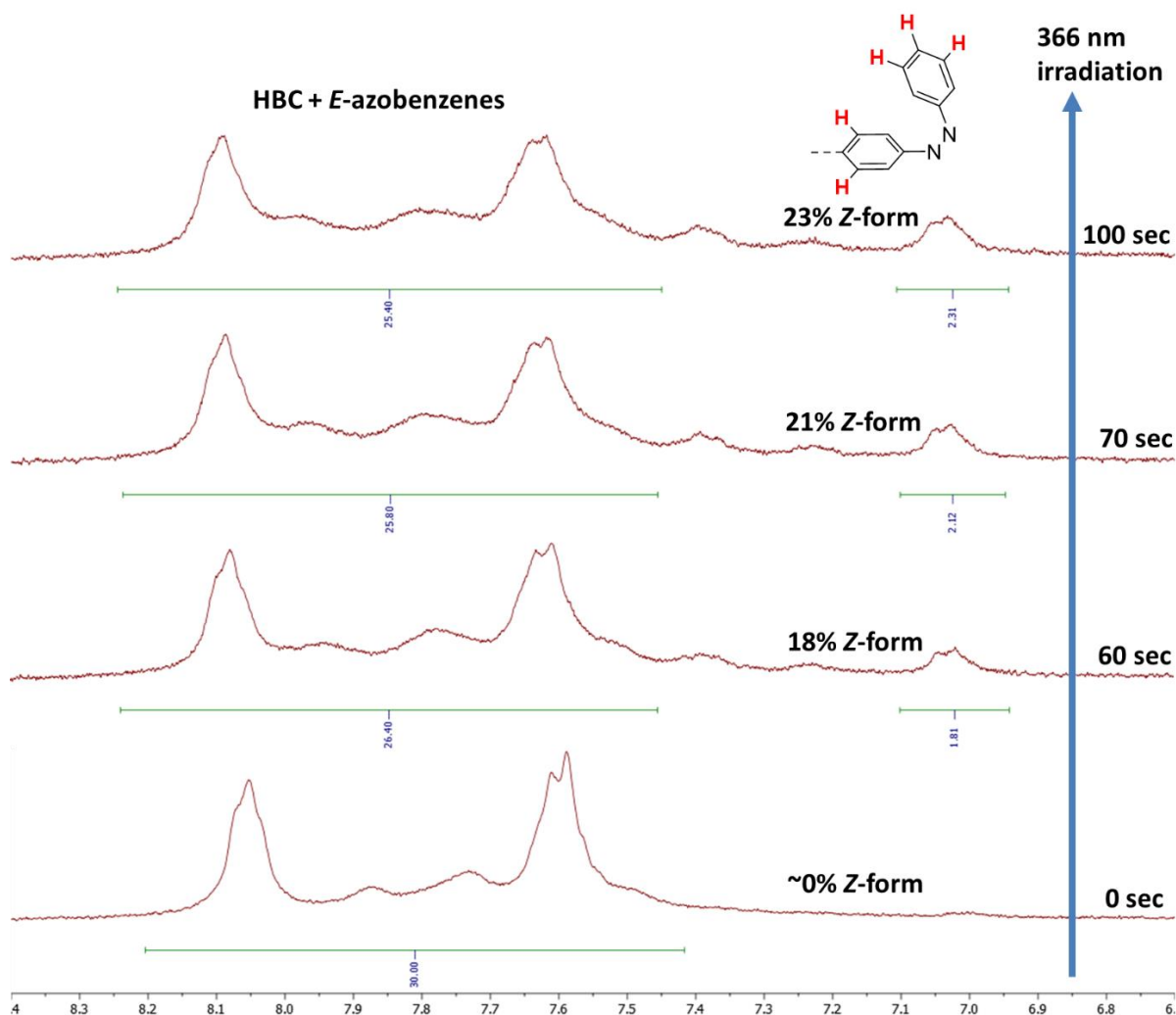


Figure S4. Aromatic region of the ^1H NMR spectra of **oAHA** in $\text{THF-}d_8$ recorded after different time of direct irradiation of the solution in NMR tube with 366 nm light until the PSS was reached. The broad peak at around 6.95–7.10 ppm is assigned to the signals of the protons of Z-azobenzene labeled in red. The integration of this peak is compared with the integration of the protons on HBC and E-azobenzene (7.15–7.45 ppm) to estimate the

percentage of photoisomerization. An integration of 10 protons (2 azobenzenes) corresponds to 100% of Z-form. Note that the rest of the signals of Z-azobenzene appear at around 7.15–7.45 ppm. The broadening and shifting of the signal around 7.4–8.2 ppm is an indication of changing of the aggregation of HBCs caused by variation of the composition of isomers.

STM images Figure S5, S6 and the summarized Table S1

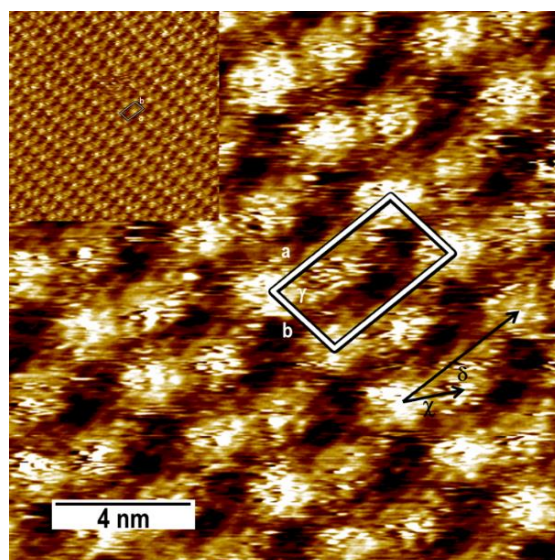


Figure S5. STM images recorded at the interface of HOPG and a 0.1 mM TCB solution of **oAHA**. The image corresponds to **oAHA** ori2 in Table S1. Inset: the same crystal packing taken in a larger area of 50 nm × 50 nm. Tunneling parameters: $V_T = -750$ mV, $I_T = 20$ pA.

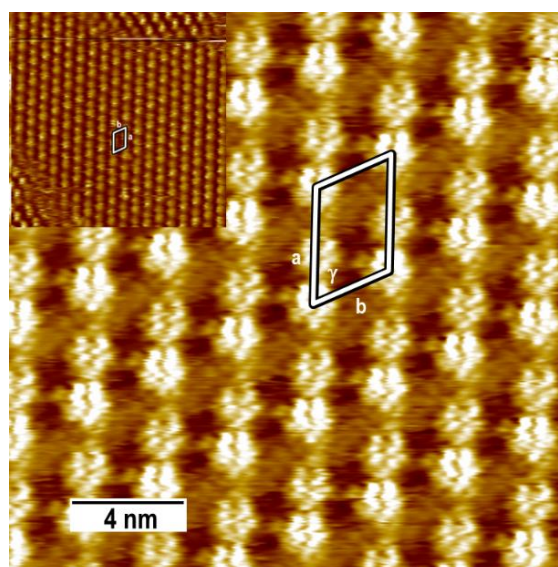


Figure S6. STM images recorded at the interface of HOPG and a 0.1 mM TCB solution of **pAHA** after irradiation with 366 nm light. The image corresponds to **pAHA** irr2 in Table S1. Inset: the same crystal packing taken in larger area of 50 nm × 50 nm. The newly formed dimer row crystal packing is found coexist with the oblique packing formed before irradiation with a clear border as can be seen in the inset of (b). Tunneling parameters: $V_T = -300$ mV, $I_T = 20$ pA.

6.6 Supporting information

Table S1. Lattice constants of the additional experimental 2D crystal packing of **pAHA** and **oAHA**.

	a (nm)	b (nm)	γ (°)	χ (nm) ^b	δ (°) ^c	Area per molecule (nm ²)
pAHA irr2 ^a	4.3 ± 0.2	3.00 ± 0.04	63 ± 2	1.74 ± 0.05	-0.1 ± 0.9	5.7 ± 0.3
oAHA ori2	4.3 ± 0.3	2.65 ± 0.08	80 ± 4	2.4 ± 0.2	17 ± 4	5.6 ± 0.4

^aOnly formed after 366 nm light irradiation. ^bThe inter-row distance, specified in the STM Figures. ^cThe inter-row angle, specified in the STM Figures.

MM/MD simulations results Figure S7 and Table S2

The adsorption energies E_{ads} of both *E,Z* and *Z,Z* present lower energy values respect to the *E,E* isomer (~5 kcal/mol for *E,Z* and ~15 kcal/mol for *Z,Z*) due to the lower π - π interactions caused by the non-planar configuration of the *Z*-form. However, due to the large aromaticity of the HBC, the magnitude of E_{ads} is one order of magnitude higher than *BE*. As a consequence, this factor is dominating the assembly process, thus explaining the highly packed patterns observed in the STM images.

In the case of the binding energy *BE*, comparing first this energy among the two structural models of **pAHA** for the *E,E* form, it is found that model II presents an energy twice higher than model I, thus demonstrating the importance of alkyl chains interdigitation in the intermolecular stabilization. Nevertheless, in most of the cases *BE* increases with the number of *Z* units, thus showing that the intermolecular interactions help to stabilize the *Z*-forms within the assembly.

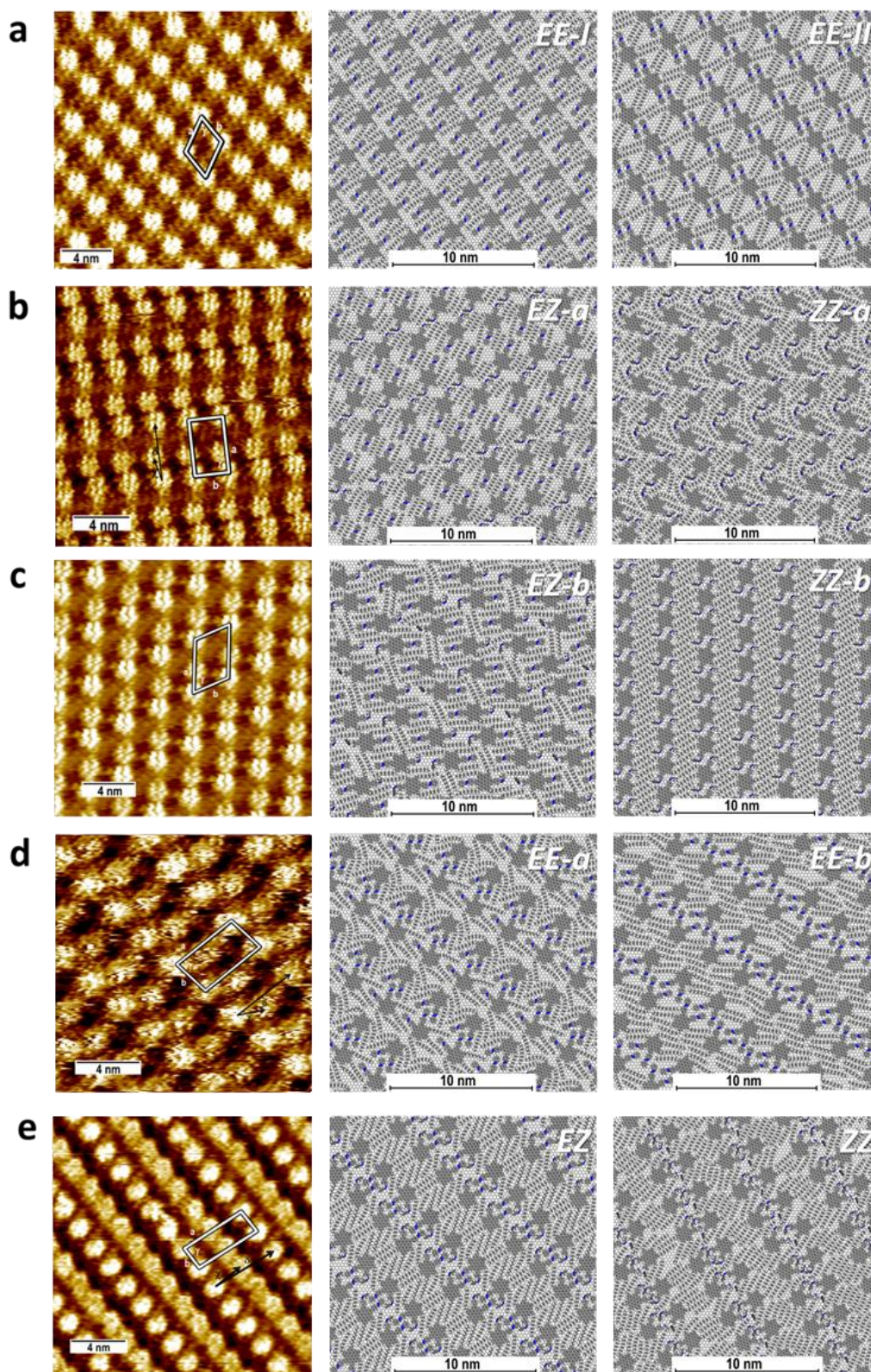


Figure S7. Summary of the STM images of ordered domains of **pAHA** found (a) before and (b)(c) after the 366 nm irradiation; and **oAHA** found (d) before and (e) after the 366 nm irradiation. Right side: corresponding supramolecular packing models of various isomers obtained by MM/MD simulations for each STM pattern on the left sides.

6.6 Supporting information

Table S2. Experimental (*ori*- for original and *irr*- for irradiated) and theoretical unit cell parameters (lateral dimensions *a* and *b*, corresponding angle γ , area occupied per molecule *A*, center to center distance χ between non-equivalent molecules in the unit cell and angle δ formed by the vector connecting the non-equivalent molecules and the *b* lateral vector) and calculated thermodynamic quantities (adsorption (E_{ads}) and binding (*BE*) energies). The highlighted rows are used to help making a direct comparison between the experimental (numbers in parentheses) and the best fitting theoretical models. Only the first model is formed by one molecule in the unit cell while the rest of the models are composed by two molecules in the unit cell.

HBC	Model	<i>a</i> (nm)	<i>b</i> (nm)	γ (°)	<i>A</i> (nm ²)	χ (nm)	δ (°)	E_{ads} (kcal/mol)	<i>BE</i> (kcal/mol)
	<i>ori</i>	(3.0)	(2.5)	(65)	(6.8)	-	-	-	-
	<i>EE-I</i>	3.0	2.5	64	6.8	-	-	-212.71	-11.09
	<i>EE-II</i>	3.2	2.5	62	6.9	-	-	-210.89	-23.35
	<i>irr</i>	(4.2)	(2.52)	(88)	(5.3)	(1.6)	(11)	-	-
pAHA	<i>EZ-a</i>	5.0	2.66	83	6.6	2.3	9.4	-204.57	-13.83
	<i>ZZ-a</i>	4.3	2.80	89	6.0	2.0	17	-195.99	-17.15
	<i>irr2</i>	(4.3)	(3.00)	(63)	(5.7)	(1.74)	(-0.1)	-	-
	<i>EZ-b</i>	4.6	3.10	62	6.3	1.80	22	-204.96	-17.13
	<i>ZZ-b</i>	4.1	3.18	62	5.7	2.04	0.1	-194.96	-24.36
	<i>ori</i>	(4.4)	(2.7)	(81)	(5.9)	(2.0)	(25)	-	-
	<i>EE-a</i>	4.9	2.8	79	6.7	2.4	24	-211.58	-17.27
	<i>ori2</i>	(4.3)	(2.65)	(80)	(5.6)	(2.4)	(17)	-	-
oAHA	<i>EE-b</i>	4.6	2.93	84	6.7	2.1	16	-208.47	-13.51
	<i>irr</i>	(5.2)	(1.77)	(83)	(4.6)	(2.4)	(-4)	-	-
	<i>EZ</i>	5.4	2.28	80	6.1	2.6	11	-205.72	-19.50
	<i>ZZ</i>	5.1	2.27	79	5.7	2.4	16	-192.53	-25.70

^1H NMR and ^{13}C NMR APT spectra of *p*AHA and *o*AHA

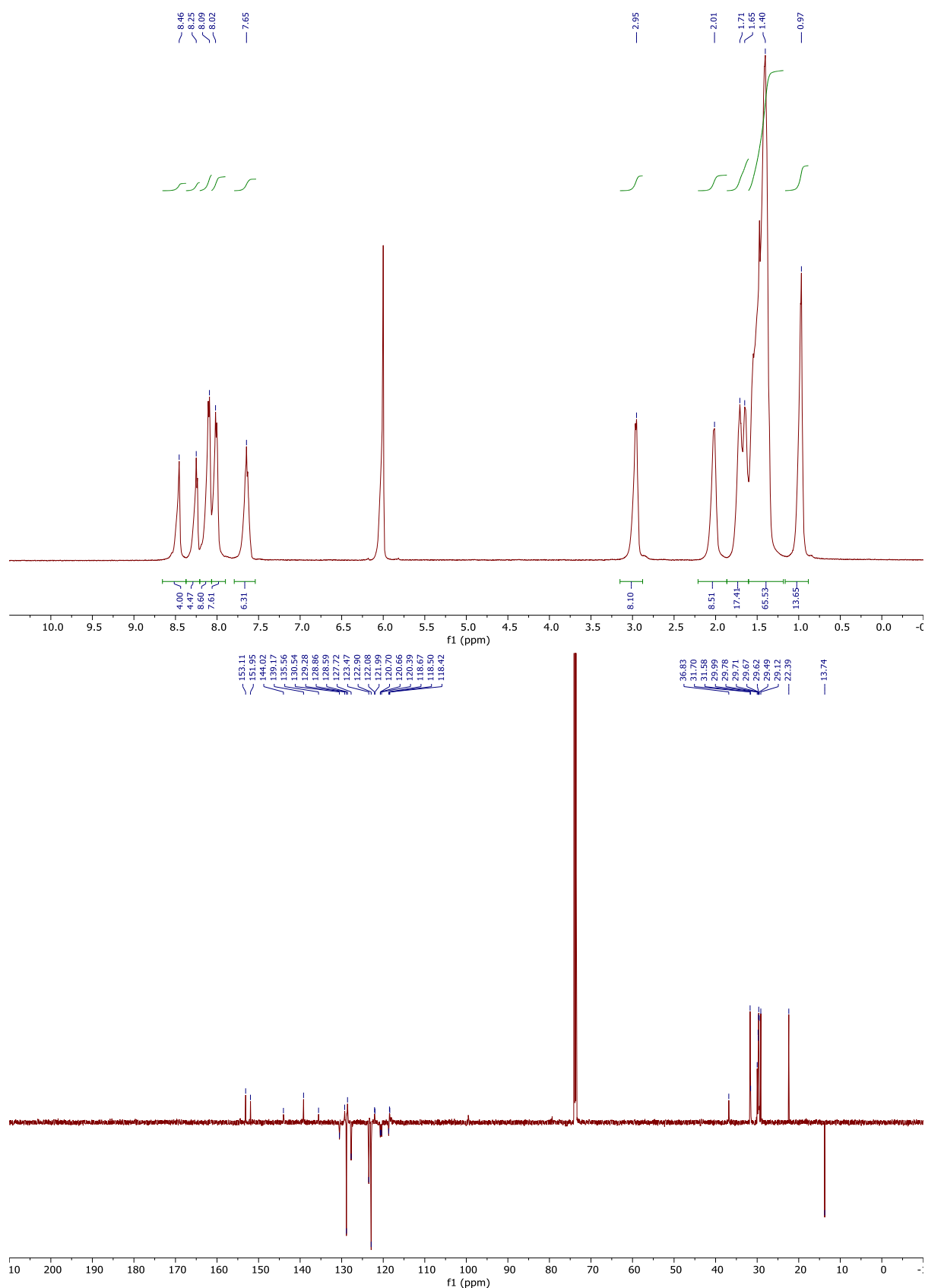


Figure S8. ^1H NMR (Up, 500 MHz, $\text{C}_2\text{D}_2\text{Cl}_4$, 373 K) and ^{13}C NMR APT spectra (Down, 126 MHz, $\text{C}_2\text{D}_2\text{Cl}_4$, 373 K) of *p*AHA.

6.6 Supporting information

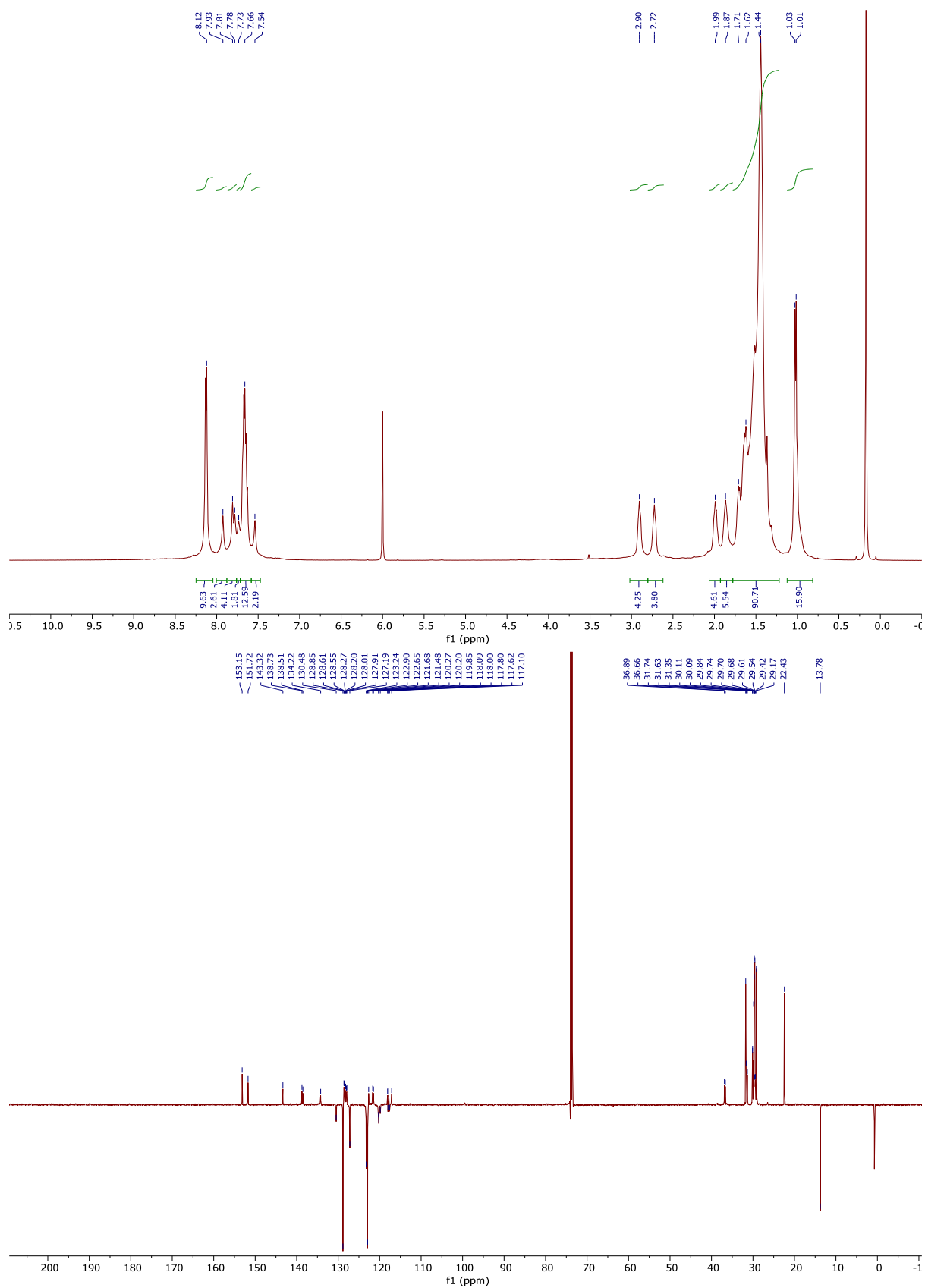


Figure S9. ^1H NMR (Up, 500 MHz, $\text{C}_2\text{D}_2\text{Cl}_4$, 373 K) and ^{13}C NMR APT spectra (Down, 126 MHz, $\text{C}_2\text{D}_2\text{Cl}_4$, 373 K) of *o*AHA.

6.7 References

- (1) Narita, A.; Wang, X. Y.; Feng, X.; Müllen, K. New Advances in Nanographene Chemistry. *Chem. Soc. Rev.* **2015**, *44* (18), 6616–6643.
- (2) Wang, X.-Y.; Narita, A.; Müllen, K. Precision Synthesis versus Bulk-Scale Fabrication of Graphenes. *Nat. Rev. Chem.* **2017**, *2* (1), 0100.
- (3) Narita, A.; Chen, Z.; Chen, Q.; Müllen, K. Solution and On-Surface Synthesis of Structurally Defined Graphene Nanoribbons as a New Family of Semiconductors. *Chem. Sci.* **2019**, *10* (4), 964–975.
- (4) Chen, Q.; Brambilla, L.; Daukiya, L.; Mali, K. S.; De Feyter, S.; Tommasini, M.; Müllen, K.; Narita, A. Synthesis of Triply Fused Porphyrin-Nanographene Conjugates. *Angew. Chem. Int. Ed.* **2018**, *57* (35), 11233–11237.
- (5) Yen, H. J.; Tsai, H.; Zhou, M.; Holby, E. F.; Choudhury, S.; Chen, A.; Adamska, L.; Tretiak, S.; Sanchez, T.; Iyer, S.; et al. Structurally Defined 3D Nanographene Assemblies via Bottom-Up Chemical Synthesis for Highly Efficient Lithium Storage. *Adv. Mater.* **2016**, *28* (46), 10250–10256.
- (6) Wu, J.; Pisula, W.; Müllen, K. Graphenes as Potential Material for Electronics. *Chem. Rev.* **2007**, *107* (3), 718–747.
- (7) Wang, Y.; Yin, Z.; Zhu, Y.; Gu, J.; Li, Y.; Wang, J. Hexapole [9]Helicene. *Angew. Chem. Int. Ed.* **2019**, *58* (2), 587–591.
- (8) Evans, P. J.; Ouyang, J.; Favereau, L.; Crassous, J.; Fernández, I.; Perles, J.; Martín, N. Synthesis of a Helical Bilayer Nanographene. *Angew. Chem. Int. Ed.* **2018**, *57* (23), 6774–6779.
- (9) Ziogos, O. G.; Konstantinopoulos, S.; Tsetseris, L.; Theodorou, D. N. Computational Studies of Nanographene Systems: Extended Discotics, Covalently Linked “Supermolecules,” and Functionalized Supramolecular Assemblies. *J. Phys. Chem. C* **2018**, *122* (32), 18715–18731.
- (10) Feng, X.; Pisula, W.; Kudernac, T.; Wu, D.; Zhi, L.; De Feyter, S.; Müllen, K. Controlled Self-Assembly of C3-Symmetric Hexa-*Peri*-Hexabenzocoronenes with Alternating Hydrophilic and Hydrophobic Substituents in Solution, in the Bulk, and on a Surface. *J. Am. Chem. Soc.* **2009**, *131* (12), 4439–4448.
- (11) Zhou, Y.; Zhang, M. Y.; Gu, K. H.; Zhu, Y. F.; Fan, X. H.; Shen, Z. Facile Synthesis and Phase Behaviors of Monofunctionalized Hexa-*Peri*-Hexabenzocoronenes. *Asian J. Org. Chem.* **2015**, *4* (8), 746–755.
- (12) Wong, W. W. H.; Birendra Singh, T.; Vak, D.; Pisula, W.; Yan, C.; Feng, X.; Williams, E. L.; Chan, K. L.; Mao, Q.; Jones, D. J.; et al. Solution Processable Fluorenyl Hexa-*Peri*-Hexabenzocoronenes in Organic Field-Effect Transistors and Solar Cells. *Adv. Funct. Mater.* **2010**, *20* (6), 927–928.
- (13) Gu, K.; Zhang, M.; Zhou, Y.; Han, M.; Zhang, W.; Shen, Z.; Fan, X. Hierarchical Self-Assembly of Disc-Rod Shape Amphiphiles Having Hexa-*Peri*-Hexabenzocoronene and a Relatively Long Rod. *Langmuir* **2017**, *33* (13), 3311–3316.
- (14) Hu, Y.; Dössel, L. F.; Wang, X.-Y.; Mahesh, S.; Pisula, W.; De Feyter, S.; Feng, X.; Müllen, K.; Narita, A. Synthesis, Photophysical Characterization, and Self-Assembly of Hexa-*Peri*-Hexabenzocoronene/Benzothiadiazole Donor-Acceptor Structure. *ChemPlusChem* **2017**, *82* (7), 1030–1033.
- (15) Keerthi, A.; Hou, I. C. Y.; Marszalek, T.; Pisula, W.; Baumgarten, M.; Narita, A. Hexa-*Peri*-Hexabenzocoronene with Different Acceptor Units for Tuning Optoelectronic Properties. *Chem. - An Asian J.* **2016**, *11* (19), 2710–2714.
- (16) Hinkel, F.; Cho, D.; Pisula, W.; Baumgarten, M.; Müllen, K. Alternating Donor-Acceptor Arrays from Hexa-*Peri*hexabenzocoronene and Benzothiadiazole: Synthesis, Optical Properties, and Self-Assembly. *Chem. - A Eur. J.* **2015**, *21* (1), 86–90.
- (17) Wu, S. H.; Chen, H. H. Self-Assembling Behavior of Binary Mixture of Hexa-*Peri*-Hexabenzocoronene Derivatives with Different Molecular Symmetry. *Tetrahedron* **2018**, *75* (2), 220–229.
- (18) Dumsloff, T.; Yang, B.; Maghsoumi, A.; Velpula, G.; Mali, K. S.; Castiglioni, C.; De Feyter, S.; Tommasini, M.; Narita, A.; Feng, X.; et al. Adding Four Extra K-Regions to Hexa-*Peri*-Hexabenzocoronene. *J. Am. Chem. Soc.* **2016**, *138* (14), 4726–4729.

6.7 References

- (19) Ai, M.; Groeper, S.; Zhuang, W.; Dou, X.; Feng, X.; Müllen, K.; Rabe, J. P. Optical Switching Studies of an Azobenzene Rigidly Linked to a Hexa-Peri-Hexabenzocoronene Derivative in Solution and at a Solid-Liquid Interface. *Appl. Phys. A* **2008**, *93* (2), 277–283.
- (20) Pisula, W.; Zorn, M.; Chang, J. Y.; Müllen, K.; Zentel, R. Liquid Crystalline Ordering and Charge Transport In Semiconducting Materials. *Macromol. Rapid Commun.* **2009**, *30* (14), 1179–1202.
- (21) Fleischmann, E. K.; Zentel, R. Liquid-Crystalline Ordering as a Concept in Materials Science: From Semiconductors to Stimuli-Responsive Devices. *Angew. Chem. Int. Ed.* **2013**, *52* (34), 8810–8827.
- (22) Oda, K.; Hiroto, S.; Shinokubo, H. NIR Mechanochromic Behaviours of a Tetracyanoethylene-Bridged Hexa-: Peri-Hexabenzocoronene Dimer and Trimer through Dissociation of C-C Bonds. *J. Mater. Chem. C* **2017**, *5* (22), 5310–5315.
- (23) Feringa, B. L.; Browne, W. R. *Molecular Switches, Second Edition*; Feringa, B. L., Browne, W. R., Eds.; Wiley-VCH Verlag GmbH & Co. KGaA: Weinheim, Germany, 2011; Vol. 1.
- (24) Lubbe, A. S.; Szymanski, W.; Feringa, B. L. Recent Developments in Reversible Photoregulation of Oligonucleotide Structure and Function. *Chem. Soc. Rev.* **2017**, *46* (4), 1052–1079.
- (25) Balzani, V.; Credi, A.; Venturi, M. *Molecular Devices and Machines: Concepts and Perspectives for the Nanoworld: Second Edition*; Wiley-VCH Verlag GmbH & Co. KGaA: Weinheim, Germany, 2008; Vol. 2.
- (26) Zhang, X.; Hou, L.; Samorì, P. Coupling Carbon Nanomaterials with Photochromic Molecules for the Generation of Optically Responsive Materials. *Nat. Commun.* **2016**, *7* (1), 11118.
- (27) Barrett, C. J.; Mamiya, J. I.; Yager, K. G.; Ikeda, T. Photo-Mechanical Effects in Azobenzene-Containing Soft Materials. *Soft Matter* **2007**, *3* (10), 1249–1261.
- (28) Naumov, P.; Chizhik, S.; Panda, M. K.; Nath, N. K.; Boldyreva, E. Mechanically Responsive Molecular Crystals. *Chem. Rev.* **2015**, *115* (22), 12440–12490.
- (29) Bisoyi, H. K.; Li, Q. Light-Driven Liquid Crystalline Materials: From Photo-Induced Phase Transitions and Property Modulations to Applications. *Chem. Rev.* **2016**, *116* (24), 15089–15166.
- (30) Yagai, S.; Kitamura, A. Recent Advances in Photoresponsive Supramolecular Self-Assemblies. *Chem. Soc. Rev.* **2008**, *37* (8), 1520–1529.
- (31) Orgiu, E.; Samorì, P. 25th Anniversary Article: Organic Electronics Marries Photochromism: Generation of Multifunctional Interfaces, Materials, and Devices. *Adv. Mater.* **2014**, *26* (12), 1827–1844.
- (32) Scheil, K.; Gopakumar, T. G.; Bahrenburg, J.; Temps, F.; Maurer, R. J.; Reuter, K.; Berndt, R. Switching of an Azobenzene-Tripod Molecule on Ag(111). *J. Phys. Chem. Lett.* **2016**, *7* (11), 2080–2084.
- (33) Jaekel, S.; Richter, A.; Lindner, R.; Bechstein, R.; Nacci, C.; Hecht, S.; Kühnle, A.; Grill, L. Reversible and Efficient Light-Induced Molecular Switching on an Insulator Surface. *ACS Nano* **2018**, *12* (2), 1821–1828.
- (34) Mielke, J.; Selvanathan, S.; Peters, M.; Schwarz, J.; Hecht, S.; Grill, L. Molecules with Multiple Switching Units on a Au(111) Surface: Self-Organization and Single-Molecule Manipulation. *J. Phys. Condens. Matter* **2012**, *24* (39), 394013.
- (35) Tegeder, P. Optically and Thermally Induced Molecular Switching Processes at Metal Surfaces. *J. Phys. Condens. Matter* **2012**, *24* (39), 394001.
- (36) Nacci, C.; Baroncini, M.; Credi, A.; Grill, L. Reversible Photoswitching and Isomer-Dependent Diffusion of Single Azobenzene Tetramers on a Metal Surface. *Angew. Chem. Int. Ed.* **2018**, *57* (46), 15034–15039.
- (37) Galanti, A.; Diez-Cabanes, V.; Santoro, J.; Valášek, M.; Minoia, A.; Mayor, M.; Cornil, J.; Samorì, P. Electronic Decoupling in C3-Symmetrical Light-Responsive Tris(Azobenzene) Scaffolds: Self-Assembly and Multiphotochromism. *J. Am. Chem. Soc.* **2018**, *140* (47), 16062–16070.
- (38) Frath, D.; Yokoyama, S.; Hirose, T.; Matsuda, K. Photoresponsive Supramolecular Self-Assemblies at the Liquid/Solid Interface. *J. Photochem. Photobiol. C* **2018**, *34*, 29–40.
- (39) Garah, M. El; Borré, E.; Ciesielski, A.; Dianat, A.; Gutierrez, R.; Cuniberti, G.; Bellemin-Lapponaz, S.; Mauro, M.;

- Samorì, P. Light-Induced Contraction/Expansion of 1D Photoswitchable Metallopolymer Monitored at the Solid–Liquid Interface. *Small* **2017**, *13* (40), 1701790.
- (40) Zeitouny, J.; Aurisicchio, C.; Bonifazi, D.; De Zorzi, R.; Geremia, S.; Bonini, M.; Palma, C. A.; Samorì, P.; Listorti, A.; Belbakra, A.; et al. Photoinduced Structural Modifications in Multicomponent Architectures Containing Azobenzene Moieties as Photoswitchable Core. *J. Mater. Chem.* **2009**, *19* (27), 4715–4724.
- (41) Liu, Y.; Mu, L.; Liu, B.; Kong, J. Controlled Switchable Surface. *Chem. - A Eur. J.* **2005**, *11* (9), 2622–2631.
- (42) Tahara, K.; Inukai, K.; Adisojoso, J.; Yamaga, H.; Balandina, T.; Blunt, M. O.; De Feyter, S.; Tobe, Y. Tailoring Surface-Confined Nanopores with Photoresponsive Groups. *Angew. Chem. Int. Ed.* **2013**, *52* (32), 8373–8376.
- (43) Ito, S.; Wehmeier, M.; Brand, J. D.; Kübel, C.; Epsch, R.; Rabe, J. P.; Müllen, K. Synthesis and Self-Assembly of Functionalized Hexa-*Peri*-Hexabenzocoronenes. *Chem. - A Eur. J.* **2000**, *6* (23), 4327–4342.
- (44) Harvey, J. H.; Butler, B. K.; Trauner, D. Functionalized Azobenzenes through Cross-Coupling with Organotrifluoroborates. *Tetrahedron Lett.* **2007**, *48* (9), 1661–1664.
- (45) Bléger, D.; Ciesielski, A.; Samorì, P.; Hecht, S. Photoswitching Vertically Oriented Azobenzene Self-Assembled Monolayers at the Solid-Liquid Interface. *Chem. - A Eur. J.* **2010**, *16* (48), 14256–14260.
- (46) Samorì, P.; Fechtenkötter, A.; Jäckel, F.; Böhme, T.; Müllen, K.; Rabe, J. P. Supramolecular Staircase via Self-Assembly of Disklike Molecules at the Solid–Liquid Interface. *J. Am. Chem. Soc.* **2001**, *123* (46), 11462–11467.
- (47) Piot, L.; Marchenko, A.; Wu, J.; Müllen, K.; Fichou, D. Structural Evolution of Hexa-*Peri*-Hexabenzocoronene Adlayers in Heteroepitaxy on n-Pentacotane Template Monolayers. *J. Am. Chem. Soc.* **2005**, *127* (46), 16245–16250.
- (48) Müllen, K.; Fichou, D.; Silly, F.; Marie, C.; Torteck, L. Tuning the Packing Density of 2D Supramolecular Self-Assemblies at the Solid–Liquid Interface Using Variable Temperature. *ACS Nano* **2010**, *4* (3), 1288–1292.
- (49) Cojal González, J. D.; Iyoda, M.; Rabe, J. P. Reversible Photoisomerization of Monolayers of π -Expanded Oligothiophene Macrocycles at Solid-Liquid Interfaces. *Angew. Chem. Int. Ed.* **2018**, *57* (52), 17038–17042.
- (50) Tahara, K.; Inukai, K.; Adisojoso, J.; Yamaga, H.; Balandina, T.; Blunt, M. O.; De Feyter, S.; Tobe, Y. Tailoring Surface-Confined Nanopores with Photoresponsive Groups. *Angew. Chem. Int. Ed.* **2013**, *52* (32), 8373–8376.
- (51) Weippert, J.; Hauns, J.; Bachmann, J.; Böttcher, A.; Yao, X.; Yang, B.; Narita, A.; Müllen, K.; Kappes, M. M. A TPD-Based Determination of the Graphite Interlayer Cohesion Energy. *J. Chem. Phys.* **2018**, *149* (19), 194701.
- (52) Mayo, S. L.; Olafson, B. D.; Goddard, W. A. DREIDING: A Generic Force Field for Molecular Simulations. *J. Phys. Chem.* **1990**, *94* (26), 8897–8909.
- (53) MS Modeling, V7. Accelrys Software Inc.: San Diego, CA 2015.
- (54) Gasteiger, J.; Marsili, M. A New Model for Calculating Atomic Charges in Molecules. *Tetrahedron Lett.* **1978**, *19* (34), 3181–3184.

Chapter 7. Hexa-*peri*-hexabenzocoronene with Different Acceptor Units for Tuning Optoelectronic Properties

■■■■■■■■■■¹, **Ian Cheng-Yi Hou**,¹ ■■■■■■■■■■¹, ■■■■■■■■■■^{1,2}, ■■■■■■■■■■^{1,*}

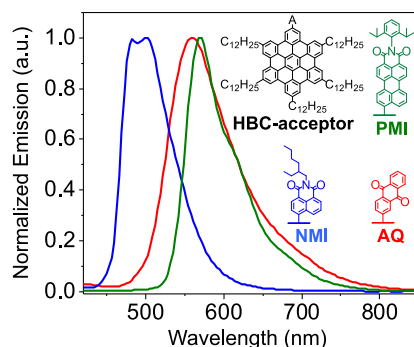
¹Max Planck Institute for Polymer Research, Ackermannweg 10, D-55128 Mainz, Germany

²Department of Molecular Physics, Faculty of Chemistry, Lodz University of Technology, Zeromskiego 116, 90-924 Lodz, Poland

Published in: *Chem. - An Asian J.* **2016**, *11* (19), 2710–2714. DOI: 10.1002/asia.201600638. Reprinted with permission. Copyright: 2016, WILEY-VCH.

Contribution: Organic synthesis and characterization (excluding acceptor building blocks). UV-Vis, CV measurements.

7.1 Abstract



ToC Figure. Hexa-*peri*-hexabenzocoronene (HBC)-based donor-acceptor dyads were synthesized with three different acceptor units, 9,10-anthraquinone (AQ), naphthalene-1,8-dicarboximide (NMI), and perylene-3,4-dicarboximide (PMI). The three HBC-acceptor dyads demonstrated varying degrees of intramolecular charge-transfer interactions, allowing tuning of their photophysical and optoelectronic properties.

Hexa-*peri*-hexabenzocoronene (HBC)-based donor-acceptor dyads were synthesized with three different acceptor units, through two pathways: 1) “pre-functionalization” of monobromo-substituted hexaphenylbenzene prior to the cyclodehydrogenation; and 2) “post-functionalization” of monobromo-substituted HBC after the cyclodehydrogenation. The HBC-acceptor dyads demonstrated varying degrees of intramolecular charge-transfer interactions, depending on the attached acceptor units, which allowed tuning of their photophysical and optoelectronic properties, including the energy gaps. The two synthetic pathways described here can be complementary and potentially be applied for the synthesis of nanographene-acceptor dyads with larger aromatic cores, including one-dimensionally extended graphene nanoribbons.

7.2 Main text

Large polycyclic aromatic hydrocarbons (PAHs), as represented by hexa-*peri*-hexabenzocoronene (HBC), have been attracting a renewed attention as nanographene molecules, having defined nanoscale graphene structures with distinct optical and electronic properties.¹⁻³ Such nanographene molecules bear high potential not only for applications in electronic and optoelectronic devices as organic semiconductors or structurally defined graphene quantum dots,^{1, 4-9} but also as models for studying chemical functionalization and structural modification of graphene and graphene nanoribbons (GNRs).¹⁻³ A series of nanographene molecules with different structures, e.g., size and edge configuration, as well as heteroatom doping, have thus far been synthesized, demonstrating the possibility of fine-tuning their photophysical and optoelectronic properties through the structural modulation.^{1, 4, 10-15} Nevertheless, the peripheral functionalization of such nanographene molecules with different functional groups has been relatively underdeveloped, despite the vast opportunities of bestowing new functions on them as well as modulating their properties without changing the aromatic core structures.¹⁶⁻²⁴ In particular, nanographene molecules coupled with acceptor units are of great interest for lowering their energy gaps through charge-transfer interactions, although only a few such examples are known in the literature.²⁵⁻²⁹

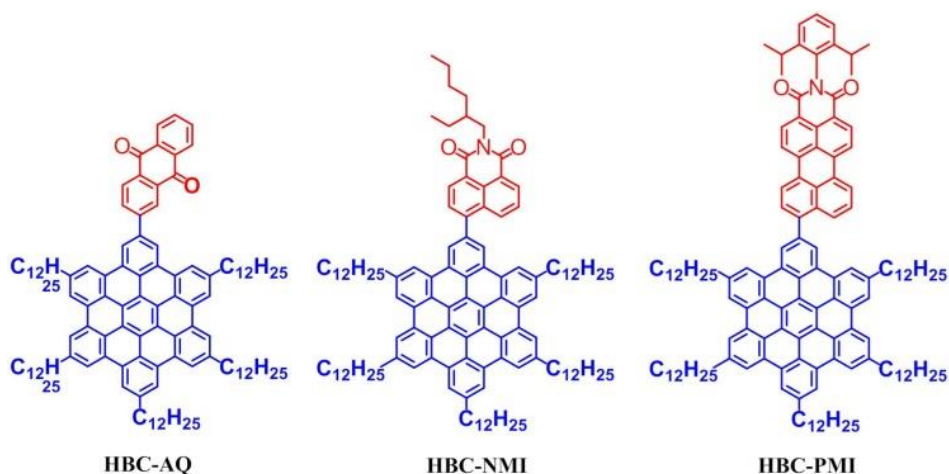


Figure 1. Chemical structures of *HBC-AQ*, *-NMI*, and *-PMI*.

To this end we have selected HBC as a model system for exploring the functionalization of nanographene molecules with different acceptor units. HBC derivatives have gained great interest as organic functional materials with phase-forming behavior, serving as donor materials in organic photovoltaics (OPV)²⁹⁻³¹ as well as p-type semiconductors in organic field-effect transistors (OFETs).³²⁻³⁴ Herein we report syntheses of three HBC-acceptor dyads

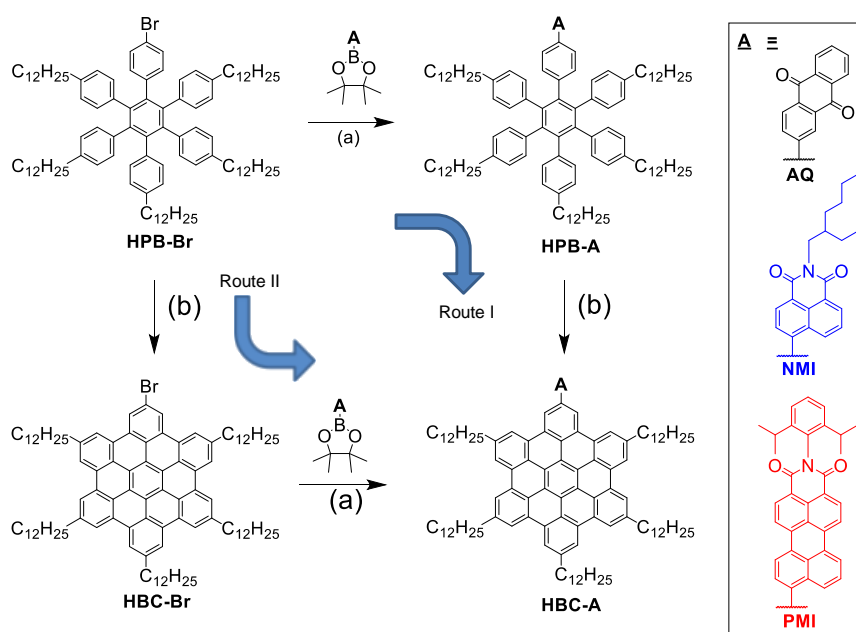
7.2 Main text

(**HBC-A**) bearing different acceptor units, i.e., 9,10-anthraquinone (**AQ**),³⁵ naphthalene-1,8-dicarboximide (**NMI**),³⁶ and perylene-3,4-dicarboximide (**PMI**)³⁷ (Figure 1). The three HBC-acceptor dyads demonstrate varied photophysical and optoelectronic properties and, depending on the acceptor unit, allowed for a fine control of their optical properties and energy gaps.

The synthesis of HBC-acceptor dyads started from monobromo-substituted hexaphenylbenzene derivative **HPB-Br**²⁴ and two synthetic routes were investigated in comparison: 1) “pre-functionalization” of **HPB-Br** with an acceptor unit (**A**) through a Suzuki coupling to obtain **HPB-A**, followed by oxidative cyclodehydrogenation to afford **HBC-A** (Route I, Scheme 1); 2) cyclodehydrogenation of **HPB-Br** to monobromo-substituted HBC derivative **HBC-Br**,²⁴ followed by “post-functionalization” to provide **HBC-A** (Route II, Scheme 1). The pre-functionalization protocol enables facile and complete purification of the soluble, functionalized precursor **HPB-A**, although the acceptor unit might compromise the efficiency of the cyclodehydrogenation, and/or be unstable under the reaction conditions. On the other hand, the post-functionalization protocol can ensure the completion of the cyclodehydrogenation, i.e., from **HPB-Br** to **HBC-Br**, and is more straightforward for preparing various **HBC-A** with different acceptor units, whereas the separation of the resulting **HBC-A** from debrominated byproducts could be difficult, depending on their solubility. Thus, these two protocols can be complementary to each other and are worthwhile studying in comparison.

First, the synthesis was carried out through the pre-functionalization route: **HPB-Br** was coupled with boronic esters of the acceptor units, namely, 2-(4,4,5,5-tetramethyl-1,3,2-dioxaborolan-2-yl)anthracene-9,10-dione (**AQ-boro**), N-(2-ethylhexyl)-4-(4,4,5,5-tetramethyl-1,3,2-dioxaborolan-2-yl)naphthalene-1,8-dicarboximide (**NMI-boro**), and N-(2,6-diisopropylphenyl)-9-(4,4,5,5-tetramethyl-1,3,2-dioxaborolan-2-yl)perylene-3,4-dicarboximide (**PMI-boro**)³⁸ via the Suzuki coupling to obtain **HPB-AQ**, **-NMI**, and **-PMI**, respectively (Scheme 1). Subsequently, the oxidative cyclodehydrogenation of these precursors was carried out using FeCl₃ in dichloromethane and nitromethane at room temperature, providing **HBC-AQ**, **-NMI**, and **-PMI**, respectively. The products were highly soluble in common organic solvents such as dichloromethane (DCM), toluene, tetrahydrofuran (THF), and ethyl acetate, which allowed for purification by silica gel column chromatography and comprehensive characterizations in solution. Structural proof was thus obtained by ¹H and ¹³C NMR as well as matrix-assisted laser desorption/ionization time-of-flight (MALDI-TOF) mass spectrometry (MS) analyses (see SI), indicating that all three

acceptor units did not hinder the complete cyclodehydrogenation. Nevertheless, MALDI-TOF MS analysis displayed relatively intense peaks of chlorinated byproducts for **HBC-NMI** and **-PMI**, in comparison to **HBC-AQ**, which could not be removed by the silica gel column chromatography (see Figures S17–S19). These characterizations also confirmed that no extra C-C bond was formed between the HBC core and the acceptor units during the cyclodehydrogenation, which would make a five-membered ring particularly in the cases of **HBC-NMI** and **-PMI** (Figure S1).



*Scheme 1. Scheme Caption Synthetic routes towards HBC-acceptor dyads; a) toluene/ethanol/2 M K₂CO₃, 90 °C, 16 h; pre-functionalization: **HPB-AQ**: 74%; **HPB-NMI**: 90%; **HPB-PMI**: 54%; post-functionalization: **HBC-AQ**: 79%; **HBC-NMI**: 94%; **HBC-PMI**: 81% b) FeCl₃, nitromethane, dichloromethane, rt, 1 h; post-functionalization: **HBC-Br**: 83%; pre-functionalization: **HBC-AQ**: 46%; **HBC-NMI**: 91%; **HBC-PMI**: 32%.*

Next, the second, post-functionalization route was applied for the syntheses of **HBC-AQ**, **-NMI**, and **-PMI**, which was expected to suppress the undesired chlorinated byproducts. **HPB-Br** was first subjected to the cyclodehydrogenation to obtain **HBC-Br**,²⁴ and then to Suzuki coupling with **AQ-boro**, **NMI-boro**, and **PMI-boro** to afford **HBC-AQ**, **-NMI**, and **-PMI**, respectively (Scheme 1). The MALDI-TOF MS analyses of thus obtained **HBC-NMI** and **-PMI** samples showed significantly smaller signals from the chlorinated byproducts. Although the relative intensities in the MALDI-TOF MS analysis do not correspond to the actual ratios between different chemical species, the obvious suppression of the byproduct signals under the same measurement condition indicated the superiority of the post-

functionalization route for the preparation of soluble HBC-acceptor dyads. On the other hand, the pre-functionalization route can be useful for HBC derivatives with limited solubility, which cannot be separated from debrominated byproducts through column chromatography although the cyclodehydrogenation conditions need to be carefully optimized to suppress the chlorination. It should be noted that the UV-Vis absorption and emission spectra of the HBC-acceptor dyads prepared by the pre- and post-functionalization methods were almost identical (Figures S8–10), showing that the chlorinated byproducts detected by MALDI-TOF MS had negligible influences on the optical properties of **HBC-AQ**, **-NMI**, and **-PMI**. These results indicated that both pre- and post-functionalization routes can be complementarily employed for the synthesis of different HBC-acceptor dyads, and eventually also applied for coupling larger nanographene molecules and GNRs with acceptor units.

The optical and electrochemical properties of the three HBC-acceptor dyads were investigated in comparison. UV-Vis absorption spectra of **HBC-AQ**, **-NMI**, and **-PMI** all showed the β -band of the HBC core at ~ 360 nm along with the p-band at ~ 390 nm (Figure 2A).³⁹ A broad red-shifted band observed for **HBC-AQ** at 400–520 nm and for **HBC-NMI** at 400–460 nm could presumably be assigned to the intramolecular charge-transfer (CT) interactions between donor and acceptor units, although it was difficult to confirm its dependence on the polarity of the solvent²⁵ due to the small absorbance (Figure S6). It should be noted that these broad bands also overlap with the α -band of the HBC core, which nevertheless does not extend over 425 nm (Figure 2A).³⁹ On the other hand, no red-shifted absorption band was visible in the absorption spectrum of **HBC-PMI**, compared to the absorption of the **PMI** unit itself,³⁷ suggesting the absence of the ground-state CT.

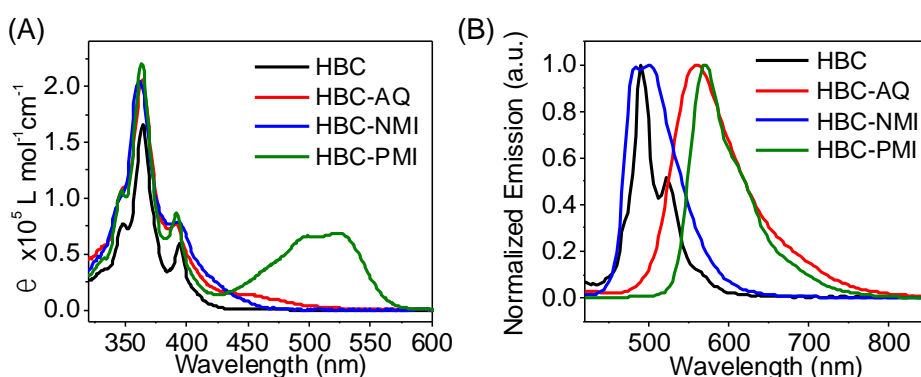


Figure 2. (A) Absorption and (B) emission spectra of the HBC-acceptor dyads in comparison with pristine HBC bearing six dodecyl chains, recorded in toluene solutions at a concentration of 10^{-5} mol/L. Excitation wavelength in the photoluminescence spectroscopy measurements was 400 nm.

In the emission spectra, **HBC-NMI** revealed peaks at ~480 and ~500 nm in toluene, which were red-shifted to ~550 nm in THF, due to the intramolecular CT (Figures 2B and S7).⁴⁰ Interestingly, **HBC-AQ** showed the emission maxima (λ_{em}) at ~560 nm in toluene with large Stokes shift of approximately 110 nm, based on the absorption maxima of the CT band at ~450 nm. The emission maxima of **HBC-AQ** further red-shifted to 680 nm when the solvent was changed to THF, corroborating the strong intramolecular donor-acceptor interactions in **HBC-AQ** (Figures 2B and S7). Additionally, **HBC-AQ** exhibited dual fluorescence in THF with an emission peak at 492 nm from local excitation of the HBC moiety, in addition to the CT peak. This observation might be due to stabilization of different conformations of the molecule, depending on the solvent.⁴¹ **HBC-PMI** displayed a small red-shift of emission peak (λ_{em} : 571 nm) from that of pristine **PMI** at ~550 nm (Figure 2B).²⁶ The red-shift of the emission peak, comparing the spectra in toluene and THF, was also very limited (10 nm) (Figures S7), which provided further evidence for the weak intramolecular CT interactions between the **HBC** and **PMI** units. Among the three systems, **HBC-PMI** gave the highest quantum yield of 45% whereas **HBC-AQ** and **-NMI** exhibited that of around 8–9%. The optical energy gaps were estimated from the absorption onset in toluene to be 2.41 eV (**HBC-AQ**), 2.70 eV (**HBC-NMI**), and 2.16 eV (**HBC-PMI**), which demonstrated the possibility of fine-tuning the optical properties by changing the acceptor units.

Table 1. Photophysical and electrochemical properties of the HBC-acceptor dyads

Compound	λ_{abs} (nm) ^[a]	λ_{em} (nm) ^[a]	Φ_F (%) ^[a]	E_{HOMO} (eV) ^[b]	$E_{LUMO,CV}$ (eV) ^[c]	$E_{g,opt}$ (eV) ^[d]
HBC-AQ	364; 392; 448	558	8.2	-5.83	-3.42	2.41
HBC-NMI	361; 394; 410; 450	482; 502	8.8	-6.01	-3.31	2.70
HBC-PMI	363; 392; 498; 523	571	45	-5.67	-3.51	2.16

[a] Absorption peaks (λ_{abs}), emission maxima (λ_{em}), and fluorescence quantum yields (Φ_F) were recorded in toluene. [b] HOMO level (E_{HOMO}) was calculated by $E_{HOMO} = E_{LUMO,CV} - E_{g,opt}$. [c] LUMO level ($E_{LUMO,CV}$) was determined by CV. [d] Optical energy gaps ($E_{g,opt}$) were estimated from the onset of the absorption spectra in toluene.

Cyclic voltammetry (CV) analyses of the HBC-acceptor dyads were performed in THF with 0.1 M $Bu_4N^+PF_6^-$ electrolyte, an Ag reference electrode, and a platinum counter electrode, giving reversible reduction (Table 1 and Figure S5). The lowest unoccupied molecular orbitals (LUMO) energy levels were estimated from the onset of reduction and found to be

shifted, depending on the attached acceptor units: -3.42 , -3.31 , and -3.51 eV for **HBC-AQ**, **-NMI**, and **-PMI**, respectively. The highest occupied molecular orbital (HOMO) energy levels could then be calculated using the estimated optical energy gaps to be -5.83 , -6.01 , and -5.67 eV for **HBC-AQ**, **-NMI**, and **-PMI**, respectively.

Density functional theory (DFT) calculations provided further insight into the CT interactions of the HBC-acceptor dyads, which disclosed that the LUMOs were generally distributed over the acceptor units whereas the HOMOs were distributed on the HBC unit (Figure 3). Especially, in the case of **HBC-AQ**, LUMO and HOMO were completely separated onto the acceptor (**AQ**) and donor (**HBC**) units, respectively, which suggested strong CT interactions. On the other hand, LUMO of **HBC-NMI** was partially extended to the HBC moiety. Moreover, the HOMO of **HBC-PMI** was moderately spread on to the **PMI** unit. These theoretical results were in agreement with experimental observation showing strong CT interactions in **HBC-AQ** and weaker interactions in **HBC-NMI** and **-PMI**. Additionally, the calculated dihedral angle (θ) between **HBC** and **AQ** units at the covalently attached bond was found to be 36° . The dihedral angles were similar for **HBC-NMI** and **-PMI** ($\sim 54^\circ$) due to the comparable steric demand (Table S2).

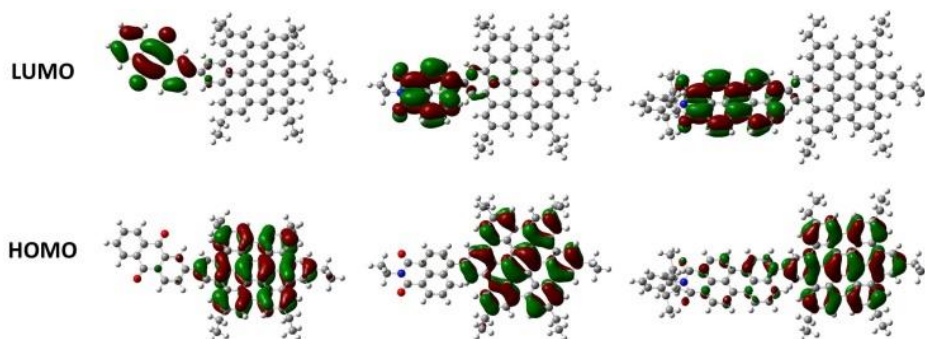


Figure 3. Calculated HOMOs and LUMOs of **HBC-AQ** (left), **-NMI** (middle), and **-PMI** (right) using DFT, B3LYP/6-31G (d).

The influence of the different acceptor units on the supramolecular organization of the HBC-acceptor dyads was next investigated by differential scanning calorimetry (DSC) and two-dimensional wide-angle X-ray scattering (2D-WAXS) (Figure 4). The DSC scans of **HBC-AQ** and **-NMI** exhibited one phase transition between the crystalline and liquid crystalline phase at 82.2 and 96.7 °C, respectively (Figure 4A and S3). The slightly higher temperature for **HBC-NMI** was surprising, considering that the **NMI** unit possessed additional branched alkyl side chains, which were supposed to weaken the molecular interactions. In contrast to

the observation of phase transitions for **HBC-AQ** and **-NMI**, **HBC-PMI** did not reveal any peak in the DSC measurement.

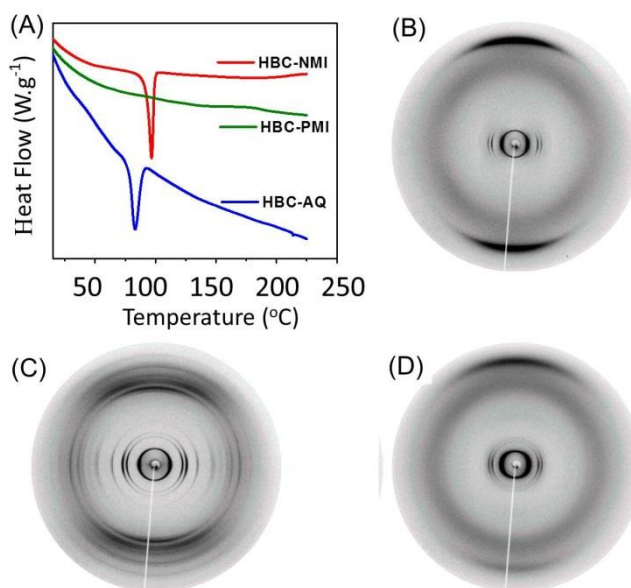


Figure 4. (A) DSC curves of HBC derivatives recorded at 10 °C/min under N₂ atm. (B–D) 2D-WAXS of **HBC-NMI** recorded at (B) 120 °C and (C) 30 °C and (D) **HBC-PMI** at 30 °C. The fiber samples were placed vertically in front of the detector.

Based on the DSC results, the supramolecular organization in bulk was investigated by using X-ray scattering. For these measurements, macroscopically aligned fiber samples were obtained through extrusion.⁴²⁻⁴³ The scattering was collected by an area detector in the wide-angle range. As shown in Figure 4B and C, two typical 2D-WAXS patterns of **HBC-NMI** recorded at 120 and 30 °C, respectively, indicated its discotic LC columnar organization. In the LC phase, the disc-shaped molecules were packed on top of each other forming columnar structures (Figure 4B). The intracolumnar π -stacking distance of 0.35 nm was derived from meridional reflections, while the equatorial ones were attributed to the intercolumnar arrangement with stacks being oriented along the fiber axis. From the position of these scattering intensities a hexagonal unit cell with a parameter of $a_{\text{hex}} = 2.94$ nm was determined. Interestingly, **HBC-AQ** assembled in an identical hexagonal fashion, as the observation for **HBC-NMI**, in the LC phase ($a_{\text{hex}} = 2.88$ nm) (Figure 4). In the crystalline phase, **HBC-AQ** and **-NMI** organized also in similar supramolecular structures (Figure 4C and S4), where the columnar hexagonal organization was maintained with a slightly smaller a_{hex} parameter of 2.40 nm. In the stacks, the molecules displayed a herringbone tilting towards the columnar axis. In contrast to **HBC-AQ** and **-NMI**, **HBC-PMI** revealed solely a LC phase over the

7.2 Main text

investigated temperature range without becoming crystalline (Figure 4D). The packing parameter was $a_{\text{hex}} = 2.92$ nm for the hexagonal unit cell and 0.35 nm for the π -stacking distance.

In summary, three HBC-acceptor dyads, bearing 9,10-anthraquinone, naphthalene-1,8-dicarboximide, and perylene-3,4-dicarboximide units, were prepared through two synthetic routes, namely via the coupling of the acceptor unit before and after the cyclodehydrogenation of the HBC core. Photophysical, electrochemical, and liquid-crystalline properties of the HBC-acceptor dyads were studied, which demonstrated different degrees of intramolecular CT interactions and modulation of the energy gaps, depending on the acceptor units. These results marked the possibility of sensitively controlling the optoelectronic properties of such nanographene molecules through coupling with different acceptor units. Furthermore, the reported synthetic protocols can now be applied to larger nanographene molecules and graphene nanoribbons, paving the way towards new generation of nanographene-acceptor systems.

7.3 Supporting information

General

All reagents were purchased from commercial sources and used without further purification unless otherwise stated. Thin layer chromatography was carried out using pre-coated aluminum sheets with silica gel 60 F254 (Merck). Column chromatography was performed using Merck silica gel 60, 40-63 μm (230-400 mesh). ^1H NMR and ^{13}C NMR spectra were recorded in the listed deuterated solvents on a Bruker AVANCE 250, 300, and 500 MHz spectrometers. Mass spectra were obtained using Field desorption mass spectra were obtained on a VG Instruments ZAB 2-SE-FPD spectrometer. Matrix-assisted laser desorption time-of-flight mass spectrometer (MALDI-TOF) mass spectra were taken on a Bruker Reflex II MALDI-TOF mass spectrometer with dithranol as matrix and calibrated against a mixture of $\text{C}_{60}/\text{C}_{70}$. The UV-vis spectra were recorded at 298 K on a Perking-Elmer Lambda 900 spectrophotometer.

CV measurements were carried out on a computer-controlled GSTAT12 in a three-electrode cell in a THF solution of Bu_4NPF_6 (0.1 M) with a scan rate of 100 mV/s at room temperature, with using glassy carbon electrode as the working electrode, Pt wire as the counter electrode, Ag electrode as the reference electrode. HOMO and LUMO energy levels were calculated from the onsets of the first oxidation and reduction peak by empirical formulas $E_{\text{HOMO}} = -(E_{\text{onset}}^{\text{ox1}} + 4.8)$ eV, $E_{\text{LUMO}} = -(E_{\text{onset}}^{\text{red1}} + 4.8)$ eV while the potentials were determined using ferrocene (Fc) as standard. Density functional theory (DFT) calculations were carried out at the B3LYP/6-31G (d) level using Gaussian 09⁴⁴ and molecular structures were generated using GaussView 5.0.9⁴⁵. The side chains were set to CH_2CH_3 (ethyl) to simplify the calculation. Thermogravimetry analysis (TGA) was carried out on a Mettler 500 Thermogravimetry Analyzer with heating rates of 10 K/min. Differential scanning calorimetry (DSC) were measured on a Mettler DSC 30 with heating and cooling rates of 10 K/min.

Synthesis

Unless otherwise noted, materials were purchased from Aldrich, Acros, TCI, and other commercial suppliers and used as received unless otherwise specified. The monobromo-substituted HPB and HBC derivatives, 4-bromo-4'-dodecyl-3',4',5',6'-tetrakis(4-dodecylphenyl)-1,1':2',1''-terphenyl (**HPB-Br**) and 2-bromo-5,8,11,14,17-pentadodecylhexa-peri-hexabenzocoronene (**HBC-Br**), respectively,²⁴ 4-bromo-N-(2-ethylhexyl)-1,8-naphthalimide,⁴⁶ and boronic acids N-(2,6-diisopropylphenyl)-9-(4,4,5,5-tetramethyl-1,3,2-

7.3 Supporting information

dioxaborolan-2-yl)perylene-3,4-dicarboximide (**PMI-boro**)³⁸ and 2-(4,4,5,5-tetramethyl-1,3,2-dioxaborolan-2-yl)anthracene-9,10-dione (**AQ-boro**)⁴⁷ were prepared following the reported procedures.

N-(2-ethylhexyl)-4-(4,4,5,5-tetramethyl-1,3,2-dioxaborolan-2-yl)naphthalene-1,8-

dicarboximide (NMI-boro): Pd(dppf)Cl₂ (300 mg, 0.41 mmol) was added to a well-degassed solution of 4-Bromo-N-(2-ethylhexyl)-1,8-naphthalimide (3.88 g, 10.0 mmol), bis(pinacolato)diboron (2.54 g, 10.0 mmol), and KOAc (2.00 g, 20.4 mmol) in anhydrous 1,4-dioxane (100 mL). The resulting mixture was stirred at 70 °C for 16 h under argon atmosphere. After cooling, the mixture was evaporated to dryness and taken up with dichloromethane (DCM). The organic layer was washed with water, dried over MgSO₄, filtered, and evaporated to dryness. Purification by column chromatography (SiO₂, 1:4 DCM/hexane) afforded **NMI-boro** in 85% yield (3.70 g). ¹H NMR (250 MHz, CDCl₃) δ = 9.12 (d, *J* = 7.5 Hz, 1H), 8.61 (d, *J* = 7.5 Hz, 1H), 8.57 (d, *J* = 7.5 Hz, 1H), 8.30 (d, *J* = 7.5 Hz, 1H), 7.78 (t, *J*₁ = *J*₂ = 7.5 Hz, 1H), 4.16–4.08 (m, 2H), 1.98–1.93 (m, 1H), 1.45 (s, 12H), 1.40–1.31 (m, 8H), 0.96–0.84 (m, 6H). ¹³C NMR (75 MHz, CDCl₃) δ = 164.71, 164.70, 135.77, 135.25, 134.84, 130.88, 129.79, 127.91, 127.07, 124.78, 122.66, 84.55, 44.18, 37.90, 30.77, 28.73, 24.97, 24.10, 23.06, 14.08, 10.66. MS (FD): calcd. for C₂₆H₃₄BNO₄ [*M*]⁺ 435.4 (100.0%, *m/z*) found 435.3.

Suzuki coupling reaction procedure: To a solution of **HPB-Br** or **HBC-Br** (1 eq.) and corresponding aryl boronic ester (2 eq.) in toluene (2 mL) was added a solution of K₂CO₃ (4 eq.) in water and EtOH (1:1, 2 mL). The reaction mixture was degassed and the catalyst (Pd(PPh₃)₄, 0.1 eq) along with ligand (SPhos, 0.2 eq) were added under the argon flow. The reaction mixture was stirred at 90 °C for 16 hours under argon atmosphere. After cooling down to room temperature, methanol was added followed by extraction with chloroform. The combined organic layers were washed with water and dried over Na₂SO₄. The solvents were removed in vacuo and the crude was further purified by column chromatography on silica gel to afford the desired products.

Synthesis of HPB-AQ: Following the Suzuki coupling procedure, reaction between **HPB-Br** (50 mg, 0.034 mmol) and **AQ-boro** (28.7 mg, 0.086 mmol) afforded **HPB-AQ** after flash column chromatography (3 % ethyl acetate in hexane) as yellow powder (40 mg, 74%). ¹H

NMR (250 MHz, CD₂Cl₂) δ = 8.36–8.35 (1H, AN), 8.29–8.22 (m, 3H, AN), 7.87–7.78 (m, 3H, AN), 7.28 (d, J = 12 Hz, 2H), 6.99 (d, J = 12 Hz, 2H), 6.78–6.66 (m, 20H), 2.39–2.34 (m, 10H), 1.55–1.11 (m, 100H), 0.88–0.83 (m, 15H). ¹³C NMR (63 MHz, CD₂Cl₂) δ = 183.48, 183.12, 146.90, 142.89, 141.32, 141.06, 140.76, 140.25, 140.07, 138.72, 138.65, 138.56, 135.58, 134.50, 134.29, 134.19, 134.13, 132.86, 132.35, 132.33, 131.79, 128.21, 127.56, 127.49, 127.24, 127.04, 125.75, 125.37, 35.85, 35.73, 32.51, 32.48, 31.89, 31.76, 30.33, 30.32, 30.27, 30.16, 30.11, 29.97, 29.91, 29.47, 29.25, 23.27, 23.24, 14.46. MS (FD): calcd. for C₁₁₆H₁₅₆O₂ [M]⁺ 1583 (100.0%, m/z) found 1582.

Synthesis of HPB-NMI: Following the Suzuki coupling procedure, reaction between **HPB-Br** (50 mg, 0.034 mmol) and 1,8-naphthalene monoimide boronic ester (**NMI-boro**, 29.4 mg, 0.068 mmol) afforded **HPB-NMI** after flash column chromatography (20% DCM in hexane) as colorless oil (52 mg, 90%). ¹H NMR (300 MHz, CD₂Cl₂) δ = 8.56 (d, J = 6.3 Hz, 1H), 8.51 (d, J = 7.5 Hz, 1H), 7.85 (d, J = 7.5 Hz, 1H), 7.63 (t, J = 7.5 Hz, 1H), 7.50 (d, J = 7.5 Hz, 1H), 6.99 (s, 2H), 6.98 (s, 2H), 6.82–6.67 (m, 20H), 4.09 (m, 2H), 2.43–2.35 (m, 10H), 1.95–1.91 (m, 1H), 1.41–1.10 (m, 109H), 0.92–0.85 (m, 22H). ¹³C NMR (75 MHz, CD₂Cl₂) δ = 165.03, 164.81, 147.44, 142.35, 141.44, 141.05, 140.82, 140.38, 140.34, 140.18, 140.14, 138.74, 138.70, 135.96, 133.00, 132.28, 131.99, 131.87, 131.33, 129.16, 128.50, 127.94, 127.24, 127.13, 123.48, 122.20, 44.47, 38.51, 35.94, 35.89, 32.55, 32.52, 31.95, 31.93, 31.91, 31.33, 30.37, 30.35, 30.30, 30.26, 30.23, 30.19, 30.14, 30.07, 30.00, 29.95, 29.50, 29.46, 29.29, 24.61, 23.67, 23.30, 23.28, 14.48, 14.46, 11.01. MS (MALDI-TOF, positive) m/z (%) calcd. for C₁₂₂H₁₇₁NO₂ [M]⁺ 1683.3 (27), 1684.3 (36), 1685.3 (24), 1686.3 (11), 1687.4 (4), found 1683.6 (29), 1684.6 (36), 1685.6 (21), 1686.6 (11), 1687.7 (3).

Synthesis of HPB-PMI: The Suzuki coupling reaction of **HPB-Br** (40 mg, 0.028 mmol) and **PMI-boro** (41.8 mg, 0.069 mmol) was performed at 105 °C subsequent purification by flash column chromatography using hot toluene as eluent afforded **HPB-PMI** as red oil (28 mg, 54%). ¹H NMR (250 MHz, CD₂Cl₂) δ = 8.62 (d, J = 7.5 Hz, 2H), 8.52, 8.49–8.45 (m, 4H), 7.75–7.41 (m, 8H), 7.37–7.34 (d, J = 7.5 Hz, 2H), 6.85–6.66 (m, 20H), 2.81–2.70 (m, 2H), 2.45–2.35 (m, 10H), 1.44–1.08 (m, 100H), 0.88–0.78 (m, 27H). ¹³C NMR (176 MHz, CD₂Cl₂) δ = 164.62, 146.71, 144.31, 141.88, 141.39, 141.02, 140.86, 140.58, 140.30, 140.18, 140.13, 138.81, 138.74, 138.45, 138.32, 136.87, 133.35, 132.77, 132.71, 132.41, 132.22, 132.01, 131.89, 131.19, 130.17, 129.80, 129.69, 129.10, 129.03, 128.80, 128.66, 128.59, 128.44,

7.3 Supporting information

127.46, 127.25, 127.13, 124.55, 124.18, 121.38, 121.23, 120.86, 120.58, 35.98, 35.89, 32.54, 32.45, 31.98, 31.90, 30.34, 30.30, 30.24, 30.17, 30.14, 29.99, 29.89, 29.64, 29.50, 24.28, 23.30, 23.22, 14.48, 14.43. MS (FD): calcd. for C₁₃₆H₁₇₅NO₂ [*M*]⁺ 1856 (100.0%, *m/z*) found 1855.

General method of cyclodehydrogenation using FeCl₃: A solution of **HPB** derivative (0.01 mmol) in dichloromethane (10 mL) was degassed by bubbling with argon for 15 min. To this solution was added FeCl₃ (0.4 mmol) in nitromethane (0.5 mL). The mixture was allowed to react at room temperature for 1 h under continuous stream of argon (bubbling). Methanol was then added to the reaction mixture, inducing precipitation of the product. The precipitate was collected by filtration and the crude product was purified by flash column chromatography using hot toluene as eluent to afford the HBC-acceptor dyads.

Synthesis of HBC-AQ:

Cyclodehydrogenation reaction of **HPB-AQ** (10 mg) afforded **HBC-AQ** as orange-red solid (4.5 mg, 46% yield).

Suzuki coupling reaction of **HBC-Br** (5 mg) and **AQ-boro** gave **HBC-AQ** as orange-red solid (4.3 mg, 79% yield).

¹H NMR (500 MHz, 110 °C, C₂D₂Cl₄) δ = 8.79 (s, 2H), 8.54–8.20 (m, 15H), 7.92–7.89 (m, 2H), 3.16 (m, 6H), 3.08–3.07 (m, 4H), 2.14–2.05 (m, 10H), 1.77–1.36 (m, 90H), 0.98–0.96 (m, 3H). ¹³C NMR (126 MHz, 110 °C, J-mod, C₂D₂Cl₄) δ = 183.01, 182.45, 147.42, 140.10, 140.06, 139.94, 134.16, 134.07, 133.93, 133.82, 132.48, 132.17, 129.93, 129.81, 129.60, 129.48, 129.01, 127.91, 127.28, 127.15, 125.69, 124.65, 122.96, 122.89, 121.40, 121.15, 121.01, 119.79, 119.41, 119.16, 119.01, 118.25, 37.20, 37.07, 31.92, 31.89, 31.87, 31.75, 30.10, 29.92, 29.86, 29.83, 29.76, 29.67, 29.65, 29.29, 29.27, 22.56, 22.54, 13.85. MS (MALDI-TOF, positive) *m/z* (%) calcd. for C₁₁₆H₁₄₄O₂ [*M*]⁺ 1569.1 (28), 1570.1 (36), 1571.1 (23), 1572.1 (10), 1573.1 (3), 1574.1 (2), found 1569.0 (25), 1569.9 (34), 1570.9 (24), 1572.0 (12), 1572.9 (3), 1574.0 (2).

Synthesis of HBC-NMI:

Cyclodehydrogenation reaction of **HPB-NMI** (20 mg) delivered **HBC-NMI** (18 mg, 91% yield) as yellow-orange solid.

Following Suzuki coupling procedure, reaction between HBC-Br (25 mg, 0.017 mmol) and NMI-boro (25 mg, 0.053 mmol) afforded HBC-NMI after column chromatography as yellow-orange powder (28 mg, 94%).

^1H NMR (500 MHz, 100 °C, $\text{C}_2\text{D}_2\text{Cl}_4$) δ = 9.07 (b, 2H), 8.95 (b, 1H), 8.77-8.61 (m, 11H), 8.25 (b, H), 7.81 (b, 1H), 4.33 (m, 2H), 3.20 (m, 10H), 2.18–2.06 (m, 12H), 1.71–1.35 (m, 108H), 1.11–0.94 (m, 21H). ^{13}C NMR (126 MHz, 100 °C, J-mod, $\text{C}_2\text{D}_2\text{Cl}_4$) δ = 164.54, 164.38, 147.64, 140.97, 140.85, 140.77, 136.27, 132.70, 131.24, 130.85, 130.80, 130.60, 130.27, 130.11, 130.06, 129.88, 129.70, 129.11, 128.57, 127.12, 125.20, 123.73, 123.58, 123.38, 123.32, 122.72, 122.48, 122.25, 121.75, 121.70, 121.64, 120.21, 120.00, 44.55, 38.35, 37.16, 31.99, 31.92, 31.89, 31.85, 31.27, 29.90, 29.87, 29.82, 29.77, 29.72, 29.67, 29.65, 29.60, 29.29, 29.25, 28.93, 24.53, 23.14, 22.59, 22.56, 14.00, 13.94, 13.92, 10.88. MS (MALDI-TOF, positive) m/z (%) calcd. for $\text{C}_{122}\text{H}_{159}\text{NO}_2$ $[M]^+$ 1670.2 (26), 1671.2 (35), 1672.2 (24), 1673.2 (11), 1674.3 (4), 1675.3 (1), found 1670.1 (26), 1671.1 (34), 1672.1 (23), 1673.1 (12), 1674.2 (4), 1675.2 (1).

Synthesis of HBC-PMI:

Following cyclodehydrogenation procedure, HPB-PMI (30 mg, 0.016 mmol) gave HBC-PMI (9.6 mg, 32%) as black solid. The relatively low yield is presumably due to the loss of the product while performing the silica gel column chromatography.

Suzuki coupling reaction between HBC-Br (25 mg, 0.017 mmol) and PMI-boro (25 mg, 0.041 mmol) at 90 °C afforded HBC-PMI after column chromatography as black solid (26 mg, 81%).

^1H NMR (500 MHz, 110 °C, $\text{C}_2\text{D}_2\text{Cl}_4$) δ = 9.17 (s, 2H), 8.80–8.56 (m, 16H), 8.38 (d, J = 7.5 Hz, 1H), 8.16(d, J = 7.5 Hz, 1H), 7.69 (t, J = 7.5 Hz, 1H), 7.54, (t, J = 7.5 Hz, 1H), 7.41 (d, J = 7.5 Hz, 2H), 3.23 (m, 10H), 2.91 (m, 2H), 2.12 (m, 10H), 1.73–1.31 (m, 102), 0.95–0.91 (m, 15H). ^{13}C NMR (126 MHz, 110 °C, J-mod, $\text{C}_2\text{D}_2\text{Cl}_4$) δ = 163.84, 163.83, 146.12, 144.38, 140.91, 140.71, 137.70, 137.60, 137.33, 133.51, 131.86, 131.83, 131.73, 130.73, 130.60, 130.36, 130.12, 129.96, 129.93, 129.75, 129.72, 129.15, 129.13, 128.90, 127.37, 127.25, 125.84, 125.06, 123.93, 123.89, 123.80, 123.55, 123.53, 123.45, 123.02, 123.01, 122.16, 121.75, 121.73, 121.62, 120.57, 120.33, 120.23, 120.02, 119.38, 37.17, 31.93, 31.84, 31.81, 29.89, 29.85, 29.79, 29.74, 29.69, 29.61, 29.57, 29.31, 29.23, 29.19, 23.98, 22.53, 22.49, 13.85, 13.82. MS (MALDI-TOF, positive) m/z (%) calcd. for $\text{C}_{136}\text{H}_{163}\text{NO}_2$ $[M]^+$ 1842.3 (23), 1843.3 (34), 1844.3 (26), 1845.3 (13), 1846.3 (5), found 1842.2 (23), 1843.3 (32), 1844.2 (27), 1845.3 (14), 1846.2 (5).

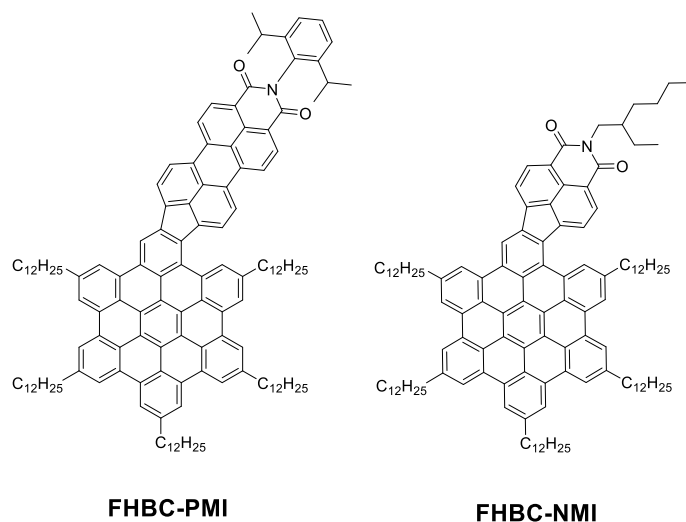


Figure S1: Possible five-membered-ring formation during the cyclodehydrogenation reaction of *HPB-PMI* and *HPB-NMI* using FeCl_3 as reagent.

Thermal properties

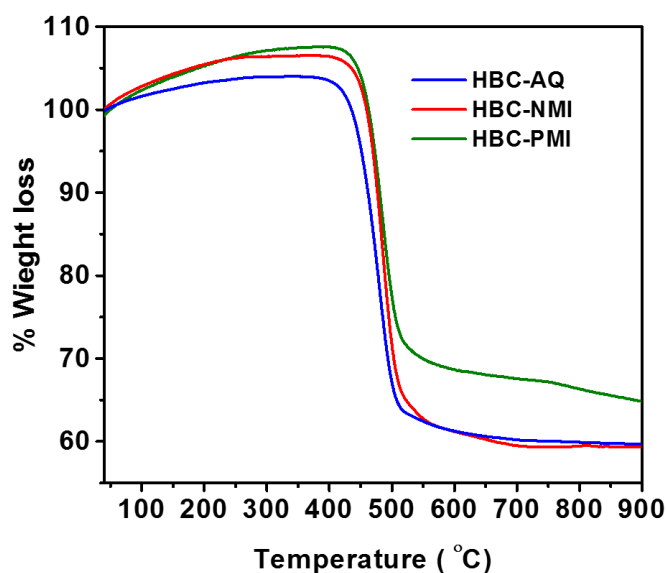


Figure S2. TGA curves of the *HBC-acceptor dyads* measured under a nitrogen atmosphere at a heating rate of 10 °C/min.

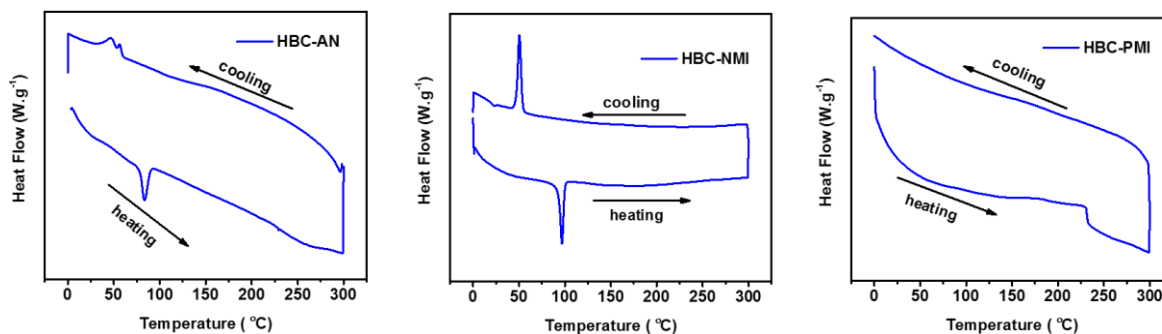


Figure S3. DSC heating and cooling curves of the *HBC-acceptor dyads* measured under a nitrogen atmosphere at a heating and cooling rate of 10 °C/min.

Two-dimensional wide-angle X-ray scattering (2D-WAXS)

2D-WAXS measurements were performed using a custom setup consisting of the Siemens Kristalloflex X-ray source (copper anode X-ray tube, operated at 35 kV/20 mA), Osmic confocal MaxFlux optics, two collimating pinholes (1.0 and 0.5 mm Owis, Germany) and an antiscattering pinhole (0.7 mm–Owis, Germany). The patterns were recorded on a MAR345 image plate detector (Marresearch, Germany). The samples were prepared by filament extrusion using a home-built mini-extruder.

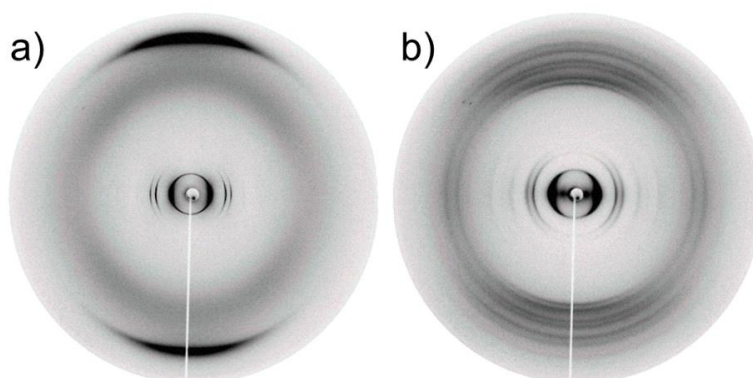


Figure S4. 2DWAXS of **HBC-AQ** recorded at a) 120 °C and b) 30 °C. The fiber sample was placed vertically in front of the detector.

Cyclic voltammetry

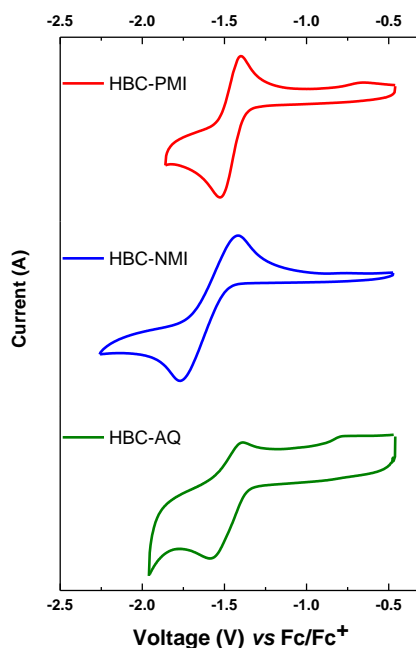


Figure S5. Cyclic voltammograms of **HBC-acceptor dyads** in THF with 0.1 M $\text{Bu}_4\text{N}^+\text{PF}_6^-$ electrolyte, an Ag reference electrode, a platinum counter electrode, and ferrocene as an external standard.

7.3 Supporting information

UV-vis absorption and photoluminescence spectra in different solvents

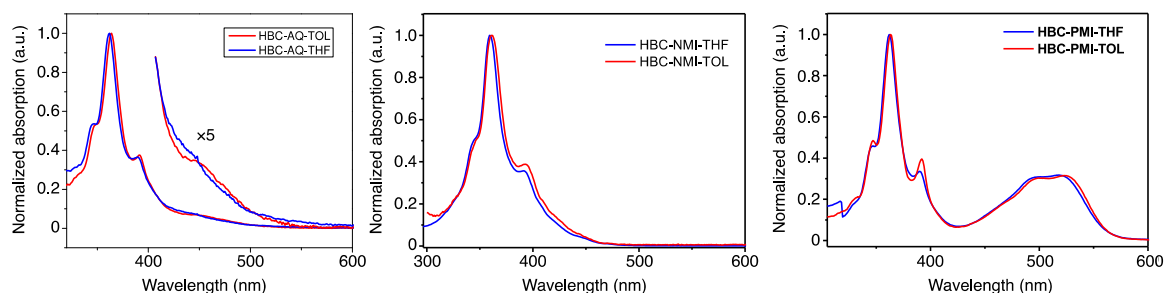


Figure S6. Normalized UV-vis absorption spectra of HBC-acceptor dyads in THF and toluene solvents at room temperature.

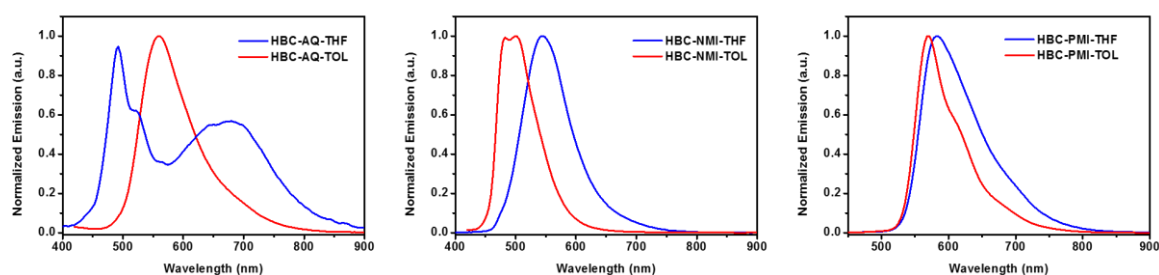


Figure S7. Normalized photoluminescence spectra of HBC-acceptor dyads in THF and toluene solvents at room temperature.

Table S1.

Compound	λ_{abs} (nm)		λ_{em} (nm)		Φ_{F} (%)
	THF	Toluene	THF	Toluene	
HBC-AQ	361; 391; ~450	364; 392; 448	492; 680	561	8.2
HBC-NMI	359; 392; 450	361; 394; 410; 450	545	482; 502	8.8
HBC-PMI	362; 390; 496; 519	363; 392; 498; 523	581	571	45

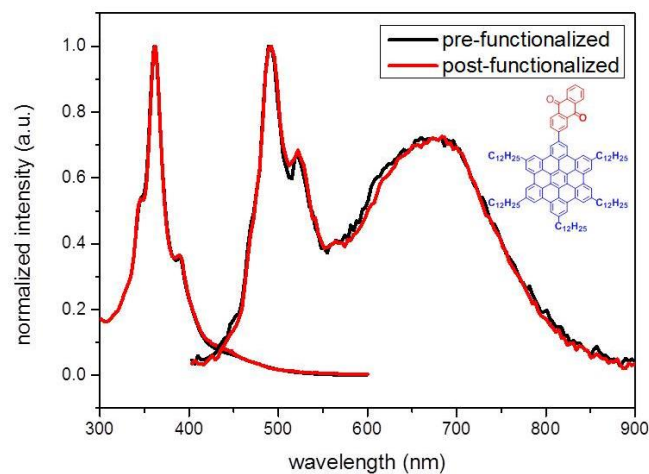


Figure S8. Normalized absorption and emission spectra of pre- and post-functionalized HBC-AQ, recorded in THF solutions at a concentration of 10^{-5} mol/L. Excitation wavelength in the photoluminescence spectroscopy measurements was 400 nm.

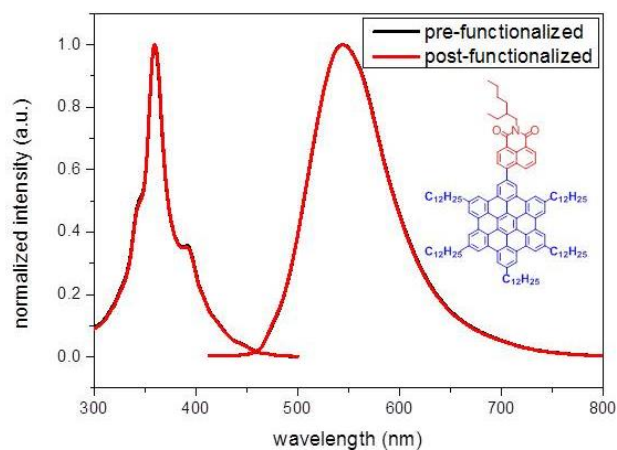


Figure S9. Normalized absorption and emission spectra of pre- and post-functionalized **HBC-NMI**, recorded in THF solutions at a concentration of 10^{-5} mol/L. Excitation wavelength in the photoluminescence spectroscopy measurements was 400 nm.

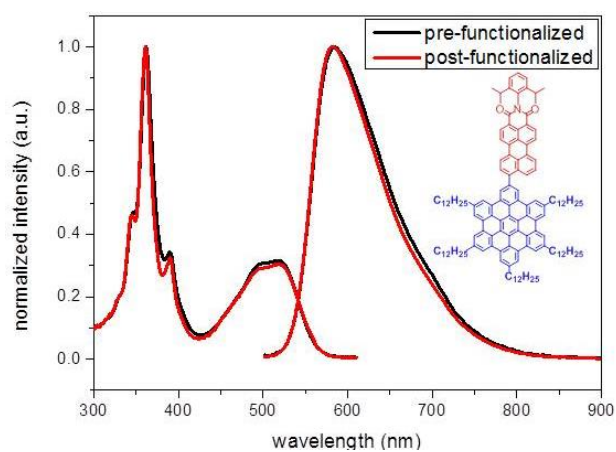
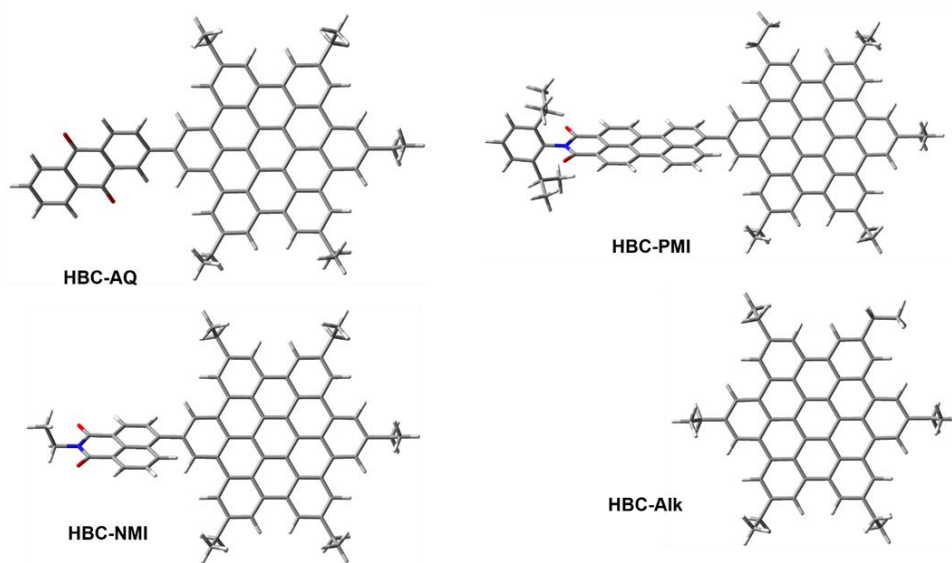
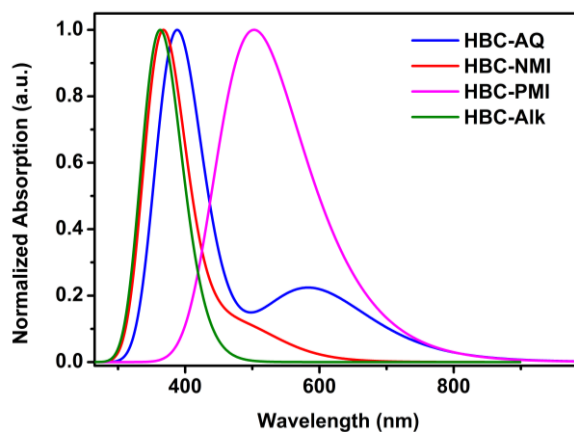


Figure S10. Normalized absorption and emission spectra of pre- and post-functionalized **HBC-PMI**, recorded in THF solutions at a concentration of 10^{-5} mol/L. Excitation wavelength in the photoluminescence spectroscopy measurements was 400 nm.

Theoretical calculations

Figure S11. Geometry optimized structures of **HBC** derivatives.Figure S12. Calculated UV-vis absorption spectra of the **HBC**-acceptor dyads (TD-SCF, B3LYP/6-31G(d)).Table S2. Calculated HOMO and LUMO levels, energy gap, absorption maxima, and dihedral angles (θ) of functionalized **HBC** dyads using DFT, B3LYP/6-31G (d).

COMPOU ND	$E_{\text{HOMO, CALC}}$ (eV)	$E_{\text{LUMO, C ALC}}$ (eV)	$E_{\text{G, C ALC}}$ (eV)	$\lambda_{\text{ABS, CALC}}$ (nm)	θ ($^{\circ}$)
HBC-AQ	-5.16	-2.76	2.40	388; 585	35.8
HBC-NMI	-5.23	-2.35	2.88	368; 471	53.5
HBC-PMI	-5.19	-2.77	2.42	503	54.3
HBC-Alk	-5.01	-1.48	3.53	363	—

^1H and ^{13}C NMR spectra

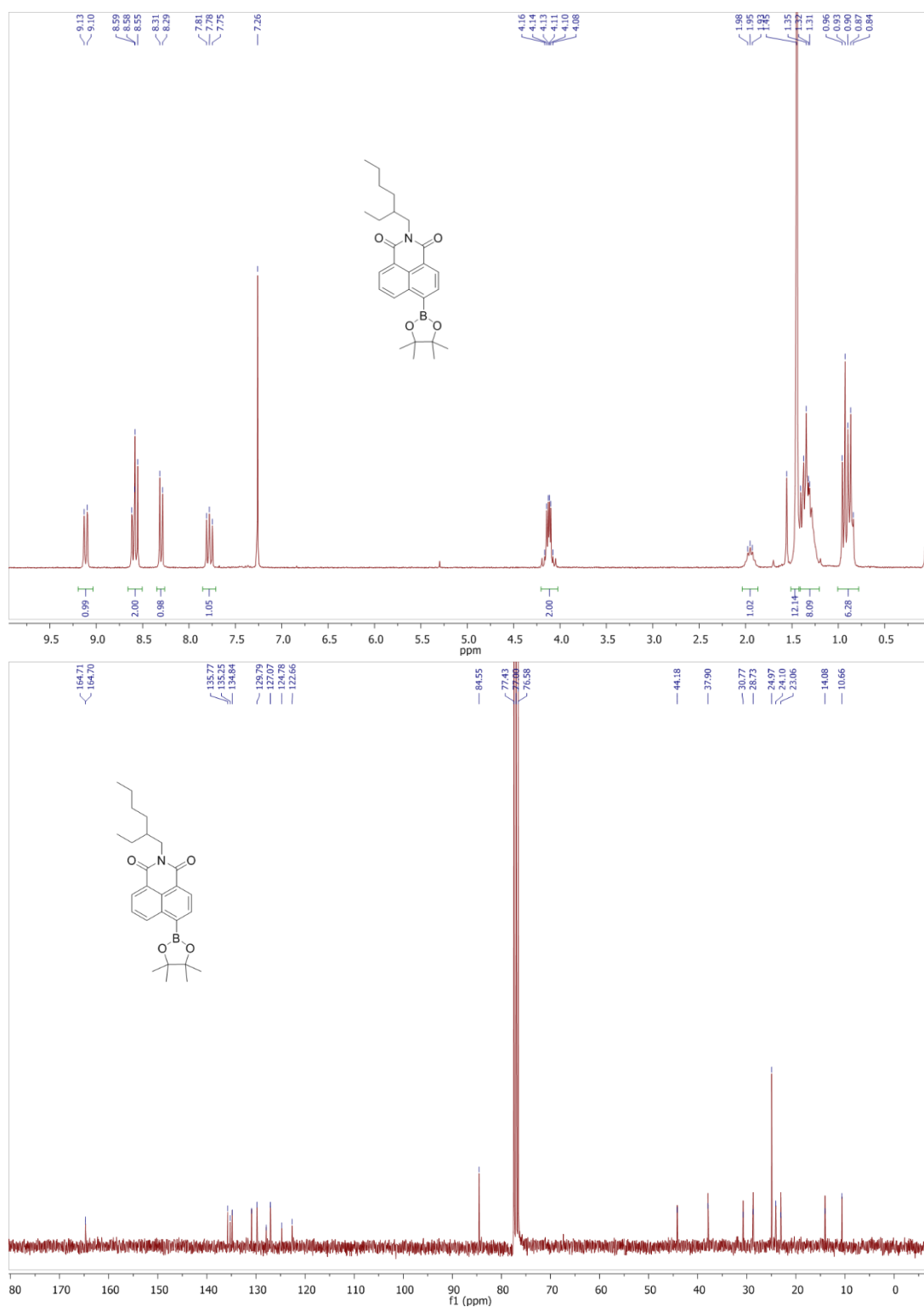


Figure S13. ^1H (above) and ^{13}C NMR (below) spectra of NMI-boro in CDCl_3 .

7.3 Supporting information

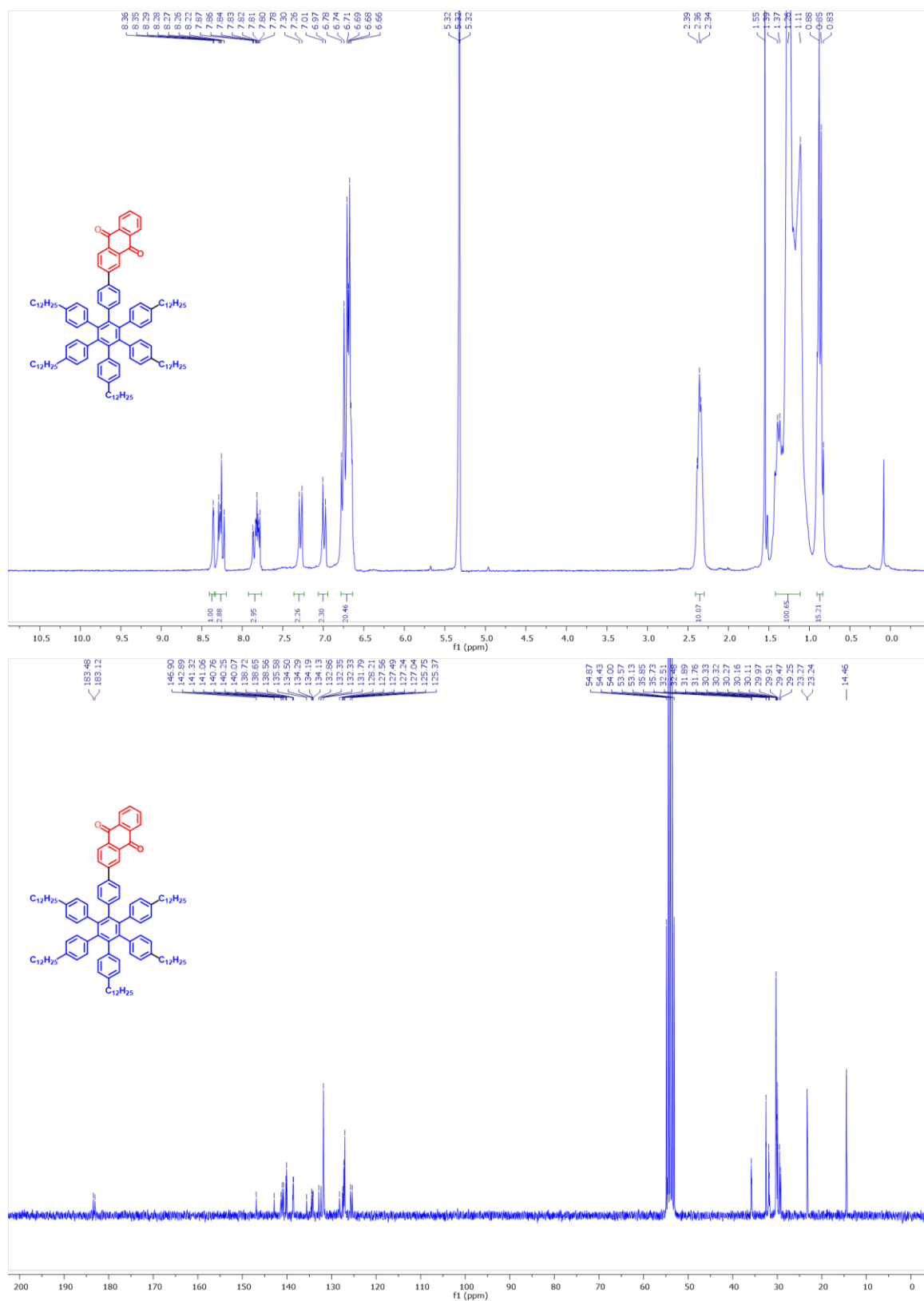


Figure S14. ¹H (above) and ¹³C NMR (below) spectra of HPB-AQ in CD₂Cl₂.

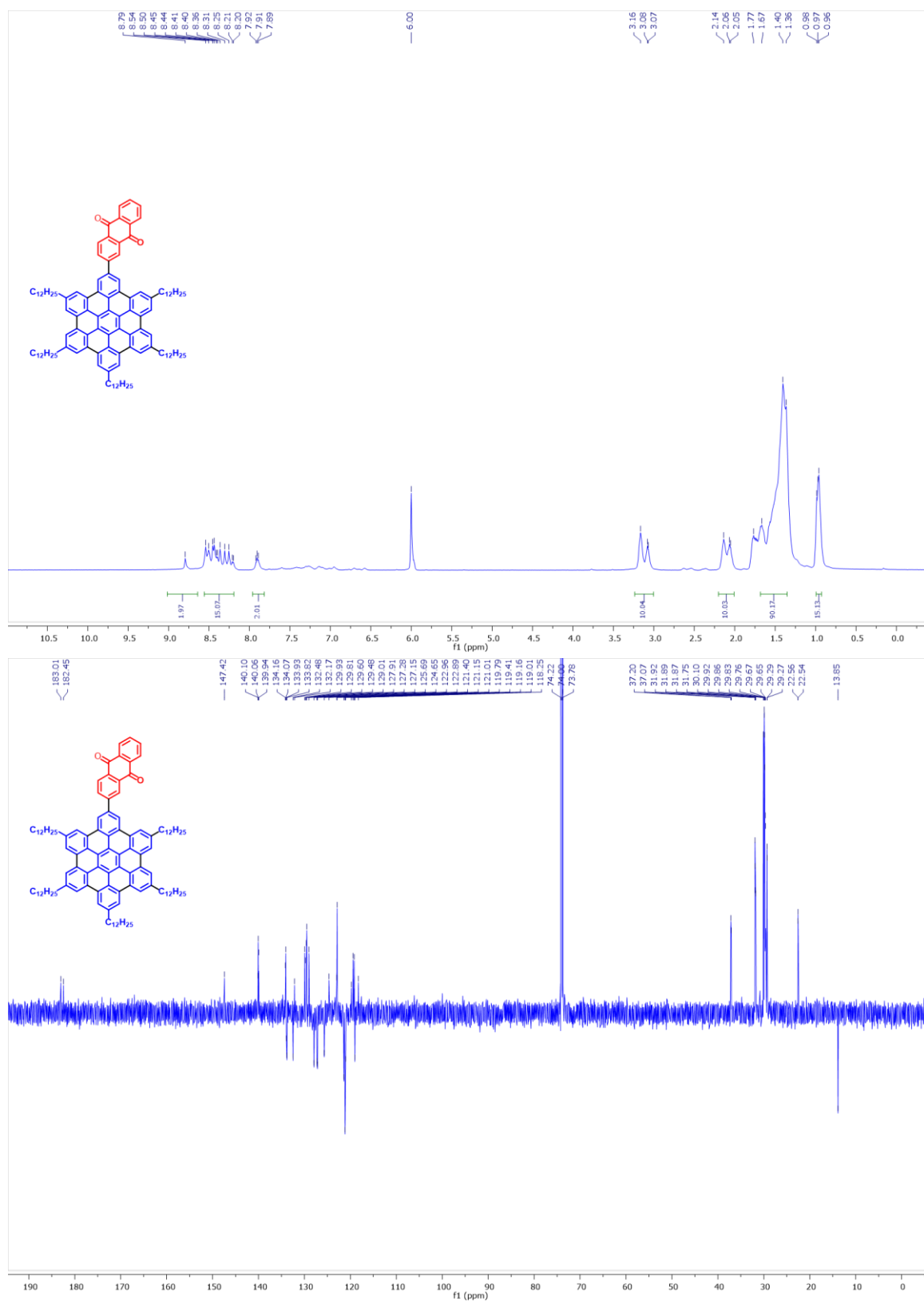


Figure S15. ^1H (above) and ^{13}C NMR (below) spectra of HBC-AQ in $\text{C}_2\text{D}_2\text{Cl}_4$.

7.3 Supporting information

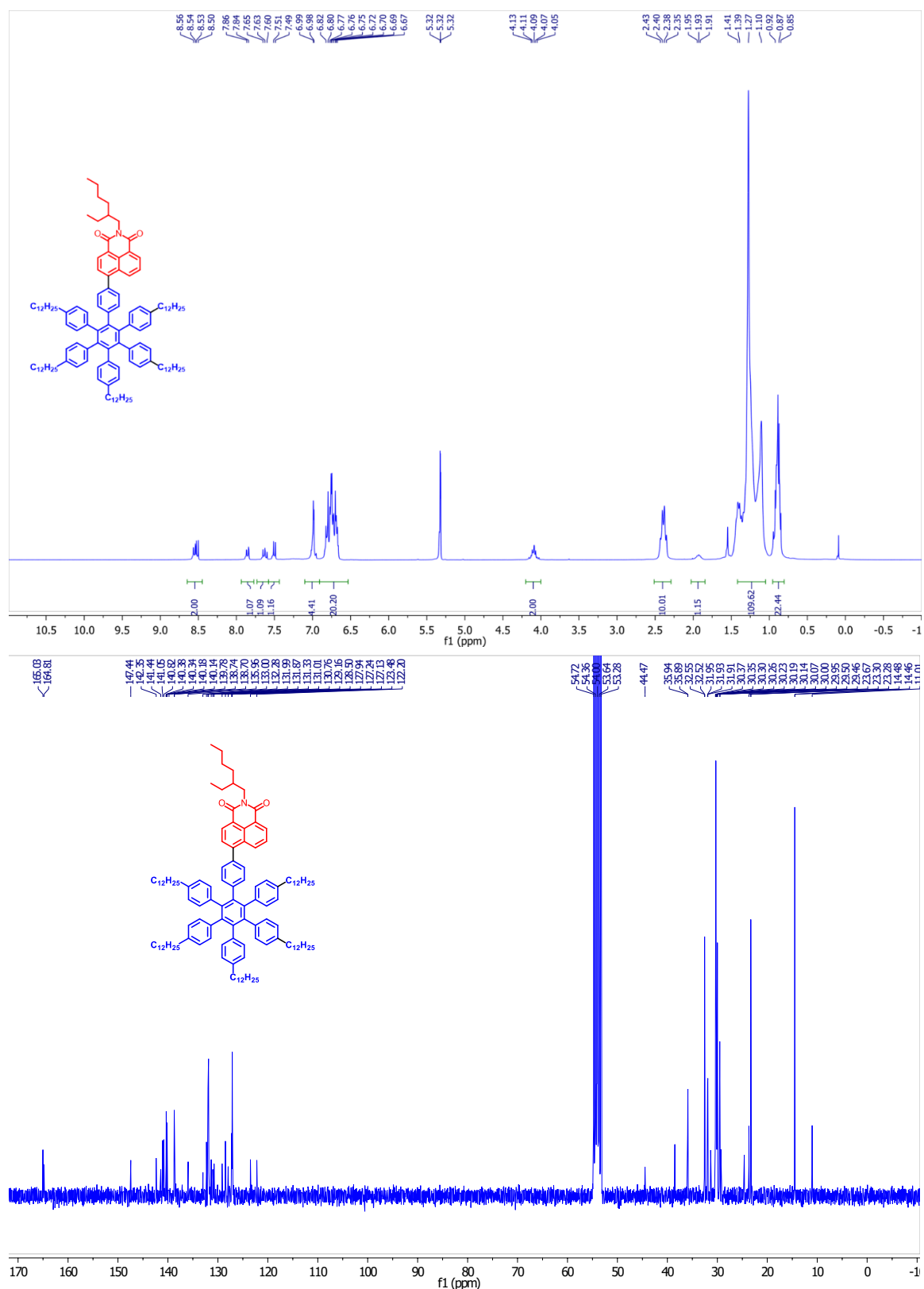


Figure S16. ¹H (above) and ¹³C NMR (below) spectra of HPB-NMI in CD₂Cl₂.

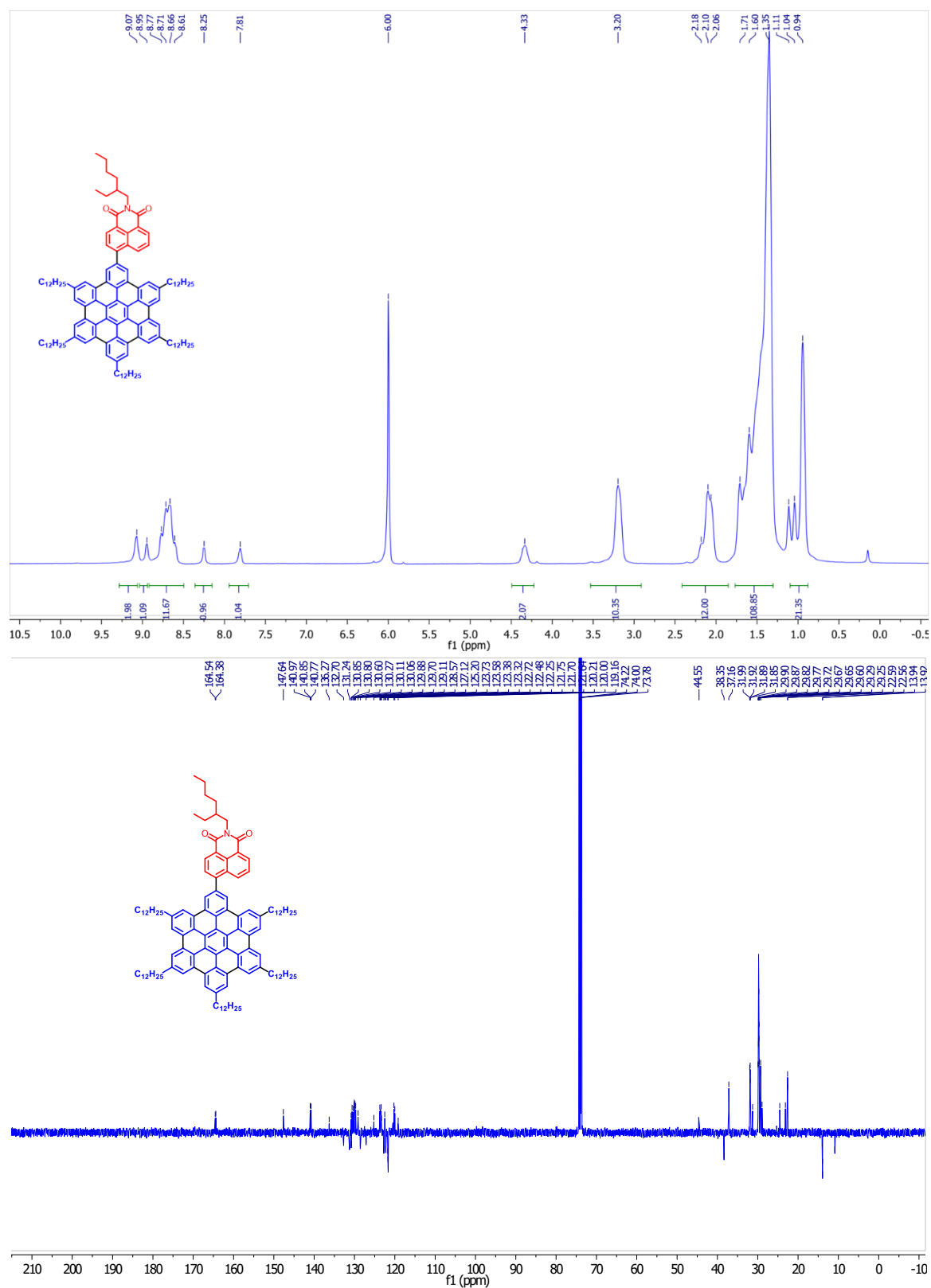


Figure S17. 1H (above) and ^{13}C NMR (below) spectra of **HBC-NMI** in $C_2D_2Cl_4$.

7.3 Supporting information

MALDI TOF MS spectra of HBC-acceptor dyads

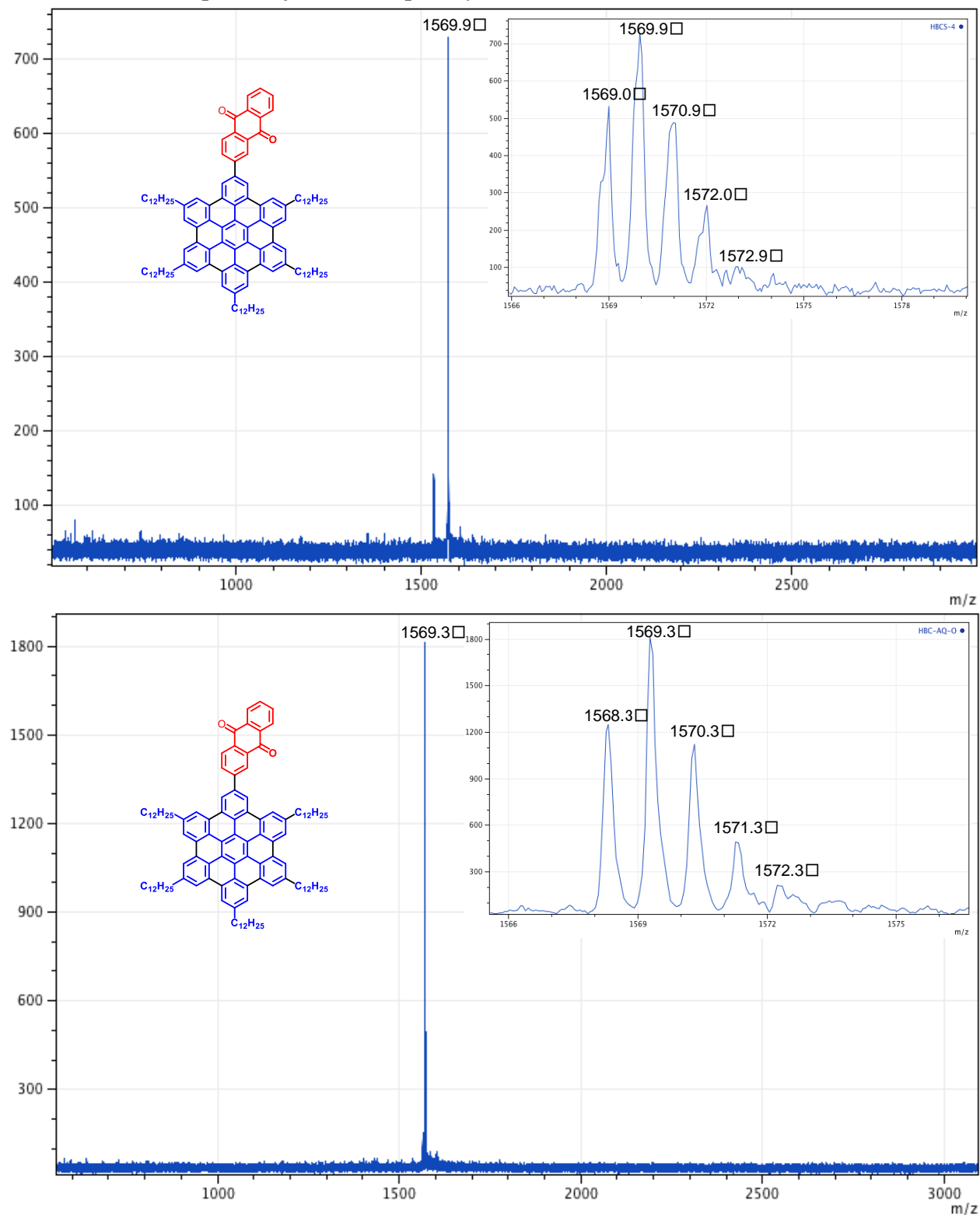


Figure S20. MALDI-TOF spectra of **HBC-AQ** prepared through the pre-functionalization (top) and the post-functionalization (bottom) protocols.

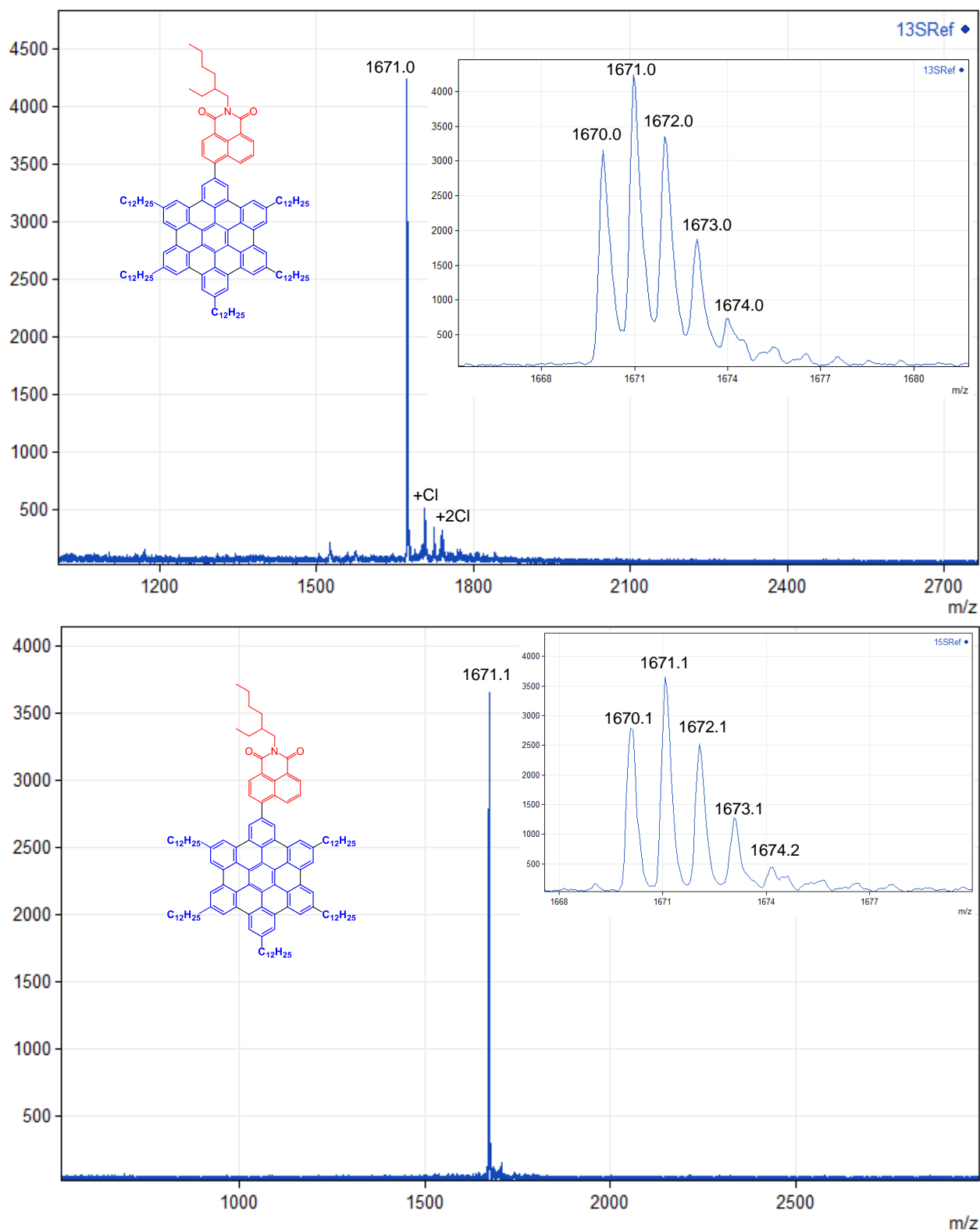


Figure S21. MALDI-TOF spectra of **HBC-NMI** prepared through the pre-functionalization (top) and the post-functionalization (bottom) protocols.

7.3 Supporting information

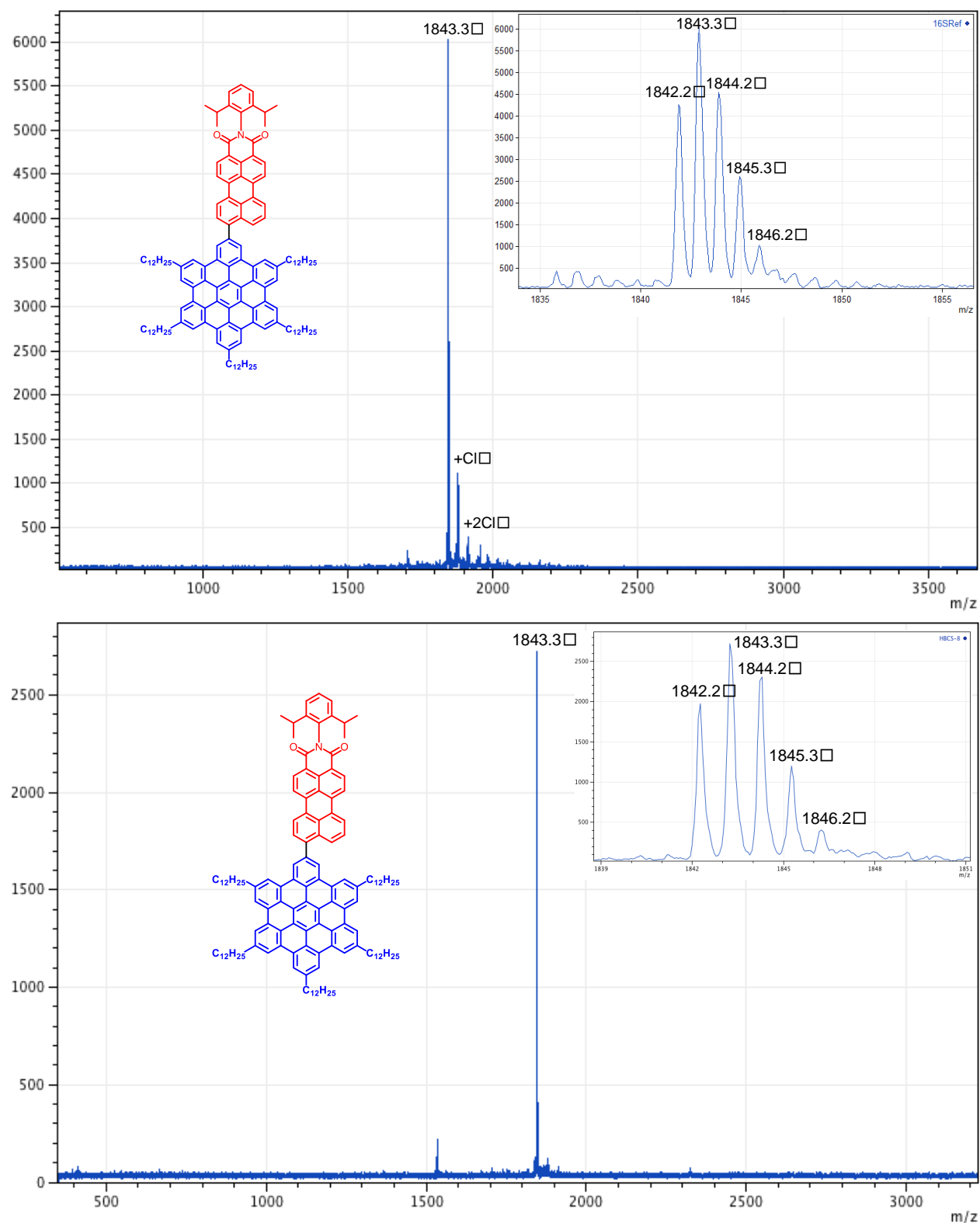


Figure S22. MALDI-TOF spectra of **HBC-PMI** prepared through the pre-functionalization (top) and the post-functionalization (bottom) protocols.

7.4 References

- (1) Narita, A.; Wang, X.-Y.; Feng, X.; Müllen, K., New advances in nanographene chemistry. *Chem. Soc. Rev.* **2015**, *44* (18), 6616-6643.
- (2) Narita, A.; Feng, X.; Hernandez, Y.; Jensen, S. A.; Bonn, M.; Yang, H.; Verzhbitskiy, I. A.; Casiraghi, C.; Hansen, M. R.; Koch, A. H. R.; Fytas, G.; Ivasenko, O.; Li, B.; Mali, K. S.; Balandina, T.; Mahesh, S.; De Feyter, S.; Müllen, K., Structurally Well-Defined and Liquid-Phase-Processable Graphene Nanoribbons. *Nature Chem.* **2014**, *6*, 126-132.
- (3) Vo, T. H.; Shekhirev, M.; Kunkel, D. A.; Morton, M. D.; Berglund, E.; Kong, L.; Wilson, P. M.; Dowben, P. A.; Enders, A.; Sinitiskii, A., Large-scale solution synthesis of narrow graphene nanoribbons. *Nat. Commun.* **2014**, *5*, 3189.
- (4) Wu, J.; Pisula, W.; Müllen, K., Graphenes as Potential Material for Electronics. *Chem. Rev.* **2007**, *107* (3), 718-747.
- (5) Li, X.; Rui, M.; Song, J.; Shen, Z.; Zeng, H., Carbon and Graphene Quantum Dots for Optoelectronic and Energy Devices: A Review. *Adv. Funct. Mater.* **2015**, *25* (31), 4929-4947.
- (6) Loh, K. P.; Tong, S. W.; Wu, J., Graphene and Graphene-like Molecules: Prospects in Solar Cells. *J. Am. Chem. Soc.* **2016**, *138* (4), 1095-1102.
- (7) Soldano, C.; Mahmood, A.; Dujardin, E., Production, properties and potential of graphene. *Carbon* **2010**, *48* (8), 2127-2150.
- (8) Yan, X.; Li, B.; Li, L.-S., Colloidal Graphene Quantum Dots with Well-Defined Structures. *Acc. Chem. Res.* **2013**, *46* (10), 2254-2262.
- (9) Segawa, Y.; Ito, H.; Itami, K., Structurally uniform and atomically precise carbon nanostructures. *Nat. Rev. Mater.* **2016**, *1*, 15002.
- (10) Berger, R.; Giannakopoulos, A.; Ravat, P.; Wagner, M.; Beljonne, D.; Feng, X.; Müllen, K., Synthesis of Nitrogen-Doped ZigZag-Edge Peripheries: Dibenzo-9a-azaphenylene as Repeating Unit. *Angew. Chem. Int. Ed.* **2014**, *53* (39), 10520-10524.
- (11) Wang, X.-Y.; Wang, J.-Y.; Pei, J., BN Heterosuperbenzenes: Synthesis and Properties. *Chem.—Eur. J.* **2015**, *21* (9), 3528-3539.
- (12) Jiang, W.; Li, Y.; Wang, Z., Heteroarenes as high performance organic semiconductors. *Chem. Soc. Rev.* **2013**, *42* (14), 6113-6127.
- (13) Segura, J. L.; Juarez, R.; Ramos, M.; Seoane, C., Hexaazatriphenylene (HAT) derivatives: from synthesis to molecular design, self-organization and device applications. *Chem. Soc. Rev.* **2015**, *44* (19), 6850-6885.
- (14) Ball, M.; Zhong, Y.; Wu, Y.; Schenck, C.; Ng, F.; Steigerwald, M.; Xiao, S.; Nuckolls, C., Contorted Polycyclic Aromatics. *Acc. Chem. Res.* **2015**, *48* (2), 267-276.
- (15) Dou, C.; Saito, S.; Matsuo, K.; Hisaki, I.; Yamaguchi, S., A Boron-Containing PAH as a Substructure of Boron-Doped Graphene. *Angew. Chem. Int. Ed.* **2012**, *51* (49), 12206-12210.
- (16) Tan, Y.-Z.; Osella, S.; Liu, Y.; Yang, B.; Beljonne, D.; Feng, X.; Müllen, K., Sulfur-Annulated Hexa-peri-hexabenzocoronene Decorated with Phenylthio Groups at the Periphery. *Angew. Chem. Int. Ed.* **2015**, *54* (10), 2927-2931.
- (17) Yamaguchi, R.; Ito, S.; Lee, B. S.; Hiroto, S.; Kim, D.; Shinokubo, H., Functionalization of Hexa-peri-hexabenzocoronenes: Investigation of the Substituent Effects on a Superbenzene. *Chem. Asian J.* **2013**, *8* (1), 178-190.
- (18) Yamaguchi, R.; Hiroto, S.; Shinokubo, H., Synthesis of Oxygen-Substituted Hexa-peri-hexabenzocoronenes through Ir-Catalyzed Direct Borylation. *Org. Lett.* **2012**, *14* (10), 2472-2475.

7.4 References

- (19) Tan, Y.-Z.; Osella, S.; Liu, Y.; Yang, B.; Beljonne, D.; Feng, X.; Müllen, K., Sulfur-Annulated Hexa-peri-hexabenzocoronene Decorated with Phenylthio Groups at the Periphery. *Angew. Chem. Int. Ed.* **2015**, *54* (10), 2927-2931.
- (20) Wong, W. W. H.; Subbiah, J.; Puniredd, S. R.; Purushothaman, B.; Pisula, W.; Kirby, N.; Müllen, K.; Jones, D. J.; Holmes, A. B., Liquid crystalline hexa-peri-hexabenzocoronene-diketopyrrolopyrrole organic dyes for photovoltaic applications. *J. Mater. Chem.* **2012**, *22* (39), 21131-21137.
- (21) Lungerich, D.; Hitzengerger, J. F.; Marcia, M.; Hampel, F.; Drewello, T.; Jux, N., Superbenzene–Porphyrin Conjugates. *Angew. Chem. Int. Ed.* **2014**, *53* (45), 12231-12235.
- (22) Hill, J. P.; Jin, W.; Kosaka, A.; Fukushima, T.; Ichihara, H.; Shimomura, T.; Ito, K.; Hashizume, T.; Ishii, N.; Aida, T., Self-Assembled Hexa-peri-hexabenzocoronene Graphitic Nanotube. *Science* **2004**, *304* (5676), 1481-1483.
- (23) Ravat, P.; Marszalek, T.; Pisula, W.; Müllen, K.; Baumgarten, M., Positive Magneto-LC Effect in Conjugated Spin-Bearing Hexabenzocoronene. *J. Am. Chem. Soc.* **2014**, *136* (37), 12860-12863.
- (24) Ito, S.; Wehmeier, M.; Brand, J. D.; Kübel, C.; Epsch, R.; Rabe, J. P.; Müllen, K., Synthesis and Self-Assembly of Functionalized Hexa-peri-hexabenzocoronenes. *Chem.–Eur. J.* **2000**, *6* (23), 4327-4342.
- (25) Hinkel, F.; Cho, D.; Pisula, W.; Baumgarten, M.; Müllen, K., Alternating Donor–Acceptor Arrays from Hexa-peri-hexabenzocoronene and Benzothiadiazole: Synthesis, Optical Properties, and Self-Assembly. *Chem. Eur. J.* **2015**, *21* (1), 86-90.
- (26) Dössel, L. F.; Kamm, V.; Howard, I. A.; Laquai, F.; Pisula, W.; Feng, X.; Li, C.; Takase, M.; Kudernac, T.; De Feyter, S.; Müllen, K., Synthesis and Controlled Self-Assembly of Covalently Linked Hexa-peri-hexabenzocoronene/Perylene Diimide Dyads as Models To Study Fundamental Energy and Electron Transfer Processes. *J. Am. Chem. Soc.* **2012**, *134* (13), 5876-5886.
- (27) Samorì, P.; Fechtenkötter, A.; Reuther, E.; Watson, M. D.; Severin, N.; Müllen, K.; Rabe, J. P., Self-Assembly of Perylene Monoimide Substituted Hexa-peri-hexabenzocoronenes: Dyads and Triads at Surfaces. *Adv. Mater.* **2006**, *18* (10), 1317-1321.
- (28) Wong, W. W. H.; Subbiah, J.; Puniredd, S. R.; Purushothaman, B.; Pisula, W.; Kirby, N.; Mullen, K.; Jones, D. J.; Holmes, A. B., Liquid crystalline hexa-peri-hexabenzocoronene-diketopyrrolopyrrole organic dyes for photovoltaic applications. *J. Mater. Chem.* **2012**, *22* (39), 21131-21137.
- (29) Ren, S.; Yan, C.; Vak, D.; Jones, D. J.; Holmes, A. B.; Wong, W. W. H., Solution Processable Monosubstituted Hexa-Peri-Hexabenzocoronene Self-Assembling Dyes. *Adv. Funct. Mater.* **2012**, *22* (10), 2015-2026.
- (30) Li, J. L.; Kastler, M.; Pisula, W.; Robertson, J. W. F.; Wasserfallen, D.; Grimsdale, A. C.; Wu, J. S.; Müllen, K., Organic Bulk-Heterojunction Photovoltaics Based on Alkyl Substituted Discotics. *Adv. Funct. Mater.* **2007**, *17* (14), 2528-2533.
- (31) Haßheider, T.; Benning, S. A.; Lauhof, M. W.; Kitzerow, H. S.; Bock, H.; Watson, M. D.; Müllen, K., ORGANIC HETEROJUNCTION PHOTOVOLTAIC CELLS MADE OF DISCOTIC, MESOGENIC MATERIALS. *Molecular Crystals and Liquid Crystals* **2004**, *413* (1), 461-472.
- (32) Mativetsky, J. M.; Kastler, M.; Savage, R. C.; Gentilini, D.; Palma, M.; Pisula, W.; Müllen, K.; Samorì, P., Self-Assembly of a Donor-Acceptor Dyad Across Multiple Length Scales: Functional Architectures for Organic Electronics. *Adv. Funct. Mater.* **2009**, *19* (15), 2486-2494.
- (33) Yamamoto, Y.; Jin, W.; Fukushima, T.; Minari, T.; Tsukagoshi, K.; Saeki, A.; Seki, S.; Tagawa, S.; Aida, T., Charge Transport Properties of Hexabenzocoronene Nanotubes by Field Effect: Influence of the Oligoether Side Chains on the Mobility. *Chem. Lett.* **2009**, *38* (9), 888-889.
- (34) Craats, A. M. v. d.; Warman, J. M.; Fechtenkötter, A.; Brand, J. D.; Harbison, M. A.; Müllen, K., Record Charge Carrier Mobility in a Room-Temperature Discotic Liquid-Crystalline Derivative of Hexabenzocoronene. *Adv. Mater.* **1999**, *11* (17), 1469-1472.

- (35) Samori, P.; Yin, X.; Tchegotareva, N.; Wang, Z.; Pakula, T.; Jäckel, F.; Watson, M. D.; Venturini, A.; Müllen, K.; Rabe, J. P., Self-Assembly of Electron Donor–Acceptor Dyads into Ordered Architectures in Two and Three Dimensions: Surface Patterning and Columnar “Double Cables”. *J. Am. Chem. Soc.* **2004**, *126* (11), 3567-3575.
- (36) Bullock, J. E.; Vagnini, M. T.; Ramanan, C.; Co, D. T.; Wilson, T. M.; Dicke, J. W.; Marks, T. J.; Wasielewski, M. R., Photophysics and Redox Properties of Rylene Imide and Diimide Dyes Alkylated Ortho to the Imide Groups. *J. Phys. Chem. B* **2010**, *114* (5), 1794-1802.
- (37) Keerthi, A.; Liu, Y.; Wang, Q.; Valiyaveetil, S., Synthesis of Perylene Dyes with Multiple Triphenylamine Substituents. *Chem. Eur. J.* **2012**, *18* (37), 11669-11676.
- (38) Stappert, S.; Li, C.; Müllen, K.; Basché, T., Synthesis of an Acceptor–Donor–Acceptor Multichromophore Consisting of Terrylene and Perylene Diimides for Multistep Energy Transfer Studies. *Chem. Mater.* **2016**, *28* (3), 906-914.
- (39) Rieger, R.; Müllen, K., Forever young: polycyclic aromatic hydrocarbons as model cases for structural and optical studies. *J. Phys. Org. Chem.* **2010**, *23*, 315-325.
- (40) Zhao, G.-J.; Chen, R.-K.; Sun, M.-T.; Liu, J.-Y.; Li, G.-Y.; Gao, Y.-L.; Han, K.-L.; Yang, X.-C.; Sun, L., Photoinduced Intramolecular Charge Transfer and S2 Fluorescence in Thiophene- π -Conjugated Donor–Acceptor Systems: Experimental and TDDFT Studies. *Chem. Eur. J.* **2008**, *14* (23), 6935-6947.
- (41) Thiagarajan, V.; Selvaraju, C.; Malar, E. J. P.; Ramamurthy, P., A Novel Fluorophore with Dual Fluorescence: Local Excited State and Photoinduced Electron-Transfer-Promoted Charge-Transfer State. *ChemPhysChem* **2004**, *5* (8), 1200-1209.
- (42) Pisula, W.; Tomović, Ž.; Watson, M. D.; Müllen, K.; Kussmann, J.; Ochsenfeld, C.; Metzroth, T.; Gauss, J., Helical Packing of Discotic Hexaphenyl Hexa-peri-hexabenzocoronenes: Theory and Experiment. *J. Phys. Chem. B* **2007**, *111* (26), 7481-7487.
- (43) Hansen, M. R.; Schnitzler, T.; Pisula, W.; Graf, R.; Müllen, K.; Spiess, H. W., Cooperative Molecular Motion within a Self-Assembled Liquid-Crystalline Molecular Wire: The Case of a TEG-Substituted Perylenediimide Disc. *Angew. Chem. Int. Ed.* **2009**, *48* (25), 4621-4624.
- (44) Frisch, M. J.; Trucks, G. W.; Schlegel, H. B.; Scuseria, G. E.; Robb, M. A.; Cheeseman, J. R.; Scalmani, G.; Barone, V.; Mennucci, B.; Petersson, G. A.; Nakatsuji, H.; Caricato, M.; Li, X.; Hratchian, H. P.; Izmaylov, A. F.; Bloino, J.; Zheng, G.; Sonnenberg, J. L.; Hada, M.; Ehara, M.; Toyota, K.; Fukuda, R.; Hasegawa, J.; Ishida, M.; Nakajima, T.; Honda, Y.; Kitao, O.; Nakai, H.; Vreven, T.; Montgomery Jr., J. A.; Peralta, J. E.; Ogliaro, F.; Bearpark, M. J.; Heyd, J.; Brothers, E. N.; Kudin, K. N.; Staroverov, V. N.; Kobayashi, R.; Normand, J.; Raghavachari, K.; Rendell, A. P.; Burant, J. C.; Iyengar, S. S.; Tomasi, J.; Cossi, M.; Rega, N.; Millam, N. J.; Klene, M.; Knox, J. E.; Cross, J. B.; Bakken, V.; Adamo, C.; Jaramillo, J.; Gomperts, R.; Stratmann, R. E.; Yazyev, O.; Austin, A. J.; Cammi, R.; Pomelli, C.; Ochterski, J. W.; Martin, R. L.; Morokuma, K.; Zakrzewski, V. G.; Voth, G. A.; Salvador, P.; Dannenberg, J. J.; Dapprich, S.; Daniels, A. D.; Farkas, Ö.; Foresman, J. B.; Ortiz, J. V.; Cioslowski, J.; Fox, D. J. *Gaussian 09*, Gaussian, Inc.: Wallingford, CT, USA, 2009.
- (45) Roy Dennington, T. K., John Millam *GaussView*, 5; Semichem Inc.: 2009.
- (46) Gudeika, D.; Lygaitis, R.; Mimaitė, V.; Grazulevicius, J. V.; Jankauskas, V.; Lapkowski, M.; Data, P., Hydrazones containing electron-accepting and electron-donating moieties. *Dyes Pigm.* **2011**, *91* (1), 13-19.
- (47) Hankache, J.; Wenger, O. S., Microsecond charge recombination in a linear triarylamine-Ru(bpy)₃²⁺-anthraquinone triad. *Chem. Commun.* **2011**, *47* (36), 10145-10147.

Chapter 8. Chemisorption of Atomically Precise 42-Carbon Graphene Quantum Dots on Metal Oxide Films Greatly Accelerates Interfacial Electron Transfer

██████████¹, Ian Cheng-Yi Hou¹, ██████████¹, ██████████¹, ██████████^{1,2}, ██████████¹, ██████████^{1,3}, ██████████^{1,4,*}

¹Max Planck Institute for Polymer Research, Ackermannweg 10, 55128 Mainz, Germany.

²Institute of Physical Chemistry, Johannes Gutenberg University Mainz, Duesbergweg 10-14, 55128 Mainz, Germany.

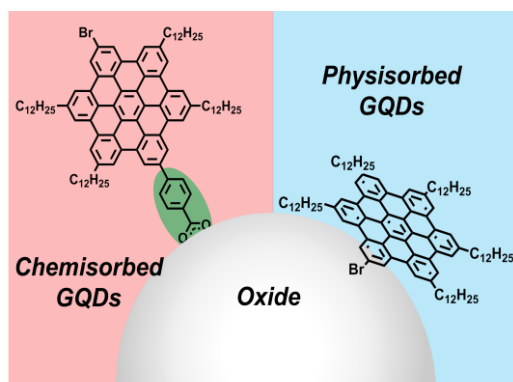
³Organic and Carbon Nanomaterials Unit, Okinawa Institute of Science and Technology Graduate University, Okinawa 904-0495, Japan.

⁴Instituto Madrileño de Estudios Avanzados en Nanociencia (IMDEA Nanociencia), Faraday 9, 28049 Madrid, Spain.

Published in: *J. Phys. Chem. Lett.* **2019**, *10* (7), 1431–1436. DOI: 10.1021/acs.jpcllett.9b00399. Reprinted with permission. Copyright: 2019, American Chemical Society.

Contribution: Organic synthesis and characterization. Measuring UV-Vis spectra. Assist on surface adsorption experiments. Assist on ToC Figure and the organic synthetic parts in main text and SI.

8.1 Abstract



ToC Figure.

Graphene quantum dots (GQDs) are emerging as environmentally friendly, low-cost and highly tunable building blocks in solar energy conversion architectures, such as solar (fuel) cells. Specifically, GQDs constitute a promising alternative for organometallic dyes in sensitized oxide systems. Current sensitized solar cells employing atomically precise GQDs are based on physisorbed sensitizers, with typically limited efficiencies. Chemisorption has been pointed out as a solution to boost photoconversion efficiencies, by allowing improved control over sensitizer surface coverage and sensitizer-oxide coupling strength. Here, employing time-resolved THz spectroscopy, we demonstrate that chemisorption of atomically precise C42-GQDs (hexa-*peri*-hexabenzocoronene derivatives consisting of 42 sp² carbon

atoms) onto mesoporous metal oxides, enabled by their functionalization with a carboxyl group, enhances electron transfer (ET) rates by almost two orders of magnitude when compared with physisorbed sensitizers. Density functional theory (DFT) calculations, absorption spectroscopy and valence band X-ray photoelectron spectroscopy reveal that the enhanced ET rates can be traced to stronger donor-acceptor coupling strength enabled by chemisorption.

8.2 Main Text

Graphene quantum dots (GQDs) are nano-sized graphene fragments, which have non-zero, size-dependent bandgaps due to quantum confinement effects.¹⁻³ Moreover, GQDs are metal-free and hence potentially low-cost and environment-friendly. These features have motivated researchers to apply GQDs in solar energy conversion schemes (e.g. solar cells⁴⁻⁷ and photocatalytic devices^{8,9}). GQDs are typically prepared by hydrothermal treatment of graphene or small molecules¹⁻³; although certain control of GQD size has been achieved following this synthesis protocol², samples are generally defined by broad absorption features induced by inhomogeneous broadening (i.e. samples does not consist on a narrow distribution of chemical structures), an aspect that is detrimental for optoelectronic applications.

Alternatively, large polycyclic aromatic hydrocarbons (PAHs) have been synthesized in the field of organic chemistry over the last decades, being hexa-*peri*-hexabenzocoronene (HBC), consisting of 42 sp² carbon atoms, a representative example^{10,11}. Recently, ■■■ *et al.* reported the synthesis of large PAHs consisting of 132, 168, and 170 sp² carbon atoms and referred to them as colloidal GQDs.^{12,13} Such PAHs, sometimes also called nanographenes, can indeed serve as atomically precise zero dimensional GQDs, owing to their well-defined size- and shape-dependent optoelectronic properties as predicted by theoretical predictions¹⁴⁻¹⁶. ■■■ *et al.* also reported the use of such well-defined GQDs as absorbers in a sensitized solar cell geometry.¹⁷ However, these initial solar cell devices revealed low photo-conversion efficiencies, mainly linked with low short-circuit currents. The poor photocurrent produced in the cells was tentatively correlated with the low affinity of the employed GQDs sensitizers, which were physisorbed onto the mesoporous oxide surface. In a follow up report from the same group, functionalization of the colloidal GQDs by carboxyl groups was reported to allow better control on the interfacial bonding geometry on polar surfaces (specifically on mica) by chemisorption.¹⁸ Furthermore, theoretical studies have shown that chemisorption – instead of physisorption - of sensitizers should favor donor-acceptor coupling and hence boost electron transfer at GQD/oxide interfaces^{19,20}. Although all these works have suggested that chemisorption of GQDs onto metal oxides might improve photoconversion efficiencies in sensitized systems, there is at present no experimental evidence to support that claim. Here, we quantify interfacial electron transfer (ET) rates for atomically precise GQD_{C42} (HBC with 42 sp² carbon atoms) chemisorbed and physisorbed on mesoporous SnO₂ by optical pump-terahertz probe (OPTP) spectroscopy. We demonstrate that sensitizer chemisorption onto the oxide electrode substantially improves ET rates induced by strong overlap (hybridization)

between donor and acceptor wavefunctions, which is triggered by the functionalization of the $\text{GQD}_{\text{C}42}$ by a carboxyl group. This claim is directly evident from the OPTP data and is further supported by absorption spectroscopy, valence band X-ray photoelectron spectroscopy (VBXPS) and density functional theory (DFT) calculations.

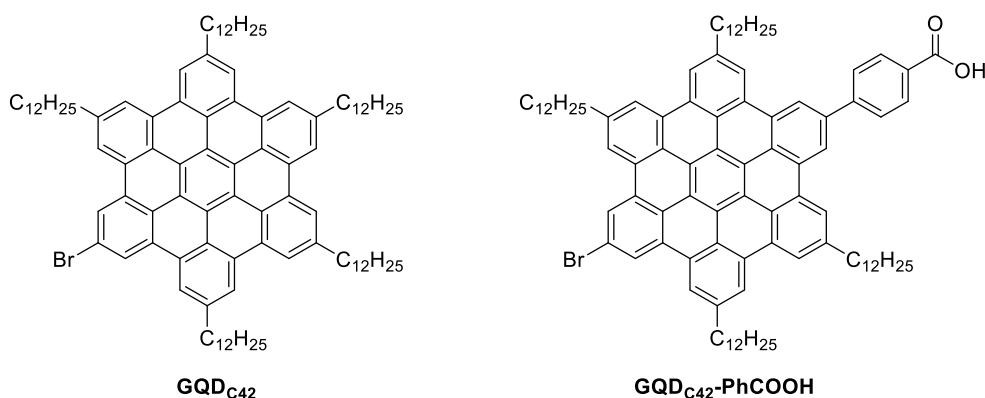


Figure 1. Chemical structures of the graphene quantum dots, $\text{GQD}_{\text{C}42}$ and $\text{GQD}_{\text{C}42}\text{-PhCOOH}$, analyzed in this study; they differ on the presence of a carboxyl functional group which is expected to serve as a covalent link to the oxide electrode.

The molecular structures of the two $\text{GQD}_{\text{C}42}$ samples used in this study are shown in Figure 1. For clarity, we name our samples as $\text{GQD}_{\text{C}42}$ and $\text{GQD}_{\text{C}42}\text{-PhCOOH}$ for the sensitizer without and with a phenyl carboxylic acid functional group respectively. The $\text{GQD}_{\text{C}42}$ sample was prepared following a protocol described previously²¹ and the synthesis of $\text{GQD}_{\text{C}42}\text{-PhCOOH}$ is described in the supporting information (SI). In brief, $\text{GQD}_{\text{C}42}\text{-PhCOOH}$ was synthesized starting from a hexaphenylbenzene derivative bearing bromo- and iodo-groups through a Suzuki-coupling reaction to selectively introduce a phenyl ester moiety and subsequent cyclodehydrogenation reaction to convert the hexaphenylbenzene core into HBC. Finally, the ester group was hydrolyzed under basic conditions to the desired carboxylic acid anchoring group. The synthesized samples were diluted in toluene, and the obtained suspensions were employed for sensitizing the mesoporous oxide films (see SI for sample preparation details). The functionalized films were subsequently characterized by OPTP spectroscopy; the measurements were performed under nitrogen conditions to prevent any potential sensitizer photo-oxidation.

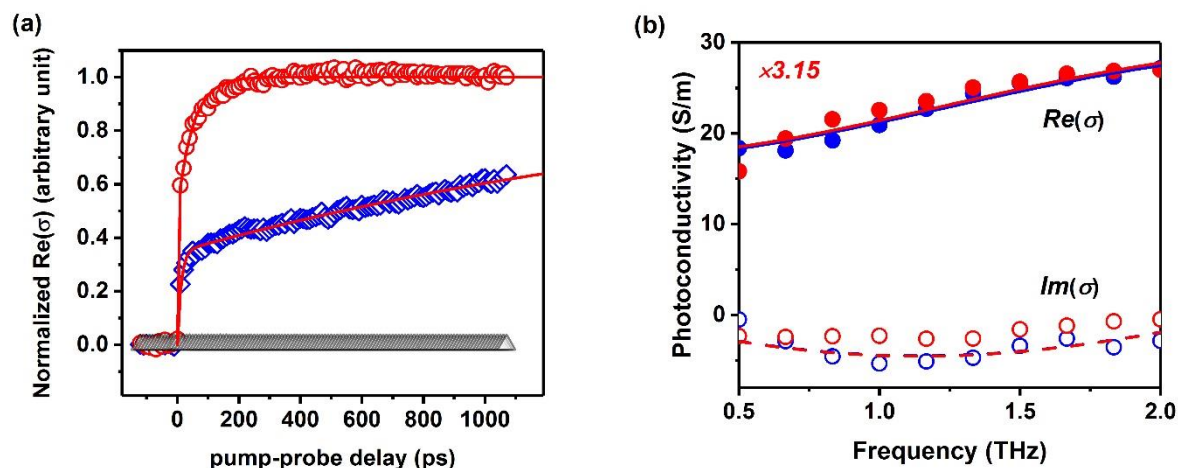


Figure 2. (a) OPTP dynamics of GQDC₄₂ (open blue diamonds) and GQDC₄₂-PhCOOH (open red circles) sensitizing SnO₂ films (400 nm pump excitation, 0.6 mJ cm⁻²). Traces are normalized to the plateau of the bi-exponential fits (solid red lines). Black open triangles are OPTP dynamics for a bare SnO₂ film. (b) Frequency-resolved complex photoconductivity for both sensitized systems (1 ns after photoexcitation); solid and dashed lines correspond to Drude-Smith fits for the real and imaginary components of the frequency dependent conductivity.

OPTP spectroscopy is a powerful tool to investigate ultrafast interfacial dynamics for dye-²²⁻²⁶ and QD-²⁷⁻²⁹ sensitized oxide systems. As the employed THz probe (~1.5 THz bandwidth) is primarily sensitive to free carrier motion (i.e. photoconductivity), an OPTP measurement in a sensitized oxide neatly probes the emergence of photoconductivity in the oxide electrode after selective excitation of the sensitizer. As such, it resolves, in time, the arrival of electrons from the sensitizer's populated molecular orbitals (e.g. LUMO) into the oxide's conduction band (CB). Figure 2a shows normalized OPTP dynamics for GQDC₄₂ and GQDC₄₂-PhCOOH sensitizing SnO₂ mesoporous films (blue diamonds and red circles respectively; 400nm pump excitation, 0.6 mJ/cm²); these dynamics were collected in the linear single-exciton regime (see figure S1). The lack of response under 400 nm pump excitation of a bare SnO₂ mesoporous oxide film is also presented in figure 2a (black triangles). As evident from figure 2a, the sensitization of mesoporous SnO₂ by the sensitizer functionalized with a phenyl carboxyl group (GQDC₄₂-PhCOOH, figure 1) – which is expected to chemisorb at the oxide surface – results in faster ET rates when compared with the sensitizer lacking functionalization (GQDC₄₂ in figure 1), which is expected to physisorb at the oxide surface. Both traces can be well described phenomenologically by a bi-phasic exponential model (solid red lines in figure 2), providing time constants of $\tau_1 = 12 \pm 1$ ps and $\tau_2 = 2025 \pm 450$ ps for GQDC₄₂ sensitized SnO₂ films; and $\tau_1 = 0.2 \pm 0.1$ ps and

$\tau_2 = 51 \pm 3$ ps for GQD_{C42}-PhCOOH sensitized SnO₂ films. Biphasic ET dynamics are a common observable for dye- and QD- sensitized oxide systems that have been generally explained in terms of two distinct transfer channels towards the oxide electrode. They might be linked with “hot” and “cold” ET channels^{30,31}, or, alternatively, to “cold” ET channels induced by two donor-acceptor interfacial conformations (i.e., providing distinct donor-acceptor energetics)³². Biphasic dynamics have been also rationalized by considering effects induced by molecules loosely attached (physisorbed) to the surface or those present in form of the aggregates^{29,33,34}. Even though it is difficult to rule out any of these scenarios from the current data, the fact that both ET components become faster when QDs are chemisorbed onto the oxide matrix support the view that two ET channels define our interfacial dynamics. A deeper analysis of the nature of the bi-phasic signals is underway and will be reported elsewhere.

To validate the conclusion of faster ET rates for the chemisorbed sensitizers inferred from the OTP data, we analyze the frequency-resolved complex photoconductivity in the samples. This approach can tell whether OTP dynamics indeed refer uniquely to electrons populating the oxide conduction band. Figure 2b presents the real and imaginary (closed and open symbols) components of the complex conductivity for GQD_{C42} (blue), and GQD_{C42}-PhCOOH (red) sensitized oxide films (1ns after excitation, 1.5 THz bandwidth). As evident from figure 2b, the complex photoconductivity spectra for chemisorbed and physisorbed dots onto the oxide overlap quite well, indicating that the nature of the monitored photoconductivity for both samples is identical, as expected for electrons in SnO₂. The resolved complex spectra can be well described by the phenomenological Drude-Smith (DS) model³⁵:

$$\tilde{\sigma}(\omega) = \frac{\omega_p^2 \epsilon_0 \tau_s}{1 - i\omega \tau_s} * \left(1 + \frac{c}{1 - i\omega \tau_s} \right) \quad (\text{Eq. 1})$$

where ω_p , ϵ_0 , τ_s and c refers to the plasma frequency, vacuum permittivity, scattering time and localization factor respectively. Within the DS model, the measurable frequency resolved photoconductivity can be attributed to free carriers experiencing preferential backscattering at the boundaries of the nanocrystalline mesoporous oxide electrode^{22,36}. The strength of the localization is parametrized by c , which ranges between 0 (free carrier-Drude response) and -1 (representing full localization of charges). Best fit to the data using equation 1 for both samples provide the same fitting parameters within error; a scattering rate of $\tau_s = 46 \pm 2$ fs and localization factor of $c = -0.69 \pm 0.1$. These results are in good agreement with

8.2 Main Text

previous values inferred for nanostructured SnO₂ films^{37–39}, and hence demonstrate that the monitored signal in figure 2a refers uniquely to electrons populating the oxide conduction band. These results support our conclusion that the changes in the monitored interfacial ET rates can be traced uniquely to the presence of the phenyl carboxyl group functionalizing the GQD_{C42}-PhCOOH, allowing for chemisorption. Furthermore, these results reveal that electron transport within the analyzed SnO₂ electrode is unaffected by the type of functionalization (chemisorption or physisorption).

To check the generality of our observation that ET is accelerated for chemisorbed sensitizers, we also measured interfacial ET dynamics for both sensitizers onto mesoporous ZnO and TiO₂ films (figure S3). For ZnO samples we observed as well faster ET rates for the chemisorbed sensitizers, analogous to the case of SnO₂ based samples (figure 2). For titania, ET occurs faster than our experimental sub-ps time resolution for both sensitizers, so we are unable to determine changes in ET rates for this set of samples. The overall slower ET rates observed for ZnO and SnO₂ electrodes when compared to titania – generally explained in terms of larger density of states for the latter improving donor-acceptor coupling strength—agree qualitatively with those reported for organo-metallic dye sensitizers onto the same electrodes⁴⁰. Overall, the results support the view that the presence of a phenyl carboxyl group facilitates ET transfer towards the electrode independently of its nature.

To rationalize our finding of faster ET for chemisorbed GQD_{C42}, we investigate the nature of the interaction between sensitizer donor and oxide acceptor. Figure 3 presents the relative energy level alignments. For the SnO₂ electrode, the energy positions are obtained from ultraviolet photoelectron spectroscopy (UPS, see figure S5) and absorbance. For the two molecules, the highest occupied molecular orbital (HOMO) and lowest unoccupied molecular orbital (LUMO) were obtained from gas-phase DFT calculations. When the interaction of the metal oxide with the molecules is not taken into account, upon sensitization, the slightly larger ΔG (the energy difference between the LUMO of the sensitizer and the CB of the electron-accepting oxide, see figure 3) for the GQD_{C42} lacking a carboxyl group should lead to faster ET for the physisorbed sensitizers²⁹. From the OTP data shown in figure 2a, it is clear that this is not the case, which shows that the chemical interaction between chemisorbed GQD_{C42}-PhCOOH and the oxide electrode affects donor-acceptor energetics (and hence coupling strength). The frontier orbitals obtained from DFT calculations offer some insight on this aspect. As shown in figure 3, the sensitizer expected to chemisorb to the oxide surface (GQD_{C42}-PhCOOH) reveals a substantial LUMO distribution on carboxyl group, which is expected to deprotonate and bond to the oxide surface. The localization of the LUMO nearer

the oxide surface will provide enhanced donor-acceptor coupling strength (donor-acceptor wavefunction overlap) when compared with the physisorbed case, in line with the OPTP data shown in figure 2a. Faster ET rates as a function of shorter donor-acceptor orbital distances between sensitizers and metal oxides have been demonstrated in quantum dot-oxide⁴¹ and dye-oxide⁴⁰ systems.

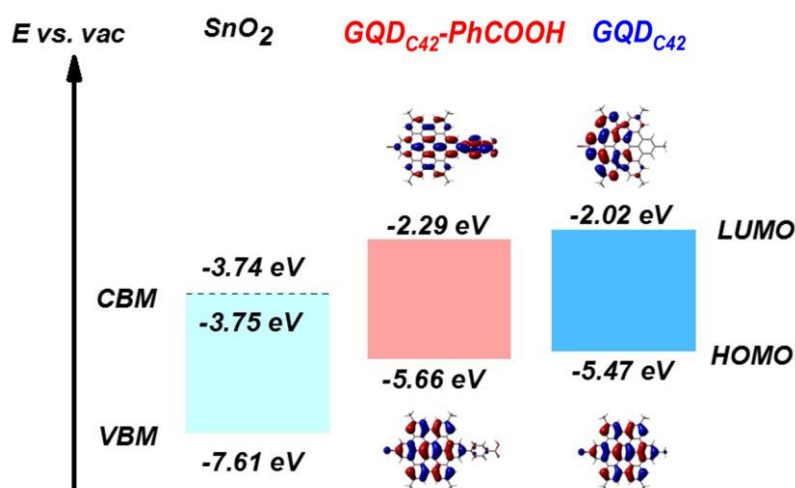


Figure 3. Interfacial donor-acceptor energetics derived from gas-phase DFT calculations for GQD_{C42} and GQD_{C42}-PhCOOH sensitizers and from UPS for tin oxide. Frontier orbital distributions of HOMO and LUMO for both sensitizers are also presented. The Fermi level for the tin oxide sample is within the oxide CB, indicating strong n-type character.

To reveal a stronger interaction between chemisorbed GQD_{C42} orbitals and the oxide conduction band, we analyzed the samples by optical absorption and valence band X-ray photoelectron spectroscopy. In figure 4a we present the UV-VIS absorbance spectrum of both sensitized systems (solid red and blue lines for chemisorbed and physisorbed GQD_{C42} respectively) along with the bare oxide film (black line). Figure 4a also provides the spectra of the toluene solution of both sensitizers (dashed red and blue lines for chemisorbed and physisorbed GQD_{C42} respectively); the absorption profiles peak at 3.45 eV and 3.39 eV for GQD_{C42} and GQD_{C42}-PhCOOHs respectively. Whereas the peak absorbance for GQD_{C42} remains essentially identical upon sensitization, a clear blue shift is resolved for the peak absorbance of the GQD_{C42}-PhCOOH sensitizers after binding to the oxide electrode (dotted and solid red lines in figure 4a). A similar blue shift in the absorbance after sensitization has been previously reported for dye-sensitized films and explained in terms of the strong coupling induced by deprotonation of the dyes⁴²⁻⁴⁵ induced by chemisorption; in good agreement with our expectations.

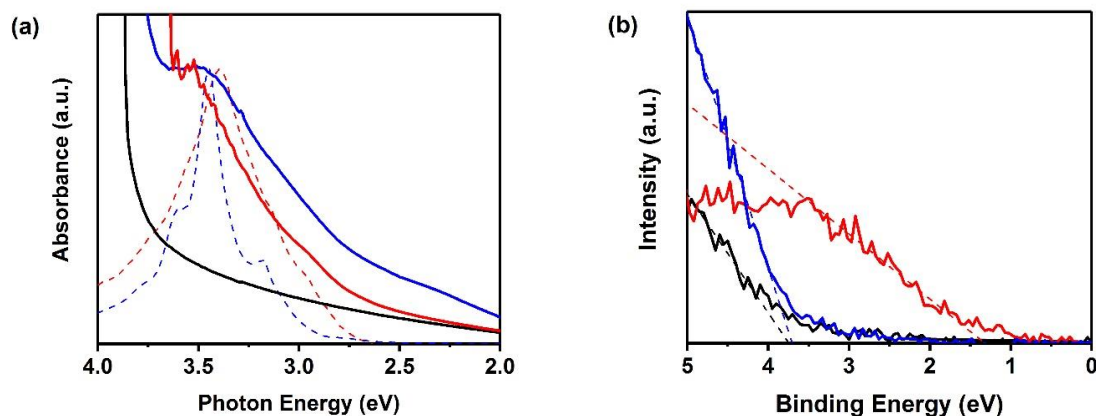


Figure 4. (a) UV-VIS absorbance spectrum of GQD_{C42} (blue) and GQD_{C42}-PhCOOH (red) sensitized SnO₂ films and for sensitizers dispersed in solution (dashed lines). The spectrum of bare SnO₂ film is also shown (solid black line). (b) Valence band X-ray spectra of GQD_{C42} (blue) and GQD_{C42}-PhCOOH (red) sensitized and bare (black) SnO₂ electrodes. The dashed lines are linear fits enabling binding energy estimates for the analyzed systems.

In figure 4b we present VBXPS data for a bare SnO₂ mesoporous film (solid black line) and oxide electrodes functionalized by GQD_{C42}-PhCOOH and GQD_{C42} sensitizers (red and blue line respectively). As evident from the plot, the physisorbed GQD_{C42} sensitized and the bare tin oxide electrodes reveal identical electron binding energies. However, the electron binding energy is reduced by approximately 2 eV upon chemisorption of GQD_{C42}-PhCOOHs, indicating significant/efficient modification/decoration of the surface of the oxide, which was absent upon the physisorption (the results were reproducible within ~50 meV for samples produced in three different batches). The observed change in electron binding energy can be explained by chemical modification at the oxide interface (e.g. deprotonation of COOH groups able to modify the Fermi energy at the oxide) and/or by dipolar effects (modifying vacuum levels induced by the presence of a surface electric field induced by sensitization)⁴⁶. In any case, it reveals a strong donor-acceptor interaction for the chemisorbed GQD_{C42}, in qualitative agreement with absorbance spectra shown in figure 4a and the expected closer proximity of frontier orbitals inferred by DFT calculation (figure 3). All these results support qualitatively the experimentally resolved effect on interfacial OTP dynamics, i.e. the main conclusion of this work: chemisorption of GQD_{C42}, enabled by their functionalization with a carboxyl group, substantially enhances ET rates.

In summary, we investigated the rates of electron transfer from physisorbed and chemisorbed GQD sensitizers to metal oxides, using HBC derivatives as atomically precise GQDs. An increase of ET rates as large as two orders of magnitude is observed for chemisorbed

sensitizers when compared with physisorbed ones. Accelerated electron transfer is correlated with enhanced donor-acceptor coupling (i.e., wavefunction hybridization). These results demonstrate that functionalization of GQDs with anchoring head groups represents a potential path for improved photoconversion efficiencies in carbon-based sensitizer/oxide electrodes employed in solar energy conversion schemes.

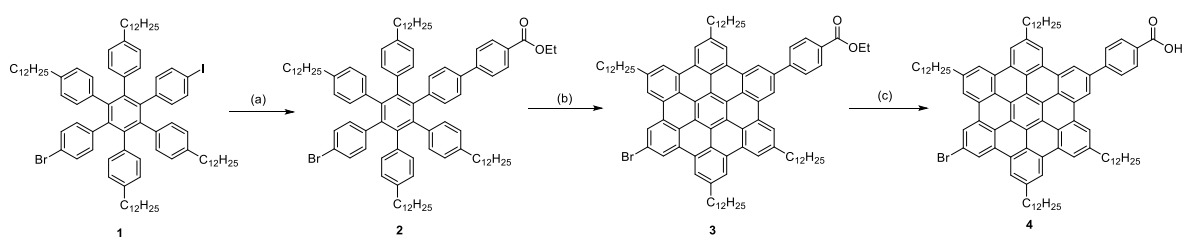
8.3 Supporting information

Materials and methods

General methods. All reactions working with air- or moisture-sensitive compounds were carried out under argon atmosphere using standard Schlenk line techniques. Unless otherwise noted, all starting materials and reagents were purchased from commercial sources (such as Alfa Aesar, Sigma-Aldrich, Acros and TCI) and used without further purification. Thin layer chromatography (TLC) was performed on silica gel coated aluminum sheets with F254 indicator and silica gel column chromatography separation was performed with the 0.063–0.200 mm particle size. NMR spectra were recorded in deuterated solvents using Bruker AVANCE III 500 and Bruker AVANCE III 700 MHz NMR spectrometers. Chemical shifts (δ) were expressed in ppm relative to the residual of solvent (CD_2Cl_2 @ 5.32 ppm for ^1H NMR, 54.00 ppm for ^{13}C NMR, $\text{C}_2\text{D}_2\text{Cl}_4$ @ 6.00 ppm for ^1H NMR, 73.78 ppm for ^{13}C NMR). Coupling constants (J) were recorded in Hertz (Hz) with multiplicities explained by the following abbreviations: s = singlet, d = doublet, t = triplet, q = quartet, dd = double of doublets, dt = doublet of triplets, m = multiplet, br = broad. The micro-FT-IR spectra were recorded through a diamond anvil cell (transmission mode) with a Nicolet Nexus FT-IR spectrometer coupled with a Thermo Electron Continuum IR microscope. The wavenumber (ν) is expressed in cm^{-1} . UV–vis absorption spectra were measured on a Perkin-Elmer Lambda 900 spectrophotometer at room temperature. High-resolution mass spectra (HRMS) were recorded by matrix-assisted laser decomposition/ionization (MALDI) using 7,7,8,8-tetracyanoquinodimethane (TCNQ) as matrix on a Bruker Reflex II-TOF spectrometer (MALDI-TOF HRMS).

Synthesis of ethyl 5'-(4-bromophenyl)-4-dodecyl-3',4',6'-tris(4-dodecylphenyl)-[1,1':2',1'':4'',1''':quaterphenyl]-4''-carboxylic acid (2 in scheme S1). To a suspension of 4-bromo-4''-dodecyl-3',5',6'-tris(4-dodecylphenyl)-4'-(4-iodophenyl)-1,1':2',1''-terphenyl²¹ (0.18 g, 0.12 mmol) and 4-ethoxycarbonylphenylboronic acid (77 mg, 0.40 mmol) in toluene (5 mL) was added a solution of K_2CO_3 (0.9 g, 7 mmol) in water (1 mL) and ethanol (1 mL). This mixture was degassed by freeze-pump-thaw technique (1 cycle). $\text{Pd}(\text{PPh}_3)_4$ (15 mg, 0.013 mmol) was then added to the mixture, which was further degassed by freeze-pump-thaw technique for another 2 cycles. The mixture was then heated at 70 °C under vigorous stirring and monitored by TLC until the starting material was consumed (about 1 h). After cooling to a room temperature, the mixture was diluted with diethyl ether and washed with water and brine. The organic layer was then dried over MgSO_4 and the solvent was removed

in vacuo. The residue was purified by silica gel column chromatography (eluent: ethyl acetate/hexane = 1/6) to afford the title compound as pale yellow oil (0.14 g, 81%). ^1H NMR (700 MHz, CD_2Cl_2): δ 7.98 (d, $J = 8.4$ Hz, 2H), 7.49 (d, $J = 8.4$ Hz, 2H), 7.17 (d, $J = 8.1$ Hz, 2H), 6.98 (d, $J = 8.4$ Hz, 2H), 6.93 (d, $J = 8.1$ Hz, 2H), 6.76–6.69 (m, 14 H) 6.67 (d, $J = 8.0$ Hz, 4H), 4.33 (q, $J = 7.1$ Hz, 2H), 2.39 (t, $J = 7.5$ Hz, 4H), 2.35 (t, $J = 7.5$ Hz, 4H), 1.41 (quint, $J = 7.9$ Hz, 8H), 1.39–1.02 (m, 75 H), 0.92–0.85 (m, 12 H). ^{13}C NMR (126 MHz, CD_2Cl_2) δ 166.78, 145.49, 141.85, 141.06, 140.91, 140.86, 140.69, 140.50, 140.41, 139.84, 138.42, 138.32, 136.77, 133.81, 132.67, 131.78, 131.76, 130.34, 130.10, 129.61, 127.34, 127.26, 126.99, 125.66, 119.64, 61.41, 54.43, 54.22, 54.00, 53.79, 53.57, 35.81, 32.52, 31.84, 31.80, 30.34, 30.30, 30.27, 30.20, 30.10, 30.04, 29.97, 29.95, 29.39, 29.36, 23.28, 14.68, 14.46. HRMS (MALDI-TOF) calcd. for $\text{C}_{99}\text{H}_{133}\text{BrO}_2$ $[\text{M}]^+$, 1432.9489. Found $[\text{M}]^+$ 1432.9426.



Scheme S1. The synthesis of $\text{GQD}_{\text{C}42}\text{-PhCOOH}$. Reagents and conditions: (a) $\text{Pd}(\text{PPh}_3)_4$, K_2CO_3 , toluene/water/ethanol, 70°C , 1 h. (b) FeCl_3 , DCM/nitromethane, rt, 1 h. (c) KOtBu , H_2O (3 eq.), THF, rt, overnight.

Synthesis of ethyl 4-(11-bromo-5,8,14,17-tetradodecylhexa-*peri*-hexabenzocoronene-2-yl)benzoate (3 in scheme S1). A solution of **2** (0.17 g, 0.12 mmol) in unstabilized dichloromethane (50 mL) was degassed by argon bubbling for 5 min. The argon bubbling was continued for the whole reaction period. To this solution was added a solution of FeCl_3 (0.6 g, 4 mmol) in nitromethane (5 mL). The reaction mixture turned dark brown immediately. The mixture was stirred at a room temperature for 1 h and then poured into methanol (400 mL). Two drops of brine was added to the mixture to facilitate precipitation. The precipitates were collected by vacuum filtration and purified by silica gel column chromatography (eluent: hot toluene) to afford the title compound as a bright yellow solid (161 mg, 95%). ^1H NMR (700 MHz, $\text{C}_2\text{D}_2\text{Cl}_4$, 373 K): δ 8.37 (d, $J = 7.0$ Hz, 2H), 8.17 (br, 2H), 7.92 (d, $J = 7.0$ Hz, 2H), 7.83 (br, 2H), 7.77 (br, 2H), 7.63 (br, 2H), 7.60 (br, 2H), 7.49 (br, 2H), 4.60 (q, $J = 7.2$ Hz, 2H), 2.78 (br, 4H), 2.70 (br, 4H), 1.90 (br, 4H), 1.83 (br, 4H), 1.73–1.18 (m, 75H), 1.02–0.87 (m, 12H). ^{13}C NMR (176 MHz, $\text{C}_2\text{D}_2\text{Cl}_4$, 373 K): δ 166.25, 145.96, 139.03, 138.99,

8.3 Supporting information

135.37, 135.25, 135.21, 130.25, 130.10, 129.46, 128.97, 128.19, 128.15, 127.03, 123.01, 122.58, 121.72, 121.70, 121.53, 121.47, 120.86, 120.52, 120.25, 120.04, 118.62, 118.00, 117.60, 117.48, 117.28, 60.79, 36.77, 36.67, 31.72, 31.56, 31.46, 29.95, 29.77, 29.74, 29.66, 29.63, 29.52, 29.14, 22.41, 14.33, 13.74. IR: $\nu = 3063, 2952, 2917, 2849, 1719, 1609, 1576, 1466, 1271, 1104, 1021, 861, 849, 771, 721, 705$. HRMS (MALDI-TOF) calcd. for $C_{99}H_{121}BrO_2 [M]^+$, 1420.8550. Found $[M]^+$ 1420.8501.

Synthesis of 4-(11-bromo-5,8,14,17-tetradodecylhexa-*peri*-hexabenzocoronene-2-yl)benzoic acid (4 in scheme S1). To a solution of **3** (30 mg, 21 μ mol) and water (1.1 mg, 62 μ mol) in tetrahydrofuran (7 mL) was added a tetrahydrofuran solution of KO t Bu (0.19 mL, 1 M, 190 μ mol) at a room temperature. The mixture was stirred overnight and poured into methanol (50 mL). The precipitates were collected by vacuum filtration and washed with water, methanol and acetone to afford the title compound as a brownish orange solid (29 mg, 99%). HRMS (MALDI-TOF) calcd. for $C_{97}H_{117}BrO_2 [M]^+$, 1392.8237. Found $[M]^+$ 1392.8180. IR: $\nu = 3062, 2952, 2919, 2849, 1687, 1609, 1576, 1464, 1414, 1367, 1181, 861, 849, 774, 719, 613, 553, 492$. Because of the strong aggregation of **3** in solution, NMR spectra could not be resolved.

Preparation of GQDs sensitized metal oxide films. Mesoporous metal oxide films (SnO₂, ZnO, TiO₂) were prepared by doctor-blading method. After sintering at 450 °C for 2h, they were left to cool down to 80 °C. After this, we immersed the mesoporous films in an anhydrous toluene solution containing the GQDs (1 mg/5 mL). To allow the sensitization, the samples remained in a N₂ purged glovebox overnight. The obtained sensitized films were rinsed in Toluene and dried under N₂ environment without applying any thermal treatment during the process.

OPTP Spectroscopy. The detailed working principle of OPTP spectroscopy has been introduced elsewhere⁴⁷. A Ti:sapphire amplified laser system (Spitfire ACE by Spectra-Physics) producing ultra-short laser pulses of ~40 fs duration at 800 nm at 1 kHz repetition rate was used to drive our OPTP set-up. About ~ 900 mW energy is used to run the optical pump-THz probe spectrometer setup. For the THz generation and detection, 10% of the incoming laser beam is used (90 mW). THz radiation is generated in a phase-matched manner by optical rectification in a ZnTe crystal (<110> orientation, 10×10×1 mm thickness, purchased from MaTeck). The ZnTe generation crystal is pumped with a slightly focused

beam (~ 3 mm diameter) of 800 nm light (80 mW power, 50 fs FWHM). The THz light exits the ZnTe generation crystal slightly divergent and is first collimated and subsequently focused on the sample using a pair of off-axis parabolic mirrors. The transmitted THz pulses are recollimated and focused on a second ZnTe detection crystal by another pair of parabolic mirrors, where the instantaneous THz field strength is detected through electro-optical sampling. In our experiment, graphene quantum dots were selectively excited by a 400nm optical pulse which was generated by frequency doubling of the fundamental 800 nm in a BBO crystal. Assuming thin film approximation applies and fixing the arriving time of sampling beam at the THz peak, the magnitude of the real part of photoconductivity as a function of pump-probe time delay (up to 1 ns for our setup) was provided. This measurement gives information about the product of the photo-induced charge carrier density and their average mobility. To deconvolute these two factors and interrogate the nature of interfacial ET frequency-resolved photoconductivity needs to be measured. In this measurement, the recorded photo-induced change in amplitude and phase of the propagating THz pulses yield information on, respectively, the real and imaginary parts of the complex-valued photoconductivity of the sample under study.

UPS, VBXPS, and XPS. UPS and VBXPS measurements were conducted on a Kratos Axis Ultra^{DL}D spectrometer (Kratos, Manchester, England). In these measurements, the samples were transported from an inert-atmosphere glovebox (<1 ppm of O₂) to the vacuum system (2×10^{-7} mbar) immediately after they were prepared. In UPS measurement, electrical contact was always applied. The sample was held at a bias of -9 V with respect to the spectrometer. Illumination at 21.2 eV is provided by the He(I) emission line from a helium discharge lamp, and the chamber pressure increases from $\sim 10^{-10}$ to $\sim 10^{-7}$ mbar. Photoelectron emission was collected at 0° from the surface normal of the samples. The spectra were taken in three different spots to confirm the spectra reproducibility and irradiation exposure time was kept under one minute. VBXPS spectra were collected using an Al K α excitation source with a photon energy of 1487 eV. Spectra were acquired in hybrid mode of the analyzer lens, using a 0° take-off angle, which is defined as the angle between the surface normal and the axis of the analyzer lens.

First-Principles Calculations. DFT calculations were performed using the Gaussian 09 software package.⁴⁸ The geometry and energies were calculated at the B3LYP/6-311+G(d,p) level. All alkyl chains were replaced with methyl groups for computational simplicity.

Supplementary figures

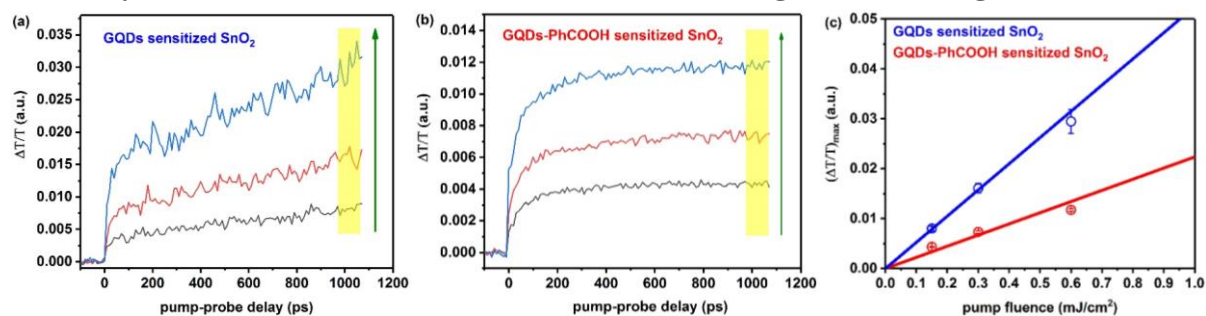
OPTP dynamics of GQDs Sensitized SnO₂ in Linear Single-Exciton Regime

Figure S1. OPTP dynamics of (a) GQDs sensitized SnO₂ and (b) GQDs-PhCOOH sensitized SnO₂ as a function of 400 nm pump excitation fluence. The data demonstrate that excitation in the linear regime (i.e., the signals scale linearly with fluence, hence no change of oxide mobility in the oxide is resolved).

Oscillations in frequency-resolved photoconductivity spectra

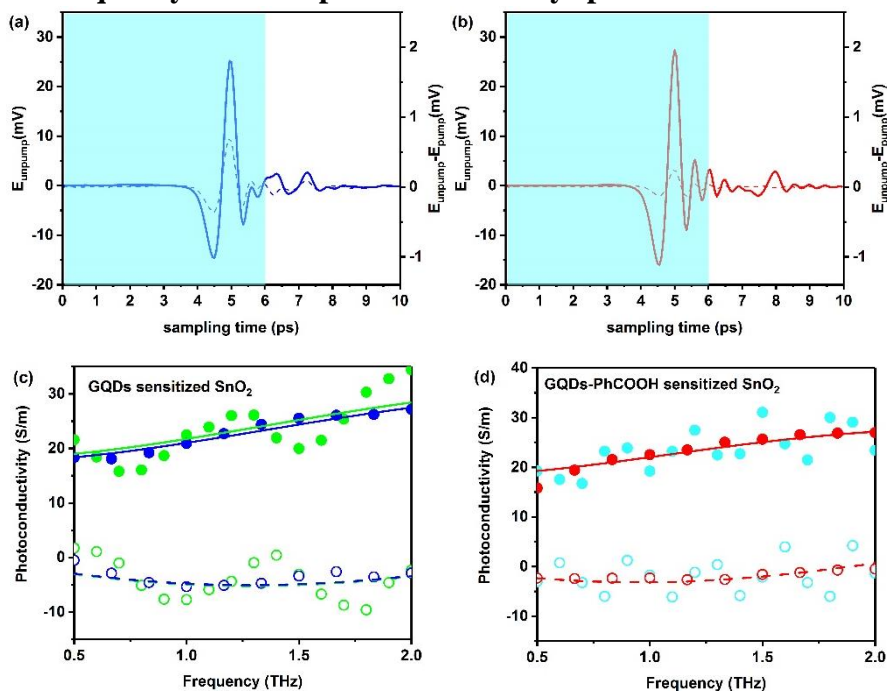


Figure S2. (Top figures) THz probe line shapes in the time domain for both samples. A series of oscillations appear at time delays above 6 ps that we tentatively correlate with multiple reflections of the pump excitation for our sample/substrate geometry (QD-oxide film/fused silica). Fourier transformation of bare data reveals oscillations in the complex conductivity line shape in the frequency domain (bottom panels). The oscillations can be filtered out by shorting the time span (from 0 to 6ps) prior Fourier transformation. Fits to the Drude-Smith model for bare and filtered data in the frequency domain (solid and dashed lines in bottom panel) demonstrate that the filtering protocol is barely affecting the inferred photophysical response of the analyzed systems.

OPTP dynamics of GQDs Sensitized ZnO/TiO₂

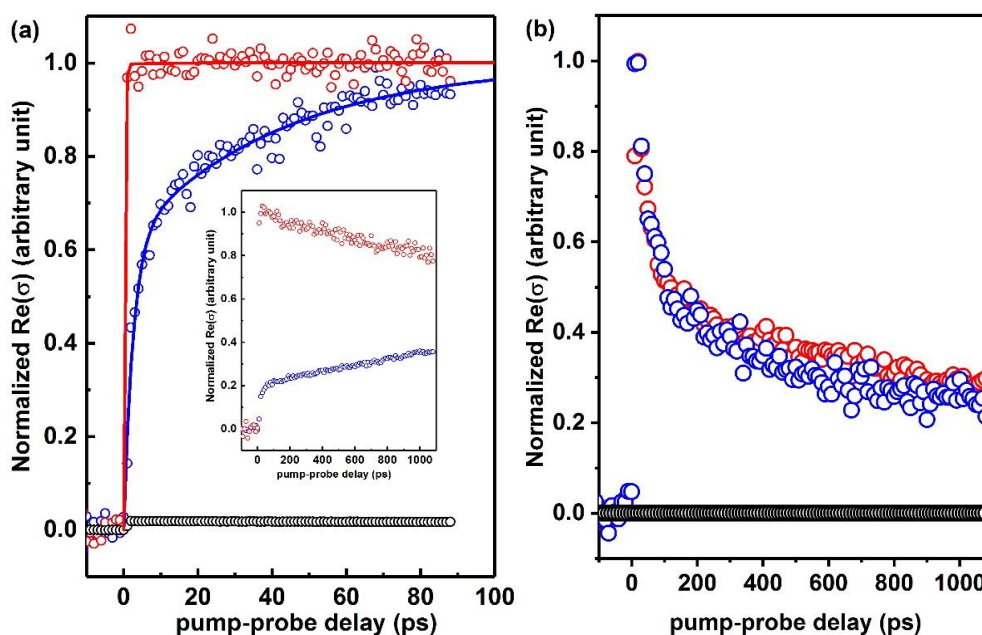


Figure S3. Normalized OPTP dynamics of GQDs sensitized ZnO films (a) and TiO₂ films (b) excited under the same conditions employed for sensitized SnO₂ films for fig 2a in the manuscript. Dynamics in bare ZnO and TiO₂ films are also shown (black open circles). Biphasic fits for the ZnO case provide ET time constant $\tau_1 = 3$ ps, $\tau_2 = 42$ ps for physisorbed case and $\tau_1 = 0.3$ ps, $\tau_2 = 13$ ps for chemisorbed case respectively. The ET components for TiO₂ are faster than our setup resolution (sub 100fs).

Frequency-Resolved Photoconductivity of GQDs Sensitized ZnO/TiO₂

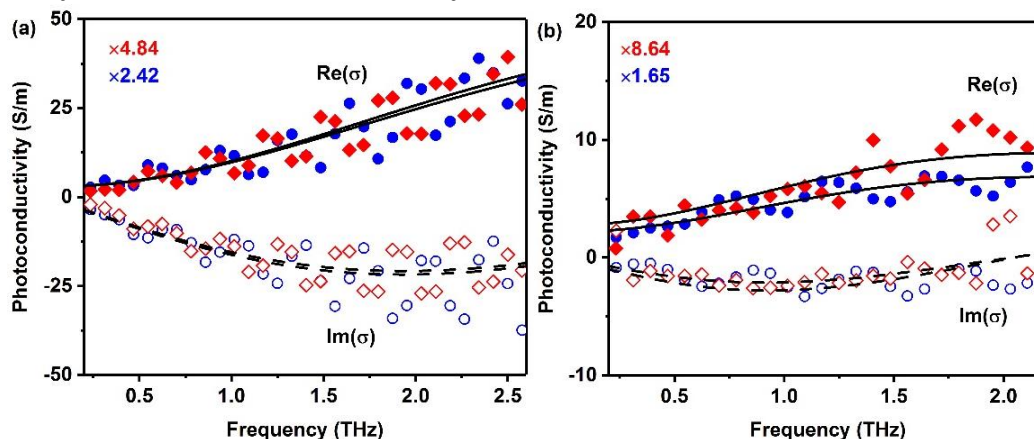


Figure S4. Frequency-resolved complex photoconductivity (solid and open dots for the real and imaginary components) for (a) sensitized ZnO systems and (b) TiO₂ system (1ns after excitation). Solid and dashed lines are best fits to the DS model. Best fit in mesoporous ZnO films provides a scattering rate and localization parameter of $\tau_s = 33.6$ fs and $c = -0.97$, which agrees well with previous reports.⁴⁹ For titania, we obtain from the DS fits $\tau_s = 64.5$ fs and $c = -0.84$, also in agreement with literature.⁵⁰

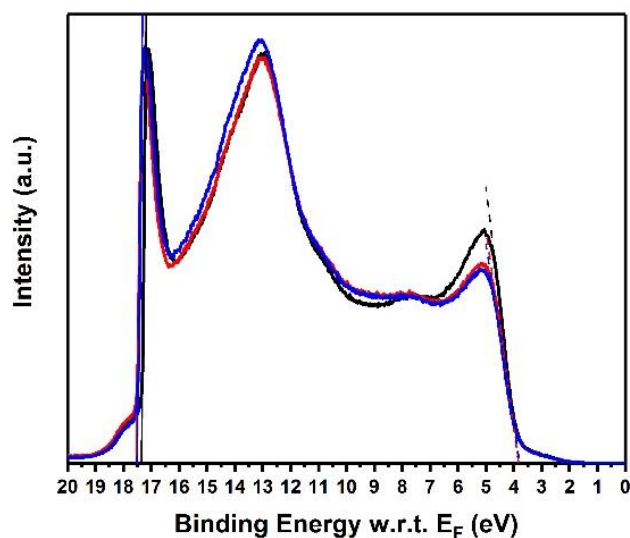
UPS data of Mesoporous SnO₂ Film

Figure S5. Ultraviolet photoelectron spectroscopy (UPS) data of three spots on the same SnO₂ film (solid lines). Two cutoffs were resolved for each spectrum: the one close to the Fermi level representing valence band edge (VBE) of SnO₂; the one far from the Fermi level representing vacuum level in each spot. From these cutoffs, we can obtain the workfunction of the system.

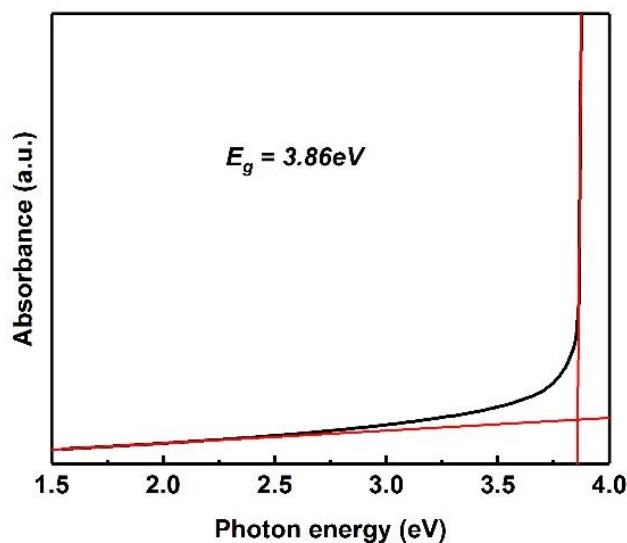
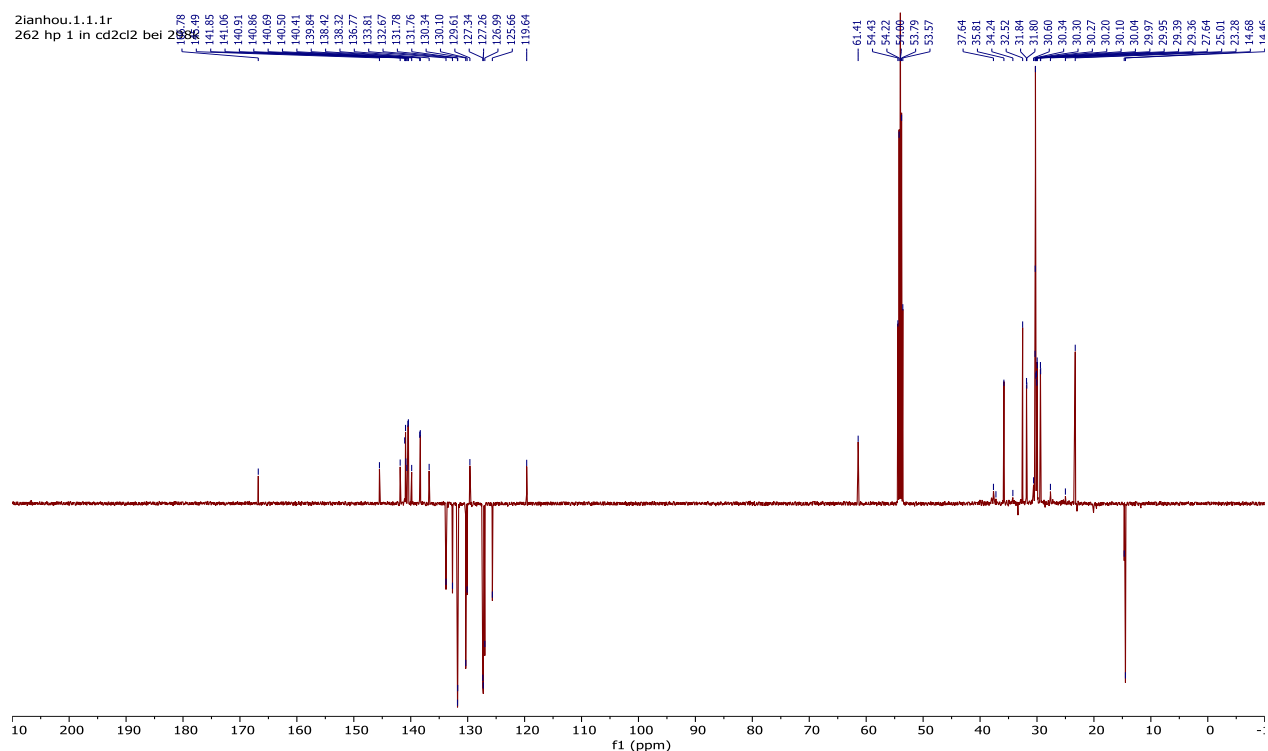
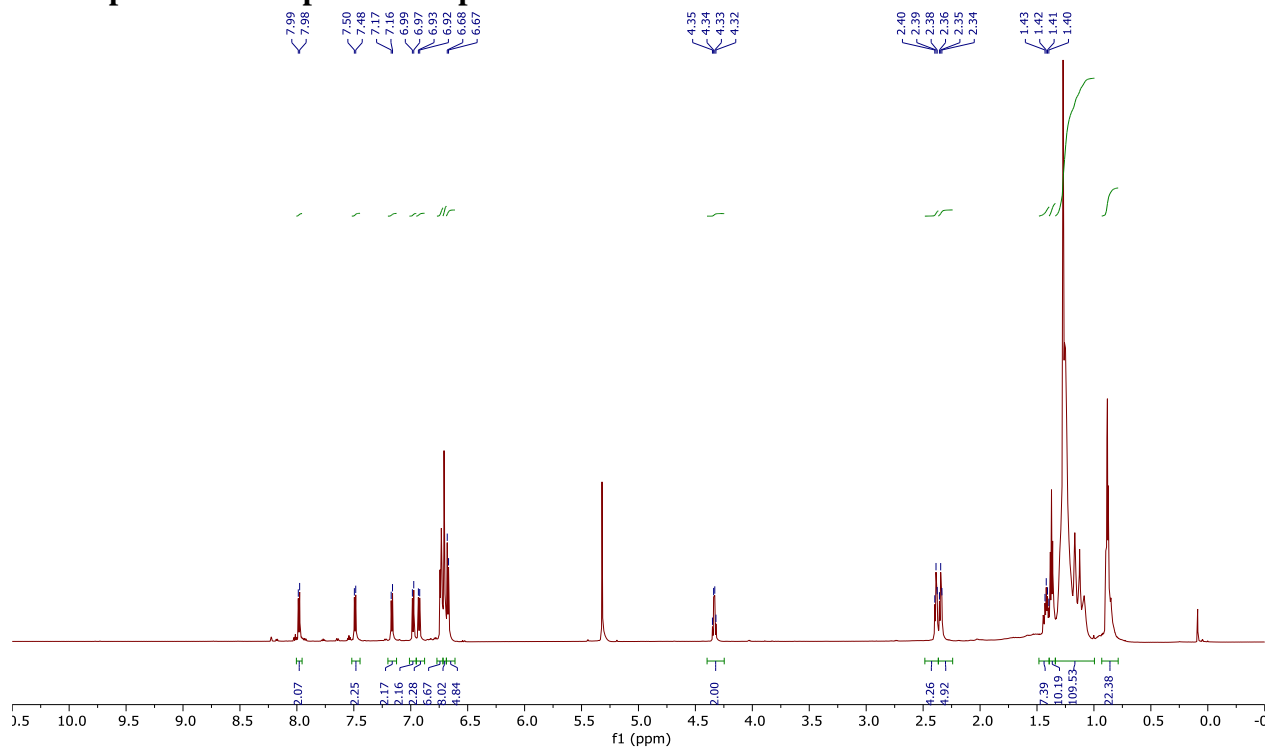
Absorption Spectrum of Mesoporous SnO₂ Film

Figure S6. Absorption spectrum of bare SnO₂ film. A bandgap of 3.86 eV can be inferred by linear extrapolation.

NMR spectra of unreported compounds



8.3 Supporting information

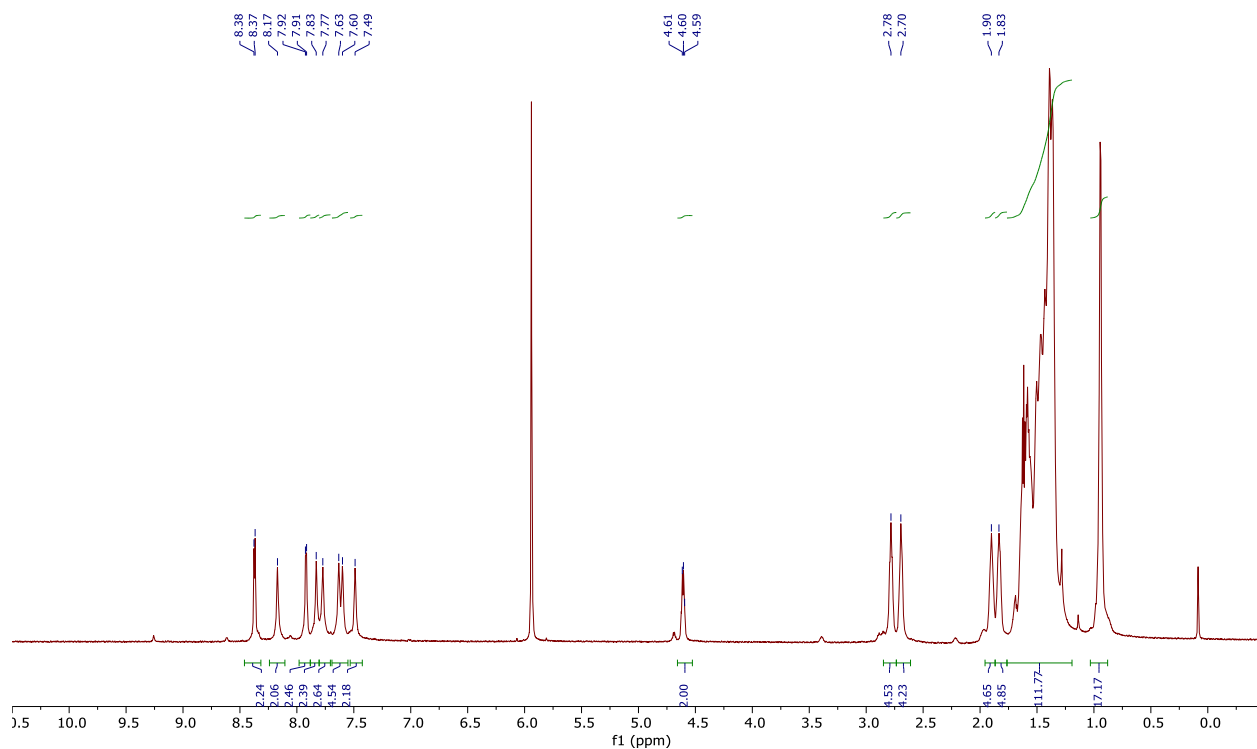


Figure S9. ^1H NMR spectrum of **3** in $\text{C}_2\text{D}_2\text{Cl}_4$ (700 MHz, 373 K).

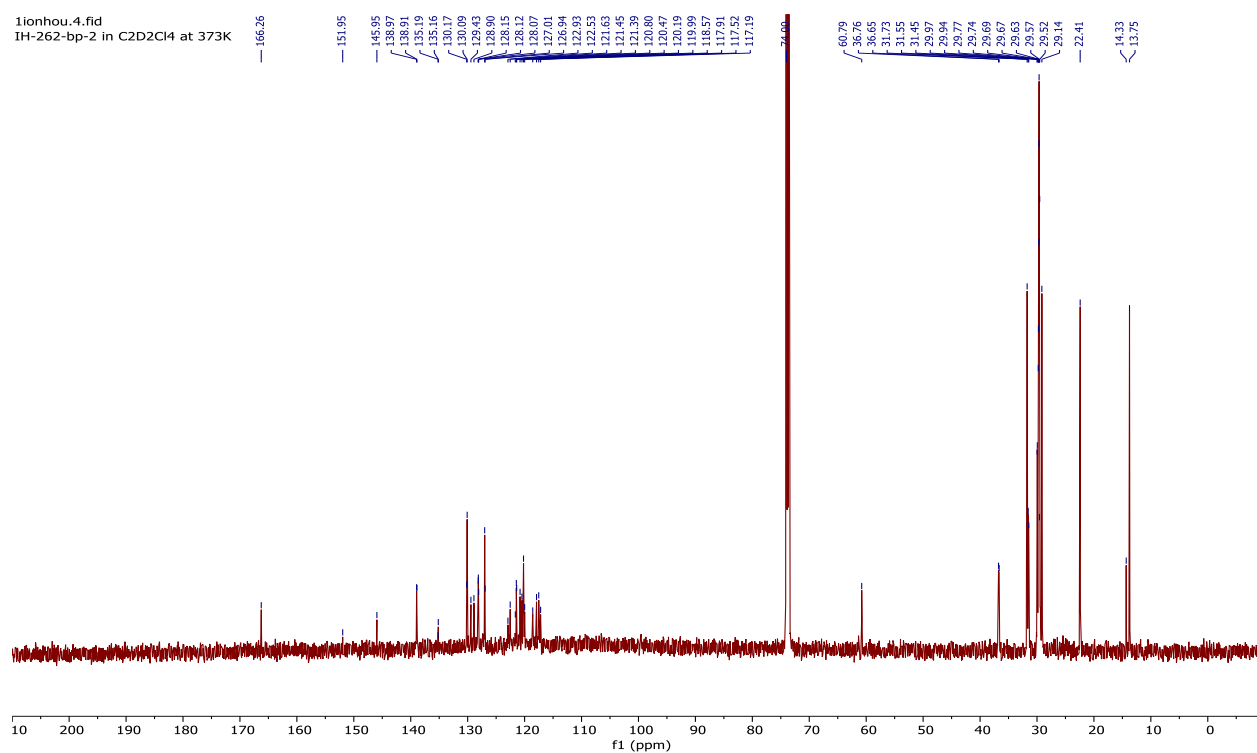


Figure S10. ^{13}C NMR spectrum of **3** in $\text{C}_2\text{D}_2\text{Cl}_4$ (176 MHz, 373 K).

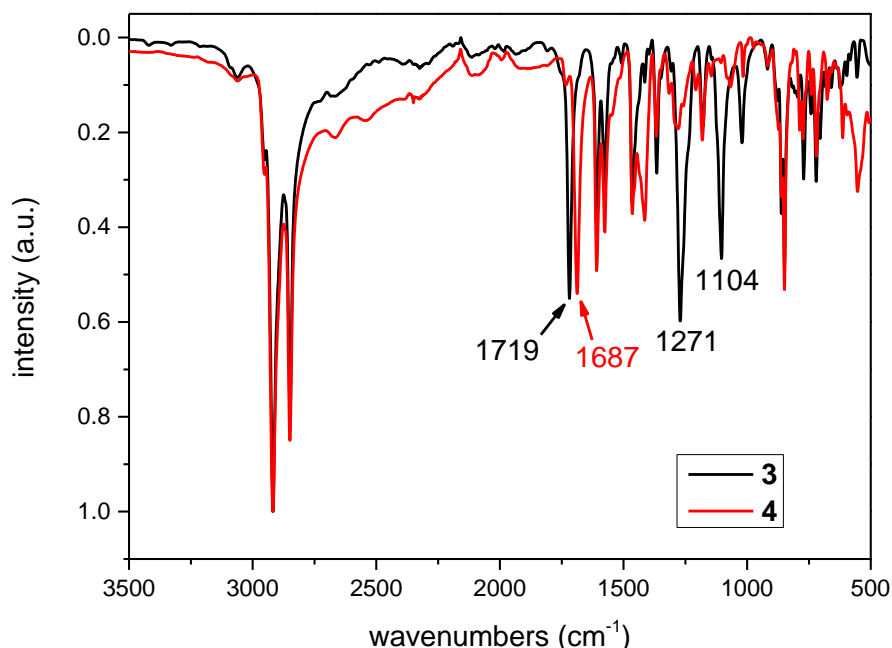


Figure S11. Infrared absorption spectra of **3** and **4**. The complete transformation of ester functional group into carboxyl group is clearly demonstrated by the infrared absorption spectral change of carbonyl functional groups, which shifts from 1719 cm⁻¹ (benzoic ester) to 1687 cm⁻¹ (benzoic acid).

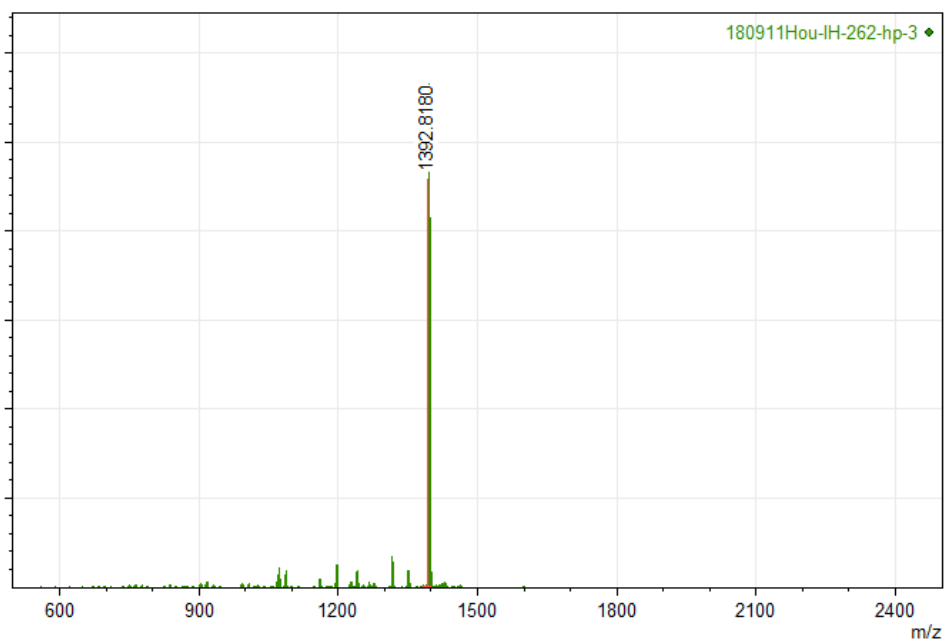


Figure S12. HRMS (MALDI-TOF) spectrum of **4** (matrix: TCNQ).

8.4 References

- (1) Zheng, P.; Wu, N. Fluorescence and Sensing Applications of Graphene Oxide and Graphene Quantum Dots: A Review. *Chem. - An Asian J.* **2017**, *12* (18), 2343–2353.
- (2) Li, X.; Rui, M.; Song, J.; Shen, Z.; Zeng, H. Carbon and Graphene Quantum Dots for Optoelectronic and Energy Devices: A Review. *Adv. Funct. Mater.* **2015**, *25* (31), 4929–4947.
- (3) Li, L.; Wu, G.; Yang, G.; Peng, J.; Zhao, J.; Zhu, J. J. Focusing on Luminescent Graphene Quantum Dots: Current Status and Future Perspectives. *Nanoscale* **2013**, *5* (10), 4015–4039.
- (4) Zamiri, G.; Bagheri, S. Fabrication of Green Dye-Sensitized Solar Cell Based on ZnO Nanoparticles as a Photoanode and Graphene Quantum Dots as a Photo-Sensitizer. *J. Colloid Interf. Sci.* **2018**, *511*, 318–324.
- (5) Chen, L.; Guo, C. X.; Zhang, Q.; Lei, Y.; Xie, J.; Ee, S.; Guai, G.; Song, Q.; Li, C. M. Graphene Quantum-Dot-Doped Polypyrrole Counter Electrode for High-Performance Dye-Sensitized Solar Cells. *ACS Appl. Mater. Interfaces* **2013**, *5* (6), 2047–2052.
- (6) Dinari, M.; Momeni, M. M.; Goudarzirad, M. Dye-Sensitized Solar Cells Based on Nanocomposite of Polyaniline/Graphene Quantum Dots. *J. Mater. Sci.* **2016**, *51* (6), 2964–2971.
- (7) Mihalache, I.; Radoi, A.; Mihaila, M.; Munteanu, C.; Marin, A.; Danila, M.; Kusko, M.; Kusko, C. Charge and Energy Transfer Interplay in Hybrid Sensitized Solar Cells Mediated by Graphene Quantum Dots. *Electrochim. Acta* **2015**, *153*, 306–315.
- (8) Bayat, A.; Saievar-Iranizad, E. Graphene Quantum Dots Decorated Rutile TiO₂ Nanoflowers for Water Splitting Application. *J. Energy Chem.* **2018**, *27* (1), 306–310.
- (9) Rajender, G.; Kumar, J.; Giri, P. K. Interfacial Charge Transfer in Oxygen Deficient TiO₂-Graphene Quantum Dot Hybrid and Its Influence on the Enhanced Visible Light Photocatalysis. *Appl. Catal. B Environ.* **2018**, *224*, 960–972.
- (10) Narita, A.; Wang, X. Y.; Feng, X.; Müllen, K. New Advances in Nanographene Chemistry. *Chem. Soc. Rev.* **2015**, *44* (18), 6616–6643.
- (11) Wu, J.; Pisula, W.; Müllen, K. Graphenes as Potential Material for Electronics. *Chem. Rev.* **2007**, *107* (3), 718–747.
- (12) Yan, X.; Li, B.; Li, L. S. Colloidal Graphene Quantum Dots with Well-Defined Structures. *Acc. Chem. Res.* **2013**, *46* (10), 2254–2262.
- (13) Yan, X.; Cui, X.; Li, L. S. Synthesis of Large, Stable Colloidal Graphene Quantum Dots with Tunable Size. *J. Am. Chem. Soc.* **2010**, *132* (17), 5944–5945.
- (14) Rieger, R.; Müllen, K. Forever Young: Polycyclic Aromatic Hydrocarbons as Model Cases for Structural and Optical Studies. *J. Phys. Org. Chem.* **2010**, *23* (4), 315–325.
- (15) Tan, Y. Z.; Yang, B.; Parvez, K.; Narita, A.; Osella, S.; Beljonne, D.; Feng, X.; Müllen, K. Atomically Precise Edge Chlorination of Nanographenes and Its Application in Graphene Nanoribbons. *Nat. Commun.* **2013**, *4* (1), 2646.
- (16) Wang, X.-Y.; Narita, A.; Müllen, K. Precision Synthesis versus Bulk-Scale Fabrication of Graphenes. *Nat. Rev. Chem.* **2017**, *2* (1), 0100.
- (17) Yan, X.; Cui, X.; Li, B.; Li, L.-S. Large, Solution-Processable Graphene Quantum Dots as Light Absorbers for Photovoltaics. *Nano Lett.* **2010**, *10* (5), 1869–1873.
- (18) Hamilton, I. P.; Li, B.; Yan, X.; Li, L. S. Alignment of Colloidal Graphene Quantum Dots on Polar Surfaces. *Nano Lett.* **2011**, *11* (4), 1524–1529.
- (19) Seyed-Talebi, S. M.; Beheshtian, J.; Neek-Amal, M. Doping Effect on the Adsorption of NH₃ Molecule onto Graphene Quantum Dot: From the Physisorption to the Chemisorption. *J. Appl. Phys.* **2013**, *114* (12), 124307.
- (20) Long, R. Understanding the Electronic Structures of Graphene Quantum Dot Physisorption and Chemisorption onto the TiO₂ (110) Surface: A First-Principles Calculation. *ChemPhysChem* **2013**, *14* (3), 579–582.
- (21) Ito, S.; Wehmeier, M.; Brand, J. D.; Kübel, C.; Epsch, R.; Rabe, J. P.; Müllen, K. Synthesis and Self-Assembly of Functionalized Hexa-Peri-Hexabenzocoronenes. *Chem. - A Eur. J.* **2000**, *6* (23), 4327–4342.

Chapter 8. Chemisorption of Atomically Precise 42-Carbon Graphene Quantum Dots on Metal Oxide Films Greatly Accelerates Interfacial Electron Transfer

- (22) Turner, G. M.; Beard, M. C.; Schmittenmaer, C. A. Carrier Localization and Cooling in Dye-Sensitized Nanocrystalline Titanium Dioxide. *J. Phys. Chem. B* **2002**, *106* (45), 11716–11719.
- (23) Tiwana, P.; Docampo, P.; Johnston, M. B.; Snaith, H. J.; Herz, L. M. Electron Mobility and Injection Dynamics in Mesoporous ZnO, SnO₂, and TiO₂ Films Used in Dye-Sensitized Solar Cells. *ACS Nano* **2011**, *5* (6), 5158–5166.
- (24) Karakus, M.; Zhang, W.; Räder, H. J.; Bonn, M.; Cánovas, E. Electron Transfer from Bi-Isonicotinic Acid Emerges upon Photodegradation of N3-Sensitized TiO₂ Electrodes. *ACS Appl. Mater. Interfaces* **2017**, *9* (40), 35376–35382.
- (25) Tiwana, P.; Parkinson, P.; Johnston, M. B.; Snaith, H. J.; Herz, L. M. Ultrafast Terahertz Conductivity Dynamics in Mesoporous TiO₂: Influence of Dye Sensitization and Surface Treatment in Solid-State Dye-Sensitized Solar Cells. *J. Phys. Chem. C* **2010**, *114* (2), 1365–1371.
- (26) Brauer, J. C.; Moser, J.-E. Transient Photoconductivity of Dye-Sensitized TiO₂ Nanocrystalline Films Probed by Optical Pump-THz Probe Spectroscopy. *Ultrafast Phenom.* **2011**, 358–360.
- (27) Wang, H.; Barceló, I.; Lana-Villarreal, T.; Gómez, R.; Bonn, M.; Cánovas, E. Interplay between Structure, Stoichiometry, and Electron Transfer Dynamics in SILAR-Based Quantum Dot-Sensitized Oxides. *Nano Lett.* **2014**, *14* (10), 5780–5786.
- (28) Zhao, K.; Pan, Z.; Mora-Seró, I.; Cánovas, E.; Wang, H.; Song, Y.; Gong, X.; Wang, J.; Bonn, M.; Bisquert, J.; et al. Boosting Power Conversion Efficiencies of Quantum-Dot-Sensitized Solar Cells beyond 8% by Recombination Control. *J. Am. Chem. Soc.* **2015**, *137* (16), 5602–5609.
- (29) Cánovas, E.; Moll, P.; Jensen, S. A.; Gao, Y.; Houtepen, A. J.; Siebbeles, L. D. A.; Kinge, S.; Bonn, M. Size-Dependent Electron Transfer from PbSe Quantum Dots to SnO₂ Monitored by Picosecond Terahertz Spectroscopy. *Nano Lett.* **2011**, *11* (12), 5234–5239.
- (30) Wang, H. I.; Infante, I.; Brinck, S. Ten; Cánovas, E.; Bonn, M. Efficient Hot Electron Transfer in Quantum Dot-Sensitized Mesoporous Oxides at Room Temperature. *Nano Lett.* **2018**, *18* (8), 5111–5115.
- (31) Benkő, G.; Kallioinen, J.; Korppi-Tommola, J. E. I.; Yartsev, A. P.; Sundström, V. Photoinduced Ultrafast Dye-to-Semiconductor Electron Injection from Nonthermalized and Thermalized Donor States. *J. Am. Chem. Soc.* **2002**, *124* (3), 489–493.
- (32) Furube, A.; Katoh, R.; Yoshihara, T.; Hara, K.; Murata, S.; Arakawa, H.; Tachiya, M. Ultrafast Direct and Indirect Electron-Injection Processes in a Photoexcited Dye-Sensitized Nanocrystalline Zinc Oxide Film: The Importance of Exciplex Intermediates at the Surface. *J. Phys. Chem. B* **2004**, *108* (33), 12583–12592.
- (33) Wenger, B.; Grätzel, M.; Moser, J. E. Rationale for Kinetic Heterogeneity of Ultrafast Light-Induced Electron Transfer from Ru(II) Complex Sensitizers to Nanocrystalline TiO₂. *J. Am. Chem. Soc.* **2005**, *127* (35), 12150–12151.
- (34) Cánovas, E.; Wang, H.; Karakus, M.; Bonn, M. Hot Electron Transfer from PbSe Quantum Dots Molecularly Bridged to Mesoporous Tin and Titanium Oxide Films. *Chem. Phys.* **2016**, *471*, 54–58.
- (35) Smith, N. V. Classical Generalization of the Drude Formula for the Optical Conductivity. *Phys. Rev. B - Condens. Matter Mater. Phys.* **2001**, *64* (15), 155106.
- (36) Ulbricht, R.; Hendry, E.; Shan, J.; Heinz, T. F.; Bonn, M. Carrier Dynamics in Semiconductors Studied with Time-Resolved Terahertz Spectroscopy. *Rev. Mod. Phys.* **2011**, *83* (2), 543–586.
- (37) Tsokkou, D.; Othonos, A.; Zervos, M. Carrier Dynamics and Conductivity of SnO₂ Nanowires Investigated by Time-Resolved Terahertz Spectroscopy. *Appl. Phys. Lett.* **2012**, *100* (13), 133101.
- (38) Regan, K. P.; Swierk, J. R.; Neu, J.; Schmittenmaer, C. A. Frequency-Dependent Terahertz Transient Photoconductivity of Mesoporous SnO₂ Films. *J. Phys. Chem. C* **2017**, *121* (29), 15949–15956.
- (39) Zou, X.; Luo, J.; Lee, D.; Cheng, C.; Springer, D.; Nair, S. K.; Cheong, S. A.; Fan, H. J.; Chia, E. E. M. Temperature-Dependent Terahertz Conductivity of Tin Oxide Nanowire Films. *J. Phys. D: Appl. Phys.* **2012**, *45* (46), 465101.
- (40) Asbury, J. B.; Hao, E.; Wang, Y.; Ghosh, H. N.; Lian, T. Ultrafast Electron Transfer Dynamics from Molecular

8.4 References

- Adsorbates to Semiconductor Nanocrystalline Thin Films. *J. Phys. Chem. B* **2001**, *105* (20), 4545–4557.
- (41) Wang, H.; McNellis, E. R.; Kinge, S.; Bonn, M.; Cánovas, E. Tuning Electron Transfer Rates through Molecular Bridges in Quantum Dot Sensitized Oxides. *Nano Lett.* **2013**, *13* (11), 5311–5315.
- (42) Hagberg, D. P.; Edvinsson, T.; Marinado, T.; Boschloo, G.; Hagfeldt, A.; Sun, L. A Novel Organic Chromophore for Dye-Sensitized Nanostructured Solar Cells. *Chem. Commun.* **2006**, No. 21, 2245–2247.
- (43) Wang, Z. S.; Sugihara, H. N3-Sensitized TiO₂ Films: In Situ Proton Exchange toward Open-Circuit Photovoltage Enhancement. *Langmuir* **2006**, *22* (23), 9718–9722.
- (44) Lin, L. Y.; Tsai, C. H.; Wong, K. T.; Huang, T. W.; Hsieh, L.; Liu, S. H.; Lin, H. W.; Wu, C. C.; Chou, S. H.; Chen, S. H.; et al. Organic Dyes Containing Coplanar Diphenyl-Substituted Dithienosilole Core for Efficient Dye-Sensitized Solar Cells. *J. Org. Chem.* **2010**, *75* (14), 4778–4785.
- (45) Nazeeruddin, M. K.; Humphry-Baker, R.; Liska, P.; Grätzel, M. Investigation of Sensitizer Adsorption and the Influence of Protons on Current and Voltage of a Dye-Sensitized Nanocrystalline TiO₂ Solar Cell. *J. Phys. Chem. B* **2003**, *107* (34), 8981–8987.
- (46) Cahen, D.; Kahn, A. Electron Energetics at Surfaces and Interfaces: Concepts and Experiments. *Adv. Mater.* **2003**, *15* (4), 271–277.
- (47) Wang, H. I.; Lu, H.; Nagata, Y.; Bonn, M.; Cánovas, E. Dipolar Molecular Capping in Quantum Dot-Sensitized Oxides: Fermi Level Pinning Precludes Tuning Donor-Acceptor Energetics. *ACS Nano* **2017**, *11* (5), 4760–4767.
- (48) Frisch, M. J.; Trucks, G. W.; Schlegel, H. B.; Scuseria, G. E.; Robb, M. A.; Cheeseman, J. R.; Scalmani, G.; Barone, V.; Mennucci, B.; Petersson, G. A.; et al. Gaussian 09, Revision D.01. Gaussian, Inc.: Wallingford CT 2013.
- (49) Baxter, J. B.; Schmittenmaer, C. A. Conductivity of ZnO Nanowires, Nanoparticles, and Thin Films Using Time-Resolved Terahertz Spectroscopy. *J. Phys. Chem. B* **2006**, *110* (50), 25229–25239.
- (50) Turner, G. M.; Beard, M. C.; Schmittenmaer, C. A. Carrier Localization and Cooling in Dye-Sensitized Nanocrystalline Titanium Dioxide. *J. Phys. Chem. B* **2002**, *106* (45), 11716–11719.

Chapter 9. Summary and Outlook

This thesis deals with synthesis of precursors and model nanostructures that are related to graphene quantization and defects at GBs. It is especially intriguing for synthetic approach of NGs and its precursor at a length scale of 5–10 nm. Thus, in *Chapter 2* and *Chapter 3*, we have developed synthetic protocols for PP nanostructures that extend until 5 nm length scale in both quasi-1D and quasi-2D. Besides, constructing carbon-nanostructures with multiple pentagon-heptagon-pair is challenging, although such nanostructures are essential for understanding and even tailoring nanostructure at graphene GB. Therefore, in *Chapter 4* and *Chapter 5*, we have employed azulene in solution-based chemistry combined with on-surface synthesis for building sp^2 -carbon-nanostructures that correlate to both theoretical and experimental graphene GBs. Furthermore, nano-sized graphene behaves like molecule. Controlling their assembly can be leveraged against several difficulties in various disciplines of material applications. In *Chapter 6–8*, we attempt to control assembly of HBC in 2D as well as 3D.

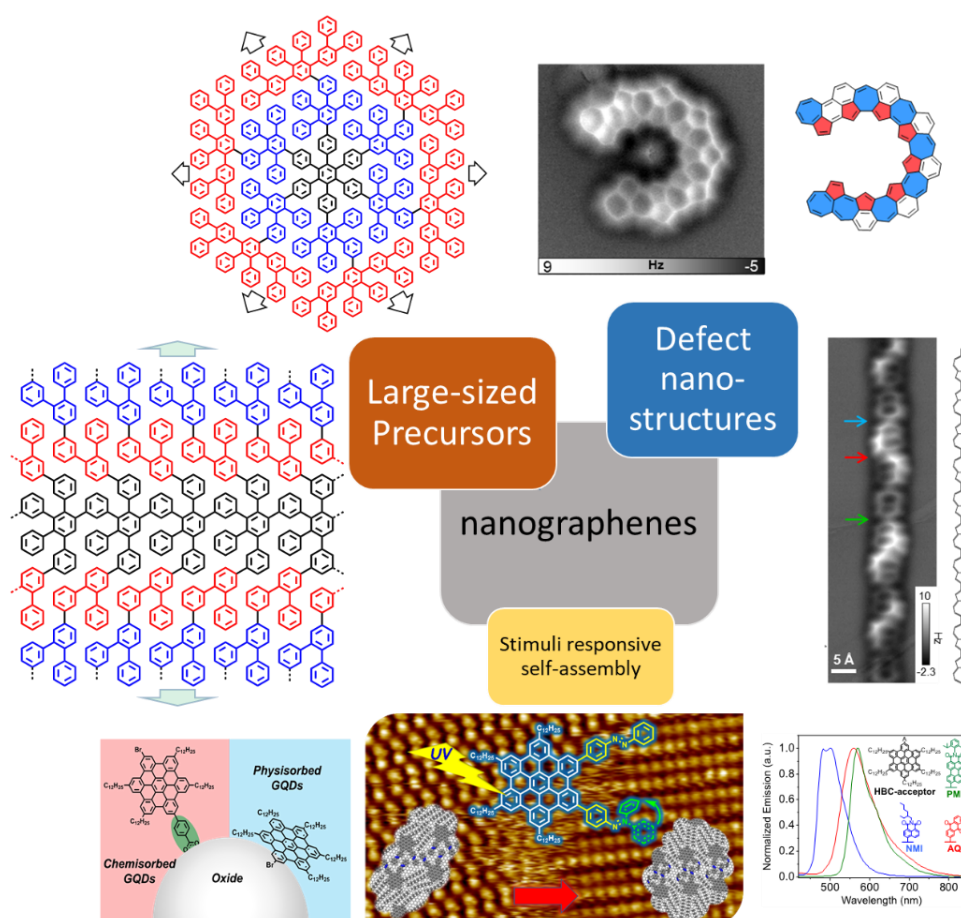
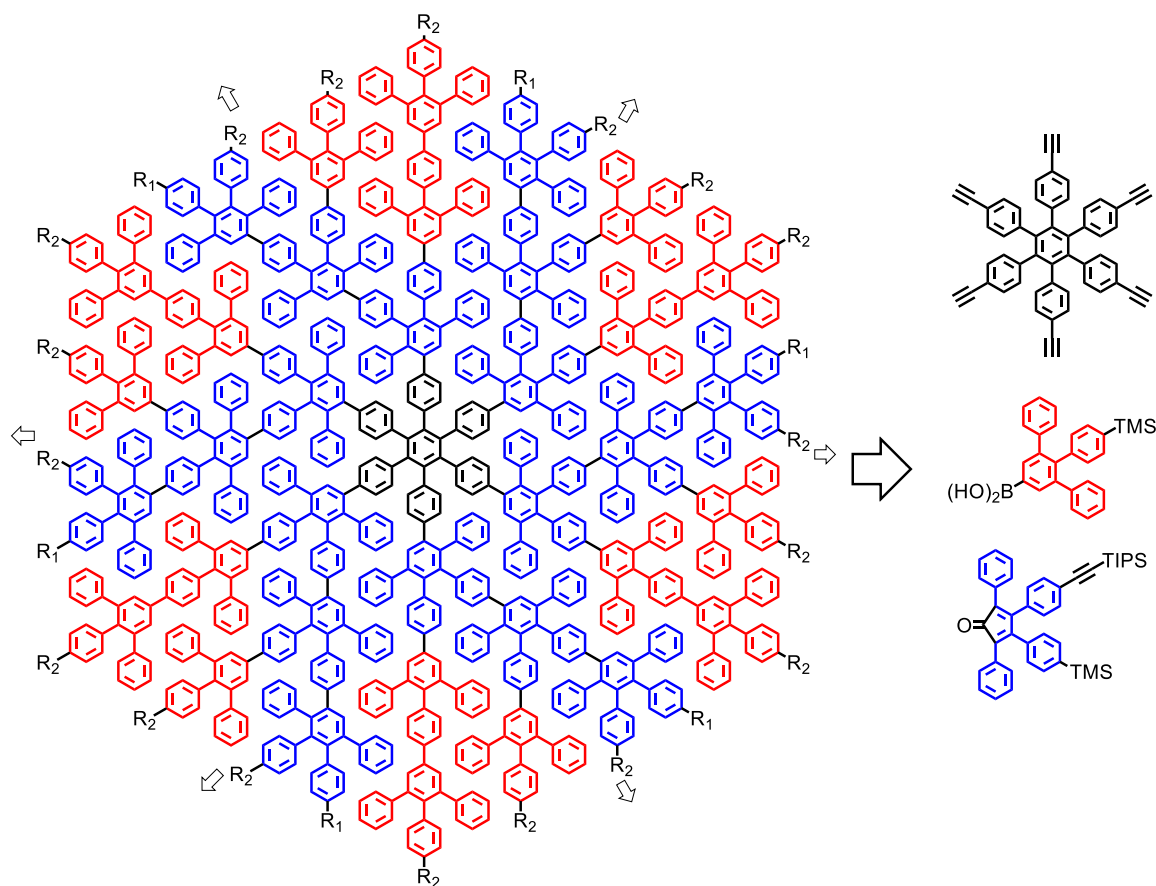


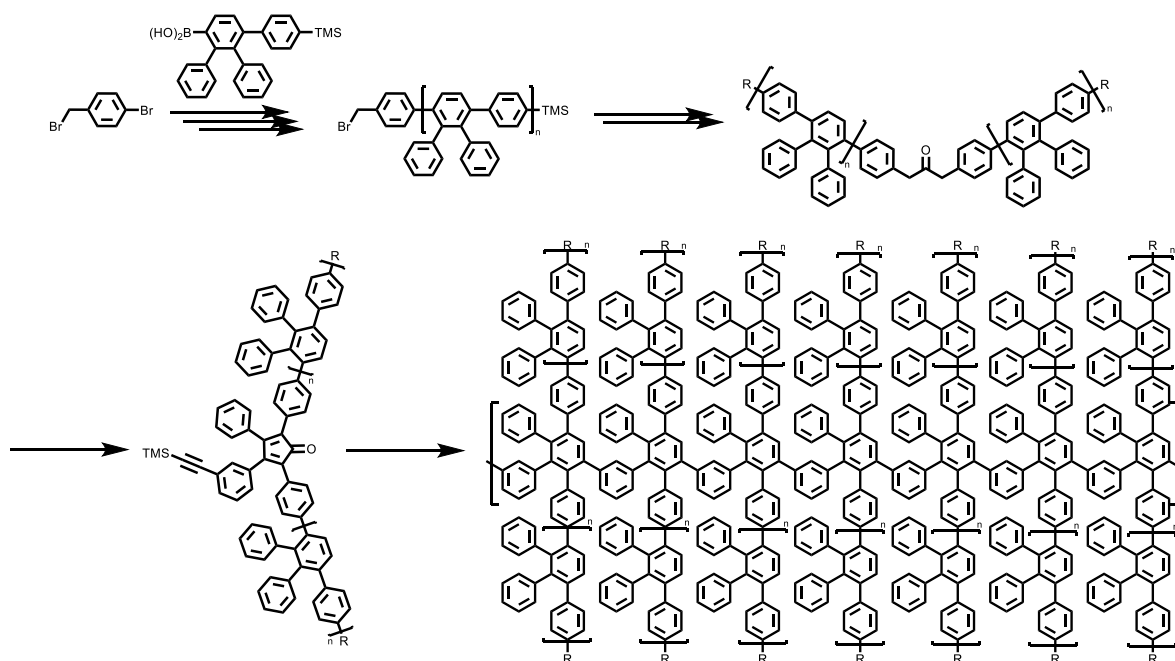
Figure 1. Schematic summary of achievements in this thesis.

9.1 Synthesis of large-sized Polyphenylenes

In *Chapter 2*, we constructed large-sized dendritic PP utilizing divergent synthetic strategies. Such strategies relied on first synthesizing skeletons with multiple ethynyl or ethynylene functional groups, followed by their D-A reactions with CP to introduce enormous benzene rings. Dendritic PPs was achieved containing up to 546 carbon atoms. In parallel, in *Chapter 3* we developed a stepwise D-A reaction protocol based on two different types of cyclopenta-2,4-dien-1-one derivatives. In principle, applying this protocol, linear PPs with tailored width can be achieved. PPs synthesized in *Chapter 2* and *Chapter 3* were characterized by NMR, IR spectroscopy as well as MALDI MS and GPC, confirming the power of employing D-A reaction between CP and ethynyl/ethynylene functional group for large-sized PPs synthesis.¹ Despite the successfulness, the complete cyclodehydrogenations of large-sized PPs in solution encountered enormous difficulties. Cyclodehydrogenations of large-sized dendritic PPs stopped at partially planarized intermediates. Similarly, cyclodehydrogenated product of wide linear PPs resulted in graphitic materials with large band gap. This indicated that we would be standing at the limited-size that current in-solution synthesis could achieve. Nevertheless, with the help of electrospray deposition, we were able to visualize dendritic PPs on surface and monitor their thermal reaction products. Further investigation such as low temperature nc-AFM shall be applied for unraveling the detail of the resulted nanostructures.² In addition, modifying the syntheses could provide other precursors that would perform better in cyclodehydrogenation reactions. Notably, dendritic PPs can be more easily purified in a “polymeric reaction” than those for linear PPs, which have wide molecular weight distribution. Accordingly, as shown in Scheme 1, using a stepwise synthetic strategy similar as what we used in *Chapter 4*, dendritic PP with various size can derive from a HPB core and two other building blocks, employing an additional Suzuki reaction step. Notably, these dendritic PPs do not possess HPB sub-structures. Consequently, cease of reaction at some partial planarized structures containing small-sized NGs would be avoided. In parallel, for the extension of linear PPs, it would be wiser now coming back to monomer extension approach, for an ease of purification. It has been shown that cyclodehydrogenation of poly[*p*-phenylene-*alt*-(2,3-diphenyl-*p*-phenylene)] leads to 6AGNR with high quality.³ Accordingly, a plausible two-building-blocks-synthesis shown in Scheme 2 can produce a series of CP monomer that is suitable for polymerization into linear PP. Such PPs shall serve as attractive precursors for lateral extended high quality GNRs.



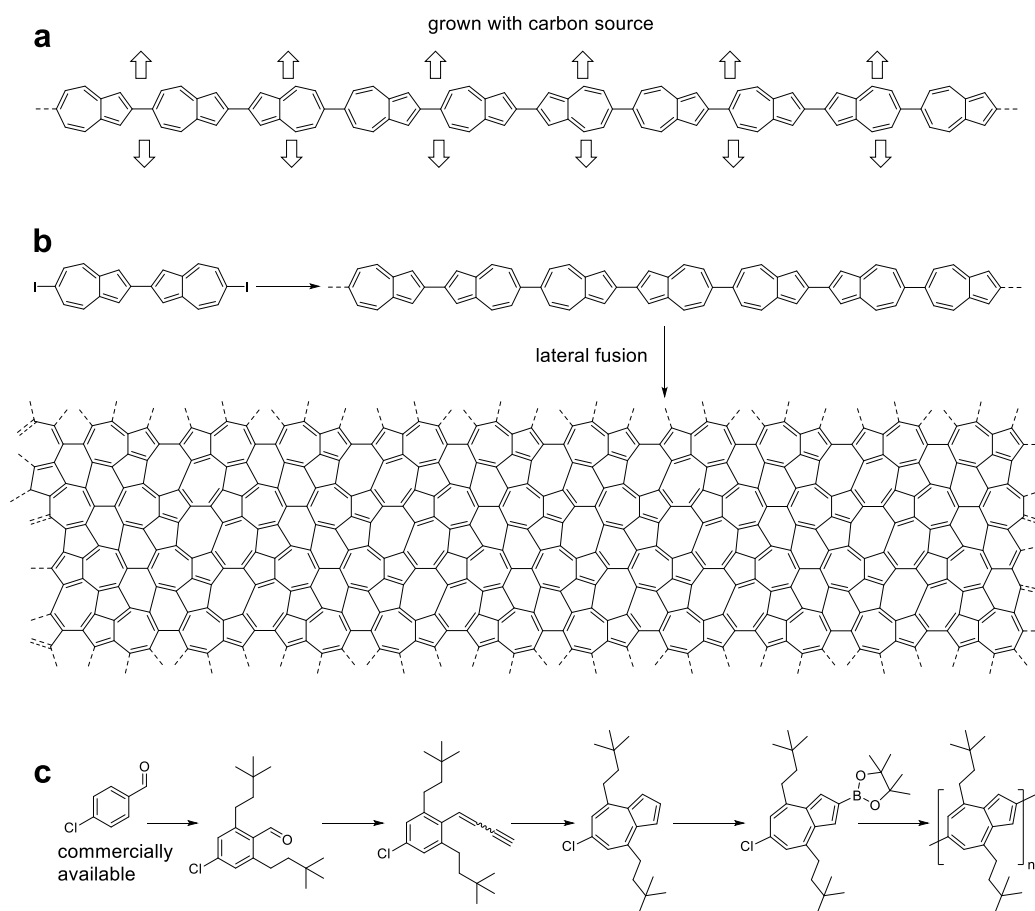
Scheme 1. A "stepwise" synthesis of extended dendritic PPs.



Scheme 2. An approach for lateral extended CP monomer by stepwise synthesis of oligo[p-phenylene-alt-(2,3-diphenyl-p-phenylene)].

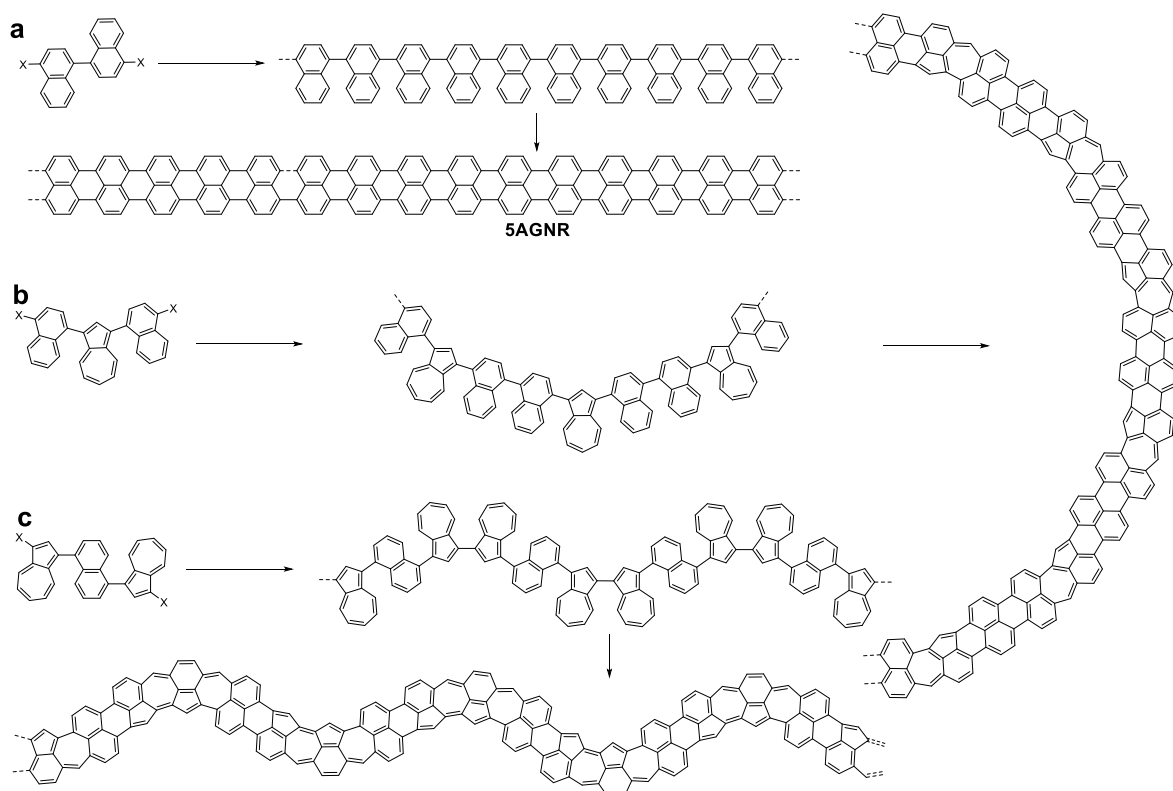
9.2 Synthesis of sp^2 -carbon-nanostructures with multiple heptagon-pentagon-pairs

In *Chapter 4* we have synthesized poly(2,6-azulenylene) on Au(111) surface. Although a dipole-moment-guided polymerization did not occur, and 2,6-azulenylene randomly linked on-surface, the lower-lying-energy of the CB and VB bands of the poly(2,6-azulenylene) marked it as a unique sp^2 -carbon materials, in comparison with GNRs synthesized on-surface. Despite to serve as a possible GB structure in graphene 2,6-azulenylene shall align in a head-to-tail manner,⁴ it would be still interesting to grow graphene flakes starting from the poly(2,6-azulenylene) on-surface to see whether tilt angle between resulted graphene grains could be controlled (Scheme 3a). In addition, using azulene dimer with higher symmetry can avoid the uncontrolled connection during on-surface polymerization, and result in a more ordered polymer that would serve as candidate for not only constructing GB in graphene but also lateral fusion into graphene allotropes such as Haeckelites (Scheme 3b).⁵ Besides, solution-synthesis could provide orderly linked poly(2,6-azulenylene) by differentiating functional groups on 2,6-positions, such as applying Suzuki polymerization (Scheme 3c). Orderly linked poly(2,6-azulenylene) is interesting as a rigid nanorod with aligned dipole moments.⁶



Scheme 3. Possible further works based on on-surface synthesis of poly(2,6-azulenylene).

In *Chapter 5*, we have succeeded on applying cyclodehydrogenation of poly(1,3-azulenylylene) on-surface, which was accompanied by a “methylene walk” rearrangement of azulene skeleton that led to a unique nanostructure of fused multiple heptagon-pentagon-pairs. Such nanostructure is highly related to those experimentally observed at graphene GB. Importantly, so far similar nanostructure cannot be constructed using other synthetic protocols. Future works can be focused on applying this azulene on-surface reaction for the synthesis of ribbon-like structure, especially for analogs of 5AGNRs, with high content of heptagons and pentagons. Notably, on-surface synthesis of 5AGNR is still challenging acquiring long nanoribbons due to a lack of proper monomeric precursor that could polymerize into long polymer.⁷ Inspired by the fact that we can achieve poly(1,3-azulenylylene) on-surface with high DP, 4,4'-dihalo-1,1'-binaphthalenyl, an isomer of 3,3'-dihalo-1,1'-biazulenyl used in our present work, can be a good candidate to polymerize on-surface into long poly(1,4-naphthalenylylene) (Scheme 4a). If the cyclodehydrogenation of poly(1,4-naphthalene) into 5AGNR worked well, several different monomers of combinations of 1,3-azulenylylene and 1,4-naphthalenylylene could fertilize synthesis of novel 5AGNR analogues (Scheme 4b,c).

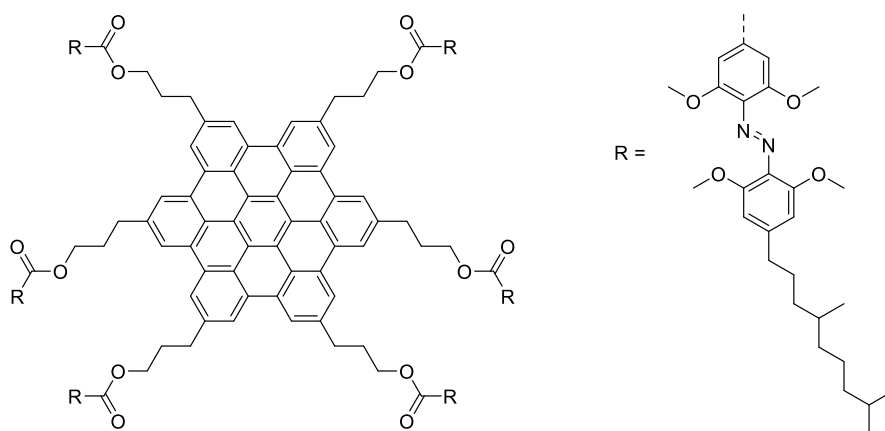


Scheme 3. Possible further works based on on-surface cyclodehydrogenation of 1,3-azulenylylene.

9.3 Stimuli responsive self-assembly of nanographenes

In *Chapter 6*, monitored by STM, we have demonstrated photomodulation of 2D self-assembly patterns of two azobenzene-HBC-azobenzene triads at liquid/HOPG interface. This is a huge step forward from our earlier work of a HBC-azobenzene dyad that did not show such stimuli-responsive behavior.⁸ Besides, in *Chapter 7*, we have seen that both the electronic properties as well as 3D self-assembly behavior of HBC can be fine-tuned by conjugation with electron-withdrawing π -systems (NMI, PMI, and anthraquinone). This work piloted our recent work on functionalization of GNR with electron withdrawing groups.⁹ Furthermore, in *Chapter 8*, employing VB XPS, we demonstrated that HBCs can physisorb or chemisorb on mesoporous TiO_2 and SnO_2 , where the chemisorption was enabled by a carboxyl functional group. Applying OTP, the much faster photoinduced ET from HBC to metal oxide was revealed for chemisorption over physisorption.

The achievements in *Chapter 6* is one of the rare demonstration of photoswitching of NGs functionalized with photoswitches. However, the UV-Vis absorption of azobenzene is overshadowed by that of HBC. Thus, employing azobenzene derivatives that can be switched by longer wavelength irradiation, such as 2,2',6,6'-tetramethoxyazobenzene, would be necessary for future works.¹⁰ Furthermore, it can be helpful for photophysical decouple of HBC with azobenzene to avoid through bond energy transfer or interruption of the two π -systems. Also, employing branched or multiple alkyl side chains could lower the DLC phase transition temperature.¹¹ With a careful screening of different substitutions, a HBC-azobenzene material that is photoswitchable between crystalline and DLC phase at a room temperature could be realized (Scheme 4).



Scheme 4. Improved design of a HBC functionalized with multiple azobenzenes.

Organic synthesis and graphene science are seemingly unrelated fields. However, establishing on nanoscience, the two fields can benefit on each other and even create new research directions. Especially, organic synthesis provide model compounds for understanding defects in graphene. Currently, synthesis of fully embedded defect structure in sub-nano graphene lattice is still highly underdeveloped. In particular, circumazulene, circumpentaheptafulvalene, and related structures, although not reported yet, possess nanoenvironment that is required for a first approximation of force field surrounding dislocation defects in graphene.¹² Their synthesis shall offer a fundamental understanding of line defects and GB in graphene. It is expected that organic synthesis in a spirit of graphene science will continually rise and shine in the near future.

9.4 References

- (1) Hou, I. C. Y.; Hu, Y.; Narita, A.; Müllen, K. Diels-Alder Polymerization: A Versatile Synthetic Method toward Functional Polyphenylenes, Ladder Polymers and Graphene Nanoribbons. *Polym. J.* **2018**, *50* (1), 3–20.
- (2) Hinaut, A.; Meier, T.; Pawlak, R.; Feund, S.; Jöhr, R.; Kawai, S.; Glatzel, T.; Decurtins, S.; Müllen, K.; Narita, A.; et al. Electrospray Deposition of Structurally Complex Molecules Revealed by Atomic Force Microscopy. *Nanoscale* **2018**, *10* (3), 1337–1344.
- (3) Li, G.; Yoon, K.-Y.; Zhong, X.; Wang, J.; Zhang, R.; Guest, J. R.; Wen, J.; Zhu, X.-Y.; Dong, G. A Modular Synthetic Approach for Band-Gap Engineering of Armchair Graphene Nanoribbons. *Nat. Commun.* **2018**, *9* (1), 1687.
- (4) Yazyev, O. V.; Louie, S. G. Topological Defects in Graphene: Dislocations and Grain Boundaries. *Phys. Rev. B* **2010**, *81* (19), 195420.
- (5) Fan, Q.; Martin-Jimenez, D.; Ebeling, D.; Krug, C. K.; Brechmann, L.; Kohlmeyer, C.; Hilt, G.; Hieringer, W.; Schirmeisen, A.; Gottfried, J. M. Nanoribbons with Nonalternant Topology from Fusion of Polyazulene: Carbon Allotropes beyond Graphene. *J. Am. Chem. Soc.* **2019**, *141* (44), 17713–17720.
- (6) Steer, R. P. Photophysics of Molecules Containing Multiples of the Azulene Carbon Framework. *J. Photochem. Photobiol. C* **2019**, *40*, 68–80.
- (7) Zhang, H.; Lin, H.; Sun, K.; Chen, L.; Zagranyski, Y.; Aghdassi, N.; Duhm, S.; Li, Q.; Zhong, D.; Li, Y.; et al. On-Surface Synthesis of Rylene-Type Graphene Nanoribbons. *J. Am. Chem. Soc.* **2015**, *137* (12), 4022–4025.
- (8) Ai, M.; Groeper, S.; Zhuang, W.; Dou, X.; Feng, X.; Müllen, K.; Rabe, J. P. Optical Switching Studies of an Azobenzene Rigidly Linked to a Hexa-Peri-Hexabenzocoronene Derivative in Solution and at a Solid-Liquid Interface. *Appl. Phys. A* **2008**, *93* (2), 277–283.
- (9) Keerthi, A.; Radha, B.; Rizzo, D.; Lu, H.; Diez Cabanes, V.; Hou, I. C. Y.; Beljonne, D.; Cornil, J.; Casiraghi, C.; Baumgarten, M.; et al. Edge Functionalization of Structurally Defined Graphene Nanoribbons for Modulating the Self-Assembled Structures. *J. Am. Chem. Soc.* **2017**, *139* (46), 16454–16457.
- (10) Bléger, D.; Hecht, S. Visible-Light-Activated Molecular Switches. *Angew. Chem. Int. Ed.* **2015**, *54* (39), 11338–11349.
- (11) Pisula, W.; Feng, X.; Müllen, K. Tuning the Columnar Organization of Discotic Polycyclic Aromatic Hydrocarbons. *Adv. Mater.* **2010**, *22* (33), 3634–3649.
- (12) Yazyev, O. V.; Chen, Y. P. Polycrystalline Graphene and Other Two-Dimensional Materials. *Nat. Nanotechnol.* **2014**, *9* (10), 755–767.

Acknowledgement

Time flies. The almost-five-year PhD of mine looks so long. But in the end, it feels like everything stops suddenly. Frankly speaking, I was not so well prepared when I first came to Mainz. Looking back, I would say I had dived into my PhD without planning. It is followed up with heavy work-loading and little time left for thinking. Thinking, along the time of my thesis writing, is what I realize so important and would like to do better if I could start all-over again. My immaturity made other people's life more difficult. Yet I still could be standing here at the last stage of my PhD. That is why I must acknowledge so many people who work together with me during my PhD study. Without them, I think I would have spent much more time.

Most importantly, I would like express my gratitude to my supervisor Prof. [REDACTED]. Although I could not occupy much of his precious time (and I should not), every chance we communicate through quarterly reports or face-to-face inspire and challenge me for a higher place. His high working efficiency and enormous knowledge is what I would like to learn from. He also demonstrates how to be an organic chemist who is not just doing synthesis for others, but has his own insight into material development. Working with Prof. [REDACTED] has really sharpened my mind and remolded me.

As importantly, I shall thank to my project leader Prof. [REDACTED]. Prof. [REDACTED] is always the first person to correct my unrealistic and shabby manuscripts. We have discussed among many research subjects and it has been always inspiring. Prof. [REDACTED] also trained me to work in a precise and scientific way for the good of my carrier. Massive time he spent and friendship he offered is beyond description.

I would also like to thank Prof. [REDACTED] who recruited me at the very beginning. Because of Prof. [REDACTED], I can have the chance involving in "iSwitch" project, which gave me so many advantages considering salary, training opportunities, collaborations etc. I do not know whether I deserve them or not but could only work even harder. Also, Prof. [REDACTED] was the landlord of my apartment. This helps me so much in a city where foreigner hardly get a two-person apartment with a decent rent.

Furthermore, I am thankful for the company and assistance provided by AK [REDACTED] people, with you guys we can always have some fun along the daily hardworking. Especially,

The people who shared lab space with me. I am lucky for staying in lots of labs during my PhD. Firstly, special thanks to Prof. [REDACTED], Dr. [REDACTED], and Dr. [REDACTED] for

helping me and showing me around at the beginning when I first came to Mainz; as well as Dr. [REDACTED], Prof. [REDACTED], and Dr. [REDACTED] who are good neighbours in my first lab. Secondly, thanks to Dr. [REDACTED] and Dr. [REDACTED] who helped us moving in their lab, which is our second one. Thirdly, thanks Dr. [REDACTED], Dr. [REDACTED] and [REDACTED] who joined us in our third lab; Dr. [REDACTED], [REDACTED], Dr. [REDACTED] and [REDACTED] in our fourth lab; and Dr. [REDACTED] and [REDACTED] in our fifth lab in the University. The abovementioned people established a nice working place in the five labs and together we made great times.

I would also like to address my gratefulness to people who share office with me. Prof. [REDACTED], Dr. [REDACTED], Dr. [REDACTED], [REDACTED], Dr. [REDACTED], Dr. [REDACTED], and Dr. [REDACTED], in the office MPIP; and Dr. [REDACTED] in the office University. We had so many great times. Also, [REDACTED], who passed away in an airplane crash just one month before finishing of this thesis. I only hope you could have seen me reaching the final stage.

In addition, I need to address my gratefulness to AK [REDACTED] in JGU. Especially Prof. [REDACTED], [REDACTED], [REDACTED], [REDACTED], Prof. [REDACTED], and [REDACTED], who embrace me with a nice and warm place to stay and fun things to do for my last PhD year.

Also, I am thankful for involving in Marie Skłodowska-Curie ITN “iSwitch” that gave me a chance to meet and learn with many talented young researchers. Thanks the coordinator Prof. [REDACTED] and project manager Dr. [REDACTED] for their dedicated works. Especially, thanks Prof. [REDACTED] and Dr. [REDACTED] for providing me a nice, comfortable and fruitful secondment at Strasbourg. Thanks Prof. [REDACTED], Dr. [REDACTED], and Dr. [REDACTED] for their hospitality during my secondment in Berlin. Also thanks to all the collaborators within iSwitch projects.

Also, thanks all the people from NMR, thermal analysis, Mass analysis, and polymer analysis departments, as well as cafeteria in MPIP. Thank you for making daily life easier. Thanks Dr. [REDACTED] for organizing every week football game. Thanks all the collaborators in and out MPIP for realizing our fruitful results. Also thanks to everyone I have encountered during this almost five years staying in Mainz.

In the end, I would like to thank my lovely wife [REDACTED], the mi-gi-ga. You delight my life with so many joys (also pains). We are so different but that is why we are interested by each other. I wish you a happy-everyday life, and I will work the very best for that.